Quantifying cooling and exhumation patterns in a bivergent metamorphic core complex: the central Menderes Massif, western Turkey

Von der Naturwissenschaftlichen Fakultät der

Gottfried Wilhelm Leibniz Universität Hannover

zur Erlangung des Grades

Doktor der Naturwissenschaften (Dr. rer. nat.)

genehmigte Dissertation

von

Nils-Peter Nilius, M. Sc.

[2019]

Referent: [Jun. -Prof. Dr. rer. nat. habil. Christoph Glotzbach]

Korreferent: [Prof. Dr. rer. nat. Francois Holtz]

Tag der Promotion: [06.09.2019]

Acknowledgements

Foremost, I would like to thank my supervisor Dr. Christoph Glotzbach for giving me the opportunity to pursue my dissertation within this project. I deeply appreciate that I could freely follow and implement my scientific ideas on one side and always count on your help and enjoyable discussions on the other side. I am also very grateful to Prof. Dr. François Holtz for his kindness to co-examine this thesis and Prof. Dr. Ulrich Heimhofer for his support as a chairman of the examination committee.

This thesis benefited greatly by the assistance of Prof. Dr. Andrea Hampel, whose comments on manuscripts and her guidance and encouragement through the last years had a great deal on the completion of this thesis. The same accounts for the inspiring discussions with Prof. Dr. Ralf Hetzel, who also introduced me to the geology of the central Menderes Massif. I have some fond memories about geological and non-geological discussions with Dr. Andreas Wölfler and I am grateful for his efforts to teach me the fission track technique. I also enjoyed being a guest in Dr. István Dunkl's thermochronology lab in Göttingen. Only by his great experience, I got at least some apatite (U-Th)/He ages from my rebellious "potting soil'' samples. Although based in Münster, I enjoyed the company of my PhD fellow Caroline Heineke in the last years, especially during the fieldwork seasons. A great deal of the successful fieldwork seasons owes to the help and support by Dr. Cüneyt Akal, who was within reach for Caro and me almost 24/7 and was an outstanding host for us. Furthermore, I would like to thank Katharina[2], Fanfan, Maurits, Conny, George and Gang at the Institute of Geology in Hannover.

Coming home after a day full of microscopy, modelling and writing, the time with the non-geologists Laila, Lars, Jule, Agathe, Matze, Leonie, Timo, Janna and Carina was always a mental holyday from numbers, minerals and tectonic models. I can't count the number of dinners I owe you. I am also very grateful to my parents and their support and trust during all the years. Most of the thanks are due to Luise for accompanying me with her patience and humour also in the more stressful phases during the last years but also for hours of proofreading and critical suggestions.

Zusammenfassung

Die Entwicklung von metamorphen Kernkomplexen ist eng verbunden mit dem Auftreten von ausgeprägter kontinentaler Extension. Begünstigende tektonische Rahmenbedingungen findet man beispielsweise in Orogenen, deren überdickte Lithosphäre durch nachlassende Konvergenzraten gravitativen Ausgleichsbewegungen ausgesetzt ist, oder im Hangenden einer zurückrollenden Subduktionszone. Ein markantes Merkmal von metamorphen Kernkomplexen ist, dass der größte Teil der Extension entlang einer flacheinfallenden Abschiebung (Detachment Fault) aufgenommen wird. Detachments sind in der Lage, durch die mit der Extension einhergehenden sehr großen Versatzbeträge, in Ihrem Liegendblock metamorph überprägte Gesteine aus tiefen Bereichen der kontinentalen Kruste an die Erdoberfläche zu befördern, während sich im Hangendblock niedrigmetamorphe Gesteine oder erodierte Sedimente des exhumierten Liegendblocks befinden. Da in klassischen Modellen eines metamorphen Kernkomplexes die Extension im Wesentlichen auf die Bewegung entlang eines einzelnen Detachments konzentriert ist, weisen die meisten metamorphen Kernkomplexe eine starke Asymmetrie im Exhumationsmuster ihres Liegenblocks auf.

Seit Mitte der 1990er Jahre wurden jedoch im zentralen Menderes Massiv in der Westtürkei und in der westlichen Ägäis auch Bereiche stark gedehnter Kruste identifiziert, bei denen die Dehnung der Lithosphäre zu bivergenter Extension entlang gegensätzlich einfallender Detachments geführt hat. Dieser bivergente Extensionsmodus führt folglich zu einer symmetrischen Exhumation metamorpher Einheiten im Liegenden der beteiligten Detachments. Bis heute fehlt jedoch eine fundierte Datengrundlage, mit der die Entwicklung eines symmetrisch exhumierten Kernkomplexes räumlich und zeitlich eingegrenzt werden kann, sowie Informationen über die Raten und Beträge der Exhumation und Extension entlang der beteiligten Detachments.

Das Ziel dieser Arbeit ist, diese Datenlücke mit der Anwendung strukturgeologischer und thermochronologischer Methoden zu schließen. Das Untersuchungsgebiet ist das zentrale Menderes Massiv in der Westtürkei, welches aus zwei Ost-West verlaufenden Bergmassiven besteht. Im Norden des zentralen Menderes Massiv wurde das Bozdağ Massiv im Liegenden des nordwärts einfallenden Gediz Detachments exhumiert, während im Süden das Aydın Massiv im Liegenden des südwärts einfallenden Büyük Menderes Detachments exhumiert wurde. Vorwiegend auf Grundlage dieser symmetrischen Anordnung der Detachments, wurde eine zeitgleiche Aktivität sowie ähnliche Versatzbeträge entlang der Detachments angenommen. Jedoch ist nur im östlichen Teil des Bozdağ Massivs die extensionale Geschichte gut untersucht, wohingegen im Aydın Massiv sowie im westlichen Teil des Bozdağ Massivs weder eine solide thermo- und geochronologische Datenbasis noch strukturgeologische Felddaten zur extensionalen Entwicklung vorhanden sind. Die Daten dieser Arbeit ermöglichen es daher erstmals räumlich-zeitliche Variationen im Exhumations- und Extensionsmuster eines bivergenten metamorphen Kernkomplexes zu erfassen.

Thermochronologische Datierungsmethoden ermöglichen es die Temperatur- beziehungsweise die Abkühlgeschichte von Gesteinen zu bestimmen, wobei in dieser Studie vor allem die Apatit und Zirkon Spaltspur- und (U-Th)/He-Datierung angewendet wurden (AFT, ZFT und AHe, ZHe). Jedes dieser vier Systeme weist eine spezifische Schließungstemperatur auf, die es

ermöglicht die Abkühlgeschichte von Gesteinsproben über einen Temperaturbereich von ~240 °C bis ~60 °C nachzuvollziehen. Auf Basis der Abkühlgeschichte werden mit Hilfe einer thermokinematischen Modellierung die Exhumationsraten sowie mögliche zeitliche Änderungen der Exhumationsraten im Zuge der Entwicklung des zentralen Menderes Massiv bestimmt. In Kooperation mit Projektpartnern der Universität Münster wurden zudem mit der K-Ar Datierung von authigenen Illit in Störungsmehl die zeitliche Aktivität der Detachments näher bestimmt. Die räumliche Variabilität der Erosionsraten im zentralen Menderes Massiv wurde mit Hilfe von kosmogenen Nukliden untersucht.

Die Resultate dieser Studie bestätigen erstmals die zuvor angenommene bivergente Extension und symmetrische Exhumation des zentralen Menderes Massivs. Die bessere räumliche und zeitliche Auflösung der neuen Daten, erlaubt die Feststellung zeitlich-räumlicher Variationen sowie ausgeprägter Unterschiede in den Bewegungs- und Exhumationsraten der untersuchten Detachments. Im Unterschied zum Bozdağ Massiv, welches kontinuierlich seit dem mittleren Miozän entlang des Gediz Detachments exhumiert wird, zeigt sich im Aydın Massiv, dass das Büyük Menderes Detachment vorwiegend im mittleren Miozän aktiv war, wohingegen im späten Miozän und Pliozän die Extension vom hier erstmals beschriebenen Demirhan Detachment aufgenommen wurde. Dabei betragen die Exhumationsraten im mittleren Miozän im Liegenden des Büyük Menderes Detachments ca. 0.5 km/Ma, während der westliche Teil des Bozdağ Massiv mit ca. 0.6 km/Ma exhumiert wird. Im späten Miozän, zwischen 9 und 6 Ma, steigen die Exhumationsraten jedoch entlang des Gediz Detachments auf 1.0 bis 1.5 km/Ma an, während in diesem Zeitraum nur relativ wenig Aktivität am Büyük Menderes Detachment auftritt. Dies ändert sich jedoch mit dem Beginn der Aktivität des Demirhan Detachments, welches sich im Hangenden des östlichen Büyük Menderes Detachment befindet und eine Bewegungsrate entlang der Störung von ca. 2 km/Ma sowie eine Exhumationsrate von ca. 0.4 km/Ma zwischen 7 und 3 Ma aufweist. Zeitgleich verlagert sich die Hauptaktivität des Gediz Detachment weiter nach Osten, wo der östliche Teil des Bozdağ Massiv mit ca. 1.5 km/Ma exhumiert wird. Die Bewegung entlang des Gediz Detachment erreichte in dieser Zeit eine Rate von ca. 5 km/Ma.

Die Ergebnisse verdeutlichen, dass die Exhumationsgeschichte des zentralen Menderes Massiv in vier Dimensionen beschrieben werden muss, da die bivergente Extension entlang der Detachments sowohl räumlich als auch zeitlich variabel war. So ist nicht nur eine laterale Verschiebung des Exhumationsfokus im Aydın und Bozdağ Massiv mit der Zeit in Richtung Osten zu beobachten, sondern auch unterschiedlich starke Exhumationsraten und Extensionsraten zwischen Büyük Menderes und Gediz Detachment. Im Vergleich zeigt sich, dass sowohl das Büyük Menderes und Demirhan Detachment, als auch das Gediz Detachment zur symmetrischen Exhumation beigetragen haben. Bilanziert betrachtet waren jedoch die Exhumationsraten und Extensionstiefe am Gediz Detachment doppelt so hoch wie entlang der Büyük Menderes und Demirhan Detachments.

Abstract

The development of metamorphic core complexes is closely associated with the occurrence of pronounced continental extension. Tectonic conditions promoting core complex evolution can be found, for example, in orogens whose thickened lithosphere is exposed to gravitational instability due to decreasing convergence rates, or in the overriding plate during the rolling-back of a subduction zone. A striking feature of metamorphic core complexes is that the major part of the extension is accommodated along a shallow dipping detachment fault. The resulting large displacement along the detachment allows to exhume metamorphic rocks from deep levels of the continental crust to the earth's surface, while low-metamorphic rocks or eroded sediments of the exhumed footwall are located in the hanging wall. In classical models of metamorphic core complexes, the extension is largely focused on the movement along a single the detachment fault, causing a strongly asymmetric exhumation pattern in the core. However, since the mid-1990s areas of highly extended crust have been identified in the central Menderes Massif (western Turkey) and more recently in the western Aegean, where lithospheric extension was accommodated not along a single detachment fault, but by bivergent extension along oppositely dipping detachments. This bivergent extension mode would result in a more symmetrical exhumation of metamorphic units. To date, however, a comprehensive data basis with which the development of a symmetrically exhumed core complex can be spatially and temporally constrained is missing. Furthermore, information on the rates and amounts of exhumation and extension along the involved detachments are missing. Therefore, the study area of this work is the central Menderes Massif in western Turkey, which consists of two east-west striking mountain Massifs. In the north of the central Menderes Massif, the Bozdağ Massif was exhumed in the footwall of the northward-dipping Gediz Detachment, while in the south the Aydın Massif was exhumed along the southward-dipping Büyük Menderes detachment. Mainly on the basis of this symmetrical geometry of the detachments, a simultaneous activity and similar offset amounts along the detachments were assumed. However, only in the eastern part of the Bozdağ Massif the extensional history is well constrained, whereas in the Aydın Massif and in the western part of the Bozdağ Massif few thermo- and geochronological as well as structural geological field data for extensional development exist. The intention of this work is therefore to gain better insights into formation processes of bivergent core complexes by quantifying the rates and the timing associated with the extensional evolution of the central Mender Massif by applying mainly thermochronological methods.

Thermochronological dating methods make it possible to determine the temperature and cooling history of rocks, whereby in this study the apatite and zircon fission track and (U-Th)/He-dating (AFT, ZFT and AHe, ZHe) were applied. Each of these four systems has a specific closure temperature, which makes it possible to trace the cooling history of rock samples over a temperature range from ~240 °C to ~60 °C. On the basis of the cooling history, the exhumation rates and possible temporal changes of the exhumation rates during the development of the central Mender Massif are determined by means of thermokinematic modelling. In cooperation with project partners of the University of Münster, the K-Ar dating of authigenic illite in fault gouges was used to further limit the

temporal activity of the detachments and to investigate the spatial variability of the erosion rates in the central Menderes Massif with the aid of cosmogenic nuclides.

The results of this study confirm the previously assumed bivergent extension and symmetrical exhumation of the central Menderes Massif. Due to the better spatial and temporal resolution of the new data, spatio-temporal variations as well as pronounced differences in the motion and exhumation rates of the detachments between Aydin Massif and Bozdağ Massif could be detected. In contrast to the Bozdağ Massif, which has been continuously exhumed along the Gediz detachment since the Middle Miocene, exhumation rates of the Aydın Massif reveal two main exhumation phases. During the first phase, the Aydın range was predominantly exhumed along the Büyük Menderes detachment, whereas the second phase is associated with exhumation in the footwall of the newly discovered Demirhan detachment since the latest Miocene and Pliocene. In the late Miocene, between 9 and 6 Ma, the exhumation rates along the Gediz detachment increase to 1.0 to 1.5 km/Ma, while during this period relatively little activity occurs at the Büyük Menderes detachment. However, this changes with the beginning of the activity of the Demirhan detachment, which is located in the hanging wall of the eastern Büyük Menderes detachment and comprises a slip rate of ~2 km/Ma and an exhumation rate of ~0.4 km/Ma between 7 and 3 Ma. At the same time, the main activity of Gediz detachment shifts further to the east, where the eastern part of the Bozdağ Massif is exhumed with ~1.5 km/Ma along the Gediz detachment with a slip rate of ~5 km/Ma.

The results show that the exhumation history of the central Menders Massif has to be described in four dimensions, since the bivergent extension along the detachments is spatially and temporally variable. Thus, not only a lateral shift of the exhumation focus in the Aydın and Bozdağ Massif can be observed with time towards the east, also different exhumation and extension rates occur between Büyük Menderes and Gediz detachment. Comparing the exhumation and slip rates between the detachments show that the Büyük Menderes and Demirhan detachment as well as Gediz detachment contributed to the symmetrical exhumation of the central Menderes Massif, on balance however, the exhumation rates and extension depth at Gediz detachment were twice as high as along Büyük Menderes and Demirhan detachments.

Table of contents

List of abbreviation

^{4}He	Helium isotope
^{10}Be	Beryllium isotope
^{147}Sm	Samarium isotope
^{232}Th	Thorium isotope
^{235}U, ^{238}U	Uranium isotopes
^{40}Ar/^{39}Ar	Argon isotopes
^{40}K	Potassium isotope
AFT	apatite fission track
AHe	apatite (U-Th)/He
D_{par}	length of fission track etch figure
Ft correction	He ejection correction factor
PAZ	partial annealing zone
PRZ	partial retention zone expelled from the crystal
Tc	closure temperature
tT-model	time-temperature model
ZFT	zircon fission track

Definitions

In this thesis, I follow the suggested terminology and their definitions used to describe processes related to the exhumation of rocks by Ring et al. (1999)

Erosion	the removal of material at a spatial point on the Earth's surface by mechanical and chemical processes.
Denudation	removal of rock at by tectonic and or surface processes at a specific point at or under the Earth's surface
Exhumation	Motion of rock relative (towards) to the Earth's surface – the unroofing history of a rock

1. Introduction and Background

1.1   Introduction

Lithospheric extension occurs in many geodynamic environments and dominates the tectonic processes of continental break-up, syn- and post-orogenic extension, active and passive intracontinental rifting and extension in the overriding plate of a retreating subduction zone. Although the causes for post-orogenic extension and back-arc extension due to slab-rollback are different, both scenarios favour the formation of low-angle normal faults to accommodate the extensional strain. By the large normal-sense offsets, low-angle normal faults (or detachment faults) are capable to exhume rocks from middle or lower crustal levels and separate the metamorphic units in the footwall from lower or unmetamorphosed rocks in the hanging wall. Therefore, the exposed deeper crustal units in the footwall of the detachment form a tectonic window, which is called a metamorphic core complex. An interesting feature of highly extended continental lithosphere is that the extension in the brittle crust is not symmetrically accommodated by multiple faults and comparable offsets, but by a strong asymmetry, where a single detachment accommodates the bulk amount of extensional deformation (Figure 1). This asymmetric pattern of exhumation implies that large scale lithospheric extension is dominated by a simple shear mode of extension rather than by pure shear as observed in most graben systems related to rift tectonics (e.g. European Cenozoic Rift System or East African Rift).
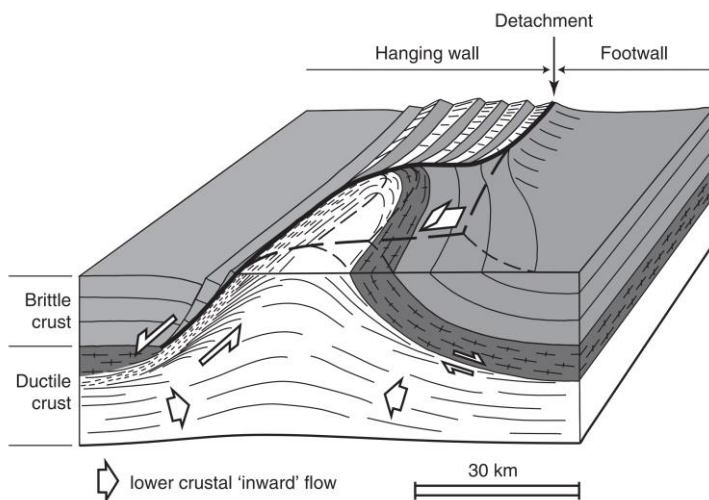
Figure 1: Conceptual sketch illustrating the general features and lithospheric processes of a metamorphic core complex (from Tirel et al. 2009 based on Brun & van der Driessche 1994).

These observations rely mostly on the intensively studied detachment faults of the highly extended lithosphere of the Basin and Range Province (western U.S.) (Davis & Coney 1979; Lister et al. 1984) and the Aegean extensional province in the 1980s and 1990s (e.g. Lister et al. 1984), until the bivergent extension with a more symmetric exhumation pattern in the central Menderes Massif was proposed by Hetzel et al. (1995a). In contrast to most core complexes, which either comprise a single detachment fault or multiple detachment faults but with the same sense of faulting, the central Menderes Massif comprises a symmetric architecture with two detachments of opposite dip and sense of shear (Gessner et al. 2001; Ring et al. 2003). Within the central Menderes Massif late Cenozoic extension was accommodated by the north-dipping Gediz detachment and the south-dipping Büyük Menderes detachment and led to the exhumation of the Bozdağ and Aydın mountain ranges, respectively. Further examples of bivergent extension resulting in a symmetric exhumation of

a core complex are proposed for a short-lived bivergent phase of extension in the Rhodope core complex during the Oligocene and for the western part of the Cycladic Extensional Province in the Aegean Sea (Figure 2) (Grasemann et al. 2012). However, in the Rhodopes, the bivergent extension only occurred during a short time period and most of the extension in the Miocene was accommodated by simple shear extension along a single detachment fault, whereas the interrelationship between the isolated exposures of detachment segments in the Cycladic Extensional Province is difficult to reconcile as large portions of the region are submerged below sea level. Consequently, few constraints on the evolution of symmetric core complexes exist, for which this thesis focuses on the extensional development of the central Menderes Massif. Prior to this thesis, most studies on the extensional development of the central Menderes Massif only focused on the eastern part of the Gediz detachment, where the spectacularly exposed footwall hosts a syntectonic Salihli granodiorite – well suited for dating purposes. Hence, the proposed synchronous extension along both detachments relies mainly on thermo- and geochronological data from the Salihli granodiorite and only on few AFT ages from the Büyük Menderes detachment.
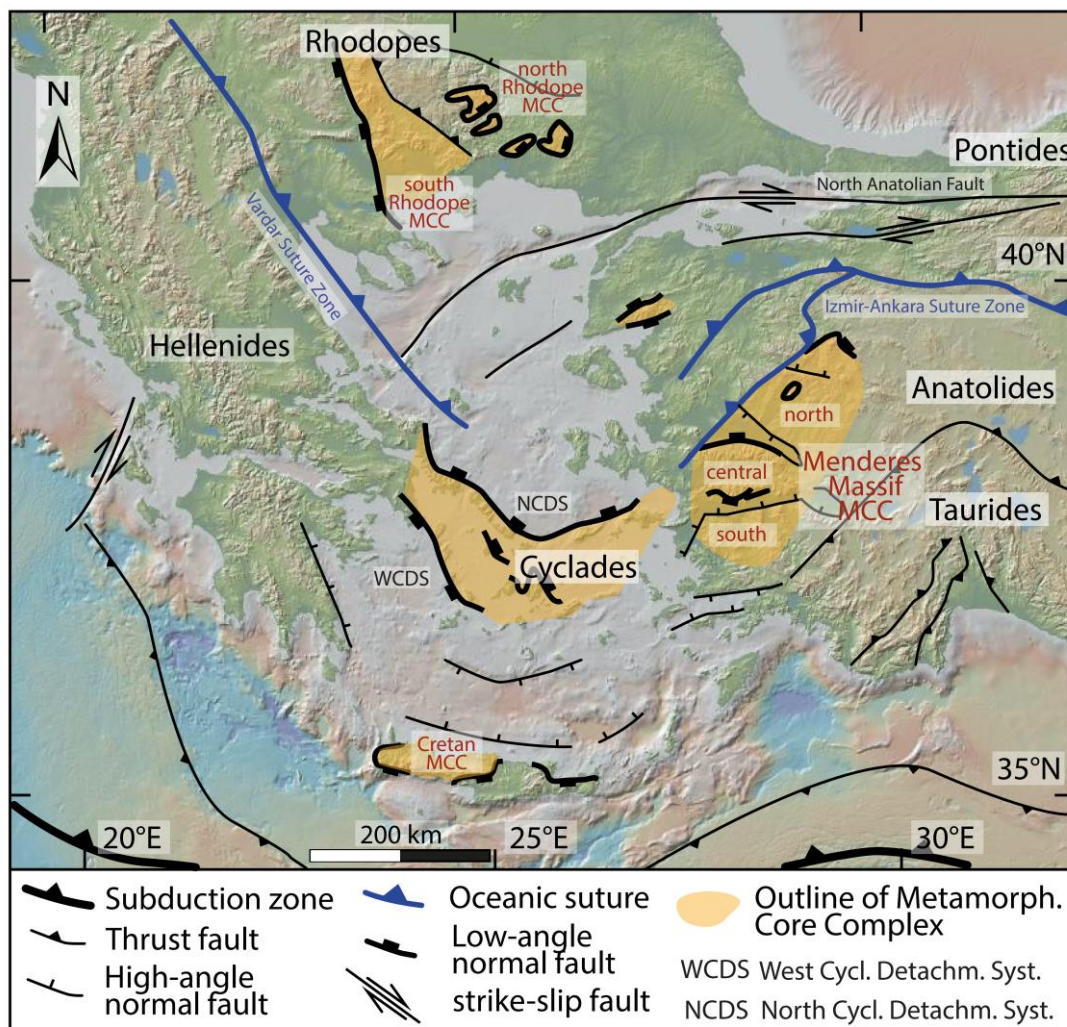
Figure 2: Overview map of the Aegean and western Turkey including the main tectonic features, based on Jolivet et al. (2015).

A fundamental part in the scope of this thesis is to detect spatial and temporal changes during the evolution of the central Menderes Massif by constraining the time-temperature history with apatite and zircon (U-Th/He) and fission track thermochronology. In a second step, this information is used to calculate the slip rates of the detachment faults and to infer the exhumation rates by thermokinematik modelling of footwall and hanging wall units of the central Menderes Massif. Within this thesis the following questions will be addressed:

1. **What are the times and rates of footwall cooling related to the late Cenozoic extension in the Aydın range?**

2. **Given the proposed symmetric exhumation model – why does the Aydın range show different structural and geomorphological characteristics compared to the Bozdağ range?**

3. **Did the proposed bivergent extension along the detachments occur synchronously or asynchronously?**

4. **What are the rates of exhumation and slip along the detachment faults?**

Figure 3: Geological map of the central Menderes Massif (western Turkey). Inset in the lower left corner illustrates the position of the central Menderes Massif within the Aegean region.

5. **What are the erosion rates in the central Menderes Massif and how high is the contribution of erosional denudation to rock exhumation (as the total exhumation is the product of tectonic and erosional denudation) in an actively extending region?**

Accordingly, the subchapters of **Chapter 1** include a short description about the unique features of continental core complexes, gives an introduction to the alpine and post-alpine evolution of the Aegean and western Turkey and introduces the methodological principles of the zircon and apatite (U-Th)/He (ZHe and AHe) and fission track thermochronology (ZFT and AFT) as well as K-Ar fault gouge dating and erosion rates derived from cosmogenic ^{10}Be. **Chapter 2** presents the first comprehensive investigation of low-temperature thermochronology data exploring the cooling history in the southern central Menderes Massif (Aydın range) as well as catchment and ridge-crest erosion rates derived by cosmogenic ^{10}Be. The thermochronological data presented in Chapter 2 are complemented by additional apatite and zircon (U-Th)/He and fission track data in the western and northern part of the Aydın range, but also structural data in **chapter 3**. On the basis of the new thermochronological dataset and the mapping of the structures related to the extensional development of the Aydın range, a new tectonic model for the extensional evolution of the southern part of the central Menderes Massif is presented. Furthermore, the obtained cooling ages are used to quantify the exhumation rates of the Aydın range and slip rates of the Demirhan detachment. Constraints on the timing of increased faulting along the Gediz and Büyük Menderes detachments is not only gained by low-temperature thermochronology but also by K-Ar dating of fault gouges presented in **chapter 4**. In the subsequent **chapter 5**, new apatite and zircon (U-Th)/He and fission track data from the north-western part and additional ZFT and AFT data from the north-eastern part of the central Menderes Massif are used to establish a comprehensive tectonic model on the extensional evolution of the central Menderes Massif. As erosion and tectonic denudation contribute to exhumation, the relative proportion of erosion to rock exhumation and landscape change during active continental extension is evaluated by using cosmogenic ^{10}Be to constrain the spatial pattern of erosion across the central Menderes Massif in **chapter 6**. Finally, the thesis is concluded with a discussion on implications of the Oligocene to late Miocene tectonic evolution of western Turkey, with emphasis on the extend of the Simav detachment. The second part of the discussion addresses the contribution of each detachment to the symmetric exhumation in the central Menderes Massif. The third part discusses the possible causes of the imbalance of the symmetric exhumation pattern of the central Menderes Massif in comparison with the prevalent top-to-the north extensional detachment faulting in the Aegean domain.

1.2   Background

Continental Core Complexes

Extensional tectonics are an integral part of the plate tectonic concept, as it is responsible for the collapse of orogenic systems, the break-up of continents and the formation of oceanic basins. The earliest tectonic structures that have been associated with extensional stresses in the continental lithosphere are rift basins like the East African Rift System (Gregory 1896) and the upper Rhine Graben (e.g. Cloos 1939). However, only one decade after the concept of plate tectonics became largely accepted among the geoscience community in the late 1960s, the recognition of large-scale continental extension and the exhumation of mid-crustal rocks in the Basin and Range Province (western United States) by low-angle normal faults attracted large scientific attention (e.g. Davis & Coney 1979; Lister et al. 1984). From a mechanical point of view, the low-angle orientation (<30°) of these normal faults contradict the principles of the Andersonian mechanics, which predict that normal faults are unable to initiate and slip at angles less than 20° to 30° dip (Anderson 1951). However, similar observations were reported from other geodynamic environments like in the back-arc setting of the Aegean (Lister et al. 1984) and even within overall contractional tectonic environments along the Alpine-Himalaya orogen (Burchfiel & Royden 1985). Although the appearance of this new category of extensional structures is highly variable in nature, they have in common that one or more extensional detachment faults separate high grade rocks with mylonitic and cataclastic textures originating from deeper crustal levels in the footwall, from unmetamorphic units in the hanging wall, for which the term metamorphic core complex has been established (e.g. Whitney et al. 2013; Platt et al. 2015). After the classification of Buck (1991), the development of metamorphic core complexes depicts one possible mode that develops, alongside with the wide rift and narrow rift mode, if the lithosphere is subjected to extension (Figure 4). Thereby, several parameters like crustal thickness, water content, strength of the lithosphere, heat flow, strain rate and the presence or absence of magma influence the resulting extensional mode (e.g. Buck & Karner 2004; Wijns et al. 2005; Rosenbaum et al. 2005; Brun & Sokoutis 2018).
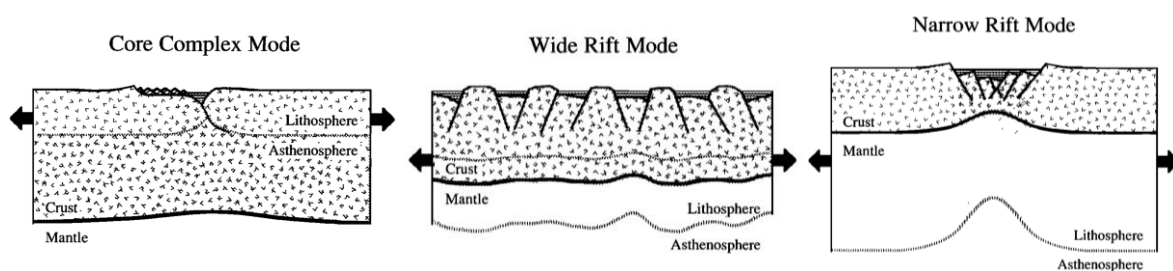
Figure 4: Sketch of the three modes of lithospheric extension proposed by Buck (1991).

A major difference between the extensional evolution of a core complex relative to the narrow and wide rift modes, is that the bulk amount of extension during the core complex formation is focused at the detachment fault, which renders an asymmetric (simple shear) response of the lithosphere to extension than symmetric graben formation described by pure shear. Consequently, the early concepts assumed that extensional detachments depict lithospheric scale features, which also crosscut and displace the Moho (Figure 5) (Wernicke 1981; Bartley & Wernicke 1984). However, this

situation was not encountered by seismic surveys in the Basin and Range Province. Instead, seismic data showed a flat geometry of the Moho with little or absent perturbations below highly extended regions (Hauser et al. 1987). As a consequence of the vertically ''immobile'' Moho and the growth of topography associated with the isostatic response during the exhumation of middle crust, the resulting gap in between is occupied by pressure-driven lateral inflow of ductile lower crust (Block & Royden 1990). Hence, detachment faults cross-cut the brittle upper crust and root in the ductile middle crust in a sub-horizontal orientation (Wernicke & Axen 1988; Davis & Lister 1986). This also explains the missing metamorphic gradient in the footwall in the direction of tectonic transport (Cooper et al. 2010).
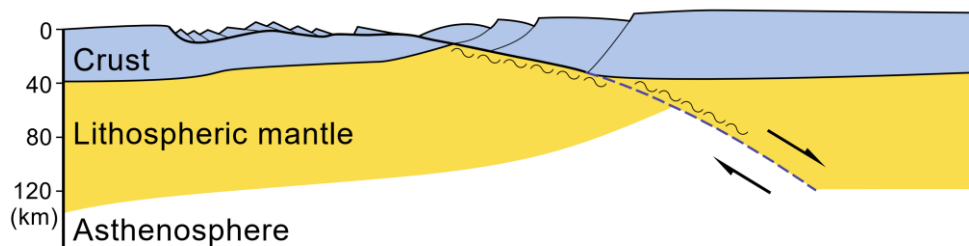
Figure 5: Detachment fault cross-cutting and displacing the lithosphere, from Brun et al. (2017), based on Wernicke (1981, 1985).

1.3   Geological evolution of the Aegean region and western Turkey

The Aegean region encompasses an arcuate orogenic belt that was formed during the prolonged history of the subduction and accretion of small oceanic basins and microcontinents, located in the western Neotethys, since the convergence between Africa and Eurasia initiated in the Cretaceous (Faccenna et al. 2003; Stampfli & Hochard 2009; Jolivet & Brun 2010; Menant et al. 2016). This part of the alpine orogenic belt is subdivided from west to east into the Hellenides (mainland Greece), the Cyclades (Aegean Sea) and the Anatolides and Taurides (Turkey) (Figure 2). The Menderes Massif in particular represents a part of the Anatolides and is described in more detail in chapters 2 and 4. This chapter aims to provide the geological framework, including the fundamental architecture of the Aegean alpine belt, as inherited orogenic structures commonly influence the geometry and style of the subsequent post-orogenic extensional phase.

Although the N-S directed convergence between Africa and Eurasia prevailed since the Cretaceous, the tectonic regime of the overriding plate can be divided into a phase of contraction, resulting into the formation of an alpine nappe stack, and its subsequent destruction in the course of post-orogenic extension and extension due to the roll-back of the African slab (Jolivet et al. 2010; Menant et al. 2016). Lateral correlations of tectonic units of the Anatolide/Tauride belt and the Hellenides are still debated due to the complicated pre-orogenic paleogeography consisting of small oceanic basins (including Vardar, Pindos and Izmir-Ankara-Erzincan Oceans) and laterally discontinuous continental ribbons (van Hinsbergen 2012). However, both regions were dominated by a southward propagation of nappe stacking.
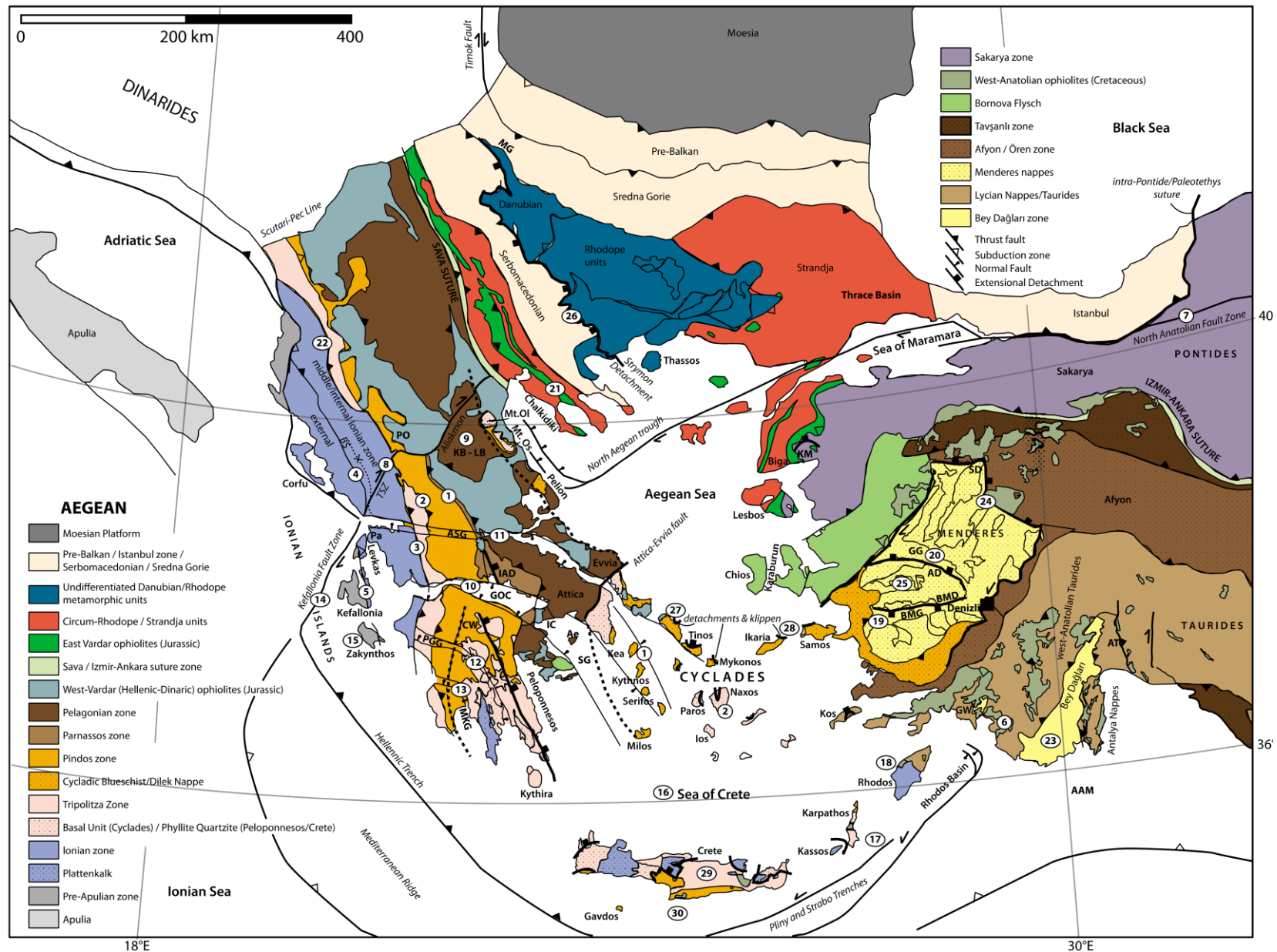
Figure 6: Geological map of the Aegean and western Turkey from van Hinsbergen & Schmid (2012). Abbreviations: AAM = Anaximander and Anaxigoras Seam Mounts; AD = Alaşehir Detachment; ASG = Amvrakikos-Sperchios Graben; AT = Aksu Thrust; BMD = Büyük Menderes Detachment; BMG = Büyük Menderes Graben; BS = Botsara syncline (and Klematia-Paramythia Basin); CW = Chelmos Window; GOC = Gulf of Corinth; GG = Gediz Graben; GW = Göçek window; IAD = Itea-Amfissa Detachment; IC = Isthmus of Corinth; KB-LB = Karditsa Basin–Larissa Basin; KM = Kazdağ; MG = Mesta Graben; MKG = Melimala-Kalamata Graben; Mt. Ol. = Mount Olympos; Mt. Os. = Mount Ossa; Pa = Paleros; PGG = Pyrgos-Gythian Graben; PO = Pindos Ophiolite; SD = Simav Detachment; SG = Saronic Gulf; TSZ = Thesprotiko Shear Zone.

Alpine architecture of mainland Greece and the Cyclades

The Aegean belt is bordered to the north by the Moesian platform, which acted as a buttress for the developing fold-and-thrust belt of the Rhodope in the Cretaceous, forming the internal part of the Aegean orogen (Figure 6) (van Hinsbergen & Schmid 2012). Since the late Cretaceous oceanic lithosphere of the Vardar ocean was subducted below the Rhodope and Moesian platform units towards the north, until the Pelagonian microcontinent entered the subduction zone, leading to the closure of the Vardar ocean and the formation of the Sava suture zone in the late Cretaceous (Lips et al. 1998; Stampfli & Borel 2002; Schmid et al. 2008; Ustaszewski et al. 2010). The upper crustal parts of Pelagonia were decoupled from lower lithospheric units, enabling ongoing subduction and accretion of marine units of the Pindos basin, whose lithospheric nature, whether thinned continental or oceanic, is unrecorded (Schmid et al. 2008; Jolivet et al. 2010). The Cycladic Blueschist Units are exposed in the central Cyclades and represent an eastern part of Pindos, which experienced high-pressure/low-temperature metamorphism between 55 and 40 Ma and a retrograde greenschist facies overprint of Oligocene age (Lagos et al. 2007; Ring et al. 2007; Jolivet et al. 2010). Concurrent to the exhumation of parts of the Pindos nappe in the Oligocene, the shallow marine platform carbonates of the Tripolitza block are accreted below the Pindos units. Below Tripolitza the lowermost structural position is occupied by the Ionian units (Sotiropoulos et al. 2003).

Alpine architecture of western Turkey

The northernmost tectonic unit in western Turkey is represented by the Istanbul zone, which was once part of the Greek/Bulgarian Moesian platform and became separated due to the mid-Cretaceous opening of the western part of the Black Sea (Okay 2008; Bozkurt et al. 2008). In contrast to the Istanbul zone, the Sakarya zone to the south is described as a continental ribbon that cannot be correlated with any part of the Hellenides and therefore represents an individual continental fragment (van Hinsbergen & Schmid 2012). The Sakarya zone defines the northern active margin of the Neotethys, which is now exposed as the Izmir-Ankara-Erzincan suture zone (Şengör & Yilmaz 1981). This suture zone is the Turkish equivalent to the Sava suture zone in Greece, separating the late Cretaceous to Eocene nappe stack in the south from the Eurasian active margin in the north (van Hinsbergen & Schmid 2012; Menant et al. 2016). The Izmir-Ankara-Erzincan suture itself is characterized by a mélange of late Triassic to Cretaceous marine sediments and oceanic volcanics (Gökten & Flyod 2007). The tectonic units located below the Izmir-Ankara-Erzincan suture zone were incorporated into the southward propagating accretionary nappe pile in the Eocene. However, the unmetamorphic ophiolites covering the Tavşanlı and Afyon-Ören units to the south of the Izmir-Ankara-Erzincan suture zone were already obducted in the late Cretaceous, indicting the existence of an intra-oceanic subduction zone (Şengör & Yilmaz 1981; Dilek et al. 1999; Menant et al. 2016). Both, the Tavşanlı zone and the Afyon-Ören units experienced high-pressure/low-temperature metamorphism at 88 to 80 Ma and 65 to 60 Ma, respectively (Candan et al. 2005; Sherlock et al. 1999; Whitney et al. 2011). Below the Ören unit, the Dilek nappe also experienced blueschist facies metamorphism in the Eocene, indicating that rocks of the Dilek nappe represent a separate alpine

nappe that was thrust over the underlying nappes of the Menderes Massif (Ring et al. 1999; Gessner et al. 2001a). The aforementioned ophiolitic and high-pressure units encompass geographically and overlay structurally the nappes attributed to the Menderes Massif. The Menderes Massif exposes the structurally deepest units of the Anatolides and consists of four nappes with the Bayındır nappe in the lowermost position (Ring et al. 1999). The Bayındır nappe consists of greenschist to amphibolite facies meta-sediments, including phyllites, marbles and quartzites, which, in contrast to the polymetamorphic history of the overlaying nappes of the Menderes Massif, only experienced alpine metamorphism with maximum temperatures of ~400°C (Ring et al. 1999). The timing of this event is only roughly constrained by a single $^{40}Ar/^{39}Ar$ white mica age of 36 Ma (Lips et al. 2001). During the Alpine orogeny, the Bozdağ nappe was emplaced onto the Bayındır nappe. The Bozdağ nappe mainly consist of metapelite and minor volumes of amphibolite, dolomite, eclogite and granitic intrusions of Triassic age (Koralay et al. 2001, 2011). These metasediments were deposited in a Pan-African foreland basin, which subsequently became incorporated into the Pan-African orogen under amphibolite-facies metamorphic conditions (Candan et al. 2001; Ring et al. 2001; Koralay 2015).

The tectonic contact to the overlaying Çine nappe is most probably of pre-Triassic age (Gessner et al. 2001a). Deformed orthogneisses with Neoproterozoic to early Cambrian intrusion ages are the dominant lithology of the Çine nappe, besides minor amounts of paragneiss, eclogite and amphibolite (Bozkurt et al. 1995; Hetzel & Reischmann 1996; Oberhänsli 1997; Loos & Reischmann 1999). Rocks of the Çine nappe experienced a poly-metamorphic history including the Cenozoic alpine Barrovian-type metamorphism between 43 and 34 Ma (Schmidt et al. 2015). The Selimiye nappe is the uppermost nappe of the Menderes Massif and was thrust over the Çine nappe in the Eocene (Ring et al. 2003). It consists of metapelites, marbles and metabasites of Palaeozoic age (Gessner et al. 2004; Regnier et al. 2003). To the southeast of the Menderes Massif, the Bey Dağları consists of Jurassic to Eocene platform carbonates that are correlated with the siliciclastic meta-sediments of the Bayındır nappe of the Menderes Massif, as the former Menderes-Bey Dağları platform (Collins & Robertson 2003). In the Miocene, the Bey Dağları platform was overthrust by the unnmetamorphosed units of the Lycian nappe, carrying on top remnants of the same ophiolitic units that were obducted in the Cretaceous onto the Tavşanlı and Afyon/Ören units, situated to the north and east of the Menderes Massif (Figure 6). This was interpreted by van Hinsbergen (2010) as an indication that the Lycian nappes were once situated above the Menderes Massif and were tectonically transported to the south during the early Miocene. The timing of this event was constrained by early Miocene sediments that were deposited south of the frontal thrust of the Lycian nappes in a foreland basin environment between ~23 and 16 Ma (Hayward 1984; van Hinsbergen 2010). Hence, this southeast-ward transport of the Lycian nappes occurred concurrently with the first signs of extensional deformation in Western Turkey and widespread extension in the Aegean.

Late Cenozoic extension

The initiation of widespread extension in the overriding plate of the African slab (or Hellenic, Aegean slab) is marked by the onset of faulting along extensional detachments in the Rhodopes during the Eocene (Figure 7) (Brun & Sokoutis 2010), which predates the first indications of the southward migration of the magmatic arc since the early Oligocene related to roll-back of the African slab (Jolivet & Brun 2010). Instead, this first phase of post-orogenic extension is rather a consequence of the slab delamination at that time, promoting asthenospheric heating and thermal weakening of the overlaying nappe pile (Kydonakis et al. 2015). The relatively low extension rate of ~0.6 km/Ma across the whole Rhodope core complex in the Eocene was accommodated along two oppositely dipping detachment faults, exhuming the northern and southern submassifs of the Rhodope core complex simultaneously (Brun & Sokoutis 2007; Burg 2012). Whereas the extensional deformation in the northern Rhodope core complex was rather short lived and ceased in the Oligocene, top-to-the south extension in the southern Rhodope core complex continued along the Kerdylion detachment until the middle Miocene (Nagel et al. 2011; Kounov et al. 2015; Brun & Sokoutis 2018). Extensional deformation of the southern Rhodope core complex was associated with a ~25° clockwise rotation of the hanging wall during the Miocene (Brun & Sokoutis 2008; van Hinsbergen et al. 2008). With the rotational pole situated in the northwest of the Rhodope core complex, the maximum amount of extension occurred at its submerged eastern rim along the Aegean coast line, accommodating ~120 km of extension, whereby only a part of this movement is attributed to detachment faulting (Brun & Sokoutis 2007). The other proportion is attributed to widespread high-angle normal faulting after extension along the Kerdylion detachment ceased in the middle Miocene. The change from a core-complex mode of extension to a wide rift mode of extension is associated to the fivefold increase of extensional deformation in the course of increasing slab roll-back rates since the middle Miocene (Brun & Sokoutis 2018).

In the central Aegean and western Turkey, increasing slab roll-back rates since the Oligocene resulted in the formation of the north-dipping North-Cycladic-Detachment-System (NCDS), exhuming the northern part of the Cyclades metamorphic core complex in the central Aegean Sea and the north-dipping Simav detachment, exhuming rocks of the northern Menderes Massif in western Turkey (Jolivet et al. 2010; Işik & Tekeli 2001; Ring & Collins 2005; Thomson & Ring 2006; Erkül 2009). Whether the NCDS represents a single detachment fault or consists of several branches remains controversial (Philippon et al. 2012), as is the relationship between the NCDS and the Simav detachment. However, their structural position within the alpine nappe stack implies for that the NCDS as well as the Simav detachment, developed in inherited zones of lithospheric weakness, which are the Vardar and Izmir-Ankara-Erzincan suture zones, respectively (Jolivet et al 2010). Faulting along the NCDS initiated at ~ 35 Ma and lasted until 15 to 10 Ma, whereas faulting along the Simav detachment initiated in the latest Oligocene and ceased already in the early Miocene at ~19 to 17 Ma (Brichau et al. 2006; Jolivet et al. 2010; Hetzel et al. 2013).
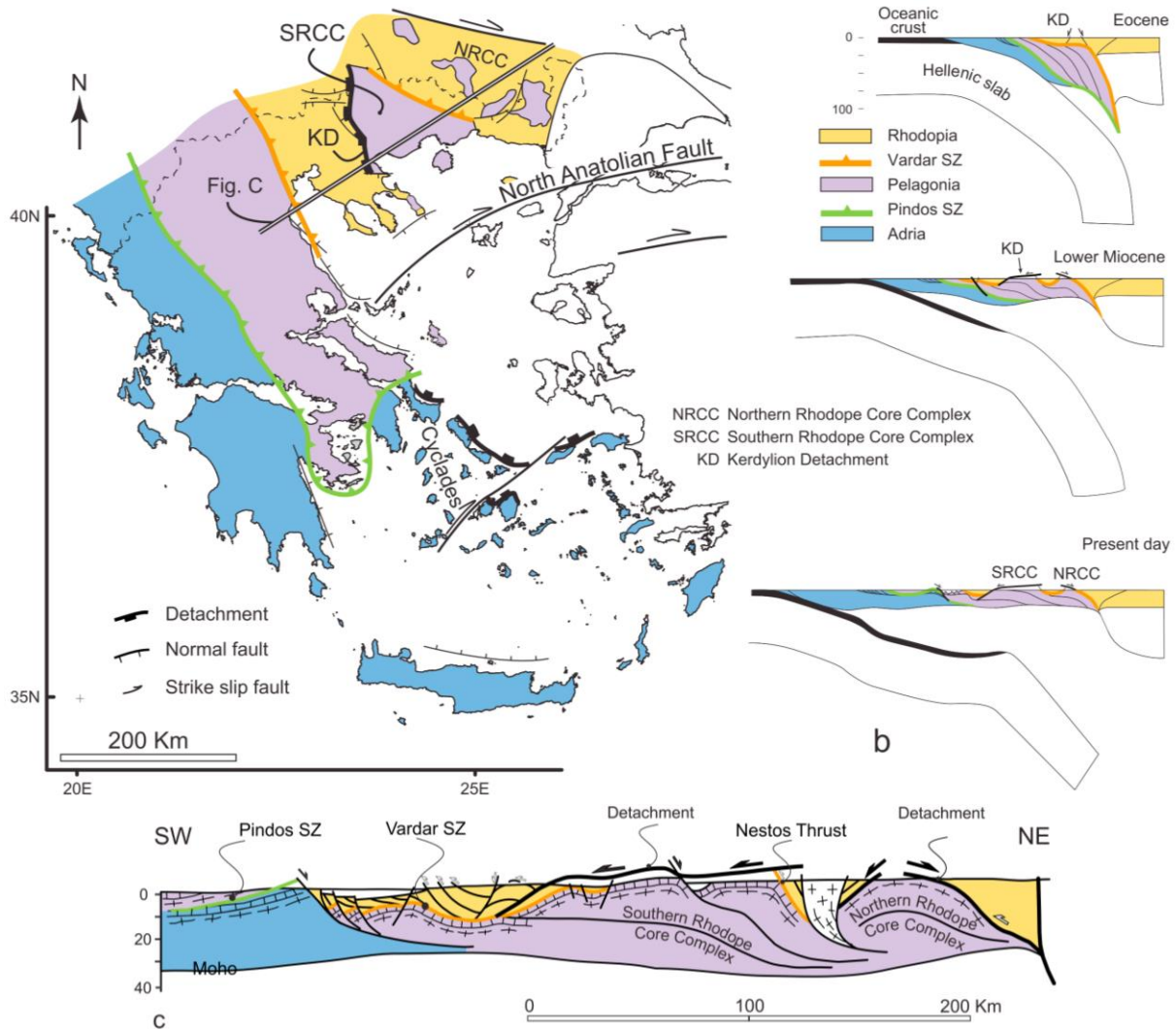
Figure 7: Simplified tectonic map of the north-eastern Aegean depicting the main extensional structures. b shows the main stages of extension and exhumation of the northern (NRCC) and southern (SRCC) Rhodope core complexes since the Eocene. c: Lithospere scale cross section through the Rhodope core complex after Brun & Sokoutis (2018). Abbreviations: NRCC = Northern Rhodope Core Complex, SRCC = Southern Rhodope Core Complex, KD = Kerdylion detachment.

In the western Aegean, top-to-the north faulting of the NCDS was accompanied by top-to-the south faulting along the Western-Cycladic-Detachment System (WCDS) (Figure 8) (Grasemann et al. 2012). The WCDS probably extends until the recently proposed Santorini detachment, which is also interpreted as a top-to-the south extensional detachment fault (Schneider et al. 2018). The WCDS and Santorini detachments show a similar timing. Both were constrained to be active between early Miocene until late Miocene, with a phase of high activity in the middle Miocene. A similar symmetric pattern of core complex exhumation as in the Cyclades (Grasemann et al. 2012) is also attributed to the exhumation history of the central Menderes Massif in western Turkey (Hetzel et al. 1995a; Hetzel et al. 2001b; Ring et al. 2003; Wölfler et al. 2017; Nilius et al. 2019). The Menderes Massif comprises a two-stage extensional evolution, of which the first stage is related to the extension along the Simav detachment and the exhumation of the northern Menderes Massif (Işik & Tekeli 2001; Işik et al. 2004; Thomson & Ring 2006; Erkül 2009; Hasözbek et al. 2011; Cenki-Tok et al. 2016). Since the middle Miocene, the second stage led to the exhumation of the central Menderes Massif by two

oppositely-dipping detachment faults (Hetzel et al. 1995a, b; Hetzel et al. 1998; Gessner et al. 2001a; Gessner et al. 2001b; Seyitoğlu et al. 2002; Bozkurt & Sözbilir 2004; Buscher et al. 2013).

The second stage initiated with the emplacement of synorogenic granodiorites into the footwall of the northward-dipping Gediz detachment at 16 and 15 Ma (Glodny & Hetzel 2007; Rosetti et al. 2017) and the fast exhumation in the footwall of south-dipping Büyük Menderes and Demirhan detachments (Figure 3) (Wölfler et al. 2017; Nilius et al. 2019). In the hanging wall of the Büyük Menderes detachment, the Büyük Menderes graben limits the central Menderes Massif to the south and the Gediz graben in the hanging wall of the Gediz detachment limits the central Menderes Massif to the north (Figure 3). As with the clockwise rotation of the Rhodope core complex at the northwestern border of the Aegean extensional province, the extensional deformation of the central Menderes Massif accommodated an oppositely counterclockwise rotation at the eastern rim of the Aegean extensional province (van Hinsbergen 2010). The counterclockwise rotation of ~30° between the tectonic units situated north and south of the central Menderes Massif are also evident from the cooling and exhumation history of the footwall rocks (Chapter 5). Since the late Pliocene/Pleistocene,
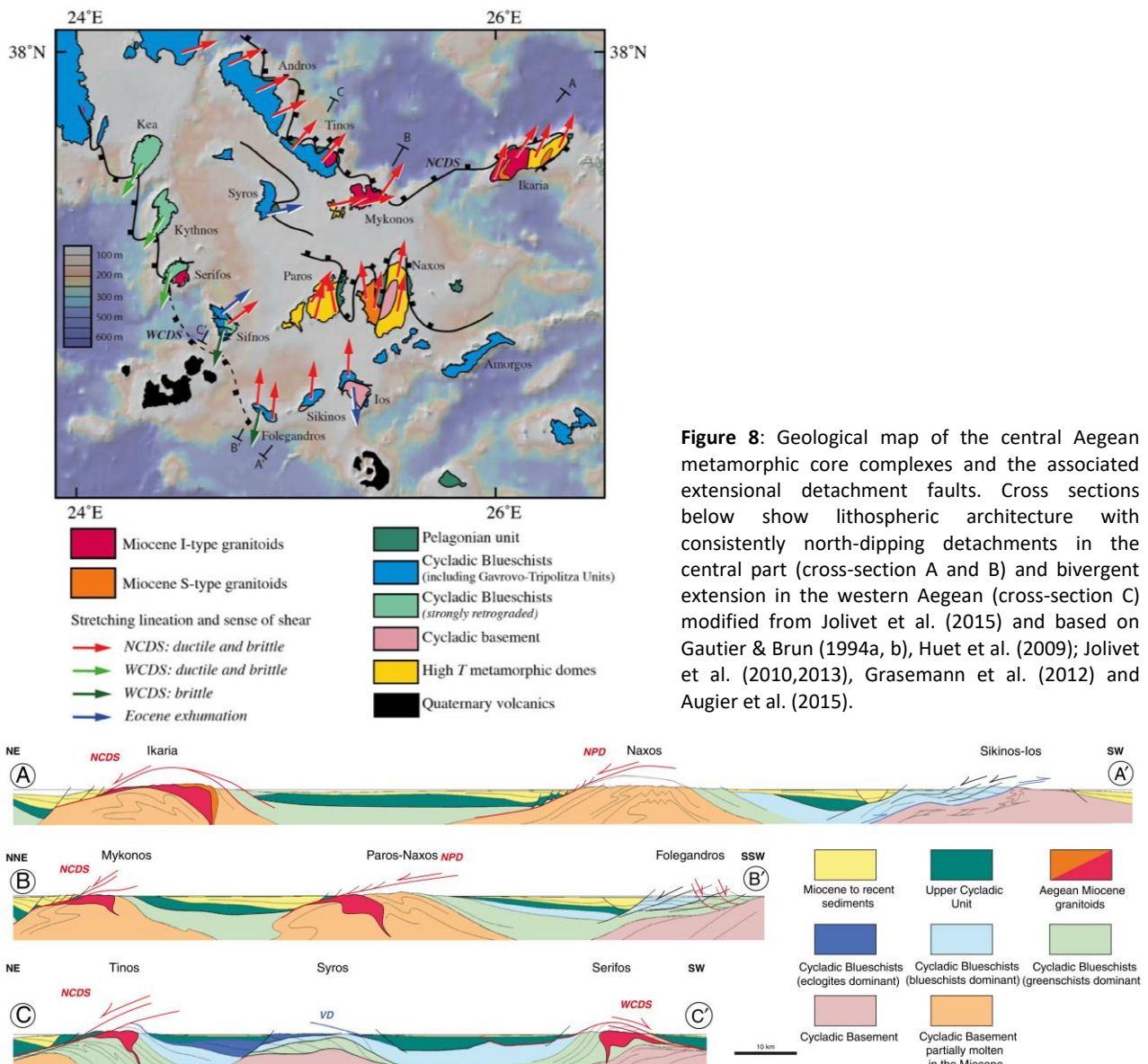
Figure 8: Geological map of the central Aegean metamorphic core complexes and the associated extensional detachment faults. Cross sections below show lithospheric architecture with consistently north-dipping detachments in the central part (cross-section A and B) and bivergent extension in the western Aegean (cross-section C) modified from Jolivet et al. (2015) and based on Gautier & Brun (1994a, b), Huet et al. (2009); Jolivet et al. (2010,2013), Grasemann et al. (2012) and Augier et al. (2015).

faulting along the detachments terminated and changed to the high-angle normal faulting along the southern and northern graben margins of the Gediz and Büyük Menderes grabens, respectively (Bozkurt & Sözbilir 2004; Gürer et al. 2009; Buscher et al. 2013; Kent et al. 2016; Wölfler et al. 2017; Nilius et al. 2019).

1.4   Methods to derive the extensional history of the central Menderes Massif

Thermochronology

The first absolute date of a mineral was derived by Rutherford (1905) by measuring the amount of U and its decay product He, trapped within a sample of fergusonite. Although, the idea to measure the radiogenic He of actinide bearing minerals was originally intended to infer the age of a rock, the modern use of this technique is used to constrain the temperature history of a rock. In contrast to a geochronometric dating method where the daughter product of radioactive decay stays within the mineral, the two most commonly used thermochronometric methods, fission track and U-Th/He dating, utilize the disappearance of the radioactive decay products, being it either the diffusion of He out of the crystal lattice or the annealing of fission tracks. The kinetics behind the annealing and diffusion processes are strongly dependent on the temperature and the heating-time and are specific for each mineral system used. Hence, with the two most commonly used minerals for fission track and (U-Th)/He thermochronology, apatites and zircons, one can track the cooling history of a rock from ~ 240 to ~40°C (Figure 9) (Tagami 2005; Flowers et al. 2007; Flowers et al. 2009). In the following, fission track and (U-Th)/He thermochronology for apatite and zircon are described.
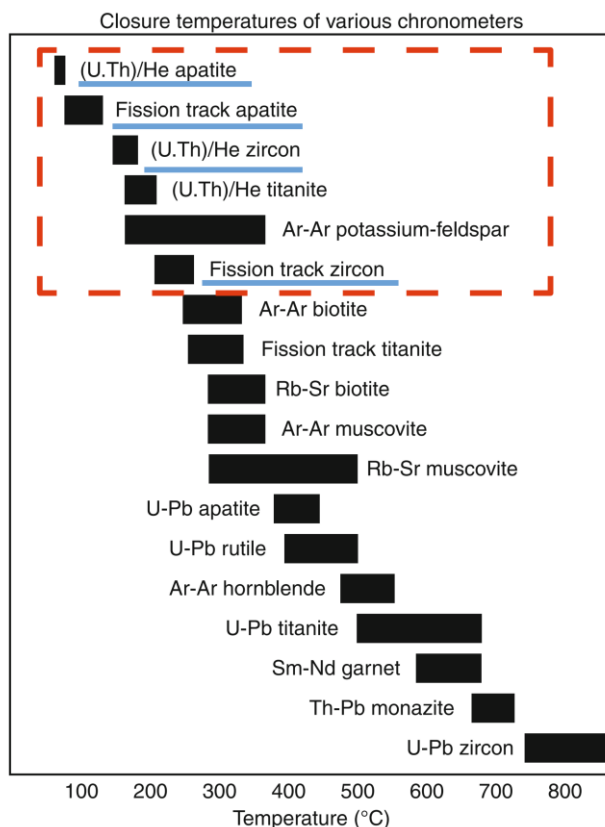
Figure 9: Summary of closure temperatures for radiometric dating methods modified from Carlson (2011). Dashed red line indicates thermochronometric systems, which are typically refered to as "low-temperature thermochronometer". Blue marked thermochronometers were used in the course of this study.

Fission track thermochronology

Fission tracks in U-bearing minerals or glass are the damage trails formed by the spontaneous fission of ^{238}U into two recoiling nuclei (Price & Walker 1963), which results in fission tracks with an initial length of ~11 µm in zircons and ~16 µm in apatites (Fleischer et al. 1975). To permit counting of fission tracks under an optical microscope, the initial width of only 25 to 50 Å has to be increased by chemical etching. The resulting track density in the sample is depending on the ^{238}U concentration, the fission track age and the decay constant. The ^{238}U content is indirectly estimated by irradiating the sample with thermal neutrons which causes the spontaneous fission of ^{235}U nuclei, and the multiplying with the constant natural ratio between ^{235}U and ^{238}U. The rate of induced fission of ^{235}U is proportional to the thermal-neutron fluence, which is determined by the irradiation of dosimeter glass with a known U content, together with the sample stack (Hurford 1990) (Figure 10). A very widely used method to analyse the ^{238}U content of the sample is the attachment of a U-free muscovite sheet on the polished surface of the sample during the irradiation (commonly referred to as external detector method), which records the induced fission of ^{235}U in the sample (Figure 10) (Hurford & Green 1982; Hurford 1990). As counting of fission tracks under the optical microscope is prone to a subjective bias, the fission track age is corrected by an individual factor named ζ, which is determined by the counting of a natural standard sample (Hurford & Green 1983). The fission track age is calculated by using the equation

$$t = \frac{1}{\lambda_D}\ln(\lambda_D \zeta \rho_d G \left(\frac{\rho_s}{\rho_i}\right)) \tag{1}$$

, where the decay constant for ^{238}U is given by λD, ζ the zeta factor, G is the geometry factor and ρ_s and ρ_i are the densities of spontaneous and induced fission tracks on the sample and the muscovite detector, respectively. Both, AFT and ZFT techniques have in common that fission tracks are either partially or completely erased with increasing temperature over a temperature range called partial annealing zone (PAZ). The lower temperature boundary of the PAZ for the AFT system is ~60 °C and for the ZFT system ~230 °C, whereas the upper boundary is ~110 and ~310 °C for the AFT and ZFT systems, respectively. Within the PAZ, shortened and long fission tracks occur together and provide valuable information that can be used to constrain the cooling rates of the sample by thermal modelling (Gallagher 1995; Ketcham 2005).
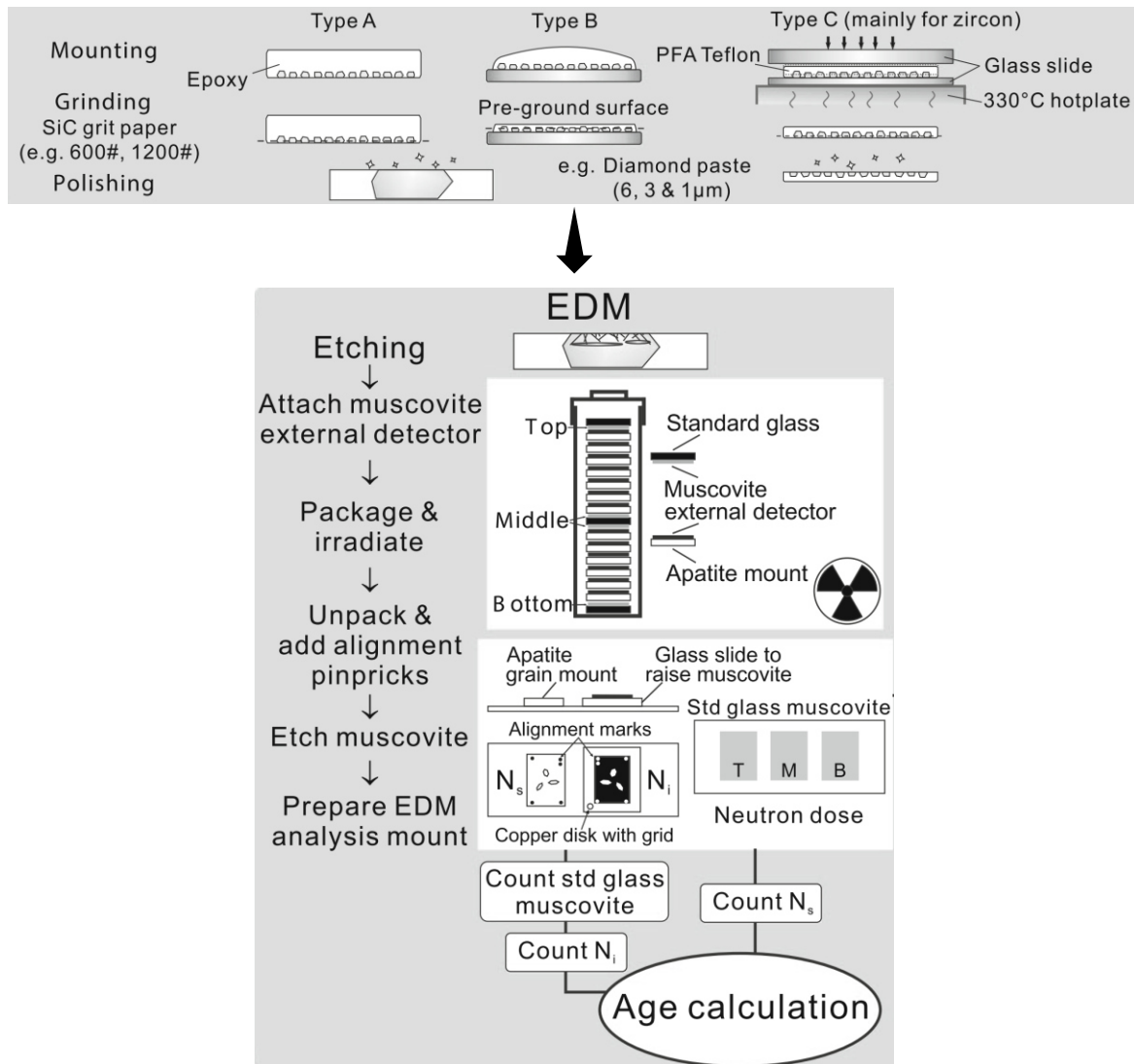
Figure 10: Sample preparation procedure to derive for zircon and apatite fission track analysis using the external detector method (EDM) of Hurford & Green (1982), modified from Kohn et al. (2019).

(U-Th)/He thermochronology

The early attempts to use radiogenic He of U and Th bearing minerals for radiometric dating purposes were soon abandoned due to the problematic diffusion of He (Rutherford 1907; Soddy 1911-1914). Since the late 1980s, the method was rediscovered with the intention to use He diffusion as a temperature dependent process for the invention of new thermochronometers (Zeitler et al. 1987). This idea was initially tested for apatites and subsequently for additional minerals like titanites (Reiners and Farley 1999), zircons (Reiners et al. 2002, Reiners 2005), monazites (Boyce et al. 2005) and some more exotic phases like the Fe-oxides magnetite (Blackburn et al. 2007) and hematite (Lippolt et al. 1993; Farley & Flowers 2012). However, the probably most challenging aspect with the (U-Th)/He method are the processes that influence the He-diffusion characteristics of the applied mineral. As these are best known for apatites and zircons, and thus are the commonly used minerals for (U-Th)/He-dating, I applied AHe and ZHe in the course of this study. Therefore, the following chapter will give additional details of AHe and ZHe thermochronology.

Diffusion experiments confirmed the low-temperature sensitivity of apatite to a temperature range as low as 40 to 70 °C (Farley 2000; Flowers et al. 2009), whereas higher temperatures from ~140 to 200 °C were inferred for the ZHe system (Reiners et al. 2003; Guenthner et al. 2013). The specific closure temperature of the AHe and ZHe systems vary within the temperature ranges, called partial retention zones (PRZ), defining the temperature range where He partially diffuses out of the mineral. Typical closure temperatures for the AHe method are ~65 °C and ~180 °C for ZHe method depend on the grain-specific diffusion characteristics (Wolf et al. 1996, 1998; Farley 2000; Reiners & Brandon 2006; Guenthner et al. 2013). Therefore, it is crucial to understand and quantify the processes that govern the loss of He out of the crystal. He loss by diffusion is relatively well constrained for zircons (Reiners et al. 2004; Guenthner et al. 2013) and apatites (Zeitler et al. 1987; Farley 2000; Flowers et al. 2009). Factors influencing the He diffusion kinetics are the grain size and the radiation damage, where the latter is a function of the effective Uranium concentration (eU= U + 0.235*Th) and the cooling history (Flowers et al. 2009; Guenthner et al. 2013). Another process which leads to the loss of He and needs to be corrected are the long alpha-stopping distances of 5 to 22 μm compared to the typical grain widths of 50 to 200 μm of apatites and zircons (Farley et al. 1996; Ketcham et al. 2011). Hence, the resulting age calculated with the measured He-concentration would lead to a significantly younger age. The correction factor FT is the fraction of the total produced He, which is a function of the size and the morphology of the analyzed crystal, with the model relying on the assumption that the measured grains are perfectly symmetric and comprise smooth surfaces (Farley et al. 1996).

K-Ar Fault gouge dating

Faulting in the brittle regime of upper crustal levels is dominated by fracturing, crushing and subsequent grinding of wall rock material. In combination with fluids and at temperature ranges <300 °C, authigenic clays are formed as a retrograde reaction within the fault zone (Zwingmann & Mancktelow 2004). This fine-grained material mixed with authigenic clay minerals like smectite and illite are described as a fault gouge. The authigenic, potassium bearing illite of the fault gouge is separated from the whole rock and used to constrain the age of its authigenic growth, which occurs at temperatures of 120 to 160 °C, with K-Ar of $^{40}Ar/^{39}Ar$ dating techniques (e.g. van der Pluijm et al. 2001; Zwingmann & Mancktelow 2004; Hetzel et al. 2013). Different grain size fractions of illite are analyzed separately, as the smallest grain size fraction normally indicates the youngest illite growth phase and consequently is interpreted to represent the latest faulting activity (Zwingmann et al. 2010; Haines & van der Pluijm 2012). In our approach, the absolute ages constrained from K-Ar fault gouge dating are combined with thermochronological data of the adjacent wall rocks to combine the cooling history in the footwall of the detachment fault with the timing of increased fault activity by K-Ar fault gouge ages from different illite grain size fractions.

Erosion rates derived from cosmogenic ^{10}Be concentration

Beryllium-10 (^{10}Be) is a radioactive nuclide with a half-life time of 1.387 ± 0.012 Ma, which is produced via the interaction of cosmic rays with nuclei (N,O, Ar) of the Earth's atmosphere ('*meteoric*') or in the crystal lattice of minerals (mainly from spallation of Mg, Al, Si, Ca) at or close to the Earth's surface ('*in situ*') (Lal, 1991; Gosse & Phillips 2001). Although the bulk amount of ^{10}Be is *meteoric*, few high-energy particles reach the Earth's surface, where the *in situ*-production rate of ^{10}Be exponentially decreases with depth, because of the attenuation length of cosmic rays of 160 g/cm². Hence, applied to rocks with a density 2.7 g/cm³, the ^{10}Be production rate would fade 60 cm below the surface (Balco et al. 2008). With the surface production rate, the ^{10}Be concentration, the attenuation depth and the decay constant of ^{10}Be known, the erosion rate can be calculated as:

$$E = (P/C-\lambda) * z, \qquad\qquad (2)$$

with C describing the ^{10}Be concentration (at/g$_{quartz}$), P the production rate at the surface (at/g$_{quartz}$ α), λ as the decay constant of ^{10}Be (1/a) and z as the attenuation depth (cm) (Lal 1991, Granger et al. 1996). The corresponding erosion rate averages over the time needed to reach the attenuation depth z by erosion. Hence, erosion rates derived by cosmogenic nuclides typically integrate over a time range of 10^2 to 10^5 years, depending on the magnitude of erosion (von Blanckenburg 2006).

^{10}Be concentrations in quartz can be used to constrain local-scale erosion rates for example on ridge crests by sampling bedrock quartz clast (Hancock & Kirwan 2007) or to constrain erosion rates of catchment-scale by sampling from stream sediments (Biermann & Steig 1996; Granger et al. 1996). Combining catchment erosion rates, which reflect the average erosion rate over the entire catchment area and local erosion rates from adjacent ridge crest, allows to determine important perceptions about the local relief evolution (Meyer et al. 2010).

References

Anderson, E.M. 1951. The dynamics of faulting and dyke formation with applications to Britain. 2nd ed., Oliver and Boyd, Edinburgh, 206 pp.

Augier, R., Jolivet, L., Gadenne, L., Lahfid, A., Driussi, O. 2015. Exhumation kinematics of the Cycladic Blueschists unit and back-arc extension, insight from the Southern Cyclades (Sikinos and Folegandros Islands, Greece). Tectonics 34(1), 152-185.

Balco, G., Stone, J.O., Lifton, N.A., Dunai, T.J. 2008. A complete and easily accessible means of calculating surface exposure ages or erosion rates from 10Be and 26Al measurements. Quaternary geochronology 3(3), 174-195.

Bartley, J.M., Wernicke, B.P. 1984. The Snake Range decollement interpreted as a major extensional shear zone. Tectonics 3(6), 647-657.

Bierman, P., Steig, E.J. 1996. Estimating rates of denudation using cosmogenic isotope abundances in sediment. Earth surface processes and landforms 21(2), 125-139.

Blackburn, T.J., Stockli, D.F., Walker, J.D. 2007. Magnetite (U–Th)/He dating and its application to the geochronology of intermediate to mafic volcanic rocks. Earth and Planetary Science Letters 259(3-4), 360-371.

Block, L., Royden, L.H. 1999. Core complex geometries and regional scale flow in the lower crust. Tectonics 9(4), 557-567.

Bozkurt, E., Winchester, J.A., Park, R.G., 1995. Geochemistry and tectonic significance of augen gneisses from the southern Menderes Massif (West Turkey). Geological Magazine 132(3), 287–301.

Bozkurt, E., Sözbilir, H., 2004. Tectonic evolution of the Gediz Graben: field evidence for an episodic, two-stage extension in western Turkey. Geological Magazine 141, 63–79.

Bozkurt, E., Winchester, J.A., Yiğitbaş, E., Ottley, C.J. 2008. Proterozoic ophiolites and mafic–ultramafic complexes marginal to the Istanbul Block: an exotic terrane of Avalonian affinity in NW Turkey. Tectonophysics 461(1-4), 240-251.

Boyce, J.W., Hodges, K.V., Olszewski, W.J., Jercinovic, M.J. 2005. He diffusion in monazite: Implications for (U-Th)/He thermochronometry. Geochemistry, Geophysics, Geosystems 6(12).

Brichau, S., Ring, U., Ketcham, R.A., Carter, A., Stockli, D., Brunel, M., 2006. Constraining the long-term evolution of the slip rate for a major extensional fault system in the central Aegean, Greece, using thermochronology. Earth and Planetary Science Letters 241, 293–306.

Brun, J. P., van den Driessche, J. 1994. Extensional gneiss domes and detachment fault systems; structure and kinematics. Bulletin de la Société Géologique de France, 165(6), 519-530.

Brun, J.P., Sokoutis, D. 2007. Kinematics of the southern Rhodope core complex (North Greece). International Journal of Earth Sciences 96(6), 1079-1099.

Brun, J.P., Sokoutis, D. 2010. 45 my of Aegean crust and mantle flow driven by trench retreat. Geology, 38(9) 815-818.

Brun, J.P., Sokoutis, D., Tirel, C., Gueydan, F., Van den Driessche, J., Beslier, M. O., 2017. Crustal versus mantle core complexes. Tectonophysics. https://doi.org/10.1016/j.tecto.2017.09.017.

Brun, J.P., Sokoutis, D. 2018. Core complex segmentation in North Aegean, a dynamic view. Tectonics

37(6), 1797-1830.

Buck, W.R., 1991. Modes of continental lithospheric extension. Journal of Geophysical Research 96, 20, 161–20, 178.

Buck, W.R., Karner, G.D. 2004. Consequences of asthenospheric variability on continental rifting. In: Karner, G.D., Taylor, B., Driscoll, N.W., Kohlstedt, D.L. (Eds.), Rheology and deformation of the lithosphere at continental margins, Columbia University Press, New York, 62, 1-30.

Burchfiel, B.C., Royden, L.H. 1985. North-south extension within the convergent Himalayan region. Geology, 13(10), 679-682.

Burg, J.P. 2012. Rhodope: From Mesozoic convergence to Cenozoic extension: Review of petro-structural data in the geochronological frame. Journal of the Virtual Explorer 42, 1.

Buscher, J.T., Hampel, A., Hetzel, R., Dunkl, I., Glotzbach, C., Struffert, A., Akal, C., Rätz, M., 2013. Quantifying rates of detachment faulting and erosion in the central Menderes Massif (western Turkey) by thermochronology and cosmogenic ^{10}Be. Journal of the Geological Society, London 170, 669–683.

Candan, O., Dora, O.Ö., Oberhänsli, R., Çetinkaplan, M., Partzsch, J.H., Warkus, F.C., Dürr, S., 2001. Pan-African high-pressure metamorphism in the Precambrian basement of the Menderes Massif, western Anatolia, Turkey. International Journal of Earth Sciences 89, 793–811.

Candan, O., Çetinkaplan, M., Oberhänsli, R., Rimmelé, G., Akal, C., 2005. Alpine high-P/low-T metamorphism of the Afyon Zone and implications for the metamorphic evolution of Western Anatolia, Turkey. Lithos 84 (1-2), 102-124.

Carlson W.R. 2011. Absolute age determinations: Radiometric. In Gupta, H.K. Encyclopaedia of Solid Earth Geophysics. Springer Netherlands. 1539pp.

Cenki-Tok, B., Expert, M., Işık, V., Candan, O., Monie, P., Bruguier, O., 2016. Complete Alpine reworking of the northern Menderes Massif, western Turkey. International Journal of Earth Sciences 105(5), 1507-1524.

Cloos, H., 1939. Hebung – Spaltung – Vulkanismus. Elemente einer geometrischen Analyse irdischer Großformen. Geologische Rundschau 30, 401–527.

Collins, A.S., Robertson, A.H. 2003. Kinematic evidence for Late Mesozoic–Miocene emplacement of the Lycian Allochthon over the western Anatolide belt, SW Turkey. Geological Journal 38(3-4), 295-310.

Cooper, F.J., Platt, J.P., Anczkiewicz, R., Whitehouse, M.J. 2010. Footwall dip of a core complex detachment fault: Thermobarometric constraints from the northern Snake Range (Basin and Range, USA). Journal of Metamorphic Geology 28(9), 997-1020.

Davis, G.H., Coney, P.J. 1979. Geologic development of the Cordilleran metamorphic core complexes. Geology 7(3), 120-124.

Davis, G.A., Lister, G.S., Reynolds, S.J. 1986. Structural evolution of the Whipple and South Mountains shear zones, southwestern United States. Geology 14(1), 7-10.

Dilek, Y., Thy, P., Hacker, B., Grundvig, S. 1999. Structure and petrology of Tauride ophiolites and mafic dike intrusions (Turkey): Implications for the Neotethyan ocean. Geological Society of America Bulletin 111(8), 1192-1216.

Erkül, F., 2009. Tectonic significance of synextensional ductile shear zones within the Early Miocene Alaçamdağ granites, northwestern Turkey. Geological Magazine 147(4), 611–637.

Faccenna, C., Jolivet, L., Piromallo, C., Morelli, A. 2003. Subduction and the depth of convection in the Mediterranean mantle. Journal of Geophysical Research: Solid Earth 108(B2).

Farley, K.A., Wolf, R.A., Silver, L.T., 1996. The effects of long alpha-stopping distances on (U-Th)/He ages. Geochimica et Cosmochimica Acta 60, 4223–4229.

Farley, K.A., 2000. Helium diffusion from apatite: General behavior as illustrated by Durango fluorapatite. Journal of Geophysical Research 105, 2903–2914.

Farley, K.A., Flowers, R.M., 2012. (U–Th)/Ne and multidomain (U–Th)/He systematics of a hydrothermal hematite from eastern Grand Canyon. Earth and Planetary Science Letters 359, 131-140.

Fleischer, R.L., Price, P.B., Walker, R.M., Walker, R.M. 1975. Nuclear tracks in solids: principles and applications. Univ of California Press.

Flowers, R.M., Shuster, D.L. Farley, K.A., 2007. Radiation damage control on apatite (U-Th)/He dates from the Grand Canyon region, Colorado Plateau. Geology 35, 447–450.

Flowers, R.M., Ketcham, R.A., Shuster, D.L., Farley, K.A. 2009. Apatite (U–Th)/He thermochronometry using a radiation damage accumulation and annealing model. Geochimica et Cosmochimica acta 73(8), 2347-2365.

Gallagher, K. 1999. Evolving temperature histories from apatite fission-track data. Earth and Planetary Science Letters 136(3-4), 421-435.

Gautier, P., Brun, J.P. 1994a. Crustal-scale geometry and kinematics of late-orogenic extension in the central Aegean (Cyclades and Ewia Island). Tectonophysics 238(1-4), 399-424.

Gautier, P., Brun, J.P. 1994b. Ductile crust exhumation and extensional detachments in the central Aegean (Cyclades and Evvia Islands). Geodinamica Acta 7(2), 57-85.

Gessner, K., Ring, U., Passchier, C.W., Güngör, T., 2001a. How to resist subduction: Eocene post-high-pressure emplacement of the Cycladic blueschist unit onto the Menderes nappes, Anatolide belt, western Turkey. Geological Society of London Journal 158, 769–780.

Gessner, K., Ring, U., Johnson, C., Hetzel, R., Passchier, C.W., Güngör, T., 2001b. An active bivergent rolling-hinge detachment system: Central Menderes metamorphic core complex in western Turkey. Geology 29, 611–614.

Gessner, K., Collins, A.S., Ring, U., Güngör, T., 2004. Structural and thermal history of poly-orogenic basement: U-Pb geochronology of granitoid rocks in the southern Menderes Massif, Western Turkey. Journal of the Geological Society, London 161, 93–101.

Glodny, J., Hetzel, R., 2007. Precise U-Pb ages of syn-extensional Miocene intrusions in the central Menderes Massif, western Turkey. Geological Magazine 144, 235–246.

Gökten, E., Floyd, P.A. 2007. Stratigraphy and geochemistry of pillow basalts within the ophiolitic mélange of the İzmir–Ankara–Erzincan suture zone: implications for the geotectonic character of the northern branch of Neotethys. International Journal of Earth Sciences 96(4), 725-741.

Gosse, J.C., Phillips, F.M. 2001. Terrestrial in situ cosmogenic nuclides: theory and application. Quaternary Science Reviews 20(14), 1475-1560.

Granger, D.E., Kirchner, J.W., Finkel, R. 1996. Spatially averaged long-term erosion rates measured from in situ-produced cosmogenic nuclides in alluvial sediment. The Journal of Geology 104(3), 249-257.

Grasemann, B., Schneider, D. A., Stöckli, D. F., Iglseder, C. 2012. Miocene bivergent crustal extension in the Aegean: Evidence from the western Cyclades (Greece). Lithosphere, 4(1), 23-39.

Gregory J.W., 1896: The Great Rift Valley. Murray, London, 422.

Guenthner, W.R., Reiners, P.W., Ketcham, R.A., Nasdala, L., Giester, G., 2013. Helium diffusion in natural zircon: Radiation damage, anisotropy, and the interpretation of zircon (U-Th)/He thermochronology. American Journal of Science 313, 145–198.

Gürer, Ö.F., Sarica-Filoreau, N., Özburan, M., Sangu, E., Doğan, B. 2009. Progressive development of the Büyük Menderes Graben based on new data, western Turkey. Geological Magazine 146(5), 652-673.

Haines, S.H., van der Pluijm, B.A., 2008. Clay quantification and Ar–Ar dating of synthetic and natural gouge: application to the Miocene Sierra Mazatán detachment fault, Sonora, Mexico. Journal of Structural Geology 30(4), 525-538.

Hancock, G., Kirwan, M. 2007. Summit erosion rates deduced from 10Be: Implications for relief production in the central Appalachians. Geology 35(1), 89-92.

Hasözbek, A., Satır, M., Erdoğan, B., Akay, E., Siebel, W., 2011. Early Miocene post-collisional magmatism in NW Turkey: geochemical and geochronological constraints. International Geology Review 53(9), 1098–1119.

Hauser, E. C., Gephart, J., Latham, T., Oliver, J., Kaufman, S., Brown, L., & Lucchitta, I. (1987). COCORP Arizona transect: Strong crustal reflections and offset Moho beneath the transition zone. Geology, 15(12), 1103-1106.

Hayward, A.B. 1984. Miocene clastic sedimentation related to the emplacement of the Lycian Nappes and the Antalya Complex, SW Turkey. Geological Society, London, Special Publications 17(1), 287-300.

Hetzel, R., Passchier, C.W., Ring, U., Dora, O.Ö., 1995a. Bivergent extension in orogenic belts: The Menderes Massif (southwestern Turkey). Geology 23, 455–458.

Hetzel, R., Ring, U., Akal, C., Troesch, M., 1995b. Miocene NNE-directed extensional unroofing in the Menderes Massif, southwestern Turkey. Journal of the Geological Society, London 152, 639–654.

Hetzel, R., Reischmann, T., 1996. Intrusion of Pan-African gneisses in the southern Menderes massif and the age of cooling after Alpine ductile extensional deformation. Geological Magazine 133, 565–572.

Hetzel, R., Zwingmann, H., Mulch, A., Gessner, K., Akal, C., Hampel, A., Güngör, T., Petschick, R., Mikes, T., 2013. Spatiotemporal evolution of brittle normal faulting and fluid infiltration in detachment fault systems: A case study from the Menderes Massif, western Turkey. Tectonics 32, 1–13; doi:10.1002/tect.20031.

Huet, B., Labrousse, L., Jolivet, L. 2009. Thrust or detachment? Exhumation processes in the Aegean: Insight from a field study on Ios (Cyclades, Greece). Tectonics 28(3).

Hurford, A. J., Green, P. F. 1982. A users' guide to fission track dating calibration. Earth and Planetary

Science Letters 59(2), 343-354.

Hurford A.J., Green, P.F., 1983. The zeta age calibration of fission-track dating. Chemical Geology 1, 285–317.

Hurford, A.J. 1990. Standardization of fission track dating calibration: Recommendation by the Fission Track Working Group of the IUGS Subcommission on Geochronology. Chemical Geology: Isotope Geoscience Section 80(2), 171-178.

Işik, V., Tekeli, O., 2001. Late orogenic crustal extension in the northern Menderes massif (western Turkey): Evidences for metamorphic core complex formation. International Journal of Earth Sciences 89, 757–765.

Işik, V., Tekeli, O., Seyitoğlu, G., 2004, The ^{40}Ar/^{39}Ar age of extensional ductile deformation and granitoid intrusion in the northern Menderes core complex: implications for the initiation of extensional tectonics in western Turkey. Journal of Asian Earth Sciences 23, 555–566.

Jolivet, L., Brun, J.-P., 2010. Cenozoic geodynamic evolution of the Aegean. International Journal of Earth Sciences 99, 109–138.

Jolivet, L., Lecomte, E., Huet, B., Denéle, Y., Lacombe, O., Labrousse, L., Le Pourhiet, L., Mehl, C., 2010. The North Cycladic Detachment System. Earth and Planetary Science Letters 289, 87–104.

Jolivet, L., Faccenna, C., Huet, B., Labrousse, L., Le Pourhiet, L., Lacombe, O., et al. 2013. Aegean tectonics: Strain localisation, slab tearing and trench retreat. In: The Aegean: a natural laboratory for tectonics - Neotectonics 597-598, S. 1–33. DOI: 10.1016/j.tecto.2012.06.011.

Jolivet, L., Menant, A., Sternai, P., Rabillard, A., Arbaret, L., Augier, R., Laurent, V., Beaudoin, A., Grasemann, B., Huet, B., Labrousse, L. Le Pourhiet, L. (2015). The geological signature of a slab tear below the Aegean. Tectonophysics, 659, 166-182.

Kent, E., Boulton, S.J., Stewart, I.S., Whittaker, A.C., Alçiçek, M C. 2016. Geomorphic and geological constraints on the active normal faulting of the Gediz (Alaşehir) Graben, Western Turkey. Journal of the Geological Society 173(4), 666-678.

Ketcham, R.A., Carter, A., Donelick, R.A., Barbarand, J., Hurford, A.J., 2007. Improved modeling of fission-track annealing in apatite. American Mineralogist 92(5-6), 799-810.

Ketcham, R.A., Gautheron, C., Tassan-Got, L. 2011. Accounting for long alpha-particle stopping distances in (U–Th–Sm)/He geochronology: Refinement of the baseline case. Geochimica et Cosmochimica Acta 75(24), 7779-7791.

Kohn, B., Chung, L., Gleadow, A. 2019. Fission-Track Analysis: Field Collection, Sample Preparation and Data Acquisition. In Malusà M., Fitzgerald P. (eds). Fission-Track Thermochronology and its Application to Geology (pp. 25-48). Springer Textbooks in Earth Sciences, Geography and Environment. Springer, Cham.

Koralay, O.E., Satır, M., Dora, O.Ö., 2001. Geochemical and geochronological evidence for Early Triassic calc-alkaline magmatism in the Menderes Massif, western Turkey. International Journal of Earth Sciences 89, 822–835.

Koralay, O.E., Candan, O., Akal, C., Dora, O.Ö., Chen, F., Satır, M., Oberhänsli, R., 2011. Geology and geochronology of the Pan-African and Triassic metagranitoids in the Menderes Massif, Western Anatolia, Turkey. Bulletin of the Mineral Research and Exploration 142, 69–121.

Koralay, O.E., 2015. Late Neoproterozoic granulite facies metamorphism in the Menderes Massif, Western Anatolia/Turkey: implication for the assembly of Gondwana. Geodinamica Acta 27, 244–266.

Kounov, A., Wüthrich, E., Seward, D., Burg, J.P., Stockli, D. 2015. Low-temperature constraints on the Cenozoic thermal evolution of the Southern Rhodope Core Complex (Northern Greece). International journal of earth sciences 104(5), 1337-1352.

Kydonakis, K., Brun, J.P., Sokoutis, D. 2015. North Aegean core complexes, the gravity spreading of a thrust wedge. Journal of Geophysical Research. Solid Earth 120(1), 595-616.

Lagos, M., Scherer, E.E., Tomaschek, F., Münker, C., Keiter, M., Berndt, J., Ballhaus, C. 2007. High precision Lu–Hf geochronology of Eocene eclogite-facies rocks from Syros, Cyclades, Greece. Chemical Geology 243(1-2), 16-35.

Lal, D. 1991. Cosmic ray labeling of erosion surfaces: in situ nuclide production rates and erosion models. Earth and Planetary Science Letters, 104(2-4) 424-439.

Lippolt, H.J., Wernicke, R.S., Boschmann, W., 1993. 4 He diffusion in specular hematite. Physics and Chemistry of Minerals 20(6), 415-418.

Lips, A.L.W., White, S.H., Wijbrans, J.R. 1998. 40Ar/39Ar laserprobe direct dating of discrete deformational events: a continuous record of early Alpine tectonics in the Pelagonian Zone, NW Aegean area, Greece. Tectonophysics 298(1-3), 133-153.

Lips, A.L.W., Cassard, D., Sözbilir, H., Yilmaz, H., Wijbrans, J.R., 2001. Multistage exhumation of the Menderes Massif, western Anatolia (Turkey). International Journal of Earth Sciences 89, 781–792.

Lister, G.S., Banga, G., Feenstra, A., 1984. Metamorphic core complexes of Cordilleran type in the Cyclades, Aegean Sea, Greece. Geology 12(4), 221–225.

Loos, S., Reischmann, T., 1999. The evolution of the southern Menderes Massif in SW Turkey as revealed by zircon dating. Journal of the Geological Society of London 156, 1021–1030.

Menant, A., Jolivet, L., Vrielynck, B. 2016. Kinematic reconstructions and magmatic evolution illuminating crustal and mantle dynamics of the eastern Mediterranean region since the late Cretaceous. Tectonophysics 675, 103-140.

Meyer, H., Hetzel, R., Strauss, H. 2010. Erosion rates on different timescales derived from cosmogenic 10 Be and river loads: implications for landscape evolution in the Rhenish Massif, Germany. International Journal of Earth Sciences 99(2), 395-412.

Nagel, T.J., Schmidt, S., Janák, M., Froitzheim, N., Jahn-Awe, S., Georgiev, N. 2011. The exposed base of a collapsing wedge: the Nestos shear zone (Rhodope Metamorphic Province, Greece). Tectonics, 30(4).

Nilius, N. P., Glotzbach, C., Wölfler, A., Hampel, A., Dunkl, I., Akal, C., Heineke, C., Hetzel, R. 2019. Exhumation history of the Aydın range and the role of the Büyük Menderes detachment system during bivergent extension of the central Menderes Massif, western Turkey. Journal of the Geological Society, jgs2018-162.

Oberhänsli, R., Candan, O., Dora, O.Ö., Dürr, S., 1997. Eclogites within the Menderes Massif/western Turkey. Lithos 41, 135–150.

Okay, A. I. 2008. Geology of Turkey: a synopsis. Anschnitt 21, 19-42.

Philippon, M., Brun, J.P., Gueydan, F. 2012. Deciphering subduction from exhumation in the segmented Cycladic Blueschist unit (Central Aegean, Greece). Tectonophysics 524, 116-134.

Platt, J.P., Behr, W.M., Cooper, F.J. 2015. Metamorphic core complexes: windows into the mechanics and rheology of the crust. Journal of the Geological Society 172(1), 9-27.

Price, P.B., Walker, R.M. 1963. Fossil tracks of charged particles in mica and the age of minerals. Journal of Geophysical Research 68(16), 4847-4862.

Regnier, J.L., Ring, U., Passchier, C.W., Gessner, K., Güngör, T., 2003. Contrasting metamorphic evolution of metasedimantary rocks from the Çine and Selimiye nappes in the Anatolide belt, western Turkey. Journal of Metamorphic Geology 21, 699–721.

Reiners, P.W., Farley, K.A. 1999. Helium diffusion and (U–Th)/He thermochronometry of titanite. Geochimica et Cosmochimica Acta, 63(22), 3845-3859.

Reiners, P.W., Farley, K.A., Hickes, H.J. 2002. He diffusion and (U–Th)/He thermochronometry of zircon: initial results from Fish Canyon Tuff and Gold Butte. Tectonophysics, 349(1-4), 297-308.

Reiners, P.W., Zhou, Z., Ehlers, T.A., Xu, C., Brandon, M.T., Donelick, R.A., Nicolescu, S., 2003. Post-orogenic evolution of the Dabie Shan, eastern China, from (U-Th)/He and fission track thermochronology. American Journal of Science 303, 489–518.

Reiners, P.W., Spell, T.I., Nicolescu, S., Zanetti, K. 2004. Zircon (U-Th)/He thermochronometry: He diffusion and comparisons with ^{40}Ar/^{39}Ar dating. Geochimica et Cosmochimica Acta 68, 1857–1887.

Reiners, P.W., 2005. Zircon (U-Th)/He thermochronometry. Reviews in Mineralogy and Geochemistry 58, 151–179.

Reiners, P.W., Brandon, M.T., 2006. Using thermochronology to understand orogenic erosion. Annual Review of Earth and Planetary Sciences 34, 419–466.

Ring, U., Gessner, K., Güngör, T., Passchier, C.S., 1999. The Menderes Massif of western Turkey and the Cycladic Massif in the Aegean – do they really correlate? Journal of the Geological Society, London 156, 3–6.

Ring, U., Willner, A., Lackmann, W., 2001. Nappe stacking with different pressure-temperature paths: An example from the Menderes nappes of western Turkey. American Journal of Science 301, 912–944.

Ring, U., Johnson, C., Hetzel, R., Gessner, K., 2003. Tectonic denudation of a Late Cretaceous-Tertiary collisional belt: regionally symmetric cooling patterns and their relation to extensional faults in the Anatolide belt of western Turkey. Geological Magazine 140, 421–441.

Ring, U., Collins, A.S., 2005. U–Pb SIMS dating of synkinematic granites: timing of core-complex formation in the northern Anatolide belt of western Turkey. Journal of the Geological Society 162(2), 289–298.

Ring, U., Will, T., Glodny, J., Kumerics, C., Gessner, K., Thomson, S., Güngör, T., Monie, P., Okrusch, M., Drüppel, K. 2007. Early exhumation of high-pressure rocks in extrusion wedges: Cycladic blueschist unit in the eastern Aegean, Greece, and Turkey. Tectonics 26(2).

Rosenbaum, G., Regenauer-Lieb, K., Weinberg, R. 2005. Continental extension: From core complexes to rigid block faulting. Geology 33(7), 609-612.

Rutherford, E., 1905. Present problems in radioactivity. Popular Science Monthly, May, 1–34.

Rutherford, E., 1907. Some cosmical aspects of radioactivity. Journal of the Royal Astronomical Society of Canada, 145–165.

Schmid, S.M., Bernoulli, D., Fügenschuh, B., Matenco, L., Schefer, S., Schuster, R., Tischler, M., Ustaszewski, K. 2008. The Alpine-Carpathian-Dinaridic orogenic system: correlation and evolution of tectonic units. Swiss Journal of Geosciences 101(1), 139-183.

Schmidt, A., Pourteau, A., Candan, O., Oberhänsli, R., 2015. Lu-Hf geochronology on cm-sized garnets using microsampling: New constraints on garnet growth rates and duration of metamorphism during continental collision (Menderes Massif, Turkey). Earth and Planetary Science Letters 432, 24–35.

Schneider, D.A., Grasemann, B., Lion, A., Soukis, K., Draganits, E. 2018. Geodynamic significance of the Santorini Detachment System (Cyclades, Greece). Terra Nova, 30(6), 414-422.

Schwarz, G., 1978. Estimating the dimension of a model. The annals of statistics 6(2), 461–464.

Sherlock, S., Kelley, S., Inger, S., Harris, N., Okay, A. 1999. 40 Ar-39 Ar and Rb-Sr geochronology of high-pressure metamorphism and exhumation history of the Tavsanli Zone, NW Turkey. Contributions to Mineralogy and Petrology 137(1-2), 46-58.

Şengör, A.M.C., Yilmaz, Y., 1981. Tethyan evolution of Turkey: a plate tectonic approach. Tectonophysics, 75(3-4) 181-241.

Soddy, F., 1911-1914. Chemistry of the radio-elements; Parts I and II, London, Longmans, Green & Co.

Sotiropoulos, S., Kamberis, E., Triantaphyllou, M. V., Doutsos, T. 2003. Thrust sequences in the central part of the External Hellenides. Geological Magazine 140(6) 661-668.

Stampfli, G.M., Borel, G.D. 2002. A plate tectonic model for the Paleozoic and Mesozoic constrained by dynamic plate boundaries and restored synthetic oceanic isochrons. Earth and Planetary Science Letters 196(1-2), 17-33.

Stampfli, G.M., Hochard, C. 2009. Plate tectonics of the Alpine realm. Geological Society, London, Special Publications 327(1), 89-111.

Tagami, T., O'Sullivan, P.B. 2005. Fundamentals of fission-track thermochronology. Reviews in Mineralogy and Geochemistry 58(1), 19-47.

Thomson, S.N., Ring, U., 2006. Thermochronologic evaluation of postcollision extension in the Anatolide orogen, western Turkey. Tectonics 25, TC3005, doi:10.1029/2005TC001833.

Tirel, C., Gautier, P., Van Hinsbergen, D.J.J., Wortel, M.J.R. 2009. Sequential development of interfering metamorphic core complexes: numerical experiments and comparison with the Cyclades, Greece. Geological Society, London, Special Publications, 311(1), 257-292.

Ustaszewski, K., Kounov, A., Schmid, S.M., Schaltegger, U., Krenn, E., Frank, W., Fügenschuh, B. 2010. Evolution of the Adria-Europe plate boundary in the northern Dinarides: From continent-continent collision to back-arc extension. Tectonics 29(6).

van Hinsbergen, D.J., Dupont-Nivet, G., Nakov, R., Oud, K., Panaiotu, C. 2008. No significant post-Eocene rotation of the Moesian Platform and Rhodope (Bulgaria): implications for the kinematic evolution of the Carpathian and Aegean arcs. Earth and Planetary Science Letters 273(3-4), 345-

358.

van Hinsbergen, D.J., 2010. A key extensional metamorphic complex reviewed and restored: the Menderes Massif of western Turkey. Earth-Science Reviews 102(1-2), 60-76.

van Hinsbergen, D.J.J., Schmid, S.M. 2012. Map view restoration of Aegean–West Anatolian accretion and extension since the Eocene. Tectonics 31, TC5005.

van der Pluijm, B.A., Hall, C.M., Vrolijk, P. J., Pevear, D. R., Covey, M.C. 2001. The dating of shallow faults in the Earth's crust. Nature 412(6843), 172.

von Blanckenburg, F. 2006. The control mechanisms of erosion and weathering at basin scale from cosmogenic nuclides in river sediment. Earth and Planetary Science Letters 242(3-4), 224-239.

Vrolijk, P., van der Pluijm, B. A., 1999. Clay gouge. Journal of structural Geology 21(8-9), 1039-1048.

Wernicke, B. 1981. Low-angle normal faults in the Basin and Range Province: nappe tectonics in an extending orogen. Nature 291(5817), 645.

Wernicke, B., Axen, G.J. 1988. On the role of isostasy in the evolution of normal fault systems. Geology 16(9), 848-851.

Whitney, D.L., Teyssier, C., Toraman, E., Seaton, N.C.A., Fayon, A.K. 2011. Metamorphic and tectonic evolution of a structurally continuous blueschist-to-Barrovian terrane, Sivrihisar Massif, Turkey. Journal of Metamorphic Geology 29(2), 193-212.

Whitney, D.L., Teyssier, C., Rey, P., Buck, W.R. 2013. Continental and oceanic core complexes. Bulletin 125(3-4), 273-298.

Wijns, C., Weinberg, R., Gessner, K., Moresi, L. 2005. Mode of crustal extension determined by rheological layering. Earth and Planetary Science Letters, 236(1-2) 120-134.

Wolf, R.A., Farley, K.A., Silver, L.T., 1996. Helium diffusion and low temperature thermochronology of apatite. Geochimica et Cosmochimica Acta 60, 4231–4240.

Wolf, R.A., Farley, K.A. Kass, D.M., 1998. Modeling of the temperature sensitivity of the apatite (U-Th)/He thermochronometer. Chemical Geology 148, 105–114.

Wölfler, A., Glotzbach, C., Heineke, C., Nilius, N.P., Hetzel, R., Hampel, A., Akal, C., Dunkl, I., Christl, M., 2017. Late Cenozoic cooling history of the central Menderes Massif: Timing of the Büyük Menderes detachment and the relative contribution of normal faulting and erosion to rock exhumation. Tectonophysics 717, 585-598.

Zeitler, P.K., Herczeg, A.L., McDougall, I., Honda, M., 1987. U-Th-He dating of apatite: A potential thermochronometer. Geochimica et Cosmochimica Acta 51, 2865–2868.

Zwingmann, H., Mancktelow, N., 2004. Timing of Alpine fault gouges. Earth and Planetary Science Letters 223(3-4), 415-425.

Zwingmann, H., Mancktelow, N., Antognini, M., Lucchini, R., 2010. Dating of shallow faults: New constraints from the AlpTransit tunnel site (Switzerland). Geology 38(6), 487-490.

2. Late Cenozoic cooling history of the central Menderes Massif: Timing of the Büyük Menderes detachment and the relative contribution of normal faulting and erosion to rock exhumation

Andreas Wölfler[a], Christoph Glotzbach[a,b], Caroline Heineke [c] , Nils-Peter Nilius[a], Ralf Hetzel [c], Andrea Hampel [a], Cüneyt Akal [d], István Dunkl[e], Marcus Christl [d],

[a] Institut für Geologie, Leibniz Universität Hannover, Callinstraße 30, D-30167 Hannover, Germany, nilius@geowi.uni-hannover.de, hampel@geowi.uni-hannover.de

[b] Institut für Geologie und Geodynamik, Universität Tübingen, Wilhelmstraße 56, D-72074 Tübingen, Germany, christoph.glotzbach@uni-tuebingen.de

[c] Institut für Geologie und Paläontologie, Westfälische Wilhelms-Universität Münster, Corrensstraße 24, D-48149 Münster, Germany, rahetzel@uni-muenster.de

[d] Dokuz Eylül University, Engineering Faculty, Department of Geological Engineering, Tınaztepe Campus, Buca, TR-35160 Izmir, Turkey, cuneyt.akal@deu.edu.tr

[e] University of Göttingen, Geoscience Center, Sedimentology and Environment Geology. Goldschmidstraße 3, 37077 Göttingen, Germany

[e] Laboratory of Ion Beam Physics, ETH Zurich, Otto-Stern-Weg 5, HPK G23, 8093 Zurich, Switzerland

Own contribution: Fieldwork, Preparation of figures and cross-sections of figure 2c,d.

Late Cenozoic cooling history of the central Menderes Massif: Timing of the Büyük Menderes detachment and the relative contribution of normal faulting and erosion to rock exhumation

Andreas Wölfler [a,*], Christoph Glotzbach [a,b], Caroline Heineke [c], Nils-Peter Nilius [a], Ralf Hetzel [c], Andrea Hampel [a], Cüneyt Akal [d], István Dunkl [e], Marcus Christl [f]

[a] Institute of Geology, Leibniz University of Hannover, Callinstraße 30, 30167 Hannover, Germany
[b] Department of Geoscience, University of Tübingen, Wilhelmstraße 56, 72074 Tübingen, Germany
[c] Institute of Geology and Palaeontology, University of Münster, Corrensstraße 24, 48149 Münster, Germany
[d] Dokuz Eylül University, Engineering Faculty, Department of Geological Engineering, Tınaztepe Campus, Buca, 35160, Izmir, Turkey
[e] University of Göttingen, Geoscience Center, Sedimentology and Environment Geology, Goldschmidstraße 3, 37077 Göttingen, Germany
[f] Laboratory of Ion Beam Physics, ETH Zurich, Otto-Stern-Weg 5, HPK G23, 8093 Zurich, Switzerland

ARTICLE INFO

ABSTRACT

Based on new thermochronological data and [10]Be-derived erosion rates from the southern part of the central Menderes Massif (Aydın block) in western Turkey, we provide new insights into the tectonic evolution and landscape development of an area that undergoes active continental extension. Fission-track and (U-Th)/He data reveal that the footwall of the Büyük Menderes detachment experienced two episodes of enhanced cooling and exhumation. Assuming an elevated geothermal gradient of ~50 °C/km, the first phase occurred with an average rate of ~0.90 km/Myr in the middle Miocene and the second one in the latest Miocene and Pliocene with a rate of ~0.43 km/Myr. The exhumation rates between these two phases were lower and range from ~0.14 to ~0.24 km/Myr, depending on the distance to the detachment. Cosmogenic nuclide-based erosion rates for catchments in the Aydın block range from ~0.1 to ~0.4 km/Myr. The similarity of the erosion rates on both sides of the Aydın block (northern and southern flank) indicate that a rather symmetric erosion pattern has prevailed during the Holocene. If these millennial erosion rates are representative on a million-year timescale they indicate that, apart from normal faulting, erosion in the hanging wall of the Büyük Menderes detachment fault did also contribute to the exhumation of the metamorphic rocks.

© 2017 Elsevier B.V. All rights reserved.

1. Introduction

Low-angle normal faults play a crucial role for the exhumation of metamorphosed rocks from mid-crustal levels and usually form during late-orogenic extension (e.g. Dewey, 1988). Extensional settings have been intensively studied all over the world including the Basin-and-Range Province (e.g. Wernicke et al., 1988; Lister and Davis, 1989), the European Alps (e.g. Mancktelow, 1992; Selverstone, 1988; Campani et al., 2010; Scharf et al., 2013a) and the Aegean region (e.g. Lee and Lister, 1992; Gautier and Brun, 1994; Ring et al., 1999a; Brichau et al., 2006; Grasemann et al., 2012). The rapid cooling of metamorphic rocks exposed in these regions has commonly been interpreted to indicate that erosion has played a minor role to rock exhumation. However, the relative contribution of tectonic denudation and erosion to rock

exhumation has rarely been quantified (e.g. Brichau et al., 2008; Buscher et al., 2013).

In the past decades, low-temperature thermochronology has proven to be a powerful tool to determine the cooling and exhumation history of rocks exhumed by detachment faulting (e.g. Dokka et al., 1986; Fitzgerald et al., 1991; Axen et al., 2000; Armstrong et al., 2003; Reiners and Ehlers, 2005). By using multiple thermochronometers with different closure temperatures, cooling paths can be constrained and converted into exhumation rates, provided the geo-thermal gradient can be satisfactorily approximated. To quantify rates of erosion, cosmogenic nuclides such as [10]Be can be used (Lal, 1991; Granger et al., 1996; von Blanckenburg, 2006). A combination of these methods allows resolving both the relative contribution of tectonic denudation and erosion to exhumation (e.g. Buscher et al., 2013). Since each method has a typical timescale over which it integrates, the multi-method approach is essential to gain quantitative insights into landscape evolution across different timescales.

We conducted this study in the central Menderes Massif, an active extensional region in western Turkey (Fig. 1), which provides excellent exposures, including spectacular detachment faults, and quartz-bearing metamorphic rocks enabling the determination of [10]Be-based erosion rates. The metamorphic rocks of the central Menderes Massif are bound by two E-W-striking low-angle detachment faults: the Gediz detachment in the northern part of the Bozdağ block and the Büyük Menderes detachment in the southern part of the Aydın block (Fig. 1). Based on structural investigations and a limited set of apatite fission track ages it has been proposed that these two detachment faults were active during bivergent extension, which controlled the exhumation of the central Menderes Massif (Gessner et al., 2001a; Ring et al., 2003). A recent study

by Buscher et al. (2013) combined several thermochronometers and cosmogenic nuclides to decipher the cooling and exhumation history of the metamorphic rocks in the Boz Dağ region in more detail (Fig. 1a). In contrast, the exhumation pattern of the Aydın block is only documented by a limited set of thermochronometers (Gessner et al., 2001a). Hence, to understand the history of faulting and bivergent extension in more detail, better temporal constraints on the exhumation of the Aydın block as well as on the timing of the Büyük Menderes detachment faulting are required. Here we present new apatite and zircon (U-Th)/He and fission-track ages as well as cosmogenic [10]Be data to place constraints on the cooling and erosion history of the Aydın block.
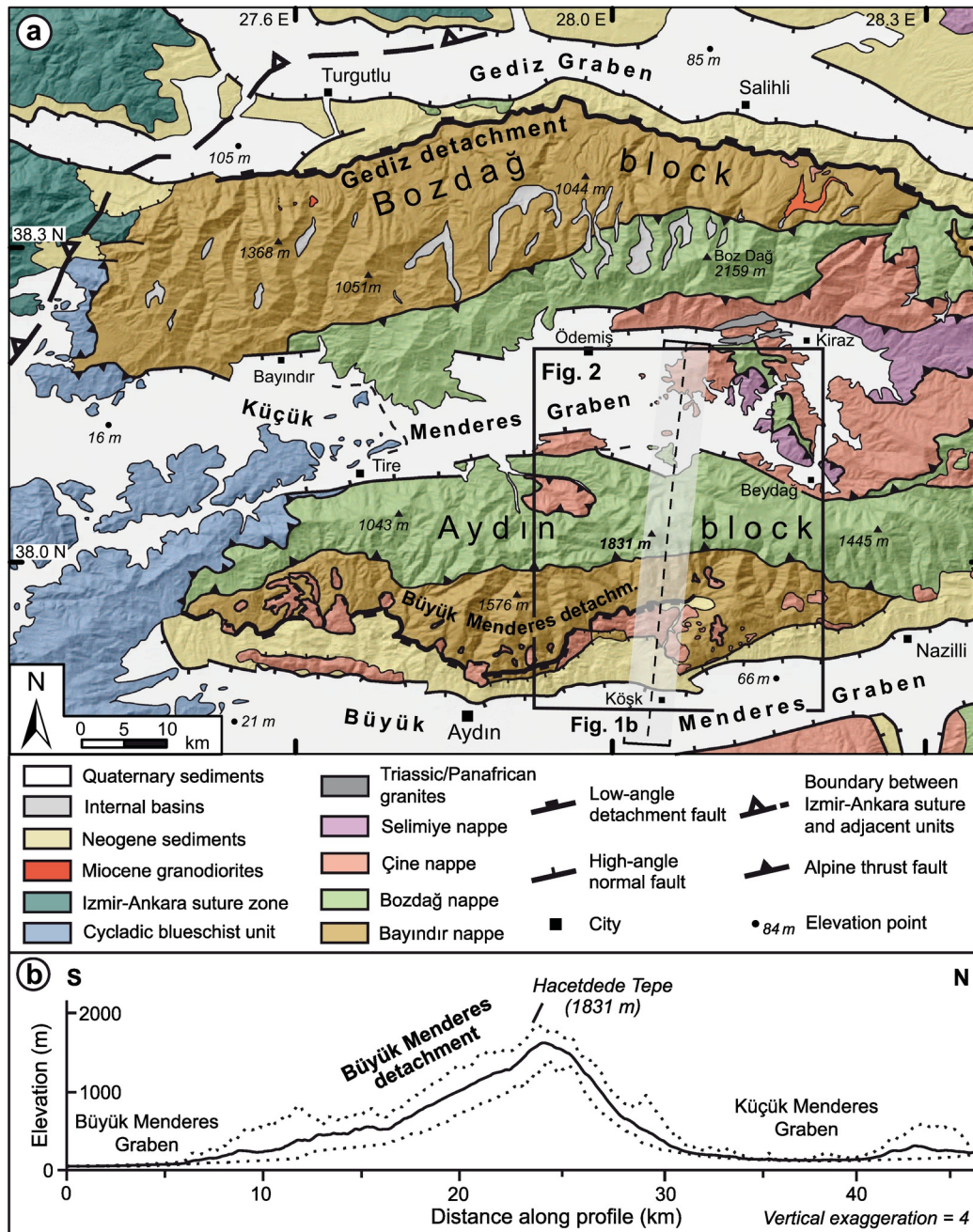
Fig. 1. (a) Geological map of the central Menderes Massif, western Turkey (compiled from Candan et al., 1992; Hetzel et al., 1995a; Hetzel et al., 1998; Gessner et al., 2001b; Özer and Sözbilir, 2003; Gürer et al., 2009; Candan et al., 2011; Koralay et al., 2011; Sözbilir et al., 2011; Gessner et al., 2013 and own field observations). (b) Swath profile across the Aydın block and the eastern Küçük Menderes Graben. Location is shown in (a). Note the topographic asymmetry of the Aydın block with the relative steep northern flank and the shallow-dipping Büyük Menderes detachment on its southern flank.

2. Geological setting of the central Menderes Massif

The Menderes Massif consists of a northern, central, and southern submassif, which are separated by tectonically active E-W trending graben systems (e.g. Seyitoğlu and Scott, 1991; Yılmaz et al., 2000; Bozkurt and Sözbilir, 2004). The central Menderes Massif can be divided into the northern Bozdağ and the southern Aydın block, which are separated by the Küçük Menderes Graben and bound by the Gediz and Büyük Menderes grabens in the north and south, respectively (Fig. 1). The main normal faults of the Gediz and Büyük Menderes grabens separate Neogene sediments in the footwalls from Quaternary sediments in the hanging walls (Çiftçi and Bozkurt, 2010; Gessner et al., 2013). Both graben-bounding faults are seismically active and have produced surface-rupturing earthquakes in 1899 and 1969 (Schaffer, 1900; Ambraseys, 1971; Eyidoğan and Jackson, 1985). The Küçük Menderes Graben is bound by steeply dipping normal faults, which were mainly active in the Pliocene and Quaternary (Rojay et al., 2005; Sümer, 2015). Although Miocene sediments are documented, the graben mainly developed in the Pliocene and Quaternary but has not experienced as much as extension as recorded in the Gediz and Büyük Menderes grabens (Gessner et al., 2001a; Gessner et al., 2013; Rojay et al., 2005).

The metamorphic rocks of the Menderes Massif consist of a nappe pile that formed by thrusting and crustal thickening during the Eocene (Şengör et al., 1984; Ring et al., 1999b; Ring et al., 2001; Regnier et al., 2003; Gessner et al., 2013). Available isotopic age data indicate that upper greenschist- to lower amphibolate-facies conditions occurred during Alpine metamorphism in late Eocene and Oligocene (Satir and Friedrichsen, 1986; Hetzel and Reischmann, 1996; Lips et al., 2001; Ring et al., 2003; Schmidt et al., 2015), although some rock units also experienced older, pre-Alpine phases of metamorphism (e.g. Bozkurt and Oberhänsli, 2001; Candan et al., 2001; Candan et al., 2011; Koralay, 2015). Here we use the tectonic subdivision of the Menderes Massif into four nappes, which was proposed by Gessner et al. (1998) and Ring et al. (1999b). According to these authors the nappe stack includes, from top to bottom, (1) the Selimiye nappe, (2) the Çine nappe, (3) the Bozdağ nappe, and (4) the Bayındır nappe (Figs. 1, 2). The Selimiye nappe mainly contains Paleozoic metapelites, metabasites, and marbles (e.g. Loos and Reischmann, 1999; Regnier et al., 2003; Gessner et al., 2004). The Çine nappe is made up of orthogneisses with intrusion ages of 560–530 Ma, metagranites, pelitic gneisses, and minor amphibolites and eclogites (e.g. Hetzel and Reischmann, 1996; Oberhänsli et al., 1997; Hetzel et al., 1998; Gessner et al., 2004; Zlatkin et al., 2012). The Bozdağ nappe mainly consists of mica schists and minor amounts of marbles and amphibolites (e.g. Koralay et al., 2001; Gessner et al., 2004; Candan et al., 2011). The metamorphic rocks of the Çine and Bozdağ nappes have Precambrian protolith ages (e.g. Candan et al., 2011; Gessner et al., 2001b; Gessner et al., 2004) and experienced high-grade metamorphism in Precambrian times (e.g. Bozkurt and Oberhänsli, 2001; Candan et al., 2001; Candan et al., 2011; Koralay, 2015). The Bayındır nappe contains mica schists, quarzites, phyllites, and marbles that were affected by greenschist-facies metamorphism in the Eocene (Lips et al., 2001; Özer and Sözbilir, 2003; Çemen et al., 2006). Fossils discovered in these marbles near the Büyük Menderes Graben document a Cretaceous depositional age and subsequent metamorphism during the Alpine orogenesis (Özer and Sözbilir, 2003).

Previous studies based on low-temperature thermochronology revealed a two-stage cooling history of the Menderes Massif (Gessner et al., 2001a; Ring et al., 2003; Işık et al., 2004; Thomson and Ring, 2006). The first stage occurred in the late Oligocene and early Miocene, when rocks of the northern and southern submassifs cooled to near-surface temperatures of ~110 °C (Ring et al., 2003; Thomson and Ring, 2006). The second stage is related to the late Miocene to Pliocene exhumation of the central Menderes Massif, which was driven by N-S to NNE-SSW directed extension along the Gediz and Büyük Menderes detachment faults (Fig. 1a) (e.g. Hetzel et al., 1995a, 1995b; Emre and Sözbilir, 1997; Gessner et al., 2001a; Bozkurt and Sözbilir, 2004).

The Gediz detachment dips about 15° to the NNE with a stretching lineation in the underlying mylonites plunging gently to the NNE (Hetzel et al., 1995a; Emre, 1996; Işık et al., 2003). The detachment was active from the middle Miocene until the Pliocene or possibly the early Quaternary (Buscher et al., 2013). The Büyük Menderes detachment is exposed along the southern flank of the central Menderes Massif (Figs. 1–3) as a mainly cataclastic shear zone with a dip of 0–15° and a top-to-the-S to SSW sense of movement (Gessner et al., 2001a) (Fig. 2c, d). So far, only a few apatite fission-track ages document early Miocene cooling of hanging wall units and late Miocene cooling of footwall units of the Büyük Menderes detachment, respectively (Gessner et al., 2001a; Ring et al., 2003).

The study area is located in the Aydın block, which exposes all four metamorphic nappes described above (Figs. 1, 2). The Aydın block is characterized by a pronounced topographic asymmetry, with a steep northern flank facing the Küçük Menderes Graben and a gently-dipping southern flank dominated by the Büyük Menderes detachment (Fig. 1b). The metamorphic rocks are overlain by faulted and northward tilted Neogene fluvio-lacustrine sediments (Figs. 1, 2) with northward dips of 15° to 30° (Fig. 2c). The oldest strata of the Neogene sediments are early to middle Miocene in age (Seyitoğlu and Scott, 1991; Sen and Seyitoğlu, 2009). The sediments are locally folded and overlain by undeformed Pliocene to Pleistocene sediments (Bozkurt, 2000, 2001). Historical earthquakes and geomorphological indicators such as well-preserved fault scarps document that the steep normal faults bounding the Büyük Menderes Graben to the north are still active (Fig. 2; Schaffer, 1900; Gürer et al., 2009). Active normal faulting on these steep faults is locally accompanied by hydrothermal activity and hot springs with temperatures of up to 100 °C (Karamanderesi and Helvacı, 2003).

3. Methods, sampling and sample preparation

3.1. Zircon and apatite fission-track analysis

We used the zircon and apatite fission-track (ZFT, AFT) methods, whose temperature sensitivity intervals are referred to as ZFT and AFT partial annealing zones, ranging from 380 to 190 °C and 120 to 60 °C, respectively (e.g. Wagner and van den Haute, 1992; Green et al., 1986; Rahn et al., 2004). Although closure temperatures can vary depending on factors such as cooling rate, chemistry, and accumulated radiation damage, typical closure temperatures for ZFT and AFT samples are ~240 °C and ~110 °C, respectively (Wagner and van den Haute, 1992; Gleadow and Duddy, 1981).

For fission-track analysis, we collected a total of 18 samples. Sample locations, lithologies, and structural positions are given in Fig. 2 and Table 1. Twelve samples are from the southern flank of the Aydın block (14M30–14M41). Eight of these samples are from the footwall of the Büyük Menderes detachment while the remaining four are from small augen gneiss klippen (i.e. remnants of the Çine nappe) in the hanging wall (Table 1). Five samples were taken from the northern flank of the Aydın block and one (14M23) from an augen gneiss unit exposed in the eastern Küçük Menderes Graben (Fig. 2a).

Zircon and apatite grains were separated using conventional magnetic and heavy liquid separation techniques and embedded in PDA Teflon™ and epoxy, respectively, grounded and polished. Zircon mounts were etched in a KOH-NaOH eutectic melt at 215 °C (Zaun and Wagner, 1985); the apatites were etched with 5 M HNO_3 for 20 s at 21 °C (Donelick et al., 1999). The samples were irradiated with thermal neutrons at the FRM-II reactor facility in Garching (Technical University Munich, Germany). Fission-track counting was carried out with an Olympus BX-51 microscope under 1000× magnification at the Institute of Geology in Hannover. We used the external detector method (Gleadow, 1981) with uranium-free muscovite sheets and the zeta calibration approach (e.g. Naeser, 1978; Hurford and Green, 1983) with dosimeter glass IRMM-540R and IRMM-541 and Durango apatite and Fish Canyon zircon age standards. For the assessment of annealing
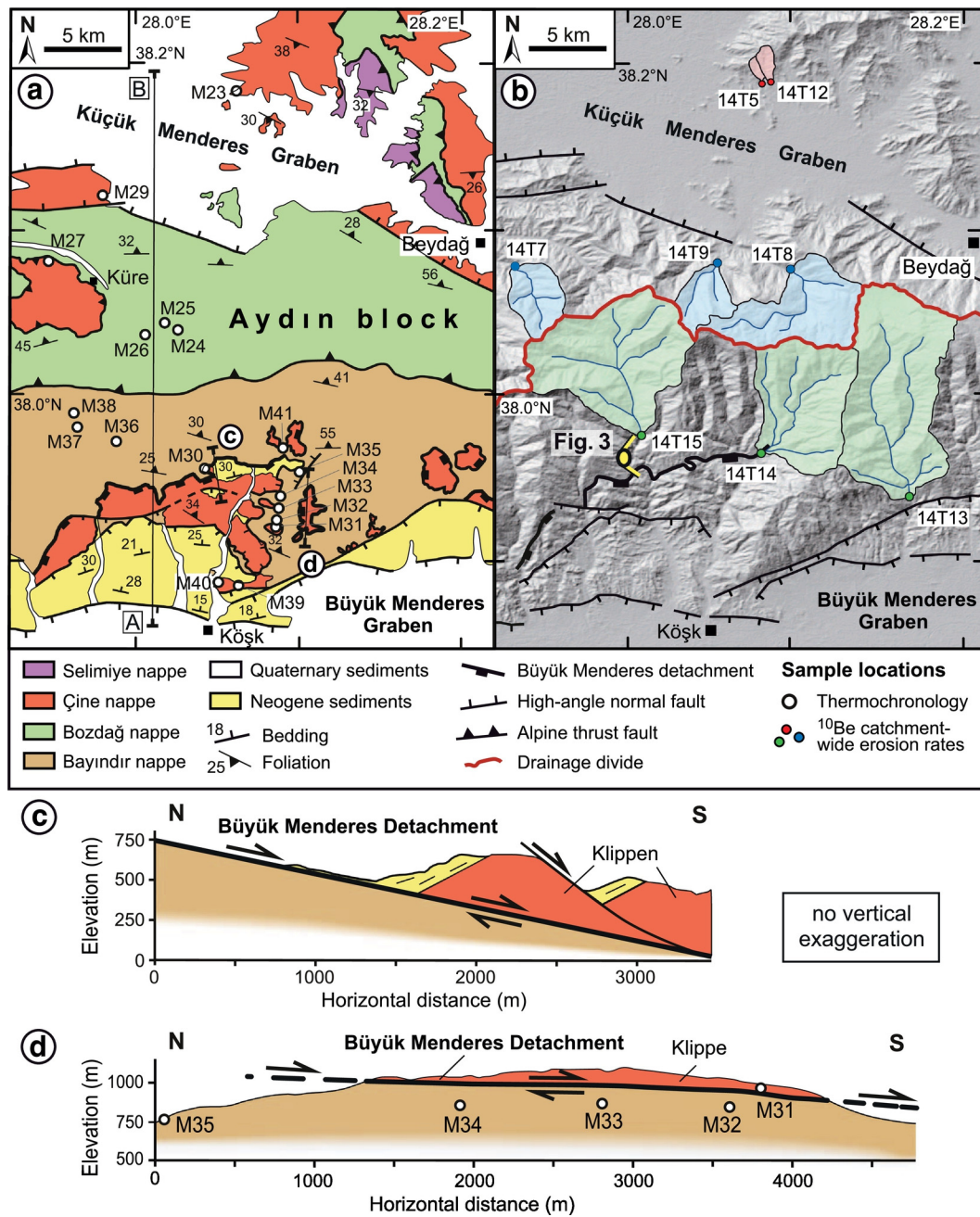
Fig. 2. (a, b) Geological map and shaded relief image of the study area north of Köşk. Note that both figures cover exactly the same region. The locations of the thermochronological samples are shown in the geological map (note that the first two numbers of the sample IDs (i.e. 14) are omitted for clarity). Rectangles with letters A and B denote the trace of the profile in Fig. 5. Bold letters in white circles (c and d) refer to the cross sections depicted below. The map is based on Candan et al., 1992; Emre and Sözbilir, 1997; Gürer et al., 2009; Hetzel et al., 1998; Özer and Sözbilir, 2003; Emre and Sözbilir, 2007; Candan et al., 2011; Koralay et al., 2011 and own field observations. The sampling sites for ¹⁰Be-derived erosion rates and the respective catchments are indicated in the shaded-relief image. The yellow symbol near sample 14T15 indicates the view shown in the field photograph of Fig. 3. (c) N-S profile across the Büyük Menderes detachment. (d) Cross-section showing the flat-lying Büyük Menderes detachment. Sample 14M31 is from augen gneisses that occur in the hanging wall of the Büyük Menderes detachment.

Fig. 3. Photograph of the Büyük Menderes detachment (for location see Fig. 2b). Black arrows delineate the detachment fault. Coordinates of viewpoint: 37.9584°N, 28.0000°E.

kinetics in apatites we used Dpar values (mean diameter of etch figures on prismatic surfaces of apatite parallel to the crystallographic c-axis) (Burtner et al., 1994). The mean track lengths from horizontal confined tracks were corrected for c-axis orientation (Donelick et al., 1999). Fission-track ages were calculated with the TRACKKEY software version 4.2 (Dunkl, 2002) and are reported in Tables 2 and 3 with 1σ errors.

3.2. Zircon and apatite (U-Th)/He analysis

Zircon and apatite (U-Th)/He thermochronology (ZHe, AHe) is based on the accumulation of radiogenic helium produced by the α-

Table 1
Location, lithology, and structural position of samples for low-temperature thermochronology.

Sample	Latitude (°N) (WGS 84)	Longitude (°E) (WGS 84)	Elevation (m)	Lithology	Structural position	Thermochronometers applied
14M23	38.1841	28.0610	135	Augen gneiss	Çine nappe	AHe, AFT, ZHe
14M24	38.0392	28.0265	1600	Paragneiss	Bozdağ nappe, footwall of Büyük Menderes detachment	AFT, ZHe
14M25	38.0438	28.0186	1187	Paragneiss	Bozdağ nappe, footwall of Büyük Menderes detachment	AFT, ZHe
14M26	38.0361	28.0066	887	Paragneiss	Bozdağ nappe, footwall of Büyük Menderes detachment	AFT, ZHe
14M27	38.0814	27.9482	556	Augen gneiss	Çine nappe	AFT, ZHe
14M29	38.1207	27.9806	177	Augen gneiss	Çine nappe	AHe, AFT, ZHe, ZFT
14M30	37.9553	28.0443	671	Augen gneiss	Çine nappe, hanging wall of Büyük Menderes detachment	AFT, ZHe
14M31	37.9227	28.0861	829	Augen gneiss	Çine nappe, hanging wall of Büyük Menderes detachment	AHe, AFT, ZHe, ZFT
14M32	37.9241	28.0864	830	Mica schist	Bayındır nappe, footwall of Büyük Menderes detachment	AFT, ZHe, ZFT
14M33	37.9310	28.0876	849	Mica schist	Bayındır nappe, footwall of Büyük Menderes detachment	AFT
14M34	37.9387	28.0884	831	Mica schist	Bayındır nappe, footwall of Büyük Menderes detachment	AHe, AFT, ZHe
14M35	37.9537	28.1034	766	Mica schist	Bayındır nappe, footwall of Büyük Menderes detachment	AHe, AFT, ZHe
14M36	37.9721	27.9892	846	Mica schist	Bayındır nappe, footwall of Büyük Menderes detachment	AFT, ZHe, ZFT
14M37	37.9803	27.9663	1087	Mica schist	Bayındır nappe, footwall of Büyük Menderes detachment	AHe, AFT, ZHe
14M38	37.9892	27.9641	1167	Mica schist	Bayındır nappe, footwall of Büyük Menderes detachment	AFT
14M39	37.8846	28.0630	287	Augen gneiss	Çine nappe, hanging wall of Büyük Menderes detachment	AFT, ZHe
14M40	37.8862	28.0476	181	Augen gneiss	Çine nappe, hanging wall of Büyük Menderes detachment	AHe, AFT
14M41	37.9682	28.0899	406	Mica schist	Bayındır nappe, footwall of Büyük Menderes detachment	AFT, ZHe

decay of ^{238}U, ^{235}U, ^{232}Th, and ^{147}Sm (e.g. Zeitler et al., 1987; Lippolt et al., 1994; Farley, 2002; Reiners et al., 2003). The temperature intervals at which helium diffusion approaches production (by alpha decay) is referred to as zircon and apatite helium partial retention zones with temperature ranges from 190 to 120 °C and 80 to 60 °C, respectively (Wolf et al., 1996, 1998; Farley, 2000; Reiners et al., 2003). The typical closure temperatures are 180 °C and 70 °C for the ZHe and AHe systems, respectively (Ehlers and Farley, 2003; Reiners et al., 2004; Reiners and Brandon, 2006; Flowers et al., 2007; Herman et al., 2007; Guenthner et al., 2013).

We employed (U-Th)/He dating on samples that yielded apatites and zircons of sufficient quality (Table 1). Apatite and zircon crystals were hand-picked using a stereo- and polarizing microscope and selected under 200× magnification following the selection criteria of Farley (2002) and Reiners (2005). The dimension of the selected crystals was measured to determine alpha-ejection correction factors (Farley et al., 1996). Single crystals were loaded into pre-cleaned Pt tubes for He analysis carried out at the GÖochron Laboratory at the University of Göttingen (Germany). Extraction of helium from crystals was performed by heating the encapsulated grains in vacuum using an IR laser. The extracted gas was purified by an SAES Ti-Zr getter and the He content was measured by a Hiden Hal-3F/PIC triple-filter quadrupole mass spectrometer. For measurements of the alpha-emitting elements U, Th, and Sm, the crystals were dissolved and spiked with calibrated ^{233}U, ^{230}Th, and ^{149}Sm solutions. Zircons were dissolved in Teflon bombs with 48% HF and 65% HNO_3 at 220 °C for five days. Apatites were dissolved in 2% ultrapure HNO_3 (+0.05% HF) in an ultrasonic bath. The actinide and Sm concentrations were measured by inductively coupled plasma mass spectrometry using the isotope dilution method with a Perkin Elmer Elan DRC II system equipped with an APEX microflow nebulizer. Errors for the single-grain ZHe and AHe analyses are

attributed to uncertainties in the He, U, Th, and Sm measurements and the estimated uncertainty of the Ft correction factor. The zircon and apatite (U-Th)/He ages were calculated as unweighted mean ages from the single-grain ages of each sample and are reported in Tables 4 and 5 with an uncertainty of 2 standard errors.

3.3. Catchment-wide erosion rates from cosmogenic ^{10}Be

Spatially averaged erosion rates of river catchments can be determined from the ^{10}Be concentration in sand samples taken from active streams (e.g. Granger et al., 1996; von Blanckenburg, 2006). This approach assumes that the sediment in the stream channels is well mixed, that erosion is uniform through time, and that nuclide production in the catchment equals the outflux of nuclides via erosion and radioactive decay (e.g. Bierman and Steig, 1996).

To quantify spatially integrated erosion rates in the study area, we took stream sediment samples at the outlets of eight catchments that range in size between 1 and 102 km^2 (Fig. 2). Three samples were collected from streams draining the south-facing slope of the Aydın block, whereas three samples were taken from catchments that drain northwards into the Küçük Menderes graben (Fig. 2). The bedrock in these six catchments is dominated by greenschist- to amphibolite-facies mica schists, which constitute the main lithology in the Bozdağ and Bayındır nappes in this part of the Aydın block. We note that the three southern samples were taken relatively far upstream along the respective rivers to ensure that rocks of the Çine nappe are absent in these catchments. We also collected two samples from small ephemeral streams at the eastern end of the Küçük Menderes Graben (Fig. 2). These two catchments are entirely located in coarse-grained augen gneisses of the Çine nappe. In general, the position of all sampling

Table 2
Results of zircon fission track analyses.

Sample	Number of grains	ρs	Ns	ρi	Ni	ρd	Nd	P($χ^2$) (%)	Dispersion	Central age ± 1σ (Ma)	U (ppm)
14M29	20	75.474	717	92.737	881	6.815	2583	10	0.13	**30.3 ± 2.1**	607
14M31	20	75.225	835	96.757	1074	6.814	2583	8	0.13	**29.0 ± 1.9**	585
14M32	20	75.714	583	111.299	857	6.814	2583	61	0.04	**25.3 ± 1.7**	689
14M36	20	38.485	508	53.864	711	6.812	2583	0	0.32	**26.4 ± 2.6**	349

ρs (ρi) is the spontaneous (induced) track density (10^5 tracks/cm^2); Ns (Ni) is the number of counted spontaneous (induced) tracks; ρd is the dosimeter track density (10^5 tracks/cm^2); Nd is the number of tracks counted on the dosimeter; P($χ^2$) is the probability of obtaining a Chi-square value ($χ^2$) for n degree of freedom (where n is the number of crystals minus 1); ages were calculated using the zeta calibration method (Hurford and Green, 1983), glass dosimeter IRMM541, and a zeta value of 109 ± 3 a/cm^2 calculated with Fish Canyon Tuff zircon standards.

Table 3
Results of apatite fission track analyses.

Sample	Number of grains	ρs	Ns	ρi	Ni	ρd	Nd	P(χ²) (%)	Dispersion	Central age ±1σ (Ma)	U (ppm)	Mean track length (μm)	SD (μm)	Number of track lengths measured	Dpar (μm)
14M23*	20	2.587	52	15.473	311	8.3118	3032	26	0	**17.7 ± 2.8**	26	13.78	1.20	34	1.56
14M24*	20	1.129	14	10.081	125	8.2999	3032	85	0	**11.8 ± 3.4**	18	12.98	0.88	50	1.57
14M25*	20	1.176	18	9.477	145	8.1326	3032	12	0.32	**13.1 ± 3.6**	15				1.79
14M26	20	2.665	105	20.787	819	8.276	3032	99	0	**12.4 ± 1.4**	37				1.68
14M27*	20	4.135	43	24.135	251	8.264	3032	90	0	**18.0 ± 3.1**	32	13.26	1.12	23	1.60
14M29*	20	3.254	82	17.143	432	8.2541	3032	0.11	0.56	**21.1 ± 3.8**	27	13.96	1.20	53	1.67
14M30*	20	2.586	30	13.621	158	8.2401	3032	85	0	**19.9 ± 4.0**	22	13.56	1.18	22	1.67
14M31*	15	2.887	41	17.042	242	8.2282	3032	50	0	**17.8 ± 3.1**	31	13.66	1.24	43	1.73
14M32*	15	0.655	11	16.190	272	8.2162	3032	77	0	**4.2 ± 1.3**	25				1.56
14M33	4	0.635	4	14.603	92	8.2034	3032	78	0	**4.2 ± 2.1**	28				1.57
14M34	17	0.512	19	11.402	423	8.1923	3032	2	0.67	**4.8 ± 1.4**	20				1.61
14M35*	11	0.788	7	15.444	139	8.1684	3032	50	0	**5.2 ± 2.0**	27				1.55
14M36	20	1.395	47	23.383	788	8.1565	3032	86	0	**5.7 ± 0.9**	41				1.53
14M37	20	1.762	77	12.586	550	8.145	3032	2	0.42	**14.7 ± 2.4**	21	13.09	1.11	16	1.64
14M38*	15	1.772	14	11.772	93	7.972	3032	99	0	**15.3 ± 4.4**	19	13.33	1.13	21	1.62
14M39	20	1.869	37	9.949	197	8.12	3032	9	0.54	**18.9 ± 4.2**	21	13.44	1.22	18	1.58
14M40*	20	0.649	32	2.677	132	8.1087	3032	12	0.61	**22.8 ± 5.8**	4	13.28	0.89	11	1.66
14M41	11	0.847	16	18.201	344	8.097	3032	29	0	**4.4 ± 1.1**	33				1.54

ρs (ρi) is the spontaneous (induced) track density (10^5 tracks/cm²); Ns (Ni) is the number of counted spontaneous (induced) tracks; ρd is the dosimeter track density (10^5 tracks/cm²); Nd is the number of tracks counted on the dosimeter; P(χ²) is the probability of obtaining Chi-square value (χ²) for n degree of freedom (where n is the number of crystals minus 1); ages were calculated using the zeta calibration method (Hurford and Green, 1983), glass dosimeter IRMM540, and zeta values of 235 ± 9 a/cm² (samples without asterisk) and 255 ± 9 a/cm² (samples with asterisk) calculated with Durango apatite standards.

sites, either at the boundary between the metamorphic rocks and the Neogene or Quaternary sediments or within the metamorphic rocks, ensures that the sediment source area of all samples encompasses only metamorphic rocks.

The 250–500 μm grain size fractions of the stream sediments obtained by sieving in the field were split into a magnetic and a non-magnetic fraction using a Frantz magnetic separator. The subsequent leaching procedure consisted of one etching step in 6 M HCl at 80 °C, four etching steps in dilute HF/HNO₃ in a heated ultrasonic bath (Kohl and Nishiizumi, 1992), and two alternating etching steps in aqua regia and 8 M HF to obtain pure quartz (Goethals et al., 2009). For beryllium extraction, ~0.3 mg of Be carrier was added to each sample. Following complete dissolution of quartz in HF (40%), samples were redissolved and converted into chloride form using 6 M HCl. Beryllium was separated by successive anion and cation exchange columns and precipitated as Be(OH)₂ at pH 8–9. Following the transformation to BeO at 1000 °C and target preparation for accelerator mass spectrometry (AMS), ^{10}Be was analyzed at the compact AMS facility "TANDY" of the ETH Zurich (Christl et al., 2013). The measured ^{10}Be/^{9}Be ratios are normalized to the secondary ETH standard S2007N with a nominal ^{10}Be/^{9}Be ratio of 28.1×10^{-12} (Kubik and Christl, 2010), considering the ^{10}Be half-life of 1.387 ± 0.012 Ma (Chmeleff et al., 2010; Korschinek et al., 2010). The secondary standard has been calibrated to the primary standard ICN 01-5-1 (Nishiizumi et al., 2007; Kubik and Christl, 2010).

Catchment-wide erosion rates were calculated from the blank-corrected ^{10}Be concentrations with the CRONUS-Earth online calculator (Balco et al., 2008; version 2.2; http://hess.ess.washington.edu) using the time-invariant production rate scaling model of Lal (1991) and Stone (2000) (Table 6). We note that the results of four samples (14T7, −8, −13 and −14) have been included in a manuscript that focusses on the lifetimes of water reservoirs in the Menderes Massif (Heineke et al., manuscript in revision). To account for the shielding of cosmic rays by the surrounding topography, a shielding factor was calculated for each catchment using the MATLAB script provided by Greg Balco (http://depts.washington.edu/cosmolab/shielding.m) and a digital elevation model with a horizontal resolution of 30 m (ASTER GDEM; http://www.gdem.aster.ersdac.or.jp). Erosion rates determined with cosmogenic nuclides approximately integrate over the time interval needed to remove a ~60 cm thick layer of bedrock from the surface: commonly a period of 10^3–10^5 years (e.g. Granger et al., 1996).

4. Results

4.1. Results from fission-track and (U-Th)/He analysis

The results from low-temperature thermochronology (Tables 2–5) reveal distinct ages for the rock samples from the footwall and hanging wall of the Büyük Menderes detachment fault, respectively (Fig. 4). The youngest ages are obtained from samples located below the Büyük Menderes detachment in the southern part of the study area (samples 14M32, −33, −34, −35, −36, −41). This group of samples yield AFT ages from 5.7 ± 0.9 to 4.2 ± 1.3 Ma and two AHe ages of 3.0 ± 0.3 Ma, respectively (Figs. 4, 5). The ZHe and ZFT ages of these samples are significantly older and range from 15.7 ± 3.6 to 12.2 ± 0.7 Ma and from 26.4 ± 2.6 to 25.3 ± 1.7 Ma, respectively (Figs. 4, 5). A second sample group is defined by footwall samples from the central and northern part of the Aydın block (14M24, −25, −26, −37, −38). AFT and ZHe ages of these samples range from 15.3 ± 4.4 to 11.8 ± 3.4 Ma and from 16.5 ± 0.8 to 13.0 ± 0.8 Ma, respectively. The third group of samples is defined by the oldest ages and comprises four augen gneiss samples from the hanging wall of the Büyük Menderes detachment (14M30, −31, −39, −40), one sample from the northern flank of the Aydın block (14M27), and two samples of augen gneisses in the Küçük Menderes Graben (14M23, −29). The two ZFT ages from this group are 30.3 ± 2.1 Ma and 29.0 ± 1.9 Ma, whereas the ZHe and AFT ages range from 25.7 ± 0.9 to 20.0 ± 1.6 Ma and from 22.8 ± 5.8 to 17.7 ± 2.8 Ma, respectively (black symbols in Fig. 5). The augen gneisses from the Küçük Menderes Graben yield AHe ages of 21.9 ± 1.2 Ma and 17.5 ± 1.7 Ma. In contrast, two samples from the hanging wall of the Büyük Menderes detachment (14M31, −40) yield AHe ages of 1.6 ± 0.2 and 0.5 ± 0.1 Ma (Fig. 5).

The apatite samples from all three age groups are characterized by unimodal track length distributions and relatively long mean track lengths (13.0 to 13.8 μm, with standard deviations of 0.9 to 1.2 μm) (Table 3). The track length data suggest a moderately fast cooling through the apatite partial annealing zone in the Miocene to Pliocene. Mean Dpar values of the samples range from 1.53 to 1.79 μm (Table 3), pointing to a homogeneous chemical composition of the samples, typical for fluorine-apatite.

By using the closure temperatures mentioned in Section 3 (i.e. ZFT: 240 °C, ZHe: 180 °C, AFT: 110 °C, AHe: 70 °C) and a mean annual surface

Table 4
Results of zircon (U-Th)/He geochronology.

Sample	Aliq.	He Vol. (10^-9 cm^3)	1σ (%)	238U Mass (ng)	1σ (%)	Conc. (ppm)	232Th Mass (ng)	1σ (%)	Conc. (ppm)	Th/U ratio	Sm Mass (ng)	1σ (%)	Conc. (ppm)	Ejection correction	Uncorr. age (Ma)	FT-corr. age (Ma)	2σ (Ma)	Sample age (Ma)	2se (Ma)
14M23	#1	2.105	1.2	1.132	1.8	499	0.134	2.4	59	0.12	0.031	7.6	14	0.68	15.0	**22.02**	2.30	**21.8**	0.3
	#2	4.243	1.1	2.340	1.8	829	0.103	2.4	37	0.04	0.005	18.5	2	0.69	14.9	**21.53**	2.19		
14M24	#1	1.551	1.2	1.128	1.8	268	0.410	2.4	98	0.36	0.010	12.7	2	0.80	10.5	**13.10**	0.95	**13.9**	1.3
	#2	1.081	1.2	0.850	1.8	276	0.345	2.4	112	0.41	0.012	13.2	4	0.72	9.6	**13.34**	1.25		
	#3	0.836	1.3	0.546	1.8	149	0.373	2.4	101	0.68	0.006	18.0	2	0.71	10.9	**15.38**	1.48		
14M25	#1	4.983	0.8	3.415	1.8	404	1.977	2.4	234	0.58	0.042	9.0	5	0.82	10.6	**12.95**	0.84	**13.0**	0.8
14M26	#1	0.852	1.0	0.559	1.8	248	0.102	2.4	45	0.18	0.008	15.4	4	0.71	12.10	**17.04**	1.63	**16.5**	0.8
	#2	2.999	0.9	1.674	1.8	262	1.063	2.4	166	0.64	0.042	10.5	7	0.81	12.89	**15.91**	1.07		
14M27	#1	7.941	0.9	3.845	1.8	258	0.771	2.4	52	0.20	0.039	10.8	3	0.83	16.32	**19.66**	1.24	**19.9**	0.2
	#2	2.554	0.9	1.231	1.8	229	0.615	2.4	114	0.50	0.039	11.5	7	0.76	15.35	**20.20**	1.63		
	#3	2.108	0.9	1.099	1.8	277	0.163	2.4	41	0.15	0.014	14.7	4	0.77	15.34	**19.92**	1.57		
14M29	#1	19.300	0.8	9.024	1.8	1756	1.307	2.4	254	0.14	0.016	19.0	3	0.84	17.11	**20.37**	1.24	**24.6**	2.1
	#2	7.266	0.8	3.088	1.8	652	0.264	2.4	56	0.09	0.040	11.3	8	0.72	19.08	**26.51**	2.44		
	#3	9.940	0.9	3.583	1.8	377	0.617	2.4	65	0.17	0.067	10.1	7	0.82	22.05	**26.89**	1.77		
14M30	#1	3.482	1.2	1.544	1.8	367	0.142	2.4	34	0.09	0.006	20.6	1	0.71	18.3	**25.73**	2.48	**25.7**	0.9
	#2	2.879	1.2	1.186	1.8	299	0.113	2.4	28	0.09	0.004	22.9	1	0.74	19.6	**26.55**	2.35		
	#3	13.137	1.1	5.219	1.8	467	1.204	2.4	108	0.23	0.091	5.3	8	0.80	19.7	**24.69**	1.78		
14M31	#1	1.476	1.2	0.812	1.8	231	0.180	2.4	51	0.22	0.013	10.2	4	0.76	14.3	**18.80**	1.56	**20.0**	1.6
	#2	8.919	1.1	4.403	1.8	737	0.580	2.4	97	0.13	0.108	5.0	18	0.77	16.3	**21.11**	1.69		
14M32	#1	2.982	0.9	2.494	1.8	1012	0.733	2.4	298	0.29	0.101	9.6	41	0.69	9.26	**13.42**	1.34	**14.5**	0.6
	#2	0.328	1.2	0.199	1.9	55	0.227	2.4	63	1.14	0.012	13.3	3	0.75	10.75	**14.34**	1.21		
	#3	0.724	1.1	0.529	1.8	235	0.081	2.5	36	0.15	0.004	22.9	2	0.70	10.94	**15.62**	1.54		
14M34	#1	5.532	0.8	2.304	1.8	594	3.831	2.4	988	1.66	0.028	11.5	7	0.77	14.25	**18.51**	1.42	**15.5**	1.6
	#2	0.581	1.1	0.439	1.8	72	0.106	2.4	17	0.24	0.010	15.8	2	0.70	10.37	**14.81**	1.46		
	#3	0.402	1.1	0.332	1.9	166	0.130	2.4	65	0.39	0.006	22.0	3	0.69	9.16	**13.27**	1.34		
14M35	#1	1.398	0.9	0.944	1.8	248	0.849	2.4	223	0.90	0.241	9.6	63	0.77	10.09	**13.10**	1.01	**15.7**	3.6
	#2	3.577	0.9	1.806	1.8	340	1.261	2.4	238	0.70	0.216	9.6	41	0.77	14.06	**18.26**	1.41		
	#3	1.636	0.9	0.753	1.8	604	0.260	2.4	208	0.34	0.025	11.3	20	0.64	16.61	**25.96***	2.97		
14M36	#1	0.429	1.1	0.314	1.9	207	0.155	2.4	102	0.49	0.011	14.2	7	0.67	10.13	**15.12**	1.62	**15.3**	1.1
	#2	1.622	0.9	1.170	1.8	231	0.396	2.4	78	0.34	0.013	13.6	3	0.79	10.63	**13.46**	0.99		
	#3	2.672	0.9	1.409	1.8	200	0.757	2.4	108	0.54	0.035	10.9	5	0.80	13.92	**17.40**	1.22		
14M37	#1	0.936	1.0	0.636	1.8	195	0.325	2.4	100	0.51	0.029	11.3	9	0.76	10.87	**14.30**	1.16	**14.8**	0.3
	#2	1.546	0.9	1.151	1.8	553	0.359	2.4	172	0.31	0.004	22.2	2	0.70	10.35	**14.79**	1.44		
	#3	2.378	0.9	1.691	1.8	529	0.297	2.4	93	0.18	0.005	20.4	2	0.73	11.18	**15.32**	1.37		
14M39	#1	1.810	1.3	1.132	1.8	266	0.517	2.4	121	0.46	0.101	5.6	24	0.71	11.9	**16.81**	1.62	**21.0**	5.9
	#2	4.275	1.2	1.802	1.8	366	0.851	2.4	173	0.47	0.059	6.2	12	0.70	17.7	**25.22**	2.48		
14M41	#1	3.125	1.2	2.314	1.8	286	0.613	2.4	76	0.27	0.006	16.4	1	0.81	10.5	**12.99**	0.91	**12.2**	0.7
	#2	0.909	1.3	0.810	1.8	258	0.228	2.4	73	0.28	0.003	25.8	1	0.73	8.7	**11.93**	1.09		
	#3	1.773	0.9	1.576	1.8	422	0.484	2.4	129	0.31	0.035	10.5	9	0.74	8.7	**11.74**	1.02		

Ejection correction (Ft): correction factor for alpha-ejection (according to Farley et al., 1996 and Hourigan et al., 2005). Uncertainty of the single-grain ages includes both the analytical uncertainty and the estimated uncertainty of the ejection correction. Sample age is the unweighted average age of all Ft-corrected (U-Th)/He ages. Results from aliquots marked with asterisk are not considered in the calculation of the sample age.

temperature of 10 °C, we determined exhumation rates from the cooling ages of mineral pairs. We calculated the exhumation rates by dividing cooling rates with an estimated value for the paleo-geothermal gradient. At present, the average surface heat flow of ~110 mW/m² in the Menderes Massif (Ilkişik, 1995) and heat flow models for the continental crust (Chapman and Furlong, 1992) indicate an average geothermal gradient of about 40 °C/km. During periods of extension however, the geothermal gradient may have increased to values of 50 °C/km or more (cf. Foster et al., 1991; Lund et al., 1993). For instance, Foster et al. (1991) calculated a geo-thermal gradient of 50 ± 20 °C/km for the Mojave extensional belt and Blackwell (1983) reported a high geothermal gradient of about 50 °C/km in the extensional Basin-and-Range Province. Based on geophysical data, the geothermal gradient for western Anatolia was calculated to range between 50 and 70 °C/km (Dolmaz et al., 2005). Thermal-kinematic modelling of low-angle normal faults indicates that within a few kilometres around the fault, the geothermal gradients in the hanging wall as well as the footwall are spatially invariant (e.g. Grasemann and Dunkl, 2003). To account for the above mentioned uncertainties of the paleo-geothermal gradient, we calculated exhumation rates for three different geothermal gradients of 30, 50, and 70 °C/km for the three sample groups defined above (Fig. 6a–i). For each of these three scenarios alternating phases of relatively fast

and slow exhumation can be recognized and will be discussed in Section 5.1.

4.2. Results from cosmogenic ¹⁰Be analysis

The erosion rates determined for the eight catchments in the Aydın block and the Küçük Menderes Graben range from ~50 to ~400 mm/kyr and are shown in Fig. 4. Blank-corrected ¹⁰Be concentrations of the samples, production rates due to spallation and muons, and spatially integrated erosion rates for the respective catchments are presented in Table 6. The lowest erosion rates of 54 ± 5 and 64 ± 6 m/Myr were obtained for the two small catchments that are entirely located in augen gneisses of the Çine nappe at the eastern end of the Küçük Menderes Graben. These rates can be explained by the low erodibility of the coarse-grained orthogneisses and the rather low mean hillslope angles of the two catchments of ~16° and ~18°, respectively (Table 6). The sediment samples from the six larger catchments in the Aydın block yielded higher, albeit quite variable erosion rates between 84 ± 8 and 390 ± 39 m/Myr. The faster erosion documented for these catchments likely reflects the higher erodibility of the fragile mica schists and the generally steeper hillslopes of these catchments, which have mean hillslope

Table 5
Results of apatite (U-Th)/He geochronology.

Sample	Aliq.	He Vol. (10⁻⁹ cm³)	1σ (%)	²³⁸U Mass (ng)	1σ (%)	Conc. (ppm)	²³²Th Mass (ng)	1σ (%)	Conc. (ppm)	Th/U ratio	Sm Mass (ng)	1σ (%)	Conc. (ppm)	Ejection correction	Uncorr. age (Ma)	FT-corr. age (Ma)	2σ (Ma)	Sample age (Ma)	2se (Ma)
14M23	#1	0.032	3.3	0.019	3.4	3.9	0.004	4.0	0.9	0.23	0.680	6.4	139	0.73	10.25	**14.04**	1.67	**17.5**	1.7
	#2	0.014	4.8	0.006	8.5	2.9	0.002	5.7	1.1	0.37	0.263	6.7	121	0.65	12.64	**19.44**	3.60		
	#3	0.047	2.6	0.022	3.0	4.2	0.006	3.7	1.1	0.26	0.861	6.0	161	0.66	12.55	**19.02**	2.37		
14M29	#1	0.295	1.2	0.120	1.9	14.4	0.022	2.9	2.7	0.19	1.998	5.8	240	0.80	17.19	**21.49**	1.56	**21.9**	1.2
	#2	0.423	1.1	0.163	1.8	17.6	0.031	2.7	3.3	0.19	2.204	5.8	238	0.77	18.59	**24.15**	1.92		
	#3	0.365	1.2	0.153	1.8	14.1	0.048	2.6	4.4	0.31	2.543	5.8	235	0.81	16.31	**20.13**	1.41		
14M31	#1	0.131	1.5	0.615	1.8	56.5	0.277	2.4	25.4	0.45	0.650	6.2	60	0.81	1.58	**1.95**	0.14	**1.6**	0.2
	#2	0.163	1.5	1.190	1.8	79.2	0.036	2.7	2.4	0.03	0.720	6.0	48	0.80	1.12	**1.40**	0.11		
	#3	0.171	1.4	1.190	1.8	79.4	0.058	2.6	3.9	0.05	0.771	6.0	51	0.80	1.17	**1.46**	0.11		
14M34	#1	0.001	12.3	0.002	31.5	0.6	0.002	7.7	0.7	1.12	0.035	13.6	12	0.75	2.10	**2.81**	1.40	**3.0**	0.3
	#2	0.010	5.8	0.028	2.6	7.1	0.029	2.7	7.1	1.00	0.149	7.2	37	0.72	2.28	**3.16**	0.47		
14M35	#1	0.008	6.3	0.011	5.2	6.7	0.007	3.7	4.3	0.64	0.076	9.1	48	0.65	5.14	**7.90***	1.45	**3.0**	0.3
	#2	0.027	3.6	0.081	1.9	11.6	0.056	2.6	8.0	0.69	0.318	6.5	46	0.77	2.29	**2.98**	0.31		
14M37	#1	0.013	5.1	0.010	5.5	4.2	0.018	3.0	7.3	1.75	0.055	9.3	23	0.76	7.39	**9.73**	1.41	**9.7**	1.4
14M40	#1	0.001	11.7	0.008	7.1	2.7	0.003	5.2	0.8	0.31	0.295	9.4	95	0.68	0.48	**0.70**	0.19	**0.5**	0.1
	#2	0.001	12.2	0.014	4.6	3.9	0.010	3.4	2.8	0.71	0.090	10.1	26	0.68	0.25	**0.37**	0.10		
	#3	0.001	12.2	0.020	3.4	9.1	0.007	3.6	3.2	0.35	0.028	13.1	13	0.66	0.29	**0.43**	0.12		

Ejection correction (Ft): correction factor for alpha-ejection (according to Farley et al., 1996). Uncertainty of the single-grain ages includes both the analytical uncertainty and the estimated uncertainty of the ejection correction. Sample age is the unweighted average age of all Ft-corrected (U-Th)/He ages (see: standard error). Results from aliquots marked with asterisk are not considered in the calculation of the sample age.

angles between 20 and 29 degrees (Table 6). The integration times of our eight samples range from ~1.5 to ~11 ka (Table 6).

5. Interpretation and discussion

5.1. Late Miocene/Pliocene to Oligocene cooling pattern of the Aydın block

As discussed earlier, the geothermal gradient in regions of active extension is relatively high, compared to stable regions (e.g. Foster et al., 1991). Therefore we consider a geothermal gradient of more than 30 °C/km as the most realistic scenario. In the following discussion we only refer to exhumation rates calculated for a geothermal gradient of 50 °C/km (Fig. 6b, e, h), however, we cannot exclude the possibility of a temporally higher gradient, for instance due to local fluid circulation near active faults.

The new thermochronological data from the Aydın block and the Küçük Menderes Graben define three groups of samples with different cooling paths and exhumation histories (Fig. 6). In particular, the data reveal two phases of footwall exhumation during the Miocene/Pliocene and the middle Miocene, respectively. The first group is defined by the youngest AFT and AHe ages from the southern flank of the Aydın block, which range between ~6 and ~3 Ma (Fig. 7). The exhumation rate of ~0.43 km/Myr for the latest Miocene and Pliocene (Fig. 6b) was likely caused by slip on the Büyük Menderes detachment fault and consequent tectonic denudation of the fault footwall. The link between footwall exhumation and detachment faulting is supported by K-Ar data from a fault gouge sample of the Büyük Menderes detachment that yielded ages between ~5 and ~3 Ma for three different grain size fractions (Hetzel et al. (2013), sample 09Me-NM01). These data corroborate the interpretation of Gessner et al. (2001a), who inferred rapid

Table 6
¹⁰Be concentrations, production rates, and catchment-wide erosion rates in the central Menderes Massif, Turkey.

Sample	Latitude (WGS 84) (°N)	Longitude (WGS 84) (°E)	Sample elevation (m)	Mean catchment elevation[a] (m)	Mean hillslope angle of catchment[a] (°)	Topographic shielding factor[a] (–)	Production rate[a] (Spallation) (at/g/yr)	Production rate[a] (Muons) (at/g/yr)	¹⁰Be concentration[b] (10⁴ at/g)	Erosion rate[c] (mm/kyr)	Internal uncertainty (1σ) (mm/kyr)	External uncertainty (1σ) (mm/kyr)	Time scale (kyr)
14T5	38.1843	28.0838	174	270	15.7	0.9984	5.20	0.198	7.86 ± 0.39	**64.3**	± 3.3	± 5.6	9.3
14T7	38.0732	27.9323	416	887	24.3	0.9933	8.53	0.244	2.99 ± 0.18	**254**	± 15	± 24	2.4
14T8	38.0703	28.0990	398	1127	20.1	0.9955	10.28	0.264	10.25 ± 0.51	**83.6**	± 4.2	± 7.5	7.2
14T9	38.0752	28.0565	402	1100	28.8	0.9871	9.98	0.262	5.39 ± 0.29	**157.8**	± 8.5	± 14.3	3.8
14T12	38.1849	28.0870	185	345	17.5	0.9978	5.54	0.203	9.66 ± 0.41	**54.2**	± 2.4	± 4.5	11
14T13	37.9342	28.1713	232	1011	23.0	0.9917	9.35	0.254	7.01 ± 0.31	**114.4**	± 5.2	± 9.8	5.2
14T14	37.9593	28.0818	359	968	25.3	0.9914	9.05	0.251	2.05 ± 0.14	**390**	± 28	± 39	1.5
14T15	37.9716	28.0102	487	998	25.5	0.9909	9.25	0.253	4.36 ± 0.22	**184.1**	± 9.3	± 16.3	3.3

[a] The mean elevation of the catchments, their mean hillslope angles, and the topographic shielding factors were calculated using a 30 m Aster Digital Elevation Model. We calculated the topographic shielding factor with the MATLAB script of Greg Balco (http://depts.washington.edu/cosmolab/shielding.m). The ¹⁰Be production rates were calculated with the CRONUS-Earth ¹⁰Be–²⁶Al calculator (Balco et al., 2008; http://hess.ess.washington.edu/; version 2.2), using the time-invariant production rate scaling model of Lal (1991)–Stone (2000).

[b] Blank-corrected ¹⁰Be concentrations. The uncertainty of the ¹⁰Be concentration includes the error of the blank correction and the propagated error of the analytical uncertainty. The analytical error (1σ) takes into account the error based on counting statistics, the scatter of the repeated measurement of the same sample, as well as the uncertainty of the standard normalization. ¹⁰Be concentrations were measured by AMS using the compact ETH Zurich Tandy system (Christl et al., 2013). Measured ¹⁰Be/⁹Be ratios are normalized to the secondary standard S2007N with a nominal ¹⁰Be/⁹Be ratio of 28.1 × 10⁻¹² (Kubik and Christl, 2010), considering the ¹⁰Be half-life of 1.387 ± 0.012 Ma (Chmeleff et al., 2010; Korschinek et al., 2010). The secondary standard has been calibrated relative to the primary standard ICN 01-5-1 (Nishiizumi et al., 2007; Kubik and Christl, 2010).

[c] Erosion rates were calculated with the CRONUS-Earth ¹⁰Be–²⁶Al online calculator (Balco et al., 2008; http://hess.ess.washington.edu/; version 2.2). Internal uncertainties (1σ) include the analytical uncertainty and the error of the blank correction, whereas external uncertainties (1σ) also include the systematic uncertainty of the sea-level high-latitude production rate. Note that the 2.7 % error (1σ) associated with the ¹⁰Be/⁹Be ratio of the standard S2007N is also included in the external uncertainty (Kubik and Christl, 2010). For the calculation of the catchment-wide erosion rates, we used a density of 2.5 g/cm³ and the mean elevation of the catchments. The time over which the erosion rate integrates is calculated by dividing the absorption depth scale of 60 cm by the erosion rate.
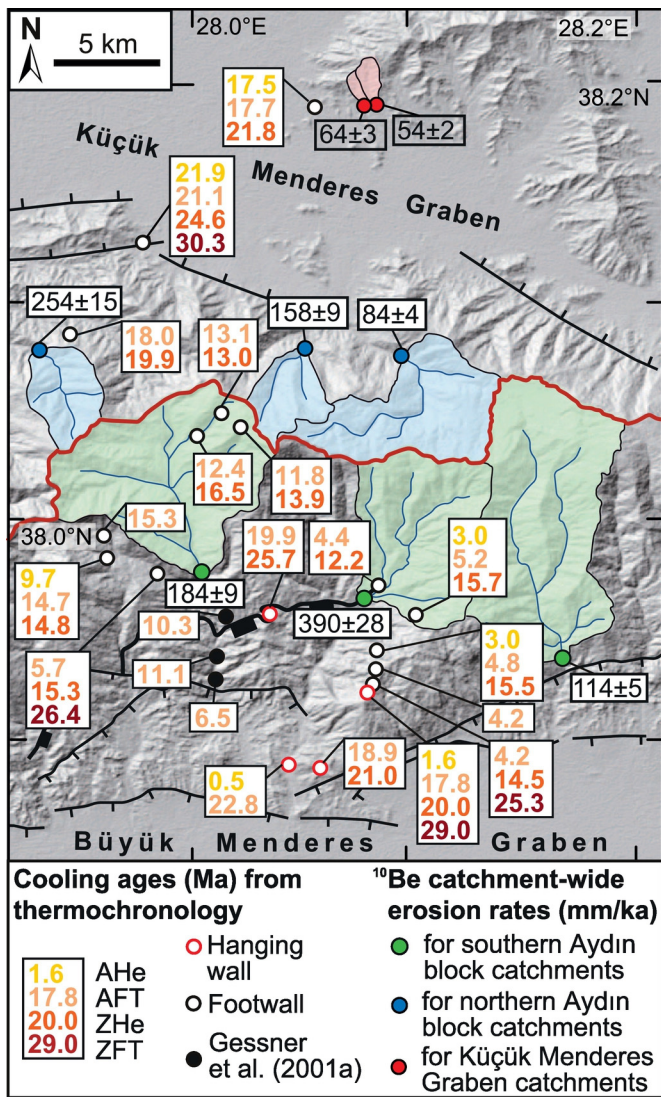
Fig. 4. Shaded-relief map of the study area with cooling ages derived from thermochronology and catchment-wide erosion rates (black numbers) based on cosmogenic ¹⁰Be concentrations of stream sediments.

Fig. 5. Cooling ages from this study plotted versus distance along the profile A to B (for location see Fig. 2a).

cooling and coeval normal faulting on the Büyük Menderes and Gediz detachment faults in the Pliocene based on thermochronological data from the Gediz detachment only. The samples from the first group have ZFT ages of ~25 Ma and ZHe ages between 16 and 12 Ma, which are significantly older than their respective AFT and AHe ages and indicate an exhumation rate of ~0.1 km/Myr before ~5 Ma (Fig. 6b).

The samples from the second group are footwall samples from the central and northern part of the Aydın block and display early to middle Miocene ZHe and AFT ages and one AHe age of 9.7 ± 1.4 Ma. The exhumation rates derived from these ages decrease through time from ~0.9 to ~0.12 km/Myr between ~15 and ~10 Ma (Fig. 6e). These data document another phase of rather rapid cooling and exhumation in the middle Miocene, which may reflect a first phase of activity of the Büyük Menderes detachment fault. Such an older phase of detachment faulting was also inferred from a K-Ar age of 21.6 ± 0.6 Ma for a cataclasite from the Büyük Menderes detachment and a K-Ar fault gouge age of 22.3 ± 0.7 Ma for a normal fault in its hanging wall (Hetzel et al., 2013, samples 09Me-NM02 and 10Me18), however, more data are needed to bolster this interpretation and constrain the beginning of deformation. It is also important to note that during the first phase of detachment faulting the samples of group 1 (Fig. 6a–c) remained at temperatures above the partial annealing zone of fission tracks in apatite (i.e. 110–60 °C). Hence,

the two distinct cooling paths recorded by the sample groups 1 and 2 indicate that two phases of relatively rapid exhumation were separated by a late Miocene period with little or no tectonic activity.

The third sample group – augen gneisses from the hanging wall (Çine nappe) exposed as klippen above the Büyük Menderes and in the Küçük Menderes Graben – gave the oldest thermochronological ages, indicating that these rocks cooled from ~240 to ~70 °C between ~30 Ma and ~18 Ma (Fig. 6h). This phase of cooling and exhumation occurred after the stacking of the Menderes nappes (e.g. Ring et al., 1999b; Gessner et al., 2013) and the Alpine prograde metamorphic evolution. Although the ZHe and AFT ages show some variability, the data seem to indicate that exhumation has accelerated in the late Oligocene/early Miocene from about ~0.16 to ~0.57 km/Myr (Fig. 6h). This interpretation is consistent with previous studies that reported a phase of rapid cooling during the late Oligocene and early Miocene for the Çine nappe (Gessner et al., 2001a; Ring et al., 2003). The subsequent exhumation occurred at a much lower mean rate of ~0.06 km/Myr (Fig. 6h). Only two samples (14M31, −40) from augen gneiss klippen in the vicinity of the Büyük Menderes graben yielded young AHe ages of 1.6 ± 0.2 Ma and 0.5 ± 0.1 Ma (Figs. 4, 5), which demonstrate that the final cooling of these klippen occurred in the Pleistocene. Similar observations were made at the Gediz detachment, where two AHe ages from augen gneiss klippen near the Gediz graben are ~2.9 and ~0.8 Ma (Buscher et al., 2013). As such young AHe ages are only found near the active graben structures, they probably record recent activity of graben-bounding normal faults. The presence of active normal faults is also evident from borehole logs in the Büyük Menderes Graben (e.g. Karamanderesi and Helvacı, 2003).

In summary, our new thermochronological data suggest that the Büyük Menderes detachment system was active during two phases that caused enhanced footwall cooling and exhumation. The first phase occurred during the middle Miocene and a second phase during the latest Miocene and Pliocene (Fig. 7). A similar temporal evolution is documented for the Gediz detachment fault, where detachment faulting was also operating in the mid-Miocene, as documented by U-Pb ages of 16.1 ± 0.2 Ma and 15.0 ± 0.3 Ma for two synextensional granodiorites that intruded the detachment-related mylonites (Glodny and Hetzel, 2007). This early stage of the Gediz detachment system was followed by enhanced cooling and footwall exhumation in the late Miocene and Pliocene, as indicated by apatite and zircon fission track and (U-Th)/He ages (Fig. 7) (Buscher et al., 2013). This younger
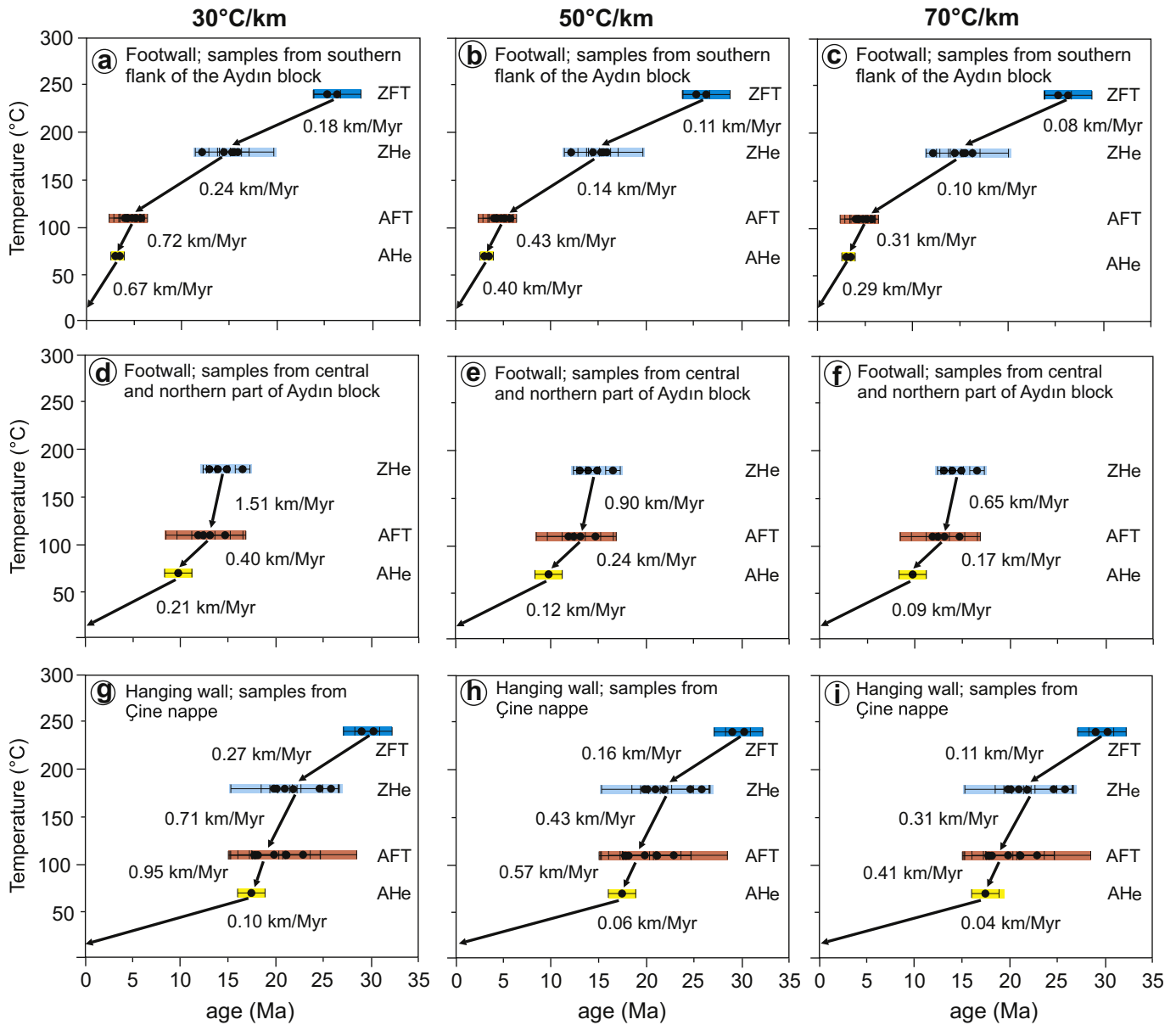
Fig. 6. (a–c) Average exhumation rates calculated from the cooling ages of mineral pairs for samples from the footwall (a–f) and hanging wall (g–i) of the Büyük Menderes detachment fault (see Section 4.1 for details). Left, middle and right columns are calculated with a geothermal gradient of 30, 50, and 70 °C/km, respectively.

phase of detachment faulting is supported by one Ar-Ar age of 7 ± 1 Ma for synkinematic white mica from the Gediz detachment (Lips et al., 2001). Hence, both detachment faults acted simultaneously in the middle Miocene as well as during the latest Miocene/Pliocene, as suggested by Gessner et al. (2001a). The similarity between two ZFT ages of ~25 Ma from the footwall and one ZFT age of ~29 Ma from hanging wall of the Büyük Menderes detachment (Fig. 5) indicates that this detachment fault was largely active at temperatures below ~250 °C. It was thus operating at a slightly shallower crustal level than the Gediz detachment. This interpretation is consistent with our field observations along the studied section, where features indicating a recrystallization of quartz (i.e. stretching lineations and mm-scale foliation in quartz veins) are conspicuously absent.

Our interpretation of two phases of detachment faulting, as described above, implies that the Büyük Menderes and Gediz detachments did not experience significant rotation over time. In other words, we argue that the detachments were active at a rather low angle during both phases of enhanced activity. Our interpretation is based on (i) the early to middle Miocene K-Ar ages on fault gouge and cataclasite

from both detachments (Hetzel et al., 2013), (ii) the syntectonic emplacement of two granodiorites at the Gediz detachment at ~15 and ~16 Ma, respectively (Glodny and Hetzel, 2007) and (iii) the occurrence of early to middle Miocene sedimentary successions, which were interpreted as the infill of supra-detachment sedimentary basins (e.g. Purvis and Robertson, 2004; Sen and Seyitoğlu, 2009; Oner and Dilek, 2011; Oner and Dilek, 2013). Low-angle detachment faulting would be mechanically feasible (cf. Melosh, 1990; Forsyth, 1992; Collettini, 2011) and represents an efficient way to accommodate long-lasting extension (e.g., Wernicke, 1995; Jolivet et al., 2010; Morley, 2014). Note, however, that the actual geometry and dip of the detachments during the first phase of activity are poorly constrained and alternative interpretations are possible. In particular, the detachments could have been initially formed as high-angle normal faults in the early Miocene and could then have been reactivated in the Pliocene as rolling hinge detachment faults, which resulted in their present-day low dip (e.g., Gessner et al., 2001a; Ring et al., 2017). This interpretation would imply that the Büyük Menderes and Gediz detachments did not exist before the Pliocene (Ring et al., 2017). Note that a rolling-hinge style
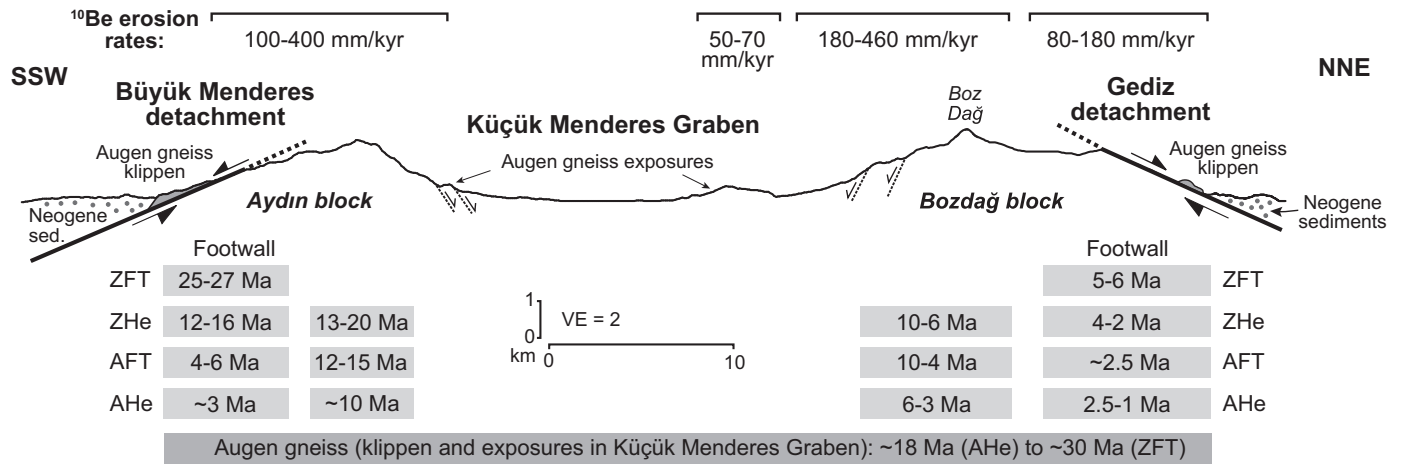
Fig. 7. Schematic profile across the central Menderes Massif summarizing cooling ages and catchment-wide erosion rates from this study and Buscher et al. (2013 and references therein).

of extension would also be mechanically feasible, as shown by numerical models (e.g., Lavier et al., 1999; Gessner et al., 2007).

5.2. Erosion pattern of the Aydın block and comparison with the Bozdağ block

The catchment-wide ^{10}Be-based erosion rates for the watersheds in the Aydın block range from ~100 to ~400 mm/kyr (Table 6, Fig. 7). Although the rates show some variability from catchment to catchment, they are quite similar on both the northern and southern mountain slopes of the Aydın block (Fig. 4). Given that the erosion rates integrate over several thousand years (Table 6), we infer that a relatively symmetric pattern of erosion has prevailed in the Aydın block during the Holocene. We argue that this pattern is likely controlled by the lithological similarities of the mica schists, which dominate both the Bozdağ and Bayındır nappes in the studied region of the Aydın block. The significantly lower erosion rates of ~54 and ~64 mm/kyr obtained for two catchments with resistant augen gneisses at the eastern end of the Küçük Menderes Graben corroborate the pronounced effect of lithology on erosion and are consistent with previous findings in other tectonically active mountain belts (Palumbo et al., 2010; Scharf et al., 2013b).

The symmetric erosion pattern in the Aydın block is in contrast to the spatial pattern of erosion documented for the Bozdağ block, where ^{10}Be-based erosion rates show an asymmetric distribution (Buscher et al., 2013). On the steep escarpment facing the Küçük Menderes Graben, erosion proceeds at rates that are about three times higher than those on the gently N-dipping mountain slope facing the Gediz Graben (Fig. 7). We attribute this marked difference in erosion rates to the presence of resistant, slowly-eroding cataclasites and quartzites in the footwall of the Gediz detachment, which constitutes a well-preserved geomorphic feature. The cataclasites associated with the Büyük Menderes detachment in the Aydın block are rather thin and resistant quartzites do not occur here, which is the reason why this detachment constitutes a less prominent feature in the landscape. In conclusion, despite having a similar relief, the lithological differences between the Gediz and Aydın blocks explain the contrasting geomorphologic appearance of the two detachment faults, which otherwise experienced a similar temporal and structural evolution.

The magnitude of the catchment-wide erosion rates of ~50 up to ~400 mm/kyr (or 0.05 to 0.4 km/Myr) as well as the presence of Neogene and Quaternary sediments on the Büyük Menderes detachment fault and in the adjacent graben suggests that, apart from normal faulting, erosion did also contribute to the exhumation of the metamorphic rocks in the central Menderes Massif. This hypothesis raises the question of how far back in time the erosion rates can be extrapolated. In this respect it is noteworthy that Holocene and late Pleistocene

erosion rates estimated from the volumes of sediments in the deltas of the Büyük and Küçük Menderes rivers indicate no significant glacial-interglacial variations in erosion (Westaway, 1994). The Holocene erosion rates for these two river basins of 0.08 and 0.19 km/Myr, respectively, are similar to erosion rates of 0.09 and 0.15 km/Myr during the late Pleistocene (i.e. the period of 60–18 ka) (Westaway, 1994, his Tables 5 and 7). Importantly, the rates of 0.15 and 0.19 km/Myr for the entire Küçük Menderes basin agree quite well with our ^{10}Be-based rates of ~0.25, ~0.16, and ~0.08 km/Myr for the three large catchments that drain into the Küçük Menderes Graben (samples 14T7, −8, −9 in Table 6). These arguments suggest that erosion rates in the central Menderes Massif did probably not change significantly over the last glacial-interglacial cycle and may be at least roughly representative for the Quaternary period with its repeated glacial-interglacial cycles (cf. Lisiecki and Raymo, 2005). In order to better resolve the relative importance of erosion and normal faulting on the exhumation of the metamorphic rocks, the evolution of the topography through time needs to be better constrained, because local relief and hillslope angles constitute another major control on erosion apart from climate and lithology.

6. Conclusions

In this study we present new low-temperature thermochronological data and ^{10}Be-based catchment-wide erosion rates to quantify the interplay between extensional faulting and erosion in the central Menderes Massif in western Turkey. The fission-track and (U-Th)/He data document that the Büyük Menderes detachment fault, which defines the southern flank of the central Menderes Massif, experienced two phases of tectonic activity in the middle Miocene and in the latest Miocene/Pliocene. In contrast to the footwall, the hanging wall units cooled already in the early and middle Miocene to temperatures below ~70 °C. Erosion rates from cosmogenic ^{10}Be for catchments in the metamorphic rocks range mainly from 100 to 400 mm/kyr. If these erosion rates are representative for the last few million years, erosion may have made a significant contribution to the exhumation of the metamorphic rocks, even during the most rapid phases of exhumation. However, clarification of this issue requires data that allow to reconstruct the paleotopographic evolution of the Menderes Massif during the Late Cenozoic.

References

Ambraseys, N.N., 1971. Value of historical records of earthquakes. Nature 232, 375–379.

Armstrong, P.A., Ehlers, T.A., Chapman, D.S., Farley, K.A., Kamp, P.J.J., 2003. Exhumation of the central Wasatch Mountains, Utah: 1. Patterns and timing of exhumation deduced from low-temperature thermochronology data. J. Geophys. Res. 108 (2172). http://dx.doi.org/10.1029/2001JB001708.

Axen, G.J., Grove, M., Stockli, D., Lovera, O.M., Rothstein, D.A., Fletcher, J.M., Farley, K.A., Abbott, P.L., 2000. Thermal evolution of Monte Blanco dome: low-angle normal falting during Gulf of California rifting and late Eocene denudation of the eastern Peninsular Ranges. Tectonics 19, 197–212.

Balco, G., Stone, J.O., Lifton, N.A., Dunai, T.J., 2008. A complete and easily accessible means of calculating surface exposure ages or erosion rates from ^{10}Be and ^{26}Al measurements. Quat. Geochronol. 3, 174–195.

Bierman, R., Steig, E.J., 1996. Estimating rates of denudation using cosmogenic isotope abundances in sediment. Earth Surf. Process. Landf. 21, 125–139.

Blackwell, D.D., 1983. Heat flow in the northern Basin and Range province. In: Geothermal Resources Council (Ed.), The Role of Heat in the Development of Energy and Mineral Resources in the Northern Basin and Range Province, Special Report 13, pp. 81–92.

von Blanckenburg, F., 2006. The control mechanisms of erosion and weathering at basin scale from cosmogenic nuclides in river sediment. Earth Planet. Sci. Lett. 242, 224–239.

Bozkurt, E., 2000. Origin on N-S extensional tectonic in western Anatolia (Turkey): evidence from the Büyük Menderes Graben. In: Bozkurt, E., Winchester, J.A., Piper, J.D.A. (Eds.), Tectonics and Magmatism in Turkey and Its Surrounding Areas. The Geological Society of London, Special Publications 173, pp. 385–403.

Bozkurt, E., 2001. Late Alpine evolution of the central Menderes Massif, western Turkey. Int. J. Earth Sci. 89, 728–744.

Bozkurt, E., Oberhänsli, R., 2001. Menderes Massif (Western Turkey): structural, metamorphic and magmatic evolution – a synthesis. Int. J. Earth Sci. 89, 79–708.

Bozkurt, E., Sözbilir, H., 2004. Tectonic evolution of the Gediz Graben: field evidence for an episodic, two-stage extension in western Turkey. Geol. Mag. 141, 63–79.

Brichau, S., Ring, U., Ketcham, R.A., Carter, A., Stockli, D., Brunel, M., 2006. Constraining the long-term evolution of the slip rate for a major extensional fault system in the central Aegean, Greece, using thermochronology. Earth Planet. Sci. Lett. 241, 293–306.

Brichau, S., Ring, U., Carter, A., Bolhar, R., Monié, P., Stockli, D., Brunel, M., 2008. Timing, slip rate, displacement and cooling history of the Mykonos detachment footwall, Cyclades, Greece, and implications for the opening of the Aegean Sea basin. J. Geol. Soc. Lond. 165, 263–277.

Burtner, R., Nigrini, A., Donelick, R.A., 1994. Thermochronology of Lower Cretaceous source rocks in the Idaho-Wyoming Thrust belt. Bull. Am. Assoc. Pet. Geol. 78, 1613–1636.

Buscher, J.T., Hampel, A., Hetzel, R., Dunkl, I., Glotzbach, C., Struffert, A., Akal, C., Rätz, M., 2013. Quantifying rates of detachment faulting and erosion in the central Menderes Massif (western Turkey) by thermochronology and cosmogenic ^{10}Be. J. Geol. Soc. Lond. 170, 669–683.

Campani, M., Mancktelow, N., Seward, D., Rolland, Y., Müller, I., Guerra, I., 2010. Geochronological evidence for continuous exhumation through the ductile-brittle transition along a crustal-scale low-angle normal fault: Simplon Fault Zone, central Alps. Tectonics 29, TC3002. http://dx.doi.org/10.1029/2009TC002582.

Candan, O., Dora, O.Ö., Kun, N., Akal, C., Koraly, E., 1992. Allochthonous metamorphic units at the southern part of Aydın Mountains, Menderes Massif. Turk. Assoc. Pet. Geol. 4 (1), 93–110.

Candan, O., Dora, O.Ö., Oberhänsli, R., Çetinkaplan, M., Partzsch, J.H., Warkus, F.C., Dürr, S., 2001. Pan-African high-pressure metamorphism in the Precambrian basement of the Menderes Massif, western Anatolia, Turkey. Int. J. Earth Sci. 89, 793–811.

Candan, O., Oberhänsli, R., Dora, O.Ö., Çetinkaplan, M., Koralay, E., Rimmelé, G., Chen, F., Akal, C., 2011. Polymetamorphic evolution of the Pan-African basement and Palaeozoic-Early Tertiary Cover Series of the Menderes Massif. Bull. Mineral Res. Explor. 142, 121–163.

Çemen, I., Catlos, E.J., Gogus, O., Ozerdem, C., 2006. Post-collisional extensional tectonics and exhumation of the Menderes massif in the western Anatolia Extended Terrrane, Turkey. In: Dilek, Y., Pavlis, S. (Eds.), Postcollisional Tectonics and Magmatism in the Eastern Mediterranean Region. Geological Society of America, Special Papers 409, pp. 353–379.

Chapman, D.S., Furlong, K.P., 1992. Thermal state of the continental lower crust. In: Fountain, D.M., Arculus, R., Kay, R.W. (Eds.), Continental Lower Crust. Elsevier, Amsterdam, pp. 179–199.

Chmeleff, J., von Blanckenburg, F., Kossert, K., Jakob, D., 2010. Determination of the ^{10}Be half-life by multicollector ICP-MS and liquid scintillation counting. Nucl. Inst. Methods Phys. Res. B 268, 192–199.

Christl, M., Vockenhuber, C., Kubik, P.W., Wacker, L., Lachner, J., Alfimov, V., Synal, H.A., 2013. The ETH Zürich AMS facilities: performance parameters and reference materials. Nucl. Instrum. Methods Phys. Res., Sect. B 294, 29–38.

Çiftçi, N.B., Bozkurt, E., 2010. Structural evolution of the Gediz Graben, SW Turkey: temporal and spatial variation of the graben basin. Basin Res. 22, 846–873.

Collettini, C., 2011. The mechanical paradox of low-angle normal faults: current understanding and open questions. Tectonophysics 510, 253–268.

Dewey, J.F., 1988. Extensional collapse of orogens. Tectonics 7, 1123–1139.

Dokka, R.K., Mahaffie, M.J., Snoke, A.W., 1986. Thermochronologic evidence of major tectonic denudation associated with detachment faulting, Northern Ruby Mountains – East Humboldt Range, Nevada. Tectonics 5, 995–1006.

Dolmaz, M.N., Hisarli, Z.M., Ustaömer, T., Orbay, N., 2005. Curie point depths based on spectrum analysis of aeromagnetic data, west Anatolian extensional province, Turkey. Pure Appl. Geophys. 162, 571–590.

Donelick, R.A., Ketcham, R.A., Carlson, W.D., 1999. Variability of apatite fission track annealing kinetics II: crystallographic orientation effects. Am. Mineral. 84, 1224–1234.

Dunkl, I., 2002. TRAKKEY: a window program for calculation and graphical presentation of fission track data. Comput. Geosci. 28, 3–12.

Ehlers, T.A., Farley, K.A., 2003. Apatite (U-Th)/He thermochronometry: methods and applications to problems in tectonics and surface processes. Earth Planet. Sci. Lett. 206, 1–14.

Emre, T., 1996. The tectonic evolution of the Gediz graben. Geol. Bull. Turk. 39, 1–18.

Emre, T., Sözbilir, H., 1997. Field evidence for metamorphic core complex, detachment faulting and accommodation faults in the Gediz and Büyük Menderes Grabens, Western Anatolia. International Earth Science Colloquium on the Aegean and Surrounding Regions, Proceedings, 1995, 1, pp. 73–94.

Emre, T., Sözbilir, H., 2007. Tectonic evolution of the Kiraz Basin, Küçük Menderes Graben: evidence for compression/uplift-related basin formation overprinted by extensional tectonics in West Anatolia. Turk. J. Earth Sci. 16, 441–470.

Eyidoğan, H., Jackson, J., 1985. A seismological study of normal faulting in the Demirci, Alaşehir and Gediz earthquakes of 1969–70 in western Turkey: implications for the nature and geometry of deformation in the continental crust. Geophys. J. R. Astron. Soc. 81, 569–607.

Farley, K.A., 2000. Helium diffusion from apatite: general behavior as illustrated by Durango fluorapatite. J. Geophys. Res. 105, 2903–2914.

Farley, K.A., 2002. (U-Th)/He dating: techniques, calibrations and applications. Mineralogical Society of America. Rev. Mineral. Geochem. 47, 819–844.

Farley, K.A., Wolf, R.A., Silver, L.T., 1996. The effects of long alpha-stopping distances on (U-Th)/He ages. Geochim. Cosmochim. Acta 60, 4223–4229.

Fitzgerald, P.G., Fryxell, J.E., Wernicke, B.P., 1991. Miocene crustal extension and uplift in southeastern Nevada: constraints from fission track analysis. Geology 19, 1013–1016.

Flowers, R.M., Shuster, D.L., Farley, K.A., 2007. Radiation damage control on apatite (U-Th)/He dates from the Grand Canyon region, Colorado Plateau. Geology 35, 447–450.

Forsyth, D.W., 1992. Finite extension and low-angle normal faulting. Geology 20, 27–30.

Foster, D.A., Miller, D.S., Miller, C.F., 1991. Tertiary extension in the Old Woman Mountains area, California: evidence from apatite fission track analysis. Tectonics 10, 875–886.

Gautier, P., Brun, J.P., 1994. Ductile crust exhumation and extensional detachments in the central Aegean (Cyclades and Evvia islands). Geodin. Acta 7, 57–85.

Gessner, K., Ring, U., Lackmann, W., Passchier, C.W., Güngör, T., 1998. Structure and crustal thickening of the Menderes Massif, southwest Turkey, and consequences for large-scale correlations between Greece and Turkey. Bull. Geol. Soc. Greece 1, 145–152.

Gessner, K., Ring, U., Johnson, C., Hetzel, R., Passchier, C.W., Güngör, T., 2001a. An active bivergent rolling-hinge detachment system: Central Menderes metamorphic core complex in western Turkey. Geology 29, 611–614.

Gessner, K., Piazolo, S., Güngör, T., Ring, U., Kröner, A., Passchier, C.W., 2001b. Tectonic significance of deformation patterns in granitoid rocks of the Menderes nappes, Anatolide belt, southwest Turkey. Int. J. Earth Sci. 89, 766–780.

Gessner, K., Collins, A.S., Ring, U., Gungor, T., 2004. Structural and thermal history of polyorogenic basement: U-Pb geochronology of granitoid rocks in the southern Menderes Massif, Western Turkey. J. Geol. Soc. Lond. 161, 93–101.

Gessner, K., Wijns, C., Moresi, L., 2007. Significance of strain localization in the lower crust for structural evolution and thermal history of metamorphic core complexes. Tectonics 26, TC2012. http://dx.doi.org/10.1029/2004TC001768.

Gessner, K., Gallardo, L.A., Markwitz, V., Ring, U., Thomson, S.N., 2013. What caused the denudation of the Menderes Massif: review of crustal evolution, lithosphere structure, and dynamic topography in southwest Turkey. Gondwana Res. 24, 243–274.

Gleadow, A.J.W., 1981. Fission-track dating methods: what are the real alternatives? Nucl. Tracks 5, 3–14.

Gleadow, A.J.W., Duddy, I.R., 1981. A natural long-term track annealing experiment for apatite. Nucl. Tracks 5, 169–174.

Glodny, J., Hetzel, R., 2007. Precise U-Pb ages of syn-extensional Miocene intrusions in the central Menderes Massif, western Turkey. Geol. Mag. 144, 235–246.

Goethals, M.M., Hetzel, R., Niedermann, S., Wittmann, H., Fenton, C.R., Kubik, P.W., Christl, M., von Blanckenburg, F., 2009. An improved experimental determination of cosmogenic ^{10}Be/^{21}Ne and ^{26}Al/^{21}Ne production ratios in quartz. Earth Planet. Sci. Lett. 284, 187–198.

Granger, D.E., Kirchner, J.W., Finkel, R., 1996. Spatially averaged long-term erosion rates measured from in situ-produced cosmogenic nuclides in alluvial sediment. J. Geol. 104, 249–257.

Grasemann, B., Dunkl, I., 2003. Effects of the geometry of normal faulting on the near surface heat flow during extension: the example of the Rechnitz Metamorphic Core Complex (Austria). Mitt. Österr. Geol. Ges. 92, 87–103.

Grasemann, B., Schneider, D.A., Stockli, D.F., Iglseder, C., 2012. Miocene divergent crustal extension in the Cyclades (Greece). Lithosphere 4, 23–39.

Green, P.F., Duddy, I.R., Gleadow, A.J.W., Tingate, P.R., Laslett, G.M., 1986. Thermal annealing of fission tracks in apatite 1. A qualitative description. Chem. Geol. 59, 237–253.

Guenthner, W.R., Reiners, P.W., Ketcham, R.A., Nasdala, L., Giester, G., 2013. Helium diffusion in natural zircon: radiation damage, anisotropy, and the interpretation of zircon (U-Th)/He thermochronology. Am. J. Sci. 313, 145–198.

Gürer, Ö.F., Sarıca-Filoreau, N., Özburan, M., Sangu, E., Doğan, B., 2009. Progressive development of the Büyük Menderes Graben based on new data, western Turkey. Geol. Mag. 146, 652–673.

Heineke, C., Hetzel, R., Akal, C., Christl, M., 2017. Lifespan of water reservoirs estimated from cosmogenic ^{10}Be in stream sediment. Water Resour. Res. (manuscript in revision).

Herman, F., Braun, J., Senden, T.J., Dunlap, W.J., 2007. (U-Th)/He thermochronometry: mapping 3D geometry using micro-X-ray tomography and solving the associated production-diffusion equation. Chem. Geol. 242, 126–136.

Hetzel, R., Reischmann, T., 1996. Intrusion of Pan-African gneisses in the southern Menderes massif and the age of cooling after Alpine ductile extensional deformation. Geol. Mag. 133, 565–572.

Hetzel, R., Ring, U., Akal, C., Troesch, M., 1995a. Miocene NNE-directed extensional unroofing in the Menderes Massif, southwestern Turkey. J. Geol. Soc. Lond. 152, 639–654.

Hetzel, R., Passchier, C.W., Ring, U., Dora, O.Ö., 1995b. Bivergent extension in orogenic belts: the Menderes Massif (southwestern Turkey). Geology 23, 455–458.

Hetzel, R., Romer, R.L., Candan, O., Passchier, C.W., 1998. Geology of the Bozdağ area, central Menderes massif, SW Turkey: Pan-African basement and Alpine deformation. Int. J. Earth Sci. 87, 394–406.

Hetzel, R., Zwingmann, H., Mulch, A., Gessner, K., Akal, C., Hampel, A., Güngör, T., Petschick, R., Mikes, T., 2013. Spatiotemporal evolution of brittle normal faulting and fluid infiltration in detachment fault systems: a case study from the Menderes Massif, western Turkey. Tectonics 32:1–13. http://dx.doi.org/10.1002/tect.20031.

Hourigan, J.K., Reiners, P.W., Brandon, M.T., 2005. U-Th zonation-dependent alpha-ejection in (U-Th)/He chronometry. Geochim. Cosmochim. Acta 69, 3349–3365.

Hurford, A.J., Green, P.F., 1983. The zeta age calibration of fission-track dating. Chem. Geol. 1, 285–317.

Ilkişik, O.M., 1995. Regional heat flow in western Anatolia using silica temperature estimates from thermal springs. Tectonophysics 244, 175–184.

Işik, V., Tekeli, O., Seyitoglu, G., 2004. The $^{40}Ar/^{39}Ar$ age of extensional ductile deformation and granitoid intrusion in the northern Menderes core complex: implications for the initiation of extensional tectonics in western Turkey. J. Asian Earth Sci. 23, 555–566.

Işik, V., Seyitoğlu, G., Çemen, I., 2003. Ductile-brittle transition along the Alaşehir detachment fault and its structural relationship with the Simav detachment fault, Menderes massif, western Turkey. Tectonophysics 374, 1–18.

Jolivet, L., Lecomte, E., Huet, B., Denéle, Y., Lacombe, O., Labrousse, L., Le Pourhiet, L., Mehl, C., 2010. The North Cycladic Detachment System. Earth Planet. Sci. Lett. 289, 87–104.

Karamanderesi, I.H., Helvacı, C., 2003. Geology and hydrothermal alteration of the Aydın-Salavatlı Geothermal Field, Western Anatolia, Turkey. Turk. J. Earth Sci. 12, 175–198.

Kohl, C.P., Nishiizumi, K., 1992. Chemical isolation of quartz for measurement of in-situ produced cosmogenic nuclides. Geochim. Cosmochim. Acta 56, 3583–3587.

Koralay, O.E., 2015. Late Neoproterozoic granulite facies metamorphism in the Menderes Massif, Western Anatolia/Turkey: implication for the assembly of Gondwana. Geodin. Acta 27, 244–266.

Koralay, O.E., Satir, M., Dora, O.Ö., 2001. Geochemical and geochronological evidence for Early Triassic calc-alkaline magmatism in the Menderes Massif, western Turkey. Int. J. Earth Sci. 89, 822–835.

Koralay, O.E., Candan, O., Akal, C., Dora, O.Ö., Chen, F., Satir, M., Oberhänsli, R., 2011. Geology and geochronology of the Pan-African and Triassic metagranitoids in the Menderes Massif, Western Anatolia, Turkey. Bull. Mineral Res. Explor. 142, 69–121.

Korschinek, G., Bergmaier, A., Faestermann, T., Gerstmann, U.C., Knie, K., Rugel, G., Wallner, A., Dillmann, I., Dollinger, G., von Gostomski, Ch.L., Kossert, K., Maiti, M., Poutivtsev, M., Remmert, A., 2010. A new value for the half-life of ^{10}Be by heavy-ion elastic recoil detection and liquid scintillation counting. Nucl. Inst. Methods Phys. Res. B 268, 187–191.

Kubik, P.W., Christl, M., 2010. ^{10}Be and ^{26}Al measurements at the Zurich 6 MV Tandem AMS facility. Nucl. Inst. Methods Phys. Res. B 268, 880–883.

Lal, D., 1991. Cosmic ray labeling of erosion surfaces: in situ nuclide production rates and erosion models. Earth Planet. Sci. Lett. 104, 424–439.

Lavier, L.L., Buck, W.R., Poliakov, A.N.B., 1999. Self-consistent rolling-hinge model for the evolution of large-offset low-angle normal faults. Geology 27, 1127–1130.

Lee, J., Lister, G.S., 1992. Late Miocene ductile extension and detachment faulting, Mykonos, Greece. Geology 20, 121–124.

Lippolt, H.J., Leitz, M., Wernicke, R.S., Hagerdon, B., 1994. (Uranium + thorium)/helium dating of apatite: experience with samples from different geochemical environments. Chem. Geol. 112, 179–191.

Lips, A.L.W., Cassard, D., Sözbilir, H., Yilmaz, H., Wijbrans, J.R., 2001. Multistage exhumation of the Menderes Massif, western Anatolia (Turkey). Int. J. Earth Sci. 89, 781–792.

Lisiecki, L.E., Raymo, M.E., 2005. A Pliocene-Pleistocene stack of 57 globally distributed benthic $\delta^{18}O$ records. Paleoceanography 20, PA1003. http://dx.doi.org/10.1029/2004PA001071.

Lister, G.S., Davis, G.A., 1989. The origin of metamorphic core complexes and detachment faults formed during Tertiary continental extension in the northern Colorado River region, U.S.A. J. Struct. Geol. 11, 65–94.

Loos, S., Reischmann, T., 1999. The evolution of the southern Menderes Massif in SW Turkey as revealed by zircon dating. J. Geol. Soc. Lond. 156, 1021–1030.

Lund, K., Beard, L.S., Perry, W.J., 1993. Relation between extensional geometry of the northern Grant Range and oil occurrences in Railroad Valley, east-central Nevada. Am. Assoc. Pet. Geol. 77, 945–962.

Mancktelow, N.S., 1992. Neogene lateral extension during convergence in the Central Alps: evidence from interrelated faulting and backfolding around the Simplonpass (Switzerland). Tectonophysics 215, 295–317.

Melosh, H.J., 1990. Mechanical basis for low-angle normal faulting. Nature 343, 331–335.

Morley, C.K., 2014. The widespread occurrence of low-angle normal faults in a rift setting: review of examples from Thailand, and implications for their origin and evolution. Earth Sci. Rev. 133, 18–42.

Naeser, C.W., 1978. Fission track dating. U.S. Geological Survey Open File Report 76–190 (31 pp.).

Nishiizumi, K., Imamura, M., Caffee, M.W., Southon, J.R., Finkel, R.C., McAninch, J., 2007. Absolute calibration of ^{10}Be AMS standards. Nucl. Inst. Methods Phys. Res. B 258, 403–413.

Oberhänsli, R., Candan, O., Dora, O.Ö., Dürr, S., 1997. Eclogites within the Menderes Massif/western Turkey. Lithos 41, 135–150.

Oner, Z., Dilek, Y., 2011. Supradetachment basin evolution during continental extension: the Aegean province of western Anatolia, Turkey. Geol. Soc. Am. Bull. 123, 2115–2141.

Oner, Z., Dilek, Y., 2013. Fault kinematics in supradetachment basin formation, Menderes core complex in western Turkey. Tectonophysics 608, 1394–1412.

Özer, S., Sözbilir, H., 2003. Presence and tectonic significance of Cretaceous rudist species in the so-called Permo-Carboniferous Göktepe Formation, central Menderes metamorphic massif, western Turkey. Int. J. Earth Sci. 92, 397–404.

Palumbo, L., Hetzel, R., Tao, M., Li, X., 2010. Topographic and lithologic control on catchment-wide denudation rates derived from cosmogenic ^{10}Be in two mountain ranges at the margin of NE Tibet. Geomorphology 117, 130–142.

Purvis, M., Robertson, A., 2004. A pulsed extension model for the Neogene–Recent E–W-trending Alaşehir Graben and the NE–SW-trending Selendi and Gördes Basins, western Turkey. Tectonophysics 391, 171–201.

Rahn, M.K., Brandon, M.T., Batt, G.E., Garver, J.I., 2004. A zero-damage model for fission-track annealing in zircon. Am. Mineral. 89, 473–484.

Regnier, J.L., Ring, U., Passchier, C.W., Gessner, K., Güngör, T., 2003. Contrasting metamorphic evolution of metasedimantary rocks from the Çine and Selimiye nappes in the Anatolide belt, western Turkey. J. Metamorph. Geol. 21, 699–721.

Reiners, P.W., 2005. Zircon (U-Th)/He thermochronometry. Rev. Mineral. Geochem. 58, 151–179.

Reiners, P.W., Brandon, M.T., 2006. Using thermochronology to understand orogenic erosion. Annu. Rev. Earth Planet. Sci. 34, 419–466.

Reiners, P.W., Ehlers, T.A. (Eds.), 2005. Low-temperature thermochronology: techniques, interpretations, and applications. Rev. Mineral. Geochem. (622 pp.).

Reiners, P.W., Zhou, Z., Ehlers, T.A., Xu, C., Brandon, M.T., Donelick, R.A., Nicolescu, S., 2003. Post-orogenic evolution of the Dabie Shan, eastern China, from (U-Th)/He and fission track thermochronology. Am. J. Sci. 303, 489–518.

Reiners, P.W., Spell, T.I., Nicolescu, S., Zanetti, K., 2004. Zircon (U-Th)/He thermochronometry: He diffusion and comparisons with $^{40}Ar/^{39}Ar$ dating. Geochim. Cosmochim. Acta 68, 1857–1887.

Ring, U., Brandon, M.T., Lister, G.S., Willett, S.D., 1999a. Exhumation processes. In: Ring, U., Brandon, M.T., Lister, G.S., Willett, S.D. (Eds.), Exhumation Processes: Normal Faulting, Ductile Flow, and Erosion. The Geological Society of London, Special Publications 154, pp. 1–27.

Ring, U., Gessner, K., Güngör, T., Passchier, C.S., 1999b. The Menderes Massif of western Turkey and the Cycladic Massif in the Aegean – do they really correlate? J. Geol. Soc. Lond. 156, 3–6.

Ring, U., Willner, A., Lackmann, W., 2001. Nappe stacking and clockwise versus anticlockwise pressure-temperature paths: an example from the Menderes nappes of western Turkey. Am. J. Sci. 301, 912–944.

Ring, U., Johnson, C., Hetzel, R., Gessner, K., 2003. Tectonic denudation of a Late Cretaceous-Tertiary collisional belt: regionally symmetric cooling patterns and their relation to extensional faults in the Anatolide belt of western Turkey. Geol. Mag. 140, 421–441.

Ring, U., Gessner, K., Thomson, S., 2017. Variations in fault-slip data and cooling history reveal corridor of heterogeneous backarc extension in the eastern Aegean Sea region. Tectonophysics 700–701, 108–130.

Rojay, B., Toprak, V., Demirci, C., Süzen, L., 2005. Plio-Quaternary evolution of the Küçük Menderes Graben Southwestern Anatolia, Turkey. Geodin. Acta 18, 317–331.

Satir, M., Friedrichsen, H., 1986. The origin and evolution of the Menderes Massif, W-Turkey: a rubidium/strontium and oxygen isotope study. Int. J. Earth Sci. 75, 703–714.

Schaffer, F., 1900. Das Maeanderthalbeben vom 20 September 1899. Mitteilungen der kaiserlichen-königlichen geographischen Gesellschaft Wien. vol. 43, pp. 221–230.

Scharf, A., Handy, M.R., Favaro, S., Schmid, S.M., Bertrand, A., 2013a. Modes of orogen-parallel stretching and extensional exhumation in response to microplate indentation and roll-back subduction (Tauern Window, Eastern Alps). Int. J. Earth Sci. 102, 1627–1654.

Scharf, T.E., Codilean, A.T., de Wit, M., Jansen, J.D., Kubik, P.W., 2013b. Strong rocks sustain ancient postorogenic topography in southern Africa. Geology 41, 331–334.

Schmidt, A., Pourteau, A., Candan, O., Oberhänsli, R., 2015. Lu-Hf geochronology on cm-sized garnets using microsampling: new constraints on garnet growth rates and duration of metamorphism during continental collision (Menderes Massif, Turkey). Earth Planet. Sci. Lett. 432, 24–35.

Selverstone, J., 1988. Evidence for east-west crustal extension in the Eastern Alps. Implications for unroofing history of the Tauern Window. Tectonics 7, 87–105.

Sen, S., Seyitoğlu, G., 2009. Magnetostratigraphy of early-middle Miocene deposits from east-west trending Alaşehir and Büyük Menderes grabens in western Turkey, and its tectonic implications. In: van Hinsbergen, D.J.J., Edwards, M.A., Govers, R. (Eds.), Collision and Collapse at the Africa-Arabia-Eurasia Subduction Zone. The Geological Society of London, Special Publications 311, pp. 321–342.

Şengör, A.M.C., Satir, M., Akkör, R., 1984. Timing of tectonic events in the Menderes Massif, western Turkey: implications for tectonic evolution and evidence for Pan-African basement in Turkey. Tectonics 3, 693–707.

Seyitoğlu, G., Scott, B.C., 1991. Late Cenozoic crustal extension and basin formation in west Turkey. Geol. Mag. 128, 155–166.

Sözbilir, H., Sarı, B., Uzel, B., Sümer, Ö., Akkiraz, S., 2011. Tectonic implications of transtensional supradetachment basin development in an extension-parallel transfer zone: the Kocaçay Basin, western Anatolia, Turkey. Basin Res. 23, 423–448.

Stone, J.O., 2000. Air pressure and cosmogenic isotope production. J. Geophys. Res. 105, 23753–23759.

Sümer, Ö., 2015. Evidence for the reactivation of a pre-existing zone of weakness and its contributions to the evolution of the Küçük Menderes Graben: a study of the Ephesus Fault, Western Anatolia, Turkey. Geodin. Acta 27, 130–154.

Thomson, S.N., Ring, U., 2006. Thermochronologic evaluation of postcollision extension in the Anatolide orogen, western Turkey. Tectonics 25, TC3005. http://dx.doi.org/10.1029/2005TC001833.

Wagner, G.A., van den Haute, P., 1992. Fission-track Dating. Kluwer Academic Publishers, The Netherlands (285 pp.).

Wernicke, B., 1995. Low-angle normal faults and seismicity: a review. J. Geophys. Res. 100, 20159–20174.

Wernicke, B., Axen, G.J., Snow, J.K., 1988. Basin and range extensional tectonics at the latitude of Las Vegas, Nevada. Geol. Soc. Am. Bull. 100, 1738–1757.

Westaway, R., 1994. Evidence for dynamic coupling of surface processes with isostatic compensation in the lower crust during active extension in western Turkey. J. Geophys. Res. 99, 203–223.

Wolf, R.A., Farley, K.A., Silver, L.T., 1996. Helium diffusion and low temperature thermochronology of apatite. Geochim. Cosmochim. Acta 60, 4231–4240.

Wolf, R.A., Farley, K.A., Kass, D.M., 1998. Modeling of the temperature sensitivity of the apatite (U-Th)/He thermochronometer. Chem. Geol. 148, 105–114.

Yılmaz, Y., Genç, S.C., Gürer, F., Bozcu, M., Yılmaz, Z., Karacik, S., Altunakynak, A., Elmas, A., 2000. When did the western Anatolian grabens begin to develop? In: Bozkurt, E., Winchester, J.A., Piper, J.D.A. (Eds.), Tectonics and Magmatism in Turkey and Surrounding Regions. The Geological Society of London, Special Publication 173, pp. 353–384.

Zaun, P.E., Wagner, G.A., 1985. Fission-track stability in zircons under geological conditions. Nucl. Tracks 10, 303–307.

Zeitler, P.K., Herczeg, A.L., McDougall, I., Honda, M., 1987. U-Th-He dating of apatite: a potential thermochronometer. Geochim. Cosmochim. Acta 51, 2865–2868.

Zlatkin, O., Avigad, D., Gerdes, A., 2012. Evolution and provenance of Neoproterozoic basement and Lower Palaeozoic siliciclastic cover of the Menderes Massif (Western Taurides): coupled U-Pb-Hf zircon isotope geochemistry. Gondwana Res. 23, 682–700.

3. Exhumation history of the Aydın range and the role of the Büyük Menderes detachment system during bivergent extension of the central Menderes Massif, western Turkey

Nils-Peter Nilius[1], Christoph Glotzbach[2], Andreas Wölfler[1], Andrea Hampel[1], István´Dunkl[5], Cüneyt Akal[4], Caroline Heineke[5], Ralf Hetzel[5]*

[1]Institute of Geology, Leibniz University of Hannover, Callinstraße 30, 30167 Hannover, Germany

[2]Department of Geosciences, University of Tübingen, Wilhelmstraße 56, 72074 Tübingen, Germany

[3]University of Göttingen, Geoscience Center, Sedimentology and Environment Geology, Goldschmidstraße 3, 37077 Göttingen, Germany

[4]Dokuz Eylül University, Engineering Faculty, Department of Geological Engineering, Tınaztepe Campus, Buca, 35390 Izmir, Turkey

[5]Institute of Geology and Palaeontology, University of Münster, Corrensstraße 24, 48149 Münster, Germany

* Corresponding author, nilius@geowi.uni-hannover.de

KEYWORDS
Continental extension, Low-angle normal faulting, detachment faulting, low-temperature thermochronology, exhumation rate modelling

Exhumation history of the Aydın range and the role of the Büyük Menderes detachment system during bivergent extension of the central Menderes Massif, western Turkey

Nils-Peter Nilius[1]*, Christoph Glotzbach[2], Andreas Wölfler[1], Andrea Hampel[1], István Dunkl[3], Cüneyt Akal[4], Caroline Heineke[5] & Ralf Hetzel[5]

[1] Institute of Geology, Leibniz University of Hannover, Callinstraße 30, 30167 Hannover, Germany
[2] Department of Geosciences, University of Tübingen, Wilhelmstraße 56, 72074 Tübingen, Germany
[3] University of Göttingen, Geoscience Center, Sedimentology and Environment Geology, Goldschmidtstraße 3, 37077 Göttingen, Germany
[4] Engineering Faculty, Department of Geological Engineering, Tınaztepe Campus, Buca, 35390 Izmir, Turkey
[5] Institute of Geology and Palaeontology, University of Münster, Corrensstraße 24, 48149 Münster, Germany
  N.-P.N., 0000-0002-3936-6507
* Correspondence: nilius@geowi.uni-hannover.de

Abstract: The central Menderes Massif (western Turkey) is a prominent example of symmetrical exhumation of a core complex. It comprises the Bozdağ and Aydın ranges, which represent the footwalls of the north-dipping Gediz detachment and the south-dipping Büyük Menderes detachment, respectively. In contrast to the Gediz detachment, the role of the Büyük Menderes detachment during Late Cenozoic extension and exhumation of the central Menderes Massif is less well resolved. Here, we present results from structural and geological mapping as well as new fission-track and (U–Th)/He data to show that two low-angle normal faults contributed to the exhumation of the Aydın range. Our data indicate that the sustained activity of the Büyük Menderes detachment since the early Miocene is followed by the onset of faulting along the previously unrecognized Demirhan detachment, which is situated in the hanging wall of the Büyük Menderes detachment, in the latest Miocene/ Pliocene. Thermokinematic modelling of cooling ages from the footwalls of the Büyük Menderes and Demirhan detachments yielded exhumation rates of *c.* 0.5 and *c.* 0.4 km Ma^{-1}, respectively. Apatite fission track ages from the Demirhan detachment indicate a slip rate of *c.* 2 km Ma^{-1} during the Pliocene. High-angle normal faulting along the modern Büyük Menderes graben commenced in the Quaternary.

Supplementary material: Further results of thermal history modelling are available at https://doi.org/10.6084/m9.figshare.c.4392905

Low-angle normal faults accommodate large-scale crustal extension and have been observed in different tectonic environments, for example, in backarc (e.g. Jolivet & Brun 2010; Ustaszewski *et al.* 2010), post-orogenic (Wernicke 1992; Malavieille 1993) and syn-orogenic (e.g. Lister & Davis 1989; Burchfiel *et al.* 1992; Lee & Lister 1992; Campani *et al.* 2010; Rutte *et al.* 2017) settings. These field observations were complemented by numerical and analogue models, which identified two endmember models that are either dominated by pure shear strain, where bivergent extension leads to symmetrical exhumation (McKenzie 1978), or by asymmetrical simple shear strain (Wernicke 1985). A combination of both models has also been proposed (e.g. Lister *et al.* 1986). However, most natural examples of core complexes have been exhumed in an asymmetrical manner (Brun *et al.* 2017*a*, *b*), i.e. a single low-angle normal fault accommodates most of the regional extension. Rare examples of symmetrically exhumed core complexes occur in western Turkey (Bozkurt 2000; Gessner *et al.* 2001*a*; Ring *et al.* 2003) and in the Aegean region (Grasemann *et al.* 2012) (Fig. 1).

In the Aegean region and western Turkey, large-scale continental extension commenced after Alpine nappe stacking had ceased in the Eocene and was attributed to the collapse of the overthickened crust or to the acceleration of the retreating Aegean slab or to a combination of both processes (e.g. Jolivet & Brun 2010; Ersoy *et al.* 2017). Subsequently, vertical thinning of the crust was accommodated by low-angle normal faults leading to the formation of several core complexes, such as the Attic–Cycladic Complex in

the Aegean (e.g. Lister *et al.* 1984; Jolivet & Patriat 1999; Huet *et al.* 2009; Jolivet *et al.* 2010) and the Menderes Massif in western Turkey (e.g. Hetzel *et al.* 1995*a*, *b*; Işik & Tekeli 2001; Ring *et al.* 2003; Bozkurt & Sözbilir 2004; Gessner *et al.* 2013). Many models of the Miocene backarc tectonics in the Aegean attribute the thinning of the crust to top-to-the north shearing along the North Cycladic detachment system, implying an asymmetrical mode of extension accommodated by a single detachment fault (Lee & Lister 1992; Vanderhaeghe 2004; Huet *et al.* 2009). However, recent studies in the southern and western Cyclades proposed that top-to-the north shearing observed in the North Cycladic detachment system was accompanied by top-to-the south shearing along the South and West Cycladic detachment systems, implying a more symmetrical bivergent mode of crustal extension (Iglseder *et al.* 2011; Grasemann *et al.* 2012). The study of these detachment systems is, however, hindered by the fact that large areas are located below sea level. To investigate the nature of bivergent continental extension, we focus on the well-exposed central Menderes Massif in western Turkey where bivergent post-orogenic extension was first described by Hetzel *et al.* (1995*b*) (Fig. 1).

The Menderes Massif was exhumed in two stages. The first stage has been attributed to the exhumation of the northern Menderes Massif along the Simav detachment (Fig. 1) in the latest Oligocene to early Miocene (Işik & Tekeli 2001; Ring & Collins 2005; Thomson & Ring 2006; Erkül 2009) and the second stage to the exhumation of the central Menderes Massif since the middle
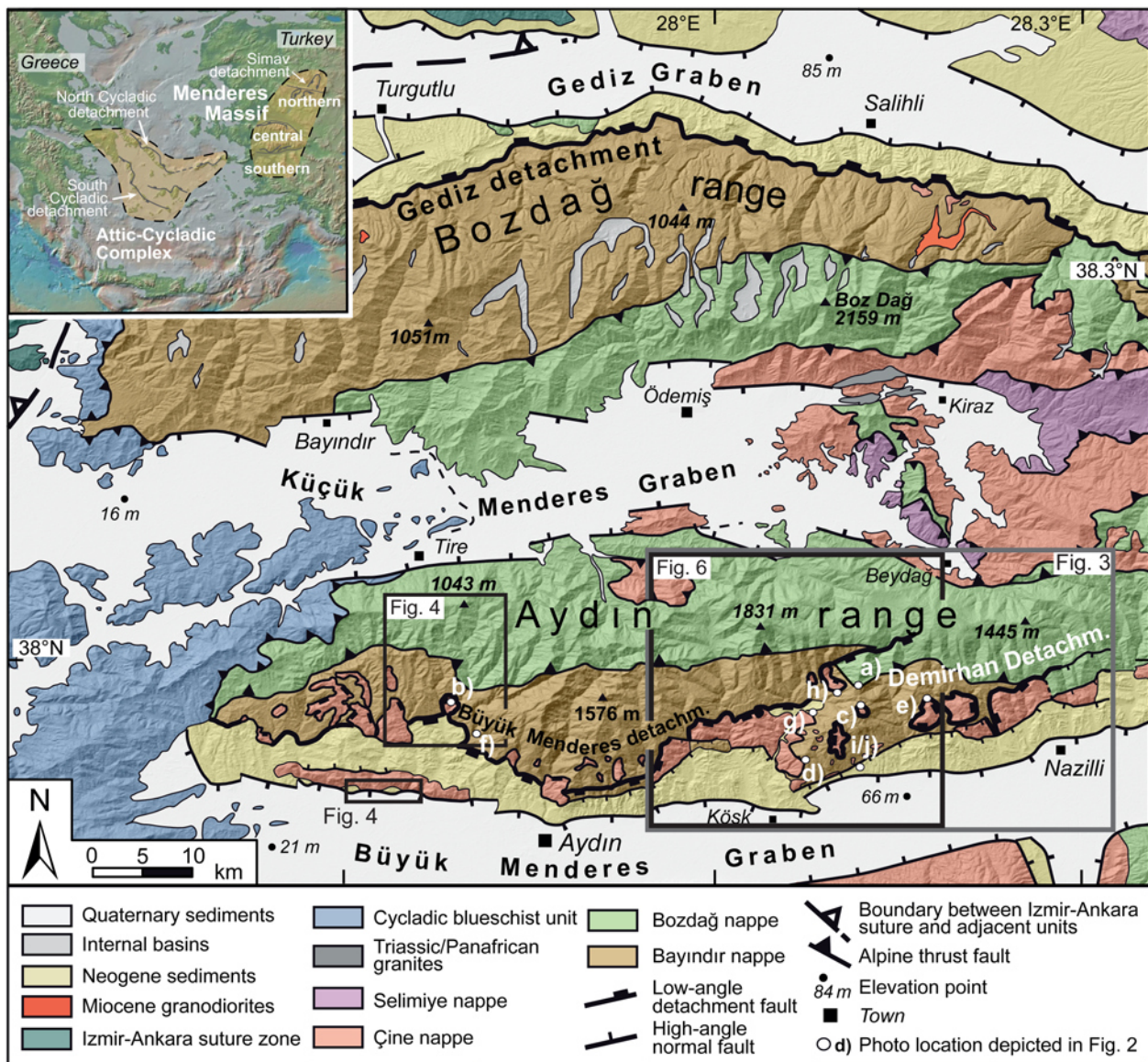
Fig. 1. Geological map of the central Menderes Massif with rectangles outlining the area shown in Figs 3, 4 and 6 (modified from Wölfler *et al.* (2017) and complemented with own field observations). The locations of the photographs in Figure 2 are also indicated.

Miocene (Hetzel *et al.* 1995*a*, *b*; Emre & Sözbilir 1997; Gessner *et al.* 2001*b*). Interestingly, the mode of exhumation of the two sub-massifs is very different, as the northern Menderes Massif was asymmetrically exhumed by top-to-the north faulting on the Simav detachment, whereas the central Menderes Massif was symmetrically exhumed along two oppositely dipping low-angle detachment faults (Hetzel *et al.* 1995*b*; Bozkurt 2001; Ring *et al.* 2003). During this bivergent extension, the north-dipping Gediz detachment exhumed the Bozdağ range, whereas the south-dipping Büyük Menderes detachment exhumed the Aydın range (Figs 1 and 2a, b). The proposed symmetrical exhumation history of the central Menderes Massif is mainly based on temporal and structural constraints derived from the Gediz detachment as it was inferred by the symmetrical architecture of the central Menderes Massif that the Aydın and the Bozdağ range share the same exhumation history (Gessner *et al.* 2001*b*). Consequently, the extensional history of the northern part of the central Menderes Massif is well constrained by geochronological data from the Bozdağ range, which indicate two phases of increased footwall cooling in the middle Miocene and since the latest Miocene/Pliocene by using $^{206}Pb/^{238}U$ dating of monazite and titanite (Glodny & Hetzel 2007; Rossetti *et al.* 2017) as well as low-temperature thermochronology (Hetzel *et al.* 1995*a*;

Gessner *et al.* 2001*a*; Ring *et al.* 2003; Buscher *et al.* 2013; Asti *et al.* 2018).

Thermochronological data of Wölfler *et al.* (2017) provided support for the interpretation that the proposed two-stage model of extension and footwall cooling in the middle Miocene and latest Miocene/Pliocene also applies to the Büyük Menderes detachment. However, most other studies from the southern central Menderes Massif focused on the evolution of the Büyük Menderes graben, which is situated in the hanging wall and south of the Büyük Menderes detachment (Sözbilir & Emre 1990; Cohen *et al.* 1995; Bozkurt 2001; Gürer *et al.* 2009; Sen & Seyitoğlu 2009). Nevertheless, the exact age of the Büyük Menderes graben is still disputed and either described as early Miocene to middle Miocene (Sözbilir & Emre 1990; Cohen *et al.* 1995; Akgün & Akyol 1999; Sen & Seyitoğlu 2009) or as latest Miocene/Pliocene (Gürer *et al.* 2009; Ring *et al.* 2017). Additionally, a prevailing extensional tectonic setting during graben formation in the Miocene has been questioned by Gürer *et al.* (2009).

Here we aim to investigate the exhumation history of the central Menderes Massif by focusing on the Aydın range as the footwall of the Büyük Menderes detachment. We have conducted field mapping of major structures related to late Cenozoic extension

Exhumation history of the Aydın range
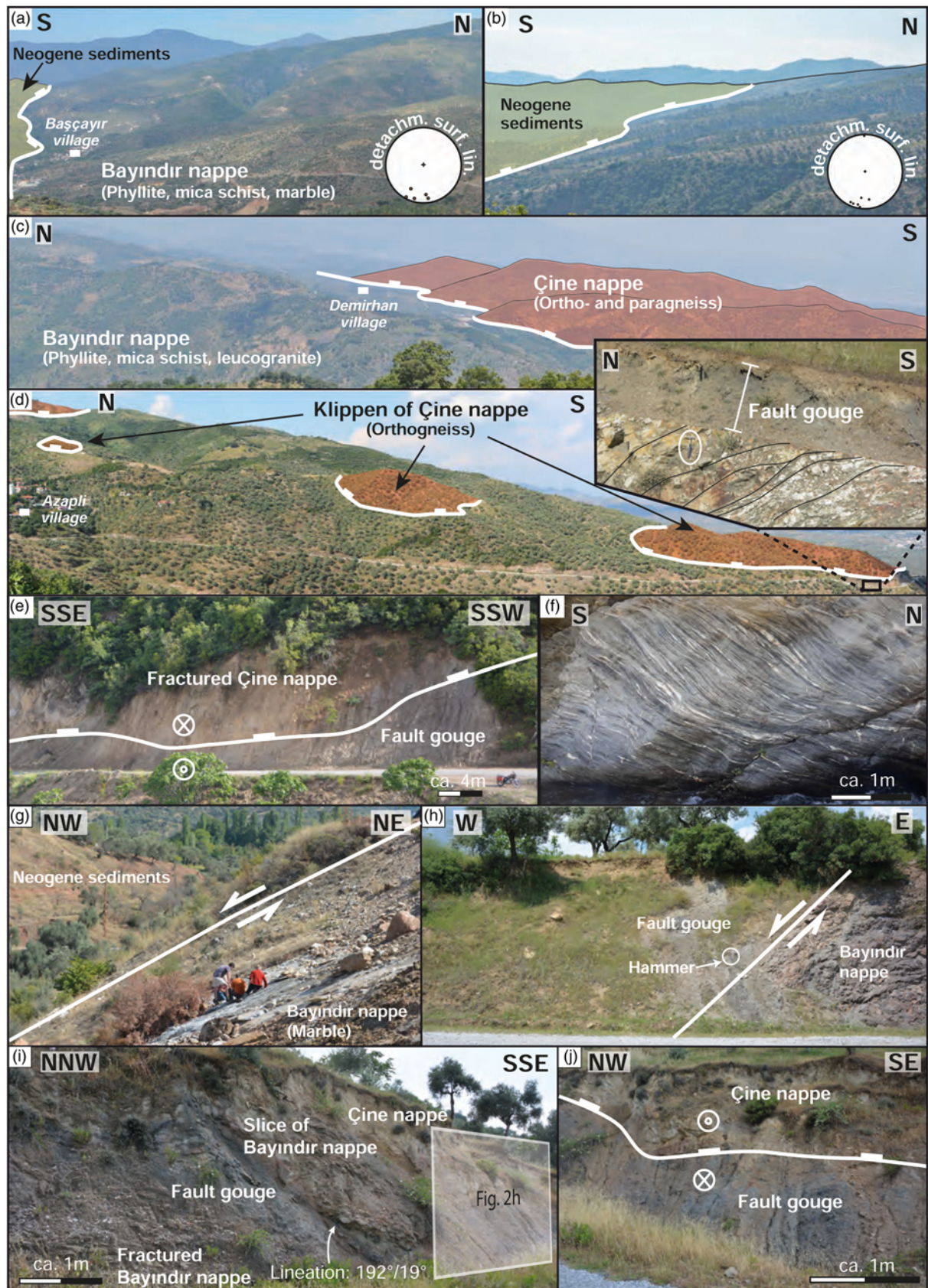
Fig. 2. (**a**) South-dipping footwall of the Büyük Menderes detachment at Başçayır village. (**b**) Erosion resistant footwall of the Büyük Menderes detachment west of Beyköy. (**c**) View to the SE on the southern flank of the Aydın range and the Demirhan detachment. (**d**) Orthogneiss of the hanging wall of the Demirhan detachment south of Karatepe. (**e**) A thick fault gouge horizon between Bayındır nappe and Çine nappe marks the Demirhan detachment west of Demirhan village. (**f**) Mylonitic footwall below the Büyük Menderes detachment near Beyköy. (**g**) Exposure of the WNW-dipping normal fault west of Başçayır village. (**h**) Outcrop of the same normal fault further north, comprising Çine nappe gneisses in the hanging wall and phyllites of the Bayındır nappe in the footwall. (**i**) Exposure of the Demirhan detachment in the uplifted part of the Büyük Menderes Graben north of Nysa. (**j**) Upper limit of the Demirhan detachment fault zone where Çine nappe of the hanging wall rests on fault gouge horizon of the Demirhan detachment. See Figure 1 for locations.

and applied low-temperature thermochronology to detect along-strike changes in the cooling history as well as thermokinematic modelling to obtain exhumation rates. Based on these new structural and thermochronological data, we suggest a new tectonic model for the evolution of the Büyük Menderes graben and improve the constraints on the bivergent exhumation of the central Menderes Massif.

Geological setting of western Turkey

The geological evolution of western Anatolia has been dominated (1) by the convergence between Africa and Eurasia since the middle Cretaceous, which led to the formation of the Anatolides in the Eocene (Şengör & Yilmaz 1981; Candan *et al.* 2005; Kaymakci *et al.* 2009; Jolivet & Brun 2010), and (2) by the ongoing continental extension since the late Oligocene/early Miocene, due to the roll-back of the Hellenic trench (e.g. Gessner *et al.* 2013; Jolivet *et al.* 2013). The proposed crustal architecture of the Menderes Massif is based on geological observations in the southern part of the Menderes Massif and the subdivision between a 'core', consisting of Precambrian metagranites and an overlying 'cover' with Paleozoic/Mesozoic sedimentary units. The sediment-ary units are (from bottom to top) composed of amphibolite-facies mica schists, greenschist-facies phyllites and marbles (Schuiling 1962). This core-cover concept was challenged by Bozkurt *et al.* (1993) and revised by Ring *et al.* (1999), who proposed that the Menderes Massif represents an Alpine nappe stack. The main argument against the core-cover concept is the observation that in the central part of the Menderes Massif, the structurally lowest position is occupied by a greenschist-facies metasedimentary unit of late Cretaceous age, which is overlain by older, amphibolite-facies garnet-mica schists and metabasites (Özer & Sözbilir 2003; Gessner *et al.* 2013).

The nappe pile consists of four nappes, with the Bayındır nappe in the lowest position (Ring *et al.* 1999; Gessner *et al.* 2001c). Most of the Bayındır nappe is composed of phyllites with intercalated marbles, quartzites and greenschist. The lack of biotite implies a lower greenschist-facies metamorphic overprint with temperatures below 400°C in the late Eocene, with the timing being still poorly constrained by a single ^{40}Ar/^{39}Ar white mica age of 36 ± 2 Ma (Lips *et al.* 2001). A rudist-bearing marble unit implies that the Bayındır nappe only experienced one Alpine metamorphic overprint and that the contact to the overlaying Bozdağ nappe must therefore be an Alpine thrust. The metasedimentary units of the Bozdağ nappe experienced amphibolites-facies metamorphic conditions during the Pan-African Orogeny (Candan *et al.* 2001; Ring *et al.* 2001; Koralay 2015). Lithologies constituting the Bozdağ nappe include mainly metapelite and minor volumes of amphibolite, dolomite, eclogite and granitic intrusions of Triassic age (Koralay *et al.* 2001, 2011). As these intrusions also penetrate the Çine nappe above, a pre-Triassic – most probably Pan-African – age for the tectonic contact between Bozdağ and Çine nappe seems likely (Gessner *et al.* 2001c). The most prominent lithologies of the Çine nappe are deformed orthogneisses (augengneiss) and minor amounts of orthogneiss, pelitic gneiss, amphibolite and eclogite (Oberhänsli *et al.* 1997). The protoliths of the orthogneisses were calc-alkaline leucogranites, which comprise late Neoproterozoic to early Cambrian intrusion ages (Bozkurt *et al.* 1995; Hetzel & Reischmann 1996; Loos & Reischmann 1999). The uppermost nappe of the Menderes Massif is the Selimiye nappe, which was affected by alpine Barrovian-type metamorphism between 43 and 34 Ma and was thrust over the Çine nappe during the Eocene (Ring *et al.* 2003; Schmidt *et al.* 2015). It consists of metapelites, marbles and metabasites of Paleozoic age (Regnier *et al.* 2003; Gessner *et al.* 2004). The Menderes nappes are overlain by remnants of the Neotethyan ocean; these remnants experienced high-pressure

metamorphism during Alpine northward subduction below the Sakarya microcontinent and are exposed north and NW of the central Menderes Massif (Okay & Tüysüz 1999).

Neogene to Recent extension of the Menderes Massif (western Turkey)

In the late Oligocene/early Miocene, the Alpine nappe stack experienced a sustained change to continental extension, leading to low-angle normal faulting and the formation of east–west-striking graben systems, which separate the Menderes Massif into three submassifs. The northern Menderes Massif is separated from the central Menderes Massif by the Gediz graben, and the central Menderes Massif is separated from the southern Menderes Massif by the Büyük Menderes graben (Fig. 1).

The first phase of post-orogenic extension in the Menderes Massif occurred between the late Oligocene to early Miocene, as revealed by apatite and zircon (U–Th)/He and fission track thermochronology as well as by U–Pb ages from syntectonic intrusions. This extension phase is recorded in the northern and southern Menderes Massif, but also in the structurally higher units of the central Menderes Massif (Gessner *et al.* 2001a; Ring & Collins 2005; Thomson & Ring 2006; Hasözbek *et al.* 2011; Buscher *et al.* 2013). Only in the northern Menderes Massif can this cooling event be unequivocally attributed to tectonic denudation along the top-to-the-north movement on the Simav detachment (Işik & Tekeli 2001; Işik *et al.* 2004; Thomson & Ring 2006; Erkül 2010).

The second phase of extension is connected to the exhumation of the central Menderes Massif along two extensional detachments with opposite dip (Fig. 1): the Gediz detachment in the north (also called the Alaşehir or Kuzey detachment) (Hetzel *et al.* 1995a, b; Gessner *et al.* 2001a; Seyitoğlu *et al.* 2002; Bozkurt & Sözbilir 2004; Buscher *et al.* 2013) and the Büyük Menderes detachment in the south (also described as the Güney detachment) (Emre & Sözbilir 1997; Bozkurt 2000). The Gediz detachment and the Büyük Menderes detachment are exposed along the Bozdağ and Aydın mountain ranges, respectively, and are separated by the Küçük Menderes Graben (Fig. 1). In the footwall of both detachments, the Bayındır nappe, as the structurally deepest unit of the Alpine nappe pile, constitutes large parts of the cataclastically overprinted footwalls, which are discordantly overlain by Neogene syn-extensional sediments and klippen of Çine nappe augengneiss (e.g. Cohen *et al.* 1995; Sen & Seyitoğlu 2009; Çiftçi & Bozkurt 2010).

The extensional history of the Bozdağ range is well constrained by age data from two granodioritic intrusions (the Turgutlu and Salihli granodiorites). The intrusion of the Salihli granodiorite into the footwall of the Gediz detachment occurred at *c.* 16 Ma and the recrystallization of titanite from mylonitic parts of the granodiorite at 14–15 Ma (U–(Th)–Pb dating) is interpreted to reflect the onset of ductile shearing (Hetzel *et al.* 1995a; Glodny & Hetzel 2007; Catlos *et al.* 2010; Rossetti *et al.* 2017) Subsequent cooling and exhumation of the footwall of the Gediz detachment is documented by ^{40}Ar/^{39}Ar ages from biotite, yielding an age of *c.* 12 Ma (Hetzel *et al* 1995a), and final exhumation during the Pliocene constrained by (U–Th)/He and fission track thermochronology of zircon and apatite (Gessner *et al.* 2001a; Ring *et al.* 2003; Buscher *et al.* 2013). Faulting along the Gediz detachment was followed by the onset of high-angle normal faulting at the southern margin of the modern Gediz graben in the late Pliocene (Oner & Dilek 2011; Buscher *et al.* 2013).

The Büyük Menderes detachment was first mapped by Candan *et al.* (1992) and later recognized as an extensional detachment fault with a top-to-the south sense of movement (Emre & Sözbilir 1997). It is exposed along the southern flank of the Aydın range and dips

5–20° to the south. First constraints on the cooling history of the Aydın range in the footwall of the Büyük Menderes detachment were given by a limited set of apatite fission track ages ranging from 16 to 6 Ma (Gessner *et al.* 2001*a*; Ring *et al.* 2003). Wölfler *et al.* (2017) presented thermochronological data along a north–south transect across the Aydın range and identified two episodes of enhanced cooling along the Büyük Menderes detachment. Their dataset implied increased exhumation rates of *c.* 0.9 km Ma^{-1} in the middle Miocene and of *c.* 0.4 km Ma^{-1} in the latest Miocene/Pliocene. This two-phase evolution is also observed in the sedimentary succession of the Büyük Menderes graben, which can be divided into a lower part comprising deformed Miocene sediments and discordantly overlaying undeformed Pliocene to Pleistocene units. The succession starts with the Hasköy formation, which is characterized by fluvio-lacustrine sediments including boulder conglomerates, sandstones and mudstones that contain lignite layers (Sözbilir & Emre 1990). The depositional ages suggested for the Hasköy formation range from early-middle Miocene to late Miocene ages (Sözbilir & Emre 1990; Seyitoğlu & Scott 1991, 1992; Akgün & Akyol 1999). The Hasköy formation is in a conformable contact with the overlying middle Miocene Gökkırantepe formation, consisting exclusively of terrestrial fluvial and alluvial sediments, whereas the boundary to the topmost late Pliocene to Pleistocene Asartepe formation is marked by an unconformity (Sözbilir & Emre 1990; Sen & Seyitoğlu 2009).

Methods

We use zircon and apatite (U–Th)/He (ZHe and AHe) and fission track (ZFT and AFT) thermochronology to derive the post-orogenic thermal history and, in combination with thermokinematic modelling, the exhumation history of the Aydın range (Table 1). The closure temperature of each system refers to a specific temperature through which the sample cooled at the measured time (the cooling age), under the assumption that the cooling path was continuous (Dodson 1973). The samples from the Büyük Menderes and Demirhan detachments were collected from hanging-wall units and in the footwall parallel to the direction of tectonic transport.

Zircon and apatite fission-track analysis

Among the total of 24 samples collected, 20 samples were used for AFT analysis and four were used for ZFT analysis (Table 1). Typical closure temperatures for the ZFT method are *c.* 240°C and for the AFT method *c.* 110°C, even though the exact closure temperature of each system may vary by different factors such as the cooling rate, mineral chemistry and radiation damage (e.g. Dodson 1973; Gleadow & Duddy 1981; Wagner & van den Haute 1992; Rahn *et al.* 2004; Ketcham *et al.* 2007). The temperature ranges from annealing to total resetting of fission tracks are *c.* 190–*c.* 380°C in zircon and *c.* 60–*c.* 120°C for apatite (Green *et al.* 1986; Wagner & van den Haute 1992; Rahn *et al.* 2004).

Conventional magnetic and heavy liquid separation techniques were applied for zircon and apatite separation. Subsequently, the zircon and apatite separates were embedded in PDA TeflonTM and epoxy, respectively, and finally grounded and polished. Zircon mounts were etched in a KOH–NaOH eutectic melt at 215°C (Zaun & Wagner 1985), whereas apatite mounts were etched with 5 M HNO$_3$ for 20 s at 21°C. We used the external detector method (Gleadow 1981) with uranium-free muscovite sheets and Durango apatite and Fish Canyon zircon age standards for the zeta calibration approach (e.g. Naeser 1978; Hurford & Green 1983). The required irradiation of the samples with thermal neutrons was performed at the FRM-II reactor facility in Garching (Technical University Munich, Germany). To monitor the neutron fluence IRMM-540R and IRMM-541 dosimeter glasses were used. Fission-track counting was carried out with an Olympus BX-51 microscope with 1000× magnification at the Institute of Geology in Hannover. For the assessment of fission track annealing kinetics in apatite we used Dpar values (mean diameter of etch figures on prismatic surfaces of apatite parallel to the crystallographic *c*-axis) (Burtner *et al.* 1994). Fission-track ages were calculated with the TRACKKEY software version 4.2 (Dunkl 2002) and are reported in Tables 2 and 3 with 1σ standard errors. We are unable to report

Table 1. *Location, lithology, and structural position of samples for low-temperature thermochronology*

Sample	Latitude (°N) (WGS 84)	Longitude (°E) (WGS 84)	Elevation (m)	Lithology	Structural position	Thermochronometers applied
15M42	37.88020	27.72991	126	Augengneiss	Çine nappe	AHe, AFT
15M44	37.96619	28.11728	970	Mica schist	Bayındır nappe, footwall	AHe, AFT, ZHe
15M45	38.02442	28.13655	1800	Mica schist	Bayındır nappe, footwall	AFT, ZFT
15M46	38.02466	28.10558	1272	Mica schist	Bayındır nappe, footwall	AHe, AFT, ZHe
15M47	38.02466	28.10558	1272	Mica schist	Bayındır nappe, footwall	AFT, ZHe, ZFT
15M48	38.00683	28.11189	922	Mica schist	Bayındır nappe, footwall	AFT
15M49	37.99857	28.10446	805	Mica schist	Bayındır nappe, footwall	AFT
15M51	37.96117	28.08538	387	Sandstone	Miocene sediments, hanging wall	AHe, AFT
15M52	38.04412	27.75315	1014	Mica schist	Bayındır nappe, footwall	AFT
15M54	38.01768	27.74109	909	Mica schist	Bozdağ nappe, footwall	AFT
15M55	38.00243	27.75802	812	Mica schist	Bozdağ nappe, footwall	AFT, ZHe
15M56	37.98357	27.76323	715	Mica schist	Bayındır nappe, footwall	AFT, ZHe
15M57	37.96844	27.76144	505	Paragneiss	Bayındır nappe, footwall	AFT, ZHe, ZFT
15M58	37.95739	27.75863	292	Mica schist	Bayındır nappe, footwall	AFT, ZHe
15M59	37.94882	27.75504	190	Paragneiss	Çine nappe, hanging wall	AHe, AFT, ZHe, ZFT
16M86	37.89713	27.62427	147	Augengneiss	Çine nappe	AHe, AFT
16M87	37.98260	28.13009	1345	Mica schist	Bozdağ nappe, footwall	AFT, ZHe
16M88	38.00618	28.13879	1226	Paragneiss	Bozdağ nappe, footwall	AFT
16M89	38.02486	28.06677	1652	Orthogneiss	Bozdağ nappe, footwall	AFT, ZHe
16M90	38.00476	28.13803	1255	Paragneiss	Bozdağ nappe, footwall	AFT, ZHe
16M91	38.00623	28.14016	1207	Paragneiss	Bozdağ nappe, footwall	ZHe
16M94	37.95898	27.75963	325	Phyllite	Bayındır nappe, footwall	AFT
16M95	38.00100	27.81659	1186	Paragneiss	Bozdağ nappe, footwall	AFT, ZHe
16M97	37.96945	27.79044	694	Mica schist	Bayındır nappe, footwall	AFT

Table 2. *Results of apatite fission-track analyses*

Sample	Number of grains	ρ_s	N_s	ρ_i	N_i	ρ_d	N_d	$P(\chi^2)$ (%)	Dispersion (%)	Central age±1σ (Ma)	U (ppm)	Dpar (μm)
15M42	17	1.016	37	3.956	144	5.5313	2796	99	0	16.1 ± 3.1	9	2.86
15M44	25	0.919	44	9.562	458	5.5103	2796	96	2	6.0 ± 1.0	26	1.36
15M45	25	3.211	122	22.105	840	5.4794	2796	64	2	9.0 ± 1.0	53	2.99
15M46*	20	3.907	53	19.388	263	5.448	2796	99	0	14.0 ± 2.2	46	1.59
15M47*	10	2.480	31	13.360	167	5.4174	2796	97	0	11.4 ± 2.3	30	2.39
15M48*	21	1.298	27	2.740	57	2.1489	2796	100	0	13.0 ± 3.1	19	1.95
15M49	21	1.507	52	7.072	244	5.3554	2796	92	18	13.3 ± 2.3	28	2.09
15M51	9	4.956	56	19.292	218	5.2934	2796	26	22	15.7 ± 2.8	58	2.39
15M52	22	3.215	79	22.543	554	7.4810	2481	100	0	12.1 ± 1.6	42	1.90
15M54	13	2.331	38	10.061	164	5.2315	2796	81	2	13.2 ± 2.6	27	2.52
15M55	17	1.641	42	8.828	226	5.2005	2796	100	0	11.0 ± 2.0	25	2.14
15M56	25	1.748	54	7.540	233	5.2005	2796	96	0	15.4 ± 2.4	21	1.81
15M57*	8	1.383	13	7.234	68	5.1285	2796	99	0	10.6 ± 3.3	20	1.99
15M58	22	1.546	45	21.306	620	5.1075	2796	80	16	4.3 ± 0.7	58	2.34
15M59	23	1.701	83	12.193	595	4.7896	2796	28	15	7.9 ± 1.3	33	1.87
16M86	20	1.763	35	5.899	137	7.185	2481	99	0	23.5 ± 4.5	13	2.08
16M87	24	3.433	110	23.061	739	7.2356	2481	78	16	12.2 ± 1.5	43	1.52
16M88	17	1.522	63	9.859	408	6.9901	2481	97	0	12.2 ± 1.8	32	1.36
16M89	17	3.513	67	18.091	345	6.9411	2481	99	0	15.3 ± 2.2	34	1.68
16M90	35	3.929	163	23.769	986	6.8920	2481	99	0	12.9 ± 1.3	48	1.86
16M94	23	1.484	42	18.297	518	6.6956	2481	100	0	6.2 ± 1.1	37	1.22
16M95	14	2.479	29	14.276	167	6.6465	2481	100	0	13.1 ± 2.8	35	1.51
16M97	7	1.538	13	11.947	101	6.5975	2481	98	0	9.6 ± 2.9	35	1.60

ρ_s (ρ_i) is the spontaneous (induced) track density (10^5 tracks per cm^2); N_s (N_i) is the number of counted spontaneous (induced) tracks; ρ_d is the dosimeter track density (10^5 tracks per cm^2); N_d is the number of tracks counted on the dosimeter; $P(\chi^2)$ is the probability of obtaining a Chi-square value (χ^2) for *n* degree of freedom (where *n* is the number of crystals minus 1); ages were calculated using the zeta calibration method (Hurford & Green 1983), glass dosimeter IRMM540, and zeta values of 226 ± 13 a cm^{-2} (samples without asterisk) and 255 ± 9 a cm^{-2} (samples with asterisk) calculated with Durango apatite standards.

track length measurements, because the apatite do not have a sufficient number of tracks owing to their low uranium content and the young cooling history of the rocks. Nevertheless, the available AFT track length data provided by Wölfler *et al.* (2017) are incorporated in our interpretation.

Zircon and apatite (U–Th)/He analysis

Zircon and apatite (U–Th)/He thermochronology (ZHe, AHe) is based on the accumulation of radiogenic helium produced by the α-decay of ^{238}U, ^{235}U, ^{232}Th and ^{147}Sm in the crystal lattice of zircon and apatite (e.g. Zeitler *et al.* 1987; Lippolt *et al.* 1994; Farley 2002; Reiners *et al.* 2003). The partial retention zone of zircon and apatite is the temperature range in which radiogenic He diffuses out of the zircon (190–120°C) and apatite (80–60°C) crystal (Wolf *et al.* 1996, 1998; Farley 2000; Reiners *et al.* 2003). The effective closure temperatures for ZHe and AHe systems can vary within the ranges of the partial retention zone but are typically reported with 190–150°C for ZHe and 75–50°C for AHe, respectively (Ehlers & Farley 2003; Reiners *et al.* 2004; Reiners & Brandon 2006; Flowers *et al.* 2007; Herman *et al.* 2007; Guenthner *et al.* 2013). The actual closure temperature depends on the He diffusion kinetics of the mineral, which is influenced by factors like its cooling history, the

grain size, the experienced radiation damage, as well as the location of the radiation damage within the grain (Flowers *et al.* 2009; Guenthner *et al.* 2013; Danišík *et al.* 2017). Helium diffusivity is higher in zircon that experienced little radiation damage, as *c*-axis parallel diffusion pathways become increasingly blocked. However, with increasing radiation damage this trend is reversed if the amount of radiation reaches a threshold value, where damage zone interconnection causes effective diffusion pathways for radiogenic He (Guenthner *et al.* 2013). The concentration of effective U (eU= (U+0.235)×Th) provides a measure of the radiation damage of a crystal. With the diffusion model of Guenthner *et al.* (2013), moderate eU values determined for our samples, in combination with the young cooling history for samples from footwall units, the thermal modelling with HeFTy implies an effective closure temperature of 170–150°C for the ZHe system. The effect of radiation damage on the He diffusion behaviour in apatite is similar to that of zircon, as He retentively also increases with increasing radiation damage (Flowers *et al.* 2009; Gautheron *et al.* 2009; Shuster & Farley 2009). Given the continuous cooling through the partial retention zone of apatite, and low eU values of 9.5– 10.5 ppm, a typical effective closure temperature of samples originating from footwall units is 62°C (Flowers *et al.* 2009). AHe samples from the hanging wall show a wider range of eU

Table 3. *Results of zircon fission-track analyses*

Sample	Number of grains	ρ_s	N_s	ρ_i	N_i	ρ_d	N_d	$P(\chi^2)$ (%)	Dispersion (%)	Central age±1σ (Ma)	U (ppm)
15M45	15	24.508	106	53.408	231	6.458	1982	13.39	5	22.7 ± 2.9	276
15M47	15	20.534	109	32.026	170	6.822	1982	18.91	24	28.2 ± 4.2	152
15M57	20	19.172	147	42.213	316	6.419	1982	19.63	20	19.1 ± 2.4	224
15M59	20	25.519	148	37.071	215	6.404	1982	93.85	1	33.6 ± 4.0	185

ρ_s (ρ_i) is the spontaneous (induced) track density (10^5 tracks per cm^2); N_s (N_i) is the number of counted spontaneous (induced) tracks; ρ_d is the dosimeter track density (10^5 tracks per cm^2); N_d is the number of tracks counted on the dosimeter; $P(\chi^2)$ is the probability of obtaining a Chi-square value (χ^2) for *n* degree of freedom (where *n* is the number of crystals minus 1); ages were calculated using the zeta calibration method (Hurford & Green 1983), glass dosimeter IRMM541, and a zeta value of 153 ± 7 a cm^{-2} calculated with Fish Canyon Tuff zircon standards.

values (3.4–234.9 ppm) and inherit a more protracted cooling history. The corresponding effective closure temperature may therefore vary between c. 50 and c. 75°C, assuming a slow cooling rate of 1°C Ma^{-1} and eU values between 4 and 150 ppm, respectively (Flowers et al. 2009).

We employed (U–Th)/He dating on samples containing apatite and zircon of sufficient quality (Table 1). Inclusion- and crack-free apatite and zircon crystals were hand-picked using a stereo- and polarizing microscope and selected under 200× magnification following the selection criteria of Farley (2002) and Reiners (2005). The dimension of the selected crystals was measured to determine alpha-ejection correction factors (Farley et al. 1996). Single crystals were loaded into pre-cleaned Pt tubes for He analysis carried out at the GÖochron Laboratory at the University of Göttingen (Germany) and one (U–Th)/He zircon analysis at the University of Tübingen (sample 16M95). At the GÖochron Laboratory at the University of Göttingen, extraction of He from crystals was performed by heating the encapsulated grains in vacuum using an IR laser. The extracted gas was purified by a SAES Ti-Zr getter and the He content was measured by a Hiden Hal-3F/PIC triple-filter quadrupole mass spectrometer. For measurements of the alpha-emitting elements U, Th and Sm, the crystals were dissolved and spiked with calibrated ^{233}U, ^{230}Th and ^{149}Sm solutions. Zircon crystals were dissolved in Teflon bombs with 48% HF and 65% HNO$_3$ at 220°C for five days. Apatite crystals were dissolved in 2% ultrapure HNO$_3$ (+0.05% HF) in an ultrasonic bath. The actinide and Sm concentrations were measured by inductively coupled plasma mass spectrometry (ICP-MS) with a Perkin Elmer Elan DRC II system equipped with an APEX micro-flow nebulizer using isotope dilution. Errors for the single-grain ZHe and AHe analyses are attributed to uncertainties in the He, U, Th and Sm measurements and the estimated uncertainty of the Ft correction factor. The zircon and apatite (U–Th)/He ages were calculated as unweighted mean ages from the single-grain ages of each sample and are reported in Tables 4 and 5 with an uncertainty of 1σ standard errors.

Thermokinematic modelling

We used a 1D thermokinematic model to constrain the exhumation history of the Aydın range. The model accounts for vertical heat transport through the Earth's crust by conduction and advection. The code is based on a modified version of Pecube (Braun 2003; Braun et al. 2012), which solves the advective–conductive heat transfer equation with implicit time stepping and uses a two-step (sampling and appraisal stages of Sambridge (1999a) and Sambridge (1999b), respectively) neighbourhood algorithm inversion. The heat production in the thermal model is 0.8 µW m^{-3} and the thermal diffusivity is 31.5 km^2 Ma^{-1}. The upper model boundary corresponds to the present-day sample elevation and surface temperature (calculated with a mean annual temperature of 20°C at sea level and an atmospheric lapse rate of 6.5°C km^{-1}). The lower model boundary has a fixed temperature of 750°C, far above the temperature range of the modelled low-temperature thermochronometers. Due to this lower boundary condition, the thickness of the model depends on the geothermal gradient. To prevent an over interpretation of the data and to choose an appropriate dimensionality of the model, we follow the procedure of Glotzbach et al. (2011). Each sample is tested for a linear, a two-step, a three-step or a four-step (inversions 1.1, 1.2, 1.3 and 1.4, respectively) exhumation history. The resulting exhumation rates and time periods are reported in Table 6. Adding complexity (such as exhumation steps) to a model generally increases its likelihood to fit the observed data but is also accompanied by an increase in the uncertainty. Relying solely on the loglikelihood function, or another misfit criterion as a selection criterion for the appropriate model setup, would imply a preference for the model with the highest

Table 4. *Results of apatite U–Th/He analyses*

Sample	Aliq.	He Vol. (10^{-9} cm^3)	He 1σ (%)	^{238}U Mass (ng)	^{238}U 1σ (%)	^{238}U Conc. (ppm)	^{232}Th Mass (ng)	^{232}Th 1σ (%)	^{232}Th Conc. (ppm)	Th/U ratio	Sm Mass (ng)	Sm 1σ (%)	Sm Conc. (ppm)	eU conc. (ppm)	Sphere equiv. radius (µm)	Ejection correction (FT)	Uncorr. age (Ma)	FT-corr. age (Ma)	2σ (Ma)	Sample age (Ma)	1 s.e. (Ma)
15M42	#2	0.029	3.6	0.050	2.2	8.4	0.175	2.4	29.1	3.46	1.635	3.5	273	15.3	77	0.80	2.28	**2.85**	0.28		
	#4	0.013	4.9	0.027	6.2	4.3	0.079	2.6	12.7	2.97	1.174	2.2	190	7.3	66	0.77	1.98	**2.57**	0.34	**2.7**	0.1
15M44	#1	0.046	2.8	0.056	2.1	5.5	0.216	2.4	21.1	3.84	3.120	3.1	305	10.5	83	0.82	2.87	**3.51**	0.29	**3.5**	0.3
15M46	#1	0.021	3.7	0.037	4.3	9.3	0.004	19.0	0.9	0.10	0.181	2.2	46	9.5	43	0.65	4.38	**6.73**	1.01	**6.7**	1.0
15M51	#1	0.033	2.9	0.074	2.0	10.8	0.052	2.6	7.6	0.70	0.194	6.8	28	12.6	80	0.81	3.10	**3.82**	0.33		
	#2	0.006	6.9	0.010	7.8	2.9	0.007	4.2	2.3	0.78	0.138	7.1	42	3.4	51	0.71	4.13	**5.85**	1.17	**4.7**	0.6
	#4	0.140	1.8	0.332	1.8	87.5	0.034	2.8	9.0	0.10	0.143	10.4	38	89.6	66	0.77	3.39	**4.38**	0.37		
15M59	#1	0.081	2.2	0.103	1.9	19.2	0.739	2.4	138.0	7.18	0.547	3.8	102	51.6	55	0.73	2.38	**3.27**	0.32		
	#3	2.564	1.2	0.934	1.8	113.2	4.269	2.4	517.5	4.57	0.890	4.2	108	234.9	70	0.78	10.86	**13.84**	1.04		
	#5	1.913	1.4	0.754	1.8	85.5	3.836	2.4	434.8	5.09	0.717	2.2	81	187.6	68	0.78	9.48	**12.18**	0.95	**9.8**	4.6
	#6	0.847	1.4	0.356	1.9	61.6	2.396	2.4	415.1	6.74	0.432	2.2	75	159.1	66	0.77	7.56	**9.79**	0.79		
16M86	#1	0.005	7.2	0.026	6.1	4.3	0.012	3.0	2.0	0.45	0.814	2.2	135	4.8	63	0.76	1.18	**1.55**	0.28		
	#2	0.002	9.3	0.015	11.0	3.5	0.006	11.5	1.4	0.39	0.453	2.2	107	3.8	51	0.70	0.86	**1.22**	0.32	**2.0**	0.7
	#3	0.005	7.1	0.014	10.3	3.1	0.005	10.3	1.2	0.37	0.389	2.2	87	3.4	52	0.71	2.39	**3.37**	0.76		

Ejection correction (Ft): correction factor for alpha-ejection (according to Farley et al. (1996)). Uncertainty of the single-grain ages includes both the analytical uncertainty and the estimated uncertainty of the ejection correction. eU is the date-effective uranium concentration ((U + 0.235)×Th). Sample age is the unweighted average age of all Ft-corrected (U–Th)/He ages (see: standard error). Only bold marked single and aliquote ages are used for interpretation.

Table 5. *Results of zircon U–Th/He analyses*

N. P. Nilius *et al.*

Sample	Aliq.	He Vol. (10⁻⁹ cm³)	1σ (%)	²³⁸U Mass (ng)	1σ (%)	Conc. (ppm)	²³²Th Mass (ng)	1σ (%)	Conc. (ppm)	Th/U ratio	Sm Mass (ng)	1σ (%)	Conc. (ppm)	eU Conc. (ppm)	Sphere equiv. radius (μm)	Ejection correct. (FT)	Uncorr. age (Ma)	FT-corr. age (Ma)	2σ (Ma)	Sample age (Ma)	1 s.e. (Ma)
15M44	#1	3.860	1.3	2.466	1.8	165.9	0.381	2.4	25.7	0.15	0.215	15.7	1	171.9	74	0.81	12.50	**15.3**	1.08		
15M44	#3	4.250	1.3	3.150	1.8	497.2	0.821	2.4	129.6	0.26	0.453	15.7	7	527.6	67	0.80	10.51	**13.2**	0.98	**14.3**	1.5
15M46	#1	8.094	1.3	4.291	1.8	1063.9	1.200	2.4	297.4	0.28	0.272	15.7	7	1133.8	51	0.74	14.64	**19.9**	1.78		
15M46	#2	0.923	1.4	0.634	1.8	264.6	0.307	2.4	128.0	0.48	0.336	15.7	14	294.6	55	0.76	10.77	**14.2**	1.21		
15M46	#3	1.287	1.4	1.008	1.8	533.0	0.202	2.4	106.9	0.20	0.155	15.7	8	558.1	48	0.70	10.08	**14.3**	1.42	**16.2**	1.9
15M47	#1	0.806	2.6	3.739	1.8	1165.3	0.609	2.4	189.9	0.16	0.368	15.7	11	1209.9	48	0.72	1.72	**2.4**	0.25		
15M47	#2	1.724	1.4	1.016	1.8	222.3	0.729	2.4	159.5	0.72	0.562	15.7	12	259.8	62	0.78	11.96	**15.3**	1.18	**15.31**	1.18
15M55	#2	1.217	1.4	0.907	1.8	159.1	0.286	2.4	50.1	0.32	0.407	15.7	7	170.9	56	0.76	10.30	**13.6**	1.14	**13.56**	1.14
15M56	#1	3.833	1.3	1.611	1.8	439.0	0.097	2.5	26.5	0.06	0.179	15.7	5	445.2	58	0.77	19.39	25.3	2.10		
15M56	#2	0.804	1.5	0.491	1.9	278.7	0.084	2.5	47.9	0.17	0.220	15.7	12	289.9	45	0.70	12.98	**18.5**	1.86	**16.8**	2.4
15M56	#3	0.375	1.5	0.264	2.0	351.4	0.127	2.4	168.1	0.48	0.116	15.7	15	390.9	44	0.69	10.51	**15.2**	1.56		
15M56	#4	1.652	1.4	0.611	1.8	457.5	0.411	2.4	308.0	0.67	0.063	15.7	5	529.9	45	0.70	19.27	27.5	2.71	26.4	1.5
15M57	#1	4.611	1.3	3.151	1.8	590.5	0.502	2.4	94.2	0.16	0.302	15.7	6	612.6	61	0.78	11.67	**15.0**	1.18		
15M57	#2	5.701	1.3	3.664	1.8	831.9	0.273	2.4	62.1	0.07	0.210	15.7	5	846.5	231	0.94	12.66	**13.5**	0.63		
15M57	#3	6.538	1.3	4.883	1.8	1291.1	0.528	2.4	139.6	0.11	0.406	15.7	11	1323.9	57	0.76	10.81	**14.1**	1.17	**14.2**	0.4
15M58	#1	4.466	1.3	3.068	1.8	92.7	1.271	2.4	38.4	0.41	0.994	15.7	3	101.7	96	0.86	10.95	**12.8**	0.76		
15M58	#2	11.496	1.3	8.473	1.8	476.2	1.118	2.4	62.9	0.13	0.408	15.7	2	491.0	88	0.84	10.89	**12.9**	0.82		
15M58	#3	9.012	1.3	5.666	1.8	351.4	2.050	2.4	127.1	0.36	0.740	15.7	5	381.2	92	0.85	12.12	**14.3**	0.87	**13.3**	0.5
15M59	#1	1.085	2.3	3.221	1.8	604.4	0.270	2.4	50.6	0.08	0.335	15.7	6	616.3	79	0.83	2.74	**3.3**	0.26		
15M59	#2	1.598	1.4	0.692	1.8	57.3	0.333	2.4	27.6	0.48	0.327	15.7	3	63.8	77	0.82	17.09	**20.8**	1.42		
15M59	#3	3.984	1.3	1.734	1.8	192.0	0.316	2.4	35.0	0.18	0.768	15.7	9	200.2	75	0.82	18.17	**22.2**	1.53	**21.5**	1.0
16M87	#1	4.81	1.1	2.33	1.8	167	1.94	2.4	139	0.83	0.050	11.9	4	199.8	87	0.84	14.3	**17.0**	1.0		
16M87	#2	3.62	1.1	2.37	1.8	432	0.56	2.4	103	0.24	0.024	8.6	4	456.5	54	0.75	12.0	**15.9**	1.3		
16M87	#3	2.45	1.1	1.13	1.8	672	0.37	2.4	220	0.33	0.014	11.1	8	723.7	45	0.70	16.7	**23.9**	2.4	**18.9**	2.5
16M89	#1	3.69	1.0	2.34	1.8	504	0.12	2.4	25	0.05	0.012	5.0	3	510.4	68	0.80	12.9	**16.1**	1.2		
16M89	#3	5.71	1.1	3.25	1.8	754	0.68	2.4	158	0.21	0.028	3.3	7	791.4	68	0.80	13.9	**17.4**	1.3	**16.8**	0.9
16M90	#2	4.47	1.1	2.49	1.8	462	1.60	2.4	297	0.64	0.027	9.5	5	532.1	54	0.75	12.9	**17.3**	1.5		
16M90	#3	3.64	1.0	2.04	1.8	406	0.13	2.4	25	0.06	0.009	15.8	2	411.7	46	0.71	14.5	**20.4**	2.0	**18.9**	2.2
16M91	#1	1.65	1.1	1.06	1.8	104	0.51	2.4	50	0.48	0.041	5.9	4	115.4	69	0.80	11.6	**14.5**	1.0		
16M91	#2	1.00	1.2	0.43	1.9	129	0.51	2.4	152	1.18	0.011	6.7	3	164.3	53	0.75	15.1	**20.2**	1.7		
16M91	#3	6.74	1.0	3.15	1.8	121	2.70	2.4	103	0.86	0.064	8.9	2	145.0	118	0.88	14.7	**16.7**	0.8	**17.1**	1.7
16M95*	#1	0.99	1.2	0.61	3.5	-	0.39	3.8	-	0.63	-	-	-	433.3	35	0.62	11.5	**18.5**	0.4		
16M95*	#2	2.30	1.2	1.25	5.0	-	0.46	4.8	-	0.37	-	-	-	206.6	298	0.95	14.0	**14.7**	0.7		
16M95*	#3	0.23	1.3	0.14	7.4	-	0.11	5.6	-	0.75	-	-	-	206.2	36	0.63	11.6	**18.4**	0.7	**17.2**	1.2

Ejection correction (Ft): correction factor for alpha-ejection (according to Farley *et al.* (1996) and Hourigan *et al.* (2005)). Uncertainty of the single-grain ages includes both the analytical uncertainty and the estimated uncertainty of the ejection correction. Sample age is the unweighted average age of all Ft-corrected (U–Th)/He ages. eU is the date-effective uranium concentration ((U + 0.235)×Th). Results from aliquots marked with an asterisk were measured in the laboratory in Tübingen. Single and aliquot ages marked in grey indicate hanging-wall population in sample 15M56.

Table 6. *Parameters for inversions 1.1 to 1.4 and resulting exhumation rates (E) for different time periods (T)*

			Inversion results							
			1.1		**1.2**		**1.3**		**1.4**	
Parameter	Unit	Range	Mean	s.e.	Mean	s.e.	Mean	s.e.	Mean	s.e.
Sample 14M31 (ZFT, ZHe, AFT, AHe)										
E_1 (0 Ma–T_1)	(km Ma^{-1})	0–1.5	0.52	0.10	0.94	0.29	0.98	0.21	1.04	0.26
T_1	(Ma)	0–35			2.18	1.37	2.95	0.65	1.96	1.12
E_2 (T_1–T_2)	(km Ma^{-1})	0–1.5			0.13	0.03	0.30	0.35	0.11	0.12
T_2	(Ma)	0–35					6.65	8.50	15.29	11.40
E_3 (T_2–T_3)	(km Ma^{-1})	0–1.5					0.56	0.45	0.43	0.38
T_3	(Ma)	0–35							21.30	8.95
E_4 (T_3–T_{max})	(km Ma^{-1})	0–1.5							0.63	0.38
Geothermal gradient	(C° km^{-1})	30–50	38.84	5.76	39.61	5.51	37.76	5.78	36.72	4.41
Number of iterations			50		150		400		450	
Number of parameters			2		4		6		8	
Number of observations			7		7		7		7	
Log-likelihood			−175.45		−13.69		−8.40		−7.73	
BIC			354.80		35.17		**28.48**		31.04	
Sample 14M37 (ZFT, ZHe, AFT, AHe)										
E_1 (0 Ma–T_1)	(km Ma^{-1})	0–1.5	0.20	0.04	0.14	0.09	0.12	0.10	0.11	0.08
T_1	(Ma)	0–26			14.29	6.32	13.81	5.32	14.06	5.45
E_2 (T_1–T_2)	(km Ma^{-1})	0–1.5			0.47	0.32	0.63	0.39	0.55	0.39
T_2	(Ma)	0–26					14.16	5.88	15.05	6.02
E_3 (T_2–T_3)	(km Ma^{-1})	0–1.5					0.49	0.33	0.65	0.42
T_3	(Ma)	0–26							16.28	4.04
E_4 (T_3–T_{max})	(km Ma^{-1})	0–1.5							0.48	0.36
Geothermal gradient	(C° km^{-1})	30–50	39.32	5.75	38.40	5.36	38.76	5.31	36.91	5.35
Number of iterations			50		150		300		350	
Number of parameters			2		4		6		8	
Number of observations			6		6		6		6	
Log-likelihood			−17.20		−2.73		−1.38		−2.37	
BIC			37.18		**12.63**		13.50		19.08	
Sample 15M44 (ZFT, ZHe, AFT, AHe)										
E_1 (0 Ma–T_1)	(km Ma^{-1})	0–1.5	0.27	0.05	0.53	0.26	0.42	0.17	0.42	0.19
T_1	(Ma)	0–26			7.74	7.24	7.29	6.36	12.74	8.91
E_2 (T_1–T_2)	(km Ma^{-1})	0–1.5			0.24	0.26	0.29	0.29	0.19	0.22
T_2	(Ma)	0–26					9.62	8.05	12.72	8.30
E_3 (T_2–T_3)	(km Ma^{-1})	0–1.5					0.37	0.37	0.44	0.42
T_3	(Ma)	0–26							13.98	5.97
E_4 (T_3–T_{max})	(km Ma^{-1})	0–1.5							0.41	0.36
Geothermal gradient	(C° km^{-1})	30–50	39.12	5.86	37.62	5.32	37.49	5.00	36.33	5.60
Number of iterations			50		150		300		350	
Number of parameters			2		4		6		8	

(continued)

N. P. Nilius *et al.*

Table 6. (Continued)

Parameter	Unit	Range	Inversion results 1.1 Mean	s.e.	1.2 Mean	s.e.	1.3 Mean	s.e.	1.4 Mean	s.e.
Number of observations			5		5		5		5	
Log-likelihood			−24.15		−14.72		−11.88		−12.79	
BIC			50.49		35.88		**33.42**		38.45	
Sample 15M57/16M97 (ZFT, ZHe, AFT)										
E_1 (0 Ma–T_1)	(km Ma^{-1})	0–1.5	0.25	0.05	0.18	0.10	0.18	0.14	0.18	0.13
T_1	(Ma)	0–25			13.45	4.93	12.18	4.99	12.41	4.45
E_2 (T_1–T_2)	(km Ma^{-1})	0–1.5			0.79	0.39	0.68	0.41	0.58	0.36
T_2	(Ma)	0–25					14.30	4.53	14.43	4.94
E_3 (T_2–T_3)	(km Ma^{-1})	0–1.5					0.81	0.37	0.73	0.41
T_3	(Ma)	0–25							16.05	3.88
E_4 (T_3–T_{max})	(km Ma^{-1})	0–1.5							0.78	0.40
Geothermal gradient	(C° km^{-1})	30–50	39.46	5.78	38.93	5.77	38.39	5.90	38.35	5.40
Number of iterations			50		150		300		350	
Number of parameters			2		4		6		8	
Number of observations			5		5		5		5	
Log-likelihood			−15.19		−3.83		−0.93		−3.51	
BIC			33.61		14.10		**10.17**		19.90	

BIC, Bayesian information criterion. Parameters T_1 and T_2 denote the time (from 0 Ma to T_{max}) at which exhumation rates change. Parameters E_1, E_2, E_3 and E_4 are the exhumation rates (from 0 to 1.5 km Ma^{-1}) between 0 Ma and T_1 (E_1), between T_1 and T_2 (E_2), between T_2 and T_3 (E_3) and T_3 and T_{max} (E_4). Entries in grey indicate parameters that resulted in the arithmetic mean of their boundary limits and are not used for interpretation.
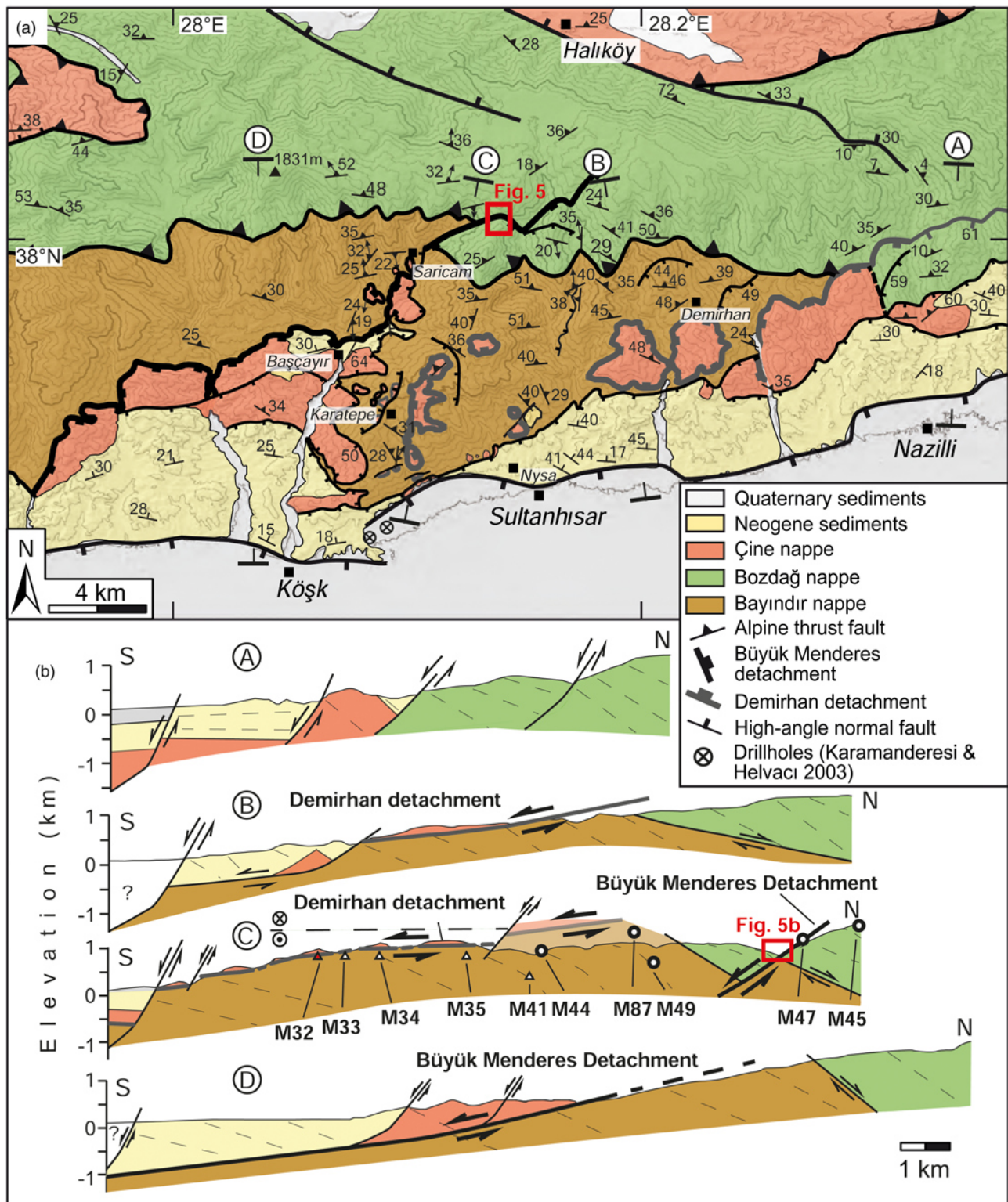
Fig. 3. (**a**) Geological map of the eastern part of the Aydın range between Köşk and Nazilli. (**b**) Geological cross-sections along the southern flank of the Aydın range. Map and profiles are based on our own observations and data from previous studies (Karamanderesi & Helvacı 2003; Rojay *et al.* 2005; Çemen *et al.* 2006; Emre & Sözbilir 2007; Sen & Seyitoğlu 2009; Candan *et al.* 2011; Yal *et al.* 2017).

complexity. Therefore, we employ the Bayesian information criterion (BIC), which provides a measure of the ratio between the likelihood (fitting) and the model complexity (Schwarz 1978):

$$BIC = -2 \cdot \ln L + k \cdot \ln(n) \qquad (1)$$

whereby ln*L* denotes the log-likelihood for the model, and k and n are the numbers of free parameters and observations, respectively. Thus, the lowest *BIC* value indicates the preferred model setup.

Depending on the number of time/exhumation steps, we model 5000 to 35 000 thermal histories, over the last 26 Ma for footwall samples from the Demirhan and Büyük Menderes detachment, and 5000 to 45 000 thermal histories over the last 35 Ma for samples from the hanging wall. Free parameters are the geothermal gradient (30–50°C km^{-1}), the exhumation rates (0–1.5 km Ma^{-1}) and the time at which the exhumation rate changes (in the period between 0–26 and 0–35 Ma for the footwall and hanging wall, respectively). The

thermokinematic model traces the cooling history of rocks based on the modelled exhumation paths and calculates thermochronological ages with the annealing algorithms of Ketcham *et al.* (2007) and Tagami *et al.* (1998) for AFT and ZFT, and the diffusion algorithms of Flowers *et al.* (2009) and Guenthner *et al.* (2013) for AHe and ZHe. The probability of each free input parameter is derived from the appraisal stage of the neighbourhood inversion (Sambridge 1999*b*) and is visualized as 1D and 2D marginal probability density functions (PDFs). Probable exhumation paths are visualized as synoptic 2D marginal PDFs, in which re-sampled exhumation rates and the time at which exhumation rates changed were linked to visualize the exhumation rate changing with time. For details on the modelling approach the reader is referred to Glotzbach *et al.* (2011) and recent studies of Schultz *et al.* (2017), Thiede & Ehlers (2013) and Whipp *et al.* (2007), which also used the advances of comparable 1D thermokinematic modelling approaches to infer exhumation rates from low-temperature thermochronology data.

Results

Geological mapping of extensional structures

Mapping in the Aydın range aimed at (a) identifying the tectonic structures that document the Cenozoic extensional history of the southern part of the central Menderes Massif and (b) linking these structures to the low-temperature thermochronological data. The

field relations revealed that two detachment faults are exposed along the southern flank of the Aydın range, which we call the Büyük Menderes and Demirhan detachments, respectively. We focused our thermochronological and structural studies on two areas where the Büyük Menderes and Demirhan detachments are particularly well exposed; the region between Başçayır and Nazilli (Fig. 3) and the area around Beyköy (Fig. 4).

The western part of the south-dipping Büyük Menderes detachment fault strikes WSW–ENE and can be traced from Beyköy in the west (Fig. 2b) to the central part of the Aydın range, *c.* 9 km south of Halıköy (Fig. 2a). The footwall of the detachment dips with 14–20° to the south or SSE and shows consistent south- to SSW-dipping slickenline lineations on the detachment surface. The cataclasites overprint a mylonitic footwall with top-to-the-south shear sense indicators (Fig. 2f). Apart from the eastern termination of the Büyük Menderes detachment, where the footwall consists of garnet-bearing mica schists of the Bozdağ nappe, footwall rocks of the Büyük Menderes detachment exclusively consist of phyllites, marble lenses and mica schists of the Bayındır nappe. The hanging wall is comprised of augengneisses and partly paragneisses of the Çine nappe which are overlain by northward-dipping Neogene sediments. Gürer *et al.* (2009) previously reported that the trace of the Büyük Menderes detachment east of Başçayır village is displaced by an approximately north–south-striking fault, which explained the reappearance of the detachment SE of Başçayır village at Karatepe (Fig. 3a). Instead, our own mapping in the area around Başçayır
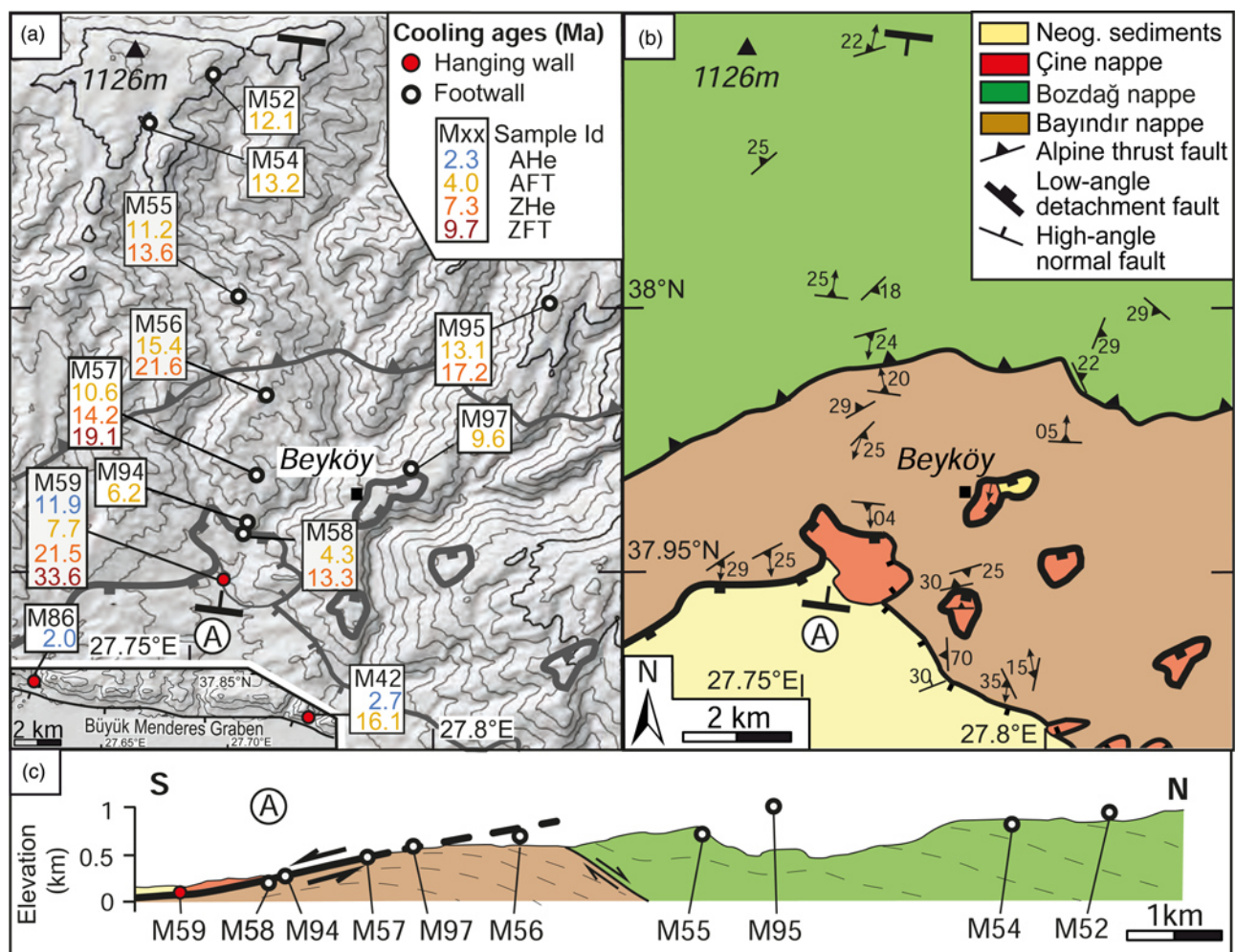
Fig. 4. (**a**) Shaded relief image of the western part of the Aydın range with thermochronological sample locations and the associated cooling ages. Note that for clarity the first two digits of the thermochronological sample identifiers are omitted. Inset shows the position of AHe samples from the northern rim of the Büyük Menderes graben. (**b**) Geological map of the same area showing relics of Çine nappe klippen at Beyköy resting on phyllites of the Bayındır nappe. (**c**) Position of the low-temperature thermochronology samples projected orthogonally into the NNE–SSW-trending geological cross-section.
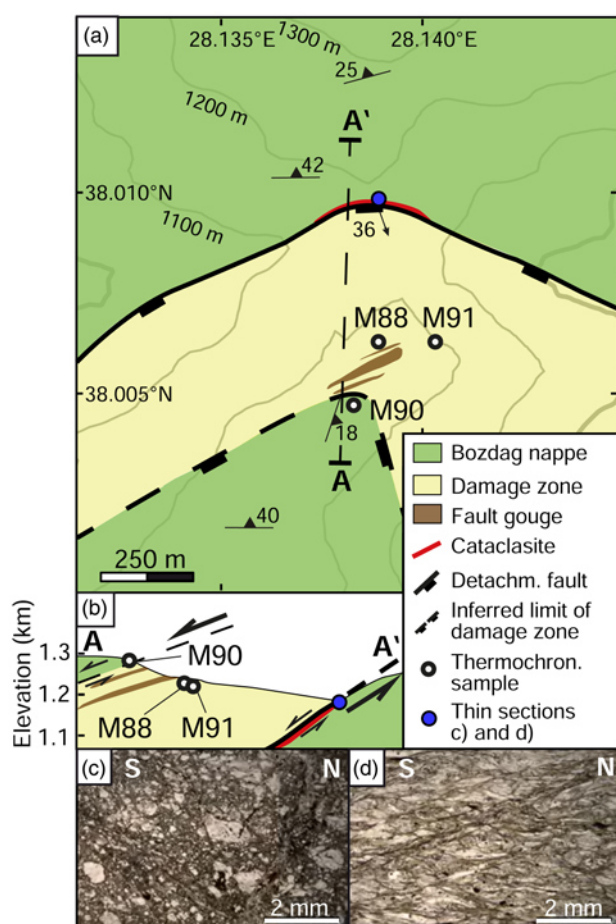
Fig. 5. (a) Detailed geological map of the eastern part of the Büyük Menderes detachment, NE of Sariçam village. (b) Cross-section of the fault zone which is characterized by a wide damage zone above a cataclasite and *c.* 3 m thick fault gouge horizons. Open circles indicate the position of the thermochronology samples. (c) Thin section of the cataclastic footwall showing cataclastically reworked components. (d) Thin section of a footwall sample taken 2 m below the cataclasite revealing mylonitic textures with C/S fabrics indicating dextral (top-south) shearing.

village revealed that the Büyük Menderes detachment can be traced further to the NE of Sariçam village (Fig. 3a). Here, the Büyük Menderes detachment occurs as a 1–2 m thick south-dipping (185°/36°) cataclasite with slickenlines dipping 168°/22° (Fig. 5a and b). Thin sections document the cataclastic overprint of a ductilely deformed footwall (Fig. 5c). Ductile top-to-the-south shearing is documented by S–C fabrics and mica fish in thin section (Fig. 5d). A *c.* 300 m thick damage zone above the cataclasite contains 3–6 m thick fault gouge horizons that seem to represent the upper limit of the damage zone (Fig. 5b). In contrast to other parts of the Büyük Menderes detachment, both hanging wall and footwall consist of garnet mica schist of the Bozdağ nappe, which implies that the outcrop represents a structurally higher part of the detachment fault. The eastern termination of the Büyük Menderes detachment, *c.* 9 km south of Halıköy (Fig. 3a), is characterized by scarce cataclasite relics and fractured mica schists with thin fault gouge horizons.

The Demirhan detachment

The NE-trending trace of the southward-dipping Büyük Menderes detachment in the Başçayır area (Fig. 2a), and the tectonic contact between the Bayındır nappe and the Çine nappe exposed farther south and east of Karatepe (Fig. 2c–e), indicate that they cannot be part of the same detachment fault (Fig. 3, cross-section C). Instead,

we propose that this fault contact represents a separate, eastern branch of the Büyük Menderes detachment system, which we have called the Demirhan detachment. The Demirhan detachment is structurally located in the hanging wall of the Büyük Menderes detachment and can be traced as a WSW–ENE-striking fault, from the mountains north of Sultanhisar over *c.* 20 km to the mountains north of Nazilli (Figs 2c and 3). The dip of the Demirhan detachment changes along strike, from a subhorizontal orientation at Karatepe to a 13–16° dip near Demirhan village. Here, the fault contact between phyllites in the footwall and orthogneisses in the hanging wall is well exposed by a cataclastic footwall and *c.* 5 m thick fault gouge horizons (Fig. 2e). A progressive change to high-angle normal faults, which dip with *c.* 60° to the south, occurs in the area north of Nazilli, implying a decreasing fault offset towards the east (Fig. 3b, section A). At Karatepe, a SSW–NNE-striking and NW-dipping normal fault, which can be traced from Sarıçam to Karatepe, cuts and displaces the Demirhan detachment. This fault is exposed along the western slope of the Karatepe ridge, between the Çine and Bayındır nappes. South of Sarıçam, this normal fault dips with 42° to the WNW (Fig. 2h). East of Başçayır, the same normal fault has an orientation of (299°/30°) and the marble-bearing footwall shows slickenlines plunging towards the WNW (298°/30°) (Fig. 2g), indicating a top-to-the-WNW displacement. Therefore, the western termination of the Demirhan detachment is not exposed.

Along the southern part of the Aydın range, east–west-striking high-angle normal faults crosscut and displace the Demirhan detachment towards the uplifted Neogene sediments, which are located north of the active graben-bounding normal fault of the Büyük Menderes graben. In the vicinity of the ancient city of Nysa (Fig. 3a), the eastern branch of the Büyük Menderes detachment crops out as a 3–5 m thick fault gouge zone between phyllites in the footwall and strongly fractured orthogneiss covered by Neogene sediments in the hanging wall (Fig. 2i and j). The southward continuation of the detachment was also encountered in two boreholes in the northern Büyük Menderes graben located *c.* 5 km NE of Köşk (Karamanderesi & Helvacı 2003). In the boreholes, the fault zone is located at a depth of *c.* 500 m and separates orthogneisses from phyllites.

Results from fission-track and (U–Th)/He analysis

Our new low-temperature thermochronology data reveal three distinct age groups, which can be attributed to the cooling and exhumation of the footwall and hanging-wall units of the Büyük Menderes and Demirhan detachments (Figs 6 and 7).

Two AHe ages from the footwalls of both detachments are 3.5 ± 0.3 Ma (sample 15M44) and 6.7 ± 1.0 Ma (sample 14M46). The AFT ages of footwall samples from the Büyük Menderes detachment range from 15.4 ± 2.4 (15M56) to 4.3 ± 0.7 Ma (15M58) and samples from below the Demirhan detachment yielded ages of 12.9 ± 1.3 to 6.0 ± 1.0 Ma (Table 2). The AFT track lengths of 13.0 ± 0.9 to 13.8 ± 1.2 μm for footwall samples of the Büyük Menderes detachment require moderate to fast cooling through the partial annealing zone of the AFT system (Wölfler *et al.* 2017). The majority of AFT samples have similar annealing kinetics, as shown by Dpar values (the arithmetic mean fission-track etch figure parallel to the crystallographic *c*-axis) of 1.2 to 2.2 μm, indicative of F-apatite (Carlson *et al.* 1999). The two AFT samples with Dpar values close to 3 μm (14M42 and 14M45) might be more resistant to annealing (Ketcham *et al.* 1999). ZHe analysis from footwall samples yielded ages between 18.9 ± 2.2 Ma (sample 16M90) and 13.3 ± 0.5 Ma (sample 15M58) (Fig. 6 and Table 5). These ages are mean ages calculated from single grain ages (neglecting one outlier in 15M47). Two age groups were identified within the single-grain analyses of sample 15M56 (Table 5), whereas single grain ages reveal a positive age–eU relationship,
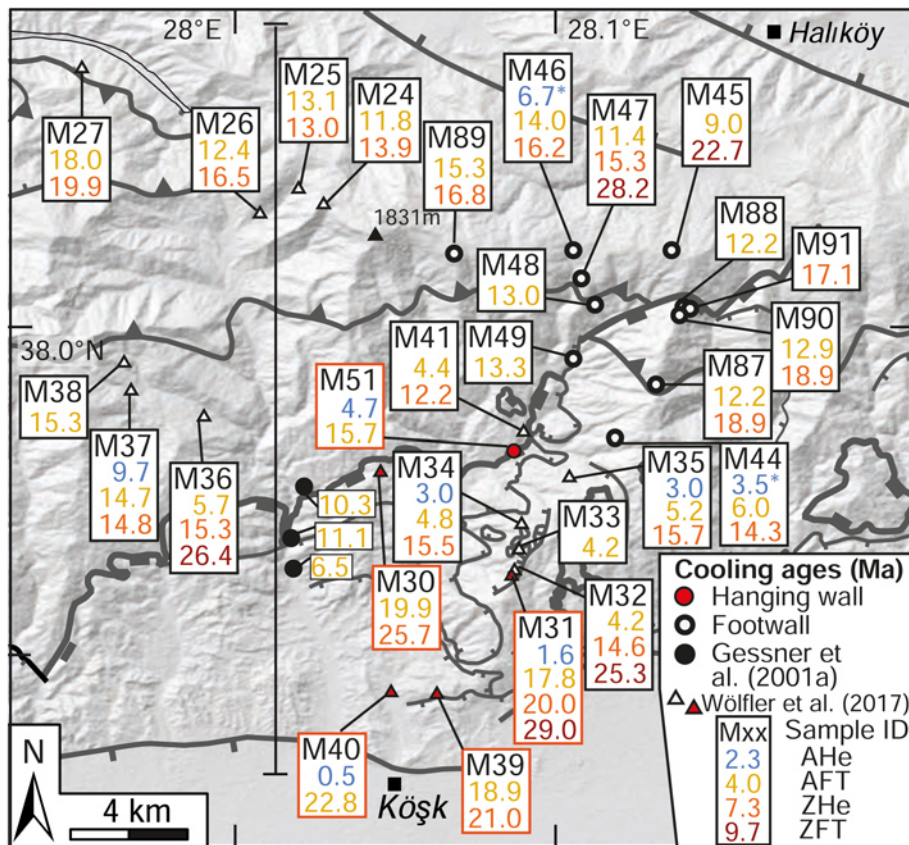
Fig. 6. Shaded relief image of the Aydın range north of Köşk showing thermochronological sampling sites and results of new data presented in this study and data of Wölfler *et al.* (2017) and Gessner *et al.* (2001*a*).

with an eU value of 390.9 ppm for the youngest grain (15.2 ± 1.6 Ma) and an eU value of 529.9 ppm for the oldest grain (27.5 ± 2.7 Ma), which might explain the observed dispersion. However, thermal history modelling taking into account differences in diffusion kinetics caused by grain size and accumulated radiation damage revealed that the grains of the aliquot cannot have experienced the same cooling path. Hence, the two mean ages of 26.4 ± 1.1 Ma and 16.8 ± 1.7 Ma might rather reflect hanging-wall and footwall cooling ages, respectively, as 15M56 shows a strong cataclastic overprint and may include slices of hanging-wall material (Fig. 7b). The youngest and oldest ZFT ages obtained from footwall units are 19.1 ± 2.4 Ma and 28.2 ± 4.2 Ma, respectively (Fig. 7 and Table 3).

AHe ages obtained from samples in the hanging wall of the Büyük Menderes detachment comprise ages ranging from 11.9 ± 1.2 to 2.0 ± 0.7 Ma. The youngest AHe ages of 2.0 Ma (16M86) and 2.7 Ma (15M42) stem from samples near the active normal fault of the Büyük Menderes graben (Fig. 4a). Sample 15M59 from the hanging wall of the Büyük Menderes detachment experienced a slow cooling history, as seen from a late Oligocene ZFT age of 33.6 ± 4.0 Ma, an early Miocene ZHe age (21.5 ± 1.0 Ma) and a late Miocene AFT age of 7.9 ± 1.3 Ma. Four AHe analyses of this sample gave a large range of single grain ages of 13.8 to 3.3 Ma (Table 4). The single grain ages show a positive age–eU relationship, suggesting slow cooling through the partial retention zone. Thermal modelling with HeFty (Ketcham 2005) implies slow cooling since *c.* 20 Ma and an effective closure temperature of *c.* 68°C for the high eU apatite (grains #3, #5, #6) and 60°C for the low eU apatite (grain #1), with a young AHe age of 3.3 Ma.

Data interpretation and discussion

Cooling history of the Aydın range

To analyse the cooling and exhumation history of the rocks in the Aydın range, we complement our new thermochronological data

with the data published by Wölfler *et al.* (2017). The combined dataset shows that rocks of the Aydın range can be classified into three groups with different cooling histories. Two groups are attributed to contrasting cooling histories in the footwalls of the Büyük Menderes and the Demirhan detachments, respectively, whereas the third data group documents the cooling of the hanging-wall units above both detachments. Samples from the eastern (Fig. 7a) and western thermochronological transects (Fig. 7b) of the footwall of the Büyük Menderes detachment (Fig. 4a) have in common that both share a rapid cooling event between ZHe and AFT closure temperatures during the middle Miocene. In the eastern part of the footwall of the Büyük Menderes detachment, late Oligocene to early Miocene ZFT ages suggest moderate cooling rates in the early Miocene between ZFT and ZHe systems and an interval of increased rates in the middle Miocene between ZHe and AFT systems – i.e. in a temperature range from *c.* 160–*c.* 110°C (Fig. 7a). In contrast, sample 15M57 in the footwall of the western part of the Büyük Menderes detachment reveals a more progressive cooling from *c.* 19–*c.* 10 Ma between ZFT and AFT systems. This suggests that the detachment operated at higher temperatures, which is supported by intense ductile top-to-the south shearing in the footwall near Beyköy (Fig. 2f). The middle Miocene episode of fast cooling along the footwall of the Büyük Menderes detachment is not observed in thermochronological data from the footwall of the Demirhan detachment (14M32 to 14M35 and 15M44, 16M87, 16M90). Instead, an episode of rapid cooling is recorded between AFT ages ranging between *c.* 6 and *c.* 4 Ma and AHe ages ranging between *c.* 3.5 and *c.* 3.0 Ma in the latest Miocene and Pliocene. Two footwall samples in the Aydın range (16M87 and 16M90) neither show the middle Miocene nor the latest Miocene/Pliocene episodes of enhanced cooling (Fig. 6). The slow and continuous Miocene cooling of these samples can be explained by their structural position in the hanging wall of the Büyük Menderes detachment and the large distance to the Demirhan detachment (Fig. 6). The third group of thermochronological
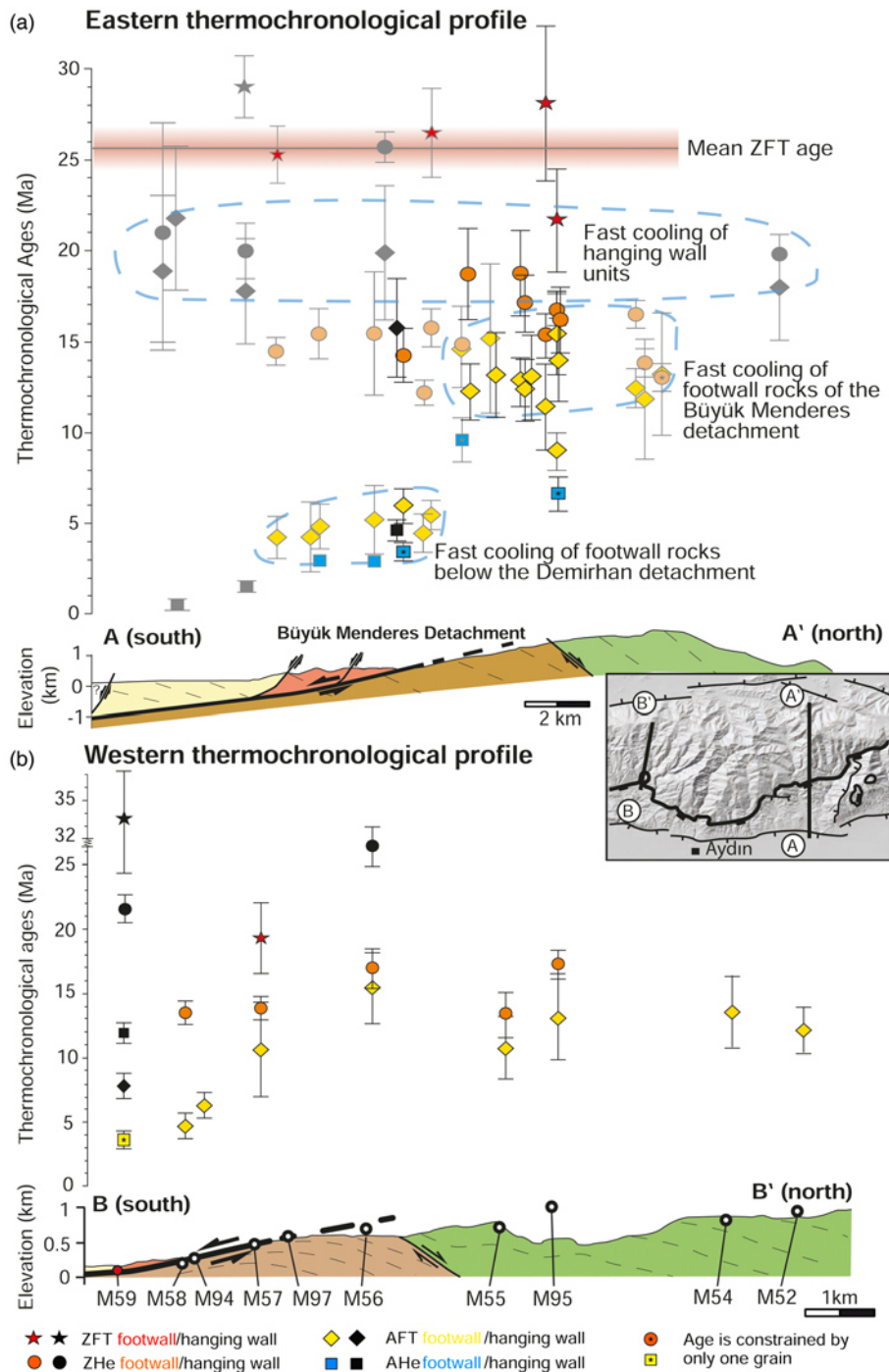
Fig. 7. (**a**) Thermochronological results projected perpendicularly into the extended north–south profile D shown in Figure 3b and depicted in the map inset. (**b**) Thermochronological results of the western thermochronological profile. The ages are projected perpendicular to the NNE–SSW-trending cross-section of Figure 4c. Note that the cooling age axis is not continuous between 26.5 and 32 Ma.

data represents the augengneisses of the Çine nappe that are found as klippen in the hanging walls of the Büyük Menderes and Demirhan detachments. The distinctly older cooling ages of these klippen reveal a phase of relatively rapid cooling in the late Oligocene/early Miocene, which is also described in the Bozdağ range and in the northern Menderes sub-massifs (Gessner *et al.* 2001*b*; Thomson & Ring 2006; Buscher *et al.* 2013; Wölfler *et al.* 2017). However, only in the northern sub-massif can this cooling episode be clearly linked to tectonic denudation along the Simav detachment (Ring *et al.* 2003; Thomson & Ring 2006; Cenki-Tok *et al.* 2016). The AHe ages derived from hanging-wall samples, which are situated in the vicinity of the Büyük Menderes graben, consistently reveal enhanced late Pliocene/Quaternary cooling (Figs 4a and 6) that we interpret to be related to the exhumation in the footwall of the northern graben-bounding normal fault.

Thermokinematic modelling results

To obtain precise predictions on the magnitude and temporal changes in the exhumation history, thermokinematic modelling was performed on samples for which ages from at least three out of the four thermochronometers (AHe, AFT, ZHe, ZFT) were available. Using less thermochronometers usually results in models with limited quantitative information, which was also reported in similar thermokinematic modelling approaches by Valla *et al.* (2010) and van der Beek *et al.* (2010). Two samples from the footwall of the Büyük Menderes detachment (14M37, 15M57), one sample from the footwall of the Demirhan detachment (15M44) and one sample from the hanging wall of the Demirhan detachment (14M31) passed these criteria. The modelled ages of these samples reproduce well the observed thermochronological ages and were used to constrain the exhumation history of the Aydın range (Fig. 8). As samples
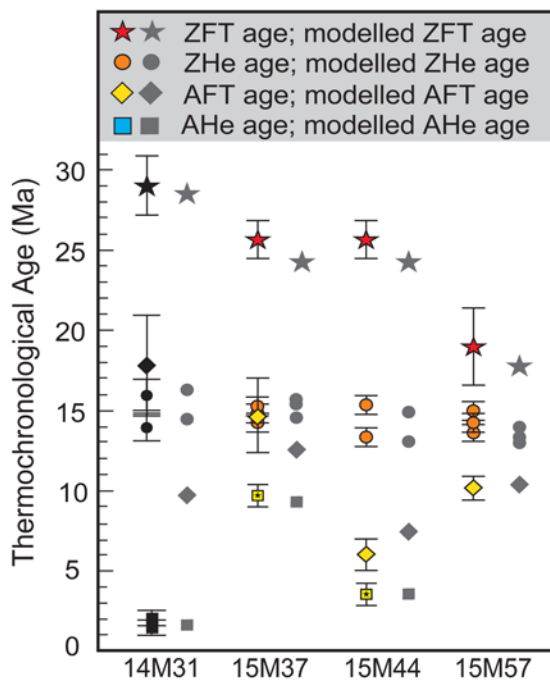
Fig. 8. Observed v. modelled cooling ages, using the same symbols for the thermochronological systems as in Figure 7.

14M37 and 15M44 do not comprise ZFT ages, we used the mean of all available ZFT ages from footwall units in the Aydın range (25.7 ± 1.1 Ma) for the modelling of samples 14M37 and 15M44. The procedure is justified by similar ZFT ages in the footwall and hanging wall of the Aydın range (29–23 Ma), supporting the interpretation of Wölfler *et al.* (2017) that detachment faulting in the eastern part of the Aydın range mainly occurred at or below *c.* 250°C.

The activity of the Büyük Menderes detachment is constrained by samples 15M57 and 14M37 from the western and eastern parts of its footwall. The exhumation history of sample 14M37 is best described by two time-steps (inversion 1.2, Table 6) with a lower BIC value compared to a three-step model or a continuous exhumation model. The model reflects an exhumation history where an early to middle Miocene period with exhumation rates of 0.5 km Ma^{-1} is followed by slower rates of *c.* 0.1 km Ma^{-1} since *c.* 10 Ma (Fig. 9a). The predicted lower exhumation rates since the Serravallian are also evident in the exhumation pattern of sample 15M57 from the western footwall of the Büyük Menderes detachment. The thermochronological ages of this sample can be fitted with a continuous exhumation model, which is primarily an effect of the large AFT error (± 3.3 Ma). Although the best model predicts an AFT age of 7.5 Ma within error of the observed age (10.6 ± 3.3 Ma), there is evidence from sample 16M97 that the correct AFT age is *c.* 10 Ma, as sample 16M97 is located nearby at the same lateral position in the footwall and yields an AFT age of 9.7 ± 2.9 Ma (Fig. 4a). Combining both samples, by calculating the mean AFT age and the standard error, results in an AFT age of 10.2 ± 0.5 Ma. Repeating the inverse thermokinematic modelling of sample 15M57 with this merged AFT age requires a two-step model (best model AFT age is 10.3 Ma) with a transition from high exhumation rates of >0.5 km Ma^{-1} to lower rates of *c.* 0.2 km Ma^{-1} at 13.5 ± 4.9 Ma (Fig. 9b).

In contrast to the middle Miocene activity observed along the Büyük Menderes detachment, the exhumation in the footwall of the Demirhan detachment commenced in the late Miocene. Sample 15M44 requires a three-step exhumation (lowest BIC value, Table 6), with a change from a relatively vaguely constrained

time period of increased exhumation rates in the early Miocene, to slow exhumation rates of *c.* 0.25 km Ma^{-1} in the middle Miocene to higher exhumation rates of *c.* 0.4 km Ma^{-1} at *c.* 7 Ma (Figs 9a and 10c). The increase in exhumation is likely associated with the onset of faulting along the Demirhan detachment. This younger phase of higher late Miocene/Pliocene exhumation rates is also described by Wölfler *et al.* (2017) for a group of samples from the southern part of the Aydın range. They derived exhumation rates of 0.7 km Ma^{-1} assuming a 30°C geothermal gradient and 0.4 km Ma^{-1} assuming a 50°C geothermal gradient, which is in accordance with our modelled exhumation rate of 0.4 km Ma^{-1} with a geothermal gradient of *c.* 38°C km^{-1} (Table 6).

The cessation of extension along the Demirhan detachment can be constrained by the onset of exhumation associated with high-angle normal faulting along the Büyük Menderes graben. This is reflected by the onset of fast exhumation, indicated by sample 14M31 from the hanging wall of the Demirhan detachment. Sample 14M31 requires three exhumation steps to fit the thermochronological data (Table 6). The older time step, at which exhumation rates changed from *c.* 0.6 to *c.* 0.3 km Ma^{-1} is roughly constrained to be in the Oligocene to early Miocene (Fig. 9a). For this time period, a possible extensional reactivation of the basal thrust of the Lycian nappes has been proposed (Ring *et al.* 2003; van Hinsbergen 2010). At 2.9 ± 0.6 Ma, exhumation rates increase to 1.0 ± 0.2 km Ma^{-1} (Table 6). We interpret this increase to be related to the onset of high-angle normal faulting along the northern part of the Büyük Menderes graben, which simultaneously marks the cessation of faulting along the Demirhan detachment. Note that there is a trade-off between exhumation rate and the onset time of faster exhumation (Fig. 9c), i.e. a more recent onset would require higher exhumation rates and vice versa.

The slip rate of the Demirhan detachment

There are two widely used approaches to derive the total slip rate accommodated along low-angle detachments from thermochronological data: (1) plotting the decrease of cooling ages in the down-dip direction of the footwall v. the distance between the samples in the direction of tectonic transport (e.g. Foster & John 1999; Brady 2002; Stockli 2005; Brichau *et al.* 2006; Buscher *et al.* 2013; Singleton *et al.* 2014); and (2) deriving the total slip rate by simple trigonometry from vertical exhumation rates of the footwall (e.g. Schultz *et al.* 2017). The first approach is based on the assumptions that the isotherms have been stable and subhorizontal, that the orientation of the fault did not change and that exhumation was solely caused by tectonic denudation. We also note that the AFT samples should have the same annealing kinetics, and hence similar effective closure temperatures. This is supported for our samples by consistent Dpar values of 1.36 to 1.53 μm, reflecting typical flourine–apatite composition, and the uniform cooling history. The second approach requires one to estimate the original dip angle at which the fault was active. The thermochronological dataset presented in this study and by Wölfler *et al.* (2017) allow us to apply both approaches to constrain the slip rate of the Demirhan detachment.

Firstly, the AFT age of sample 15M44 is combined with four AFT samples from Wölfler *et al.* (2017), which together show decreasing cooling ages in the down-dip direction of the detachment (Fig. 11). A linear regression of the data with *Isoplot* (Ludwig 2003) gives an error-weighted slip rate of 2.6 ± 2.1 (1σ) km Ma^{-1} (or mm a^{-1}) (Fig. 11). The uncertainty of the slip rate is mainly caused by the large errors in the AFT ages. Secondly, based on a modelled exhumation rate of 0.42 ± 0.17 km Ma^{-1} for the samples in the footwall of the Demirhan detachment (sample 15M44, Fig. 9a) and present-day dip of *c.* 15° of the detachment, we calculate a slip rate of 1.6 ± 0.65 km Ma^{-1}. For a steeper dip of 30°, the resulting slip rate
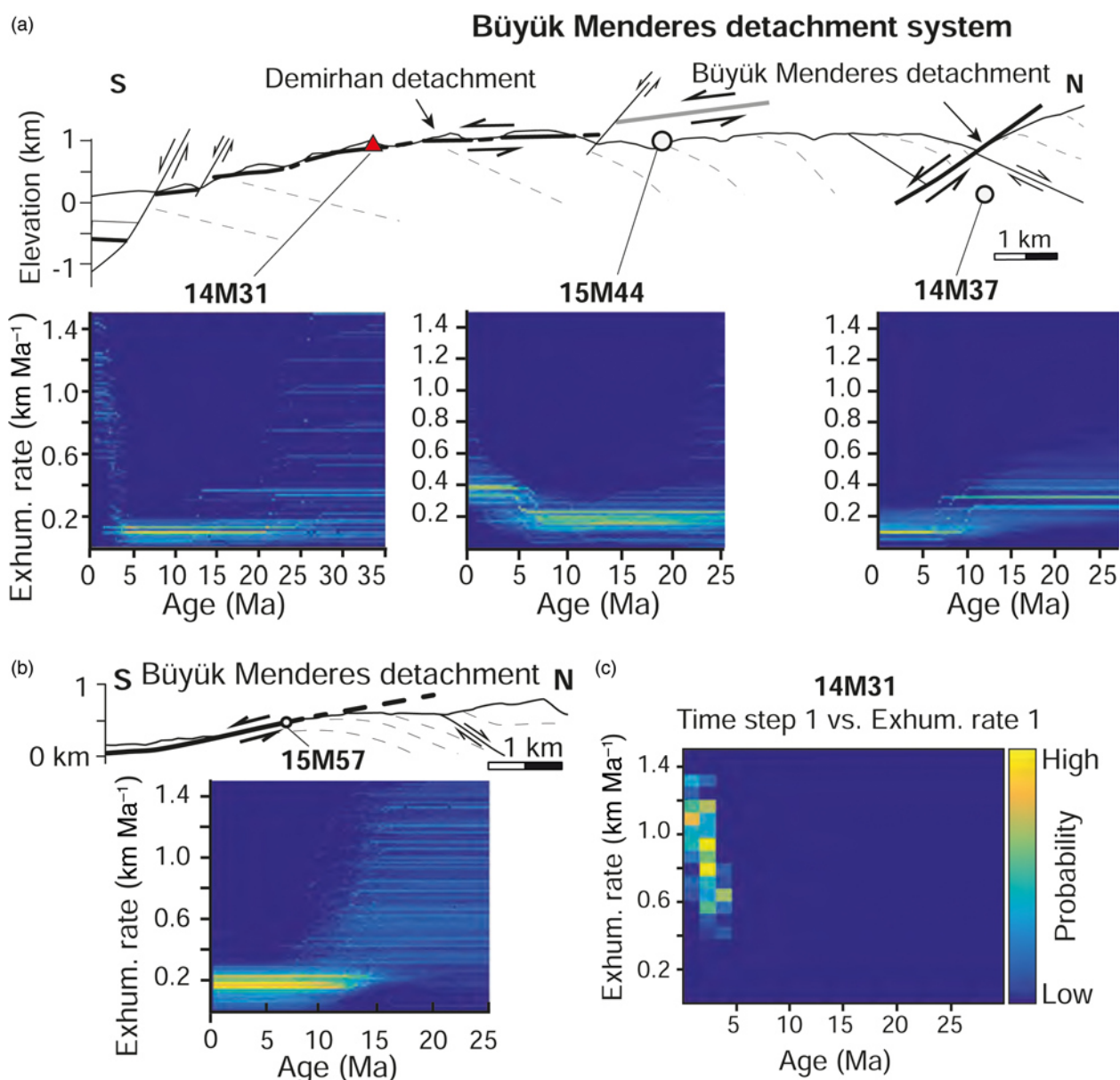
Fig. 9. (**a**) Modelled exhumation rates for the eastern part of the footwall of the Büyük Menderes detachment (14M37) and the Demirhan detachment footwall (15M44) and hanging wall (14M31). (**b**) Modelled exhumation rate for sample 15M57 from the western part of the Büyük Menderes detachment. (**c**) Two-dimensional probability density function showing the linear relationship between T_1 and E_1 of sample 14M31 (exhumation rate for the time between 0 Ma and T_1).

would be 0.8 ± 0.34 km Ma^{-1}. Although both approaches (to determine the slip rate) are associated with high uncertainties, they constrain the slip rate of the Demirhan detachment to be c. 2 km Ma^{-1}, which is about half the rate obtained for the Gediz detachment during the same period (4.3 (+3.0/−1.2) km Ma^{-1}; Buscher et al. 2013). Considering that faulting along the Demirhan detachment started between the modelled inception at c. 7 Ma (Table 6, sample 15M44) and 6 Ma (AFT age of sample 15M44) until its cessation at c. 3 Ma, indicated by the onset of high-angle graben faulting at the northern rim of the Büyük Menderes graben, the total displacement along the footwall of the Demirhan detachment is in the order of c. 6–c. 8 km.

Tectonic implications for the extensional history of the Aydın range

Based on exhumation histories (derived from thermokinematic modelling) and new field observations, we propose a new tectonic model for the Miocene to Recent extensional history of the Aydın range and the evolution of the Büyük Menderes graben (Figs 1 and 2).

The timing of initiation of the extensional tectonic regime, leading to the formation of the central Menderes Massif and the east–west-striking basins, is an ongoing discussion and centres around the question of whether the extension commenced in the early to middle Miocene (Bozkurt 2001) or in the latest Miocene/Pliocene (Gürer et al. 2009; Ring et al. 2017). For the Bozdağ range, the initiation of detachment faulting along the Gediz detachment is well constrained by the U–Pb intrusion ages of the syntectonic Salihli and Turgutlu granodiorites of c. 15 to c. 16 Ma, respectively (Glodny & Hetzel 2007). This approach cannot be applied in the Aydın range due to the lack of syntectonic intrusions along the Büyük Menderes detachment. Therefore, most studies inferred the onset of north–south extensional faulting and graben formation indirectly by constraining the depositional ages of the syntectonic Neogene sediments in the Büyük Menderes graben (e.g. Sözbilir & Emre 1990; Seyitoğlu & Scott 1991; Cohen et al. 1995). The
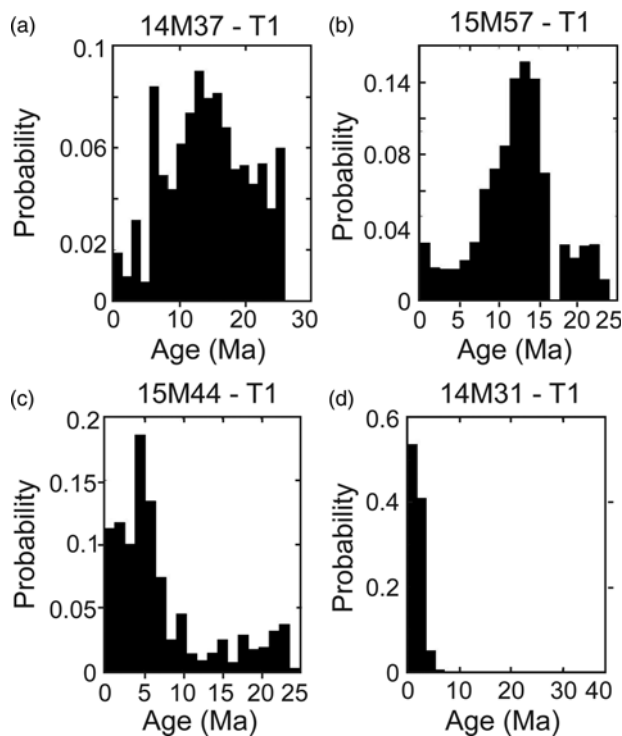
Fig. 10. PDFs (probability density functions) of parameter T_1 (time at which the exhumation rate is changed): (**a**) parameter T_1 of sample 14M37 indicates a middle Miocene change in exhumation rates; (**b**) similarly to the T_1 of 14M37, parameter T_1 of sample 15M57 shows a middle Miocene age; (**c**) sample 15M44 indicates a change from slow to high exhumation rates initiated during the late Miocene; (**d**) sample 14M31 shows the latest Miocene/Pliocene change from slow to high exhumation rates.

Fig. 11. Slip rate derived from AFT ages (1σ errors) in the footwall of the Demirhan detachment, plotted against distance in slip direction. The observed scatter of the data points from the best-fit line is given as MSWD (mean square of weighted deviates).

difficulty of this approach is the uncertain age of the oldest sedimentary unit, the Hasköy formation.

The depositional ages of the Hasköy formation are either based on palynological dating, yielding ages from early Miocene to late Miocene (Sözbilir & Emre 1990; Seyitoğlu & Scott 1991; Cohen *et al.* 1995; Akgün & Akyol 1999), or on the palaeomagnetic data of Sen & Seyitoğlu (2009) who tentatively suggest a 16–15 Ma depositional age for the Hasköy formation. Alternatively, Gürer *et al.* (2009) proposed that the Hasköy formation was deposited during the formation of the NE- and NW-trending basins in the northern and southern Menderes submassifs, which are inferred to result from a north–south-oriented contractional tectonic regime during the Miocene until the late Pliocene. However, this interpretation is not supported by our thermochronological and structural data, which demonstrate a persistent north–south-directed extension since the Miocene and do not comply with seismic reflection profiles of the Gediz and Büyük Menderes graben, which showed that the Miocene units in both basins were deposited in an extensional half-graben setting (Çiftçi & Bozkurt 2010; Çiftçi *et al.* 2011). Early Miocene (*c.* 22–20 Ma) K–Ar ages for a cataclasite of the Büyük Menderes detachment footwall and for a normal fault in the hanging wall of the detachment, may date the onset of normal faulting in the Aydın range (Hetzel *et al.* 2013).

The first stage of enhanced early to middle Miocene exhumation in the Aydın range was proposed by Wölfler *et al.* (2017) and is corroborated by the additional thermochronological data obtained in this study. Within the context of our new structural model for the Aydın range, almost all samples situated in the footwall of the Büyük Menderes detachment show fast early to middle Miocene exhumation rates of 0.5 ± 0.3 to 0.8 ± 0.4 km Ma^{-1} between the ZHe (mean ZHe ages: 14.9 Ma) and AFT (mean AFT ages: 12.9 Ma)
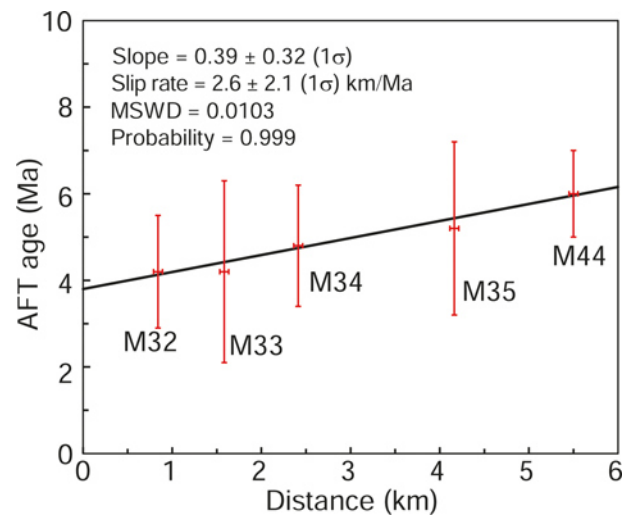
systems (Fig. 10a). However, this exhumation phase is not seen in samples from the footwall of the Demirhan detachment due to their position in the hanging wall of the Büyük Menderes detachment at this time. The relatively large errors associated with the AFT ages prevent resolving the timing of fast exhumation rates during the first stage exhumation event in the middle Miocene by thermokinematic modelling. However, the samples from the eastern part of the Büyük Menderes detachment show fast cooling between *c.* 16 and *c.* 13 Ma (Fig. 6) and samples from the western part show a similar timing with fast cooling occurring at *c.* 13 Ma (Fig. 4a). The middle Miocene activity along the Büyük Menderes detachment coincides with some major tectonic changes in the Aegean and western Turkey, due to the lithospheric response to an accelerated southward roll-back of the Aegean slab commencing at *c.* 15 Ma (e.g. Menant *et al.* 2016). In western Turkey, this is expressed by a southward movement of volcanism and an associated shift to more asthenosphere-derived melts due to the position of western Anatolia above the eastern edge of the Aegean slab (Prelević *et al.* 2012; Menant *et al.* 2016). The extensional processes in western Anatolia are marked by the cessation of detachment faulting along the Simav detachment (Ring & Collins 2005) and the onset of high-angle normal faulting at 17 to 16 Ma (Hetzel *et al.* 2013). Subsequently, the exhumation of the Bozdağ range by the initiation of faulting along the Gediz detachment commences at *c.* 14.5 Ma (Rossetti *et al.* 2017) after the intrusion of granodiorites at 15 and 16 Ma (Glodny & Hetzel 2007). For this early stage movement on the Gediz detachment, Rossetti *et al.* (2017) calculated a cooling rate of *c.* 100°C km^{-1} between 14 and 12 Ma, which is followed by an interval of slow cooling (*c.* 13°C km^{-1}) before a second stage of fast cooling with rates of *c.* 100°C km^{-1} in the latest Miocene/Pliocene. Compared to the Aydın range, the cooling rates in the Bozdağ range are higher, but the similar timing indicates a synchronous activity of the Gediz and the Büyük Menderes detachments during the middle Miocene.

The second exhumation stage in the latest Miocene marks the initiation of faulting along the Demirhan detachment in the Aydın range (Fig. 12b) and the concurrent activity of the Gediz detachment in the Bozdağ range since the Pliocene (Buscher *et al.* 2013). The middle Miocene cooling ages from AFT and 10–7 Ma cooling ages from AHe (Fig. 6) indicate that the footwall rocks of the Büyük Menderes detachment were already close to the surface when faulting along the Demirhan detachment initiated in the latest
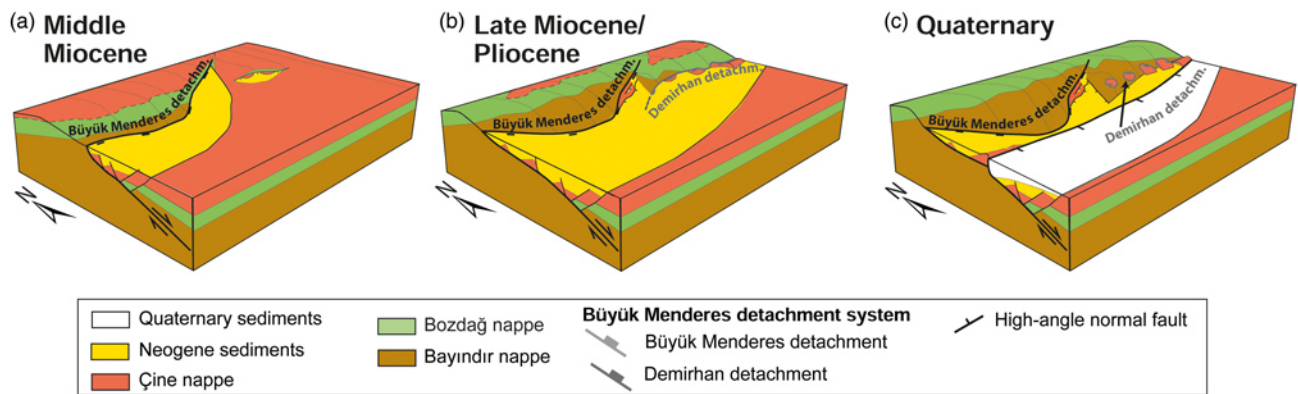
Fig. 12. Sketch illustrating the proposed extensional history of the Aydın range since the middle Miocene. (**a**) Exhumation of the Aydın range in the footwall of the Büyük Menderes detachment and probably early graben formation in the eastern parts of the Büyük Menderes graben. (**b**) Main proportion of extension is accommodated along the Demirhan detachment which exhumes the eastern part of the Aydın range. (**c**) Onset of high-angle normal faulting along the modern graben-bounding fault of the Büyük Menderes graben and uplift and erosion of the Neogene sediments in its footwall.

Miocene (Fig. 9a and Table 6). With a slip rate of about 2 km Ma^{-1}, the Demirhan detachment likely accommodated most of the extension along the southern boundary of the central Menderes Massif but young K–Ar fault gouge ages of *c.* 3–5 Ma indicate that the Büyük Menderes detachment remained active until the Pliocene (Hetzel *et al.* 2013). The inception of faulting along the Demirhan detachment goes along with a widespread tectonic reorganization in the Aegean region and western Turkey, which was caused by the westward propagation of the North Anatolian fault into the Aegean domain (Şengör *et al.* 2005) and the segmentation of the Hellenic slab by the development of a slab tear below the Corinth rift (Royden & Papanikolaou 2011; Jolivet *et al.* 2013). Since the separation from the western part of the Hellenic slab at 5 Ma ago, the trench retreat of the central part of the Hellenic slab accelerated from *c.* 1.7 cm a^{-1} to *c.* 3.2 cm a^{-1} (Brun *et al.* 2017*a*, *b*). Whether the westward propagation of the North Anatolian fault and the associated westward extrusion of Anatolia was caused by the increasing slab retreat rate or by the ongoing continental collision between Arabia and Anatolia is still disputed. In any case, faulting on this strike-slip fault in the Aegean domain is associated with the redistribution of extensional strain from the central Aegean towards the western (Evvia island and Corinth region) and eastern edges (western Anatolia) of the Aegean domain (Royden & Papanikolaou 2011; Menant *et al.* 2016). This new tectonic situation may have favoured the abandonment of the perennial Büyük Menderes detachment and the formation of the new Demirhan detachment in the hanging wall. This is a process that has also been reported from other persistent extensional detachment systems, for example along the North Cycladic Detachment System (NCDS), which accommodated its total amount of extension of 70–90 km in three successively active detachments between 30 and 9 Ma (Jolivet *et al.* 2010). However, compared to the NCDS, the Büyük Menderes detachment system accommodated less extension and most probably does not have a crustal scale pre-extensional precursor, such as the Vardar suture zone for the NCDS. Both systems show that long-lived extensional structures may become ineffective over time. The position of the Demirhan detachment, which occurs not only in the hanging wall but also to the SE of the Büyük Menderes detachment, further implies an eastward propagation of extensional structures with time.

Ongoing extension led to the formation of high-angle normal faults, which bound the modern Büyük Menderes graben to the north and cut the Büyük Menderes and Demirhan detachments. These steeper normal faults must have developed after the activity of the detachments had ceased (Fig. 12c). AHe ages in the footwall of the northern graben-bounding fault range from 2.7 to 0.5 Ma and

suggest a late Pliocene to Pleistocene onset of faulting. This is also supported by the thermal modelling results for sample 14M31, which belongs to the hanging wall of the Demirhan detachment and was exhumed in the footwall of the high-angle normal fault (Fig. 9a). Contemporaneously, the Pliocene–Pleistocene Asartepe formation was discordantly deposited above the middle Miocene Gökkırantepe formation during the Pliocene to Pleistocene in the Büyük Menderes graben (Ünay *et al.* 1995; Sarıca 2000). This sedimentary succession is currently uplifted and exposed in the footwall of Quaternary high-angle normal faults whose activity was demonstrated by the surface-rupturing earthquake near Aydın in 1899 (e.g. Altunel 1999). These high-angle normal faults appear to root into a sub-horizontal southward-dipping reflector, which has been interpreted as an active low-angle normal fault at *c.* 2.5 km depth (Çiftçi *et al.* 2011) that accommodates a proportion of the present-day extension rate of 20 mm a^{-1} in western Anatolia (Aktug *et al.* 2009).

Conclusions

The new structural and thermochronological data presented in this study allow a comprehensive interpretation of the extensional history of the Aydın range, and an evaluation of the bivergent exhumation of the central Menderes Massif. Structural mapping of extensional structures demonstrates that extension and exhumation of the Aydın range was not accomplished by slip on a single extensional detachment fault but occurred by faulting on two individual low-angle detachment faults – the Büyük Menderes detachment and the Demirhan detachment in its hanging wall. New thermochronological data shed light on the temporal sequence of the activity of the individual detachments and show that the Büyük Menderes detachment was active in the early to middle Miocene. In the latest Miocene, active detachment faulting started on the Demirhan detachment (although the western part of the Büyük Menderes detachment remained active) and continued until the onset of high-angle normal faulting along the modern Büyük Menderes graben in the Quaternary. Thermokinematic modelling reveals that the footwalls of the Büyük Menderes and Demirhan detachments were exhumed at rates of 0.5 and *c.* 0.4 km Ma^{-1}, respectively. Our results support contemporaneous exhumation of the Aydın and Bozdağ ranges during the middle Miocene and latest Miocene/Pliocene.

References

Akgün, F. & Akyol, E. 1999. Palynostratigraphy of the coal-bearing Neogene deposits graben in Büyük Menderes Western Anatolia. *Geobios*, **32**, 367–383, https://doi.org/10.1016/S0016-6995(99)80013-8

Aktug, B., Nocquet, J.M. *et al.* 2009. Deformation of western Turkey from a combination of permanent and campaign GPS data: Limits to block-like behavior. *Journal of Geophysical Research*, **114**, https://doi.org/10.1029/2008JB006000

Altunel, E. 1999. Geological and geomorphological observations in relation to the 20 September 1899 Menderes earthquake, western Turkey. *Journal of the Geological Society, London,* **156**, 241–246, https://doi.org/10.1144/gsjgs.156.2.0241

Asti, R., Malusà, M.G. & Faccenna, C. 2018. Supradetachment basin evolution unravelled by detrital apatite fission track analysis: the Gediz Graben (Menderes Massif, Western Turkey). *Basin Research*, **30**, 502–521, https://doi.org/10.1111/bre.12262

Bozkurt, E. 2000. Timing of extension on the Büyük Menderes Graben, western Turkey, and its tectonic implications. *In*: Bozkurt, E., Winchester, J. A. & Piper, J.D.A. (eds) *Tectonics and Magmatism in Turkey and its Surrounding Area*. Geological Society, London, Special Publications, **173**, 385–403, https://doi.org/10.1144/GSL.SP.2000.173.01.18

Bozkurt, E. 2001. Late Alpine evolution of the central Menderes Massif, western Turkey. *International Journal of Earth Sciences*, **89**, 728–744, https://doi.org/10.1007/s005310000141

Bozkurt, E. & Sözbilir, H. 2004. Tectonic evolution of the Gediz Graben: field evidence for an episodic, two-stage extension in western Turkey. *Geological Magazine*, **141**, 63–79, https://doi.org/10.1017/S0016756803008379

Bozkurt, E., Park, R.G. & Winchester, J.A. 1993. Evidence against the core/cover interpretation of the southern sector of the Menderes Massif, west Turkey. *Terra Nova*, **5**, 445–451, https://doi.org/10.1111/j.1365-3121.1993.tb00282.x

Bozkurt, E., Winchester, J.A. & Park, R.G. 1995. Geochemistry and tectonic significance of augen gneisses from the southern Menderes Massif (West Turkey). *Geological Magazine*, **132**, 287–301, https://doi.org/10.1017/S0016756800013613

Brady, R.J. 2002. Very high slip rates on continental extensional faults: new evidence from (U–Th)/He thermochronometry of the Buckskin Mountains, Arizona. *Earth and Planetary Science Letters*, **197**, 95–104, https://doi.org/10.1016/S0012-821X(02)00460-0

Braun, J. 2003. Pecube: A new finite-element code to solve the 3D heat transport equation including the effects of a time-varying, finite amplitude surface topography. *Computers & Geosciences*, **29**, 787–794, https://doi.org/10.1016/S0098-3004(03)00052-9

Braun, J., van der Beek, P. *et al.* 2012. Quantifying rates of landscape evolu-tion and tectonic processes by thermochronology and numerical modeling of crustal heat transport using PECUBE. *Tectonophysics*, **524–525**, 1–28, https://doi.org/10.1016/j.tecto.2011.12.035

Brichau, S., Ring, U., Ketcham, R.A., Carter, A., Stockli, D. & Brunel, M. 2006. Constraining the long-term evolution of the slip rate for a major extensional fault system in the central Aegean, Greece, using thermochronology. *Earth and Planetary Science Letters*, **241**, 293–306, https://doi.org/10.1016/j.epsl.2005.09.065

Brun, J.P., Sokoutis, D., Tirel, C., Gueydan, F., Van den Driessche, J. & Beslier, M.O. 2017*a*. Crustal *versus* mantle core complexes. *Tectonophysics*, **746**, 22–45, https://doi.org/10.1016/j.tecto.2017.09.017

Brun, J.P., Faccenna, C., Gueydan, F., Sokoutis, D., Philippon, M., Kydonakis, K. & Gorini, C. 2017*b*. Effects of slab rollback acceleration on Aegean extension. *Bulletin of the Geological Society of Greece*, **50**, 5–23, https://doi.org/10.12681/bgsg.11697

Burchfiel, B.C., Chen, Z., Hodges, K.V., Yuping, L., Royden, L.H., Changrong, D. & Jiene, X. 1992. *The South Tibetan Detachment System, Himalayan Orogen: extension contemporaneous with and parallel to shortening in a collisional mountain belt. GSociety of America Special Papers*, **269**, https://doi.org/10.1130/SPE269-p1eological

Burtner, R., Nigrini, A. & Donelick, R.A. 1994. Thermochronology of Lower Cretaceous source rocks in the Idaho-Wyoming Thrust belt. *American Association of Petroleum Geologists Bulletin*, **78**, 1613–1636.

Buscher, J.T., Hampel, A. *et al.* 2013. Quantifying rates of detachment faulting and erosion in the central Menderes Massif (western Turkey) by thermochronology and cosmogenic [10]Be. *Journal of the Geological Society, London*, **170**, 669–683, https://doi.org/10.1144/jgs2012-132

Campani, M., Mancktelow, N., Seward, D., Rolland, Y., Müller, W. & Guerra, I. 2010. Geochronological evidence for continuous exhumation through the ductile–brittle transition along a crustal scale low angle normal fault: Simplon Fault Zone, central Alps. *Tectonics*, **29**, TC3002, https://doi.org/10.1029/2009TC002582

Candan, O., Dora, OÖ, Kun, N., Akal, C. & Koraly, E. 1992. Allochthonous metamorphic units at the southern part of Aydın Mountains, Menderes Massif. *Turkish Association of Petroleum Geologists*, **4**, 93–110.

Candan, O., Dora, OÖ, Oberhänsli, R., Çetinkaplan, M., Partzsch, J.H., Warkus, F.C. & Dürr, S. 2001. Pan-African high-pressure metamorphism in the Precambrian basement of the Menderes Massif, western Anatolia, Turkey. *International Journal of Earth Sciences*, **89**, 793–811, https://doi.org/10.1007/s005310000097

Candan, O., Çetinkaplan, M., Oberhänsli, R., Rimmelé, G. & Akal, C. 2005. Alpine high-P/low-T metamorphism of the Afyon Zone and implications for the metamorphic evolution of Western Anatolia, Turkey. *Lithos*, **84**, 102–124, https://doi.org/10.1016/j.lithos.2005.02.005

Candan, O., Koralay, O.E. *et al.* 2011. Supra-Pan-African unconformity between core and cover series of the Menderes Massif/Turkey and its geological implications. *Precambrian Research*, **184**, 1–23, https://doi.org/10.1016/j.precamres.2010.09.010

Carlson, W.D., Donelick, R.A. & Ketcham, R.A. 1999. Variability of apatite fission-track annealing kinetics: I. Experimental results. *American Mineralogist*, **84**, 1213–1223, https://doi.org/10.2138/am-1999-0901

Catlos, E.J., Baker, C., Sorensen, S.S., Çemen, I. & Hançer, M. 2010. Geochemistry, geochronology, and cathodoluminescence imagery of the Salihli and Turgutlu granites (central Menderes Massif, western Turkey): Implications for Aegean tectonics. *Tectonophysics*, **488**, 110–130, https://doi.org/10.1016/j.tecto.2009.06.001

Çemen, I., Catlos, E.J., Gogus O., Ozerdem, C., 2006. Post-collisional extensional tectonics and exhumation of the Menderes massif in the western Anatolia Extended Terrrane, Turkey. *In*: Dilek, Y. & Pavlis, S. (eds) *Postcollisional Tectonics and Magmatism in the Eastern Mediterranean Region*. Geological Society of America, Special Papers, Boulder, Colorado, **409**, 353–379.

Cenki-Tok, B., Expert, M., Işık, V., Candan, O., Monie, P. & Bruguier, O. 2016. Complete Alpine reworking of the northern Menderes Massif, western Turkey. *International Journal of Earth Sciences*, **105**, 1507–1524, https://doi.org/10.1007/s00531-015-1271-2

Çiftçi, N.B. & Bozkurt, E. 2010. Structural evolution of the Gediz Graben, SW Turkey: temporal and spatial variation of the graben basin. *Basin Research*, **22**, 846–873, https://doi.org/10.1111/j.1365-2117.2009.00438.x

Çiftçi, N.B., Pamukçu, O., Çoruh, C., Çopur, S. & Sözbilir, H. 2011. Shallow and deep structure of a supradetachment basin based on geological, conventional deep seismic reflection sections and gravity data in the Buyuk Menderes Graben, Western Anatolia. *Surveys in Geophysics*, **32**, 271–290, https://doi.org/10.1007/s10712-010-9109-8

Cohen, H.A., Dart, C.J., Akyüz, H.S. & Barka, A. 1995. Syn-rift sedimentation and structural development of the Gediz and Büyük Menderes graben, western Turkey. *Journal of the Geological Society*, London, **152**, 629–638, https://doi.org/10.1144/gsjgs.152.4.0629

Danišík, M., McInnes, B.I., Kirkland, C.L., McDonald, B.J., Evans, N.J. & Becker, T. 2017. Seeing is believing: Visualization of He distribution in zircon and implications for thermal history reconstruction on single crystals. *Science Advances*, **3**, e1601121, https://doi.org/10.1126/sciadv.1601121

Dodson, M.H. 1973. Closure temperature in cooling geochronological and petrological systems. *Contributions to Mineralogy and Petrology*, **40**, 259–274, https://doi.org/10.1007/BF00373790

Dunkl, I. 2002. TRAKKEY: a window program for calculation and graphical presentation of fission track data. *Computers & Geosciences*, **28**, 3–12, https://doi.org/10.1016/S0098-3004(01)00024-3

Ehlers, T.A. & Farley, K.A. 2003. Apatite (U–Th)/He thermochronometry: Methods and applications to problems in tectonics and surface processes. *Earth and Planetary Science Letters*, **206**, 1–14, https://doi.org/10.1016/S0012-821X(02)01069-5

Emre, T. & Sözbilir, H. 1997. Field evidence for metamorphic core complex, detachment faulting and accommodation faults in the Gediz and Büyük Menderes Grabens, Western Anatolia. *In:* International Earth Science Colloquium on the Aegean and Surrounding Regions, Proceedings, 1995, **1**, 73–94.

Emre, T. & Sözbilir, H. 2007. Tectonic evolution of the Kiraz Basin, Küçük Menderes Graben: evidence for compression/uplift-related basin formation overprinted by extensional tectonics in west Anatolia. *Turkish Journal of Earth Sciences*, **16**, 441–470.

Erkül, F. 2010. Tectonic significance of synextensional ductile shear zones within the Early Miocene Alaçamdağ granites, northwestern Turkey. *Geological Magazine*, **147**, 611–637, https://doi.org/10.1017/S0016756809990719

Ersoy, E.Y., Akal, C. *et al.* 2017. U–Pb zircon geochronology of the Paleogene–Neogene volcanism in the NW Anatolia: Its implications for the Late Mesozoic–Cenozoic geodynamic evolution of the Aegean. *Tectonophysics*, **717**, 284–301, https://doi.org/10.1016/j.tecto.2017.08.016

Farley, K.A. 2000. Helium diffusion from apatite: General behavior as illustrated by Durango fluorapatite. *Journal of Geophysical Research*, **105**, 2903–2914, https://doi.org/10.1029/1999JB900348

Farley, K.A. 2002. (U–Th)/He dating: techniques, calibrations and applications. *Reviews in Mineralogy & Geochemistry*, **47**, 819–844, https://doi.org/10.2138/rmg.2002.47.18

Farley, K.A., Wolf, R.A. & Silver, L.T. 1996. The effects of long alpha-stopping distances on (U–Th)/He ages. *Geochimica et Cosmochimica Acta*, **60**, 4223–4229, https://doi.org/10.1016/S0016-7037(96)00193-7

Flowers, R.M., Shuster, D.L., Wernicke, B.P. & Farley, K.A. 2007. Radiation damage control on apatite (U–Th)/He dates from the Grand Canyon

region, Colorado Plateau. *Geology*, **35**, 447–450, https://doi.org/10.1130/G23471A.1

Flowers, R.M., Ketcham, R.A., Shuster, D.L. & Farley, K.A. 2009. Apatite (U–Th)/He thermochronometry using a radiation damage accumulation and annealing model. *Geochimica et Cosmochimica Acta*, **73**, 2347–2365, https://doi.org/10.1016/j.gca.2009.01.015

Foster, D.A. & John, B.E. 1999. Quantifying tectonic exhumation in an extensional orogen with thermochronology: examples from the southern Basin and Range Province. *In*: Ring, U., Brandon M.T., Lister G.S. & Willett S.D. (eds) *Exhumation Processes: Normal Faulting, Ductile Flow and Erosion*. Geological Society, London, Special Publications, **154**, 343–364, https://doi.org/10.1144/GSL.SP.1999.154.01.16

Gautheron, C., Tassan-Got, L., Barbarand, J. & Pagel, M. 2009. Effect of alpha-damage annealing on apatite (U–Th)/He thermochronology. *Chemical Geology*, **266**, 157–170, https://doi.org/10.1016/j.chemgeo.2009.06.001

Gessner, K., Ring, U., Johnson, C., Hetzel, R., Passchier, C.W. & Güngör, T. 2001a. An active bivergent rolling-hinge detachment system: Central Menderes metamorphic core complex in western Turkey. *Geology*, **29**, 611–614, https://doi.org/10.1130/0091-7613(2001)029<0611:AABRHD>2.0.CO;2

Gessner, K., Piazolo, S., Güngör, T., Ring, U., Kröner, A. & Passchier, C.W. 2001b. Tectonic significance of deformation patterns in granitoid rocks of the Menderes nappes, Anatolide belt, southwest Turkey. *International Journal of Earth Sciences*, **89**, 766–780, https://doi.org/10.1007/s005310000106

Gessner, K., Ring, U., Passchier, C.W. & Güngör, T. 2001c. How to resist subduction: Eocene post-high-pressure emplacement of the Cycladic blueschist unit onto the Menderes nappes, Anatolide belt, western Turkey. *Journal of the Geological Society, London*, **158**, 769–780, https://doi.org/10.1144/jgs.158.5.769

Gessner, K., Collins, A.S., Ring, U. & Güngör, T. 2004. Structural and thermal history of poly-orogenic basement: U–Pb geochronology of granitoid rocks in the southern Menderes Massif, Western Turkey. *Journal of the Geological Society, London*, **161**, 93–101, https://doi.org/10.1144/0016-764902-166

Gessner, K., Gallardo, L.A., Markwitz, V., Ring, U. & Thomson, S.N. 2013. What caused the denudation of the Menderes Massif: Review of crustal evolution, lithosphere structure, and dynamic topography in southwest Turkey. *Gondwana Research*, **24**, 243–274, https://doi.org/10.1016/j.gr.2013.01.005

Gleadow, A.J.W. 1981. Fission-track dating methods: what are the real alternatives? *Nuclear Tracks*, **5**, 3–14, https://doi.org/10.1016/0191-278X(81)90021-4

Gleadow, A.J.W. & Duddy, I.R. 1981. A natural long-term track annealing experiment for apatite. *Nuclear Tracks*, **5**, 169–174, https://doi.org/10.1016/0191-278X(81)90039-1

Glodny, J. & Hetzel, R. 2007. Precise U–Pb ages of syn-extensional Miocene intrusions in the central Menderes Massif, western Turkey. *Geological Magazine*, **144**, 235–246, https://doi.org/10.1017/S0016756806003025

Glotzbach, C., Van Der Beek, P.A. & Spiegel, C. 2011. Episodic exhumation and relief growth in the Mont Blanc massif, Western Alps from numerical modelling of thermochronology data. *Earth and Planetary Science Letters*, **304**, 417–430, https://doi.org/10.1016/j.epsl.2011.02.020

Grasemann, B., Schneider, D.A., Stockli, D.F. & Iglseder, C. 2012. Miocene bivergent crustal extension in the Cyclades (Greece). *Lithosphere*, **4**, 23–39, https://doi.org/10.1130/L164.1

Green, P.F., Duddy, I.R., Gleadow, A.J.W., Tingate, P.R. & Laslett, G.M. 1986. Thermal annealing of fission tracks in apatite 1. A qualitative description. *Chemical Geology*, **59**, 237–253, https://doi.org/10.1016/0168-9622(86)90074-6

Guenthner, W.R., Reiners, P.W., Ketcham, R.A., Nasdala, L. & Giester, G. 2013. Helium diffusion in natural zircon: Radiation damage, anisotropy, and the interpretation of zircon (U–Th)/He thermochronology. *American Journal of Science*, **313**, 145–198, https://doi.org/10.2475/03.2013.01

Gürer, Ö.F., Sarıca-Filoreau, N., Özburan, M., Sangu, E. & Doğan, B. 2009. Progressive development of the Büyük Menderes Graben based on new data, western Turkey. *Geological Magazine*, **146**, 652–673, https://doi.org/10.1017/S0016756809006359

Hasözbek, A., Satır, M., Erdoğan, B., Akay, E. & Siebel, W. 2011. Early Miocene post-collisional magmatism in NW Turkey: geochemical and geochronological constraints. *International Geology Review*, **53**, 1098–1119, https://doi.org/10.1080/00206810903579302

Herman, F., Braun, J., Senden, T.J. & Dunlap, W.J. 2007. (U–Th)/He thermochronometry: Mapping 3D geometry using micro-X-ray tomography and solving the associated production-diffusion equation. *Chemical Geology*, **242**, 126–136, https://doi.org/10.1016/j.chemgeo.2007.03.009

Hetzel, R. & Reischmann, T. 1996. Intrusion of Pan-African gneisses in the southern Menderes massif and the age of cooling after Alpine ductile extensional deformation. *Geological Magazine*, **133**, 565–572, https://doi.org/10.1017/S0016756800007846

Hetzel, R., Ring, U., Akal, C. & Troesch, M. 1995a. Miocene NNE-directed extensional unroofing in the Menderes Massif, southwestern Turkey. *Journal of the Geological Society, London*, **152**, 639–654, https://doi.org/10.1144/gsjgs.152.4.0639

Hetzel, R., Passchier, C.W., Ring, U. & Dora, OÖ. 1995b. Bivergent extension in orogenic belts: The Menderes Massif (southwestern Turkey). *Geology*, **23**, 455–458, https://doi.org/10.1130/0091-7613(1995)023<0455:BEIOBT>2.3.CO;2

Hetzel, R., Zwingmann, H. et al. 2013. Spatiotemporal evolution of brittle normal faulting and fluid infiltration in detachment fault systems: A case study from the Menderes Massif, western Turkey. *Tectonics*, **32**, 1–13, https://doi.org/10.1002/tect.20031

Hourigan, J.K., Reiners, P.W. & Brandon, M.T. 2005. U–Th zonation-dependent alpha-ejection in (U–Th)/He chronometry. *Geochimica et Cosmochimica Acta*, **69**, 3349–3365, https://doi.org/10.1016/j.gca.2005.01.024

Huet, B., Labrousse, L. & Jolivet, L. 2009. Thrust or detachment? Exhumation processes in the Aegean: Insight from a field study on Ios (Cyclades, Greece). *Tectonics*, **28**, TC3007, https://doi.org/10.1029/2008TC002397

Hurford, A.J. & Green, P.F. 1983. The zeta age calibration of fission-track dating. *Chemical Geology*, **1**, 285–317, https://doi.org/10.1016/S0009-2541(83)80026-6

Iglseder, C., Grasemann, B., Rice, A.H.N., Petrakakis, K. & Schneider, D.A. 2011. Miocene south directed low-angle normal fault evolution on Kea Island (West Cycladic Detachment System, Greece). *Tectonics*, **30**, TC4013, https://doi.org/10.1029/2010TC002802

Işık, V. & Tekeli, O. 2001. Late orogenic crustal extension in the northern Menderes massif (western Turkey): Evidences for metamorphic core complex formation. *International Journal of Earth Sciences*, **89**, 757–765, https://doi.org/10.1007/s005310000105

Işık, V., Tekeli, O. & Seyitoğlu, G. 2004. The $^{40}Ar/^{39}Ar$ age of extensional ductile deformation and granitoid intrusion in the northern Menderes core complex: implications for the initiation of extensional tectonics in western Turkey. *Journal of Asian Earth Sciences*, **23**, 555–566, https://doi.org/10.1016/j.jseaes.2003.09.001

Jolivet, L. & Brun, J.-P. 2010. Cenozoic geodynamic evolution of the Aegean. *International Journal of Earth Sciences*, **99**, 109–138, https://doi.org/10.1007/s00531-008-0366-4

Jolivet, L. & Patriat, M. 1999. Ductile extension and the formation of the Aegean Sea. *In*: Durand, B., Jolivet, L., Horváth, F. & Séranne, M. (eds) *The Mediterranean Basins: Tertiary Extension within the Alpine Orogen*. Geological Society, London, Special Publications, **156**, 427–456, https://doi.org/10.1144/GSL.SP.1999.156.01.20

Jolivet, L., Lecomte, E. et al. 2010. The North Cycladic Detachment System. *Earth and Planetary Science Letters*, **289**, 87–104, https://doi.org/10.1016/j.epsl.2009.10.032

Jolivet, L., Faccenna, C., Huet, B., Labrousse, L., Le Pourhiet, L., Lacombe, O. et al. 2013. Aegean tectonics: Strain localisation, slab tearing and trench retreat. *In*: The Aegean: a natural laboratory for tectonics – *Neotectonics*, **597–598**, 1–33, https://doi.org/10.1016/j.tecto.2012.06.011

Karamanderesi, I.H. & Helvacı, C. 2003. Geology and hydrothermal alteration of the Aydın-Salavatlı Geothermal Field, Western Anatolia, Turkey. *Turkish Journal of Earth Sciences*, **12**, 175–198.

Kaymakci, N., Özçelik, Y., White, S.H. & Van Dijk, P.M. 2009. Tectono-stratigraphy of the Çankırı Basin: late Cretaceous to early Miocene evolution of the Neotethyan suture zone in Turkey. *In*: Van Hinsbergen, D. J. J., Edwards, M. A. & Govers, R. (eds) *Collision and Collapse at the Africa–Arabia–Eurasia Subduction Zone*. Geological Society, London, Special Publications, **311**, 67–106, https://doi.org/10.1144/SP311.3

Ketcham, R.A. 2005. Forward and inverse modeling of low-temperature thermochronometry data. *Reviews in Mineralogy and Geochemistry*, **58**, 275–314, https://doi.org/10.2138/rmg.2005.58.11

Ketcham, R.A., Donelick, R.A. & Carlson, W.D. 1999. Variability of apatite fission-track annealing kinetics: III. Extrapolation to geological time scales. *American Mineralogist*, **84**, 1235–1255, https://doi.org/10.2138/am-1999-0903

Ketcham, R.A., Carter, A., Donelick, R.A., Barbarand, J. & Hurford, A.J. 2007. Improved modeling of fission-track annealing in apatite. *American Mineralogist*, **92**, 799–810, https://doi.org/10.2138/am.2007.2281

Koralay, O.E. 2015. Late Neoproterozoic granulite facies metamorphism in the Menderes Massif, Western Anatolia/Turkey: implication for the assembly of Gondwana. *Geodinamica Acta*, **27**, 244–266, https://doi.org/10.1080/09853111.2015.1014987

Koralay, O.E., Satır, M. & Dora, OÖ. 2001. Geochemical and geochronological evidence for Early Triassic calc-alkaline magmatism in the Menderes Massif, western Turkey. *International Journal of Earth Sciences*, **89**, 822–835, https://doi.org/10.1007/s005310000134

Koralay, O.E., Candan, O., Akal, C., Dora, OÖ, Chen, F., Satır, M. & Oberhänsli, R. 2011. Geology and geochronology of the Pan-African and Triassic metagranitoids in the Menderes Massif, Western Anatolia, Turkey. *Bulletin of the Mineral Research and Exploration*, **142**, 69–121.

Lee, J. & Lister, G.S. 1992. Late Miocene ductile extension and detachment faulting, Mykonos, Greece. *Geology*, **20**, 121–124, https://doi.org/10.1130/0091-7613(1992)020<0121:LMDEAD>2.3.CO;2

Lippolt, H.J., Leitz, M., Wernicke, R.S. & Hagerdon, B. 1994. (Uranium + thorium)/helium dating of apatite: experience with samples from different geochemical environments. *Chemical Geology*, **112**, 179–191, https://doi.org/10.1016/0009-2541(94)90113-9

Lips, A.L.W., Cassard, D., Sözbilir, H., Yilmaz, H. & Wijbrans, J.R. 2001. Multistage exhumation of the Menderes Massif, western Anatolia (Turkey). *International Journal of Earth Sciences*, **89**, 781–792, https://doi.org/10.1007/s005310000101

Lister, G.S. & Davis, G.A. 1989. The origin of metamorphic core complexes and detachment faults formed during Tertiary continental extension in the northern

Colorado River region, USA. *Journal of Structural Geology*, **11**, 65–94, https://doi.org/10.1016/0191-8141(89)90036-9

Lister, G.S., Banga, G. & Feenstra, A. 1984. Metamorphic core complexes of Cordilleran type in the Cyclades, Aegean Sea, Greece. *Geology*, **12**, 221–225, https://doi.org/10.1130/0091-7613(1984)12<221:MCCOCT>2.0.CO;2

Lister, G.S., Etheridge, M.A. & Symonds, P.A. 1986. Detachment faulting and the evolution of passive continental margins. *Geology*, **14**, 246–250, https://doi.org/10.1130/0091-7613(1986)14<246:DFATEO>2.0.CO;2

Loos, S. & Reischmann, T. 1999. The evolution of the southern Menderes Massif in SW Turkey as revealed by zircon dating. *Journal of the Geological Society, London*, **156**, 1021–1030, https://doi.org/10.1144/gsjgs.156.5.1021

Ludwig, K.R. 2003. *User's Manual for Isoplot 3.00 A Geochronological Toolkit for Excel*. Berkeley Geochronological Center, Special Publication No. **4**.

Malavieille, J. 1993. Late orogenic extension in mountain belts: insights from the Basin and Range and the late Paleozoic Variscan belt. *Tectonics*, **12**, 1115–1130, https://doi.org/10.1029/93TC01129

McKenzie, D. 1978. Some remarks on the development of sedimentary basins. *Earth and Planetary Science Letters*, **40**, 25–32, https://doi.org/10.1016/0012-821X(78)90071-7

Menant, A., Jolivet, L. & Vrielynck, B. 2016. Kinematic reconstructions and magmatic evolution illuminating crustal and mantle dynamics of the eastern Mediterranean region since the late Cretaceous. *Tectonophysics*, **675**, 103–140, https://doi.org/10.1016/j.tecto.2016.03.007

Naeser, C.W., 1978. *Fission track dating*, US Geological Survey Open File Report 76–190.

Oberhänsli, R., Candan, O., Dora, OÖ & Dürr, S. 1997. Eclogites within the Menderes Massif/western Turkey. *Lithos*, **41**, 135–150, https://doi.org/10.1016/S0024-4937(97)82009-9

Okay, A.I., Tüysüz, O., 1999. Tethyan sutures of northern Turkey. *In*: Durand, B., Jolivet, L., Horvath, E. & Seranne, M. (eds) *The Mediterranean Basins: Tertiary Extension within the Alpine Orogen*. Geological Society, London, Special Publications, **156**, 475–515, https://doi.org/10.1144/GSL.SP.1999.156.01.22

Oner, Z. & Dilek, Y. 2011. Supradetachment basin evolution during continental extension: the Aegean province of western Anatolia, Turkey. *Geological Society of America Bulletin*, **123**, 2115–2141, https://doi.org/10.1130/B30468.1

Özer, S. & Sözbilir, H. 2003. Presence and tectonic significance of Cretaceous rudist species in the so-called Permo-Carboniferous Göktepe Formation, central Menderes metamorphic massif, western Turkey. *International Journal of Earth Sciences*, **92**, 397–404, https://doi.org/10.1007/s00531-003-0333-z

Prelević, D., Akal, C., Foley, S.F., Romer, R.L., Stracke, A. & Van Den Bogaard, P. 2012. Ultrapotassic mafic rocks as geochemical proxies for post-collisional dynamics of orogenic lithospheric mantle: the case of southwestern Anatolia, Turkey. *Journal of Petrology*, **53**, 1019–1055, https://doi.org/10.1093/petrology/egs008

Rahn, M.K., Brandon, M.T., Batt, G.E. & Garver, J.I. 2004. A zero-damage model for fission-track annealing in zircon. *American Mineralogist*, **89**, 473–484, https://doi.org/10.2138/am-2004-0401

Regnier, J.L., Ring, U., Passchier, C.W., Gessner, K. & Güngör, T. 2003. Contrasting metamorphic evolution of metasedimantary rocks from the Çine and Selimiye nappes in the Anatolide belt, western Turkey. *Journal of Metamorphic Geology*, **21**, 699–721, https://doi.org/10.1046/j.1525-1314.2003.00473.x

Reiners, P.W. 2005. Zircon (U–Th)/He thermochronometry. *Reviews in Mineralogy and Geochemistry*, **58**, 151–179, https://doi.org/10.2138/rmg.2005.58.6

Reiners, P.W. & Brandon, M.T. 2006. Using thermochronology to understand orogenic erosion. *Annual Review of Earth and Planetary Sciences*, **34**, 419–466, https://doi.org/10.1146/annurev.earth.34.031405.125202

Reiners, P.W., Zhou, Z., Ehlers, T.A., Xu, C., Brandon, M.T., Donelick, R.A. & Nicolescu, S. 2003. Post-orogenic evolution of the Dabie Shan, eastern China, from (U–Th)/He and fission track thermochronology. *American Journal of Science*, **303**, 489–518, https://doi.org/10.2475/ajs.303.6.489

Reiners, P.W., Spell, T.I., Nicolescu, S. & Zanetti, K. 2004. Zircon (U–Th)/He thermochronometry: He diffusion and comparisons with ^{40}Ar/^{39}Ar dating. *Geochimica et Cosmochimica Acta*, **68**, 1857–1887, https://doi.org/10.1016/j.gca.2003.10.021

Ring, U. & Collins, A.S. 2005. U–Pb SIMS dating of synkinematic granites: timing of core-complex formation in the northern Anatolide belt of western Turkey. *Journal of the Geological Society, London*, **162**, 289–298, https://doi.org/10.1144/0016-764904-016

Ring, U., Gessner, K., Güngör, T. & Passchier, C.S. 1999. The Menderes Massif of western Turkey and the Cycladic Massif in the Aegean – do they really correlate? *Journal of the Geological Society, London*, **156**, 3–6, https://doi.org/10.1144/gsjgs.156.1.0003

Ring, U., Willner, A. & Lackmann, W. 2001. Nappe stacking with different pressure–temperature paths: An example from the Menderes nappes of western Turkey. *American Journal of Science*, **301**, 912–944, https://doi.org/10.2475/ajs.301.10.912

Ring, U., Johnson, C., Hetzel, R. & Gessner, K. 2003. Tectonic denudation of a Late Cretaceous–Tertiary collisional belt: regionally symmetric cooling patterns and their relation to extensional faults in the Anatolide belt of western Turkey. *Geological Magazine*, **140**, 421–441, https://doi.org/10.1017/S0016756803007878

Ring, U., Gessner, K. & Thomson, S. 2017. Variations in fault-slip data and cooling history reveal corridor of heterogeneous backarc extension in the eastern Aegean Sea region. *Tectonophysics*, **700–701**, 108–130, https://doi.org/10.1016/j.tecto.2017.02.013

Rojay, B., Toprak, V., Demirci, C. & Süzen, L. 2005. Plio-Quaternary evolution of the Küçük Menderes Graben Southwestern Anatolia, Turkey. *Geodinamica Acta*, **18**, 317–331, https://doi.org/10.3166/ga.18.317-331

Rossetti, F., Asti, R., Faccenna, C., Gerdes, A., Lucci, F. & Theye, T. 2017. Magmatism and crustal extension: Constraining activation of the ductile shearing along the Gediz detachment, Menderes Massif (western Turkey). *Lithos*, **282**, 145–162, https://doi.org/10.1016/j.lithos.2017.03.003

Royden, L.H. & Papanikolaou, D.J. 2011. Slab segmentation and late Cenozoic disruption of the Hellenic arc. *Geochemistry, Geophysics, Geosystems*, **12**, https://doi.org/10.1029/2010GC003280

Rutte, D., Ratschbacher, L., Schneider, S., Stübner, K., Stearns, M.A., Gulzar, M.A. & Hacker, B.R. 2017. Building the Pamir-Tibetan Plateau—Crustal stacking, extensional collapse, and lateral extrusion in the Central Pamir: 1. Geometry and kinematics. *Tectonics*, **36**, 342–384, https://doi.org/10.1002/2016TC004293

Sambridge, M. 1999*a*. Geophysical inversion with a neighbourhood algorithm—I. Searching a parameter space. *Geophysical Journal International*, **138**, 479–494, https://doi.org/10.1046/j.1365-246X.1999.00876.x

Sambridge, M. 1999*b*. Geophysical inversion with a neighbourhood algorithm—II. Appraising the ensemble. *Geophysical Journal International*, **138**, 727–746, https://doi.org/10.1046/j.1365-246x.1999.00900.x

Sarıca, N. 2000. The Plio-Pleistocene age of Büyük Menderes and Gediz grabens and their tectonic significance on N–S extensional tectonics in West Anatolia: mammalian evidence from the continental deposits. *Geological Journal*, **35**, 1–24, https://doi.org/10.1002/(SICI)1099-1034(200001/03)35:1<1::AID-GJ834>3.0.CO;2-A

Schmidt, A., Pourteau, A., Candan, O. & Oberhänsli, R. 2015. Lu–Hf geochronology on cm-sized garnets using microsampling: New constraints on garnet growth rates and duration of metamorphism during continental collision (Menderes Massif, Turkey). *Earth and Planetary Science Letters*, **432**, 24–35, https://doi.org/10.1016/j.epsl.2015.09.015

Schuiling, R.D. 1962. On petrology, age and evolution of the Menderes Massif, W-Turkey; a rubidium/strontium and oxygen isotope study. *Bulletin of the Institute for Mineral Research and Exploration, Turkey*, **58**, 703–714.

Schultz, M.H., Hodges, K.V., Ehlers, T.A., van Soest, M. & Wartho, J.A. 2017. Thermochronologic constraints on the slip history of the South Tibetan detachment system in the Everest region, southern Tibet. *Earth and Planetary Science Letters*, **459**, 105–117, https://doi.org/10.1016/j.epsl.2016.11.022

Schwarz, G. 1978. Estimating the dimension of a model. *The Annals of Statistics*, **6**, 461–464, https://doi.org/10.1214/aos/1176344136

Sen, S. & Seyitoğlu, G., 2009. Magnetostratigraphy of early-middle Miocene deposits from east–west trending Alaşehir and Büyük Menderes grabens in western Turkey, and its tectonic implications. *In*: van Hinsbergen, D.J.J., Edwards, M.A. & Govers, R. (eds) *Collision and Collapse at the Africa-Arabia-Eurasia Subduction Zone*. Geological Society, London, Special Publications, **311**, 321–342, https://doi.org/10.1144/SP311.13

Şengör, A.M.C. & Yilmaz, Y. 1981. Tethyan evolution of Turkey: a plate tectonic approach. *Tectonophysics*, **75**, 181–241, https://doi.org/10.1016/0040-1951(81)90275-4

Şengör, A.M.C., Tüysüz, O. *et al.* 2005. The North Anatolian fault: A new look. *Annual Review of Earth and Planetary Science*, **33**, 37–112, https://doi.org/10.1146/annurev.earth.32.101802.120415

Seyitoğlu, G. & Scott, B.C. 1991. Late Cenozoic crustal extension and basin formation in west Turkey. *Geological Magazine*, **128**, 155–166, https://doi.org/10.1017/S0016756800018343

Seyitoğlu, G. & Scott, B.C. 1992. The age of the Büyük Menderes graben (west Turkey) and its tectonic implications. *Geological Magazine*, **129**, 239–242, https://doi.org/10.1017/S001675680000830X

Seyitoğlu, G., Tekeli, O., Çemen, I., Şen Ş & Işik, V. 2002. The role of the flexural rotation/rolling hinge model in the tectonic evolution of the Alaşehir graben, western Turkey. *Geological Magazine*, **139**, 15–26, https://doi.org/10.1017/S0016756801005969

Shuster, D.L. & Farley, K.A. 2009. The influence of artificial radiation damage and thermal annealing on helium diffusion kinetics in apatite. *Geochimica et Cosmochimica Acta*, **73**, 183–196, https://doi.org/10.1016/j.gca.2008.10.013

Singleton, J.S., Stockli, D.F., Gans, P.B. & Prior, M.G. 2014. Timing, rate, and magnitude of slip on the Buckskin Rawhide detachment fault, west central Arizona. *Tectonics*, **33**, 1596–1615, https://doi.org/10.1002/2013TC003517

Sözbilir H., Emre, T., 1990. Neogene stratigraphy and structure of the northern rim of the Büyük Menderes graben. *In*: Proceedings of International Earth Science Colloquium on the Aegean Region, **2**, 314–322.

Stockli, D.F. 2005. Application of low-temperature thermochronometry to extensional tectonic settings. *Reviews in Mineralogy and Geochemistry*, **58**, 411–448, https://doi.org/10.2138/rmg.2005.58.16

Tagami, T., Galbraith, R.F., Yamada R., Laslett, G.M., 1998. Revised annealing kinetics of fission tracks in zircon and geological implications. *In*: *Advances in Fission-Track Geochronology*. Springer, Dordrecht, 99–112.

Thiede, R.C. & Ehlers, T.A. 2013. Large spatial and temporal variations in Himalayan denudation. *Earth and Planetary Science Letters*, **371**, 278–293, https://doi.org/10.1016/j.epsl.2013.03.004

Thomson, S.N. & Ring, U. 2006. Thermochronologic evaluation of postcollision extension in the Anatolide orogen, western Turkey. *Tectonics*, **25**, TC3005, https://doi.org/10.1029/2005TC001833

Ünay, E., Göktaş, F., Hakyemez, H.Y., Avşar, M. & Şan, Ö. 1995. Dating the sediments exposed at the northern part of the Büyük Menderes Graben (Turkey) on the basis of Arvicolidae (Rodentia, Mammalia). *Geological Bulletin of Turkey*, **38**, 75–80.

Ustaszewski, K., Kounov, A., Schmid, S.M., Schaltegger, U., Krenn, E., Frank, W. & Fügenschuh, B. 2010. Evolution of the Adria-Europe plate boundary in the northern Dinarides: From continent-continent collision to back-arc extension. *Tectonics*, **29**, TC6017, https://doi.org/10.1029/2010TC002668

Valla, P.G., Herman, F., Van Der Beek, P.A. & Braun, J. 2010. Inversion of thermochronological age-elevation profiles to extract independent estimates of denudation and relief history—I: Theory and conceptual model. *Earth and Planetary Science Letters*, **295**, 511–522, https://doi.org/10.1016/j.epsl.2010.04.033

Van Der Beek, P.A., Valla, P.G., Herman, F., Braun, J., Persano, C., Dobson, K.J. & Labrin, E. 2010. Inversion of thermochronological age–elevation profiles to extract independent estimates of denudation and relief history—II: Application to the French Western Alps. *Earth and Planetary Science Letters*, **296**, 9–22, https://doi.org/10.1016/j.epsl.2010.04.032

van Hinsbergen, D.J. 2010. A key extensional metamorphic complex reviewed and restored: the Menderes Massif of western Turkey. *Earth-Science Reviews*, **102**, 60–76, https://doi.org/10.1016/j.earscirev.2010.05.005

Vanderhaeghe, O., 2004. Structural development of the Naxos migmatite dome *In*: Whitney, D.L., Teyssier, C. & Siddoway, C.S. (eds) *Gneiss Domes in Orogeny*. Geological Society of America Special Papers, **380**, 211–228.

Wagner, G.A. & van den Haute, P. 1992. *Fission-Track Dating*. Kluwer Academic, The Netherlands.

Wernicke, B. 1985. Uniform-sense normal simple shear of the continental lithosphere. *Canadian Journal of Earth Sciences*, **22**, 108–125, https://doi.org/10.1139/e85-009

Wernicke, B. 1992. Cenozoic extensional tectonics of the US Cordillera. *In*: Burchfiel, B.C., Lipman, P.W. & Zoback, M.L. (eds) *The Cordilleran Orogen*. Geological Society of America, Boulder, CO, 553–582, https://doi.org/10.1130/DNAG-GNA-G3.553

Whipp, D.M., Ehlers, T.A., Blythe, A.E., Huntington, K.W., Hodges, K.V. & Burbank, D.W. 2007. Plio-Quaternary exhumation history of the central Nepalese Himalaya: 2. Thermokinematic and thermochronometer age prediction model. *Tectonics*, **26**, https://doi.org/10.1029/2006TC001991

Wolf, R.A., Farley, K.A. & Silver, L.T. 1996. Helium diffusion and low temperature thermochronology of apatite. *Geochimica et Cosmochimica Acta*, **60**, 4231–4240, https://doi.org/10.1016/S0016-7037(96)00192-5

Wolf, R.A., Farley, K.A. & Kass, D.M. 1998. Modeling of the temperature sensitivity of the apatite (U–Th)/He thermochronometer. *Chemical Geology*, **148**, 105–114, https://doi.org/10.1016/S0009-2541(98)00024-2

Wölfler, A., Glotzbach, C. *et al.* 2017. Late Cenozoic cooling history of the central Menderes Massif: Timing of the Büyük Menderes detachment and the relative contribution of normal faulting and erosion to rock exhumation. *Tectonophysics*, **717**, 585–598, https://doi.org/10.1016/j.tecto.2017.07.004

Yal, G.P., Eker, A.M., Cambazoglu, S., Sen O., Akgun, H., 2017. Assessment of the early development work for Kuyucak Geothermal Field, Turkey. *In*: Proceedings, 42nd Workshop on Geothermal Reservoir Engineering, Stanford University, Stanford California, February 13–15.

Zaun, P.E. & Wagner, G.A. 1985. Fission-track stability in zircons under geological conditions. *Nuclear Tracks*, **10**, 303–307.

Zeitler, P.K., Herczeg, A.L., McDougall, I. & Honda, M. 1987. U–Th–He dating of apatite: A potential thermochronometer. *Geochimica et Cosmochimica Acta*, **51**, 2865–2868, https://doi.org/10.1016/0016-7037(87)90164-5

4. Detachment faulting in a bivergent core complex constrained by fault gouge dating and low-temperature thermochronology

Caroline Heineke [a], Ralf Hetzel [a*], Nils-Peter Nilius [b], Horst Zwingmann [c], Andrew Todd [d], Andreas Mulch [e,f], Andreas Wölfler [b], Christoph Glotzbach [g], Cüneyt Akal [h], István Dunkl [i], Mark Raven [j], Andrea Hampel [b]

[a] Institut für Geologie und Paläontologie, Westfälische Wilhelms-Universität Münster, Corrensstraße 24, D-48149 Münster, Germany

[b] Institut für Geologie, Leibniz Universität Hannover, Callinstraße 30, D-30167 Hannover, Germany

[c] Department of Geology and Mineralogy, Kyoto University, Kitashirakawa Oiwake-cho, 606-8502 Kyoto, Japan

[d] CSIRO Energy, 26 Dick Perry Ave, Kensington, WA 6151, Australia

[e] Senckenberg Biodiversity and Climate Research Centre (BiK-F), Senckenberganlage 25, D-60325 Frankfurt, Germany

[f] Institut für Geowissenschaften, Goethe-Universität Frankfurt, Altenhöferallee 1, 60438 Frankfurt, Germany

[g] Department of Geosciences, University of Tübingen, Wilhelmstraße 56, D-72074 Tübingen, Germany

[h] Dokuz Eylül University, Engineering Faculty, Department of Geological Engineering, Tınaztepe Campus, Buca, TR-35160 Izmir, Turkey

[i] Geowissenschaftliches Zentrum der Universität Göttingen, Abteilung Sedimentologie/ Umweltgeologie, Goldschmidtstraße 3, D-37077 Göttingen, Germany

[j] CSIRO Land and Water, Waite Road, Urrbrae, SA 5064, Australia

* Corresponding author, rahetzel@uni-muenster.de, Phone: +49 (0) 251 83-33908, Fax: +49 (0) 251 83-33933

Own contribution: Sampling and structural mapping, thermochronological samples and data, figure 5, manuscript comments

Highlights:

• K-Ar ages of fault gouge record detachment faulting in a bivergent core complex

• Two detachment faults were active diachronously between ~22 Ma and ~3 Ma

• The Büyük Menderes detachment experienced two phases of faulting since ~22 Ma

• The Gediz detachment was active continuously from mid-Miocene to late Pliocene

Abstract

The central Menderes Massif in western Turkey is a bivergent metamorphic core complex characterised by two detachment faults that operated with opposite sense of shear. Here, we present K-Ar ages and hydrogen isotope data for fault gouge as well as fission track and (U-Th)/He ages for apatite and zircon from bedrock samples to constrain the timing of detachment faulting. Comparison of the K-Ar ages and low-temperature thermochronologic ages indicates brittle faulting at temperatures between ~240 and ~70 °C. At the western termination of the Gediz detachment, K-Ar ages between ~12 and ~5 Ma suggest rather continuous faulting since the mid-Miocene; a Pliocene phase of rapid slip is mainly recorded in the eastern part of this detachment. In contrast, K-Ar ages from the Büyük Menderes detachment cluster at 22–16 and 9–3 Ma and provide evidence for two phases of faulting, which is in accordance with new and published low-temperature thermochronologic data. Hydrogen isotope ratios of −76 to −115‰ indicate infiltration of meteoric water during detachment faulting and gouge formation. The youngest K-Ar ages and cooling histories for hanging and footwall rocks imply that the activity of both detachments ended ~3 Ma ago when the currently active grabens were established.
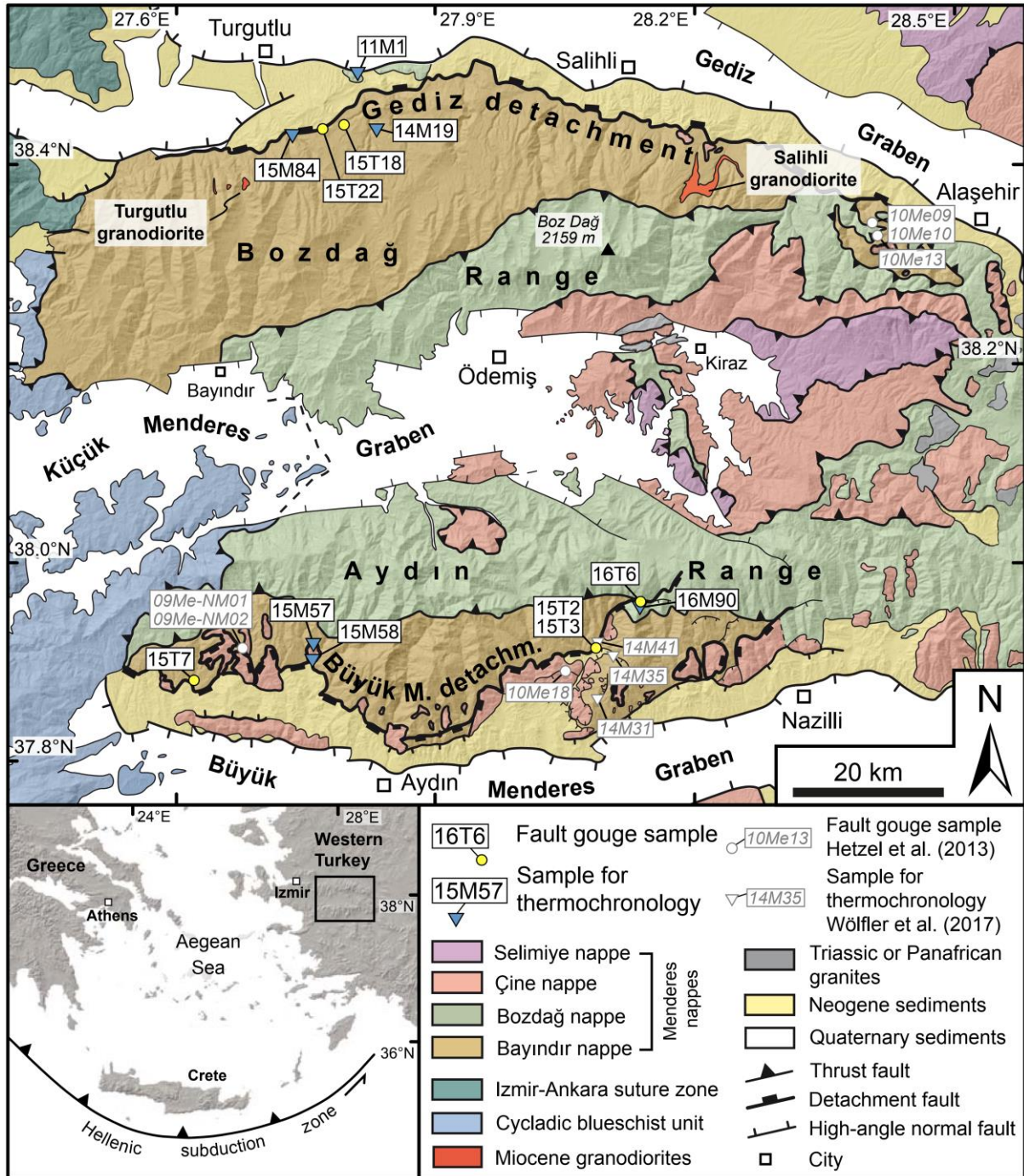
Figure 1: Geological map of the central Menderes Massif (modified from Wölfler et al., 2017 and complemented with own field observations). Note that samples 15M57, 15M58, and 16M90 are included in Nilius et al. (2019). Map in lower left part of the figure shows the location of the study area within the Aegean region.

4.1 INTRODUCTION

Brittle faulting accommodates much of the deformation in the Earth's upper crust and is a key process that governs landscape evolution in tectonically active regions. In order to understand how landscapes evolve in response to crustal shortening or extension, it is crucial to constrain the timing of brittle faulting episodes. Commonly, this is done in an indirect way by applying low-temperature

thermochronology to the hanging wall and footwall of thrust or normal faults and by thermokinematic modelling of the respective cooling paths to account for heat advection and to quantify slip-rate histories (e.g. Thiede et al., 2005; Campani et al., 2010; Braun et al., 2012; McCallister et al., 2014; Wolff et al., 2019). In contrast, direct isotopic dating of brittle fault rocks such as breccia, cataclasite, fault gouge, or pseudotachylite (e.g. Eide et al., 1997; Sherlock and Hetzel, 2001; van der Pluijm et al., 2001; Zwingmann and Mancktelow, 2004; Wölfler et al., 2010; Ault et al., 2015) is more challenging due to the fine-grained nature of most fault rocks. Against this background, the direct dating of brittle faults combined with low-temperature thermochronology is a particularly valuable approach to decipher the timing of brittle deformation phases (e.g. Duvall et al., 2011; Mancktelow et al., 2016; Ring et al., 2017).

Probably the most common rock type that forms during brittle faulting and cataclasis is clay-rich fault gouge, which typically contains the K-bearing mineral illite. The pioneering studies of Lyons and Snellenburg (1971) and Kralik et al. (1987) have shown the great potential of K-Ar and Rb-Sr dating of clay fractions from fault gouge in order to determine the age of faulting. Since then, an increasing number of studies has employed K-Ar and ^{40}Ar-^{39}Ar dating of synkinematic illite from fault gouge to provide absolute age constraints on brittle faulting (e.g. Vrolijk and van der Pluijm, 1999; Choo and Chang, 2000; Haines and van der Pluijm, 2008; Zwingmann et al., 2010, 2011; Rahl et al., 2011; Haines et al., 2016).

The combination of absolute fault gouge dating with low-temperature thermochronology has often been applied to characterise the activity of low-angle normal faults in extensional tectonic settings (e.g. Haines and van der Pluijm, 2012; Mancktelow et al., 2016). Such low-angle normal or detachment faults are a general feature of metamorphic core complexes that form during the syn-, late-, or postorogenic extension of mountain belts (e.g. Dewey, 1988; Lister and Davis, 1989; Burchfiel et al., 1992; Malavieille, 1993). Detachment faults, which represent the upward continuation of ductile shear zones, accommodate large amounts of extension and are responsible for the rapid exhumation of metamorphic rocks from mid-crustal depth (e.g. Crittenden et al., 1980; Forsyth, 1992). Regarding the geometry and kinematics of core complexes and detachment faults, two end-member types can be distinguished (Malavieille, 1993). The more common type is asymmetric and bounded by a single detachment (e.g. Wernicke and Axen, 1988; Lister and Davis, 1989). The other type is characterised by bivergent extension, which is accommodated by detachment faults with opposing dip directions on both flanks of the core complex (Malavieille, 1993; Faure et al., 1996; Vanderhaeghe et al., 1999; Gessner et al., 2001). Typical processes that occur during the evolution of metamorphic core complexes are the overprinting of older mylonitic fabrics by younger cataclastic fault zones and discrete brittle faults (e.g. Crittenden et al., 1980; Lister and Davis, 1989) and the infiltration of meteoric fluids into the detachment faults, as shown by stable isotope studies (e.g. Fricke et al., 1992;

Caine et al., 1996; Mulch and Chamberlain, 2007; Gébelin et al., 2015).

Here, we present 19 new K-Ar ages to constrain the age of detachment faulting in a key area of continental extension: the Menderes Massif in Western Turkey. The central part of this massif constitutes a bivergent metamorphic core complex that was exhumed by slip on two detachment faults with opposite dip and sense of shear. Our K-Ar ages, complemented by new and previously published low-temperature thermochronologic data, allow us to evaluate if the two detachment faults were active simultaneously or not. In addition, we quantify the hydrogen isotope composition of the dated fault gouge samples to test if meteoric fluids have infiltrated the detachment faults during periods of fault activity.

4.2   GEOLOGICAL SETTING

Since ~25 Ma, the Aegean region in the back-arc of the Hellenic subduction zone has experienced pronounced extensional deformation, which resulted in the exhumation of mid-crustal rocks exposed in numerous metamorphic massifs and core complexes (e.g. McKenzie, 1978; Jolivet and Faccenna, 2000; Brun and Sokoutis, 2010; Jolivet et al., 2013). The Menderes Massif in western Turkey is one of the largest of these metamorphic massifs. It is cut by two active E-W trending grabens – the Gediz and Büyük Menderes grabens – which subdivide the massif into three submassifs (e.g. Seyitoğlu and Scott, 1991; Yılmaz et al., 2000; Gürer et al., 2009) and bound the central Menderes Massif in the north and south (Figure 1).

The metamorphic rocks of the central Menderes Massif comprise four nappes that were stacked during late Cretaceous to Eocene plate convergence along the Izmir-Ankara suture zone (e.g. Şengör et al., 1984; Ring et al., 1999; van Hinsbergen et al., 2010; Gessner et al., 2013). From lowest to highest structural level, these nappes include the Bayındır, Bozdağ, Çine, and Selimiye nappes, which are structurally overlain by the Cycladic blueschist unit in the west (Ring et al., 1999; Gessner et al., 2013) (Figure 1). The Bozdağ, Bayındır, and Selimiye nappes consist mainly of greenschist to amphibolite facies mica schists, quartzites and phyllites; the two latter also contain some marbles (Dora et al., 1990; Hetzel et al., 1998; Özer and Sözbilir, 2003; Candan et al., 2011). The Çine nappe consists largely of orthogneisses and pelitic gneisses (e.g. Hetzel and Reischmann, 1996; Hetzel et al., 1998; Candan et al., 2001). At the northern and southern margins of the central Menderes Massif two belts of Neogene sedimentary rocks are well exposed due to ongoing footwall uplift along the active boundary faults of the Gediz and Büyük Menderes grabens (Figure 1).
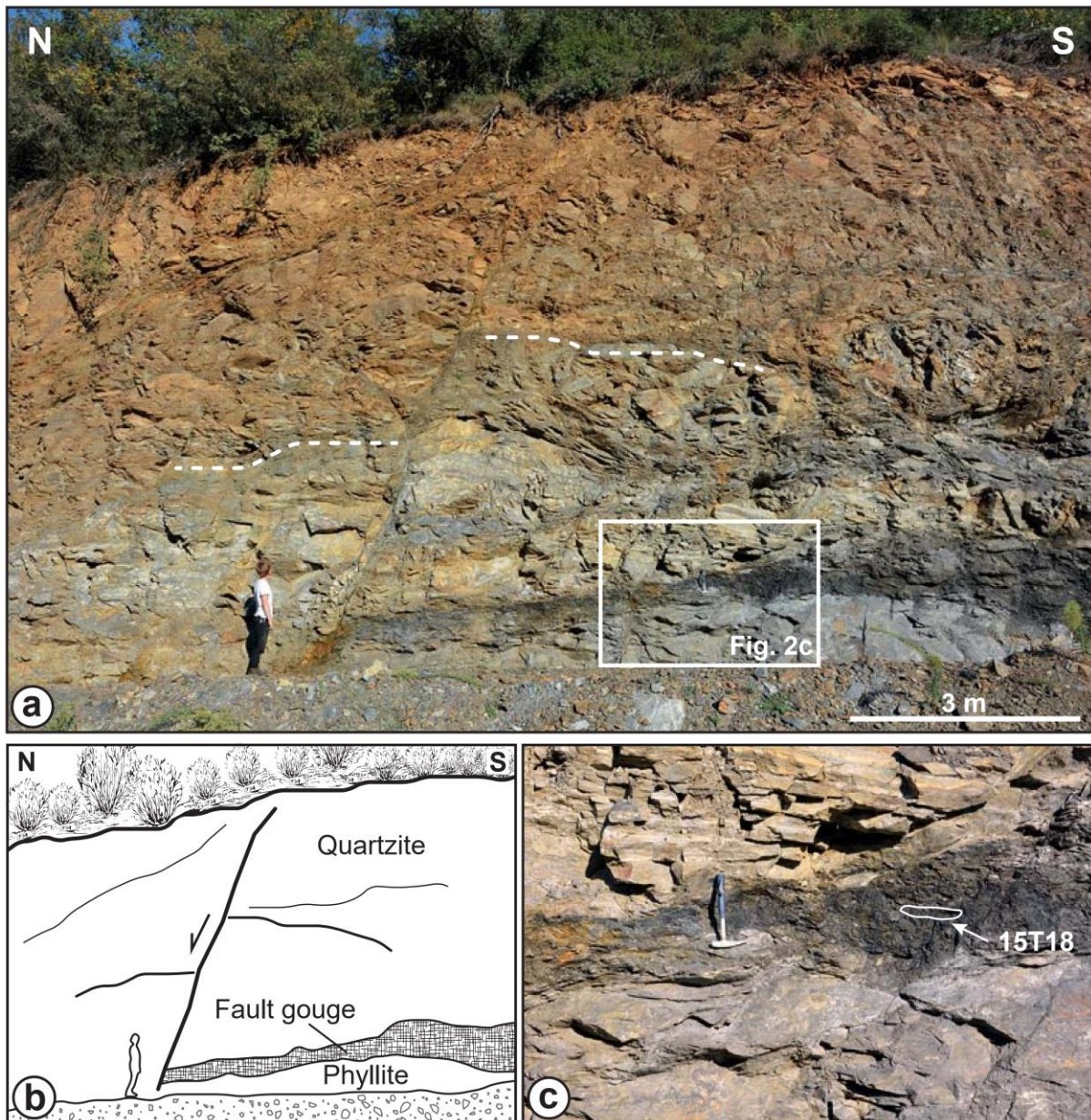
Figure 2: Photographs of sampling site 15T18. **a)** Roadcut with the low-angle normal fault in the foreground from which sample 15T18 was obtained for K-Ar dating. Hanging wall of the fault consists of mylonitic quartzite, while the footwall comprises greyish phyllite. A steep normal fault cross-cuts and displaces the low-angle normal fault. Offset of bedrock is indicated by the white dashed line. **b)** Sketch of the outcrop shown in a). **c)** Sampled fault gouge horizon with hammer for scale. White outline corresponds to area from which sample 15T18 was obtained for K-Ar dating.

The Küçük Menderes Graben separates the central Menderes Massif into the Bozdağ and Aydın mountain ranges, which are bounded by shallow-dipping detachment faults (Figure 1). The central Menderes Massif was exhumed during bivergent N-S-directed extension on these two faults and thus constitutes a symmetric core complex (Gessner et al., 2001). The rocks in the footwall of the Gediz detachment, at the northern slope of the Bozdağ Range, exhibit a top-to-the-N to NNE sense of shear (Hetzel et al., 1995), whereas the shear sense of the Büyük Menderes detachment was opposite, i.e. top-to-the-S to SSW (Emre, 1996; Gessner et al., 2001; Işık et al., 2003).

As both detachments cut obliquely through the nappe pile, the structurally higher Çine nappe was emplaced against the lower Bayındır nappe. Therefore, orthogneisses of the Çine nappe occur as klippen above the two detachments (Figure 1) (Hetzel et al., 1995; Buscher et al., 2013; Wölfler et al., 2017). Likewise, the Neogene sedimentary rocks along the northern and southern margins of the massif were tectonically emplaced on the detachment faults during progressive extension and normal faulting. Finally, both detachment faults were cut by the high-angle boundary faults of the Gediz and Büyük Menderes grabens.

The timing of detachment faulting in the central Menderes Massif has hitherto been inferred from different types of geochronological data, but is still not well resolved. At the Gediz detachment, ductile deformation and normal faulting was initially interpreted to have been underway in the mid-Miocene,
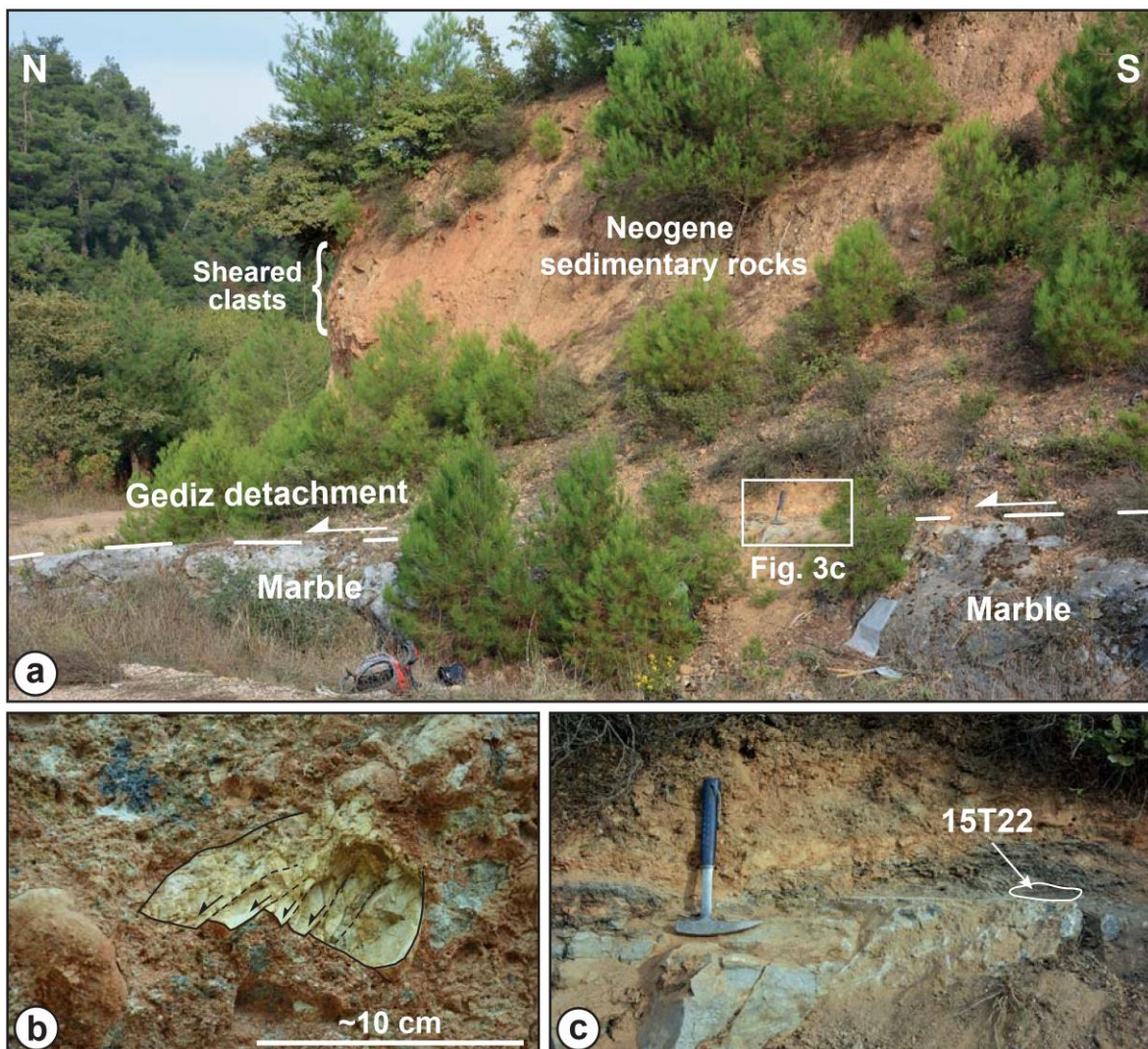
Figure 3: Photographs of sampling site 15T22. **a)** Roadcut with Gediz detachment in the foreground. The hanging wall comprises deformed Neogene sedimentary rocks with numerous sheared clasts. The footwall of the detachment fault is marble. **b)** Sheared clast in Neogene sediments. Note that the sediment contains many brecciated rock fragments of different sizes. **c)** Sampled fault gouge horizon above the detachment fault surface. White outline corresponds to area from which sample 15T22 was obtained for K-Ar dating.

based on U-Pb zircon ages of ~16–15 Ma and 40Ar-39Ar biotite ages of ~13–12 Ma for two

synextensional intrusions, the Turgutlu and Salihli granodiorites (Hetzel et al., 1995; Glodny and Hetzel, 2007) (Figure 1). More recently, in situ U–(Th)–Pb dating of titanite from the Salihli granodiorite was used to suggest that the pre-extensional emplacement and crystallization of the magma occurred at 17–16 Ma, whereas ductile extensional deformation began 1–2 Ma later at 15–14 Ma (Rossetti et al., 2017). 40Ar-39Ar laser dating of synkinematic white mica from one mylonite sample beneath the Gediz detachment yielded two single-fusion ages of 6.6±2.5 and 6.7±1.1 Ma (weighted mean: 6.7±1.0 Ma), indicating ongoing deformation at temperatures near the brittle-ductile transition zone in the latest Miocene (Lips et al., 2001). The first few apatite and zircon fission track ages from the central Menderes Massif were interpreted to indicate that both the Gediz and Büyük Menderes detachments were active simultaneously, with a period of particularly rapid cooling in the Pliocene (Gessner et al., 2001; Ring et al., 2003). The latter phase of extension was also inferred from an ion microprobe Th–Pb age of 4.5±1.0 Ma for retrograde monazite from the Salihli granodiorite (Catlos and Çemen, 2005).

This period of fast cooling and exhumation in the eastern part of the Gediz detachment took place between ~4 and ~2 Ma as shown by a detailed thermochronologic study of the Salihli granodiorite (Buscher et al., 2013). At the Büyük Menderes detachment, a similar study revealed two distinct phases of cooling in the middle Miocene and latest Miocene/Pliocene (Wölfler et al., 2017), which have been confirmed by additional data taken along strike of the detachment fault (Nilius et al., 2019). A first attempt to use K-Ar dating of fault gouge and cataclasite to provide direct age constraints on brittle faulting yielded ages of 10–9 Ma and 4–3 Ma near the eastern end of the Gediz detachment and ages of ~22 Ma and ~5–3 Ma at the Büyük Menderes detachment (Hetzel et al., 2013; for location of samples see Figure 1).
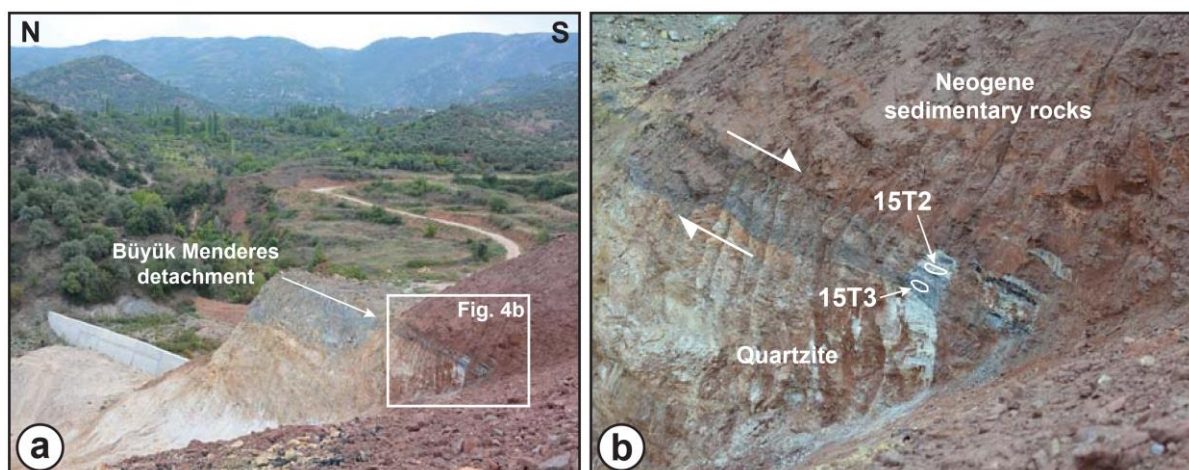
Figure 4: Photographs of sampling site at the eastern Büyük Menderes detachment. **a)** The fault footwall consists of sheared quartzite, while the hanging wall comprises reddish Neogene sedimentary rocks. **b)** Close-up view with locations of K-Ar samples 15T2 and 15T3 indicated by white lines.

4.3   Sampling sites and sample description

To better constrain the timing of detachment faulting in the central Menderes Massif, we collected six fault gouge samples for K-Ar dating at five new sites of the Gediz and Büyük Menderes detachment faults (Figure 1). At all sites, we used hammer and chisel to obtain 1–2 kg of material from weakly to moderately consolidated fault gouge. In order to define the cooling history of the country rock, we also collected three bedrock samples for low-temperature thermochronology at the Gediz detachment and three similar samples at the Büyük Menderes detachment. Note that although the three latter samples are included in a study on the exhumation of the Aydın Range (Nilius et al., 2019), they are also briefly described and presented in this study.

In the western part of the Gediz detachment, we sampled fault gouge at two recently created roadcuts (Figure 1). At the first roadcut, sample 15T18 was collected from a low-angle normal fault, which dips gently to the north in the footwall of the Gediz detachment. The bedrock below and above the fault consists of phyllites and mylonitic quartzites of the Bayındır nappe (Figure 2a). The fault zone exhibits a ~50-cm-thick layer of black to dark grey fault gouge and is cut by a steep north-dipping normal fault (85/70 N) (Figures 2a,b). The sample for K-Ar dating was taken from the center of the fault gouge layer at a distance of several metres from the high-angle normal fault (Figure 2c). About 3 km farther west, the Gediz detachment fault is well exposed in another roadcut. Here, the detachment is characterised by a 10–15-cm-thick dark-grey fault gouge layer, which separates light grey marbles in the footwall from reddish sedimentary rocks in the hanging wall (Figure 3a). The planar top of the detachment dips gently to the north (108/10 N) and exhibits a well-developed, NNW-plunging striation (337/08). The Neogene conglomerates in the hanging wall show numerous sheared and broken clasts (Figure 3b). For K-Ar dating, sample 15T22 was collected from the lowermost 4 cm of the fault-gouge directly above the striated marbles (Figure 3c). For low-temperature thermochronology, we took two bedrock samples from the footwall of the Gediz detachment (14M19 and 15M84) to the east and west of the two roadcuts, respectively (Figure 1). A third bedrock sample (11M1) was taken a few kilometres farther north from a bedrock klippe in the hanging wall of the detachment.
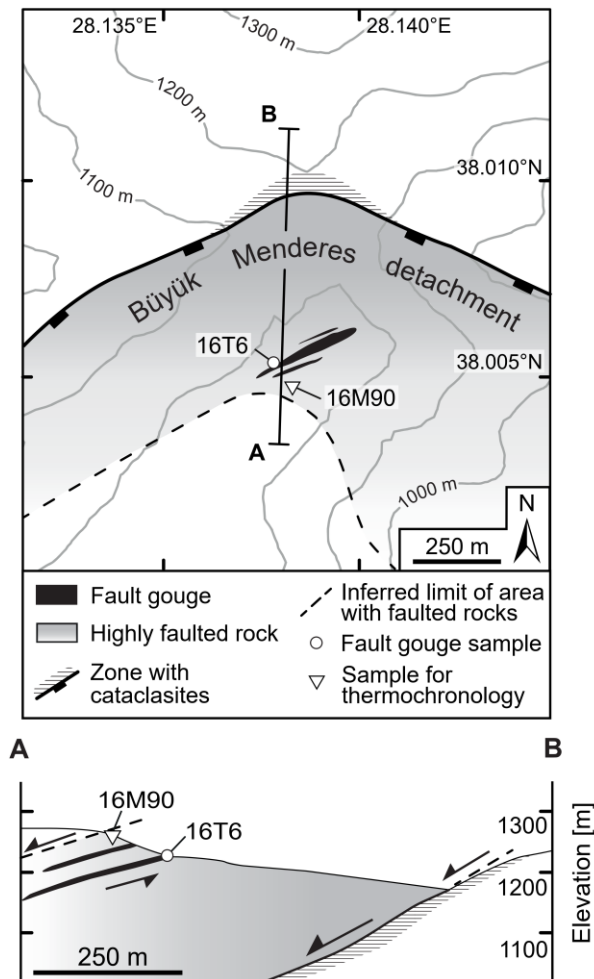
Figure 5: Map and cross section of area at eastern end of the Büyük Menderes detachment fault where we took sample 16T6 for K-Ar dating and sample 16M90 for thermochronology. Rock deformation decreases in a southerly direction as indicated by the grey shading.

At the Büyük Menderes detachment the construction of a water reservoir offered the possibility to obtain fresh gouge material from the eastern portion of the fault (samples 15T2 and 15T3) (Figure 1). The detachment separates deformed Neogene sedimentary rocks in the hanging wall from yellow quartzites in the footwall (Figure 4a). The fault zone is 50–70 cm thick and became exposed over a distance of ~12 m during excavations related to dam construction. It dips gently to the SE (60/20 SE) and the planar schistosity of the fault gouge has striations with an orientation of 160/18. The fault zone consists of two gouge layers separated by a ~10-cm-thick zone of cataclastically deformed quartzite derived from the fault footwall. The upper gouge layer is rich in clay, light grey in colour and ~15 cm thick, whereas the dark grey gouge layer underneath contains less clay and has a thickness of ~30 cm. Samples for K-Ar dating were collected from the lower part of the light grey fault gouge (15T2) and from the lowermost 20 cm of the dark grey gouge layer (15T3) (Figure 4b). As the water reservoir has been filled in the past years, the outcrop is no longer accessible.

About 7 km farther northeast, we obtained another fault gouge sample (16T6) from the Büyük Menderes detachment. This sampling site is located ~800 m higher than the outcrop at the water reservoir and the detachment forms a several hundred metres wide fault zone. The sample was collected from a >5-m-thick zone with dark grey to black fault gouge near the crest of a NNE-trending

mountain ridge (Figure 5). The rocks above and below the fault gouge comprise weathered and sheared mica schists of the Bozdağ nappe. The sampled fault gouge layer is orientated subparallel to the foliation of the mica schists (i.e. 45/20 SE) (Figure 5). We also obtained one sample (16M90) for low-temperature thermochronology from the mica schists (Nilius et al., 2019). About 400 m north of the sampling sites occur south-dipping cataclasites (Figure 5), which exhibit a top-S sense of shear but are not suitable for K-Ar dating because they contain little clayey material. At the western part of the Büyük Menderes detachment we took another fault gouge sample (15T7) in a small river valley that exposes >5-m-thick cataclastically deformed mylonites with a top-S shear sense (Figure 1). The sample was collected from a ~0.5-m-thick fault zone, which dips south at an angle of 20–25° (i.e. slightly steeper than the foliation of the cataclasites). Striations on the main fault plane plunge towards the SSW. About 15 km east of this sampling site, we collected two samples for low-temperature thermochronology (15M57 and 15M58; Nilius et al., 2019) from the footwall of the detachment (Figure 1).

4.4   K-Ar dating and hydrogen isotope analysis of fault gouges

K-Ar methodology and results

The methodology used for K-Ar dating of the fault gouges is similar to the one described by Zwingmann et al. (2010) and Hetzel et al. (2013). About 50–100 g of fresh fault gouge was gently disaggregated by repetitive freezing and thawing to avoid artificial grain-size reduction of rock components and contamination with K-bearing minerals such as K-feldspar and mica (Liewig et al., 1987). The grain-size fractions <2 and 2–6 µm were separated in distilled water by gravity settling, whereas the fractions <0.4 and <0.1 µm were separated with a high-speed centrifuge. The 2–6 µm size fraction was investigated to evaluate the influence of potential detrital contamination. The mineralogical composition of the fault gouge samples was determined by X-ray diffraction (XRD) and is provided in the supplement (Table S1).

The K-Ar dating technique follows Dalrymple and Lanphere (1969) and Faure (1986). K-Ar isotopic determinations were performed following a procedure similar to that described by Bonhomme et al. (1975) and additional details can be found in Hetzel et al. (2013). For K analysis two sample aliquots of approximately 100 mg were required. Normally, 20 mg of sample material was required for Ar analysis. During the course of this study, two different age standards and three air shots were measured. The K-Ar dating results of samples and standards are summarised in Tables 1a and 1b. The error for Ar analyses is below 1% and the average $^{40}Ar/^{36}Ar$ value for the three air shots is 295.53±0.27 (2σ) (Table 1c). Blanks for the extraction line and mass spectrometer were systematically determined and the mass discrimination factor was determined periodically by air shots. K-Ar ages were calculated using ^{40}K abundance and decay constants recommended by Steiger and Jäger (1977). The uncertainties of

the K-Ar ages are given as 2σ and take into account the errors associated with sample weighing, $^{38}Ar/^{36}Ar$ and $^{40}Ar/^{38}Ar$ measurements, and K analysis.
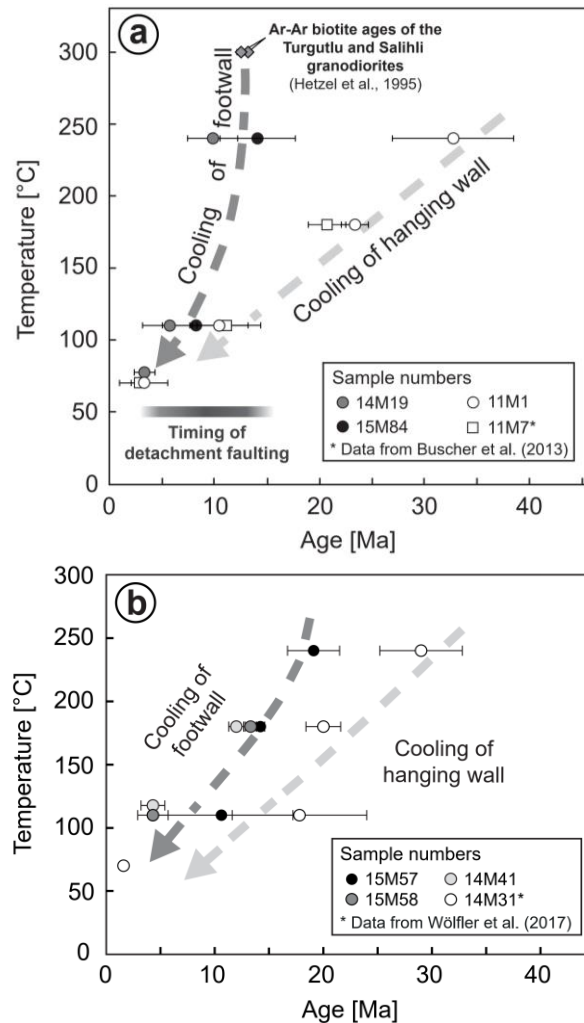
Figure 6: Cooling paths for the footwall and hanging wall of the **a)** Gediz and **b)** Büyük Menderes detachments based on thermochronologic data (Tables 3, 4). We also plotted ^{40}Ar-^{39}Ar biotite ages for the Turgutlu and Salihli granodiorites (Hetzel et al., 1995) and the ZHe, AFT, and AHe ages for sample 11M7 (an orthogneiss klippe on the Gediz detachment; Buscher et al., 2013). In plot **b)** we also show the ZFT, ZHe, AFT, and AHe ages of sample 14M31 (an orthogneiss klippe above the Büyük Menderes detachment; Wölfler et al., 2017).

The 19 K-Ar ages of the six fault gouge samples from the Büyük Menderes and Gediz normal fault systems range from ~22 to ~3 Ma (Table 1a). The K content ranges from a low 1.51% for sample 16T6 <0.4 µm to 5.18% for sample 15T3 (combined <0.1 and <0.4 µm size fractions) suggesting different mineralogy within the analysed clay fractions as confirmed by XRD results (Table S1). Radiogenic ^{40}Ar contents between 28% and 77% indicate good analytical conditions for all analyses except for the size fraction <0.1 µm of sample 15T22, which has a low radiogenic ^{40}Ar content of ~12% resulting in a relatively large error of the K-Ar age. At the Gediz detachment, K-Ar ages of 7–6 Ma were obtained from the three grain size fractions of sample 15T18, whereas sample 15T22 yielded three ages of ~12 Ma and one age of ~5 Ma for the smallest size fraction (Table 1a). The different grain size fractions of the samples 15T2 and 15T3 from the Büyük Menderes detachment have K-Ar ages of ~8.5 to

~2.8 Ma. In contrast, the size fractions of the gouge samples 15T7 and 16T6 from the Büyük Menderes detachment yielded older ages between ~22 and ~16 Ma (Table 1a).

Hydrogen isotope analysis of fault gouges and results

The hydrogen isotope (δD) values of six fault gouge samples were determined by continuous flow mass spectrometry using a high-temperature elemental analyser (Thermo Finnigan TC/EA) coupled to a mass spectrometer (Thermo Finnigan Delta V Advantage and 253). A sample weight of ca. 0.8 mg was wrapped into Ag foil and dried overnight at 200 °C under vacuum in a stainless-steel tray. Samples were rapidly transferred to a zero-blank autosampler in the stainless-steel tray and the autosampler was immediately purged with helium gas to prevent rehydration of interlayer spacing or water adsorption on clay surfaces from ambient air moisture. Three internationally referenced standard materials and additional in-house working standards were run with the samples. After correction for mass bias, daily drift of the thermal combustion reactor, and offset from the certified reference values, NBS30 (biotite), NBS22 (oil), and CH7 (polyethylene foil) had δD values of −65.3‰, −118.3‰, and −102.8‰, respectively. Repeated measurements of the different standards and unknowns resulted in a precision of ±3‰ for δD. All isotope ratios are reported relative to Vienna-Standard Mean Ocean Water (V-SMOW). The δD values of the fault gouge samples from the two fault systems fall in the range from −76 to −115‰ (Table 2).

4.5   Low-temperature thermochronology

Zircon and apatite fission-track analysis

For fission-track analysis, apatite and zircon grains were separated using conventional magnetic and heavy liquid separation techniques. Grains were embedded in PDA TeflonTM and epoxy, respectively, ground and polished. Apatites were etched with 5 M HNO_3 for 20 seconds at 21 °C (Donelick et al., 1999). Zircon mounts were etched in a KOH-NaOH eutectic melt at 215 °C (Zaun and Wagner, 1985). All samples were irradiated with thermal neutrons at the FRM-II reactor facility in Garching (Technical University Munich, Germany). Fission-track counting was carried out with an Olympus BX-51 microscope under 1000× magnification at the University Hannover. We applied the external detector method (Gleadow, 1981) with uranium-free muscovite sheets and the zeta calibration approach (e.g. Naeser, 1978; Hurford and Green, 1983) with dosimeter glass IRMM-540R and IRMM-541 and Durango apatite and Fish Canyon zircon age standards. To assess the annealing kinetics of apatite we measured D_{par} values (mean diameter of etch pits on prismatic surfaces of apatite parallel to the crystallographic c-axis) (Burtner et al., 1994). Mean track lengths from horizontal confined tracks were corrected for c-axis orientation (Donelick et al., 1999). Zircon and apatite fission-track (= ZFT and AFT) ages record

cooling below the closure temperature of ~240 °C (zircon) and ~110 °C (apatite) (e.g. Gleadow and Duddy, 1981; Wagner and van den Haute, 1992). The fission track ages were calculated with the TRACKKEY software version 4.2 (Dunkl, 2002) and are reported with an uncertainty of 2σ (Table 3).

Zircon and apatite (U-Th)/He analysis

We employed (U-Th)/He dating on samples that yielded zircons and apatites of sufficient quality (Table 4). Zircon and apatite crystals were hand-picked using a stereo and polarizing microscope under 200× magnification following the selection criteria of Farley (2002) and Reiners (2005). Dimensions of the selected crystals were measured to determine alpha-ejection correction factors (Farley et al., 1996). Single crystals were loaded into pre-cleaned Pt tubes for He analysis, which was carried out at the GÖochron Laboratory (University of Göttingen, Germany). Extraction of helium from the crystals was performed by heating the encapsulated grains in vacuum with an IR laser. The extracted gas was purified by an SAES Ti-Zr getter and the He content was measured with a Hiden Hal-3F/PIC triple-filter quadrupole mass spectrometer. For measurements of the alpha-emitting elements U, Th, and Sm, the zircon and apatite crystals were dissolved and spiked with calibrated ^{233}U, ^{230}Th, and ^{149}Sm solutions. Zircons were dissolved in Teflon bombs with 48% HF and 65% HNO_3 at 220 °C for five days, while apatites were dissolved in 2% ultrapure HNO_3 (+0.05% HF) in an ultrasonic bath. The actinide and Sm concentrations were measured by inductively coupled plasma mass spectrometry using the isotope dilution method. Measurements were carried out with a Perkin Elmer Elan DRC II system equipped with an APEX micro-flow nebulizer. Errors for the single-grain zircon and apatite (U-Th)/He ages include the uncertainties of the He, U, Th, and Sm measurements and the estimated uncertainty of the ejection correction factor. Zircon and apatite (U-Th)/He (= ZHe and AHe) ages are interpreted to record the cooling below the closure temperatures of ~180 °C (zircon) and ~70 °C (apatite), respectively (e.g. Farley, 2000; Reiners et al., 2004). Reported ZHe and AHe ages are the unweighted mean of the single-grain ages of each sample given with 2 standard errors (Table 4).

Results from low-temperature thermochronology

The two samples from the footwall of the western Gediz detachment (15M84 and 14M19; Figure 1) yielded zircon fission track (ZFT) ages of 14.1±3.6 Ma and 9.8±2.4 Ma and apatite fission track (AFT) ages of 8.2±3.2 and 5.7±2.6 Ma, respectively (Table 3). Sample 14M19 gave an AHe age of 3.3±1.0 Ma (Table 4). Taken together these ages indicate relatively rapid cooling (~240 to ~70 °C) of the footwall rocks between ~14 and ~3 Ma (Figure 6a). In contrast, the thermochronologic ages for sample 11M1 suggest that the hanging wall cooled slowly since the Oligocene (ZFT age: 32.8±5.8 Ma; ZHe age: 23.4±1.3 Ma; AFT age: 10.4±2.8 Ma; AHe age: 3.2±2.3 Ma).

The two footwall samples from the western Büyük Menderes detachment (15M57 and 15M58;

Figure 1), yielded ZHe ages of 14.2±0.4 and 13.3±0.5 Ma, respectively (Table 4), whereas sample

16M90 from the eastern end of the detachment gave a slightly older age of 18.9±2.2 Ma (Table 3). The

AFT ages of these three samples range from 12.9±2.6 to 4.3±1.4 Ma; a ZFT age was only obtained for

sample 15M57 (i.e. 19.1±4.8 Ma) (Table 3). Taken together, the ages record the cooling of the footwall

of the Büyük Menderes detachment since ~20 Ma (Figure 6b). The hanging wall of the detachment

cooled more slowly as constrained by sample 14M31 from Wölfler et al. (2017) (Figure 6b).

Table 1a. K-Ar ages of fault gouges in the central Menderes Massif (Western Turkey).

Sample number [a]	Sample description	Latitude	Longitude	Grain size	K	Radiogenic ^{40}Ar	Radiogenic ^{40}Ar	Age	Error (2σ)
		[°N]	[°E]	[µm]	[%]	[10^{-11} mol/g]	[%]	**[Ma]**	[Ma]
Gediz detachment – Bozdağ Range									
15T18	dark grey fault gouge	38.4374	27.7969	<0.1	3.73	4.035	29.5	**6.2**	0.2
15T18		"	"	<2	4.53	5.551	28.3	**7.1**	0.3
15T18	"	"	"	2–6	4.53	5.818	42.3	**7.4**	0.2
15T22	dark grey fault gouge	38.4302	27.7691	<0.1	2.78	2.259	11.8	**4.7**	0.9
15T22		"	"	<0.4	3.04	6.061	27.9	**11.5**	0.3
15T22	"	"	"	<2	2.92	6.111	33.1	**12.0**	0.4
15T22	"	"	"	2–6	2.30	4.624	33.2	**11.6**	0.8
Büyük Menderes detachment – Aydın Range									
15T2	light grey fault gouge	37.9612	28.0854	<0.1	4.62	4.432	51.4	**5.5**	0.3
15T2		"	"	<2	4.37	6.419	68.5	**8.5**	0.2
15T2	"	"	"	2–6	3.79	4.777	58.6	**7.3**	0.2
15T3	dark grey fault gouge	37.9612	28.0854	<0.1 and <0.4	5.18	2.543	39.8	**2.8**	0.2
15T3		"	"	<2	4.28	4.663	68.1	**6.3**	0.2
15T3	"	"	"	2–6	2.96	3.325	71.9	**6.5**	0.2
15T7	black fault gouge	37.9359	27.6239	<0.4	4.77	14.831	41.7	**17.8**	0.9
15T7	"	"	"	<2	3.74	10.615	72.5	**16.3**	0.4
15T7	"	"	"	2–6	3.91	14.797	76.5	**21.7**	0.5
16T6	black fault gouge	38.0059	28.1389	<0.4	1.51	4.972	51.8	**18.9**	0.6
16T6	"	"	"	<2	1.98	6.358	66.6	**18.4**	0.5
16T6	"	"	"	2–6	1.65	5.518	72.2	**19.2**	0.5

Table 1b. Age standards analysed (n=6).

Standard ID	K	Radiogenic ^{40}Ar	Radiogenic ^{40}Ar	Age	Error (2σ)	Difference to reference value [a]
	[%]	[10^{-10} mol/g]	[%]	[Ma]	[Ma]	[%]
HD-B1-132	7.96	3.404	91.27	24.50	0.38	+1.2
HD-B1-133	7.96	3.333	89.95	23.99	0.38	−0.91
HD-B1-138	7.96	3.442	93.22	24.77	0.32	+2.31
LP6-146	8.37	19.234	97.25	127.85	1.93	−0.04
LP6-147	8.37	19.292	96.78	128.22	1.92	+0.25
LP6-152	8.37	19.421	97.68	129.05	1.65	+0.90

[a] Measured age standards include HD-B1 (Hess and Lippolt, 1994) and LP6 (Odin et al., 1982).

Table 1c. ^{40}Ar-^{36}Ar values for air shots (n=3).

Airshot-ID	^{40}Ar/^{36}Ar	Difference to reference value [a]
	[−]	[± %]
AS128-AirS-1	296.05	0.31
AS129-AirS-1	293.89	0.38
AS132-AirS-2	296.66	0.11

[a] ^{40}Ar-^{36}Ar reference value of air from Steiger and Jäger (1977).

Table 2. Hydrogen isotope data of fault gouges from the central Menderes Massif.

Sample number	Weight	Grain size	δD [a]	K-Ar age [b]
	[mg]	[μm]	[‰]	[Ma]
Bozdağ Range – Gediz detachment				
15T18	0.817	<0.1	−103	6.2 ± 0.2
15T18	0.809	<2	−97	7.1 ± 0.3
15T18	0.874	2–6	−92	7.4 ± 0.2
15T22	0.861	<0.1	−115	4.7 ± 0.9
15T22	0.903	<0.4	−108	11.5 ± 0.3
15T22	0.900	<2	−111	12.0 ± 0.4
15T22	0.881	2–6	−109	11.6 ± 0.8
Aydın Range – Büyük Menderes detachment				
15T2	0.255	<0.1	−95	5.5 ± 0.3
15T2	0.811	<2	−102	8.5 ± 0.2
15T2	0.841	2–6	−104	7.3 ± 0.2
15T3	0.855	<0.1 and <0.4	−106	2.8 ± 0.2
15T3	0.873	<2	−102	6.3 ± 0.2
15T3	0.839	2–6	−97	6.5 ± 0.2
15T7	0.934	<0.4	−76	17.8 ± 0.9
15T7	0.810	<2	−87	16.3 ± 0.4
15T7	0.869*	2–6	−76*	21.7 ± 0.5
16T6	0.862*	<0.4	−85*	18.9 ± 0.6
16T6	0.891	<2	−90*	18.4 ± 0.5
16T6	0.846	2–6	−94	19.2 ± 0.5

[a] Values marked with an asterisk are mean values from sample aliquots.

[b] Ages as reported in Table 1a.

Table 3. Results of apatite and zircon fission track analysis.

Sample [a]	Latitude	Longitude	Elevation	Number of crystals	ρ_s [b]	N_s [b]	ρ_i [b]	N_i [b]	ρ_d [b]	N_d [b]	P (χ^2) [b]	Dispersion	Central age ± 2σ	U	D_{par}
	[°N]	[°E]	[m]									[%]	[Ma]	[ppm]	[μm]
Apatite fission track (AFT)															
Footwall of Gediz detachment (Bozdağ Range)															
14M19	38.4324	27.8355	556	20	0.720	29	13.325	537	8.3596	3032	39	0.35	**5.7 ± 2.6**	22	1.30
15M84	38.4309	27.7362	244	16	1.373	35	8.824	225	4.6428	2796	99	0	**8.2 ± 3.2**	31	2.74
Hanging wall of Gediz detachment (Bozdağ Range)															
11M1	38.4805	27.8105	190	20	0.885	17	18.490	355	17.087	4424	100	0	**10.4 ± 2.8**	15	1.48
Footwall of Büyük Menderes detachment (Aydın Range)															
14M35[*]	37.9537	28.1034	766	11	0.788	7	15.444	139	8.1684	3032	50	0	**5.2 ± 4.0***	27	1.55
14M41[*]	37.9682	28.0899	406	11	0.847	16	18.201	344	8.0970	3032	29	0	**4.4 ± 2.2**	33	1.54
15M57[§]	37.9684	27.7614	705	8	1.383	13	7.234	68	5.1285	2796	99	0	**10.6 ± 6.6**	20	2.00
15M58[§]	37.9574	27.7586	292	22	1.546	45	21.306	620	5.1076	2796	80	0	**4.3 ± 1.4**	58	2.34
16M90[§]	38.0048	28.1380	1255	35	3.929	163	23.769	986	6.8920	2481	99	0	**12.9 ± 2.6**	48	1.68
Hanging wall of Büyük Menderes detachment (Aydın Range)															
14M31[*]	37.9227	28.0861	829	15	2.887	41	17.042	242	8.2282	3032	50	0	**17.8 ± 6.2***	31	1.73
Zircon fission track (ZFT)															
Footwall of Gediz detachment (Bozdağ Range)															
14M19		see above		8	17.755	87	67.347	330	6.821	2583	69	0	**9.8 ± 2.4**	508	–
15M84		"		25	9.877	100	33.778	342	6.308	1982	99	0	**14.1 ± 3.6**	228	–
Hanging wall of Gediz detachment (Bozdağ Range)															
11M1		see above		20	90	531	100.678	594	6.525	2512	2	0.24	**32.8 ± 5.8**	634	–
Footwall of Büyük Menderes detachment (Aydın Range)															
15M57[§]		"		20	19.172	147	42.213	316	6.419	1982	20	0.20	**19.1 ± 4.8**	224	–
Hanging wall of Büyük Menderes detachment (Aydın Range)															
14M31[*]		see above		20	75.225	835	96.757	1074	6.814	2583	8	0.13	**29.0 ± 3.8**	585	–

[a] Samples marked with an asterisk are from Wölfler et al. (2017). Samples included in Nilius et al. (in revision) are marked with a section sign (§).

[b] The density of spontaneous and induced tracks (ρ_s and ρ_i) is given in units of 10^5 tracks/cm^2. N_s and N_i correspond to the number of counted spontaneous and induced tracks, respectively. N_d is the number of counted tracks on the dosimeter. The probability of obtaining a chi-square value (χ^2) for n degrees of freedom (where n is the number of crystals minus 1) is indicated as P (χ^2).

Table 4. Results of apatite and zircon (U-Th)/He geochronology.

Sample [a]	Aliq.	He Vol. [10^{-9} cm^3]	He 1σ [%]	^{238}U Mass [ng]	^{238}U 1σ [%]	^{238}U Conc. [ppm]	^{232}Th Mass [ng]	^{232}Th 1σ [%]	^{232}Th Conc. [ppm]	Th/U ratio [−]	Sm Mass [ng]	Sm 1σ [%]	Sm Conc. [ppm]	Ejection correction [b] [−]	Uncorrected age [Ma]	Ft-corrected age ± 2σ [c] [Ma]	Sample age ± 2 s.e. [d] [Ma]
Apatite (U/Th)/He																	
Footwall of Gediz detachment (Bozdağ Range)																	
14M19	#3	0.001	11.0	0.003	16.7	1.7	0.004	4.0	2.3	1.35	0.095	8.2	52	0.70	2.28	3.26 ± 1.03	**3.3 ± 1.0**
Hanging wall of Gediz detachment (Bozdağ Range)																	
11M1	#1	0.0004	76.5	0.001	102.4	0.4	0.005	5.3	1.6	3.51	0.031	36.7	10	0.70	1.08	1.6 (+2.8/-1.6)	**3.2 ± 2.3**
	#2	0.001	57.2	0.001	208.4	0.3	0.004	5.8	1.6	5.51	0.009	34.8	4	0.70	3.42	4.9 (+9.8/-4.9)	
Footwall of Büyük Menderes detachment (Aydın Range)																	
14M35*	#1	0.008	6.3	0.011	5.2	6.7	0.007	3.7	4.3	0.64	0.076	9.1	48	0.65	5.14	7.90 ± 1.45*	**3.0 ± 0.3**
	#2	0.027	3.6	0.081	1.9	12	0.056	2.6	8.0	0.69	0.318	6.5	46	0.77	2.29	2.98 ± 0.31	
Hanging wall of Büyük Menderes detachment (Aydın Range)																	
14M31*	#1	0.131	1.5	0.615	1.8	57	0.277	2.4	25	0.45	0.650	6.2	60	0.81	1.58	1.95 ± 0.14	**1.6 ± 0.2**
	#2	0.163	1.5	1.190	1.8	79	0.036	2.7	2.4	0.03	0.720	6.0	48	0.80	1.12	1.40 ± 0.11	
	#3	0.171	1.4	1.190	1.8	79	0.058	2.6	3.9	0.05	0.771	6.0	51	0.80	1.17	1.46 ± 0.11	
Zircon (U/Th)/He																	
Hanging wall of Gediz detachment (Bozdağ Range)																	
11M1	#1	4.682	1.7	2.222	1.8	444	0.452	2.4	9.0	0.20	0.025	12.8	0.5	0.78	16.64	21.39 ± 1.75	**23.4 ± 1.3**
	#2	1.863	1.8	0.743	1.8	148	0.589	2.4	14	0.79	0.015	14.5	0.4	0.76	17.46	22.90 ± 1.95	
	#3	2.380	1.8	0.986	1.8	197	0.210	2.4	7.1	0.21	0.005	24.3	0.2	0.73	19.01	25.92 ± 2.42	
Footwall of Büyük Menderes detachment (Aydın Range)																	
14M35*	#1	1.398	0.9	0.944	1.8	248	0.849	2.4	223	0.90	0.241	9.6	63	0.77	10.09	13.10 ± 1.01	**15.7 ± 3.6**
	#2	3.577	0.9	1.806	1.8	340	1.261	2.4	238	0.70	0.216	9.6	41	0.77	14.06	18.26 ± 1.41	
	#3	1.636	0.9	0.753	1.8	604	0.260	2.4	208	0.34	0.025	11.3	20	0.64	16.61	26.0 ± 3.0*	
14M41*	#1	3.125	1.2	2.314	1.8	286	0.613	2.4	76	0.27	0.006	16.4	1	0.81	10.50	12.99 ± 0.91	**12.2 ± 0.7**
	#2	0.909	1.3	0.810	1.8	258	0.228	2.4	73	0.28	0.003	25.8	1	0.73	8.70	11.93 ± 1.09	
	#3	1.773	0.9	1.576	1.8	422	0.484	2.4	129	0.31	0.035	10.5	9	0.74	8.70	11.74 ± 1.02	
15M57§	#1	4.611	1.3	3.151	1.8	591	0.502	2.4	94	0.16	0.302	15.7	6	0.78	11.67	14.99 ± 1.18	**14.2 ± 0.4**
	#2	5.701	1.3	3.664	1.8	832	0.273	2.4	62	0.07	0.210	15.7	5	0.94	12.66	13.47 ± 0.63	
	#3	6.538	1.3	4.883	1.8	1291	0.528	2.4	140	0.11	0.406	15.7	11	0.76	10.81	14.15 ± 1.17	
15M58§	#1	4.466	1.3	3.068	1.8	93	1.271	2.4	38	0.41	0.994	15.7	3	0.86	10.95	12.78 ± 0.76	**13.3 ± 0.5**
	#2	11.496	1.3	8.473	1.8	476	1.118	2.4	63	0.13	0.408	15.7	2	0.84	10.89	12.90 ± 0.82	
	#3	9.012	1.3	5.666	1.8	351	2.050	2.4	127	0.36	0.740	15.7	5	0.85	12.12	14.25 ± 0.87	

Table 4 (continued). Results of apatite and zircon (U-Th)/He geochronology.

Footwall of Büyük Menderes detachment (Aydın Range)

16M90§	#2	4.474	1.1	2.487	1.8	462	1.600	2.4	297	0.64	0.027	9.5	5	0.75	12.93	17.28 ± 1.46	**18.9 ± 2.2**
	#3	3.637	1.0	2.044	1.8	406	0.130	2.4	25	0.06	0.009	15.8	2	0.71	14.52	20.45 ± 1.96	

Hanging wall of Büyük Menderes detachment (Aydın Range)

14M31*	#1	1.476	1.2	0.812	1.8	231	0.180	2.4	51	0.22	0.013	10.2	4	0.76	14.30	18.80 ± 1.56	**20.0 ± 1.6**
	#2	8.919	1.1	4.403	1.8	737	0.580	2.4	97	0.13	0.108	5.0	18	0.77	16.30	21.11 ± 1.69	

[a] Samples marked with an asterisk are from Wölfler et al. (2017). Samples included in Nilius et al. (in revision) are marked with a section sign (§).

[b] Ejection correction (Ft): correction factor for alpha-ejection (according to Farley et al., 1996 and Hourigan et al., 2005).

[c] Uncertainty of the single-grain ages includes both the analytical uncertainty and the estimated uncertainty of the ejection correction. Ft-corrected (U-Th)/He ages marked with asterisk are not considered in the calculation of the sample age.

[d] Sample age is the unweighted average age of all Ft-corrected (U-Th)/He ages (±2 standard error).

4.6   Discussion

K-Ar dating of fault gouges

K-Ar dating of illite from fault gouges is increasingly applied to constrain the temporal activity of brittle faults (e.g. Vrolijk and van der Pluijm, 1999; Zwingmann and Mancktelow, 2004; Haines and van der Pluijm, 2008; Zwingmann et al., 2010; Duvall et al., 2011; Rahl et al., 2011; Mancktelow et al., 2016; Haines et al., 2016; Ring et al., 2017). Still, interpreting K-Ar ages for different clay size fractions from individual samples requires a careful examination of sample mineralogy, host rock lithology, and cooling histories to interpret the resulting bulk mineral ages in a meaningful way. For instance, protracted illite growth over a certain period of fault activity can be reflected by progressively younger ages for smaller size fractions, because larger crystals started to grow earlier than smaller ones (e.g. Zwingmann et al., 2010). On the other hand, K-Ar ages that increase with grain size may also result from contamination of the fault gouge with K-feldspar from the host rock. In this case, older ages for larger size fractions may overestimate the time of faulting if significant amounts of K-feldspar are present, whereas younger K-Ar ages for small size fractions without K-feldspar may record clay mineral growth during faulting (e.g. Haines and van der Pluijm, 2008; Hetzel et al., 2013). Knowledge of the cooling histories of crustal blocks adjacent to the studied fault can aid the evaluation of K-Ar fault gouge ages, because authigenic growth of illite during brittle faulting often occurs at temperature conditions bracketed by the annealing temperature of fission tracks in zircon (~240 °C) and the upper boundary of the partial annealing zones of apatite (~110 °C) (e.g. Zwingmann and Mancktelow, 2004; Mancktelow et al., 2016). This observation has been interpreted to indicate that K-Ar ages reflect the timing of illite growth during faulting. In the following, we discuss our results from K-Ar dating and low-temperature thermochronology to evaluate the timing of brittle faulting on the Gediz and Büyük Menderes detachment faults.

Interpretation of the K-Ar and thermochronologic data

Sample 15T22 from the Gediz detachment was obtained from a fault gouge layer at the contact between marble in the footwall and Neogene sedimentary rocks in the hanging wall of the detachment fault (Figure 3). Sheared clasts in the sedimentary rocks document brittle deformation and cataclasis of these rocks during their tectonic emplacement on the detachment surface (Figure 3b). This synextensional deformation of the sedimentary rocks explains the presence of significant amounts of quartz in the two coarse grain size fractions of sample 15T22 (i.e. 25% and 6%; Table S1), which cannot be derived from the marble unit in the fault footwall. Minor amounts of K-feldspar in the 2–6 and <2 μm grain size fractions of the sample (i.e. 3 and <1%; Table S1) must have also been derived from the hanging wall. As shown by consistent K-Ar ages of 11.6±0.8, 12.0±0.4, and 11.5±0.3 Ma for the three coarsest grain size fractions (Table 1a), the presence of minor amounts of K-feldspar does not

affect the ages in a significant way. It is noteworthy that sample 15T22 contains only the 2M1 illite polytype and is devoid of 1M illite (Table S1). The latter is often considered to be derived from transformation of the high-temperature 2M1 polytype or from muscovite (e.g. Haines and van der Pluijm, 2012). Given the lack of muscovite in the wall rocks of the Gediz detachment, we interpret the K-Ar ages to record the growth of authigenic 2M1 illite during an early stage of detachment faulting and gouge formation at 12–11 Ma. This interpretation is in accordance with ZFT and AFT ages of 14.1±3.6 and 8.2±3.2 Ma obtained from sample 15M84 in the footwall of the Gediz detachment (Table 3, Figure 7).

Fault gouge sample 15T18 was collected 3 km farther east, from a low-angle normal fault in the footwall of the Gediz detachment (Figure 2). The three grain size fractions of this sample yielded K-Ar ages from 7.4±0.2 to 6.2±0.2 Ma (Table 1a). Based on the similarity of the three K-Ar ages, we infer that the dated illite is authigenic and has grown during normal faulting in the footwall of the Gediz detachment at 7–6 Ma. Ongoing deformation of the Gediz detachment system in the late Miocene is also recorded by an ^{40}Ar-^{39}Ar age of 6.7±1.0 Ma for synkinematic white mica from a mylonite sample (Lips et al., 2001) (Figure 7) and is consistent with rapid cooling indicated by ZFT and AFT ages of 9.8±2.4 and 5.7±2.6 Ma, respectively (sample 14M19; Figures 6a and 7).

Both fault gouge samples from the western Gediz detachment (15T18 and 15T22) contain only the 2M1 illite polytype and their smallest size fractions (i.e. <0.1 µm) have relatively low 2M1 illite contents compared to the <0.4 and <2 µm fractions (Table S1). The young K-Ar ages of 6.2±0.2 and 4.7±0.9 Ma for the two <0.1 µm size fractions of these samples may therefore record the latest illite growth during faulting (Table 1a). Apart from illite, the samples contain relatively large amounts of smectite (28–68%; Table S1), a clay mineral that is only stable at temperatures below ~100–80 °C (Pytte and Reynolds, 1989; Huang et al., 1993). We infer that the growth of smectite occurred during a late stage of normal faulting when temperatures had fallen below ~100–80 °C. Two similar AHe ages of 3.3±1.0 and 3.2±2.3 Ma for bedrock samples from the footwall and hanging wall of the western Gediz detachment (14M19 and 11M1; Figures 1 and 6) suggest that the activity of the detachment system came to an end ~3 Ma ago (Figure 6a).

At the eastern Büyük Menderes detachment, sample 16T6 was collected from a thick fault gouge layer within the broad fault zone (Figure 5). The three grain size fractions analysed from this sample yielded consistent K-Ar ages of 19.2±0.5, 18.4±0.5, and 18.9±0.6 Ma (Table 1a, Figure 7). All size fractions contain significant amounts of 1M illite (13–21%) and mixed layer illite-smectite (18–32%), but only little 2M1 illite (6–8%) (Table S1), indicating gouge formation and clay mineral growth at temperatures slightly above the partial annealing zone of apatite (cf. Zwingmann et al., 2010). This inference is broadly consistent with a ZHe age of 18.9±2.2 Ma and an AFT age of 12.9±2.6 Ma for sample 16M90 (Tables 3 and 4, Figure 7), which bracket the time when the fault rocks were at

temperatures between ~180 and ~110 °C. Minor traces of K-feldspar (2–4%) in the 2–6 and <2 µm size

fractions have no recognisable effect on the K-Ar ages, probably because the small feldspar grains were

isotopically reequilibrated due to fluid-rock interaction (cf. Zwingmann et al., 2010). We thus interpret

the K-Ar ages to reflect illite growth during detachment faulting at 19–18 Ma.
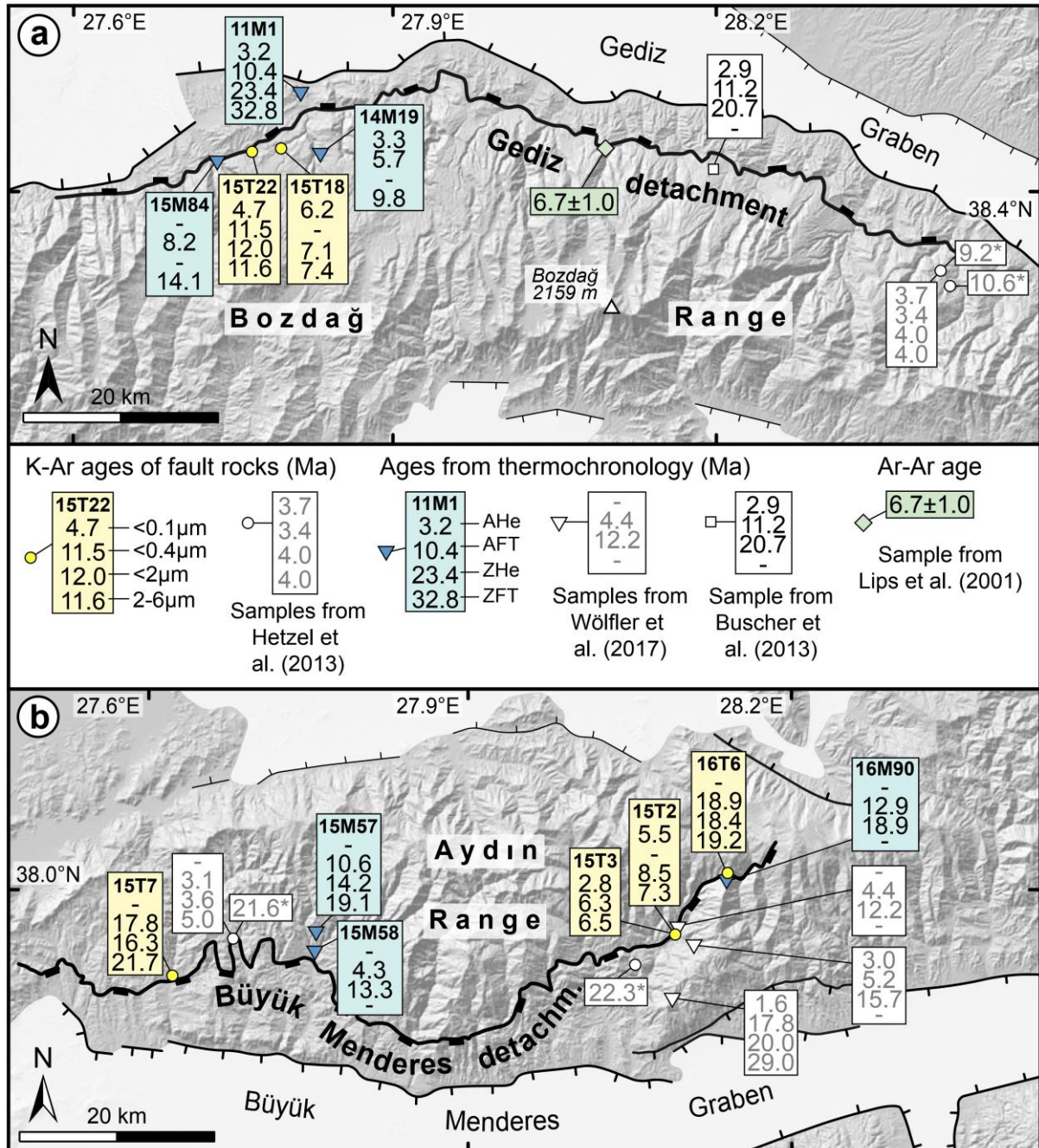
Figure 7: Shaded relief map of the **a)** Bozdağ and **b)** Aydın ranges with K-Ar ages of fault gouges and ages from low-temperature thermochronology. K-Ar ages are indicated for different grain size fractions. K-Ar ages marked with an asterisk have been determined for the <2 µm fraction. In the Bozdağ Range cooling ages from an orthogneiss klippe above the Gediz detachment (Buscher et al., 2013) and an [40]Ar-[39]Ar age from synkinematic white mica from the footwall of the Gediz detachment (Lips et al., 2001) are also indicated.

Markedly younger K-Ar ages were determined for the two fault gouge samples 15T2 and 15T3 from the outcrop at the Büyük Menderes detachment that was excavated for construction of a water reservoir (Figures 4 and 7). The two samples contain 7–15% 2M1 illite, 4–13% 1M illite (except the <0.1 μm fraction of 15T2, which is devoid of the latter), and no K-feldspar. Five out of six K-Ar ages from the size fractions of the two samples range from 8.5±0.2 to 5.5±0.3 Ma, whereas the <0.1 μm fraction of 15T2 yielded a younger age of 2.8±0.2 Ma (Table 1a, Figure 7). The quite consistent and rather young K-Ar ages, as well as the presence of quartzites in the footwall and sedimentary rocks in the hanging wall of the detachment (Figure 4) render the presence of inherited white mica from the wall rock unlikely. We thus interpret the new K-Ar ages to reflect prolonged illite growth during detachment faulting between ~9–3 Ma. As the samples 15T2 and –T3 do not contain smectite, faulting along the Büyük Menderes detachment may have ceased at a temperature above ~100 °C. The late Miocene to Pliocene phase of detachment faulting is supported by published ZHe and AFT ages of 12.2±0.7 and 4.4±2.2 Ma as well as 15.7±3.6 and 5.2±4.0 Ma for two bedrock samples from the footwall (14M41 and 14M35, Tables 3 and 4, Figure 7; Wölfler et al., 2017), which indicate prolonged cooling until the Pliocene. The entire thermochronologic dataset of that study was interpreted to record two phases of detachment faulting in the middle Miocene and latest Miocene/Pliocene (Wölfler et al., 2017). A Pliocene activity of the Büyük Menderes detachment is also in agreement with published K-Ar fault gouge ages of ~5–3 Ma for a sample in the western part of the detachment fault (Figure 7, sample 09Me-NM01; Hetzel et al., 2013).

The fault gouge sample from the western Büyük Menderes detachment (15T7) yielded similar but more variable K-Ar ages than sample 16T6 from the eastern part of the fault. The fault gouge contains large quantities of the 2M1 illite polytype (45–58%) but is devoid of 1M illite (Table S1). The three ages of 21.7±0.5, 16.3±0.4, and 17.8±0.9 Ma (Table 1a) neither correlate with the amount of 2M1 illite nor with the grain size of the analysed fractions. Given that the sampled fault developed within cataclastically deformed mylonites, faulting possibly occurred at temperatures close to the ductile-brittle transition, which would be in agreement with the growth of authigenic 2M1 illite (e.g. Haines and van der Pluijm, 2008; Ring et al., 2017). Faulting at rather high temperatures is also supported by the ZFT age of 19.1±4.8 Ma of sample 15M57, which indicates cooling below ~240 °C at about ~19 Ma (Table 3). Hence, we interpret the K-Ar ages to record detachment faulting between ~22 and ~16 Ma. This interpretation is consistent with a previously published K-Ar age of 21.6±0.6 Ma for a nearby cataclasite sample from the Büyük Menderes detachment (sample 09Me-NM02; Hetzel et al., 2013) (Figure 7).

Hydrogen isotope ratios of the analysed fault gouges range from –76 to –115‰ (Table 2, Figure 8b) and indicate interaction with infiltrating meteoric water during gouge formation and faulting (e.g. Fricke et al., 1992; Losh, 1997; Morrison and Anderson, 1998; Mulch et al., 2007). Similar δD values of

−89 to −95‰ were recently reported for two fault gouges samples from the Naxos detachment, possibly indicating a similar isotopic composition of the rainwater source for this core complex in the late Miocene (Mancktelow et al., 2016). Interestingly, the fault gouges from the Büyük Menderes detachment with early Miocene K-Ar ages exhibit δD values between −76 to −94‰, whereas those of the younger fault gouges are more negative, with values between −92 and −115‰ (Figure 8b). To evaluate whether this difference is related to changes in paleo-elevation during the formation of the Menderes metamorphic core complex is beyond the scope of the present study. The pattern is, however, consistent with a) meteoric fluid interaction in increasingly shallower levels of the extending crust and interaction with less-evolved meteoric fluids and b) with an increase in elevation of the Menderes metamorphic core complex over time.

Detachment faulting and exhumation of the central Menderes Massif

The timing of normal faulting at the Gediz and Büyük Menderes detachment systems and the question whether faulting was continuous or episodic through time has been much debated (e.g. Gessner et al., 2001; Ring et al., 2003; Purvis and Robertson, 2005; Öner and Dilek, 2011; Buscher et al., 2013; Rossetti et al., 2017; Wölfler et al., 2017). We will now use our new K-Ar ages together with previously published geochronological data to summarise the history of normal faulting and rock exhumation at both detachment faults.

In the western portion of the Gediz detachment, our oldest K-Ar ages document faulting at 12–11 Ma (sample 15T22) and are similar to two K-Ar ages of ~10.6 and ~9.2 Ma for fault gouges from the eastern part of the detachment system (Figure 7; Hetzel et al., 2013). Taken together, these ages indicate that brittle faulting was underway along the entire detachment at that time. Detachment faulting during the middle Miocene is also indicated by ^{40}Ar-^{39}Ar biotite ages of 13.1±0.2 and 12.2±0.4 Ma for the synextensional Turgutlu and Salihli granodiorites (Hetzel et al., 1995), and by slightly older U–(Th)–Pb ages of ~15–14 Ma for titanite from the Salihli granodiorite (Rossetti et al., 2017). Our younger K-Ar ages of 7–6 Ma for sample 15M18 from a normal fault in the footwall of the western Gediz detachment is remarkably similar to an ^{40}Ar-^{39}Ar age of 6.7±1.0 Ma for synkinematic white mica from a mylonite sample beneath the central part of the detachment (Figure 7; Lips et al., 2001). These ages indicate ongoing normal faulting during the late Miocene. Still younger K-Ar fault gouge ages of 4–3 Ma at the easternmost Gediz detachment (Hetzel et al., 2013) and a single K-Ar age of 4.7±0.9 Ma from the western detachment (sample 15T22) (Figure 7) suggest that faulting continued until ~3 Ma ago. Together with the cooling history of the footwall and hanging wall (Figure 6a), the presently available age data suggest that the entire Gediz detachment fault was active rather continuously between ~15 and ~3 Ma. A phase of particularly fast cooling and exhumation between ~4 and ~2 Ma has only been reported for the eastern Gediz detachment (Salihli area) (Buscher et al.,

2013) and was confirmed by Plio-Quaternary cooling ages from detrital apatite fission track analysis (Asti et al., 2018). The pronounced late Pliocene activity of the eastern Gediz detachment is in agreement with the remarkable preservation of the fault in that area, where the detachment exerts a dominant control on the current topography.
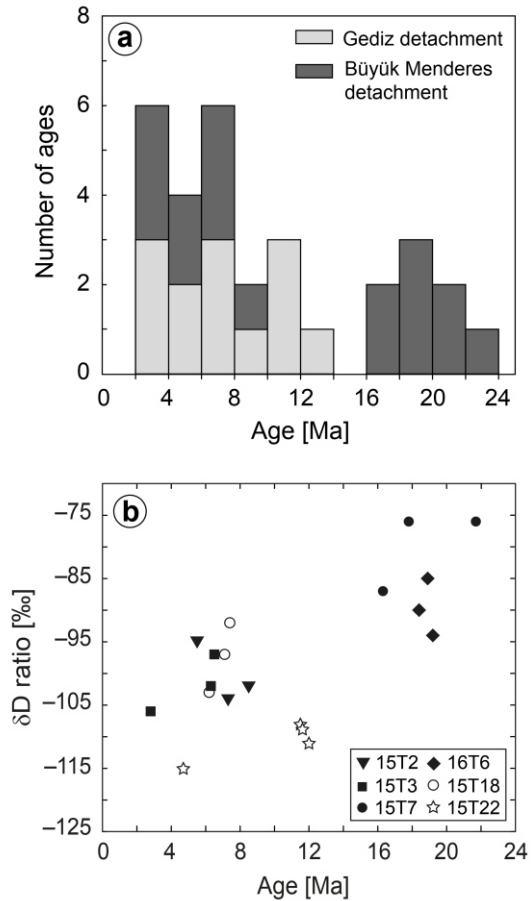
Figure 8a: K-Ar ages of fault gouge and cataclasite samples in the central Menderes Massif (data from this study and from Hetzel et al., 2013). The ages of all grain size fractions have been plotted. **b)** K-Ar ages of fault gouge samples (all grain size fractions) plotted versus δD isotope ratios. Samples from the Büyük Menderes and Gediz detachment faults are indicated with closed and open symbols, respectively.

In contrast to the Gediz detachment, K-Ar ages of fault gouge samples from the Büyük Menderes detachment system form two distinct groups (Figure 8a), suggesting that the detachment was active during two phases. Our K-Ar ages of two fault gouge samples from the eastern and western part of the Büyük Menderes detachment (Figure 7) and cooling ages from low-temperature thermochronology (Figure 6b) indicate that the first phase of normal faulting occurred at ~22–16 Ma. The thermochronologic data of Wölfler et al. (2017) and Nilius et al. (2019) indicate that cooling and rock exhumation during this phase continued into the middle Miocene. The second phase of faulting occurred between ~9 and ~3 Ma, as indicated by our new and previously published K-Ar fault gouge ages (Figures 7 and 8a). This second stage of faulting is corroborated by low-temperature thermochronologic data in the eastern part of the detachment, which document a phase of enhanced footwall cooling in the latest Miocene and Pliocene (Wölfler et al., 2017).

4.7   Conclusions

In this study, we employed K-Ar dating of fault gouges and low-temperature thermochronology to constrain the timing of detachment faulting at the Gediz and Büyük Menderes detachments in the central Menderes Massif (Western Turkey). The new K-Ar ages reveal that the Gediz detachment was active from ~12 to ~3 Ma, with a late Pliocene phase of faulting being mainly recorded in the eastern part of the detachment fault. Previously published age data indicate that detachment faulting and rapid cooling of the footwall rocks started already at ~15 Ma. In contrast to the Gediz detachment, the Büyük Menderes detachment was active during two phases. As indicated by our K-Ar ages, the first phase lasted from ~22–16 Ma, but thermochronologic data reveal that footwall cooling and rock exhumation continued during the middle Miocene. A second phase of detachment faulting occurred in the late Miocene and Pliocene and lasted from ~9–3 Ma. During this time span, both detachments were active simultaneously and caused the bivergent exhumation of the central Menderes core complex. The youngest K-Ar ages and cooling histories for hanging and footwall rocks imply that the activity of both detachments ended ~3 Ma ago. Hydrogen isotope ratios of −76 to −115‰ for fault gouges from both detachments indicate interaction with infiltrating meteoric fluids during detachment faulting and gouge formation.

References

Asti, R., Malusà, M.G., Faccenna, C., 2018. Supradetachment basin evolution unravelled by detrital apatite fission track analysis: the Gediz Graben (Menderes Massif, Western Turkey). Basin Research 30(3), 502–521.

Ault, A.K., Reiners, P.W., Evans, J.P., Thomson, S.N., 2015. Linking hematite (U-The)/He dating with the microtextural record of seismicity in the Wasatch fault damage zone, Utah, USA. Geology 43(9), 771–774.

Bonhomme, M.G., Thuizat, R., Pinault, Y., Clauer, N., Wendling, R., Winkler, R., 1975. Méthode de Datation Potassium-Argon, Appareillage et Technique, Strasbourg.

Braun, J., van der Beek, P., Valla, P., Robert, X., Herman, F., Glotzbach, C., Pedersen, V., Perry, C., Simon-Labric, T., Prigent, C., 2012. Quantifying rates of landscape evolution and tectonic processes by thermochronology and numerical modeling of crustal heat transport using PECUBE. Tectonophysics 524, 1–28.

Brun, J.-P., Sokoutis, D., 2010. 45 m.y. of Aegean crust and mantle flow driven by trench retreat. Geology 38(9), 815–818.

Burchfiel, B.C., Chen, Z., Hodges, K.V., Yuping, L., Royden, L.H., Changrong, D., Jiene, X., 1992. The South Tibetan Detachment System, Himalayan Orogen: extension contemporaneous with and parallel to shortening in a collisional mountain belt. Geological Society of America, Special Paper 269, 1–41.

Burtner, R., Nigrini, A., Donelick, R.A., 1994. Thermochronology of Lower Cretaceous source rocks in the Idaho-Wyoming Thrust belt. American Association of Petroleum Geologists, Bulletin 78, 1613–1636.

Buscher, J.T., Hampel, A., Hetzel, R., Dunkl, I., Glotzbach, C., Struffert, A., Akal, C., Rätz, M., 2013. Quantifying rates of detachment faulting and erosion in the central Menderes Massif (western Turkey) by thermochronology and cosmogenic ^{10}Be. Journal of the Geological Society, London 170(4), 669–683.

Caine, J.S., Evans, C.B., Forster, J.P., 1996. Fault zone architecture and permeability structure. Geology 24(11), 1025–1028.

Campani, M., Herman, F., Mancktelow, N., 2010. Two- and three-dimensional thermal modeling of a low-angle detachment: Exhumation history of the Simplon Fault Zone, central Alps. Journal of Geophysical Research 115, B10420, doi:10.1029/2009JB007036.

Candan, O., Dora, O.Ö., Oberhänsli, R., Çetinkaplan, M., Partzsch, J.H., Warkus, F.C., Dürr, S., 2001. Pan-African high-pressure metamorphism in the Precambrian basement of the Menderes Massif, western Anatolia, Turkey. International Journal of Earth Sciences 89, 793–811.

Candan, O., Oberhänsli, R., Dora, O.Ö., Çetinkaplan, M., Koralay, E., Rimmelé, G., Chen, F., Akal, C., 2011. Polymetamorphic evolution of the Pan-African basement and Palaeozoic-Early Tertiary Cover Series of the Menderes Massif. Bulletin of the Mineral Research and Exploration 142, 121–163.

Catlos, E.J., Çemen, I., 2005. Monazite ages and the evolution of the Menderes Massif, western Turkey. International Journal of Earth Sciences 94, 204–217.

Choo, C. O., Chang, T. W., 2000. Characteristics of clay minerals in gouges of the Dongrae fault, Southeastern Korea, and implications for fault activity. Clays and Clay Minerals 48(2), 204–212.

Crittenden, M.D., Coney, P.J., Davis G.H., 1980. Cordilleran metamorphic core complexes. Geological Society of America, Memoirs 153, 490 pp.

Dalrymple, G.B., Lanphere M.A., 1969. Potassium-Argon Dating: Principles, Techniques and Applications to Geochronology. W.H. Freeman, San Francisco.

Dewey, J.F., 1988. Extensional collapse of orogens. Tectonics 7(6), 1123–1139.

Donelick, R.A., Ketcham, R.A., Carlson, W.D., 1999. Variability of apatite fission track annealing kinetics II: crystallographic orientation effects. American Mineralogist 84, 1224–1234.

Dora, O.Ö., Kun, N., Candan, O., 1990. Metamorphic history and geotectonic evolution of the Menderes massif. In: Proceedings of International Earth Sciences Congress on Aegean Region, Izmir/Turkey 2, 102–115.

Dunkl, I., 2002. TRAKKEY: a window program for calculation and graphical presentation of fission track

data. Computers and Geosciences 28, 3–12.

Duvall, A.R., Clark, M.K., van der Pluijm, B.A., Li, C., 2011. Direct dating of Eocene reverse faulting in northeastern Tibet using Ar-dating of fault clays and low-temperature thermochronometry. Earth and Planetary Science Letters 304(3–4), 520–526.

Eide, E.A., Torsvik, T.H., Andersen, T.B., 1997. Absolute dating of brittle fault movements: Late Permian and late Jurassic extensional fault breccias in western Norway. Terra Nova 9, 135–139.

Emre, T., 1996. The tectonic evolution of the Gediz graben. Geological Bulletin of Turkey 39, 1–18.

Farley, K.A., 2000. Helium diffusion from apatite: general behavior as illustrated by Durango fluorapatite. Journal of Geophysical Research 105(B2), 2903–2914.

Farley, K.A., 2002. (U-Th)/He dating: techniques, calibrations and applications. Reviews in Mineralogy and Geochemistry 47, 819–844.

Farley, K.A., Wolf, R.A., Silver, L.T., 1996. The effects of long alpha-stopping distances on (U-Th)/He ages. Geochimica et Cosmochimica Acta 60, 4223–4229.

Faure, G., 1986. Principles of Isotope Geology. John Wiley and Sons, New York.

Faure, M., Sun, Y., Shu, L., Monié, P., Charvet, J., 1996. Extensional tectonics within a subduction-type orogen. The case study of the Wugongshan dome (Jiangxi Province, southeastern China). Tectonophysics 263(1–4), 77–106.

Forsyth, D.W., 1992. Finite extension and low-angle normal faulting. Geology 20(1), 27–30.

Fricke, H.C., Wickham, S.M., O´Neil, J.R., 1992. Oxygen and hydrogen isotope evidence for meteoric water infiltration during mylonitization and uplift in the Ruby Mountains-East Humboldt Range core complex, Nevada. Contributions to Mineralogy and Petrology 111(2), 203–221.

Gébelin, A., Teyssier, C., Heizler, M., Mulch, A., 2015. Meteoric water circulation in a rolling-hinge detachment system (northern Snake Range core complex, Nevada). Geological Society of America, Bulletin 127(1–2), 149–161.

Gessner, K., Ring, U., Johnson, C., Hetzel, R., Passchier, C.W., Güngör, T., 2001. An active bivergent rolling-hinge detachment system: Central Menderes metamorphic core complex in western Turkey, Geology 29(7), 611–614.

Gessner, K., Gallardo, L.A., Markwitz, V., Ring, U., Thomson, S.N., 2013. What caused the denudation of the Menderes Massif: Review of crustal evolution, lithosphere structure, and dynamic topography on southwest Turkey. Gondwana Research 24(1), 243–274.

Gleadow, A.J.W., 1981. Fission-track dating methods: what are the real alternatives? Nuclear Tracks 5, 3–14.

Gleadow, A.J.W., Duddy, I.R., 1981. A natural long-term track annealing experiment for apatite. Nuclear Tracks 5(1–2), 169–174.

Glodny, J., Hetzel, R., 2007. Precise U–Pb ages of syn-extensional Miocene intrusions in the central Menderes Massif, western Turkey. Geological Magazine 144(2), 235–246.

Gürer, Ö.F., Sarıca-Filoreau, N., Özburan, M., Sangu, E., Doğan, B., 2009. Progressive development of the Büyük Menderes Graben based on new data, western Turkey. Geological Magazine 146(5), 652–673.

Haines, S.H., van der Pluijm, B. A., 2008. Clay quantification and Ar–Ar dating of synthetic and natural gouge: application to the Miocene Sierra Mazatán detachment fault, Sonora, Mexico. Journal of Structural Geology 30(4), 525–538.

Haines, S.H., van der Pluijm, B. A., 2012. Patterns of mineral transformations in clay gouge, with examples from low-angle normal fault rocks in the western USA. Journal of Structural Geology 43, 2–32.

Haines, S.H., Lynch, E., Mulch, A., Valley, J.W., van der Pluijm, B., 2016. Meteoric fluid infiltration in crustal-scale normal fault systems as indicated by $\delta^{18}O$ and δ^2H geochemistry, and $^{40}Ar/^{39}Ar$ dating of neoformed clays in brittle fault rocks. Lithosphere 8(6), 587–600.

Hess, J. C., Lippolt, H.J., 1994. Compilation of K/Ar measurements on HD-B1 standard biotite; 1994 status report. In: Odin, G.S. (Ed.), Phanerozoic Time Scale. Bulletin de Liaison et d'information, IUGS Subcommission, Geochronology, Paris, 19–23.

Hetzel, R., Ring, U., Akal, C., Troesch, M., 1995. Miocene NNE-directed extensional unroofing in the

Menderes Massif, southwestern Turkey. Journal of the Geological Society, London 152(4), 639–654.

Hetzel, R., Reischmann, T., 1996. Intrusion age of Pan-African augen gneisses in the southern Menderes Massif and the age of cooling after Alpine ductile extensional deformation. Geological Magazine 133(5), 565–572.

Hetzel, R., Romer, R.L., Candan, O., Passchier, C.W., 1998. Geology of the Bozdağ area, central Menderes Massif, SW Turkey: Pan-African basement and Alpine deformation. International Journal of Earth Sciences 87(3), 394–406.

Hetzel, R., Zwingmann, H., Mulch, A., Gessner, K., Akal, C., Hampel, A., Güngör, T., Petschick, R., Mikes, T., Wedin, F., 2013. Spatiotemporal evolution of brittle normal faulting and fluid infiltration in detachment fault systems: A case study from the Menderes Massif, western Turkey. Tectonics 32, 1–13.

Hourigan, J.K., Reiners, P.W., Brandon, M.T., 2005. U-Th zonation-dependent alpha-ejection in (U-Th)/He chronometry. Geochimica et Cosmochimica Acta 69, 3349–3365.

Huang, W.L., Longo, J.M., Pevear, D.R., 1993. An experimentally derived kinetic model for smectite-to-illite conversion and its use as a geothermometer. Clays and Clay Minerals 41, 162–177.

Hurford, A.J., Green, P.F., 1983. The zeta age calibration of fission-track dating. Chemical Geology 1, 285–317.

Işık, V., Seyitoğlu, G., Çemen, I., 2003. Ductile-brittle transition along the Alaşehir detach- ment fault and its structural relationship with the Simav detachment fault, Menderes massif, western Turkey. Tectonophysics 374(1), 1–18.

Jolivet, L., Faccenna, C., 2000. Mediterranean extension and the Africa-Eurasia collision. Tectonics 19(6), 1095–1106.

Jolivet, L., Faccenna, C., Huet, B., Labrousse, L., Le Pourhiet, L., Lacombe, O., Lecomte, E., Burov, E., Denèle, Y., Brun, J.P. et al., 2013. Aegean tectonics: Strain localization, slap tearing and trench retreat. Tectonophysics 597, 1–33.

Kralik, M., Klima, K., Riedmüller, G., 1987. Dating fault gouges. Nature 327(6120), 315–317.

Liewig, N., Clauer, N., Sommer, F., 1987. Rb-Sr and K-Ar dating of clay diagenesis in Jurassic sandstone oil reservoirs, North Sea. American Association of Petroleum Geologists, Bulletin 71, 1467–1474.

Lips, A.L.W., Cassard, D., Sözbilir, H., Yilmaz, H., Wijbrans, J.R., 2001. Multistage exhumation of the Menderes massif, western Anatolia (Turkey). International Journal of Earth Sciences 89, 781–792.

Lister, G.S., Davis, G.A., 1989. The origin of metamorphic core complexes and detachment faults formed during Tertiary continental extension in the northern Colorado River region, U.S.A. Journal of Structural Geology 11(1–2), 65–94.

Losh, S., 1997. Stable isotope and modelling studies of fluid-rock interaction associated with the Snake Range and Mormon Peak detachment faults, Nevada. Geological Society of America, Bulletin 109(3), 300–323.

Lyons, J. B., Snellenburg, J., 1971. Dating faults. Geological Society of America, Bulletin 82(6), 1749–1752.

Malavieille, J., 1993. Late orogenic extension in mountain belts: insights from the Basin and Range and the Late Paleozoic Variscan belt. Tectonics 12(5), 1115–1130.

Mancktelow, N., Zwingmann, H., Mulch, A., 2016. Dating of fault gouge from the Naxos detachment (Cyclades, Greece). Tectonics 35(10), 2334–2344.

McCallister, A.T., Taylor, M.H., Murphy, M.A., Styron, R.H., Stockli, D.F., 2014. Thermochronologic constraints on the late Cenozoic exhumation history of the Gurla Mandhata metamorphic core complex, Southwestern Tibet. Tectonics 33, 27–52.

McKenzie, D., 1978. Active tectonics of the Alpine-Himalayan belt: the Aegean Sea and surrounding regions. Geophysical Journal International 55(1), 217–254.

Morrison, J., Anderson, J.L., 1998. Footwall refrigeration along a detachment fault: Implications for the thermal evolution of core complexes. Science 279(5347), 63–66.

Mulch, A., Chamberlain, C.P., 2007. Stable isotope paleoaltimetry in orogenic belts – The silicate record in surface and crustal geological archives. Reviews in Mineralogy and Geochemistry 66(1), 89–118.

Mulch, A., Teyssier, C., Cosca, M.A., Chamberlain, C.P., 2007. Stable isotope paleoaltimetry of Eocene core complexes in the North American Cordillera. Tectonics 26(4), TC4001, doi:10.1029/2006TC001995.⌷SEP⌷

Naeser, C.W., 1978. Fission track dating. U.S. Geological Survey Open File Report 76–190.

Nilius, N.-P., Glotzbach, C., Wölfler, A., Hampel, A., Dunkl, I., Akal, C., Heineke, C., Hetzel, R., (2019). Exhumation history of the Aydın range and role of the Büyük Menderes detachment system during bivergent extension of the central Menderes Massif, western Turkey. (Journal of the Geological Society, London).

Odin, G.S. and 35 collaborators, 1982. Interlaboratory standards for dating purposes. In: Odin, G.S. (Ed.), Numerical Dating in Stratigraphy, Part 1. John Wiley and Sons, Chichester, 123–148.

Öner, Z., Dilek, Y., 2011. Supradetachment basin evolution during continental extension: The Aegean province of western Anatolia, Turkey. Geological Society of America, Bulletin 123(11–12), 2115–2141.

Özer, S., Sözbilir, H., 2003. Presence and tectonic significance of Cretaceous rudist species in the so-called Permo-Carboniferous Göktepe Formation, central Menderes metamorphic massif, western Turkey. International Journal of Earth Sciences 92(3), 397–404.

Purvis, M., Robertson, A., 2005. Sedimentation of the Neogene-Recent Alaşehir (Gediz) continental graben system used to test alternative tectonic models for western (Aegean) Turkey. Sedimentary Geology 173(1–4), 373–408.

Pytte, A.M., Reynolds, R.C., 1989. The thermal transformation of smectite to illite. In: Naeser, N.D., McCulloch, T.H. (Eds.), Thermal history of sedimentary basins. Springer, New York, 133–140.

Rahl, J.M., Haines, S.H., van der Pluijm, B.A., 2011. Links between orogenic wedge deformation and erosional exhumation: Evidence from illite age analysis of fault rock and detrital thermochronology of syn-tectonic conglomerates in the Spanish Pyrenees. Earth and Planetary Science Letters 307(1–2), 180–190.

Reiners, P.W., Spell, T.I., Nicolescu, S., Zanetti, K., 2004. Zircon (U-Th)/He thermochronometry: He diffusion and comparisons with ^{40}Ar/^{39}Ar dating. Geochimica et Cosmochimica Acta 68(8), 1857–1887.

Reiners, P.W., 2005. Zircon (U-Th)/He thermochronometry. Reviews in Mineralogy and Geochemistry 58, 151–179.

Ring, U., Brandon, M.T., Lister, G.S., Willett, S.D., 1999. Exhumation processes. In: Ring, U., Brandon, M.T., Lister, G.S., Willett, S.D. (Eds.), Exhumation processes: normal faulting, ductile flow, and erosion. Geological Society of London, Special Publications 154, 1–27.

Ring, U., Johnson, C., Hetzel, R., Gessner, K., 2003. Tectonic denudation of a Late Creta- ceous-Tertiary collisional belt: regionally symmetric cooling patterns and their relation to extensional faults in the Anatolide belt of western Turkey. Geological Magazine 140(4), 421–441.

Ring, U., Uysal, I.T., Glodny, J., Cox, S.C., Little, T., Thomson, S.N., Stübner, K., Bozkaya, Ö., 2017. Fault-gouge dating in the Southern Alps, New Zealand. Tectonophysics 717, 321–338.

Rossetti, F., Asti, R., Faccenna, C., Gerdes, A., Lucci, F., Theye, T., 2017. Magmatism and crustal extension: Constraining activation of the ductile shearing along the Gediz detachment, Menderes Massif (western Turkey). Lithos 282, 145–162.

Şengör, A.M.C., Satır, M., Akkök, R., 1984. Timing of tectonic events in the Menderes Massif, western Turkey: Implications for tectonic evolution and evidence for Pan-African basement in Turkey. Tectonics 3(7), 693–707.

Seyitoğlu, G., Scott, B.C., 1991. Late Cenozoic crustal extension and basin formation in west Turkey. Geological Magazine 128(2), 155–166.

Sherlock, S. C., Hetzel, R., 2001. A laser-probe ^{40}Ar/^{39}Ar study of pseudotachylite from the Tambach Fault Zone, Kenya: direct isotopic dating of brittle faults. Journal of Structural Geology 23(1), 33–44.

Steiger, R. H., Jäger, E., 1977. Subcommission on geochronology: Convention on the use of decay constants in geo- and cosmochronology. Earth and Planetary Science Letters 36, 359–362.

Thiede, R.C., Arrowsmith, J.R., Bookhagen, B., McWilliams, M.O., Sobel, E.R., Strecker, M. R., 2005.

From tectonically to erosionally controlled development of the Himalayan orogen. Geology 33(8), 689–692.

van der Pluijm, B.A, Hall, C.M., Vrolijk, P.J., Pevear, D.R., Covey, M.C., 2001. The dating of shallow faults in the Earth's crust. Nature 412 (6843), 172–175.

van Hinsbergen, D.J., Kaymakci, N., Spakman, W., Torsvik, T.H., 2010. Reconciling the geological history of western Turkey with plate circuits and mantle tomography. Earth and Planetary Science Letters 297(3), 674–686.

Vanderhaeghe, O., Teyssier, C., Wysoczanski, R., 1999. Structural and geochronologic constraints on the role of partial melting during the formation of the Shuswap metamorphic core complex at the latitude of the Thor-Odin dome, British Columbia. Canadian Journal of Earth Sciences 36(6), 917–943.

Vrolijk, P., van der Pluijm, B.A., 1999. Clay gouge. Journal of Structural Geology 21(8–9), 1039–1048.

Wagner, G.A., van den Haute, P., 1992. Fission-track Dating. Kluwer Academic Publishers, 285 pp.

Wernicke, B.P., Axen, G.J., 1988. On the role of isostasy in the evolution of normal fault systems. Geology 16(9), 848–885.

Wölfler, A., Kurz, W., Danišík, M., Rabitsch, R., 2010. Dating of fault zone activity by apatite fission track and apatite (U-Th)/He thermochronometry: a case study from the Lavanttal fault system (Eastern Alps). Terra Nova 22(4), 274–282.

Wölfler, A., Glotzbach, C., Heineke, C., Nilius, N.-P., Hetzel, R., Hampel, A., Akal, C., Dunkl, I., Christl, M., 2017. Late Cenozoic cooling history of the central Menderes Massif: Timing of the Büyük Menderes detachment and the relative contribution of normal faulting and erosion to rock exhumation. Tectonophysics 717, 585–598.

Wolff, R., Hetzel, R., Dunkl, I., Bröcker, M., Xu, Q., Anczkiewicz, A.A., 2019. High-angle normal faulting at the Tangra Yumco graben (southern Tibet) since ~15 Ma. The Journal of Geology 127(1), 15–36.

Yılmaz, Y., Genç, S.C., Gürer, F., Bozcu, M., Yılmaz, K., Karacık, Z., Altunkaynak, S., Emlas, A., 2000. When did the western Anatolian grabens begin to develop? In: Bozkurt, E., Winchester, J.A., Piper, J.D.A. (Eds.), Tectonics and magmatism in Turkey and surrounding regions. Geological Society of London, Special Publications 173, 353–384.

Zaun, P.E., Wagner, G.A., 1985. Fission-track stability in zircons under geological conditions. Nuclear Tracks 10, 303–307.

Zwingmann, H., Mancktelow, N., 2004. Timing of Alpine fault gouges. Earth and Planetary Science Letters 223(2–4), 415–425.

Zwingmann, H., Mancktelow, N., Antognini, M., Lucchini, R., 2010. Dating of shallow faults – New constraints from the AlpTransit tunnel site (Switzerland). Geology 38(6), 487–490.

Zwingmann, H., Han, R., Ree, J.H., 2011. Cretaceous reactivation of the Deokpori Thrust, Taebaeksan Basin, South Korea, constrained by K-Ar dating of clayey fault gouge. Tectonics 30(5), TC 5015, doi:10.1029/2010TC002829.

5. Along-strike variations in the exhumation pattern of a metamorphic core complex: the central Menderes Massif, Western Turkey

Nils-Peter Nilius[1]*, Christoph Glotzbach[2], Andreas Wölfler[1], Andrea Hampel[1], István´Dunkl[5], Cüneyt Akal[4], Caroline Heineke[3], Ralf Hetzel[3]

[1]Institute of Geology, Leibniz University of Hannover, Callinstraße 30, 30167 Hannover, Germany

[2]Department of Geosciences, University of Tübingen, Wilhelmstraße 56, 72074 Tübingen, Germany

[3]Institute of Geology and Palaeontology, University of Münster, Corrensstraße 24, 48149 Münster, Germany

[4]Dokuz Eylül University, Engineering Faculty, Department of Geological Engineering, Tınaztepe Campus, Buca, 35390 Izmir, Turkey

[5]University of Göttingen, Geoscience Center, Sedimentology and Environment Geology, Goldschmidstraße 3, 37077 Göttingen, Germany

5.1   Introduction

Metamorphic core complexes are common structural features in regions where continental lithosphere is subject to extension. Since their recognition in the Basin and Range Province (western United States) almost 40 years ago (e.g. Coney 1980; Wernicke 1981; Davis et al. 1986), metamorphic core complexes have been described in syn- and post-orogenic settings (e.g. Alps, Himalaya), but also in back-arc (e.g. Aegean province) and passive margin settings. One of the diagnostic features of metamorphic core complexes is that most of the extension is accommodated along a low-angle detachment fault, which exhumes ductilely deformed metamorphic rocks from mid or lower crustal levels in its footwall and is overlain by higher crustal or unmetamorphic units in the hanging wall (Crittenden et al. 1980; Lister et al. 1984; Whitney et al. 2013). Alongside with the wide rift and the narrow rift mode, the formation of metamorphic core complexes is classically treated as one possible mode at which the lithosphere is affected by tectonic thinning (Buck 1991; Brun 1999). A typical evolution of an extensional system in a thickened post-orogenic crust begins with a core complex mode and changes with continued extension over a wide rift mode to a narrow rift mode, which would ultimately result in the exhumation of sub-lithospheric mantle and the formation of an oceanic ridge (Buck 1991). The change from a core complex mode to a wide rift mode is observed in numerical models (e.g. Rosenbaum et al. 2005), but also in nature, e.g. in the northern Aegean by segmentation of the Southern Rhodope Core Complex (Brun & Sokoutis 2018) and the Basin and Range province (Coney 1987). A complex interplay between several factors including rheological stratification, thermal state and strength of the lithosphere, as well as crustal thickness, water content, strain rate and the presence of magma characterizes tectonic extension and controls, which of the three extensional modes develop (e.g. Buck & Karner 2004; Ziegler & Cloetingh 2004; Wijns et al. 2005). The combination of thick brittle crust and/or low viscosity ductile crust in combination with low strain rates are more likely to be accommodated by localized extensional deformation on a detachment fault (Whitney et al. 2013; Kydonakis et al. 2015), whereas high strain rates favour the distributed deformation of the wide rift mode (Brun 1999). The tectonic evolution of areas that are affected by large-scale lithospheric extension are normally described in 2D, which are depth and the direction parallel to the stretching direction. However, several regions like the Rhodope and central Menderes core complexes reveal a rotational pattern of extension, which therefore need a 3D model to explain their tectonic evolution. In this case, the total amount of stretching increases with distance to the rotational pole. Hence, the mechanical conditions of the lithosphere are likely to vary laterally and may result in different modes of extension along strike.

A good natural example to study the exhumation of a core complex with a rotational component is the central Menderes Massif in western Turkey (Figure 1). It forms the central part of the Menderes Massif, which consists of the northern, the central and the southern Menderes Massif. The central Menderes Massif was symmetrically exhumed along two extensional detachment faults; (1) the Gediz detachment dipping to the north with the Gediz graben in its hanging wall and the Bozdağ range in its footwall (Figure 2a,b) and (2) by the Büyük Menderes detachment system, which consists of two southward-dipping detachments, exhuming the Aydın range in their respective footwalls and is delimited to the south by the high-angle normal faults of the Büyük Menderes

graben (Figure 2c). Paleomagnetic data from western Anatolia document that the exhumation of the central Menderes Massif is associated with an anticlockwise block rotation of ~30° between the northern and the southern Menderes Massif (van Hinsbergen et al. 2010). However, this rotational component seems to be in conflict with some observations associated with the formation of the central Menderes Massif. For instance, the oldest sedimentary units and also the deepest part of the Gediz graben are found in its eastern part, implying that the graben formation propagated from east to west (Çiftçi & Bozkurt 2010). Additionally, no large-scale block rotations have been detected by geodetic GPS measurements across western Anatolia (Aktug et al. 2009). Furthermore, in the southern part of the central Menderes Massif, structural and thermochronological data from the Aydın range imply that the exhumation in the footwall of the Büyük Menderes detachment mainly occurred during the middle Miocene and was succeeded by faulting along the Demirhan detachment since 6 Ma, extending the area of the central Menderes Massif affected by low-angle detachment faulting towards the east (Nilius et al. 2019). To explain the aforementioned ambiguous observations and to infer a new advanced exhumation model of the central Menderes Massif that incorporates
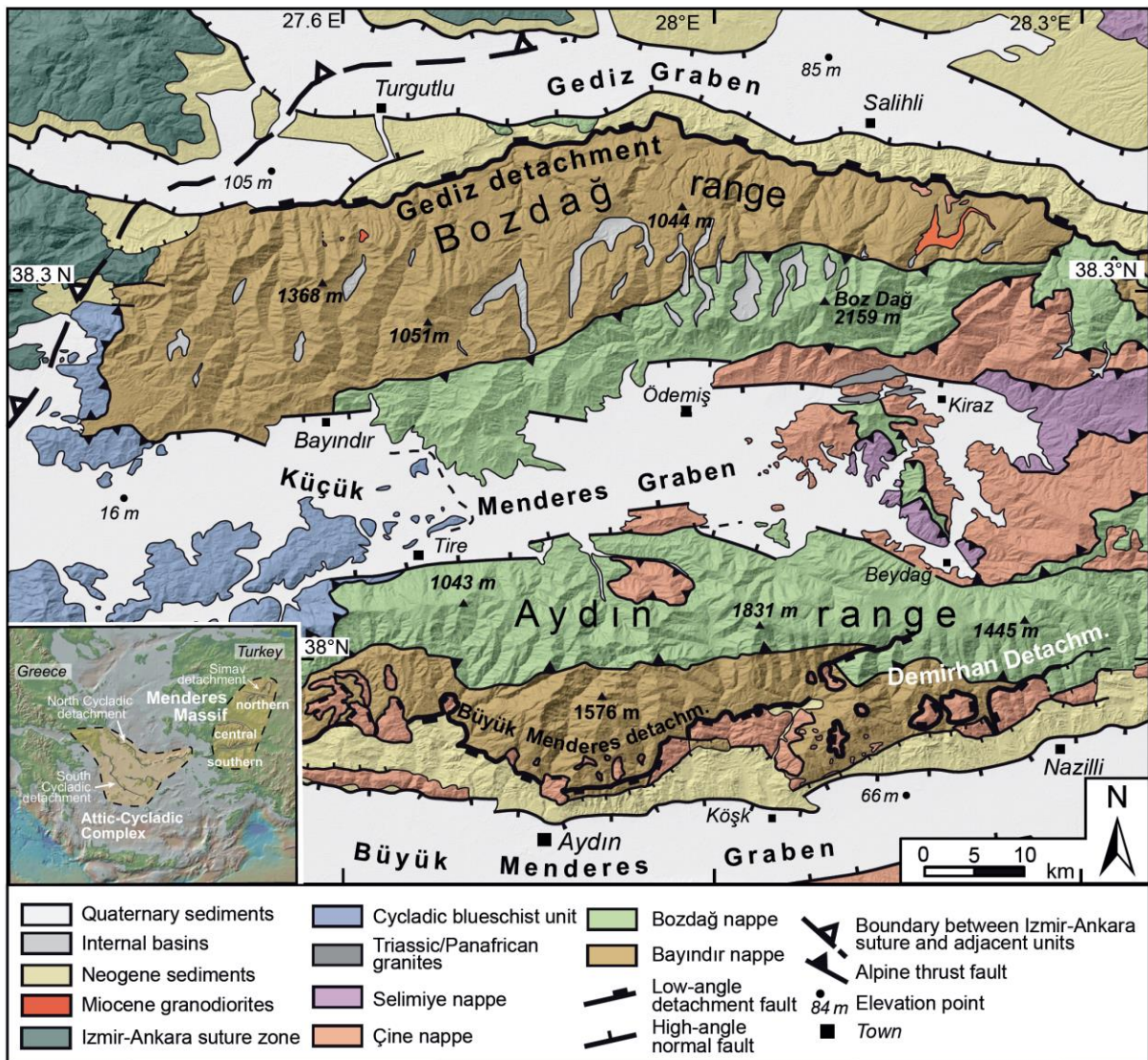
Figure 1: Geological map of the central Menderes Massif. Inset shows the position within the eastern Mediterranean. Based on own field observations and on maps of Wölfler et al. (2017) and Nilius et al. (2019).

geophysical, geomorphological and graben evolution models of the Büyük Menderes and Gediz graben, we present new thermochronological data of the Gediz detachment. These include new apatite and zircon fission track (AFT, ZFT) as well as apatite and zircon (U-Th)/He data (AHe, ZHe), which are used to infer slip rates of the Gediz detachment and the exhumation rates of the Bozdağ range by 1D thermokinematic modelling.

5.2   Geological setting

The nappe stack of the Anatolides was formed by the convergence between Africa and Anatolia since the middle Cretaceous until the Eocene and are exposed in western Turkey (Şengör & Yılmaz 1981; Candan et al. 2005; Kaymakcı et al. 2009; Jolivet & Brun 2010). The structurally deepest units of this nappe stack are exposed in the Menderes Massif and are from bottom to top: The Bayındır nappe, the Bozdağ nappe, the Çine nappe and the Selimiye nappe in the uppermost position (see Fig. 1) (Ring et al. 1999; Gessner et al. 2001c). The Bayındır nappe consists of greenschist to amphibolite facies meta-sediments including phyllites, marbles and quartzites. In contrast to the polymetamorphic history of the overlaying nappes of the Menderes Massif, the Bayındır nappe only experienced alpine metamorphism with maximum temperatures of ~400 °C. The timing of this event is only roughly constrained by a single $^{40}Ar/^{39}Ar$ white mica age of 36 Ma (Lips et al. 2001). During the Alpine orogeny, the Bozdağ nappe was emplaced onto the Bayındır nappe. The Bozdağ nappe mainly consists of metapelite and minor volumes of amphibolite, dolomite, eclogite and granitic intrusions of Triassic age (Koralay et al. 2001, 2011). The metasediments were deposited in a Pan-African foreland basin, which subsequently became incorporated into the Pan-African orogen under amphibolite-facies metamorphic conditions (Candan et al. 2001; Ring et al. 2001; Koralay 2015). The tectonic contact to the overlaying Çine nappe is most probably of pre-Triassic age (Gessner et al. 2001c). Besides minor amounts of paragneiss, eclogite and amphibolite, deformed orthogneisses with Neoproterozoic to early Cambrian intrusion ages are the dominant lithology of the Çine nappe (Bozkurt et al. 1995; Hetzel & Reischmann 1996; Oberhänsli 1997; Loos & Reischmann 1999). Rocks of the Çine nappe experienced a poly-metamorphic history including the Cenozoic alpine Barrovian-type metamorphism between 43 and 34 Ma (Schmidt et al. 2015). The Selimiye nappe is the uppermost nappe of the Menderes Massif and was thrusted over the Çine nappe in the Eocene (Ring et al. 2003). It consists of metapelites, marbles and metabasites of Palaeozoic age (Gessner et al. 2004; Regnier et al. 2003). To the north and northwest, the Menderes Massif is overlain by units of the Izmir-Ankara Suture Zone, which comprises remnants of the Neothethyan. These units experienced high-pressure metamorphism during Alpine subduction and accretion below the Sakarya microcontinent (Okay & Tüyüz 1999). After the cessation of the convergent tectonic regime in the late Eocene, the change to an extensional regime led to low-angle normal faulting and the formation of E-W striking graben systems.

The Gediz graben separates the northern Menderes Massif from the central Menderes Massif, which in turn is separated from the southern Menderes Massif to the south by the Büyük Menderes graben (Fig 1). The extensional history of the Menderes Massif can be roughly divided into two phases. During the first phase, the northern Menderes Massif was exhumed in the footwall of the top-to-the-north movement of the Simav detachment, which was active between the late

Oligocene and early Miocene (Gessner et al. 2001a; Işık & Tekeli 2001; Işik et al. 2004; Ring & Collins 2005; Thomson & Ring 2006; Erkül 2009; Hasözbek et al. 2011; Cenki-Tok et al. 2016). The second phase is attributed to the exhumation of the central Menderes Massif along three extensional detachments (Fig. 1): the northward-dipping Gediz detachment in the north (also called Alaşehir or Kuzey detachment) (Hetzel et al. 1995a, b; Hetzel et al. 1998; Gessner et al. 2001a; Seyitoğlu et al. 2002; Bozkurt & Sözbilir 2004; Buscher et al. 2013) and the southward-dipping Büyük Menderes detachment system in the south, which includes the Büyük Menderes detachment (also described as Güney detachment) (Emre & Sözbilir 1997; Bozkurt 2000) and the associated Demirhan detachment (Nilius et al. 2019). The Gediz detachment and the Büyük Menderes detachment system are exposed along the Bozdağ and Aydın mountain ranges, respectively, and are separated by the Küçük Menderes Graben (Fig. 1). In the footwall of the detachments, the Bayındır nappe, as the structurally deepest unit of the alpine nappe pile, constitutes the largest part of the cataclastically overprinted footwalls, which are discordantly overlain by Neogene syn-extensional sediments and klippen of Çine nappe augengneiss (Fig. 1) (Cohen et al. 1995; Sen & Seyitoğlu 2009; Çiftçi & Bozkurt 2010). In contrast to the Aydın range, the Bozdağ range comprises with the Turgutlu and Salihli granodiorites two intrusions in the footwall of the Gediz detachment. Both intrusions show a metamorphic grading towards the detachment surface from an isotropic granodiorite to a proto-mylonite, which in turn is overprinted to a cataclasite, implying that the Salihli and Turgutlu granodiorites reflect syntectonic intrusions (Hetzel et al. 1995a; Catlos et al. 2011). The Turgutlu granodiorite was dated using Th-Pb *in situ* ion microprobe analysis of monazites yielding an age range of 19 ± 5 to 11.5 ± 0.8 Ma (Catlos et al. 2010). U-Pb analyses of monazites yielded an intrusion age of 16.1 ± 0.2 Ma (Glodny & Hetzel 2007) and $^{40}Ar/^{39}Ar$ dating of biotite was interpreted to reflect a cooling age of 13.1 ± 0.2 Ma (Hetzel et al. 1995a). The intrusion age of the Salihli granodiorite was constrained to be at 16 Ma (Hetzel et al. 1995a; Glodny & Hetzel 2007; Catlos et al. 2010). Recent U-(Th)-Pb dating of pristine titanite from undeformed parts of the Salihli granodiorite yielded a protolith age of 16–17 Ma, whereas dating of recrystallised titanite from mylonitic parts of the granodiorite yield ages of 14–15 Ma, which is proposed to be the onset of ductile shearing of the Gediz detachment (Rossetti et al. 2017). Subsequent cooling and exhumation of the footwall of the Gediz detachment is documented by $^{40}Ar/^{39}Ar$ ages from biotite yielding an age of ~12 Ma (Hetzel et al 1995a). Constraints for the final exhumation of the Gediz detachment footwall are available in the eastern part of the footwall, where fission track and U-Th/He ages of zircon and apatite reveal fast cooling and exhumation in the Pliocene (Gessner et al. 2001a; Ring et al. 2003; Buscher et al. 2013). Faulting along the Gediz detachment was followed by the onset of high-angle normal faulting at the southern margin of the modern Gediz graben in the late Pliocene (Oner & Dilek 2011; Buscher et al. 2013).

The Büyük Menderes detachment was first mapped by Candan et al. (1992) and later described by Emre & Sözbilir (1997) as an extensional detachment fault with a top-to-the south sense of movement. It is exposed along the southern flank of the Aydın range and dips 5° to 20° to the south. Mapping of structures related to extensional deformation of the Aydın range showed that the extension of the eastern part of the Aydın range was accommodated by the Demirhan detachment, which is in a structurally higher position than the Büyük Menderes detachment (Nilius et al. 2019).

First indications of faulting along the Büyük Menderes detachment are documented by early Miocene K-Ar ages of ~22 to 20 Ma (Hetzel et al. 2013). Additional low temperature thermochronological data of Wölfler et al. (2017) and Nilius et al. (2019), which complement the few AFT ages of Gessner et al. (2001a) and Ring et al. (2003), imply that the Büyük Menderes detachment contributed to the first phase of increased cooling and exhumation in the middle Miocene, whereas most of the second phase of high cooling rates can be attributed to tectonic denudation along the Demirhan detachment in the latest Miocene and Pliocene. The exhumation rates for the footwalls of the Büyük Menderes and the Demirhan detachments, constrained by 1-dimensional thermokinematic modelling, occurred at 0.6–0.9 and 0.5 km/Ma, respectively (Nilius et al. 2019).
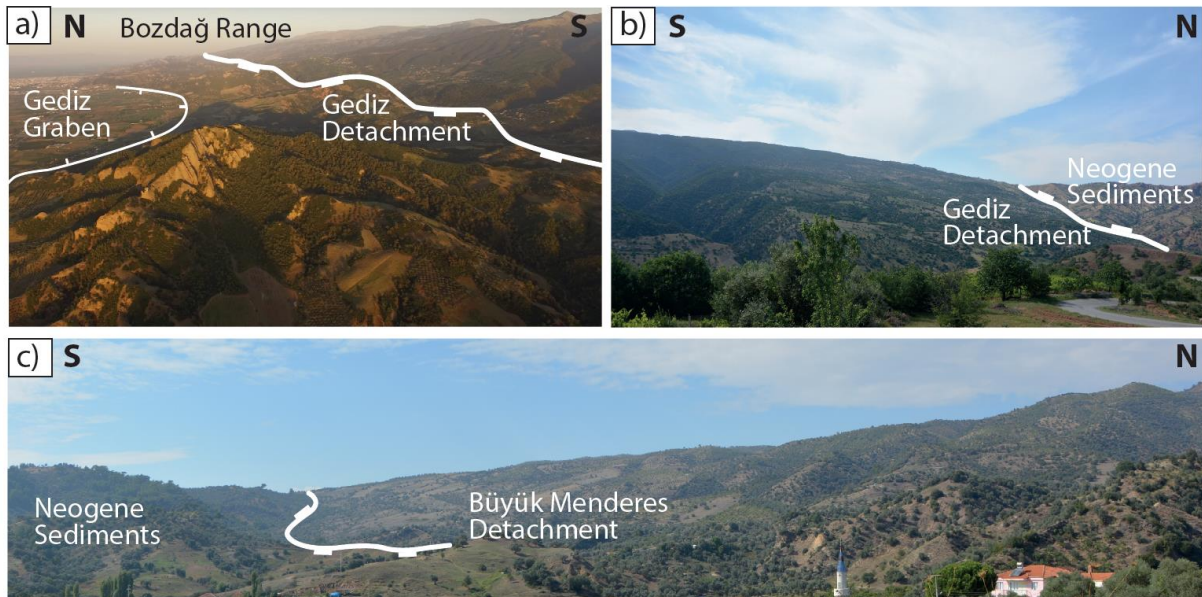
Figure 2: a) Aerial view towards the east, showing uplifted Neogene sediments in the vicinity of the ancient city of Sardis in the foreground, covering the cataclastic footwall of the Gediz detachment (Photo from the Archaeological Exploration of Sardis/President and Fellows of Harvard College). b) North-dipping Gediz detachment with steep gorges cutting through the weathering-resistant cataclasites of the Gediz detachment footwall. **c)** Exposed footwall of the Büyük Menderes detachment, dipping with ~20° to the south at Beyköy.

5.3 Sampling strategy and methods

In this study, we present new thermochronological data of 84 samples. The apatite and zircon (U-Th)/He data of samples 11M1 to 11M15 were partly published in Buscher et al. (2013) and are here complemented with new apatite and zircon fission track data. Among the 84 samples, 10 samples were used for AHe analysis, 23 samples were used for AFT analysis, 17 samples for ZHe analysis, and 19 samples were used for ZFT analysis (Table 1). With the intention to constrain the cooling in the footwall of the Gediz detachment by tectonic denudation, two N–S transects of footwall samples were taken parallel to the direction of extension. Representative samples with the information from ZFT, ZHe, AFT and AHe systems are used to constrain the sample's most reliable time-temperature path by thermal history inversion modelling with the HeFTy software v. 1.9.3 (Ketcham 2005). Furthermore, exhumation rates of individual samples are inferred by a 1D thermokinematik modelling approach, which is based on the PECUBE code of Braun (2003) and is described in more detail further below.

5.3.1   *Zircon and apatite fission track analysis*

Fission tracks in U-bearing minerals or glasses represent the damage trails formed by the spontaneous fission of ^{238}U into two recoiling nuclei (Price & Walker 1963). Typical closure temperatures for the ZFT method are ~240 °C and for the AFT method ~110 °C, even though the exact closure temperature of each system may vary by different factors such as the cooling rate, mineral chemistry and radiation damage (e.g. Wagner & van den Haute 1992; Gleadow & Duddy 1981; Rahn et al. 2004; Ketcham et al. 2007). The temperature range from annealing to total resetting of fission tracks are ~190 to ~380 °C in zircons and ~60 to ~120 °C for apatite (Green et al. 1986; Wagner & van den Haute 1992; Rahn et al. 2004).

After conventional rock crushing, sieving and density separation procedures with a Wilfley table, magnetic and heavy liquid separation techniques were applied for zircon and apatite separation. The zircon separates were embedded in PDA TeflonTM, whereas apatite grains were embedded in epoxy mounts before grounding and polishing. Zircon mounts were etched in a KOH-NaOH eutectic melt at 215 °C (Zaun & Wagner 1985) and apatites were etched with 5 M HNO$_3$ for 20 seconds at 21 °C. The external detector method (Gleadow 1981) with uranium-free muscovite sheets was used to measure the U content. We used Durango apatite and Fish Canyon zircon age standards for the zeta calibration approach (e.g. Naeser 1978; Hurford & Green 1983). The required irradiation of the samples with thermal neutrons was performed at the FRM-II reactor facility in Garching (Technical University Munich, Germany). The neutron fluence was analysed with IRMM-540R and IRMM-541 dosimeter glasses. The counting of fission-tracks was carried out with an Olympus BX-51 microscope with 1000x magnification at the Institute of Geology in Hannover. The mean diameter of etch figures on prismatic surfaces of apatite, parallel to the crystallographic c-axis, was measured and reported as Dpar value, which mimics the annealing kinetics of apatite (Burtner et al. 1994). Fission-track ages were calculated with the TRACKKEY software version 4.2 (Dunkl 2002) and are reported in Tables 2 and 3 with 1σ standard errors.

5.3.2   *Zircon and apatite U-Th/He analysis*

The accumulation of radiogenic He in the crystal lattice of ^{238}U, ^{235}U, ^{232}Th, and ^{147}Sm bearing minerals, like zircon and apatite, is measured by (U-Th)/He thermochronology (Zeitler et al. 1987; Lippolt et al. 1994; Farley 2002; Reiners et al. 2003). Radiogenic He becomes mostly trapped in the crystal lattice below a specific temperature, which is typically ~40 to 60 °C for apatite and 120 to 130 °C for zircon. The temperature at which all radiogenic He is lost due to thermal diffusion is constrained to be 80 °C for apatites and 190 °C for zircon (Wolf et al. 1996, 1998; Farley 2000; Reiners et al. 2003; Guenthner et al. 2013). The temperature range between these minima and maxima temperatures is described as the partial retention zone (Ehlers & Farley 2003; Reiners et al. 2005; Reiners & Brandon 2006; Flowers et al. 2007; Herman et al. 2007; Guenthner et al. 2013). The effective closure temperature is given under the premise, that the sample experienced a steady and monotonic cooling history. Furthermore, the closure temperature, which is typically ~70 °C for apatite and 180 °C for zircon, mainly depends on geometry and size of the crystal, the rate at which the sample cooled and the radiation damage (Wolf et al. 1996, 1998; Farley 2000; Reiners & Brandon

2006). Radiation damage is measured by the concentration of effective U (eU=U+0.235*Th) as it influences the diffusion of He in apatites and zircons. Helium diffusivity is higher in zircon and apatite if they experienced little radiation damage. However, this trend is reversed if the amount of radiation damage reaches a threshold value at which the damage zone interconnection causes effective diffusion pathways for radiogenic He (Flowers et al. 2009; Guenthner et al. 2013).

We employed (U-Th)/He dating on samples containing apatites and zircons of sufficient quality (Table 1). Inclusion and crack free apatite and zircon crystals were hand-picked using a stereo- and polarizing microscope and selected under 200x magnification following the selection criteria of Farley (2002) and Reiners (2005). The dimensions of the selected crystals were measured to determine alpha-ejection correction factors (Farley et al. 1996). Single crystals were loaded into pre-cleaned Pt tubes for He analysis carried out at the GÖochron Laboratory at the University of Göttingen (Germany) and one (U-Th)/He zircon analysis at the University of Tübingen (Sample 17M104). At the GÖochron Laboratory extraction of He from crystals was performed by heating the encapsulated grains at vacuum conditions using an IR laser. The extracted gas was purified by a SAES Ti-Zr getter and the He content was measured by a Hiden Hal-3F/PIC triple-filter quadrupole mass spectrometer. For measurements of the alpha-emitting elements U, Th, and Sm, the crystals were dissolved and spiked with calibrated ^{233}U, ^{230}Th, and ^{149}Sm solutions. Zircons were dissolved in Teflon bombs with 48 % HF and 65 % HNO_3 at 220 °C for five days. Apatites were dissolved in 2 % ultrapure HNO_3 (+0.05% HF) in an ultrasonic bath. The actinide and Sm concentrations at the GÖochron Laboratory were measured by inductively coupled plasma mass spectrometry with a Perkin Elmer Elan DRC II system equipped with an APEX micro-flow nebulizer using isotope dilution. To measure the actinide and Sm concentrations of sample 17M104, the Tübingen laboratory uses a ThermoFisher iCap quadrupole inductively coupled plasma mass spectrometer. Errors for the single-grain ZHe and AHe analyses are attributed to uncertainties in the He, U, Th, and Sm measurements and the estimated uncertainty of the Ft-correction factor. The zircon and apatite (U-Th)/He ages were calculated as unweighted mean ages from the single-grain ages of each sample and are reported in Tables 4 and 5 with an uncertainty of 1σ standard errors.

5.3.3   *Thermokinematic modelling*

1D thermokinematic modelling was used to constrain the exhumation history of the Bozdağ range. The model accounts for vertical heat transport through the Earth's crust by conduction and advection. The code is based on a modified version of *Pecube* (Braun 2003, 2012), which solves the advective – conductive heat transfer equation with implicit time stepping and uses a two-step (sampling and appraisal stages of Sambridge (1999a) and Sambridge (1999b), respectively) neighbourhood algorithm inversion. The heat production in the thermal model is 0.8 µWm^{-3} and the thermal diffusivity is 31.5 km^2/Ma. The upper model boundary corresponds to the present-day sample elevation and surface temperature (calculated with a mean annual temperature of 20 °C at sea level and an atmospheric lapse rate of 6.5 C°/km). The lower model boundary has a fixed temperature of 750 °C, which is far above the temperature range of the modelled ^{40}Ar/^{39}Ar - biotite as well as zircon and apatite (U-Th)/He and fission track thermochronometers. As this lower

boundary condition is fixed, the thickness of the model depends on the geothermal gradient. To prevent an over interpretation of the data and to choose an appropriate dimensionality of the model, we follow the procedure of Glotzbach et al. (2011). Each sample is tested for a linear-, a two-step, three-step or four-step (inversions 1.1, 1.2, 1.3 and 1.4, respectively) exhumation history (Table 6). Adding exhumation steps results in a higher complexity of the model and increases its likelihood to fit the observed data, but also increases its uncertainty. Hence, relying solely on the loglikelihood or another misfit function as a selection criterion for the appropriate model setup, would imply a preference for the model with the highest complexity. Therefore, we use the Bayesian information criterion (BIC), which provides a measure of the ratio between the likelihood (fitting) and the model complexity (Schwarz 1978):

$$BIC = -2 \cdot ln(L) + k \cdot ln(n)$$

whereby *ln(L)* denotes the log-likelihood of the model, and *k* and *n* are the numbers of free parameters and observations, respectively. The lowest *BIC* value indicates the preferred model setup. Depending on the number of time/exhumation steps, we model 5,000 to 49,000 thermal histories, over the last 15 Ma for footwall samples from the Gediz detachment, and the same number of thermal histories over the last 25 Ma for samples from the hanging wall. Free parameters are the geothermal gradient (30-50 °C/km), the exhumation rates (0-2.0 km/Ma) and the time at which the exhumation rate changes (in the period between 0-15 Ma and 0-25 Ma for the footwall and hanging wall, respectively). The thermokinematic model traces the cooling history of rocks based on the modelled exhumation paths and calculates thermochronological ages. These include the annealing algorithms of Ketcham et al. (2007) and Tagami et al. (1998) for AFT and ZFT, the He-diffusion algorithms of Flowers et al. (2009) and Guenthner et al. (2013) for AHe and ZHe, respectively, and the kinetic parameters for Ar in biotite of Grove and Harrison (1996). The probability of each free input parameter is derived from the appraisal stage of the neighbourhood inversion (Sambridge 1999b) and is visualised as 1D and 2D marginal probability density functions (PDFs). Probable exhumation paths are visualised as synoptic 2D marginal PDFs, showing re-sampled exhumation rates and the time at which exhumation rates changed were linked to visualize the exhumation rate changing with time. For details on the modelling approach we refer to Glotzbach et al. (2011) and recent studies of Schultz et al. (2017), Thiede & Ehlers (2013) and Whipp et al. (2007), which also used comparable 1D modelling approaches to infer exhumation rates from low-temperature thermochronology data.

Table 1: *Location, lithology, and structural position of samples for low-temperature thermochronology*

Sample	Latitude (°N) (WGS 84)	Longitude (°E) (WGS 84)	Elevation (m)	Lithology	Structural position	Thermochron. applied
JTB01	38.41910	28.21510	560	Augen gneiss	Çine nappe, hanging wall	ZFT
11M1	38.48050	27.81050	190	Schist	Çine nappe, hanging wall	AHe, AFT, ZHe, ZFT
11M2	38.38040	28.18260	1550	Two-mica schist	Bozdag nappe, footwall	AFT, ZFT
11M3	38.38120	28.18500	1482	Mylonitic granodiorite	Salihli granodiorite, footwall	AFT, ZFT
11M4	38.37750	28.18060	1636	Two-mica schist	Bayındır nappe, footwall	AFT
11M5	38.39630	28.18980	1201	Mylonitic granodiorite	Salihli granodiorite, footwall	AFT, ZFT
11M6	38.40730	28.19680	962	Mylonitic granodiorite	Salihli granodiorite, footwall	AFT, ZFT
11M7	38.42100	28.19640	708	Augen gneiss	Çine nappe, hanging wall	ZFT
11M8	38.42050	28.20740	560	Cataclasite	Gediz detachment	AFT
11M9	38.23500	28.58300	332	Augen gneiss	Çine nappe	AHe, AFT, ZHe,
11M11	38.29870	28.16930	636	Mica schist	Bozdağ nappe, footwall	AFT
11M12	38.33880	28.10090	1748	Mica schist	Bozdağ nappe, footwall	AFT
11M13	38.36670	28.18030	1540	Mylonitic granodiorite	Salihli granodiorite, footwall	ZFT
11M14	38.33260	28.16100	1324	Mica schist	Bozdağ nappe, footwall	AFT
11M15	38.31190	28.16700	982	Mica schist	Bozdağ nappe, footwall	AFT, ZFT
14M16	38.38287	27.67560	758	Granodiorite	Turgutlu granodiorite, footwall	AHe, AFT, ZHe, ZFT
14M17	38.40835	27.67015	238	Metatrachyte	Bayındır nappe, footwall	AHe, AFT, ZHe, ZFT
14M18	38.46559	27.81971	137	Paragneiss	Bayındır nappe, footwall	AHe, AFT, ZHe, ZFT
14M19	38.43243	27.83549	556	Mica schist	Bayındır nappe, footwall	AHe, AFT, ZHe, ZFT
14M20	38.46713	27.85341	185	Mylonite	Gediz detachment, footwall	AHe, AFT
14M21	38.40462	28.22067	773	Cataclasite	Gediz detachment	ZHe
14M22	38.40462	28.22067	1134	Mica schist	Bozdağ nappe, footwall	AHe, AFT, ZHe
15M63	38.38412	27.53777	270	Mica schist	Bayındır nappe, footwall	ZHe, ZFT
15M64	38.34749	27.54003	290	Mica schist	Bayındır nappe, footwall	AHe, ZHe
15M65	38.36472	27.53954	350	Paragneiss	Bayındır nappe, footwall	AHe, AFT, ZHe, ZFT
15M66	38.34971	27.54383	450	Paragneiss	Bayındır nappe, footwall	ZFT
15M67	38.33530	27.53455	554	Paragneiss	Bayındır nappe, footwall	ZHe
15M68	38.31144	27.52556	653	Subarkose	Bayındır nappe, footwall	ZHe
15M69	38.29848	27.54302	677	Lamprophyre	Bayındır nappe, footwall	AFT
15M70	38.27785	27.56981	290	Lamprophyre	Bayındır nappe, footwall	AFT
15M71	38.27781	27.57014	298	Paragneiss	Bayındır nappe, footwall	ZHe, ZFT
15M84	38.43098	27.73627	220	Mica schist	Bayındır nappe, footwall	AFT, ZFT
15M85	38.430043	27.769126	481	Miocene Sediments	Conglomerate, hanging wall	ZFT
16M98	38.11882	27.96952	211	Mica schist	Küyüc Menderes Graben	AFT, ZHe
17M104	38.32385	28.10209	2150	Mica schist	Bozdağ nappe, footwall	ZHe

5.4   Results

5.4.1   *Results from fission track and U-Th/He analysis*

The obtained dataset (Table 1) comprises 10 AHe ages (Table 2), 17 Zhe ages (Table 3), 23 AFT ages (Table 4) and 19 ZFT ages (Table 5). The AHe ages range between 3.2 ± 2.3 and 22.7 ± 5.0 Ma and the ZHe ages between 3.0 ± 0.3 and 23.4 ± 1.3 Ma. The AFT dataset comprises ages between 2.1 ± 0.3 and 22.3 ± 4.4 Ma and the ZFT dataset ages from 3.8 ± 0.6 to 59.0 ± 5.3 Ma. The cooling ages reveal two individual age groups. One group shows late middle Miocene and latest Miocene/Pliocene cooling ages and the second group is characterized by a wide range of cooling ages spanning from late Oligocene/early Miocene to Pliocene ages. The early Miocene cooling ages are either attributed to samples from the hanging wall of the Gediz detachment or to samples from areas that were not affected by tectonic denudation of the Gediz detachment, e.g. samples from the Küçük Menderes graben or the easternmost part of the Bozdağ range (sample 11M9). This sample group includes sample 10JTB01 yielding a ZFT age of 59 ± 5.3 Ma, which is by far the oldest thermochronological age in the central Menderes Massif.

The thermochronological profiles in the footwall of the Gediz detachment (Figure 4) show decreasing ages in the direction of the tectonic transport, but also reveal that the western part of the footwall yields older cooling ages. Thermochronological data of the western profile comprises a ZFT age of 35.5 ± 3.4 Ma, the oldest footwall ZFT age (sample 15M71) in the central Menderes Massif. Towards the north, closer to the Gediz detachment, three samples show consistent ZFT ages of ~17 Ma. The ZHe ages along the western thermochronological transect reveal a continuous decrease in ZHe ages from 13 Ma in the south to 10 Ma in the north. The youngest cooling ages in this area originate from AHe ages of ~8 Ma.

Towards the east, the samples from the Turgutlu granodiorite (14M16, 14M17), show ZFT cooling ages of ~15 Ma, which overlap within error with the intrusion age of the Turgutlu granodiorite at 16.2 Ma. However, the ZHe, AFT and AHe cooling ages of 14M16 and 14M17 cluster at ~7 Ma and hence, postdate the ages observed in the western thermochronological profile by ~3 – 5 Ma. The ZFT ages of samples 14M18 to 14M20 range from 7 to 10 Ma, respectively, and reveal cooling ages of the ZHe, AFT and AHe systems of ~5 Ma. Complementing the U-Th/He data published by Buscher et al. (2013) our new ZFT and AFT data in the eastern part of the Gediz detachment, in the region NE of the Bozdağ, reveal consistently Pliocene cooling ages close to the hanging wall. In the structurally lower parts of the Gediz detachment, the samples comprise the youngest ZFT cooling ages of the Menderes Massif yielding 5.0 to 3.8 Ma. Further to the south, middle Miocene ZHe ages (e.g. 17M104) occur together with late Miocene AFT and AHe ages (14M22/12).

5.4.2   *Results from thermokinematic modelling*

To evaluate the timing and extent of exhumation of the Bozdağ range, four samples from the footwall and one sample from the hanging wall of the Gediz detachment were modelled to obtain their thermokinematic histories (Table 6). To maximize the temporal resolution of the thermokinematic models we used samples with data of at least four thermochronometers. As shown in Table 6, samples 17M104, 11M15, 15M65 and 11M7 include ZFT, ZHe, AFT and AHe systems, whereas samples 11M6 and 14M16 additionally include ^{40}Ar/^{39}Ar–biotite ages of Hetzel et al. (1995a). This approach is justified as sample 14M16 originates from the same sample site as sample 93T18 providing ^{40}Ar/^{39}Ar ages and sample 11M6 originates from the close proximity of sample site of 93T55. The ^{40}Ar/^{39}Ar ages were interpreted as cooling ages as they originate from parts of the Turgutlu and Salihli intrusions, which were not affected by ductile deformation, and additionally yield ^{40}Ar/^{39}Ar ages, which are ~3 Ma younger than the constrained intrusion ages (Hetzel et al. 1995a).

The exhumation history of the westernmost part of the Gediz detachment is revealed by sample 15M65 and is best described with a three-step model (Table 6, inversion 1.3). The model results show exhumation rates of ~0.6 km/Ma in the middle Miocene, which then change to a relatively short intermittent phase of higher exhumation rates of 0.8 km/Ma between ~7.5 to ~6.7 Ma, followed by lower exhumation rates until present-day. The exhumation rates and the time steps at which the exhumation rate changes comprise relatively large errors and have to be interpreted with caution. However, the fundamental trend with moderate exhumation rates since the middle Miocene and a short phase of higher exhumation rates at ~8 Ma appears to be reliable. Further to the east, sample 14M16 is used to investigate the exhumation history of the western part of the Gediz detachment, south of Turgutlu (Figure 4). The exhumation history of sample 14M16 is best described by using four individual exhumation steps (inversion 1.4). The first change from a moderate exhumation rate of ~0.5 km/Ma (Figure 5a) to a short-lived high exhumation rate of 0.8 to 1.4 km/Ma occurred between ~7 and 5 Ma, and is finally followed by low exhumation rates of 0.2 km/Ma since 5 Ma.

The exhumation history of the easternmost part of the Gediz detachment and its hanging wall units is revealed by modelling of samples 11M5, 11M6 and 11M7. Sample 11M6 is the northernmost footwall sample along the thermochronological profile SE of Salihli, and hence resembles the youngest phase of faulting along the Gediz detachment. The observed data is best reproduced by using four individual exhumation phases (Table 6, inversion 1.4). The model implies that a change from slow exhumation rates of <0.3 km/Ma to high exhumation rates of ~1.5 km/Ma (Figure 5b) occurred between 6 to 5 Ma (Figure 4, 11M6). Sample 11M5 is located further south compared to sample 11M6 and occupies a structurally higher position in the footwall than sample 11M6. The lowest BIC value achieved inversion 1.3 with three individual exhumation steps. The change from relatively low to high exhumation rates also occurs at ~6 Ma, at which the exhumation changes from ~0.3 to 0.8 km/Ma. The exhumation rate of 0.8 km/Ma lasts for ~1.5 Ma until a third exhumation step at ~4.5 Ma implies a further increase in exhumation rate to 1.2 km/Ma. The exhumation history of a structurally higher part of the Gediz detachment is derived by simultaneous modelling of samples from an age elevation profile. Sample 17M104 is from the top of the Bozdağ

mountain (2150 m NN) and 11M15 is sampled from ~1100 m below (982 m NN). Considering the NNE-SSW directed faulting along the Gediz detachment, both samples represent the same structural level of the footwall, as 11M15 is situated just to the east of 17M104. The resulting two-step exhumation model depicted in Figure 4 shows that poorly constrained exhumation rates of >0.4 km/Ma during the middle Miocene are followed by slower exhumation rates of 0.3 km/Ma since the late Miocene. Sample 11M7 originates from the hanging wall of the Gediz detachment. A three step exhumation history gave the lowest BIC value and is used for the interpretation. A change from higher exhumation rates to lower exhumation rates of <0.3 km/My occurred at ~20 Ma. This phase of low exhumation rates changes at ~1 Ma, when higher exhumation rates of 0.3 to 0.5 km/Ma are predicted by the model (Figure 5c).
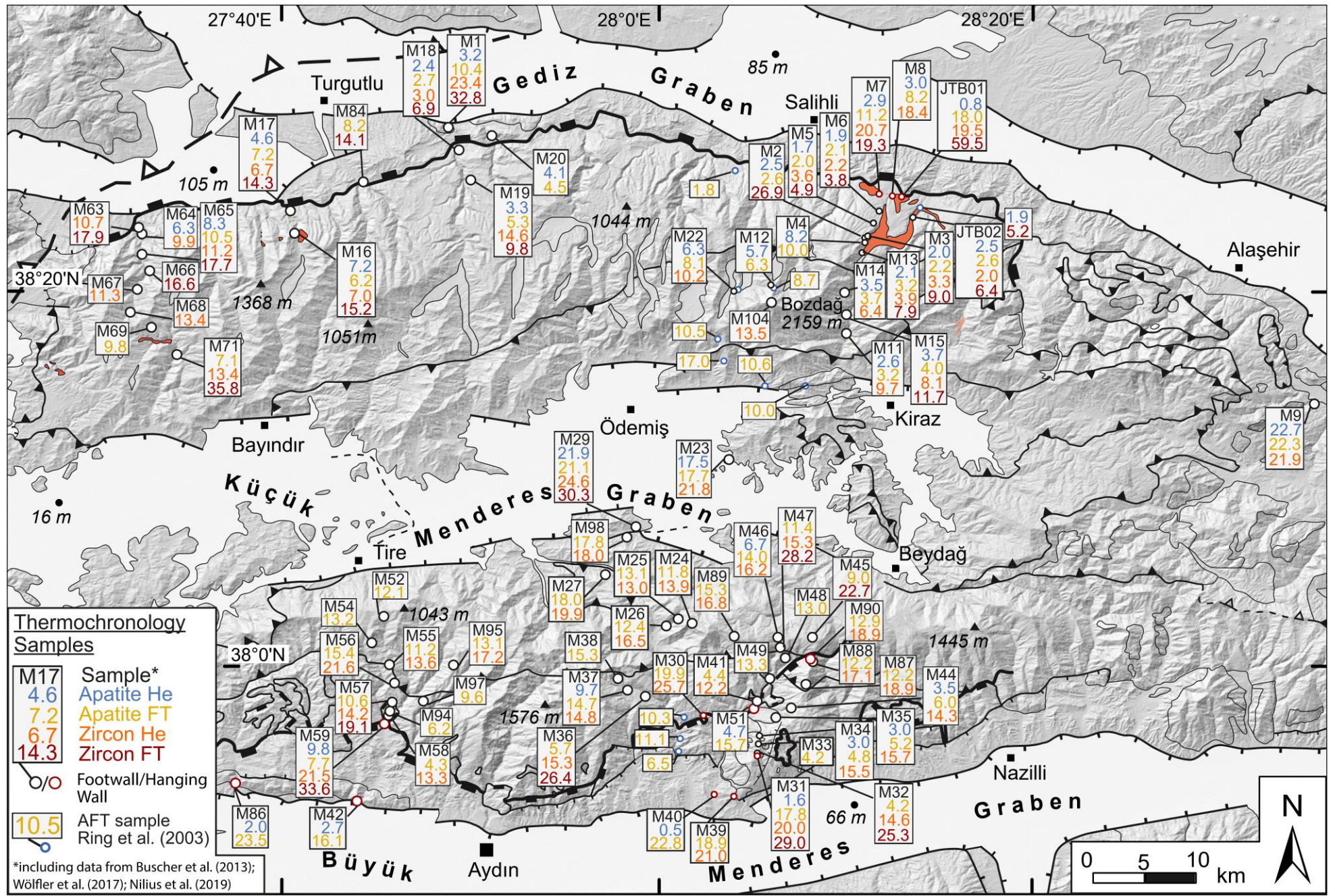
Figure 3: Shaded relief image of the central Menderes Massif showing the thermochronological ages obtained in this study together with data from Ring et al. (2003); Buscher et al. (2013); Wölfler et al. (2017) and Nilius et al. (2019). Note that the first two digits of the sample numbers are omitted for clarity.

Table 2. *Results of apatite U-Th/He analyses*

Sample	Aliq.	He Vol. (10⁻⁹ cm³)	He 1σ (%)	²³⁸U Mass (ng)	²³⁸U 1σ (%)	²³⁸U Conc. (ppm)	²³²Th Mass (ng)	²³²Th 1σ (%)	²³²Th Conc. (ppm)	Th/U ratio	Sm Mass (ng)	Sm 1σ (%)	Sm Conc. (ppm)	Ejection correction	Uncorr. age (Ma)	FT-corr. age (Ma)	2σ (Ma)	Sample age (Ma)	1 s.e. (Ma)
11M1	#1	0.000	76.5	0.001	102.4	0.4	0.005	5.3	1.57	3.51	0.031	36.7	9.88	0.69	*1.08*	**1.5**	2.8	**3.2**	2.3
	#2	0.001	57.2	0.001	208.4	0.3	0.004	5.8	1.60	5.51	0.009	34.8	3.87	0.70	*3.42*	**4.9**	9.8		
11M9	#1	0.008	11.0	0.003	45.1	1.7	0.002	6.6	0.85	0.50	0.037	22.5	20.55	0.66	*18.5*	**27.9**	21.0	**24.4**	2.7
	#2	0.020	7.3	0.007	17.2	2.0	0.005	5.4	1.32	0.65	0.065	21.5	18.68	0.74	*19.5*	**26.2**	8.3		
	#3	0.009	10.5	0.004	33.6	1.8	0.006	4.9	2.76	1.54	0.045	21.4	20.65	0.71	*13.7*	**19.2**	9.6		
14M16	#1	0.276	1.3	0.253	1.8	45.4	0.324	2.4	58.3	1.28	0.900	6.1	162	0.78	*6.8*	**8.7**	0.7	**7.2**	1.5
	#2	0.024	3.5	0.041	2.2	13.6	0.009	3.5	2.9	0.21	0.424	6.5	142	0.75	*4.3*	**5.7**	0.6		
14M17	#1	0.035	3.0	0.042	2.2	10.5	0.086	2.5	21.7	2.06	1.416	5.8	358	0.74	*3.9*	**5.3**	0.6	**4.6**	0.7
	#2	0.025	3.7	0.042	2.2	13.7	0.071	2.5	22.9	1.68	0.960	6.0	310	0.79	*3.1*	**3.9**	0.4		
14M18	#1	0.004	8.5	0.006	10.2	3.2	0.000	77.2	0.2	0.07	0.039	13.8	22	0.70	*5.0*	**7.2**	1.9	**2.4**	0.5
	#3	0.004	8.2	0.016	3.9	3.4	0.012	3.2	2.6	0.78	0.110	9.1	24	0.73	*1.8*	**2.4**	0.5		
14M19	#3	0.001	11.0	0.003	16.7	1.7	0.004	4.0	2.3	1.35	0.095	8.2	52	0.70	*2.3*	**3.3**	1.0	**3.3**	1.0
14M20	#1	0.002	10.6	0.001	48.4	0.8	0.013	3.2	9.7	11.55	0.061	9.5	45	0.69	*2.7*	**3.9**	1.3	**4.1**	1.2
	#2	0.001	10.6	0.002	31.4	1.8	0.001	23.8	0.9	0.50	0.050	10.6	50	0.67	*3.9*	**5.9**	3.0		
14M22	#2	0.039	2.7	0.057	2.0	6.5	0.010	3.4	1.2	0.18	0.895	5.9	102	0.78	*4.9*	**6.3**	0.6	**6.3**	0.6
15M64	#4	0.006	6.7	0.011	16.1	3.4	0.001	331.2	0.3	0.08	0.145	2.2	45	0.62	*3.85*	**6.3**	2.2	**6.3**	2.2
15M65	#3	0.003	8.7	0.003	33.9	2.5	0.004	4.2	3.5	1.40	0.012	29.0	10	0.70	*5.86*	**8.3**	4.3	**8.3**	4.3

Ejection correction (Ft): correction factor for alpha-ejection (according to Farley et al. (1996)). Uncertainty of the single-grain ages includes both the analytical uncertainty and the estimated uncertainty of the ejection correction. Sample age is the unweighted average age of all Ft-corrected (U-Th)/He ages (see: standard error). Results from aliquots marked with asterisk are not considered in the calculation of the sample age.

Table3: *Results of zircon (U-Th)/He-analyses*

Sample	Aliq.	He Vol. (10⁻⁹ cm³)	1σ (%)	²³⁸U Mass (ng)	1σ (%)	Conc. (ppm)	²³²Th Mass (ng)	1σ (%)	Conc. (ppm)	Th/U ratio	Sm Mass (ng)	1σ (%)	Conc. (ppm)	Ejection correction	Uncorr. age (Ma)	FT-corr. age (Ma)	2σ (Ma)	Sample age (Ma)	1 s.e. (Ma)
11M1	#1	4.682	1.7	2.222	1.8	442.4	0.452	2.4	90.1	0.20	0.025	12.8	5	0.77	*16.6*	**21.3**	1.7		
11M1	#2	1.863	1.8	0.743	1.8	179.1	0.589	2.4	142.0	0.79	0.015	14.5	4	0.76	*17.5*	**22.9**	1.9	**23.4**	1.3
11M1	#3	2.380	1.8	0.986	1.8	334.8	0.210	2.4	71.3	0.21	0.005	24.3	2	0.73	*19.0*	**25.9**	2.4		
11M9	#1	2.778	1.8	1.712	1.8	384.0	0.188	2.4	42.2	0.11	0.021	15.2	5	0.77	13.1	**16.8**	1.4		
11M9	#2	2.047	1.8	0.774	1.8	207.7	0.453	2.4	121.7	0.59	0.037	11.3	10	0.76	19.2	**25.2**	2.1	**21.1**	2.4
11M9	#3	2.880	1.7	1.432	1.8	414.3	0.260	2.4	75.2	0.18	0.026	13.2	8	0.75	15.9	**21.2**	1.8		
14M16	#1	7.128	1.1	9.248	1.8	678	1.638	2.4	120	0.18	0.052	5.8	4	0.90	*6.1*	**6.8**	0.3		
14M16	#2	16.312	1.1	19.961	1.8	2907	2.136	2.4	311	0.11	0.021	8.2	3	0.80	*6.6*	**8.3**	0.6	**7.0**	1.2
14M16	#3	4.337	1.2	7.570	1.8	1673	0.579	2.4	128	0.08	0.008	12.5	2	0.78	*4.7*	**6.0**	0.5		
14M17	#2	3.048	1.2	4.614	1.8	485	1.042	2.4	110	0.23	0.013	12.8	1	0.79	*5.2*	**6.6**	0.5		
14M17	#7	4.034	1.2	6.657	1.8	1004	1.392	2.4	210	0.21	0.010	12.6	2	0.78	*4.8*	**6.1**	0.5	**6.7**	0.6
14M17	#8	6.252	1.1	7.766	1.8	754	2.490	2.4	242	0.32	0.017	9.3	2	0.84	*6.2*	**7.4**	0.5		
14M18	#3	0.767	1.3	2.821	1.8	749	0.335	2.4	89	0.12	0.001	51.3	0	0.80	*2.2*	**2.7**	0.2		
14M18	#4	0.673	1.4	2.083	1.8	375	0.826	2.4	149	0.40	0.015	11.2	3	0.79	*2.4*	**3.1**	0.2	**3.0**	0.3
14M18	#5	0.661	1.4	2.057	1.8	457	0.173	2.4	38	0.08	0.003	21.4	1	0.79	*2.6*	**3.3**	0.3		
14M19	#2	2.790	1.2	1.785	1.8	156	0.814	2.4	71	0.46	0.027	9.4	2	0.83	*11.7*	**14.1**	0.9		
14M19	#3	1.584	1.2	0.977	1.8	338	0.888	2.4	307	0.91	0.018	9.7	6	0.73	*11.0*	**15.1**	1.4	**14.2**	0.4
14M19	#4	0.503	1.7	1.680	1.8	461	0.430	2.4	118	0.26	0.025	10.6	7	0.74	*2.3*	**3.2**	0.3		
14M21	#2	1.710	1.2	1.336	1.8	345	0.858	2.4	222	0.64	0.019	8.3	5	0.78	*9.2*	**11.8**	0.9		
14M21	#4	5.634	3.7	2.509	1.8	278	1.398	2.4	155	0.56	0.149	4.9	17	0.81	*16.4*	**20.3**	2.0	**16.0**	6.0
14M22	#2	0.684	1.0	0.751	1.8	318	0.142	2.4	60	0.19	0.004	33.6	2	0.67	*7.2*	**10.8**	1.1		
14M22	#3	4.291	0.8	3.590	1.8	480	1.694	2.4	226	0.47	0.069	8.1	9	0.77	*8.9*	**11.6**	0.9	**10.2**	1.8
14M22	#4	0.514	1.0	0.662	1.8	164	0.260	2.4	64	0.39	0.004	31.7	1	0.72	*5.9*	**8.2**	0.8		
15M63	#1	3.580	1.3	3.002	1.8	208.0	0.298	2.4	20.6	0.10	0.841	15.7	6	0.84	*9.63*	**11.5**	0.74		
15M63	#2	3.386	1.3	3.137	1.8	239.5	0.151	2.4	11.5	0.05	0.324	15.7	2	0.85	*8.83*	**10.4**	0.66	**10.7**	0.4
15M63	#3	0.300	1.6	0.265	2.0	53.4	0.235	2.4	47.3	0.88	0.432	15.7	9	0.75	*7.67*	**10.2**	0.90		
15M64	#2	0.405	1.5	0.463	1.9	186.6	0.218	2.4	87.8	0.47	0.255	15.7	10	0.67	*6.50*	**9.8**	1.07		

15M64	#3	**0.394**	8.6	**0.402**	1.9	55.6	**0.088**	2.5	12.1	0.22	**0.221**	15.7	3	**0.80**	*7.68*	**9.6**	1.78		
15M64	#4	**2.900**	1.3	**2.730**	1.8	208.8	**0.868**	2.4	66.4	0.32	**0.614**	15.7	5	**0.80**	*8.17*	**10.2**	0.75	**9.9**	0.2
15M65	#1	**1.562**	1.4	**1.528**	1.8	422.9	**0.286**	2.4	79.3	0.19	**0.203**	15.7	6	**0.69**	*8.10*	**11.7**	1.19		
15M65	#2	**0.409**	1.5	**0.409**	1.9	126.1	**0.233**	2.4	71.8	0.57	**0.289**	15.7	9	**0.69**	*7.27*	**10.5**	1.08		
15M65	#3	**1.763**	1.4	**1.604**	1.8	367.1	**0.488**	2.4	111.7	0.30	**0.275**	15.7	6	**0.74**	*8.48*	**11.4**	1.01	**11.2**	0.4
15M67	#2	**2.11**	1.3	**1.57**	1.8	255	**0.46**	2.4	74	0.29	**0.020**	12.0	3	**0.76**	*10.4*	**13.6**	1.1		
15M67	#3	**3.35**	1.4	**3.59**	1.8	474	**1.39**	2.4	184	0.39	**0.036**	6.2	5	**0.79**	*7.1*	**9.0**	0.7	**11.3**	3.3
15M68	#1	**1.42**	1.4	**0.99**	1.8	158	**0.31**	2.4	50	0.31	**0.012**	11.5	2	**0.76**	*11.1*	**14.6**	1.2		
15M68	#2	**1.43**	1.4	**1.06**	1.8	266	**0.69**	2.4	174	0.65	**0.019**	5.0	5	**0.74**	*9.7*	**13.1**	1.2		
15M68	#3	**4.54**	1.3	**3.74**	1.8	528	**0.44**	2.4	63	0.12	**0.032**	7.6	5	**0.79**	*9.8*	**12.4**	0.9		
15M68	#4	**1.90**	1.4	**1.49**	1.8	328	**0.16**	2.4	36	0.11	**0.023**	8.0	5	**0.75**	*10.3*	**13.6**	1.2	**13.4**	0.5
15M71	#1	**0.44**	1.5	**0.35**	1.9	109	**0.09**	2.4	29	0.27	**0.010**	6.4	3	**0.72**	*9.7*	**13.4**	1.3		
15M71	#2	**0.79**	1.4	**0.68**	1.8	201	**0.15**	2.4	43	0.21	**0.022**	9.3	6	**0.77**	*9.1*	**11.9**	1.0		
15M71	#3	**2.20**	1.4	**1.58**	1.8	505	**0.43**	2.4	139	0.27	**0.014**	8.1	5	**0.73**	*10.8*	**14.9**	1.4	**13.4**	0.9
16M95*	#1	**0.99**	1.2	**0.617**	3.5	377.3	**0.39**	3.8	238.1	0.63	**-**	-	-	**0.62**	11.5	**18.5**	0.4		
16M95*	#2	**2.30**	1.2	**1.254**	5.0	190.2	**0.46**	4.8	70.14	0.37	**-**	-	-	**0.95**	14.0	**14.7**	0.7	**17.2**	1.2
16M95*	#3	**0.23**	1.3	**0.142**	7.4	175.3	**0.11**	5.6	131.7	0.75	**-**	-	-	**0.63**	11.6	**18.4**	0.7		
16M98	#1	**2.76**	1.1	**1.29**	1.8	397	**0.33**	2.4	103	0.26	**0.020**	4.8	6	**0.73**	*16.7*	**22.9**	2.1	**18.2**	0.3
16M98	#2	**5.11**	1.0	**3.08**	1.8	961	**0.38**	2.4	120	0.12	**0.032**	5.4	10	**0.93**	*13.3*	**14.4**	0.6		
17M104*	#1	**3.49**	1.2	**2.993**	3.2	1447	**0.88**	3.9	427.5	0.30	**-**	-	-	**0.71**	9.0	**12.7**			
17M104*	#2	**1.48**	1.2	**1.021**	3.1	191.5	**0.93**	3.5	174.6	0.91	**-**	-	-	**0.76**	9.9	**13.0**		**13.5**	0.7
17M104*	#3	**1.08**	1.2	**0.779**	5.5	273.2	**0.29**	4.3	102.1	0.37	**-**	-	-	**0.71**	10.6	**14.9**			

Ejection correction (Ft): correction factor for alpha-ejection (according to Farley et al. (1996) and Hourigan et al. (2005)). Uncertainty of the single-grain ages includes both the analytical uncertainty and the estimated uncertainty of the ejection correction. Sample age is the unweighted average age of all Ft-corrected (U-Th)/He ages. Results from aliquots marked with asterisk were measured in the laboratory in Tübingen.

Table 4. *Results of apatite fission track analyses*

Sample	Number of grains	ρs	Ns	ρi	Ni	ρd	Nd	P(χ²) (%)	Dispersion	Central age ±1σ (Ma)	U (ppm)	Dpar (µm)
11M1**	20	0.885	17	18.490	355	1.9323	4424	99	0	11.8±3.0	13	1.48
11M3**	6	2.059	7	23.824	81	1.9238	4424	99	0	2.1±0.8	187	1.61
11M4**	5	2.308	6	7.692	20	1.9245	4424	90	0	7.4±3.4	55	1.37
11M5**	25	7.075	179	78.577	1988	1.9331	4424	0	0.83	3.1±0.6	660	1.60
11M6**	25	4.082	78	47.315	904	1.9261	4424	56	0.07	2.1±0.3	327	1.57
11M7*	10	3.478	32	7.609	70	1.9269	4424	9	0.5	11.9±3.2	63	1.53
11M8**	10	3.548	16	10.643	48	1.9272	4424	100	0	8.2±2.4	80	1.51
11M9**	25	3.049	50	3.354	55	1.9284	4424	100	0	22.3±4.4	26	1.59
11M11**	20	1.636	27	12.545	207	1.9300	4424	99	0	3.2±0.7	90	1.58
11M12**	22	2.577	50	10.000	194	1.9308	4424	97	0	6.3±1.0	77	1.61
11M13*	10	1.972	14	21.972	156	1.9316	4424	99	0	2.2±0.6	156	1.56
11M14**	25	4.217	100	28.251	670	1.9323	4424	76	0	3.7±0.4	198	1.57
11M15**	25	5.929	123	36.393	755	1.9331	4424	37	0.1	3.6±0.4	323	1.57
14M16**	23	1.701	83	12.193	595	4.7896	3032	28	0.15	7.4 ± 1.2	33	1.87
14M17**	20	0.688	24	9.3980	328	8.3835	3032	73	0	7.2±1.6	14	1.37
14M18**	18	1.463	18	57.240	710	8.3716	3023	58	0	2.7±0.7	88	1.45
14M19**	20	0.720	29	13.325	537	8.3596	3032	39	0.35	5.3±1.2	22	1.30
14M20**	7	0.223	4	4.916	88	8.3477	3032	87	0	4.5±2.3	8	8.39
14M22**	35	3.929	163	23.769	986	6.8920	2481	99	0	12.9 ± 1.3	48	1.86
15M69**	17	3.507	101	18.819	542	4.8597	2796	97	0	9.8±1.3	51	4.70
15M70	30	2.732	174	20.235	1289	4.8287	2796	100	0	7.1+-0.8	56	3.77
15M84	16	1.373	35	8.824	225	4.6428	2796	100	0	8.2±1.6	30	1.60
16M98	24	3.433	110	23.061	739	7.2356	2481	78.68	0	17.8±2.7	43	1,62

ρs (ρi) is the spontaneous (induced) track density (10^5 tracks/cm^2); Ns (Ni) is the number of counted spontaneous (induced) tracks; ρd is the dosimeter track density (10^5 tracks/cm^2); Nd is the number of tracks counted on the dosimeter; P(χ^2) is the probability of obtaining Chi-square value (χ^2) for n degree of freedom (where n is the number of crystals minus 1); ages were calculated using the zeta calibration method (Hurford and Green, 1983), glass dosimeter IRMM540, and zeta values of 226±13 a/cm^2 (samples without asterisk) and 234±9 a/cm^2 (samples with one asterisk) and 255±9 (samples with two asterisks) calculated with Durango apatite standards.

Table 5. *Results of zircon fission track analyses*

Sample	Number of grains	ρs	Ns	ρi	Ni	ρd	Nd	P(χ²) (%)	Dispersion	Central age ±1σ (Ma)	U (ppm)
10JTB01	11	51.074	459	18.694	168	3.973	2468	33	0	59.0±5.3	62
11M1	20	90.000	531	100.678	594	6.525	2512	2	0.24	32.8±2.9	634
11M2	20	120.667	543	159.556	718	6.542	2512	15	0.13	26.9±2.0	1184
11M3	20	40.707	403	160.101	1585	6.563	2512	11	0.17	9.0±0.7	1058
11M5	20	20.396	206	155.05	1566	6.576	2512	0	0.45	4.9±0.6	918
11M6	20	22.020	218	208.283	2062	6.593	2512	0	0.59	3.8±0.6	1378
11M7	20	87.705	535	147.541	900	6.609	2512	0	0.25	21.0±1.8	1016
11M13	20	28.554	237	131.205	1089	6.643	2512	59	0.02	7.9±0.6	892
11M15	20	28.723	270	88.936	836	6.677	2512	0	0.34	11.7±1.3	570
14M16	20	134.054	496	332.432	1230	6.823	2583	10	0.14	15.2±1.1	2147
14M17	16	37.895	216	100.702	574	6.822	2583	1	0.31	14.3±1.7	652
14M18	20	24.098	294	129.754	1583	6.821	2583	9	0.15	6.9±0.6	743
14M19	8	17.755	87	67.347	330	6.821	2583	69	0	9.8±1.2	508
15M63*	20	15.927	155	37.851	368	6.387	1982	28	0.27	17.9±2.3	185
15M65*	16	19.074	135	52.419	371	6.372	1982	97	0	17.7±2.0	260
15M66*	16	17.910	125	52.441	366	6.355	1982	89	0	16.6±1.9	259
15M71*	20	18.448	243	21.636	285	6.340	1982	52	0.1	35.5±3.4	109
15M84*	25	9.877	100	33.778	342	6.308	1982	99	0	14.1±1.8	228
15M85*	25	22.914	232	40.494	410	6.292	1982	94	0	27.2±2.6	21

ρs (ρi) is the spontaneous (induced) track density (10^5 tracks/cm^2); Ns (Ni) is the number of counted spontaneous (induced) tracks; ρd is the dosimeter track density (10^5 tracks/cm^2); Nd is the number of tracks counted on the dosimeter; P(χ²) is the probability of obtaining a Chi-square value (χ²) for n degree of freedom (where n is the number of crystals minus 1); ages were calculated using the zeta calibration method (Hurford & Green 1983), glass dosimeter IRMM541, and a zeta value of 109±3 and 153±7 a/cm^2 for samples marked with asterisk, calculated with Fish Canyon Tuff zircon standards.

5.5   Discussion

Late Cenozoic cooling history of the central Menders Massif

Studies concerning the tectonic evolution of the Gediz detachment either proposed that the extensional deformation along the Gediz detachment commenced with the intrusion of the Salihli and Turgutlu granodiorites in the middle Miocene (e.g. Glodny & Hetzel 2007; Catlos et al. 2010; Rosetti et al. 2017) or that faulting along the Gediz detachment commenced in the Pliocene (Gessner et al. 2013; Ring et al. 2017). An argument for the latter model was that the available footwall cooling ages at the time of publishing were mostly Pliocene in age (Ring et al. 2003; Buscher et al. 2013; Baran et al. 2017). However, the available data were restricted only to the eastern part of the Gediz detachment, south of Salihli. In contrast, our new thermochronological data show that the cooling history varies along the strike of the Gediz detachment. Although both, the Turgutlu and the Salihli granodiorites, intruded in the middle Miocene into the footwall of the Gediz detachment, our thermochronological data reveal that final cooling between the ZFT and AHe systems occurred in the westernmost part of the central Menderes Massif from Serravallian at ~13 Ma to Tortonian at ~7.5 Ma, whereas final cooling in the easternmost part occurred during the Pliocene. The Serravallian cooling ages in the western part of the Bozdağ range are the oldest cooling ages that can be attributed to cooling by tectonic denudation along the Gediz detachment. Although sample 15M71 also originates from footwall units (Bayındır nappe) of the Gediz detachment, it shows a different slow monotonic cooling history with a ZFT age of 35.8 Ma, a ZHe age of 13.4 Ma and an AFT age of 7.1 Ma, which implies that it is situated too far south to be affected by rapid footwall cooling of the Gediz detachment. Hence, the intrusions of the Turgutlu and Salihli granodiorites at 15 Ma mark the onset of extensional faulting in the Bozdağ range. However, the earliest signs of extensional deformation in the central Menderes Massif are found in the Aydın range along the Büyük Menderes detachment during the early Miocene. The activity during the early Miocene is documented by K-Ar fault gouge ages of 22 to 19 Ma as well as by cooling from the ZFT to ZHe system between 19.1 and 14.2 Ma (Hetzel et al. 2013; Nilius et al. 2019; Heineke et al. subm.). Following this rather moderate cooling in the early Miocene, faster cooling occurred in the middle Miocene at ~16 to 14 Ma along the Büyük Menderes detachment - contemporaneously with the intrusion of the Turgutlu and Salihli granodiorites in the footwall of the Gediz detachment. The proof that the intrusions are related to extensional detachment faulting are documented by in-situ U–(Th)–Pb dating of recrystallized titanite of the Salihli granodiorite yielding an age of 14.5 Ma (Rosetti et al. 2017) and from in-situ TIMS U-Pb dating of monazite yielding an age-range of 21.7 ± 4.5 to 9.6 ± 1.6 Ma, of which the younger ages were interpreted to reflect deformation ages of the Salihli granodiorite (Catlos et al. 2008; 2010). Interestingly, this ductile deformation at depth is not very prominently expressed by increased cooling rates in structurally higher parts of the Gediz detachment footwall, except for the 13.5 ± 0.7 Ma ZHe age of sample 17M104 from the peak of the Bozdağ mountain. It is also possible that the rare middle Miocene cooling ages along the Gediz detachment are the result of a sampling gap in the southern part of the Bozdağ range that comprises the structurally higher parts of the Gediz detachment footwall.
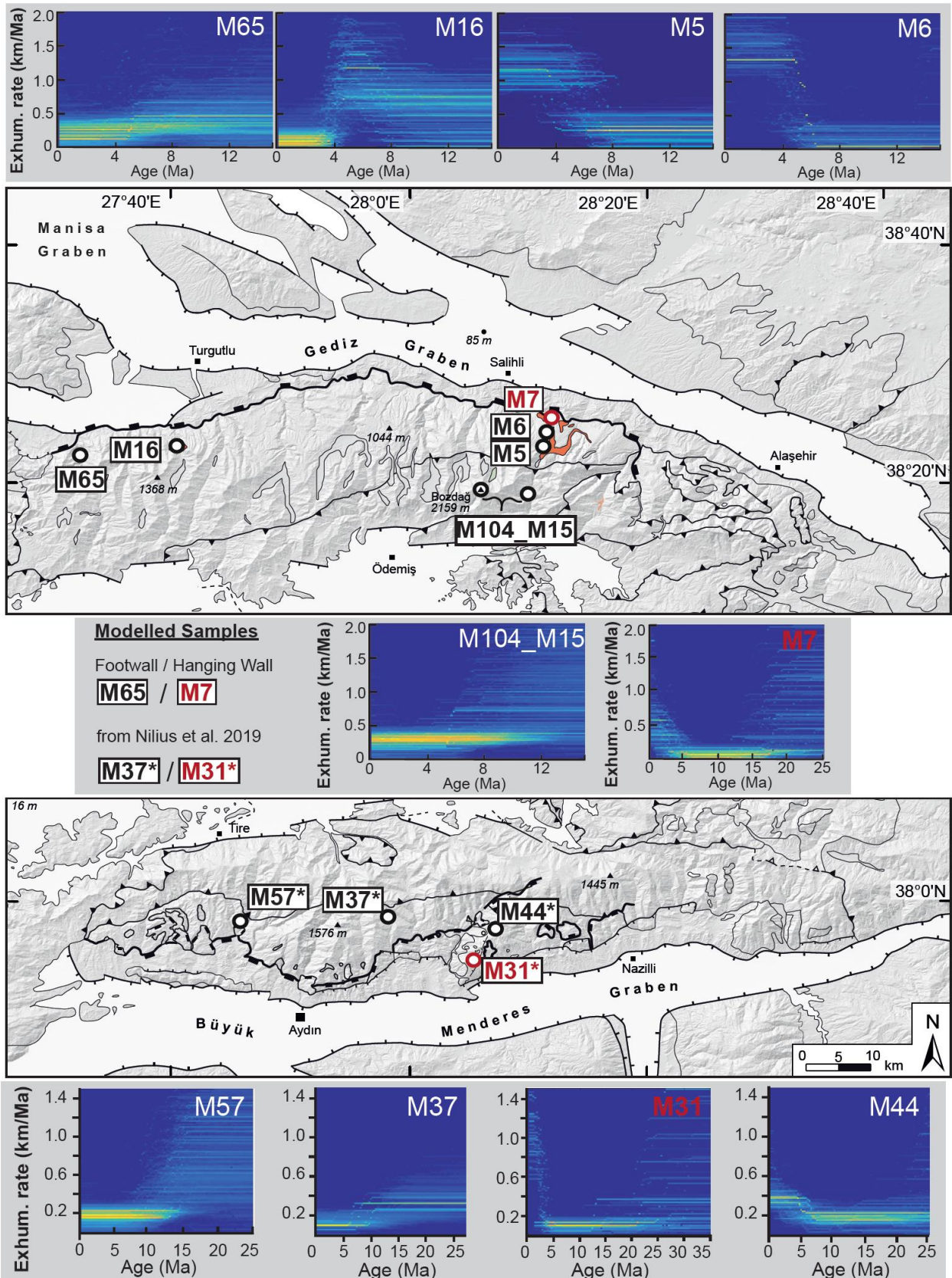
Figure 4: Exhumation rates constrained by 1-dimensional thermokinematic modelling, including modelling results of samples M57, M37, M31 and M44 of Nilius et al. (2019).

Following the middle Miocene intrusion and the subsequent shearing of the Salihli and Turgutlu granodiorites, rapid cooling of the western Gediz detachment footwall is recognized by the thermochronological samples south of Turgutlu. The timeframe for brittle faulting along the western Gediz detachment is set by the ^{40}Ar/^{39}Ar biotite age of 13.1 ± 0.2 Ma and the K – Ar fault gouge ages of ~12 to 5 Ma (Hetzel et al. 1995a; Heineke et al. subm). As the cooling of intrusions is a rapid process in the order of several ka (mainly depending on the size of the intrusive body and conductivity of the country rock) (e.g. Nabelek et al. 2012), it is very likely that the ZFT age of 15.2 ± 1.7 Ma of sample 14M16 rather reflects the post-emplacement cooling through the PAZ of the ZFT system, than cooling caused by tectonic denudation. This interpretation is supported by the ZFT annealing model of Rahn et al. (2004), which predicts effective closure temperatures of 300-330 °C for samples that experienced cooling rates of ~100 °C/Ma, causing similar or slightly higher effective closure temperatures of the ZFT system compared to the closure temperature of the ^{40}Ar/^{39}Ar biotite system. Therefore, the samples 14M17 and 15M84 are better suited to constrain the early phase of tectonic denudation by the ZFT system as they originate from country rocks of the Turgutlu granodiorite situated ~2 km north of sample 14M16 (Figure 3). Consequently, 14M17 and 15M84 reveal cooling through the PAZ of ZFT, roughly 1 Ma later than sample 14M16, at 14.3 ± 1.7 Ma and 14.1 ± 1.8 Ma, respectively. In contrast to 14M16, these samples either represent the cooling of the country rocks of the Turgutlu granodiorite by tectonic denudation along the Gediz detachment, or slow monotonic cooling through the PAZ of the ZFT system, as they likely comprise lower closure temperatures due to slower cooling rates.
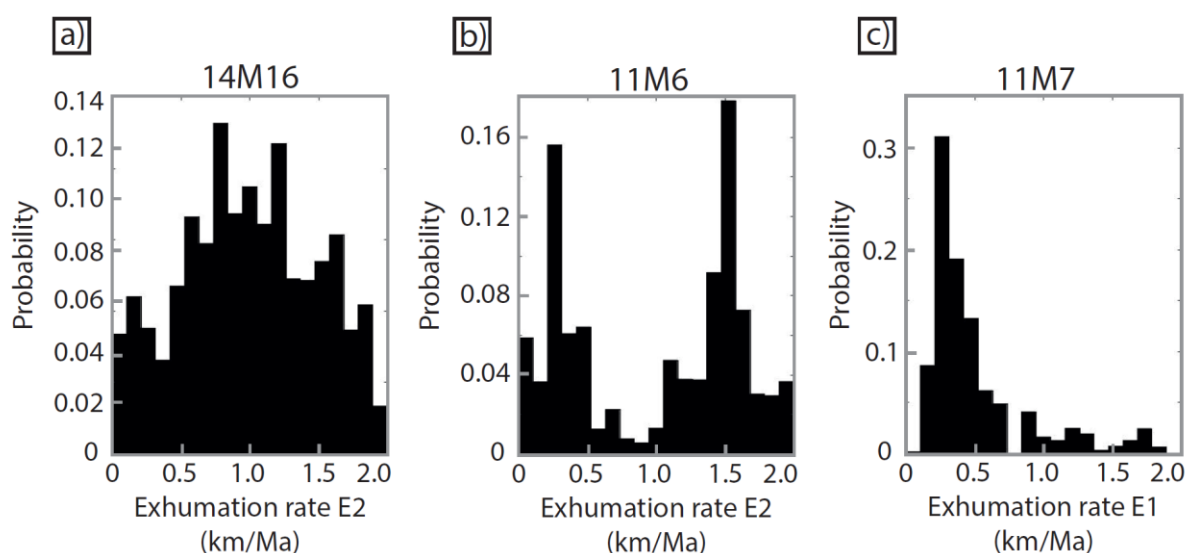
Figure 5: Probability density functions of selected parameters for samples 14M16, 11M6 and 11M7.

Although the middle Miocene cooling episode must be interpreted tentatively, all of the above discussed samples suggest fast cooling through the closure temperatures of the ZHe, AFT and AHe systems at ~7 Ma. This late Miocene episode is in accordance with the K-Ar fault gouge ages of 7.4 ± 1.2 to 6.2 ± 0.2 Ma of sample 15T18, sampled ~3 km to the east of sample 15M85. The last faulting activity of the Gediz detachment in the Turgutlu granodiorite area is documented by the K-Ar fault gouge age of 4.7 ± 0.9 Ma for the smallest grain size fraction (<0.1 µm) of sample 15T22, which

is interpreted to reflect latest illite growth phase during faulting (Heineke et al. subm) and the 4.6 ± 0.7 Ma AHe age of 14M17. However, 10 km further to the east, footwall samples 14M18 and 14M19 imply that faulting along the Gediz detachment in this area occurred since 9 to 7 Ma and lasted until ~3 Ma. This rather continuous activity of the western Gediz detachment, starting with fast cooling of the westernmost part at 13 to 10 Ma and followed by fast cooling at 7 Ma in the region of the Turgutlu granodiorite with final cooling of samples 14M18/19 at ~3 Ma, is different from the more stepwise cooling pattern observed in the Aydın range, with middle Miocene cooling along the Büyük Menderes detachment and latest Miocene/Pliocene cooling in the footwall of the Demirhan detachment (Wölfler et al. 2017; Nilius et al. 2019). The gap in cooling comprises the time between ~10 and 6 Ma implying an asynchronous activity of the Gediz and the Büyük Menderes detachment system in the late Miocene.

The large thermochronological dataset of the eastern part of the Gediz detachment presented here consists of our new ZFT and AFT data and is combined with the AFT and ZFT data from Ring et al. (2003) and the zircon and apatite (U-Th)/He data of Buscher et al. (2013) (Figure 3). With the comprehensive set of ZFT, ZHe, AFT and AHe ages, the mineral-pair method reveals two age groups within the dataset. The first age group reflects very rapid cooling from the ZFT to the AHe systems, whereas the second group of samples show rather moderate cooling with Oligocene and Miocene ZFT, ZHe and AFT ages and final cooling by Pliocene AHe ages. Samples that show the Pliocene rapid cooling constitute the vast majority and originate from the structurally lower northern part of the Gediz detachment footwall. Cooling through the closure temperatures of the ZFT to the AHe systems occurred between ~5 Ma and 2 Ma. The ZFT ages of samples from a structurally intermediate position in the footwall (11M3, 11M13) show late Miocene cooling ages, which might reflect partial resetting of fission tracks in zircon. However, the fast Pliocene cooling phase is also evident in their Pliocene ZHe, AFT and AHe cooling ages. To gain more details regarding the cooling history, samples 11M13 and 11M6 are thermally modelled with HeFTy. The resulting time-temperature histories imply that the rapid phase of cooling commenced at 5 Ma (Figure 6a) with a rate of 50 °C/Ma between 5 and 4 Ma for sample 11M13 and ~110 °C/Ma between 3.5 and 2 Ma for sample 11M6 (Figure 6b). The more moderate cooling ages of the Miocene cooling phase is observed in the structurally highest samples of the Gediz detachment footwall (11M11; 11M12; 11M15; 14M22 and 17M104). Sample 17M104 from the peak of the Bozdağ comprises the oldest ZHe age of 13 ± 0.7 Ma. Samples at lower elevation but at the same structural level as 17M104 show that moderate cooling rates in the middle Miocene are followed by a poorly defined phase of slower cooling in the late Miocene, until Pliocene AFT and AHe ages indicate a renewed phase of higher cooling rates (e.g. 11M11; 11M14 and 11M15). This trend is also evident in the thermal model of the cooling history of sample 11M15, which illustrates the aforementioned cooling path with a phase of higher cooling rates in the middle Miocene and the Pliocene and slower cooling rates between ~11 and 5 Ma (Figure 6c).
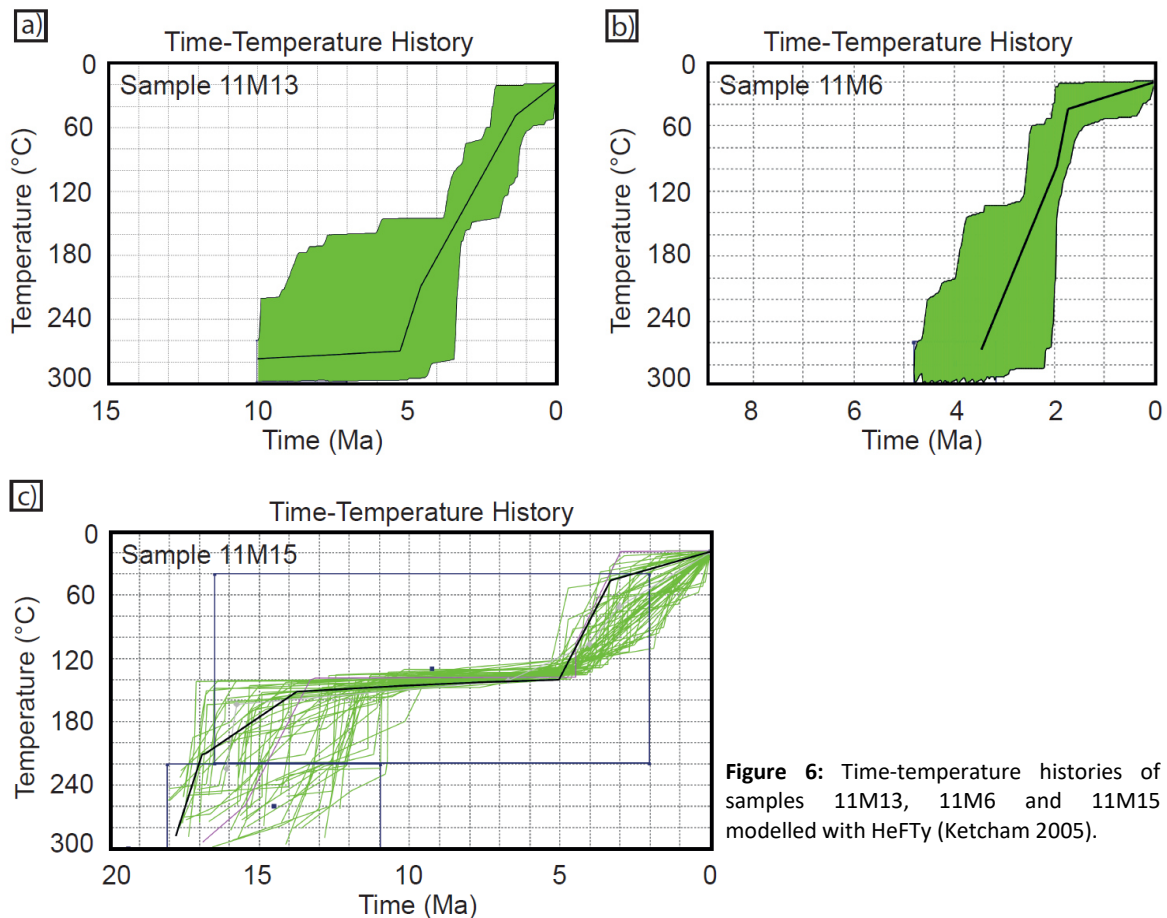
Figure 6: Time-temperature histories of samples 11M13, 11M6 and 11M15 modelled with HeFTy (Ketcham 2005).

Constraints on the slip rate of the Gediz detachment

The thermochronological transects at the Gediz detachment were taken parallel to the direction of the hanging wall transport. The systematic decrease in footwall cooling ages in the down-dip direction of the footwall reflects its movement through the closure isotherms. The slip rate is then derived by the inverse slope of cooling ages versus the distance between the samples in the direction of tectonic transport (e.g. Foster & John 1999; Brady 2002; Brichau et al. 2006; Singleton et al. 2014). The slip rate estimate is based on the assumption that the orientation of the isotherms and the fault did not change over time and that the applied thermochronometers comprise internally consistent closure temperatures.

The slip rate of the western part of the Gediz detachment is constrained by ZHe ages from samples 15M62 to 15M68, which show decreasing cooling ages towards the hanging wall from 13.4 ± 0.5 to 9.9 ± 0.4 Ma over a horizontal distance of 8.4 km. Estimated slip rates for this time interval are 2.45 ± 0.75 km/Ma (1σ), assuming that the present-day orientation of the westernmost Gediz detachment (330/20) did not change over time. First constraints on the slip rate of the eastern part of the Gediz detachment were proposed by Buscher et al. (2013) by using five ZHe samples that

show a down-dip decrease in cooling ages, yielding a slip rate of 4.3 + 3.0/- 1.2 km/Ma for the time range between 3.9 ± 0.4 and 2.5 ± 0.2 Ma. The ZHe data published by Baran et al. (2017) covers the same part of the Salihli granodiorite and comprises Pliocene cooling ages. However, the reported slip rate of 12.5 km/Ma is three times higher than the 4.3 km/Ma of Buscher et al. (2013), which we attribute to the confusion of the distances between the samples (Baran et al. 2017, Figure 3) leading to a wrong slope of the regression (Baran et al. 2017, Figure 4a). Careful re-examination and plotting of the cooling ages with the consistent distances between the samples yields a slip rate of 4.8 ± 2.8 km/Ma (2σ), which is consistent with the rate derived by Buscher et al. (2013). The slip rate constraints based on ZHe data are complemented with eight new AFT ages from the same thermochronological transect. The ages decrease over a distance of 10.27 km from 3.7 to 1.9 Ma resulting in a slip rate of 5.6 ± 2.7 km/Ma (r^2=0.98) during this time interval. Although the AHe ages also show a decrease in ages towards the hanging wall, from 3.5 ± 1.5 to 1.9 ± 0.2 Ma, the low closure temperature of the AHe system is prone to be influenced by hanging wall erosion, thermal relaxing of isotherms after faulting along the Gediz detachment ceased, or thermal resetting by hydrothermal fluids for which we exclude the AHe data from implications on the fault slip of the Gediz detachment.
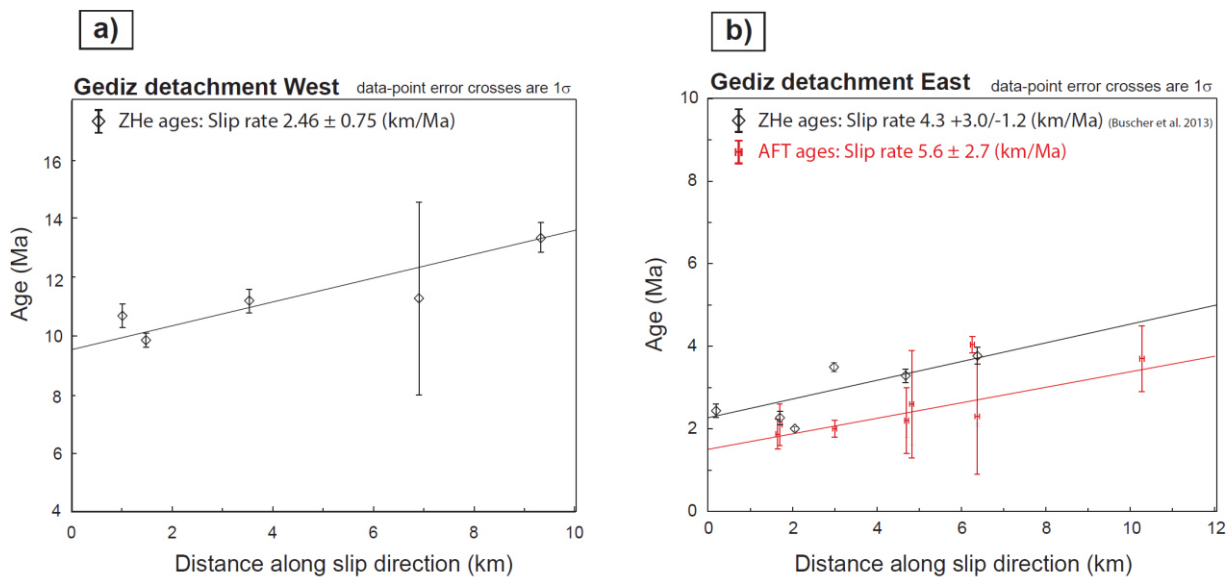
Figure 7: **a)** Slip rate for the westernmost thermochronological profile constrained by five ZHe ages. **b)** AFT ages from the eastern thermochronological profile are used to constrain the slip rates for the eastern part of the Gediz detachment. The AFT slip rate is shown together with the slip rate of Buscher et al. (2013) constrained by ZHe ages of the same samples.

The application of multiple thermochronometers for deriving fault slip rates allows us to detect temporal changes of the slip rate, because the ZHe and AFT systems record the passage of the footwall through the isotherms of ~150°C and ~120°C, respectively (Brichau et al. 2006). The slip rates derived from ZHe and AFT systems at the eastern part of the Gediz detachment are within their assigned errors (4.3 + 3.0/ - 1.2 and 5.6 ± 2.7 km/Ma). As stated above, the critical analysis of the AHe dataset results in a threefold increase of the slip rate to 14.9 ± 3.5 km/Ma. Compared to other low-angle normal faults, slip rates exceeding 10 km/Ma are rare but possible, as proven for the Maui'iu detachment fault (Papua New Guinea) comprising a slip rate of 11.7 ± 3.5 km/Ma (Webber et al. 2018). However, slip rates in the order of 10 to 15 km/Ma are rather exceptional as ~85 % of the

low-angle normal faults, included in a compilation of 49 faults, slipped at rates <10 km/Ma (Webber et al. 2018). Furthermore, a slip rate of 15 km/Ma for the Gediz detachment is not supported by exhumation rate modelling. Assuming a present-day dip of the Gediz detachment of 15°, a slip rate of 15 km/Ma would result in exhumation rates in the order of 3.9 km/Ma. In contrast, the modelled exhumation rates of 1.2 and 1.5 km/Ma (samples 11M5 and 11M6, respectively) correspond to slip rates of 4.6 and ~6 km/Ma, respectively. Hence, as the modelled exhumation rates agree very well with the slip rates derived from the ZHe and AFT ages, we suggest that the AFT derived slip rate of 5.6 ± 2.7 km/Ma is a very robust estimation. Although the ZHe and AFT derived slip rates are within their assigned errors, the slight increase from 4.3 + 3.0/ - 1.2 to of 5.6 ± 2.7 km/Ma, in combination with increasing exhumation rates in lower structural parts of the footwall might tentatively indicate an increase of tectonic denudation along the Gediz detachment during the Pliocene.

Western Anatolian block rotation and exhumation of the central Menderes Massif
The first indicators for a ~25° anticlockwise rotation of Anatolia with respect to Eurasia since the middle Miocene came from paleomagnetic measurements of the Bey Dağları carbonate platform in SW Turkey (Morris & Robertson 1993; Tatar et al. 2002). The proposed Anatolia wide rotation was later replaced by a more detailed paleomagnetic map-scale reconstruction of western Anatolia, which proposed that this rotation is only seen in domains to the south of the central Menderes Massif, but is not present north of the central Menderes Massif (van Hinsbergen et al. 2010). This observation coincides with (i) the orientation of the stretching lineation that shows a difference of ~30° between the southern and northern Menderes Massif (Hetzel et al. 1995a; Bozkurt & Satır 2000; Ring et al. 2003) and (ii) the widths of the Gediz and Büyük Menderes grabens, which both pinch out to the east and widen towards the west (Figure 4)(van Hinsbergen 2010). Hence, the resultant post-Oligocene extensional history of western Anatolia is best described by (1) a pure NE-SW extension in the early Miocene along the Simav detachment, exhuming the northern Menderes Massif without indications of block-rotations until (2) the inception of faulting along the Gediz detachment and the main phase of footwall cooling along the Büyük Menderes detachment begins at 16 Ma (van Hinsbergen et al. 2010). K-Ar fault gouge ages from the Büyük Menderes detachment of 22 to 19 Ma imply that the Büyük Menderes graben preceded the formation of the Gediz graben by ~4 to 7~ Ma (Hetzel et al. 2013; Heineke et al. subm.). In contrast to the Simav detachment, the Gediz detachment intersects the alpine nappe contacts between the Bayındır and Bozdağ nappes. Hence, it is not a reactivated structure inherited from alpine nappe stacking and it is more likely that the intrusion of the Salihli and Turgutlu granodiorites induced the inception of faulting along a zone of crustal weakness. This is supported by numerical and analogue models, which include a low viscosity heterogeneity in the lithosphere (Tirel et al. 2008; Brun et al. 2017). These models predict initiation of graben formation by crustal necking in the upper brittle crust, while strain localization at the low viscosity heterogeneity leads to ductile extensional shearing in the middle crust in the earliest phase of extension. During this phase, extension in the upper brittle crust is expressed as a pure shear extensional pattern forming a symmetric graben. Only with progressive extension, the ductile detachment ascends to upper crustal levels where the bulk amount of extension is

accommodated by simple shear on the exhumed detachment fault. This might explain why the depositional age of 16.0 ± 1.4 Ma for the lowermost sedimentary unit in the Gediz graben (Asti et al. 2016) predates the first appearance of pronounced cooling in the footwall of the Gediz detachment between 14 and 13 Ma. In other words, the sensitivity of low-temperature thermochronology might be too low to detect graben formation associated with crustal necking. The time gap between the intrusion of syn-tectonic granodiorites (16.1 and 15.0 Ma for the Turgutlu and Salihli granodiorite, respectively) along the Gediz detachment, alongside with the concurrent formation of the Gediz graben, and the first occurrence of enhanced cooling in the Bozdağ range at ~14 to 13 Ma, might therefore reflect the time needed for the detachment to reach upper crustal levels (Brun et al. 2017).
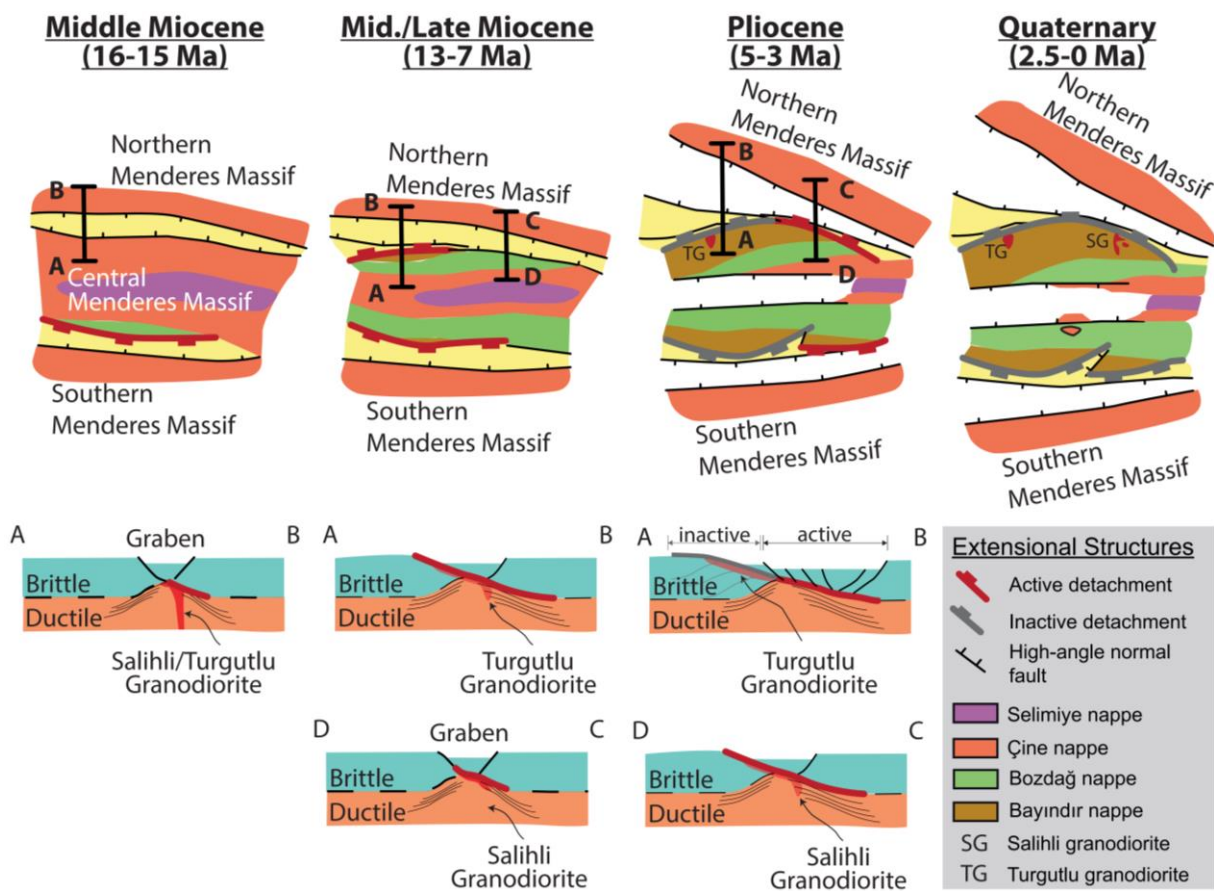
Figure 8: Sketch illustrating the extensional history of the central Menderes Massif since the middle Miocene. Upper row shows the map view evolution of the Menderes Massif. The active detachment faulting is marked in red, whereas inactive detachment segments are shown in grey. Lower row shows the evolution of the western and eastern parts of the Gediz detachment through time.

The space created by the ~30° anticlockwise rotation of the southern Menderes Massif and Lycian nappes of SW Turkey with respect to the northern Menderes Massif, can be solely attributed to the emergence of the central Menderes Massif by tectonic unroofing along extensional detachments (van Hinsbergen et al. 2010). This anticlockwise rotation and the geometry of the extensional structures define a pivot point to the east of the central Menderes Massif, which requires that the western parts of the Büyük Menderes and Gediz detachments must have accommodated larger magnitudes of extension at higher rates (if occurred simultaneously along strike) than the eastern

parts. Additionally, footwall cooling ages of the western parts of the Büyük Menderes and Gediz detachments should also reflect the youngest Pliocene phase of fast cooling. However, our thermochronological dataset depicts a different picture. In contrast to the aforementioned predictions, the youngest phase of rapid cooling is absent in the western parts of the Bozdağ and Aydın ranges. Furthermore, the western part of the Gediz apparently accommodated a similar amount of extension as the eastern part (Figure 4). Our dataset implies, that after the formation of the young Gediz graben at ~15 Ma, the Gediz detachment reached upper crustal levels first in the western part at ~13 Ma (Figure 8). The 12 to 6 Ma K-Ar fault gouge ages document sustained faulting along the western part of the Gediz detachment with exhumation rates of ~0.6 km/Ma between the middle and the late Miocene until exhumation rates increased to 1.0 to 1.5 km/Ma between 8 to 6 Ma (Figure 4, sample 14M16) (Heinecke et al. subm). In the eastern part of the Gediz detachment, the exhumation rates remained low and only the elevation difference between sample 17M104 and 11M15 document moderate exhumation rates in the order of 0.4 km/Ma between 13 and 8 Ma (Figure 4). However, at 5 Ma detachment faulting terminates in the western part of the Gediz detachment and starts in the eastern part, where fast exhumation initiates. However, termination of faulting along the western part of the Gediz detachment is not synonymous with termination of lithospheric extension in the western part of the central Menderes Massif as this would contradict the anticlockwise rotation pattern between the southern and northern Menderes Massif. Instead, it is more likely that the larger amount of finite extension in the west led to a change in the mode of lithospheric extension by switching from core complex mode faulting to a wide rift mode type at which extension in the upper brittle crust is accommodated by high-angle normal faulting. This transition at 5 Ma, when fast exhumation rates at ~5 Ma cease in the western part of the Gediz detachment, coincide with the initiation of high exhumation rates in the footwall of the eastern Gediz detachment. Exhumation history modelling of samples from different levels of the footwall (Figure 4) as well as slip rate calculations based on the ZHe and AFT cooling ages (Figure 7) imply that the slip rate along the eastern part of the Gediz detachment increased from ~4.6 to ~6 km/Ma. This is similar to the exhumation rate increase of sample 14M16 observed along the western part of the Gediz detachment (Figure 4). The change from core complex faulting to subsequent high-angle normal faulting is a relatively common feature during the evolution of extensional terrains and has been reported for the Rhodope core complex (Brun & Sokoutis 2007), the Cycladic core complexes (Phillippon et al. 2012) and the Corsica metamorphic core complex (Fournier et al. 1991). The transition is attributed to protracted thinning of the originally overthickened post-orogenic crust by tectonic denudation along the detachment faults of the core complex (Lister & Davis 1989; Rosenbaum et al. 2005). Regarding the central Menderes Massif, the scenario is supported by a lateral change of the Moho depth across the central Menderes Massif decreasing from ~35 km in the east to 28 km along its western border (Gessner et al. 2013). A further important factor in favour of the transition from localized extension of the core complex mode to more distributed extension of the wide rift mode is the maximum slip rate capability of a detachment. For the southern Rhodope core complex, it has been shown that increasing strain rates by a factor of 5 in the middle Miocene resulted in the transition of core complex faulting to high angle normal faulting (Brun & Sokoutis

2018). The mechanical conditions for the inability of the lithosphere to accommodate high strain rates along a single detachment fault are the coupling between weak ductile crust and brittle crust and high strain rates (Brun 1999; Kydonakis et al. 2014). Low brittle-ductile crust coupling at low strain rates favours localized deformation, whereas high brittle-ductile crust coupling favours distributed deformation at high strain rates. Hence, we propose that the rotational extension between the southern Menderes Massif and the northern Menderes Massif promoted the transition from detachment faulting to high-angle normal faulting in the western part of the Bozdağ range, while contemporaneously detachment faulting in the eastern part of the Bozdağ range initiated. This is also reflected in the width of the Gediz graben which increases from ~9 km near Alaşehir in the east to ~20 km near Salihli in the central part of the graben to almost 50 km at Turgutlu in the west (Figure 4). It is therefore concluded that the differences in the finite amount of lithospheric extension associated with the anticlockwise rotation between the southern and northern Menderes Massifs promoted the contemporaneous appearance of a wide rift mode in the western part and the core complex mode of extension in the eastern part of the Aydin range.

5.6   Conclusions

The thermochronological data presented in this study provide evidence for significant along-strike variations in the exhumation history of the central Menderes Massif and underlines the importance of this approach for reconstructing a complete spatio-temporal evolution of core complexes. In contrast to existing constraints on the timing of faulting along the Gediz detachment, proposing either two separate phases of extension in the middle Miocene and in the Pliocene (Hetzel et al. 2013; Rossetti et al. 2018) or continuous extension along the Gediz detachment commencing in the Pliocene (Ring et al. 2003; Ring et al. 2018), the data presented in this study reflects a rather protracted cooling history of the Gediz detachment since the middle Miocene. In detail, exhumation in the footwall of the Gediz detachment occurred in the western part of the Bozdağ range between the Serravallian and the Messinian and subsequently shifted towards the east, where rapid tectonic denudation commenced in the latest Miocene/Pliocene. This eastward propagation of detachment faulting is associated with the anticlockwise rotation of the southern Menderes Massif since the middle Miocene promoting a successive transition from a core complex mode to a wide rift mode along the western part of the Gediz detachment in the latest Miocene and concurrently initiating detachment faulting in the eastern part of the Bozdağ range.

Table 6. *Model Parameters for inversions 1.1 to 1.5.*

Parameter	Unit	Range	1.1 Mean	s.e.	1.2 Mean	s.e.	1.3 Mean	s.e.	1.4 Mean	s.e.	1.5 Mean	s.e.
			Inversion results									
Sample 11M5												
E1 (0 Ma – T1)	(km/Ma)	0 - 2.0	0.78	0.10	1.23	0.26	1.19	0.27	1.11	0.31		
T1	(Ma)	0 - 15			5.40	1.76	4.64	2.06	4.12	2.33		
E2 (T1 – T2)	(km/Ma)	0 - 2.0			0.30	0.18	0.80	0.53	0.92	0.54		
T2	(Ma)	0 - 15					6.13	2.61	6.16	2.92		
E3 (T2 – T3)	(km/Ma)	0 - 2.0					0.32	0.27	0.75	0.54		
T3	(Ma)	0 - 15							7.41	3.11		
E4 (T3 – T4)	(km/Ma)	0 - 2.0							0.36	0.35		
Geotherm. grad.	(C°/km)	30 - 50	35.46	5.07	37.29	5.17	38.47	6.14	37.56	5.16		
No. of iterations			50		150		300		450			
No. of			2		4		6		8			
No. of observ.			9		9		9		9			
Log-likelihood			-94.99		-8.99		-4.46		-5.64			
BIC			194.37		26.77		**22.10**		28.86			
Sample 11M6												
E1 (0 Ma – T1)	(km/Ma)	0 - 2.0	0.86	0.08	1.62	0.30	1.52	0.24	1.48	0.33	1.53	0.31
T1	(Ma)	0 - 15			3.77	1.46	3.57	1.54	3.26	1.55	1.51	0.28
E2 (T1 – T2)	(km/Ma)	0 - 2.0			0.24	0.13	0.87	0.64	1.00	0.62	0.86	0.64
T2	(Ma)	0 - 15					5.28	2.44	3.62	2.47	5.96	4.70
E3 (T2 – T3)	(km/Ma)	0 - 2.0					0.25	0.26	0.54	0.51	0.71	0.56
T3	(Ma)	0 - 15							6.06	2.97	5.86	3.56
E4 (T3 – T4)	(km/Ma)	0 - 2.0							0.29	0.39	0.59	0.50
T4	(Ma)	0 - 15									6.72	3.37
E5 (T4 – T5)	(km/Ma)	0 - 2.0									0.43	0.36
Geotherm. grad.	(C°/km)	30 - 50	34.27	3.97	41.09	5.96	38.05	4.51	38.92	5.45	36.95	5.19
No. of iterations			50		150		300		450		490	
No. of			2		4		6		8		10	
No. of observ.			9		9		9		9		9	
Log-likelihood			-205.29		-11.11		-7.47		-5.23		-5.97	
BIC			414.97		31.01		28.11		**28.03**		33.92	
Sample 11M7												
E1 (0 Ma – T1)	(km/Ma)	0 - 2.0	0.26	0.06	0.45	0.32	0.51	0.39	0.63	0.45		
T1	(Ma)	0 - 25			13.00	8.97	7.84	8.39	9.81	8.54		
E2 (T1 – T2)	(km/Ma)	0 - 2.0			0.71	0.68	0.61	0.51	0.40	0.41		
T2	(Ma)	0 - 25					9.28	8.19	10.44	7.83		
E3 (T2 – T3)	(km/Ma)	0 - 2.0					0.83	0.57	0.56	0.53		
T3	(Ma)	0 - 25							11.82	7.47		
E4 (T3 –T4)	(km/Ma)	0 - 2.0							0.94	0.59		
Geotherm. grad.	(C°/km)	30 - 50	39.23	5.76	39.63	5.73	38.54	5.76	37.87	5.25		
No. of iterations			50		150		300		450			
No. of			2		4		6		8			
No. of observ.			9		9		9		9			
Log-likelihood			-38.08		-13.13		-8.74		-9.02			
BIC			79.38		32.69		**27.13**		30.92			
Sample 14M16												
E1 (0 Ma – T1)	(km/Ma)	0 - 2.0	0.53	0.08	0.29	0.22	0.24	0.21	0.21	0.18		
T1	(Ma)	0 - 15			6.26	3.76	5.10	3.02	5.54	3.64		
E2 (T1 – T2)	(km/Ma)	0 - 2.0			0.75	0.33	0.99	0.49	1.07	0.56		
T2	(Ma)	0 - 15					6.70	3.34	6.47	3.06		
E3 (T2 – T3)	(km/Ma)	0 - 2.0					0.63	0.37	0.99	0.56		
T3	(Ma)	0 - 15							7.68	2.85		
E4 (T3 – T4)	(km/Ma)	0 - 2.0							0.59	0.41		
Geotherm. grad.	(C°/km)	30 - 50	39.56	5.75	38.41	5.65	38.50	5.87	37.35	5.08		
No. of iterations			50		150		300		350			
No. of			2		4		6		8			
No. of observ.			9		9		9		9			
Log-likelihood			-76.80		-46.51		-33.29		-36.36			

BIC			157.99		101.82		**79.76**		90.30		
Sample 15M65											
E1 (0 Ma – T1)	(km/Ma)	0 - 2.0	0.33	0.08	0.36	0.31	0.32	0.29	0.27	0.27	
T1	(Ma)	0 - 15			7.94	3.91	6.73	4.23	7.87	3.59	
E2 (T1 – T2)	(km/Ma)	0 - 2.0			0.58	0.44	0.83	0.56	0.84	0.56	
T2	(Ma)	0 - 15					7.48	3.89	8.01	3.73	
E3 (T2 – T3)	(km/Ma)	0 - 2.0					0.61	0.47	0.87	0.57	
T3	(Ma)	0 - 15							8.39	3.18	
E4 (T3 -T4)	(km/Ma)	0 - 2.0							0.58	0.45	
Geotherm. grad.	(C°/km)		39.31	5.76	39.91	5.85	38.11	5.59	38.13	5.53	
No. of iterations			50		150		300		490		
No. of			2		4		6		8		
No. of observ.			7		7		7		7		
Log-likelihood			-10.81		-9.11		-6.53		-7.19		
BIC			24.85		24.66		**22.72**		27.25		
Sample 17M104_11M11											
E1 (0 Ma – T1)	(km/Ma)	0 - 2.0	0.35	0.07	0.30	0.23	0.30	0.27	0.30	0.26	
T1	(Ma)	0 - 15			8.51	3.73	7.38	3.34	7.74	3.64	
E2 (T1 – T2)	(km/Ma)	0 - 2.0			0.97	0.54	0.88	0.58	0.75	0.57	
T2	(Ma)	0 - 15					8.16	3.55	8.40	3.27	
E3 (T2 – T3)	(km/Ma)	0 - 2.0					0.96	0.51	0.89	0.54	
T3	(Ma)	0 - 15							9.19	2.89	
E4 (T3 -T4)	(km/Ma)	0 - 2.0							0.91	0.51	
Geotherm. grad.	(C°/km)		39.42	5.76	39.10	5.90	38.97	5.71	38.50	5.67	
No. of iterations			50		150		300		450		
No. of			2		4		6		8		
No. of observ.			12		12		12		12		
Log-likelihood			-60.32		-56.79		-55.02		-53.67		
BIC			125.61		**123.52**		124.94		127.22		

Parameters T1 to T5 denote the time (from 0 Ma to Tmax) at which exhumation rates change. Parameters E1 to E5 are the exhumation rates (from 0 to 2.0 km/Ma) between the time steps from 0 to T1 (E1) until T5 to Tmax (E5), Greyish coloured numbers indicate parameters which resulted in the arithmetic mean of their boundary limits and are not used for interpretation.

References

Aktug, B., Nocquet, J. M., Cingöz, A., Parsons, B., Erkan, Y., England, P., Lenk, O., Gürdal, M.A., Kilicoglu, A., Akdeniz, H., Tekgül, A. 2009. Deformation of western Turkey from a combination of permanent and campaign GPS data: Limits to block-like behaviour. Journal of Geophysical Research 114(10), doi:10.1029/2008JB006000.

Asti, R., Malusà, M.G., Faccenna, C., 2018. Supradetachment basin evolution unravelled by detrital apatite fission track analysis: the Gediz Graben (Menderes Massif, Western Turkey). Basin Research 30(3), 502-521.

Bozkurt, E., Winchester, J.A., Park, R.G., 1995. Geochemistry and tectonic significance of augen gneisses from the southern Menderes Massif (West Turkey). Geological Magazine 132(3), 287–301.

Bozkurt, E., 2000. Origin on N-S extensional tectonic in western Anatolia (Turkey): evidence from the Büyük Menderes Graben. In: Bozkurt, E., Winchester, J.A., & Piper, J.D.A., (Eds) Tectonics and magmatism in Turkey and its surrounding areas. The Geological Society of London, Special Publications 173, 385–403.

Bozkurt, E., Satir, M. 2000. The southern Menderes Massif (western Turkey): geochronology and exhumation history. Geological Journal, 35(3-4), 285-296.

Bozkurt, E., Sözbilir, H., 2004. Tectonic evolution of the Gediz Graben: field evidence for an episodic, two-stage extension in western Turkey. Geological Magazine 141, 63–79.

Baran, Z.O., Dilek, Y., Stockli, D. 2017. Diachronous uplift and cooling history of the Menderes core complex, western Anatolia (Turkey), based on new Zircon (U-Th)/He ages. Tectonophysics 694, 181-196.

Brady, R.J. 2002. Very high slip rates on continental extensional faults: new evidence from (U–Th)/He thermochronometry of the Buckskin Mountains, Arizona. Earth and Planetary Science Letters 197(1-2), 95–104.

Braun, J., 2003. Pecube: A new finite-element code to solve the 3D heat transport equation including the effects of a time-varying, finite amplitude surface topography. Computers & Geosciences 29(6), 787–794.

Braun, J., van der Beek, P., Valla, P., Robert, X., Herman, F., Glotzbach, C., Pedersen, V., Perry, C., Simon-Labric, T., Prigent, C., 2012. Quantifying rates of landscape evolu-tion and tectonic processes by thermochronology and numerical modelling of crustalheat transport using PECUBE. Tectonophysics 524–525, 1–28.

Brichau, S., Ring, U., Ketcham, R.A., Carter, A., Stockli, D., Brunel, M., 2006. Constraining the long-term evolution of the slip rate for a major extensional fault system in the central Aegean, Greece, using thermochronology. Earth and Planetary Science Letters 241, 293–306.

Brun, J.P. 1999. Narrow rifts versus wide rifts: inferences for the mechanics of rifting from laboratory experiments. Philosophical Transactions of the Royal Society of London. Series A: Mathematical, Physical and Engineering Sciences 357(1753), 695-712.

Brun, J.P., Sokoutis, D. 2007. Kinematics of the southern Rhodope core complex (North Greece). International Journal of Earth Sciences 96(6), 1079-1099.

Brun, J.P., Sokoutis, D., Tirel, C., Gueydan, F., Van den Driessche, J., Beslier, M. O., 2017. Crustal versus mantle core complexes. Tectonophysics. https://doi.org/10.1016/j.tecto.2017.09.017.

Brun, J.P., Sokoutis, D. 2018. Core complex segmentation in North Aegean, a dynamic view. Tectonics 37(6), 1797-1830.

Buck, W.R., 1991. Modes of continental lithospheric extension. Journal of Geophysical Research 96, 20, 161–20, 178.

Buck, W.R., Karner, G.D. 2004. Consequences of asthenospheric variability on continental rifting. In: Karner, G.D., Taylor, B., Driscoll, N.W., Kohlstedt, D.L. (Eds.), Rheology and deformation of the lithosphere at continental margins, Columbia University Press, New York, 62, 1-30.

Burtner, R., Nigrini, A., Donelick, R.A., 1994. Thermochronology of Lower Cretaceous source rocks in the Idaho-Wyoming Thrust belt. Bulletin of the American Association of Petroleum Geologists 78, 1613–1636.

Buscher, J.T., Hampel, A., Hetzel, R., Dunkl, I., Glotzbach, C., Struffert, A., Akal, C., Rätz, M., 2013. Quantifying rates of detachment faulting and erosion in the central Menderes Massif (western Turkey) by thermochronology and cosmogenic ^{10}Be. Journal of the Geological Society, London 170, 669–683.

Candan, O., Dora, O.Ö., Kun, N., Akal, C., Koraly, E., 1992. Allochthonous metamorphic units at the southern part of Aydın Mountains, Menderes Massif. Turkish Association of Petroleum Geologists 4(1), 93–110.

Candan, O., Dora, O.Ö., Oberhänsli, R., Çetinkaplan, M., Partzsch, J.H., Warkus, F.C., Dürr, S., 2001. Pan-African high-pressure metamorphism in the Precambrian basement of the Menderes Massif, western Anatolia, Turkey. International Journal of Earth Sciences 89, 793–811.

Candan, O., Çetinkaplan, M., Oberhänsli, R., Rimmelé, G., Akal, C., 2005. Alpine high-P/low-T metamorphism of the Afyon Zone and implications for the metamorphic evolution of Western Anatolia, Turkey. Lithos 84 (1-2), 102-124.

Catlos, E.J., Baker, C., Sorensen, S.S., Çemen, I., Hançer, M., 2010. Geochemistry, geochronology, and cathodoluminescence imagery of the Salihli and Turgutlu granites (central Menderes Massif, western Turkey): Implications for Aegean tectonics. Tectonophysics 488, 110-130.

Cenki-Tok, B., Expert, M., Işık, V., Candan, O., Monie, P., Bruguier, O., 2016. Complete Alpine reworking of the northern Menderes Massif, western Turkey. International Journal of Earth Sciences 105(5), 1507-1524.

Çiftçi, N.B., Bozkurt, E., 2010. Structural evolution of the Gediz Graben, SW Turkey: temporal and spatial variation of the graben basin. Basin Research 22, 846–873.

Cohen, H.A., Dart, C.J., Akyüz, H.S., Barka, A., 1995. Syn-rift sedimentation and structural development of the Gediz and Büyük Menderes graben, western Turkey. Journal of the Geological Society 152(4), 629–638.

Coney, P.J. 1980. Cordilleran metamorphic core complexes: An overview. Cordilleran metamorphic core complexes: Geological Society of America Memoir 153, 7-31.

Coney, P.J. 1987. The regional tectonic setting and possible causes of Cenozoic extension in the North American Cordillera, in Continental Extensional Tectonics. In: M. P. Coward, J. F. Dewey, and P. L.

Hancock. Geological Society Special Publications 28, 177–186.

Crittenden, M.D., Coney, P.J., Davis, G H., Davis, G.H., 1980. Cordilleran metamorphic core complexes Vol. 153. Geological Society of America.

Davis, G.A., Lister, G.S., Reynolds, S.J. 1986. Structural evolution of the Whipple and South Mountains shear zones, southwestern United States. Geology 14(1), 7-10.

Dunkl, I., 2002. TRAKKEY: a window program for calculation and graphical presentation of fission track data. Computers & Geosciences 28, 3–12.

Ehlers, T.A., Farley, K.A., 2003. Apatite (U-Th)/He thermochronometry: Methods and applications to problems in tectonics and surface processes. Earth and Planetary Science Letters 206, 1–14.

Emre, T., Sözbilir, H., 1997. Field evidence for metamorphic core complex, detachment faulting and accommodation faults in the Gediz and Büyük Menderes Grabens, Western Anatolia. International Earth Science Colloquium on the Aegean and Surrounding Regions, Proceedings, 1995, 1, 73–94.

Erkül, F., 2009. Tectonic significance of synextensional ductile shear zones within the Early Miocene Alaçamdağ granites, northwestern Turkey. Geological Magazine 147(4), 611–637.

Farley, K.A., Wolf, R.A., Silver, L.T., 1996. The effects of long alpha-stopping distances on (U-Th)/He ages. Geochimica et Cosmochimica Acta 60, 4223–4229.

Farley, K.A., 2000. Helium diffusion from apatite: General behavior as illustrated by Durango fluorapatite. Journal of Geophysical Research 105, 2903–2914.

Farley, K.A., 2002. (U-Th)/He dating: techniques, calibrations and applications. Mineralogical Society of America. Reviews in Mineralogy & Geochemistry 47, 819–844.

Flowers, R.M., Shuster, D.L. Farley, K.A., 2007. Radiation damage control on apatite (U-Th)/He dates from the Grand Canyon region, Colorado Plateau. Geology 35, 447–450.

Foster, D.A., John, B.E., 1999. Quantifying tectonic exhumation in an extensional orogen with thermochronology: examples from the southern Basin and Range Province. Geological Society, London, Special Publications 154(1), 343–364.

Fournier, M., Jolivet, L., Goffé, B., Dubois, R. 1991. Alpine Corsica metamorphic core complex. Tectonics 10(6), 1173-1186.

Gessner, K., Ring, U., Johnson, C., Hetzel, R., Passchier, C.W., Güngör, T., 2001a. An active bivergent rolling-hinge detachment system: Central Menderes metamorphic core complex in western Turkey. Geology 29, 611–614.

Gessner, K., Ring, U., Passchier, C.W., Güngör, T., 2001c. How to resist subduction: Eocene post-high-pressure emplacement of the Cycladic blueschist unit onto the Menderes nappes, Anatolide belt, western Turkey. Geological Society of London Journal 158, 769–780.

Gessner, K., Collins, A.S., Ring, U., Güngör, T., 2004. Structural and thermal history of poly-orogenic basement: U-Pb geochronology of granitoid rocks in the southern Menderes Massif, Western Turkey. Journal of the Geological Society, London 161, 93–101.

Gessner, K., Gallardo, L.A., Markwitz, V., Ring, U., Thomson, S.N., 2013. What caused the denudation of the Menderes Massif: Review of crustal evolution, lithosphere structure, and dynamic topography in southwest Turkey. Gondwana Research 24, 243–274.

Gleadow, A.J.W., 1981. Fission-track dating methods: what are the real alternatives? Nuclear Tracks 5, 3–14.

Gleadow, A.J.W., Duddy, I.R., 1981. A natural long-term track annealing experiment for apatite. Nuclear Tracks 5, 169–174.

Glodny, J., Hetzel, R., 2007. Precise U-Pb ages of syn-extensional Miocene intrusions in the central Menderes Massif, western Turkey. Geological Magazine 144, 235–246.

Glotzbach, C., Van Der Beek, P.A., Spiegel, C., 2011. Episodic exhumation and relief growth in the Mont Blanc massif, Western Alps from numerical modelling of thermochronology data. Earth and Planetary Science Letters 304 (3-4), 417-430.

Green, P.F., Duddy, I.R., Gleadow, A.J.W., Tingate, P.R., Laslett, G.M., 1986. Thermal annealing of fission tracks in apatite 1. A qualitative description. Chemical Geology 59, 237–253.

Grove, M., Harrison, T.M. 1996. 40Ar* diffusion in Fe-rich biotite. American Mineralogist 81(7-8), 940–951.

Guenthner, W.R., Reiners, P.W., Ketcham, R.A., Nasdala, L., Giester, G., 2013. Helium diffusion in natural zircon: Radiation damage, anisotropy, and the interpretation of zircon (U-Th)/He thermochronology. American Journal of Science 313, 145–198.

Hasözbek, A., Satır, M., Erdoğan, B., Akay, E., Siebel, W., 2011. Early Miocene post-collisional magmatism in NW Turkey: geochemical and geochronological constraints. International Geology Review 53(9), 1098–1119.

Heinecke, C,. Hetzel, R., Nilius, NP., Zwingmann, H., Todd, A,. Mulch, A., Wölfler, A., Glotzbach, C., Akal, C., Dunkl, I., Raven, M., Hampel, A., subm. Detachment faulting in a bivergent core complex constrained by fault gouge dating and low-temperature thermochronology. Journal of Structural Geology.

Herman, F., Braun, J., Senden, T.J., Dunlap, W.J., 2007. (U-Th)/He thermochronometry: Mapping 3D geometry using micro-X-ray tomography and solving the associated production-diffusion equation. Chemical Geology 242, 126–136.

Hetzel, R., Ring, U., Akal, C., Troesch, M., 1995a. Miocene NNE-directed extensional unroofing in the Menderes Massif, southwestern Turkey. Journal of the Geological Society, London 152, 639–654.

Hetzel, R., Passchier, C.W., Ring, U., Dora, O.Ö., 1995b. Bivergent extension in orogenic belts: The Menderes Massif (southwestern Turkey). Geology 23, 455–458.

Hetzel, R., Reischmann, T., 1996. Intrusion of Pan-African gneisses in the southern Menderes massif and the age of cooling after Alpine ductile extensional deformation. Geological Magazine 133, 565–572.

Hetzel, R., Romer, R.L., Candan, O., Passchier, C.W., 1998. Geology of the Bozdağ area, central Menderes massif, SW Turkey: Pan-African basement and Alpine deformation. International Journal of Earth Sciences (Geologische Rundschau) 87, 394–406.

Hetzel, R., Zwingmann, H., Mulch, A., Gessner, K., Akal, C., Hampel, A., Güngör, T., Petschick, R., Mikes, T., 2013. Spatiotemporal evolution of brittle normal faulting and fluid infiltration in detachment fault systems: A case study from the Menderes Massif, western Turkey. Tectonics 32, 1–13; doi:10.1002/tect.20031.

Hourigan, J.K., Reiners, P.W., Brandon, M.T., 2005. U-Th zonation-dependent alpha-ejection in (U-Th)/He chronometry. Geochim. Cosmochim. Acta 69, 3349–3365.

Hurford A.J., Green, P.F., 1983. The zeta age calibration of fission-track dating. Chemical Geology 1, 285–317.

Işik, V., Tekeli, O., 2001. Late orogenic crustal extension in the northern Menderes massif (western Turkey): Evidences for metamorphic core complex formation. International Journal of Earth Sciences 89, 757–765.

Işik, V., Tekeli, O., Seyitoğlu, G., 2004, The $^{40}Ar/^{39}Ar$ age of extensional ductile deformation and granitoid intrusion in the northern Menderes core complex: implications for the initiation of extensional tectonics in western Turkey. Journal of Asian Earth Sciences 23, 555–566.

Jolivet, L., Brun, J.-P., 2010. Cenozoic geodynamic evolution of the Aegean. International Journal of Earth Sciences 99, 109–138.

Kaymakci, N., Özçelik, Y., White, S.H., Van Dijk, P.M. 2009. Tectono-stratigraphy of the Çankırı Basin: late Cretaceous to early Miocene evolution of the Neotethyan suture zone in Turkey. Geological Society, London, Special Publications 311(1), 67-106.

Ketcham, R.A., Carter, A., Donelick, R.A., Barbarand, J., Hurford, A.J., 2007. Improved modelling of fission-track annealing in apatite. American Mineralogist 92(5-6), 799-810.

Koralay, O.E., Satır, M., Dora, O.Ö., 2001. Geochemical and geochronological evidence for Early Triassic calc-alkaline magmatism in the Menderes Massif, western Turkey. International Journal of Earth Sciences 89, 822–835.

Koralay, O.E., Candan, O., Akal, C., Dora, O.Ö., Chen, F., Satır, M., Oberhänsli, R., 2011. Geology and geochronology of the Pan-African and Triassic metagranitoids in the Menderes Massif, Western Anatolia, Turkey. Bulletin of the Mineral Research and Exploration 142, 69–121.

Koralay, O.E., 2015. Late Neoproterozoic granulite facies metamorphism in the Menderes Massif, Western Anatolia/Turkey: implication for the assembly of Gondwana. Geodinamica Acta 27, 244–266.

Kydonakis, K., Brun, J.P., Sokoutis, D. 2015. North Aegean core complexes, the gravity spreading of a thrust wedge. Journal of Geophysical Research. Solid Earth 120(1), 595-616.

Lippolt, H.J., Leitz, M., Wernicke, R.S., Hagerdon, B., 1994. (Uranium + thorium)/helium dating of apatite: experience with samples from different geochemical environments. Chemical Geology 112, 179–191.

Lips, A.L.W., Cassard, D., Sözbilir, H., Yilmaz, H., Wijbrans, J.R., 2001. Multistage exhumation of the Menderes Massif, western Anatolia (Turkey). International Journal of Earth Sciences 89, 781–792.

Lister, G.S., Banga, G., Feenstra, A., 1984. Metamorphic core complexes of Cordilleran type in the Cyclades, Aegean Sea, Greece. Geology 12(4), 221–225.

Lister, G.S., Etheridge, M.A., Symonds, P.A., 1986. Detachment faulting and the evolution of passive continental margins. Geology 14(3), 246–250.

Lister, G. S., Davis, G. A., 1989. The origin of metamorphic core complexes and detachment faults formed during Tertiary continental extension in the northern Colorado River region, USA. Journal of Structural Geology 11(1-2), 65–94.

Loos, S., Reischmann, T., 1999. The evolution of the southern Menderes Massif in SW Turkey as revealed by zircon dating. Journal of the Geological Society of London 156, 1021–1030.

Morris, A., Robertson, A.H.F. 1993. Miocene remagnetisation of carbonate platform and Antalya Complex units within the Isparta Angle, SW Turkey. Tectonophysics 220(1-4), 243-266.

Nabelek, P.I., Hofmeister, A.M., Whittington, A.G. 2012. The influence of temperature-dependent thermal diffusivity on the conductive cooling rates of plutons and temperature-time paths in contact aureoles. Earth and Planetary Science Letters 317, 157-164.

Naeser, C.W., 1978. Fission track dating, U.S. Geological Survey Open File Report 76–190, 31 pp.

Nilius, N. P., Glotzbach, C., Wölfler, A., Hampel, A., Dunkl, I., Akal, C., Heineke, C., Hetzel, R. 2019. Exhumation history of the Aydın range and the role of the Büyük Menderes detachment system during bivergent extension of the central Menderes Massif, western Turkey. Journal of the Geological Society, jgs2018-162.

Oberhänsli, R., Candan, O., Dora, O.Ö., Dürr, S., 1997. Eclogites within the Menderes Massif/western Turkey. Lithos 41, 135–150.

Okay, A.I., Tüyüz, O., 1999. Tethyan sutures of northern Turkey. In: Durand, B., Jolivet, L., Horvath, E., Seranne, M. (Eds.), The Mediterranean Basins: Tertiary Extension within the Alpine Orogen, London, 475-515.

Oner, Z., Dilek, Y., 2011. Supradetachment basin evolution during continental extension: the Aegean province of western Anatolia, Turkey. Geological Society of America Bulletin 123, 2115–2141.

Philippon, M., Brun, J.P., Gueydan, F. 2012. Deciphering subduction from exhumation in the segmented Cycladic Blueschist unit (Central Aegean, Greece). Tectonophysics 524, 116-134.

Price, P.B., Walker, R.M. 1963. Fossil tracks of charged particles in mica and the age of minerals. Journal of Geophysical Research 68(16), 4847-4862.

Rahn, M.K., Brandon, M.T., Batt, G.E. Garver, J.I., 2004. A zero-damage model for fission-track annealing in zircon. American Mineralogist 89, 473–484.

Regnier, J.L., Ring, U., Passchier, C.W., Gessner, K., Güngör, T., 2003. Contrasting metamorphic evolution of metasedimantary rocks from the Çine and Selimiye nappes in the Anatolide belt, western Turkey. Journal of Metamorphic Geology 21, 699–721.

Reiners, P.W., 2005. Zircon (U-Th)/He thermochronometry. Reviews in Mineralogy and Geochemistry 58, 151–179.

Reiners, P.W., Zhou, Z., Ehlers, T.A., Xu, C., Brandon, M.T., Donelick, R.A., Nicolescu, S., 2003. Post-orogenic evolution of the Dabie Shan, eastern China, from (U-Th)/He and fission track thermochronology. American Journal of Science 303, 489–518.

Reiners, P.W., Spell, T.I., Nicolescu, S., Zanetti, K. 2004. Zircon (U-Th)/He thermochronometry: He diffusion and comparisons with ^{40}Ar/^{39}Ar dating. Geochimica et Cosmochimica Acta 68, 1857–1887.

Reiners, P.W., Ehlers, T.A., (Eds) 2005. Low-temperature thermochronology: techniques, interpretations, and applications. Reviews in Mineralogy and Geochemistry 622 pp.

Reiners, P.W., Brandon, M.T., 2006. Using thermochronology to understand orogenic erosion. Annual Review of Earth and Planetary Sciences 34, 419–466.

Ring, U., Gessner, K., Güngör, T., Passchier, C.S., 1999. The Menderes Massif of western Turkey and the Cycladic Massif in the Aegean – do they really correlate? Journal of the Geological Society, London 156, 3–6.

Ring, U., Willner, A., Lackmann, W., 2001. Nappe stacking with different pressure-temperature paths: An example from the Menderes nappes of western Turkey. American Journal of Science 301, 912–944.

Ring, U., Johnson, C., Hetzel, R., Gessner, K., 2003. Tectonic denudation of a Late Cretaceous-Tertiary collisional belt: regionally symmetric cooling patterns and their relation to extensional faults in the Anatolide belt of western Turkey. Geological Magazine 140, 421–441.

Ring, U., Collins, A.S., 2005. U–Pb SIMS dating of synkinematic granites: timing of core-complex formation in the northern Anatolide belt of western Turkey. Journal of the Geological Society 162(2), 289–298.

Ring, U., Gessner, K., Thomson, S., 2017. Variations in fault-slip data and cooling history reveal corridor of heterogeneous backarc extension in the eastern Aegean Sea region. Tectonophysics 700-701, 108–130.

Rosenbaum, G., Regenauer-Lieb, K., Weinberg, R. 2005. Continental extension: From core complexes to rigid block faulting. Geology 33(7), 609-612.

Rossetti, F., Asti, R., Faccenna, C., Gerdes, A., Lucci, F., Theye, T., 2017. Magmatism and crustal extension: Constraining activation of the ductile shearing along the Gediz detachment, Menderes Massif (western Turkey). Lithos 282, 145–162.

Sambridge, M., 1999a. Geophysical inversion with a neighbourhood algorithm—I. Searching a parameter space. Geophysical Journal International 138(2),479–494.

Sambridge, M., 1999b. Geophysical inversion with a neighbourhood algorithm—II. Appraising the ensemble. Geophysical Journal International 138(3), 727–746.

Schultz, M.H., Hodges, K.V., Ehlers, T.A., van Soest, M., Wartho, J.A., 2017. Thermochronologic constraints on the slip history of the South Tibetan detachment system in the Everest region, southern Tibet. Earth and Planetary Science Letters 459, 105–117.

Schmidt, A., Pourteau, A., Candan, O., Oberhänsli, R., 2015. Lu-Hf geochronology on cm-sized garnets using microsampling: New constraints on garnet growth rates and duration of metamorphism during continental collision (Menderes Massif, Turkey). Earth and Planetary Science Letters 432, 24–35.

Schwarz, G., 1978. Estimating the dimension of a model. The annals of statistics 6(2), 461–464.

Sen, S., Seyitoğlu, G., 2009. Magnetostratigraphy of early-middle Miocene deposits from east-west trending Alaşehir and Büyük Menderes grabens in western Turkey, and its tectonic implications. In: van Hinsbergen, D.J.J., Edwards, M.A., Govers, R. (Eds). Collision and Collapse at the Africa-Arabia-Eurasia Subduction Zone. The Geological Society of London, Special Publications 311, 321–342.

Şengör, A.M.C., Yilmaz, Y., 1981. Tethyan evolution of Turkey: a plate tectonic approach. Tectonophysics, 75(3-4) 181-241.

Seyitoğlu, G., Scott, B.C. 1992. The age of the Büyük Menderes graben (west Turkey) and its tectonic

implications. Geological Magazine, 129(2) 239–242.

Seyıtoğlu, G., Tekeli, O., Çemen, I., Şen, Ş., Isik, V. 2002. The role of the flexural rotation/rolling hinge model in the tectonic evolution of the Alaşehir graben, western Turkey. Geological Magazine 139(1), 15-26.

Singleton, J.S., Stockli, D.F., Gans, P.B., Prior, M. G., 2014. Timing, rate, and magnitude of slip on the Buckskin-Rawhide detachment fault, west central Arizona. Tectonics 33(8), 1596–1615.

Tagami, T., Galbraith, R.F., Yamada, R., Laslett, G.M., 1998. Revised annealing kinetics of fission tracks in zircon and geological implications. In Advances in fission-track geochronology, Springer, Dordrecht, 99–112.

Tatar, O., Gürsoy, H., Piper, J.D.A., 2002. Differential neotectonic rotations in Anatolia and the Tauride Arc: palaeomagnetic investigation of the Erenlerdağ Volcanic Complex and Isparta volcanic district, south–central Turkey. Journal of the Geological Society 159(3), 281-294.

Thiede, R.C., Ehlers, T.A., 2013. Large spatial and temporal variations in Himalayan denudation. Earth and Planetary Science Letters 371, 278–293.

Thomson, S.N., Ring, U., 2006. Thermochronologic evaluation of postcollision extension in the Anatolide orogen, western Turkey. Tectonics 25, TC3005, doi:10.1029/2005TC001833.

Tirel, C., Brun, J.P., Burov, E. 2008. Dynamics and structural development of metamorphic core complexes. Journal of Geophysical Research: Solid Earth 113(B4).

van Hinsbergen, D. J., 2010. A key extensional metamorphic complex reviewed and restored: the Menderes Massif of western Turkey. Earth-Science Reviews 102(1-2), 60-76.

Wagner, G.A., van den Haute, P., 1992. Fission-track dating. Kluwer Academic Publishers, The Netherlands, 285 pp.

Wernicke, B. 1981. Low-angle normal faults in the Basin and Range Province: nappe tectonics in an extending orogen. Nature 291(5817), 645.

Webber, S., Norton, K.P., Little, T.A., Wallace, L.M., Ellis, S. 2018. How fast can low-angle normal faults slip? Insights from cosmogenic exposure dating of the active Mai'iu fault, Papua New Guinea. Geology, 46(3), 227-230.

Whipp, D.M., Ehlers, T.A., Blythe, A.E., Huntington, K.W., Hodges, K.V., Burbank, D.W., 2007. Plio-Quaternary exhumation history of the central Nepalese Himalaya: 2. Thermokinematic and thermochronometer age prediction model. Tectonics 26(3) doi:10.1029/2006TC001991.

Whitney, D.L., Teyssier, C., Rey, P., Buck, W.R. 2013. Continental and oceanic core complexes. Bulletin 125(3-4), 273-298.

Wijns, C., Weinberg, R., Gessner, K., Moresi, L. 2005. Mode of crustal extension determined by rheological layering. Earth and Planetary Science Letters 236(1-2), 120-134.

Wolf, R.A., Farley, K.A., Silver, L.T., 1996. Helium diffusion and low temperature thermochronology of apatite. Geochimica et Cosmochimica Acta 60, 4231–4240.

Wolf, R.A., Farley, K.A. Kass, D.M., 1998. Modelling of the temperature sensitivity of the apatite (U-Th)/He thermochronometer. Chemical Geology 148, 105–114.

Wölfler, A., Glotzbach, C., Heineke, C., Nilius, N.P., Hetzel, R., Hampel, A., Akal, C., Dunkl, I., Christl, M., 2017. Late Cenozoic cooling history of the central Menderes Massif: Timing of the Büyük

Menderes detachment and the relative contribution of normal faulting and erosion to rock exhumation. Tectonophysics 717, 585-598.

Zaun, P.E., Wagner, G.A., 1985. Fission-track stability in zircons under geological conditions. Nuclear Tracks 10, 303–307.

Zeitler, P.K., Herczeg, A.L., McDougall, I., Honda, M., 1987. U-Th-He dating of apatite: A potential thermochronometer. Geochimica et Cosmochimica Acta 51, 2865–2868.

Ziegler, P.A., Cloetingh, S., 2004. Dynamic processes controlling evolution of rifted basins. Earth Science Reviews 64, 1–50.

6. Spatial patterns of erosion and landscape evolution in a bivergent metamorphic core complex revealed by cosmogenic 10Be: The central Menderes Massif (Western Turkey)

Caroline Heineke [a*], Ralf Hetzel [a], Nils-Peter Nilius [b], Christoph Glotzbach [c], Cüneyt Akal [d], Marcus Christl [e], Andrea Hampel [b]

[a] Institut für Geologie und Paläontologie, Westfälische Wilhelms-Universität Münster, Corrensstraße 24, D-48149 Münster, Germany, rahetzel@uni-muenster.de

[b] Institut für Geologie, Leibniz Universität Hannover, Callinstraße 30, D-30167 Hannover, Germany, nilius@geowi.uni-hannover.de, hampel@geowi.uni-hannover.de

[c] Institut für Geologie und Geodynamik, Universität Tübingen, Wilhelmstraße 56, D-72074 Tübingen, Germany, christoph.glotzbach@uni-tuebingen.de

[d] Dokuz Eylül University, Engineering Faculty, Department of Geological Engineering, Tınaztepe Campus, Buca, TR-35160 Izmir, Turkey, cuneyt.akal@deu.edu.tr

[e] Laboratory of Ion Beam Physics, ETH Zurich, Otto-Stern-Weg 5, HPK G23, 8093 Zurich, Switzerland, mchristl@phys.ethz.ch

* Corresponding author, caroline.heineke@uni-muenster.de, Phone: +49 (0) 251 83-33936

Own contribution: Participation of three sampling fieldtrips, discussions, manuscript comments

ABSTRACT

In extensional provinces with low-angle normal faulting – such as the Aegean region – both tectonic processes and erosion induce landscape change, but their interaction during the evolution of topography and relief accompanying continental extension has rarely been addressed. Here we present local and catchment-wide ^{10}Be erosion rates that document the spatial pattern of erosion in the central Menderes Massif, a metamorphic core complex consisting of two asymmetric mountain ranges (Bozdağ and Aydın) bound by detachment faults and active grabens. Catchment-wide erosion rates on the northern flank of the Bozdağ Range are rather low (40–110 mm/kyr), but reach values of >300 mm/kyr on the steep southern escarpment; a pattern that reflects both topography and bedrock lithology. In the Aydın Range, erosion rates are generally higher – with mean erosion rates of ~190 and ~260 mm/kyr on the northern and southern flank, respectively – and more variable along-strike. In both ranges, the erosion of ridge crests, which we determined using amalgamated bedrock clasts, proceeds at rates of 30–90 mm/kyr. The difference between local and catchment-wide erosion rates indicates that topographic relief increases in most parts of the massif in response to ongoing fault-related uplift and concomitant river incision. The analysis of river profiles, drainage divide position and mobility suggests that rock uplift is strongest in the eastern Bozdağ Range and declines along-strike. Our findings document that tectonic processes exert a significant control on landscape evolution during active continental extension and are reflected in both the topographic signature and the spatial pattern of erosion.
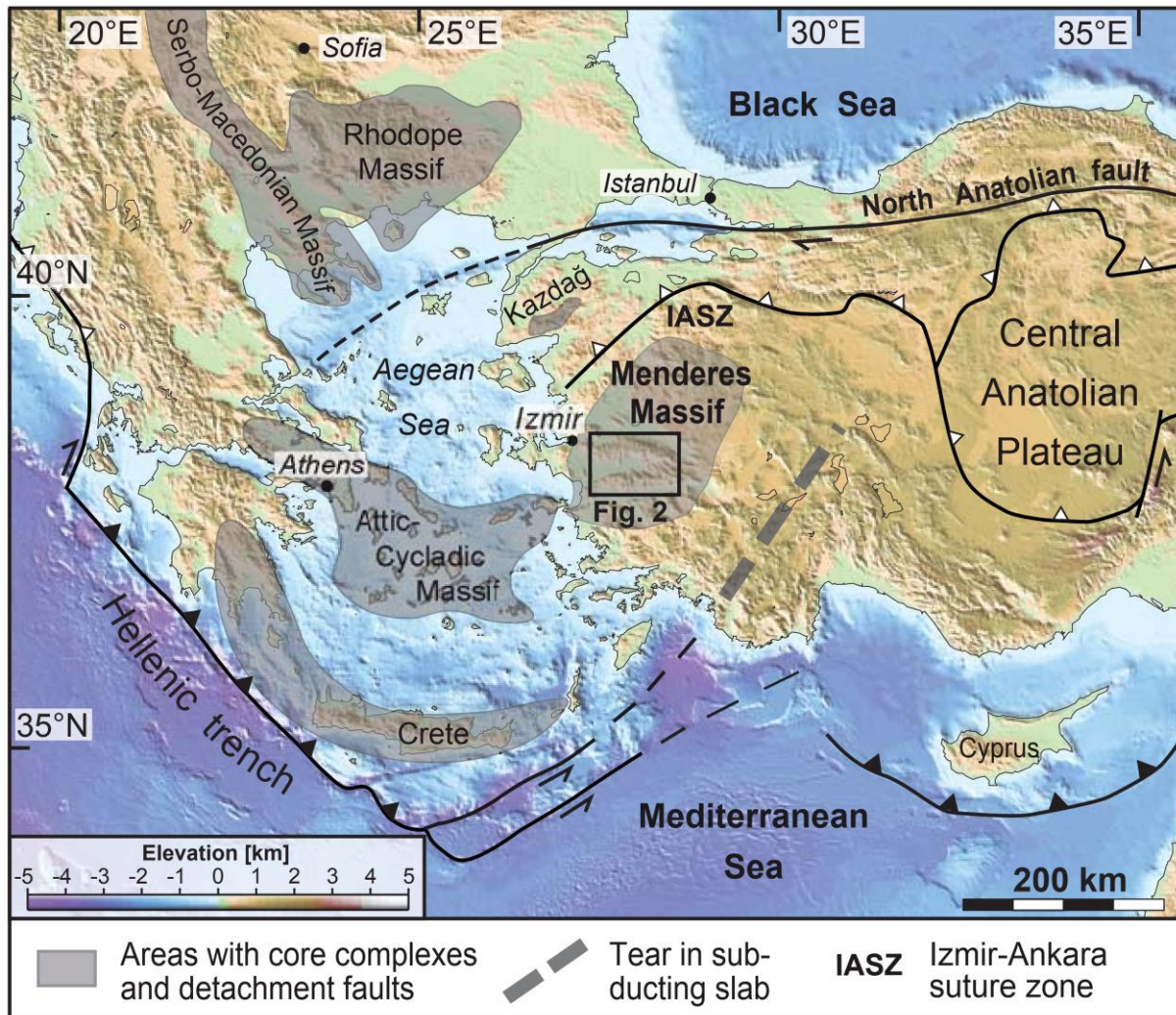
Figure 1: Map of the Eastern Mediterranean region showing the Menderes Massif and other metamorphic massifs with detachment faults (modified from Öner and Dilek, 2011).

6.1   INTRODUCTION

In tectonically active regions, tectonic and surface processes act in concert to shape the Earth's landscape (e.g., Willett et al., 2006; Bishop, 2007). These processes include the activity of faults as well as erosion, sediment transport, and deposition and ultimately lead to the exhumation of rocks. In this context, a fundamental difference between regions undergoing crustal shortening or extension exists. While in regions of shortening, rock exhumation occurs exclusively by erosion, in extensional environments both tectonic denudation (i.e., normal faulting) and erosion contribute to the exhumation of rocks (England and Molnar, 1990; Ring et al., 1999). In regions where extension has been predominantly accommodated by low-angle detachment faulting, tectonic denudation has often been considered to be the dominant mechanism for rock exhumation (e.g., Foster and John, 1999; Ring et al., 1999; Brichau et al., 2008). On the other hand, erosional denudation exerts an important control on rock exhumation and landscape evolution in mountains bounded by high-angle
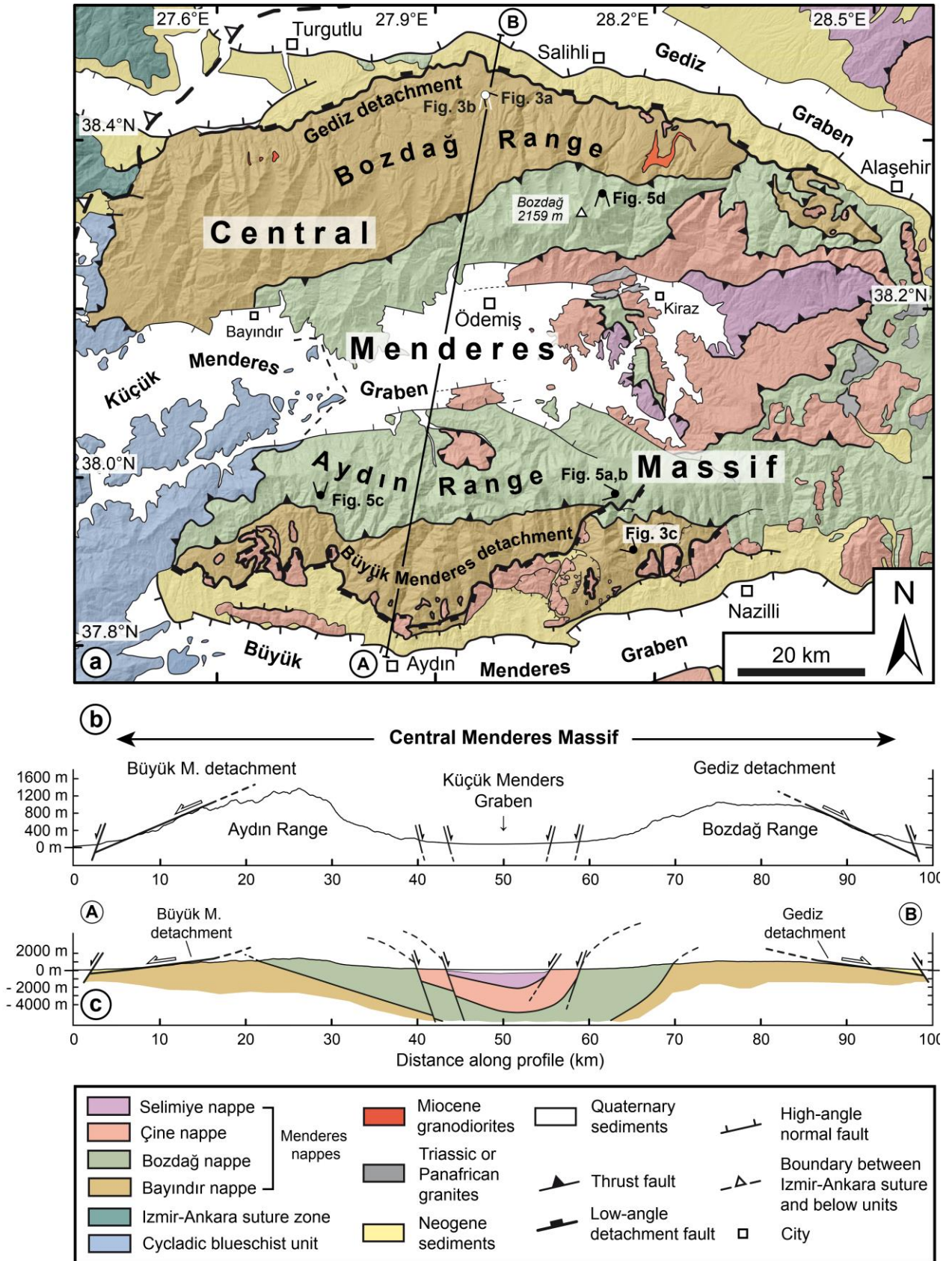
Figure 2: a) Geological map of the central Menderes Massif (modified from Wölfler et al., 2017 and complemented with own field observations). **b)** Topographic profile across the central Menderes Massif (vertical exaggeration = 5). Note the topographic asymmetry of the Bozdağ and Aydın mountain ranges with shallow dipping flanks on the sides of the two detachment faults and steep flanks toward the Küçük Menderes Graben. **c)** Geological profile (no vertical exaggeration) showing the Menderes nappe stack, which defines a synform beneath the Küçük Menderes Graben (based on Gessner et al., 2011 and own field observations).

normal faults (e.g., Harbor, 1997; Armstrong et al., 2003). In such ranges, 10Be-based erosion rates tend to be higher at the center of faults and lower near their tips, although the rates often vary considerably along strike (e.g., Reinhardt et al., 2007a; Densmore et al., 2009; Stock et al., 2009; Rossi et al., 2017; Roda-Boluda et al., 2019). In contrast to mountains bounded by high-angle normal faults, rates of erosion and the concomitant development of topography and relief have rarely been quantified in regions with low-angle detachment faults (e.g., Buscher et al., 2013).

In the Aegean extensional province, extension and detachment faulting led to the exhumation of metamorphic rocks from mid-crustal levels in several metamorphic massifs (e.g., the Rhodope Massif, the Attic-Cycladic Massif, and the Menderes Massif; Fig. 1) (e.g., Gautier et al., 1993; Hetzel et al., 1995a; Grasemann et al., 2012; Jolivet et al., 2013). In this connection, the Menderes Massif in Western Turkey was recognized as the first example of bivergent extension, i.e. the exhumation of rocks occurred along two detachments faults with opposite sense of shear (Gessner et al., 2001). This finding and the fact that the Menderes Massif is entirely located above sea-level, render it ideally suited to investigate the interplay between tectonic and surface processes and their relative contribution to exhumation in an extensional environment. So far, the contribution of erosion to rock exhumation has only been investigated along a narrow transect through the central part of the Menderes Massif by combining ^{10}Be catchment-wide erosion rates with low-temperature thermochronology (Buscher et al., 2013; Wölfler et al., 2017). However, to what extent erosion varies across the entire central Menderes Massif and how ongoing crustal extension and erosional denudation control the landscape evolution of the massif is still largely unknown.

Cosmogenic nuclides enable the quantification of erosion rates on local and catchment-scale in various geological settings (e.g., Brown et al., 1995; Small et al., 1997; Hancock and Kirwan, 2007; Meyer et al., 2010; Portenga and Bierman, 2011). Furthermore, the combination of spatially-averaged, catchment-wide erosion rates with local rates of erosion at the outcrop-scale can place constraints on the development of topography and local relief (Meyer et al., 2010; Wolff et al., 2018). Combined with digital elevation data, cosmogenic nuclide-derived erosion rates can further be used to deduce the erosional pattern of entire mountain ranges and thus aid the identification of processes that drive landscape evolution on various spatial scales. In this context, the development of new geomorphologic tools to analyze the dynamic state of river networks, river profiles, and drainage divide motion as well as the relationships between topographic parameters and erosion have proven highly valuable in identifying tectonic processes that shape the Earth's surface (e.g., DiBiase et al., 2010; Kirby and Whipple, 2012; Perron and Royden, 2013; Willett et al., 2014).

Here, we present local ^{10}Be erosion rates for 14 ridge crests and spatially-averaged erosion rates for 31 catchments in the central Menderes Massif to resolve the spatial pattern of erosion across the massif. These data allow us to draw conclusions on the development of local relief during the

ongoing extension and – in combination with the analysis of river networks – enable us to infer processes that have shaped the morphology of the central Menderes Massif during continental extension.

6.2   GEOLOGICAL SETTING

The Aegean region and Western Turkey are located in the backarc of the Hellenic subduction zone (Fig. 1) and have experienced pronounced extension during the past ~25 Ma caused by the progressive roll-back of the subducting African plate (e.g., Jolivet and Faccenna, 2000; Brun and Sokoutis, 2010; Jolivet et al., 2013). The extensional deformation, aided by erosional denudation, led to the exhumation of mid-crustal rocks, which are exposed in several metamorphic massifs in Greece, Bulgaria, and Western Turkey (Fig. 1). GPS data show that extension in this entire region is still ongoing (Reilinger et al., 2010). At present, Western Turkey – with the Menderes Massif in its central part – is extending at a rate of about 20 mm/yr in a north-south direction (Aktuğ et al., 2009).
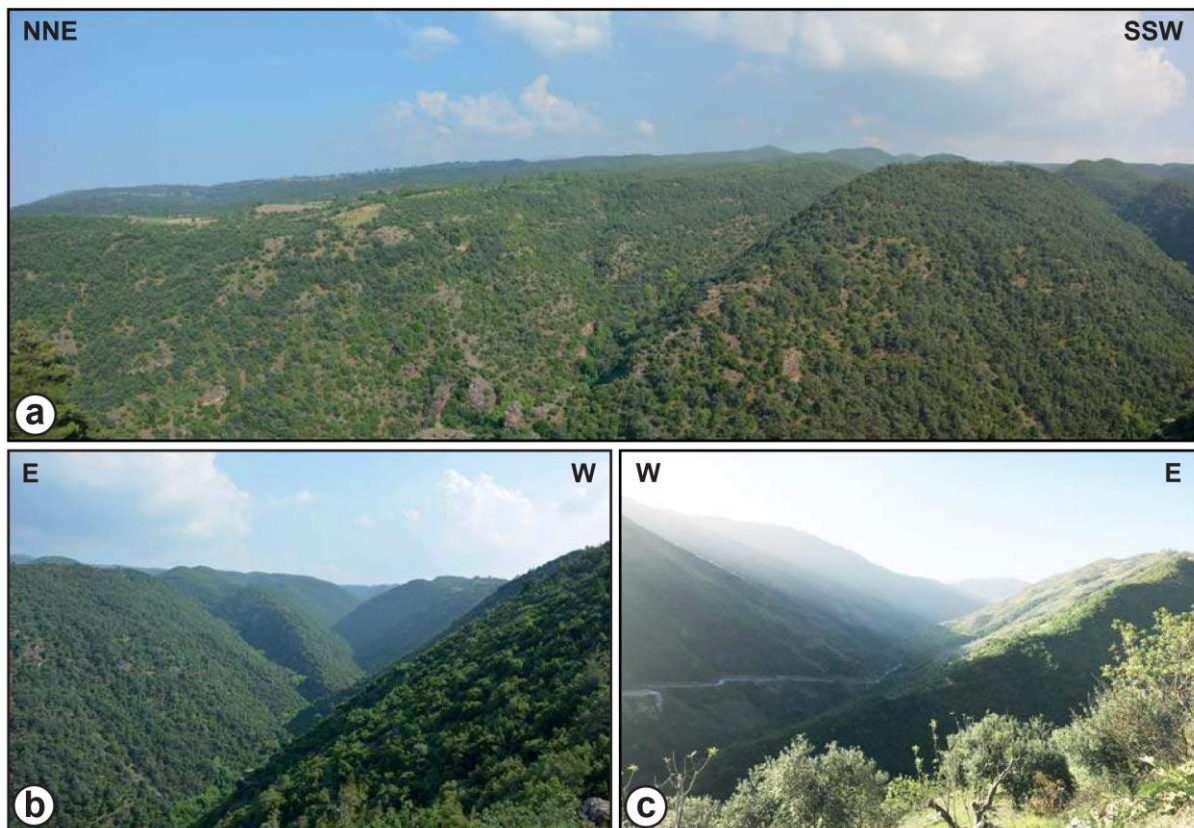
Figure 3: a) Photograph of the Gediz detachment surface dipping 15° to the N. Rivers have cut through the cataclastic detachment surface, forming steep valleys. **b)** Exemplary catchment of the northern slope of the Bozdağ Range (uphill view). Flat-topped mountain crests represent the Gediz detachment. **c)** Exemplary catchment of the southern slope of the Aydın Range (upstream view). Valleys exhibit planar hillslopes that are less steep than in the Bozdağ Range.

The Menderes Massif consists of three submassifs, which are separated by two major east-west trending grabens – the Gediz Graben and the Büyük Menderes Graben (e.g., Seyitoğlu and Scott, 1991; Yılmaz et al., 2000; Gürer et al., 2009; Çiftçi and Bozkurt, 2010) (Fig. 2a). The long-lasting history of extension of the Menderes Massif started with a first phase of extension during the late

Oligocene and the early Miocene, when the rocks of the northern submassif where largely exhumed by normal faulting (e.g., Işık and Tekeli, 2001; Thomson and Ring, 2006; Ersoy et al., 2010). Subsequently, the metamorphic rocks of the central submassif were exhumed in the footwalls of two low-angle normal faults – the Gediz and Büyük Menderes detachments – which trend east-west and dip to the north and south, respectively (e.g., Hetzel et al., 1995a,b; Emre and Sözbilir, 1997; Bozkurt and Oberhänsli, 2001; Gessner et al., 2001, 2013) (Figs. 2b,c). The Gediz detachment operated with a top-to-the-N to NNE shear sense, whereas the shear sense of the Büyük Menderes detachment is top-to-the-S to SSW (Hetzel et al., 1995b; Emre, 1996; Gessner et al., 2001; Işık et al., 2003). Both detachments are cut by the high-angle normal faults of the Gediz and Büyük Menderes grabens, which are seismically active as documented by raised fluvial terraces, fault scarps, and earthquakes (Ambraseys, 1971; Eyidoğan and Jackson, 1985; Altunel, 1999; Çiftçi and Bozkurt, 2010). Sedimentological and stratigraphic data indicate that the transition from low-angle detachment faulting to high-angle normal faulting occurred in the latest Pliocene to early Quaternary (e.g., Purvis and Robertson, 2005; Öner and Dilek, 2011).

The central Menderes Massif comprises two mountain ranges, the Bozdağ and the Aydın range, which are separated by the Küçük Menderes Graben (Fig. 2a). Both mountain ranges are characterized by a topographic asymmetry with rather steep mountain flanks facing the Küçük Menderes Graben and shallow-dipping flanks on the sides of the two detachment faults (Fig. 2b). The Gediz detachment along the northern side of the Bozdağ Range is exceptionally well-preserved owing to highly resistant cataclasites with a thickness of 20–50 m and the widespread presence of quartz-rich mylonites underneath (Hetzel et al., 1995b; Emre, 1996; Buscher et al., 2013). Therefore, streams incising the Gediz detachment form narrow valleys with steep hillslopes (Fig. 3a,b). The Büyük Menderes detachment along the southern flank of the Aydın Range is less well preserved, because the cataclasites associated with this fault are less than 5 m thick (Emre and Sözbilir, 1997; Hetzel et al., 2013; own field observations). In addition, the dominant lithologies underneath this detachment are mica schists and phyllites, which are susceptible to weathering and erosion, while resistant quartzites are absent (Wölfler et al., 2017). As a consequence, most valleys at the Büyük Menderes detachment are broader, yet deeply incised, and exhibit planar hillslopes (Fig. 3c). Apart from the metamorphic rocks, two belts of Neogene sedimentary rocks extend along the northern and southern margin of the central Menderes Massif (Fig. 2a). These strata are well exposed due to footwall uplift and ongoing normal faulting along the main boundary faults of the Gediz and Büyük Menderes Graben.
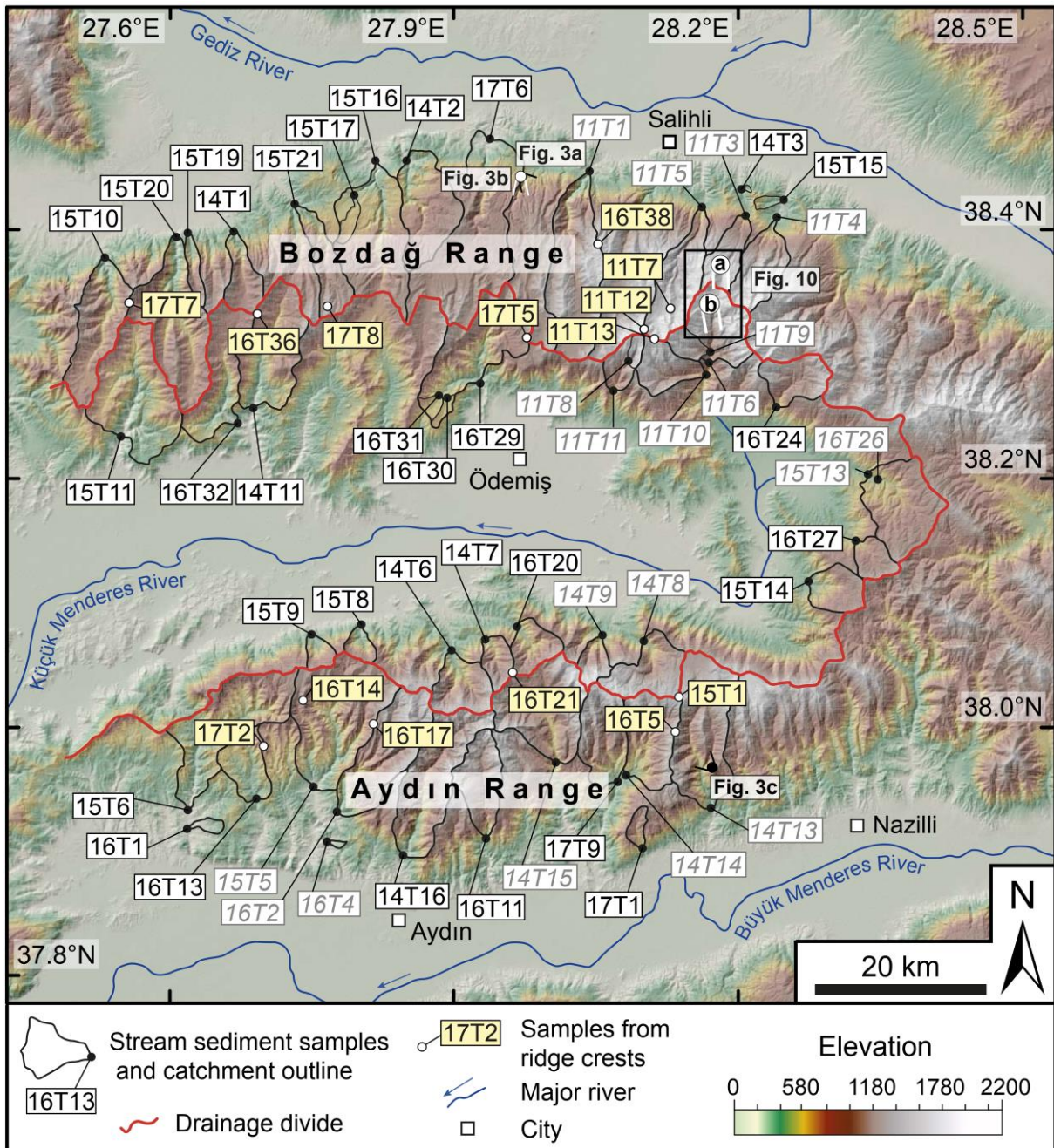
Figure 4: Shaded-relief image of the study area. Sampling sites for 10Be drainage basin erosion rates are labelled with sample numbers in white boxes. Catchment outlines are shown in black. Sample numbers in gray correspond to samples that have previously been published by Buscher et al. (2013), Wölfler et al. (2017), and Heineke et al. (2017) (for details see Table 1). Positions of ridge crest samples are labelled with sample numbers in yellow boxes.

The metamorphic rocks of the central Menderes Massif constitute a nappe pile that formed during Late Cretaceous to Eocene plate convergence and crustal shortening along the Izmir-Ankara suture zone (e.g., Şengör et al., 1984; Ring et al., 1999; van Hinsbergen et al., 2010; Gessner et al., 2013). The Menderes nappes include, from lowest to highest structural level, the Bayındır, Bozdağ, Çine, and Selimiye nappes, which in turn are overlain by the Cycladic Blueschist Unit in the west (Ring et al., 1999; Gessner et al., 2013) (Figs. 2a,c). The Gediz and Büyük Menderes detachments cut obliquely through the nappe pile and during their activity slivers of Çine nappe were emplaced as

klippen against rocks of the Bayındır nappe in their footwalls (Fig. 2a) (Hetzel et al., 1995b; Buscher et al., 2013; Wölfler et al., 2017). The boundaries of the tectonometamorphic units define an east-west trending synform, which developed during bivergent north-south extension (Gessner et al., 2001). Together with the detachment faults, this synform appears to control the present-day topography of the submassif and in particular the escarpments facing the Küçük Menderes Graben (Fig. 2c).
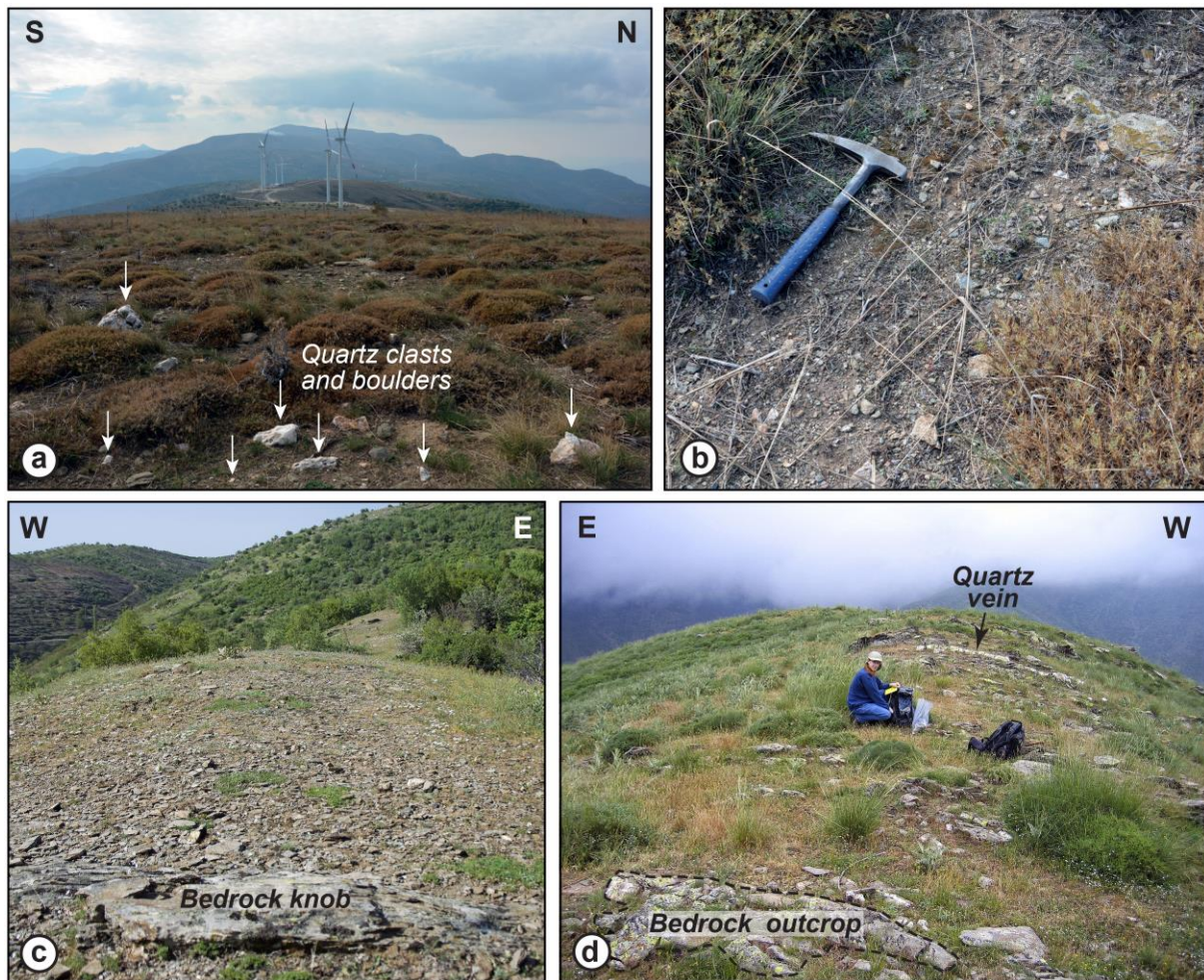
Figure 5: Representative photographs of ridge crests in the central Menderes Massif that we sampled to determine local erosion rates (see method section for details of sampling approach and Figure 2 for location of the pictures). **a)** Broad, 50–70 m wide ridge crest in the eastern Aydın Range. The area from which we collected sample 15T1 had a size of about 200 m x 50 m. White arrows indicate quartz clasts and boulders derived from quartz veins, which we avoided during sampling. **b)** Close-up view of the ridge-crest surface shown in (a) with typical bedrock clasts that were sampled (hammer for scale). Sample 15T1 yielded an erosion rate of 51±5 mm/kyr. **c)** Narrow, ~15-m-wide ridge crest in the western Aydın Range where we took sample 16T14 (the sampled area had a size of about 50 m x 10 m). Bedrock knobs such as the one visible in the foreground were avoided during sampling. Sample 16T14 yielded an erosion rate of 87±9 mm/kyr. **d)** Narrow, ~8-m-wide ridge crest in the Bozdağ Range, where we took sample 11T7 from an area of about 40 m x 5 m. Bedrock patches and quartz veins such as those seen in the foreground and background, respectively, were not sampled. Sample 11T7 gave an erosion rate of 70±6 mm/kyr.

The rocks of the Bayındır and Bozdağ nappes constitute the dominant lithological units in the central Menderes Massif. These nappes mainly consist of greenschist to amphibolite facies two-mica schists, phyllites, and quartzites, with minor amounts of marble and local amphibolite layers (Dora et al., 1990; Hetzel et al., 1998; Candan et al., 2011). In contrast, the structurally higher Çine and

Selimiye nappes are made up of orthogneisses, pelitic gneisses, as well as minor amounts of metapelites and granites (e.g., Hetzel and Reischmann, 1996; Hetzel et al., 1998; Ring et al., 1999; Candan et al., 2001). These nappes mainly occur in the eastern part of the submassif near the Küçük Menderes Graben or as tectonic klippen on the two detachment faults (Fig. 2a).

Recent studies that employed low-temperature thermochronology revealed a two-stage history of cooling and detachment faulting for the central Menderes Massif (Gessner et al., 2001; Ring et al., 2003; Buscher et al., 2013; Wölfler et al., 2017; Nilius et al., accepted manuscript) (**Fig. 2**). The first phase occurred in the middle Miocene (~16 to ~10 Ma), whereas the second phase lasted from the latest Miocene to the late Pliocene/early Quaternary (~6 to ~2 Ma). The second phase was most pronounced in the eastern part of the Bozdağ Range (i.e. in the region south of Salihli town; see Fig. 4) as evident from a phase of rapid slip (~4 mm/yr) along the Gediz detachment between 4–2 Ma (Buscher et al., 2013) and Plio-Quaternary cooling ages from detrital apatite fission track analyses (Asti et al., 2017). This interpretation is consistent with the fact that the highest topography of the entire Menderes Massif occurs in this region and with the observation that the Gediz detachment is particularly well preserved here.
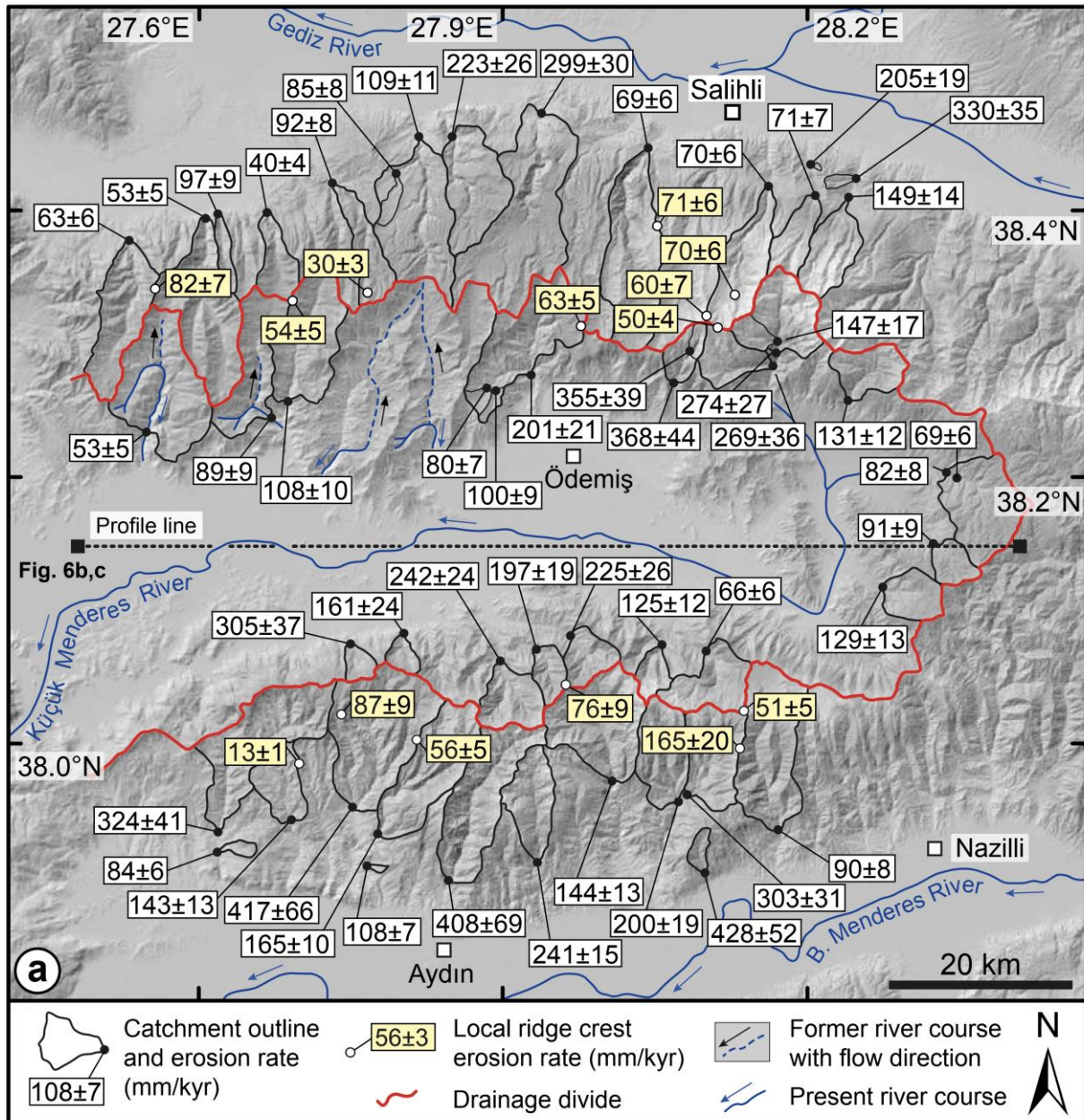
Figure 6: Shaded relief image showing local and catchment-wide erosion rates (mm/kyr) in the central Menderes Massif (1σ external uncertainties). In the western part of the Bozdağ Range, several rivers have experienced a flow reversal. The former and current river courses are indicated by white and blue arrows, respectively, following Süzen et al. (2006).

6.3   METHODS

Catchment-wide and Local Erosion Rates from Cosmogenic ^{10}Be

Cosmogenic nuclides are increasingly used to measure erosion rates over millennial timescales at outcrop or catchment scale (e.g., Cerling and Craig, 1994; Niedermann, 2002; Dunai, 2010; Portenga and Bierman, 2011). The erosion rate E (mm/kyr) of a steadily eroding bedrock surface is approximately inversely proportional to its cosmogenic nuclide concentration and given by:

$$E = [(P/C) - \lambda]\, z^{*} \qquad\qquad (1)$$

where P is the local surface production rate (at/g/yr), C is the nuclide concentration at the surface (at/g), λ is the decay constant (1/yr), and z^{*} is the absorption depth scale (i.e., the effective

attenuation length divided by rock density) (Lal, 1991). Erosion rates from cosmogenic nuclide concentrations average over the time needed to erode one absorption depth z^*. Depending on the erosion rate, this time interval typically corresponds to $10^2 - 10^5$ years (e.g., von Blanckenburg, 2006). The relationship given in equation (1) can be applied to quantify local erosion and to derive spatially averaged erosion rates for entire river catchments by determining the ^{10}Be concentration in quartz of sand samples from active streams (Brown et al., 1995; Bierman and Steig, 1996; Granger et al., 1996). This approach assumes that (1) quartz is homogeneously distributed in the eroding rocks, (2) the sediment in the stream channels is well mixed, (3) erosion in the catchment is in steady state (i.e., nuclide production is equal to the outflux of the nuclide via erosion and radioactive decay), and (4) erosion is uniform through time (e.g., von Blanckenburg, 2006; Granger and Riebe, 2007).

Sampling Strategy, Sample Preparation, and Calculation of Erosion Rates

For this study, we measured the ^{10}Be concentration of 31 stream sediment samples and 14 samples from ridge crests to derive both catchment-wide and local erosion rates across the entire central Menderes Massif (Fig. 4). We also include the catchment-wide ^{10}Be erosion rates previously published by Buscher et al. (2013), Wölfler et al. (2017), and Heineke et al. (2017) (Fig. 4, gray sample numbers). We collected our sediment samples along-strike of the Bozdağ and Aydın ranges from streams that flow into the Gediz, Küçük Menderes, and Büyük Menderes Graben, respectively. Each sediment sample was taken from several points along the respective stream over a distance of 20–60 m. Most samples are from rivers that exclusively drain metamorphic rocks. Yet, four samples (14T3, 15T15, 16T1, 16T4) were taken from streams, which flow through the Neogene sedimentary rocks exposed along the northern and southern margins of the massif (Fig. 2a). Note that the erosion rate derived from sample 16T4 has been published by Heineke et al. (2017).

To quantify the erosion of ridge crests, we took samples consisting of 1500–2600 bedrock clasts with a length of 1 to 3.5 cm on 14 mountain crests (Fig. 4). Amalgamated samples of bedrock clasts or grus were used before to quantify local erosion rates and to constrain changes in topographic relief due to river incision (Meyer et al., 2010; Strobl et al., 2012; Wolff et al., 2018). This sampling approach builds on results of previous studies, which have shown that erosion rates for bedrock outcrops may differ significantly from the actual long-term erosion rate because bedrock erosion mainly occurs by the episodic removal of small blocks or chips (Small et al., 1997, 1999; Anderson, 2002; Reinhardt et al., 2007b). Hence, erosion rates inferred from bedrock samples may be either too low or too high. Following Small et al. (1999) and Meyer et al. (2010), we argue that amalgamated clasts from soil- or regolith-covered surfaces are better suited to obtain accurate long-term erosion rates.

TABLE 1. ^{10}Be CONCENTRATIONS AND EROSION RATES FOR CATCHMENTS IN THE MENDERES MASSIF, WESTERN TURKEY.

Sample [†]	Location		Sample elevation	Mean catchment elevation	Mean slope	Catchment area	^{10}Be concen-tration [#]	Production rate		Catchment-wide erosion rate [**]	Internal uncertainty [**] (1σ)	External uncertainty [**] (1σ)	Time scale [††]
	Lat	Lon						spallation	muons				
	(°N)	(°E)	(m)	(m)	(°)	(km²)	(10⁴ at/g)	(at/g/yr)	(at/g/yr)	(mm/kyr)	(mm/kyr)	(mm/kyr)	(kyr)
Bozdağ Range													
17T6	38.4824	27.9424	175	839	16.0	157	1.93 ± 0.13	7.60	0.100	**300**	21	30	2.1
16T24	38.2639	28.2392	499	1078	21.5	34	5.10 ± 0.25	9.12	0.108	**132**	7	12	4.8
16T29	38.2853	27.9293	220	752	22.1	92	2.68 ± 0.20	7.08	0.097	**202**	15	21	3.2
16T30	38.2722	27.8909	464	585	10.9	4.3	4.77 ± 0.27	6.19	0.092	**100**	6	9	6.4
16T31	38.2738	27.8887	450	587	13.6	5.4	5.91 ± 0.29	6.20	0.092	**80**	4	7	8.0
16T32	38.2516	27.6735	166	690	20.8	65	5.71 ± 0.36	6.73	0.095	**90**	6	9	7.1
15T10	38.3876	27.5345	216	756	21.9	70	8.36 ± 0.43	7.11	0.097	**64**	3	6	10
15T11	38.2397	27.5523	131	575	20.1	112	8.75 ± 0.44	6.14	0.092	**53**	3	5	12
15T15	38.4343	28.2457	213	425	22.1	3.4	1.49 ± 0.12	5.44	0.087	**331**	26	35	2.2
15T16	38.4654	27.8197	154	707	16.0	104	4.77 ± 0.29	6.85	0.096	**109**	7	10	5.9
15T17	38.4371	27.7967	417	606	9.4	6.8	5.70 ± 0.31	6.31	0.093	**85**	5	8	7.5
15T19	38.4069	27.6234	226	781	25.5	12	5.59 ± 0.31	7.25	0.098	**98**	5	9	6.5
15T20	38.4033	27.6104	195	749	24.2	104	9.96 ± 0.50	7.07	0.097	**53**	3	5	12
15T21	38.4303	27.7355	244	869	21.7	36	6.26 ± 0.31	7.78	0.101	**93**	5	8	6.9
14T1	38.4087	27.6700	236	819	22.4	28	13.68 ± 0.63	7.41	0.099	**40**	2	4	16
14T2	38.4677	27.8534	177	746	17.1	69	2.42 ± 0.22	7.06	0.097	**223**	21	27	2.9
14T3	38.4425	28.2032	269	400	24.7	0.5	2.34 ± 0.14	5.32	0.086	**206**	12	19	3.5
14T11	38.2636	27.6912	174	706	21.1	84	4.79 ± 0.29	6.79	0.096	**108**	7	10	5.9
11T1[*]	38.4580	28.0447	190	1081	21.5	104	9.66 ± 0.42	9.17	0.108	**69**	3	6	9.3
11T3[*]	38.4205	28.2074	565	1356	18.6	28	11.36 ± 0.59	11.27	0.118	**71**	4	7	9.0
11T4[*]	38.4182	28.2389	295	1355	24.9	42	5.43 ± 0.29	11.26	0.118	**150**	8	14	4.3
11T5[*]	38.4286	28.1610	375	1455	24.7	59	12.19 ± 0.42	12.12	0.122	**71**	2	6	9.0
11T6[*]	38.3012	28.1693	645	1439	28.5	61	3.11 ± 0.20	11.95	0.122	**277**	18	28	2.3
11T8[*]	38.2990	28.0835	915	1491	32.9	6	2.47 ± 0.19	12.42	0.124	**362**	28	39	1.8
11T9[*]	38.3076	28.1685	720	1429	28.3	12	5.75 ± 0.51	11.87	0.121	**148**	13	18	4.3
11T10[*]	38.2889	28.1640	570	1228	27.5	31	2.76 ± 0.30	10.22	0.114	**271**	30	36	2.4
11T11[*]	38.2781	28.0698	594	1194	27.8	20	1.97 ± 0.18	9.96	0.112	**372**	34	44	1.7
Aydın Range													
17T1	37.9008	28.0987	421	794	22.0	7.3	1.30 ± 0.12	7.27	0.099	**430**	42	52	1.5
17T9	37.9549	28.0703	322	996	26.7	52	3.15 ± 0.19	8.51	0.105	**202**	12	19	3.2
16T1	37.9173	27.6238	131	286	14.3	4.7	5.15 ± 0.36	4.81	0.083	**84**	6	8	8.7

Sample [†]	Location		Sample elevation	Mean catchment elevation	Mean slope	Catchment area	10Be concentration [#]	Production rate		Catchment-wide erosion rates [**]	Internal uncertainty [**] (1σ)	External uncertainty [**] (1σ)	Time scale [††]
	Lat	Lon						spallation	muons				
	(°N)	(°E)	(m)	(m)	(°)	(km²)	(10⁴ at/g)	(at/g/yr)	(at/g/yr)	(mm/kyr)	(mm/kyr)	(mm/kyr)	(kyr)
16T2*	37.9299	27.7796	204	1024	25.8	84	3.89 ± 0.24	8.69	0.106	**166**	10	16	3.9
16T4*	37.9067	27.7705	173	266	14.7	1.3	3.99 ± 0.25	4.73	0.083	**108**	7	10	6.8
16T11	37.9074	27.9356	320	1106	26.1	46	2.81 ± 0.17	9.25	0.109	**243**	15	23	2.6

TABLE 1 (CONTINUED). 10Be CONCENTRATIONS AND EROSION RATES FOR CATCHMENTS IN THE MENDERES MASSIF, WESTERN TURKEY.

Sample [†]	Location		Sample elevation	Mean catchment elevation	Mean slope	Catchment area	10Be concentration [#]	Production rate		Catchment-wide erosion rates [**]	Internal uncertainty [**] (1σ)	External uncertainty [**] (1σ)	Time scale [††]
	Lat	Lon						spallation	muons				
	(°N)	(°E)	(m)	(m)	(°)	(km²)	(10⁴ at/g)	(at/g/yr)	(at/g/yr)	(mm/kyr)	(mm/kyr)	(mm/kyr)	(kyr)
16T13	37.9400	27.6936	259	515	19.5	35	3.17 ± 0.19	5.82	0.090	**144**	9	13	4.4
16T20	38.0818	27.9687	423	800	24.3	26	2.47 ± 0.22	7.33	0.099	**226**	21	27	2.8
15T5*	37.9487	27.7551	186	750	24.5	127	1.29 ± 0.18	7.03	0.097	**420**	59	66	1.5
15T6	37.9325	27.6229	153	594	23.1	102	1.49 ± 0.15	6.21	0.092	**326**	34	41	2.0
15T8	38.0855	27.8043	187	644	25.4	11	3.09 ± 0.39	6.47	0.094	**162**	21	24	4.0
15T9	38.0770	27.7514	260	706	21.8	11	1.72 ± 0.16	6.80	0.096	**306**	30	37	2.1
14T6	38.0641	27.8996	320	942	26.6	38	2.52 ± 0.17	8.17	0.104	**244**	17	24	2.6
14T7*	38.0732	27.9323	416	885	24.7	18	2.99 ± 0.18	7.84	0.102	**198**	12	19	3.2
14T8*	38.0703	28.0990	398	1124	19.9	47	10.25 ± 0.51	9.43	0.110	**67**	3	6	9.6
14T9*	38.0752	28.0565	402	1105	28.6	15	5.39 ± 0.29	9.24	0.109	**126**	7	12	5.1
14T13*	37.9342	28.1713	232	1011	23.0	103	7.01 ± 0.31	8.61	0.106	**91**	4	8	7.0
14T14*	37.9593	28.0818	359	968	25.3	60	2.05 ± 0.14	8.33	0.105	**305**	22	31	2.1
14T15*	37.9716	28.0102	487	998	25.9	92	4.36 ± 0.22	8.53	0.106	**145**	7	13	4.4
14T16	37.8959	27.8463	199	976	30.7	94	1.52 ± 0.23	8.34	0.105	**413**	63	70	1.5
Eastern Küçük Menderes													
16T26*	38.2062	28.3406	455	839	15.0	81	8.10 ± 0.31	7.57	0.100	**70**	3	6	9.1
16T27	38.1551	28.3211	495	899	16.3	21	6.49 ± 0.39	7.93	0.102	**91**	6	9	7.0
15T13*	38.2075	28.3351	424	834	15.0	83	6.86 ± 0.37	7.54	0.100	**82**	4	8	7.8
15T14	38.1177	28.2724	364	787	16.9	29	4.27 ± 0.28	7.26	0.098	**129**	8	13	5.0

[†] Samples marked with an asterisk have been published by Buscher et al. (2013), Wölfler et al. (2017), and Heineke et al. (2017).

[#] Blank-corrected 10Be concentrations. The uncertainty of the 10Be concentration (1σ) includes the error of the blank correction and the propagated error of the analytical uncertainty. The analytical error takes into account the error based on counting statistics, the scatter of the repeated measurement of the same sample, as well as the uncertainty of the standard normalization. 10Be concentrations were measured by AMS using the ETH Zurich Tandy system (Kubik and Christl, 2010; Christl et al., 2013). Measured 10Be/9Be ratios are normalized to the secondary standard S2007N with a nominal 10Be/9Be ratio of 28.1 x 10⁻¹² (Kubik and Christl, 2010), considering the 10Be half-life of 1.387 ± 0.012 Ma (Chmeleff et al., 2010; Korschinek et al., 2010). The secondary standard has been calibrated relative to the primary standard ICN 01-5-1 (Nishiizumi et al., 2007; Kubik and Christl, 2010).

** Erosion rates were calculated with the CRONUS-Earth ^{10}Be – ^{26}Al online calculator (Balco et al., 2008; http://hess.ess.washington.edu; version 2.3) using the primary calibration data set of Borchers et al. (2016) and the time-invariant production rate scaling model of Lal (1991) – Stone (2000). Note that the erosion rates previously published by Buscher et al. (2013) have been recalculated with this version of the online calculator. For calculating the erosion rates, we used a bedrock density of 2.5 g/cm^3 and the mean catchment elevation. For samples 14T3, 15T15, 16T1, and 16T4 from catchments in Neogene sedimentary rocks a density of 2.2 g/cm^3 was used. Internal uncertainties include the analytical uncertainty and the error of the blank correction, whereas external uncertainties also include the systematic uncertainty of the sea-level high-latitude production rate. Note that the 2.7 % error (1σ) associated with the ^{10}Be/^{9}Be ratio of the standard S2007N is not included in the uncertainties.

†† The time over which erosion rates integrate is calculated by dividing the absorption depth scale of 64 cm and 73 cm for metamorphic rocks and Neogene sediments, respectively, by the erosion rate.

TABLE 2. ^{10}Be CONCENTRATIONS AND LOCAL EROSION RATES FOR RIDGE CRESTS IN THE CENTRAL MENDERES MASSIF, WESTERN TURKEY

Sample	Location		Sample elevation	Topographic shielding *	^{10}Be concentration †	Production rate		Local erosion rates §	Internal uncertainty § (1σ)	External uncertainty § (1σ)	Time scale #
	Lat	Lon				spallation	muons				
	(°N)	(°E)	(m)	–	(10^4 at/g)	(at/g/yr)	(at/g/yr)	(mm/kyr)	(mm/kyr)	(mm/kyr)	(kyr)
Bozdağ Range											
17T8	38.3462	27.7693	1211	1.0	24.03 ± 0.82	10.10	0.113	30	1	3	21.3
17T7	38.3497	27.5604	1028	1.0	7.83 ± 0.37	8.78	0.107	82	4	7	7.8
17T5	38.3216	27.9790	1193	1.0	11.46 ± 0.45	9.96	0.112	63	3	5	10.2
16T38	38.3973	28.0511	1630	1.0	13.60 ± 0.53	13.76	0.129	71	3	6	9.0
16T36	38.3406	27.6946	1089	0.9999	12.20 ± 0.75	9.20	0.109	54	3	5	11.9
11T7	38.3447	28.1282	1635	1.0	13.85 ± 0.54	13.79	0.129	70	3	6	9.1
11T12	38.3269	28.0996	2015	1.0	20.50 ± 1.6	18.00	0.146	60	5	7	10.7
11T13	38.3201	28.1096	2090	1.0	25.90 ± 1.0	18.94	0.149	50	2	4	12.8
Aydın Range											
17T2	37.9833	27.7009	821	1.0	39.25 ± 0.98	7.44	0.100	13	0.4	1	49.2
16T21	38.0449	27.9628	1028	0.9999	8.47 ± 0.74	8.74	0.107	76	7	9	8.4
16T17	38.0010	27.8166	1186	0.9998	12.60 ± 0.72	9.84	0.112	56	3	5	11.4
16T14	38.0231	27.7427	1023	0.9999	7.37 ± 0.53	8.70	0.106	87	6	9	7.4
16T5	37.9942	28.1328	1467	1.0	5.26 ± 0.48	12.13	0.123	165	15	20	3.9
15T1	38.0244	28.1366	1495	1.0	16.94 ± 0.88	12.38	0.124	51	3	5	12.5

* Topographic shielding was calculated with a 30 m SRTM digital elevation model and the MATLAB script of G. Balco (http://depts.washington.edu/cosmolab/shielding.m).

† Blank-corrected ^{10}Be concentrations. The uncertainty of the ^{10}Be concentration (1σ) includes the error of the blank correction and the propagated error of the analytical uncertainty. The analytical error takes into account the error based on counting statistics, the scatter of the repeated measurement of the same sample, as well as the uncertainty of the standard normalization. ^{10}Be concentrations were measured by AMS using the ETH Zurich Tandy system (Kubik

and Christl, 2010; Christl et al., 2013). Measured $^{10}Be/^{9}Be$ ratios are normalized to the secondary standard S2007N with a nominal $^{10}Be/^{9}Be$ ratio of 28.1 x 10^{-12} (Kubik and Christl, 2010), considering the ^{10}Be half-life of 1.387 ± 0.012 Ma (Chmeleff et al., 2010; Korschinek et al., 2010). The secondary standard has been calibrated relative to the primary standard ICN 01-5-1 (Nishiizumi et al., 2007; Kubik and Christl, 2010).

§ Erosion rates were calculated with the CRONUS-Earth ^{10}Be – ^{26}Al online calculator (Balco et al., 2008; http://hess.ess.washington.edu/; version 2.3) using the primary calibration data set of Borchers et al. (2016) and the time-invariant production rate scaling model of Lal (1991) – Stone (2000). For calculating the erosion rates, we used a bedrock density of 2.5 g/cm^3. Internal uncertainties include the analytical uncertainty and the error of the blank correction, whereas external uncertainties also include the systematic uncertainty of the sea-level high-latitude production rate. Note that the 2.7 % error (1σ) associated with the $^{10}Be/^{9}Be$ ratio of the standard S2007N is not included in the uncertainties.

The time over which erosion rates integrate is calculated by dividing the absorption depth scale of 64 cm by the erosion rate.
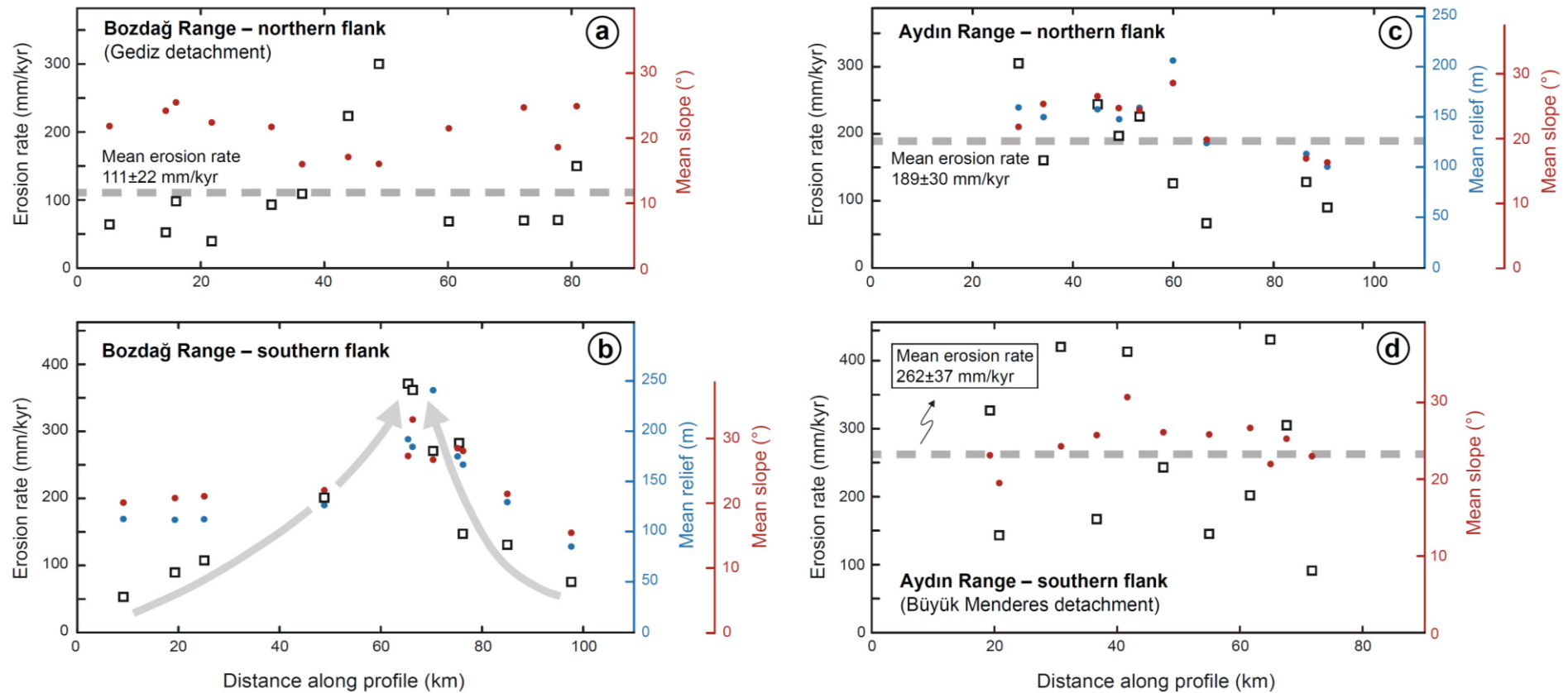
Figure 7: Catchment-wide [10]Be erosion rates (open squares) for catchments in the Bozdağ and Aydın mountain ranges plotted against mean relief (blue circles) and mean slope (red circles). The distance between the catchments along the profile corresponds to the distance between the central points of the catchments projected onto the profile line shown in Figure 6. Gray dashed line indicates mean erosion rate of the corresponding mountain range flank. Mean relief was calculated using a moving window with a diameter of 1 km. For further explanation see text. **a)** [10]Be erosion rates plotted against mean slope for catchments in the footwall of the Gediz detachment (northern flank of Bozdağ Range). **b)** [10]Be erosion rates for catchments along-strike of the southern flank of the Bozdağ Range plotted against mean catchment relief and mean slope. **c)** [10]Be erosion rates along northern flank of the Aydın Range plotted against mean catchment relief and mean slope. **d)** [10]Be erosion rates plotted against mean slope for catchments in the footwall of the Büyük Menderes detachment (southern flank of Aydın Range).

Ridge crests in the Bozdağ and Aydın mountain ranges generally exhibit smooth, convex profiles and vary in width from a few to several tens of meters (Fig. 5). Commonly, the crests are sparsely vegetated with grass, shrubs, or small trees, and the surface is covered by an up to 10 cm thick soil or regolith layer containing variable amounts of bedrock clasts (Fig. 5b). Intervening patches of bedrock outcrop occur either as bedrock knobs, sticking out from the surrounding by a few decimeters (Fig. 5c), or are nearly flush with the surface (Fig. 5d). We collected the bedrock clasts for all amalgamated samples from the thin soil or regolith on the highest, subhorizontal part of the ridge crests. To obtain representative erosion rates, the clasts were taken over distances of 40–100 m along the different crests. Depending on crest width, this procedure resulted in sampling areas of ~200 to ~1000 m^2 and 1500–2600 clasts per sample (i.e. 2–7 clasts per square meter). Although fewer clasts may also have been sufficient, we argue that a larger clast number increases the probability to obtain representative erosion rates. For reasons given above, we did not sample bedrock outcrops or collect quartz clasts derived from resistant quartz veins (Fig. 5d). Cultivated ridges or sites where wind mills have recently been constructed (Fig. 5a) were also avoided. In the western Bozdağ Range, which is partly forested, the construction of fire lanes along ridge crests made sampling in some areas impossible.

The chemical separation of Be from the amalgamated clast and stream sediment samples was carried out at the cosmogenic nuclide laboratory of the University of Münster. In a first step, all bedrock clasts from the ridge crest samples were crushed. Then all samples were sieved and washed. Subsequently, the 250–500 µm grain size fraction of all samples was split into a magnetic and a non-magnetic fraction using a Frantz magnetic separator. For two samples from ridge crests (16T36 and 16T38) we also used the 125–250 µm grain size fraction as these samples comprised fine-grained phyllites and had insufficient quantities of quartz in the coarser fraction. The subsequent chemical leaching procedure consisted of one etching step in 6 M HCl at 80 °C, four subsequent etching steps in dilute HF/HNO_3 in a heated ultrasonic bath (Kohl and Nishiizumi, 1992), and two alternating etching steps in *aqua regia* and 8 M HF to obtain pure quartz (Goethals et al., 2009). Samples 16T36, 16T38, 17T7, and 17T8 consisted of phyllitic schists and were only etched once in dilute HF/HNO_3 and then treated with fluorosilicic acid (H_2SiF_6, 30 %) to enrich quartz. After chemical cleaning of quartz, ~0.3 mg of Be carrier was added to all samples. Following complete dissolution of quartz in HF (40 %), the samples were redissolved and converted into chloride form using 6 M HCl. Beryllium was separated using successive anion and cation exchange columns and precipitated as $Be(OH)_2$ at pH 8–9. Following the transformation to BeO at 1000 °C and target preparation for accelerator mass spectrometry (AMS), [10]Be was analyzed at the AMS facility "TANDY" of the ETH Zurich (Christl et al., 2013). Local and catchment-wide erosion rates were calculated from the blank-corrected [10]Be concentrations with version 2.3 of the CRONUS-Earth online calculator (Balco et al., 2008;

http://hess.ess.washington.edu) using the time-invariant production rate scaling model of Lal (1991) and Stone (2000). Note that we did not use a topographic shielding factor for calculating the catchment-wide erosion rates, because it was shown recently that this correction is not required (DiBiase, 2018).

6.4   River Network Analysis

Normalized Channel Steepness

The evolution of topography is linked to changes in river channels, which produce relief as they erode through rock. In general, graded-river profiles can be described by a power-law relationship between channel slope (S) and the contributing upstream drainage area (A):

$$S = k_s \, A^{-\theta} \tag{2}$$

where k_s designates the channel steepness and θ the concavity index (Flint, 1974). This scaling relationship only holds downstream of a critical threshold drainage area (A_{crit}, commonly <5 km^2) over which a transition from colluvial channels to fluvial channels occurs (Montgomery and Foufoula-Georgiou, 1993; Stock and Dietrich, 2003; Wobus et al., 2006). Downstream of this transition, changes in lithology, rock uplift rate, or climate lead to the development of segmented river profiles, whereby each segment can be described by its own steepness and concavity index. At steady-state, the concavity index θ is thought to be insensitive to differences in lithology, rock uplift rate, and climate (Kirby and Whipple, 2001; Wobus et al., 2006) and commonly falls in the range of 0.4–0.6 (Snyder et al., 2000; Duvall et al., 2004; Wobus et al., 2006). In contrast, the steepness index k_s varies with these factors, rendering it a suitable metric to resolve landscape response to e.g. rock uplift. Since the steepness of a channel is an effective measure of channel slope, k_s also depends on θ (cf. Sklar and Dietrich, 1998) and a normalization of k_s is required to enable a comparison between streams of different drainage networks. For a reference concavity θ_{ref}, the normalized steepness index k_{sn} is defined as

$$k_{sn} = S \, A^{\theta ref} \tag{3}$$

and can be determined for any point in a river network (e.g., Whipple et al., 2017).

In order to derive a suitable reference concavity for streams in the central Menderes Massif, we analyzed chi-elevation plots of the sampled catchments and deduced the respective concavity index for the trunk channel of each catchment (cf., Perron and Royden, 2013). Subsequently, we calculated the mean from all concavity indices, which yielded a reference concavity of 0.4 for the study area. Finally, normalized steepness indices were determined for river segments of 1 km length for streams draining the Bozdağ and Aydın mountain ranges.

Mapping of χ for Stream Networks

Drainage divides constitute dynamic geomorphic features that migrate (either progressively or by discrete river capture) due to different rates of channel erosion on opposite sides of the divide (Gilbert, 1877; Bishop, 1995; Clark et al., 2004; Bonnet, 2009; Prince et al., 2011; Perron et al., 2012). Hence, the assessment of drainage divide stability and channel equilibrium conditions can serve as a quantitative criterion for the evaluation of landscape (dis)equilibrium and constitutes a valuable tool to infer temporal changes in river networks on various spatial scales.

Streams that originate near a common drainage divide and have the same base level, generally experience the same drop of elevation along their course. Yet, if the steady-state elevation profiles of the rivers differ (i.e., the individual profile for which erosion would balance rock uplift), the cross-divide elevation of opposing channel heads will be unequal (Willett et al., 2014). This implies that the drainage divide is unstable and the river network will adjust until a stable divide position is attained. Assessment of steady-state channel elevation throughout the river network can be achieved by mapping the parameter chi (χ), which serves as a metric for the steady-state elevation of a channel at a location x (Willett et al., 2014). Chi is defined as an integral function of position in the channel network and given by:

$$\chi = \int_{x_b}^{x} \left(\frac{A_0}{A(x')} \right)^{\frac{m}{n}} dx' \qquad (4)$$

where x_b and x correspond to the lower (base level) and upper bound (position x in the channel) of the integral, A_0 is an arbitrary scaling area (e.g., 1 km^2), m and n are parameters whose ratio corresponds to a theoretical intrinsic concavity index (Perron and Royden, 2013). Assuming spatially constant tectonic forcing and homogenous rock properties (i.e., uniform erodibility) along stream, differences in chi across a drainage divide imply disequilibrium conditions and motion of the divide in the direction of higher chi (or higher steady-state channel elevation) to attain equilibrium (Willett et al., 2014).

We generated maps of chi for the central Menderes Massif using TopoToolbox, a MATLAB-based program for the analysis of digital elevation models (Schwanghart and Scherler, 2014). We restricted our analysis to rivers that drain the slopes of the Bozdağ and Aydın mountain range, respectively, and did not consider the large streams in the three major grabens.

6.5   RESULTS

Erosion Rates from Cosmogenic ^{10}Be

In the Bozdağ Range catchment-wide erosion rates range from ~40 to ~370 mm/kyr, with distinct differences between the northern and southern flank of the mountain range (Table 1, Figs. 6, 7). Catchments on the northern range flank mostly erode at rates of ~40–110 mm/kyr, except for two

catchments in the central part of the range, which yielded higher rates (Fig. 7a). On the southern flank, high erosion rates of >350 mm/kyr occur at the steep escarpment south of Bozdağ Mountain and decrease towards the east and west (Fig. 7b). In the Aydın Range most of the [10]Be erosion rates are relatively high (~150 to ~430 mm/kyr) with considerable variations along-strike of the range (Figs. 6, 7c,d). Two small catchments in Neogene sedimentary rocks NW of Aydın town yielded erosion rates of ~84 and ~108 mm/kyr, whereas two similar catchments SE of Salihli erode at higher rates of ~206 and ~331 mm/kyr.

The local [10]Be erosion rates for ridge crests fall mainly in the range from ~30 to ~90 mm/kyr and are similar in the Bozdağ and Aydın mountains (Table 2, Fig. 6). These rates are significantly lower than most catchment-wide erosion rates, with the exception of the western Bozdağ Range where local and catchment-wide erosion rates are similar. In the Aydın Range, two samples yielded quite different rates of 13±1 and 165±20 mm/kyr, respectively. The low erosion rate of ~13 mm/kyr for sample 17T2 in the west can be attributed to the resistant bedrock lithology of the sampled crest, which is located in augen gneisses of the Çine nappe. The sample with the rate of ~165 mm/kyr was taken just above the Büyük Menderes detachment in an area with highly faulted and weathered mica schists, which may explain this rather high rate.

Channel Steepness and X Values in the Stream Network

The spatial pattern of normalized channel steepness for streams that drain the northern slope of the Bozdağ Range reveals particularly steep channels in the eastern part of the mountain range (Fig. 8). These steep channel segments, with k_{sn} values of ≥80, typically stretch over a length of 4–7 km and can be traced along strike of the Gediz detachment, occurring at approximately the same position in adjacent stream networks (Fig. 8). In a westerly direction, the channel steepness decreases and most trunk channels in the central and western part of the Bozdağ Range have k_{sn} values below 80. On the southern slope of the Bozdağ Range, steep channel segments with k_{sn} values of 80–130 are restricted to the area near Bozdağ peak, whereas farther east and west channels are generally less steep (Fig. 8). Along the northern slope of the Aydın Range, steep channel segments occur only in the upstream part of rivers that flow into the Küçük Menderes Graben. On the southern slope of the Aydın Range moderately steep channels occur in the center of the mountain range, and k_{sn} values generally decrease to the west and east.

The cross-divide pattern of chi values changes significantly along-strike of the Bozdağ Range. In the eastern part of the range, a marked difference in chi values between the northern and southern slope of the mountain range exists (Fig. 9). This difference in chi across the drainage divide disappears in a westerly direction and in the westernmost part of the Bozdağ Range chi values of streams are similar on both sides of the drainage divide. In the Aydın Range, the cross-divide

differences in chi values are generally less pronounced than in the Bozdağ Range, with streams flowing northward into the Küçük Menderes Graben having lower chi values than streams south of the drainage divide.
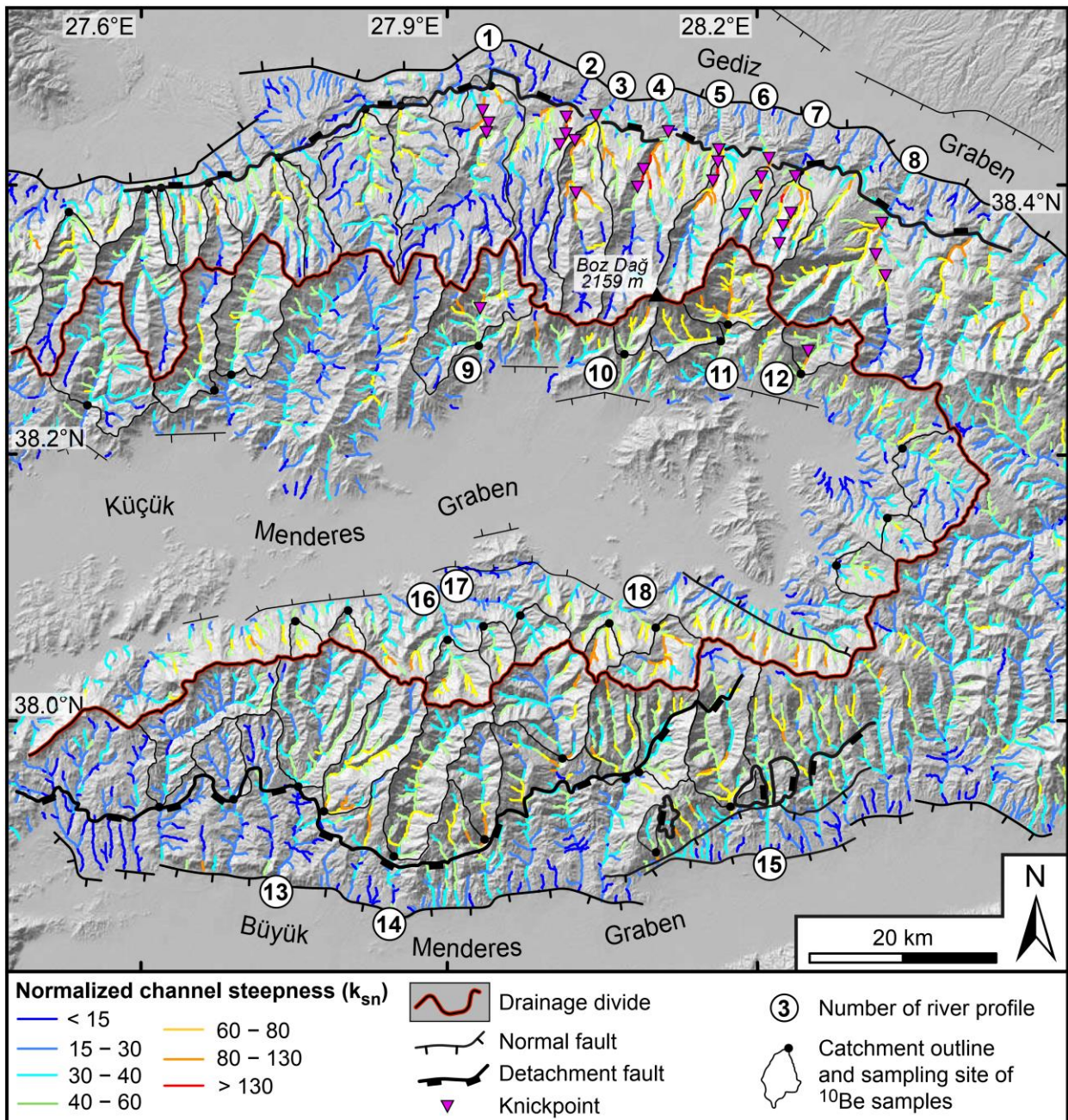
Figure 8: Map of the central Menderes Massif showing the normalized channel steepness of streams. The steepness indices (ksn) were determined for 1-km-long river segments, an upstream area of >1 km2 and a reference concavity of 0.4. The drainage divide of the Küçük Menderes Graben is delineated as red-black line. Knickpoints of streams are only indicated in the area around Bozdağ Mountain and marked by triangles. Numbers in white circles correspond to river profiles shown in Figure 10. Segments of the high-angle normal fault of the Gediz Graben are marked accordingly.
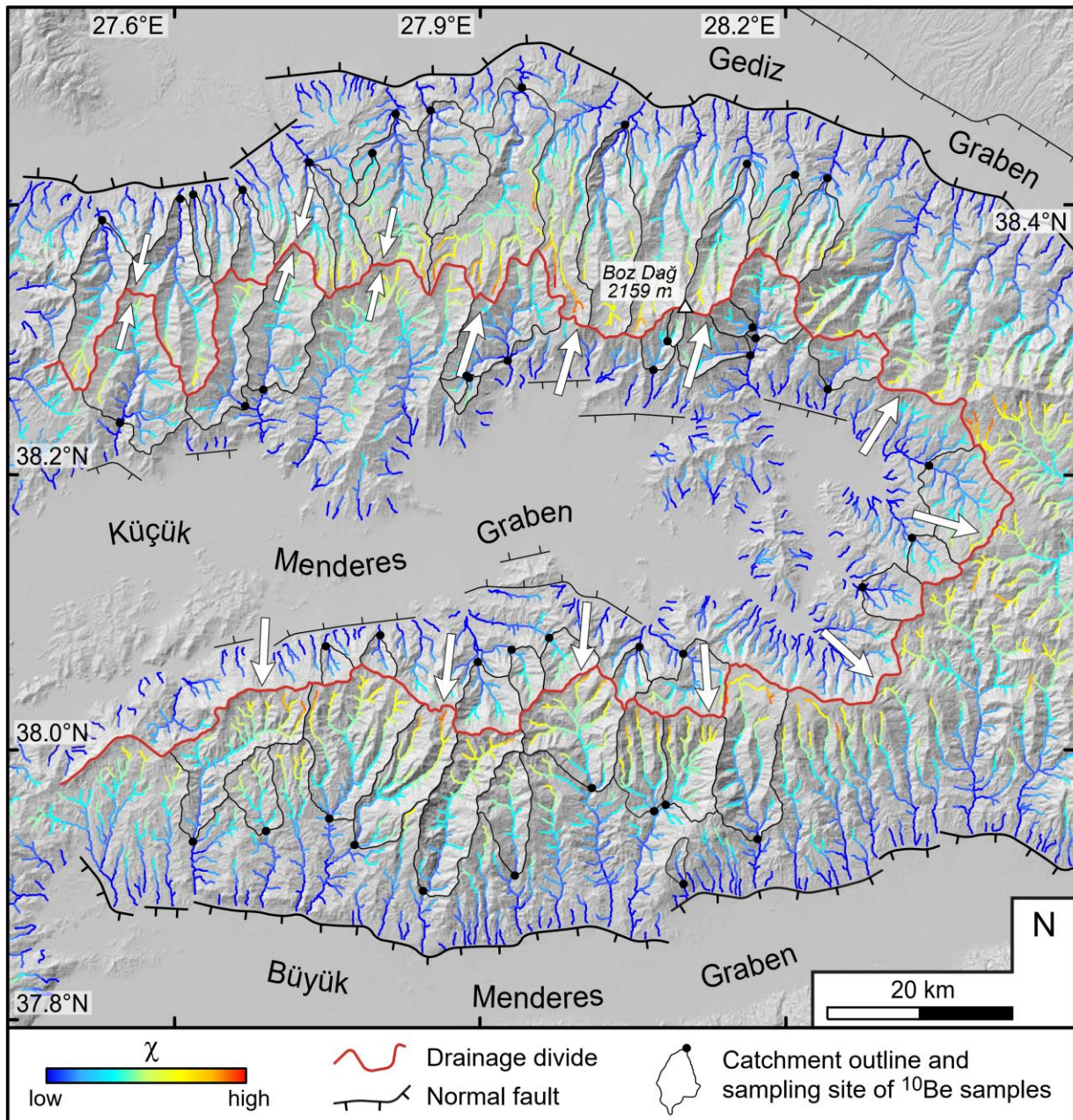
Figure 9: Map of χ for streams in the central Menderes Massif. Chi values were calculated for a scaling area A0 of 1 km2 and an m/n ratio of 0.4. Catchment outlines and sampling sites are indicated as black lines and dots, respectively (only catchments in metamorphic rocks are indicated). The drainage divide of the Küçük Menderes Graben is highlighted in red. White arrows indicate if the divide is migrating (1 arrow) or stable (2 arrows). White ellipse marks study area of Buscher et al. (2013

6.6   DISCUSSION

Footwall Erosion Along the Gediz and Büyük Menderes Detachments

The present-day topography of the central Menderes Massif is the result of a long history of extension, normal faulting, rock uplift, and erosion. The similar structural and topographic asymmetry of the Bozdağ and Aydın mountain ranges is related to their exhumation history in the footwall of the Gediz and Büyük Menderes detachments and the formation of the synform near the Küçük Menderes Graben (Fig. 2). Still, catchment-wide erosion rates in the footwalls of the two

detachment faults are markedly different (Fig. 6). We interpret the low erosion rates on the northern slope of the Bozdağ Range to result from the presence of resistant 20–50-m-thick cataclasites and quartz-rich mylonites in the footwall of the Gediz detachment (Hetzel et al., 1995b; Emre, 1996). These rocks protect the detachment from erosion due to their high rock strength (Fig. 3a,b). The rather low mean hillslope angles of the respective catchments (16°–25°; Fig. 7a) are an expression of the gently-dipping detachment surface. The mean erosion rate for all catchments on the northern mountain slope is 111±22 mm/kyr (Fig. 7a). Only two catchments in the central portion of the range erode at markedly higher rates of ~223 and ~300 mm/kyr. The high erosion rates for these catchments appear to be caused by the absence of quartz-rich mylonites as well as the presence of weak phyllites and mica schists below the Gediz detachment and are reflected by deeply incised valleys. Moreover, as the detachment has a very gentle dip in this region and the catchments are characterized by flat upstream areas, the high erosion rates may mainly reflect the incision of the trunk channels. However, to evaluate this issue in detail, an analysis of drainage basin connectivity would be required, which is beyond the scope of the present study.

In the Aydın Range, catchment-wide erosion rates are quite variable on both sides of the mountain range and – unlike in the Bozdağ Range – do not reflect its topographic asymmetry (Fig. 6). Catchments along the northern flank of the Aydın Range erode at a mean rate of 189±30 mm/kyr, whereas the average erosion rate on the shallower southern slope is 262±37 mm/kyr (Fig. 7c,d). We attribute the rapid erosion of the footwall of the Büyük Menderes detachment (as compared to the Gediz detachment) to be related to the predominance of weak phyllites and mica schists (as opposed to quartz-rich mylonites at the Gediz detachment) and to the thin (<5 m) cataclasites of the detachment (Emre and Sözbilir, 1997; Hetzel et al., 2013; own field observations), which do not shield the underlying rocks from erosion. Owing to the susceptibility of the mica schists and phyllites to erosion, the Büyük Menderes detachment is not as well preserved as the Gediz detachment (Wölfler et al., 2017). The considerable along-strike variations in erosion rates for catchments on both sides of the Aydın Range are difficult to explain. In general, such spatial variations may be caused by the occurrence of debris flows (e.g., Kober et al., 2012), variations in bedrock quartz content (e.g., Carretier et al., 2015), a violation of the steady-state erosion assumption, or other factors (cf., Dunai, 2010). However, as the quartz content of the phyllites and two-mica schists of the Bozdağ and Bayındır nappes is similar, and since debris flows have apparently no pronounced effect on measured [10]Be erosion rates in the Aydın mountains (Heineke et al., 2017), the ultimate reasons for the observed variability remains unclear.

Ridge Crest Erosion and Topographic Relief

Most of our local [10]Be erosion rates for ridge crests (i.e., 11 out of 14 values) fall in the narrow interval between ~50 and ~87 mm/kyr (Table 2, Fig. 6). The consistency of these local erosion rates across the massif shows that the amalgamation of a large number of bedrock clasts (≥1500) yields robust and representative erosion rates. Hence, this approach can overcome the problem that local erosion rates derived from bedrock outcrops may underestimate or overestimate rates of ridge crest erosion (cf., Small et al., 1999; Reinhardt et al., 2007b; Meyer et al., 2010; Strobl et al., 2012). The different sampling sites lie at elevations between ~800 and ~2100 m a.s.l. (Table 2), yet despite this significant spread there is no relation between sample elevation and erosion rate. In addition, the lowering rate of ridge crest appears to be largely independent from crest width, because the broadest of all sampled ridges erodes at a rate of 51±3 mm/kyr (Fig. 5a), which is similar to the erosion rate of 70±3 mm/kyr for the narrowest of all sampled crests (Fig. 5d).

The erosion rates for ridge crests are in most cases lower than the rates obtained for neighboring catchments, indicating that topographic relief in most parts of the central Menderes Massif is growing. Under the assumption that incision rates of rivers are similar to rates of basin erosion, the rate of relief growth equals the difference between local and catchment-wide erosion rates (Meyer et al., 2010). In the Aydın Range, the average erosion rate of 18 catchments is ~230 mm/kyr, whereas rates on intervening ridges are between 13±1 and 87±9 mm/kyr (except for one high value of ~165 mm/kyr, which we neglect for reasons explained above). Although there is a significant spread in both data sets, we attempt to provide a rough estimate for relief growth using the average value of 230 mm/kyr, to which we assign an uncertainty of ±100 mm/kyr, and a value for ridge crest lowering of 50±30 mm/kyr. The difference between these two values is 180±100 mm/kyr, which is our best estimate for the rate of relief production in the Aydın Range.

In the Bozdağ Range, we consider the western and eastern part of the range separately. In the west, local and catchment-wide erosion rates are almost similar (i.e., 30–82 mm/kyr versus 40–109 mm/kyr, respectively; Fig. 6). This similarity suggests that local relief in this part of the range does not significantly change, which implies that rock uplift and river incision rates match each other. On the northern flank of the eastern Bozdağ Range, the situation appears to be the same at first sight, as catchment erosion rates in the vicinity of Salihli are similar to rates of ridge crest lowering (Fig. 6). However, the assumption that river incision rates are similar to spatially-averaged erosion rates is unlikely to be correct in this region, because incision of the deep valleys is presumably faster than erosion of the relict Gediz detachment surface that is preserved between the valleys (Fig. 3a,b). This interpretation is supported by the observation that the north flowing rivers incising into the detachment have high channel steepness indices (Fig. 8) and are not graded (Fig. 10a). As a consequence, we argue that – in contrast to the western Bozdağ Range – local relief in the eastern

part of the range is increasing, although we do not attempt to provide an estimate for the rate at which topographic relief is growing.

Imprint of Normal Faulting on Landscape Morphology

Normal faulting and rock uplift control the current morphology of the central Menderes Massif and are reflected in the spatial pattern of normalized channel steepness and chi values in the drainage network. In the Bozdağ Range, channel segments with high k_{sn} values of >80 and locally >130 are restricted to the northeastern part of the range (i.e., region near Salihli; Fig. 8, river profiles 2–8), where the Pliocene phase of detachment faulting was most pronounced (Buscher et al., 2013; Asti et al., 2017) and caused the development of knickpoints, which can be traced along-strike of the mountain slope (Figs. 8, 10a). Another reason for the occurrence of knickpoints in this part of the Bozdağ Range is the formation of the southern boundary fault of the Gediz Graben in the early Quaternary and the subsequent linkage of its three different fault segments (Fig. 8), which caused an acceleration in fault throw rates (Kent et al., 2016a). As a consequence, the knickpoints and steep channel segments can be interpreted as a response to marked tectonic activity and normal faulting since ~6 Ma. On the southern flank of the Bozdağ Range, no comparable pattern of steep channel gradients and knickpoints exists, and stream channels are generally less steep and, in most cases, graded (Figs. 8, 10a).

In the eastern Bozdağ Range, the drainage divide is located near the crest of the steep escarpment south of Bozdağ Mountain (i.e., rather close to the Küçük Menderes Graben; Fig. 4). This position of the divide is somewhat unexpected, because fault-related rock uplift should currently be most pronounced in the vicinity of the active boundary fault of the Gediz Graben and therefore, one could expect the main divide be located farther north. We argue that the present position of the drainage divide has been inherited from the pronounced second phase of detachment faulting. During this phase of top-to-the-NNE shearing, the eastern Bozdağ Range was exhumed in the footwall of the Gediz detachment, which shifted the drainage divide far to the south. The spatial pattern of chi values for the stream network reveals marked cross-divide differences in this region, suggesting that the drainage divide is currently migrating back to the north (Fig. 9), even though normal faulting on the high-angle faults of the Gediz Graben is ongoing. The inference of a northward-migrating divide is in agreement with our catchment-wide erosion rates, which are high on the steep escarpment south of Bozdağ Mountain and much lower on the northern slope of the mountain range (Fig. 6). Hence, catchments in the south are growing at the expense of catchments north of the divide (Fig. 9). This process of divide migration has advanced most in the area east of Bozdağ Mountain. Here, the northward shift of the divide has removed the entire upstream part of the catchment north of the divide (Fig. 11a) and enlarged the deeply incised southern catchment

(Fig. 11b).

In a westerly direction along the Bozdağ Range, the drainage divide is located in a more central position within the range and cross-divide differences in chi decrease, suggesting that the drainage divide is stable (Fig. 9). This is supported by the similarity of catchment-wide erosion rates, which are of the same order of ~50–100 mm/kyr on both sides of the range (Fig. 6). Hence, the process of drainage divide migration to the north as response to faulting and rock uplift appears to be more or less completed in the western Bozdağ Range. Two reasons may be responsible for this. First, the Pliocene phase of detachment faulting was particularly rapid in the eastern part of the detachment (near Salihli, Fig. 9; Buscher et al., 2013) but less pronounced in the west, and second, the western segment of the Gediz Graben boundary fault has slipped at a lower rate than the eastern fault segment in the Quaternary (i.e., ~0.9 mm/yr vs. ~1.5 mm/yr in the last ~2 Ma; Fig. 8) (Kent et al., 2016b). Further evidence for an already accomplished northward shift of the drainage divide is provided by the bifurcation of valleys formed by streams that experienced flow reversal due to divide migration (Süzen et al., 2006) (Fig. 6). Before the northward shift of the divide, the point of confluence of the streams was located north of the drainage divide, whereas it is located south of main divide today. In summary, the spatial pattern of chi values in the Bozdağ Range indicates that the eastern and western parts of the mountain range are in different dynamic states: a quasi-equilibrium state in the west and a transient state in the east. Thus, the eastern part of the range evolves towards the state that has already been reached in western portion of the range.

In the Aydın Range, river profiles are graded on both sides of the mountains and isolated steeper channel segments with k_{sn} values >80 are restricted to the proximity of the Büyük Menderes detachment or correlate with high-angle normal faults (Figs. 8, 10b). As shown by field observations, none of the channels in the Aydın Range is colluvial and therefore we interpret the river profiles to indicate that catchment erosion and channel incision are able to keep pace with the uplift caused by the active normal faults of the Büyük Menderes Graben. In this connection, the susceptibility of the soft phyllites of the Bayındır nappe to erosion may explain why knickpoints and steeper channels segments are absent.
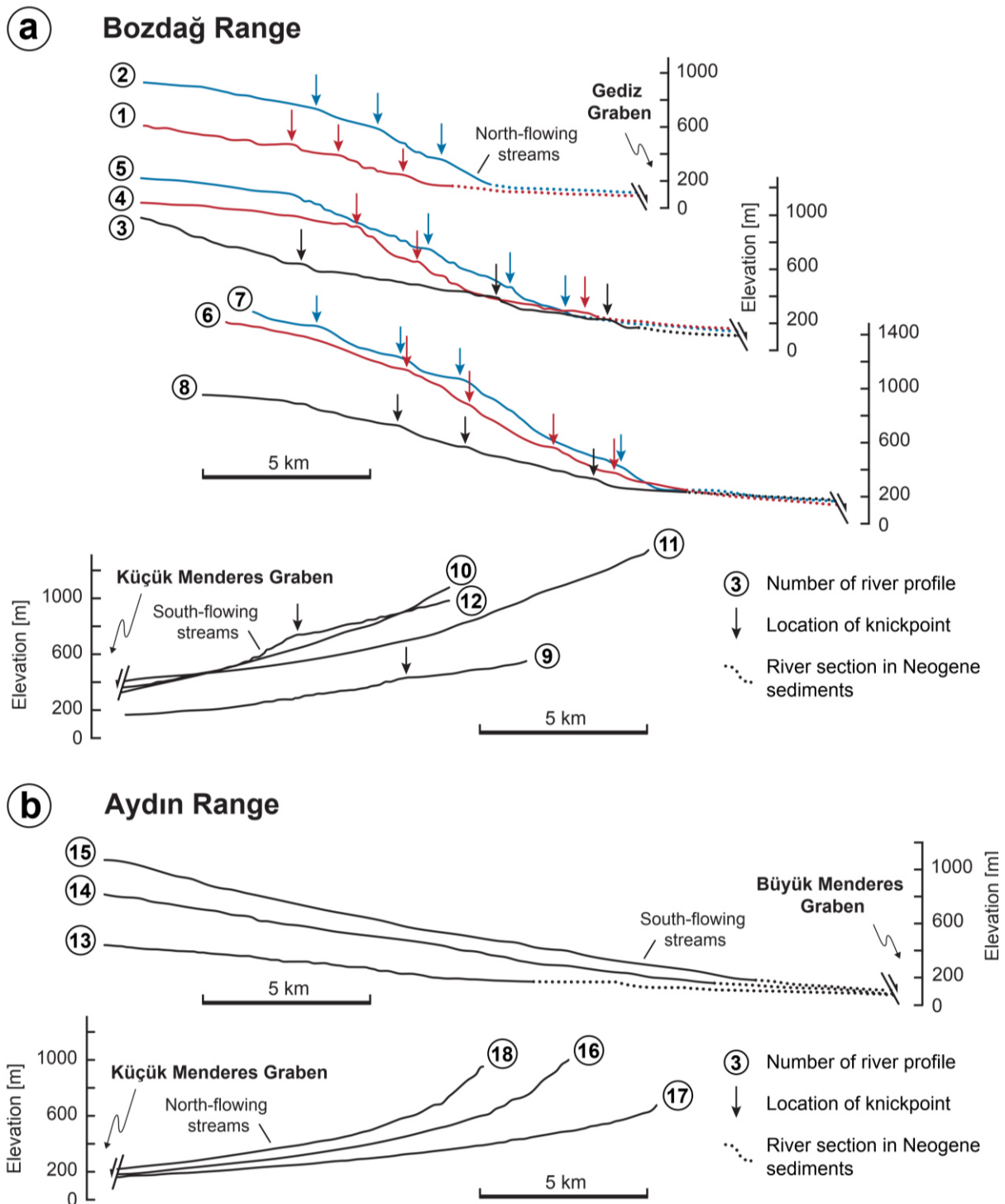
Figure10: River profiles of streams draining **a)** the Bozdağ Range and **b)** the Aydın Range. Profiles of north-flowing streams on the Bozdağ Range are shown in color only for reasons of clarity. Knickpoints are indicated with arrows. For location of streams see Figure 8. Vertical exaggeration is 4.

Like in the Bozdağ Range, normal faulting on the Büyük Menderes detachment has shifted the drainage divide to a position near the Küçük Menderes Graben (i.e., away from the detachment fault). The pattern of chi values in the Aydın Range indicates that the drainage divide is currently mobile and tends to migrate in a southward direction (Fig. 9). However, cross-divide differences in chi values are generally less pronounced than in the Bozdağ Range and not so clearly correlated with

catchment-wide erosion rates, because not all catchments having low chi values exhibit higher erosion rates – as expected if these catchments would act as aggressors and gain area (e.g., catchment 14T6 versus 14T16). In this connection, ongoing uplift of the Aydın Range and river incision in response to normal faulting along the Büyük Menderes Graben may force the drainage divide to remain close to the Küçük Menderes Graben, while the streams flowing into the Küçük Menderes Graben are unable to cause a re-migration of the divide to the south.

Landscape Evolution During Continental Extension

The determination of spatially averaged [10]Be erosion rates for catchments throughout a metamorphic core complex bounded by low-angle detachment faults allows for a thorough evaluation of along-strike variations in erosion and for resolving landscape evolution during continental extension. From our study in the central Menderes Massif, it can be deduced that surface processes exert a significant control on landscape evolution even in regions where tectonic denudation is considered to be the dominant mechanism for rock exhumation and the concomitant development of topography. In contrast to mountain ranges bounded by high-angle normal faults, the magnitude of catchment erosion along detachment faults does not tend to be higher in the center and lower near the tips of the faults, although erosion rates in both settings can vary considerably along-strike (e.g., Reinhardt et al., 2007a, Densmore et al., 2009, Roda-Boluda et al.,
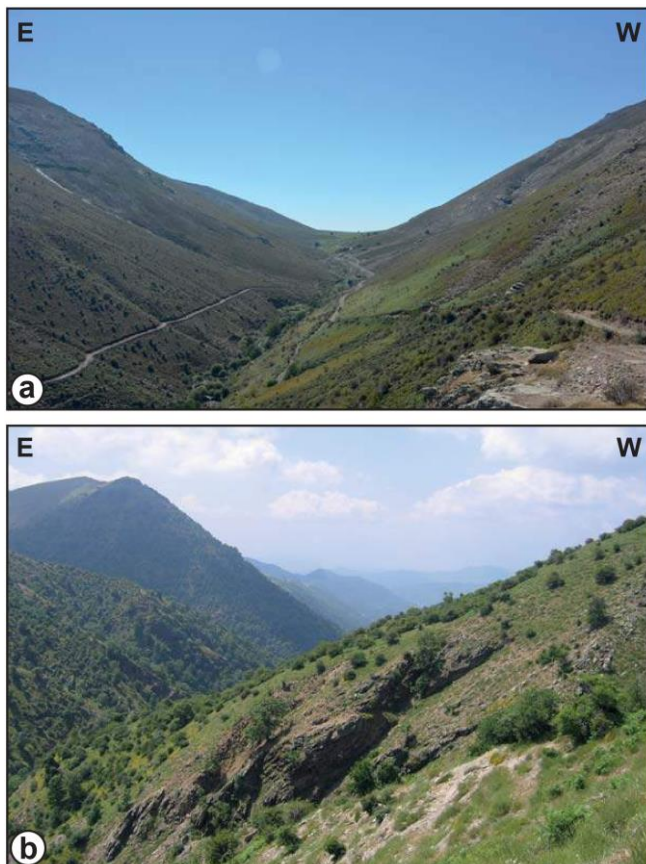
Figure 11: Field photographs in the eastern Bozdağ Range where the northward migration of the drainage divide is most advanced. Position of viewpoints is indicated in Fig. 4. a) Upstream view in catchment of sample 11T3, which drains north into the Gediz Graben. The entire head-water area of this catchment has been removed be enlargement of the aggressor catchment shown in (b). b) Downstream view in aggressor catchment south side of the drainage divide from which sample 11T6 was taken. Note steep hillslopes and rough topography compared to (a).

2019). Rather, the spatial pattern of catchment erosion in our study area largely reflects changes in topography (uplift and concomitant drainage divide migration) and relative base-level fall ultimately caused by detachment faulting. Yet, rates of catchment erosion and along-strike variations may also be influenced or caused by younger tectonic processes following detachment faulting and depend on bedrock lithology. In this regard, river network analyses can aid to evaluate the dynamic state of river channels and – in combination with catchment-wide erosion rates – to infer tectonic processes driving landscape change, which would have otherwise remained undetected.

Finally, combining ^{10}Be erosion rates with low-temperature thermochronology data enables an evaluation of the relative importance of erosion and tectonic denudation to rock exhumation along detachment faults in regions of continental extension. For the central Menderes Massif, such comparisons between catchment-wide erosion rates and exhumation rates derived from thermochronology were conducted along two transects by Buscher et al. (2013) and Wölfler et al. (2017). The new comprehensive ^{10}Be data set presented here supports the conclusion of these previous studies that the contribution of erosion to rock exhumation was higher at the Büyük Menderes detachment compared to the Gediz detachment, where tectonic denudation was the dominant mechanism for rock exhumation. From this we conclude that both tectonic denudation and erosion contribute to the exhumation of rocks in regions of continental extension, but the relative importance of both processes can vary over short distances. Erosion should consequently be included in landscape evolution models of settings with low-angle detachment faults. In this regard, the combined application of low-temperature thermochronology and ^{10}Be-derived erosion rates allows to gain quantitative insights into the landscape evolution of extensional settings across timescales.

6.7   CONCLUSIONS

New catchment-wide and the first local ^{10}Be erosion rates for ridge crests in the central Menderes Massif document the spatial pattern of erosion in the entire massif during continental extension. Rates of drainage basin erosion in combination with river network analyses reveal that the geomorphic signature of normal faulting is best preserved in the Bozdağ Range. Its preservation in the landscape is related to the resistant lithologies exposed in the footwall of the Gediz detachment, where steep channel segments and knickpoints record ongoing normal faulting and footwall uplift. In the Aydın Range, the geomorphic signal of normal faulting and uplift is less well preserved, because the lithology in the footwall of the Büyük Menderes detachment is characterized by a thin layer of cataclasites and rather weak phyllites having a low preservation potential due to their high erodibility. The spatial pattern of chi values in the drainage network, the course of the drainage divide, and cross-divide differences in catchment erosion in the central Menderes Massif document

that uplift was most pronounced in the northeastern part of the Bozdağ Range. We infer that this part of the mountain range is still in a state of transience, while the western part of the Bozdağ Range has attained a quasi-equilibrium state. By comparing catchment-wide erosion rates with local rates of ridge crest lowering, we deduce that the topographic relief in the Aydın Range and eastern Bozdağ Range increases due to ongoing uplift along the active normal faults of the Gediz, Küçük Menderes, and Büyük Menderes grabens.

ACKNOWLEDGEMENTS

REFERENCES

Aktuğ, B., Nocquet, J.M., Cingöz, A., Parsons, B., Erkan, Y., England, P., Lenk, O. Gürdal, M.A., Kilicoglu, Akdeniz, H., and Tekgül, A., 2009, Deformation of western Turkey from a combination of permanent and campaign GPS data: Limits to block-like behavior, Journal of Geophysical Research, vol. 114, B10404, doi:10.1029/2008JB006000.

Altunel, E., 1999, Geological and geomorphological observations in relation to the 20 September 1899 Menderes earthquake, western Turkey, Journal of the Geological Society, London, vol. 156, no. 2, p. 241–246.

Ambraseys, N.N., 1971, Value of historical records of earthquakes, Nature, vol. 232, no. 5310, p. 375–379.

Anderson, R.S., 2002, Modeling the tor-dotted crests, bedrock edges, and parabolic profiles of high alpine surfaces of the Wind River Range, Wyoming, Geomorphology, vol. 46, p. 35–58.

Armstrong, P. A., T. A. Ehlers, D. S. Chapman, K. A. Farley, and P. J. J. Kamp, 2003, Exhumation of the central Wasatch Mountains, Utah: 1. Patterns and timing of exhumation deduced from low-temperature thermochronology data, J. Geophys. Res., vol. 108, 2172, doi:10.1029/2001JB001708.

Asti, R., Malusà, M.G., Faccenna, C., 2017, Supradetachment basin evolution unraveled by detrital apatite fission track analysis: the Gediz Graben (Menderes Massif, Western Turkey), Basin Research, 1–20, doi:10.1111/bre.12262

Balco, G., Stone, J.O., Lifton, N.A., and Dunai, T.J., 2008, A complete and easily accessible means of calculation surface exposure ages or erosion rates from ^{10}Be and ^{26}Al measurements: Quaternary Geochronology, vol. 3, no. 3, p. 174–195.

Bierman, P., and Steig, E.J., 1996, Estimating rates of denudation using cosmogenic isotope abundances in sediment: Earth Surface Processes and Landforms, vol. 21, no. 2, p. 125–139.

Bishop, P., 1995, Drainage rearrangement by river capture, beheading and diversion, Progress in physical Geography, vol. 19, no. 4, p. 449–473.

Bishop, P., 2007, Long-term landscape evolution: linking tectonics and surface processes. Earth Surface Processes and Landforms, vol. 32, no. 3, p. 329–365.

Bonnet, S., 2009, Shrinking and splitting of drainage basins in orogenic landscapes from the migration of the main drainage divide, Nature Geoscience, vol. 2, no. 11, p. 766–771.

Borchers, B., Marrero, S., Balco, G., Caffee, M., Goehring, B., Lifton, N., Nishiizumi, K., Phillips, F., Schaefer, J., and Stone, J., 2016, Geological calibration of spallation production rates in the CRONUS-Earth project, Quaternary Geochronology, vol. 31, p. 188–198.

Bozkurt, E., and Oberhänsli, R., 2001, Menderes Massif (Western Turkey): structural, metamorphic and magmatic evolution – A synthesis. International Journal of Earth Sciences (Geologische Rundschau), vol. 89, no. 4, p. 679–708.

Brichau, S., Ring, U., Carter, A., Bolhar, R., Monié, P., Stockli, D., and Brunel, M. 2008, Timing, slip rate, displacement and cooling history of the Mykonos detachment footwall, Cyclades, Greece, and implications for the opening of the Aegean Sea basin, Journal of the Geological Society, London, vol. 165, p. 263–277.

Brown, E.T., Stallard, R.F., Larsen, M.C., Raisbeck, G.M., and Yiou, F., 1995, Denudation rates determined from the accumulation of in situ-produced ^{10}Be in the Luquillo Experimental Forest, Puerto Rico, Earth and Planetary Science Letters, vol. 129, no. 1–4, p. 193–202.

Brun, J.-P., and Sokoutis, D., 2010, 45 m.y. of Aegean crust and mantle flow driven by trench retreat, Geology, vol. 38, no. 9, p. 815–818.

Buscher, J.T., Hampel, A., Hetzel, R., Dunkl, I., Glotzbach, C., Struffert, A., Akal, C., and Rätz, M., 2013, Quantifying rates of detachment faulting and erosion in the central Menderes Massif (western Turkey) by thermochronology and cosmogenic ^{10}Be, Journal of the Geological Society, London, v. 170, no. 4, p. 669–683.

Candan, O., Dora, O.Ö., Oberhänsli, R., Çetinkaplan, M., Partzsch, J.H., Warkus, F.C., Dürr, S., 2001, Pan-African high-pressure metamorphism in the Precambrian basement of the Menderes Massif, western Anatolia, Turkey, International Journal of Earth Sciences (Geologische Rundschau), vol. 89, no. 4, p. 793–811.

Candan, O., Oberhänsli, R., Dora, O.Ö., Çetinkaplan, M., Koralay, E., Rimmelé, G., Chen, F., Akal, C., 2011, Polymetamorphic evolution of the Pan-African basement and Palaeozoic-Early Tertiary Cover Series of the Menderes Massif, Bulletin of the Mineral Research and Exploration, vol. 142, p. 121–163.

Carretier, S., Regard, V., Vasallo, R., Martinod, J., Christophoul, F., Gayer, E., Audin, L., and Lagane, C., 2015, A note on ^{10}Be-derived mean erosion rates in catchments with heterogeneous lithology: examples from the western Central Andes, Earth Surface Processes and Landforms, vol. 40, p. 1719–1729.

Cerling, T.E, and Craig, H., 1994, Geomorphology and in-situ cosmogenic isotopes, Annual Reviews of Earth and Planetary Sciences, vol. 22, no. 1, p. 273–317.

Chmeleff, J., von Blanckenburg, F., Kossert, K., and Jakob, D., 2010, Determination of the ^{10}Be half-life

by multicollector ICP-MS and liquid scintillation counting, Nuclear Instruments and Methods in Physics Research Section B: Beam Interactions with Materials and Atoms, vol. 268, no. 2, p. 192–199.

Christl, M., Vockenhuber, C., Kubik, P.W., Wacker, L., Lachner, J., Alfimov, V., and Synal, H.-A., 2013, The ETH Zurich AMS facilities: Performance parameters and reference materials, Nuclear Instruments and Methods in Physics Research Section B: Beam Interactions with Materials and Atoms, vol. 294, no. 7–8, p. 29–38.

Çiftçi, N.B., and Bozkurt, E., 2010, Structural evolution of the Gediz Graben, SW Turkey: tem- poral and spatial variation of the graben basin, Basin Research, vol. 22, no. 6, p. 846–873.

Clark, M.K., Schoenbohm, L.M., Royden, L.H., Whipple, K.X., Burchfiel, B.C., Zhang, X., Tang, W., Wang, E., and Chen, L., 2004, Surface uplift, tectonics, and erosion of eastern Tibet from large-scale drainage patterns, Tectonics, vol. 23, no. 1, TC1006.

Densmore, A.L., Hetzel, R., Ivy-Ochs, S., Krugh, W.C., Dawers, N., and Kubik, P.W., 2009, Spatial variations in catchment-averaged denudation rates from normal fault footwalls. Geology, vol. 37, p. 1139–1142.

DiBiase, R.A., Whipple, K.X., Heimsath, A.M., and Ouimet, W.B., 2010, Landscape form and millennial erosion rates in the San Gabriel Mountains, CA, Earth and Planetary Science Letters, vol. 289, no. 1, p. 134–144.

DiBiase, R.A., 2018, Increasing vertical attenuation length of cosmogenic nuclide production on steep slopes negates topographic shielding corrections for catchment erosion rates. Earth Surface Dynamics, vol. 6, p. 923–931.

Dora, O.Ö., Kun, N., Candan, O., 1990, Metamorphic history and geotectonic evolution of the Menderes massif, in Proceedings of International Earth Sciences Congress on Aegean Region, Izmir/Turkey 2, p. 102–115.

Dunai, T.J., 2010, Cosmogenic nuclides – Principles, Concepts and Applications in the Earth Surface Sciences: Cambridge University Press, 187 p.

Duvall, A., Kirby, E., and Burbank, D.W., 2004, Tectonic and lithologic controls on bedrock channel profiles and processes in coastal California, Journal of Geophysical Research: Earth Surface, vol. 109, F3, F03002.

Emre, T., 1996, The tectonic evolution of the Gediz graben, Geological Bulletin of Turkey, vol. 39, p. 1–18.

Emre, T., and Sözbilir, H., 1997, Field evidence for metamorphic core complex, detachment faulting and accommodation faults in the Gediz and Büyük Menderes grabens, Western Anatolia, in International Earth Sciences Colloquium on the Aegean and Surrounding Regions, Proceedings 1, p. 73–94.

England, P. and Molnar, P., 1990, Surface uplift, uplift of rocks, and exhumation of rocks, Geology, v. 18, no. 12, p. 1173–1177.

Ersoy, Y.E., Helvacı, C., and Sözbilir, H., 2010, Tectono-stratigraphic evolution of the NE- SW-trending superimposed Selendi basin: Implications for late Cenozoic crustal extension in Western Anatolia, Turkey, Tectonophysics, vol. 488, no. 1, p. 210–232.

Eyidoğan, H., and Jackson, J., 1985, A seismological study of normal faulting in the Demirci, Alaşehir and Gediz earthquakes of 1969-70 in western Turkey: implications for the nature and geometry of deformation in the continental crust, Geophysical Journal International, vol. 81, no. 3, p. 569–607.

Flint, J.J., 1974, Stream gradient as a function of order, magnitude, and discharge, Water Resources Research, vol. 10, no. 5, p. 969–973.

Foster, D.A., and John, B.E. 1999, Quantifying tectonic exhumation in an extensional orogen with thermochronology: examples from the southern Basin and Range Province, in Ring, U., Brandon, M.T., Lister, G.S., and Willett, S.D., eds, Exhumation processes: normal faulting, ductile flow, and erosion: Geological Society, London, Special Publications, vol. 154, p. 343–364.

Gautier, P., Brun, J.-P., and Jolivet, L., 1993, Structure and kinematics of Upper Cenozoic extensional detachment on Naxos and Paros (Cyclades Islands, Greece), Tectonics, vol. 12, no. 5, p. 1180–1194.

Gessner, K., Ring, U., Johnson, C., Hetzel, R., Passchier, C.W., and Güngör, T., 2001, An active bivergent rolling-hinge detachment system: Central Menderes metamorphic core complex in western Turkey, Geology, vol. 29, no. 7, p. 611–614.

Gessner, K., Ring, U., and Güngör, T., 2011, Field Guide to Samos and the Menderes Massif: Along-Strike Variations in the Mediterranean Tethyan Orogen: Geological Society of America Field Guide 23, 52 p., doi:10.1130/2011.0023.

Gessner, K., Gallardo, L.A., Markwitz, V., Ring, U., and Thomson, S.N., 2013, What caused the denudation of the Menderes Massif: Review of crustal evolution, lithosphere structure, and dynamic topography on southwest Turkey, Gondwana Research, vol. 24, no. 1, p. 243–274.

Gilbert, G.K., 1877, Report on the Geology of the Henry Mountains, 160 p.

Goethals, M.M., Hetzel, R., Niedermann, S., Wittmann, H., Fenton, C.R., Kubik, P.W., Christl, M., and von Blanckenburg, F., 2009, An improved experimental determination of cosmogenic ^{10}Be/^{21}Ne and ^{26}Al/^{21}Ne production ratios in quartz, Earth and Planetary Science Letters, vol. 284, no. 1, p. 187–198.

Granger, D.E., Kirchner, J.W., and Finkel, R., 1996, Spatially averaged long-term erosion rates measured from in situ produced cosmogenic nuclides in alluvial sediment, Journal of Geology, vol. 104, no. 3, p. 249–257.

Granger, D.E., and Riebe, C.S., 2007, Cosmogenic nuclides in weathering and erosion, in Holland, H.D. and Turekian, K.K., eds., Surface and Ground Water, Weathering, and Soils: Treatise on Geochemistry 5, p. 1–43.

Grasemann, B., Schneider, D.A., Stockli, D.F., and Iglseder, C., 2012, Miocene bivergent crustal extension in the Aegean: Evidence from the western Cyclades (Greece), Lithosphere, vol. 4, no. 1, p. 23–39.

Gürer, Ö.F., Sarıca-Filoreau, N., Özburan, M., Sangu, E., Doğan, B., 2009, Progressive development of the Büyük Menderes Graben based on new data, western Turkey, Geological Magazine, vol. 146, no. 5, p. 652–673.

Hancock, G. and Kirwan, M., 2007, Summit erosion rates deduced from ^{10}Be: Implications for relief

production in the central Appalachians, Geology, vol. 35, no.1, p. 89–92.

Harbor, D.J., 1997, Landscape evolution at the margin of the Basin and Range, Geology, vol. 25, p. 1111–1114.

Heineke, C., Hetzel, R., Akal, C., and Christl, M., 2017, Constraints on water reservoir lifetimes from catchment-wide ^{10}Be erosion rates − a case study from Western Turkey, Water Resources Research, vol. 53, p. 9206–9224.

Hetzel, R., Passchier, C.W., Ring, U., and Dora, O.Ö., 1995a, Bivergent extension in orogenic belts: the Menderes massif (southwestern Turkey), Geology, vol. 23, no. 5, p. 455–458.

Hetzel, R., Ring, U., Akal, C., and Troesch, M., 1995b, Miocene NNE-directed extensional unroofing in the Menderes Massif, southwestern Turkey, Journal of the Geological Society, London, vol. 152, no. 4, p. 639–654.

Hetzel, R., and Reischmann, T., 1996, Intrusion age of Pan-African augen gneisses in the southern Menderes Massif and the age of cooling after Alpine ductile extensional deformation, Geological Magazine, vol. 133, no. 5, p. 565–572.

Hetzel, R., Romer, R.L., Candan, O., and Passchier, C.W., 1998, Geology of the Bozdag area, central Menderes Massif, SW Turkey: Pan-African basement and Alpine deformation, International Journal of Earth Sciences (Geologische Rundschau), vol. 87, no. 3, p. 394–406.

Hetzel, R., Zwingmann, H., Mulch, A., Gessner, K., Akal, C., Hampel, A., Güngör, T., Petschick, R., Mikes, T., and Wedin, F., 2013, Spatio-temporal evolution of brittle normal faulting and fluid infiltration in detachment fault systems - a case study from the Menderes Massif, western Turkey, Tectonics, vol. 32, doi:10.1002/tect.20031.

Işık, V., and Tekeli, O., 2001, Late orogenic crustal extension in the northern Menderes massif (western Turkey): evidence for metamorphic core complex formation, International Journal of Earth Sciences (Geologische Rundschau), vol. 89, no. 4, p. 757–765.

Işık, V., Seyitoğlu, G., Çemen, I., 2003, Ductile-brittle transition along the Alaşehir detach- ment fault and its structural relationship with the Simav detachment fault, Menderes massif, western Turkey, Tectonophysics, vol. 374, no. 1, p. 1–18.

Jolivet, L., and Faccenna, C., 2000, Mediterranean extension and the Africa-Eurasia collision, Tectonics, vol. 19, no. 6, p. 1095–1106.

Jolivet, L., Faccenna, C., Huet, B., Labrousse, L., Le Pourhiet, L., Lacombe, O., Lecomte, E., Burov, E., Denèle, Y., Brun, J.P. et al., 2013, Aegean tectonics: Strain localization, slap tearing and trench retreat, Tectonophysics, vol. 597, p. 1–33.

Kent, E., Boulton, S.J., Whittaker, A.C., Stewart, I.S., and Alçiçek, M.C, 2016a, Normal fault growth and linkage in the Gediz (Alaşehir) Graben, Western Turkey, revealed by transient river long-profiles and slope-break knickpoints, Earth Surface Processes and Landforms, vol. 42, no. 5, p. 836–852.

Kent, E., Boulton, S.J., Stewart, I.S., Whittaker, A.C., and Alçiçek, M.C, 2016b, Geomorphic and geological constraints on the active normal faulting of the Gediz (Alaşehir) Graben, Western Turkey, Journal of the Geological Society London, vol. 173, no. 4, p. 666–678.

Kirby, E., and Whipple, K.X., 2001, Quantifying differential rock-uplift rates via stream profile analysis, Geology, vol. 29, no. 5, p. 415–418.

Kirby, E., and Whipple, K.X., 2012, Expression of active tectonics in erosional landscapes, Journal of Structural Geology, vol. 44, p. 54–75.

Kober, F., Hippe, K., Salcher, B., Ivy-Ochs, S., Kubik, P.W., Wacker, L., and Hählen N., 2012, Debris-flow-dependent variation of cosmogenically derived catchment-wide denudation rates, Geology, vol. 40, no. 10, p. 935–938.

Kohl, C.P., and Nishiizumi, K., 1992, Chemical isolation of quartz for measurement of in-situ-produced cosmogenic nuclides, Geochimica et Cosmochimica Acta, vol. 56, no. 9, p. 3583–3587.

Korschinek, G., Bergmaier, A., Faestermann, T., Gerstmann, U.C., Knie, K., Rugel, G., Wallner, A., Dillmann, I., Dollinger, G., Lierse von Gostomski, Ch., Kossert, K., Maiti, M., Poutivtsev, M., and Remmert, A., 2010, A new value for the half-life of [10]Be by Heavy-Ion Elastic Recoil Detection and liquid scintillation counting, Nuclear Instruments and Methods in Physics Research Section B: Beam Interactions with Materials and Atoms, vol. 268, no. 2, p. 187–191.

Kubik, P.W., and Christl, M., 2010, [10]Be and [26]Al measurements at the Zurich 6 MV Tandem AMS facility, Nuclear Instruments and Methods in Physics Research Section B: Beam Interactions with Materials and Atoms, vol. 268, no. 7, p. 880–883.

Lal, D., 1991, Cosmic ray labeling of erosion surfaces: in situ nuclide production rates and erosion models, Earth and Planetary Science Letters, vol. 104, no. 2–4, p. 424–439.

Meyer, H., Hetzel, R., Fügenschuh, B., and Strauss, H., 2010, Determining the growth rate of topographic relief using in situ-produced [10]Be: A case study in the Black Forest, Germany, Earth and Planetary Science Letters, vol. 290, no. 3, p. 391–402.

Montgomery, D.R., and Foufoula-Georgiou, E., 1993, Channel network source representation using digital elevation models, Water Resources Research, vol. 29, no. 12, p. 3925–3934.

Niedermann, S., 2002, Cosmic-ray-Produced Noble Gases in Terrestrial Rocks: Dating Tools for Surface Processes, in Porcelli, D., Ballentine, C.J., and Wieler, R., eds., Noble Gases in Geochemistry and Cosmochemistry: Reviews in Mineralogy and Geochemistry 47, p. 731–784.

Nilius, N.-P., Glotzbach, C., Wölfler, A., Hampel, A., Dunkl, I., Akal, C., Heineke, C., and Hetzel, R. (accepted), Exhumation history of the Aydın range and the role of the Büyük Menderes detachment system during bivergent extension of the central Menderes Massif, western Turkey, Journal of the Geological Society, London, doi:10.1144/jgs2018-162.

Nishiizumi, K., Imamura, M., Caffee, M.W., Southon, J.R., Finkel, R.C., and McAninch, J., 2007, Absolute calibration of [10]Be AMS standards, Nuclear Instruments and Methods in Physics Research Section B: Beam Interactions with Materials and Atoms, vol. 258, no. 2, p. 403–413.

Öner, Z., and Dilek, Y., 2011, Supradetachment basin evolution during continental extension: The Aegean province of western Anatolia, Turkey, Geological Society of America Bulletin, vol. 123, no. 11/12, p. 2115–2141.

Perron, J.T., Richardson, P.W., Ferrier, K.L., and Lapôtre, M., 2012, The root of branching river networks, Nature, vol. 492, no. 7427, p. 100–103.

Perron, J.T., and Royden, L., 2013, An integral approach to bedrock river profile analysis, Earth Surface Processes and Landforms, vol. 38, p. 570–576.

Portenga, E.W., and Bierman, P.R., 2011, Understanding Earth's eroding surface with [10]Be, GSA

Today, vol. 21, no. 8, p. 4–10.

Purvis, M., and Robertson, A., 2005, Sedimentation of the Neogene–Recent Alaşehir (Gediz) continental graben system used to test alternative tectonic models for western (Aegean) Turkey, Sedimentary Geology, vol. 173, no. 1–4, p. 373–408.

Prince, P.S., Spotila J.A., and Henika, W.S., 2011, Stream capture as driver of transient landscape evolution in a tectonically quiescent setting, Geology, vol. 39, no. 9, p. 823–826.

Reilinger, R., McClusky, S., Paradissis, D., Ergintav, S., and Vernant, P., 2010, Geodetic constraints on the tectonic evolution of the Aegean region and strain accumulation along the Hellenic subduction zone, Tectonophysics, vol. 488, no. 1–4, p. 22–30.

Reinhardt, L.J., Dempster, T.J., Shroder, J.F., and Persano, C., 2007a, Tectonic denudation and topographic development in the Spanish Sierra Nevada, Tectonics, vol. 26, TC3001, doi:10.1029/2006TC001954.

Reinhardt, L.J., Hoey, T.B., Barrows, T.T., Dempster, T.J., Bishop, P., and Fifield, L.K., 2007b, Interpreting erosion rates from cosmogenic radionuclide concentrations measured in rapidly eroding terrain, Earth Surface Processes and Landforms, vol. 32, p. 390–406.

Ring, U., Brandon, M.T., Lister, G.S., and Willett, S.D., 1999, Exhumation processes, *in* Ring, U., Brandon, M.T., Lister, G.S., and Willett, S.D., eds., Exhumation processes: normal faulting, ductile flow, and erosion: Geological Society, London, Special Publications vol., 154, p. 1–27.

Ring, U., Johnson, C., Hetzel, R., and Gessner, K., 2003, Tectonic denudation of a Late Cretaceous–Tertiary collisional belt: regionally symmetric cooling patterns and their relation to extensional faults in the Anatolide belt of western Turkey, Geological Magazine, vol. 140, no. 4, p. 421–441.

Roda-Boluda, D.C., D'Arcy, M., Whittaker, A.C., Gheorghiu, D.M., and Rodés, Á., 2019, ^{10}Be erosion rates controlled by transient response to normal faulting through incision and landliding, Earth and Planetary Science Letters, vol. 507, p. 140–153.

Rossi, M.W., Quigley, M.C., Fletcher, J.M., Whipple, K.X., Díaz-Torres, J.J., Seiler, C., Fifield, K.L., and Heimsath, A.M., 2017, Along-strike variation in catchment morphology and cosmogenic denudation rates reveal the pattern and history of footwall uplift, Main Gulf Escarpment, Baja California, Geological Society of America Bulletin vol. 129, p. 837–854.

Schwanghart, W., and Scherler, D., 2014, TopoToolbox 2 – MATLAB-based software for topographic analysis and modeling in Earth surface sciences, Earth Surface Dynamics, vol. 2, p. 1–7.

Şengör, A.M.C., Satır, M., and Akkök, R., 1984, Timing of tectonic events in the Menderes Massif, western Turkey: Implications for tectonic evolution and evidence for Pan-African basement in Turkey, Tectonics, vol. 3, no. 7, p. 693–707.

Seyitoğlu, G., and Scott, B.C., 1991, Late Cenozoic crustal extension and basin formation in west Turkey, Geological Magazine, vol. 128, no. 2, p. 155–166.

Sklar, L.S., and Dietrich, W.E., 1998, River longitudinal profiles and bedrock incision models: Stream power and the influence of sediment supply, *in* Tinkler, K., and Wohl, E.E., eds., Rivers over rock: Fluvial processes in bedrock channels: American Geophysical Union, Geophysical Monograph 107, p. 237–260.

Small, E.E., Anderson, R.S., Repka, J.L., and Finkel, R., 1997, Erosion rates of alpine bedrock summit

surfaces deduced from in situ [10]Be and [26]Al, Earth and Planetary Science Letters, vol. 150, no. 3–4, p. 413–425.

Small, E.E., Anderson, R.S., and Hancock, G.S., 1999, Estimates of the rate of regolith production using [10]Be and [26]Al from an alpine hillslope, Geomorphology, vol. 27, no. 1–2, p. 131–150.

Snyder, N., Whipple, K.X., Tucker, G., and Merritts, D.J., 2000, Landscape response to tectonic forcing: digital elevation model analysis of stream profiles in the Mendocino triple junction region, northern California, Geological Society of America Bulletin, vol. 112, no. 8, p. 1250–1263.

Stock, J., and Dietrich, W.E., 2003, Valley incision by debris flows: Evidence of a topographic signature, Water Resources Research, vol. 39, no. 4, 1089, doi:10.1029/2001WR001057.

Stock, G.M., Frankel, K.L. Ehlers, T.A. Schaller, M. Briggs, S.M., and Finkel, R.C., 2009, Spatial and temporal variations in denudation of the Wasatch Mountains, Utah, USA, Lithosphere, vol. 1, p. 34–40.

Stone, J.O., 2000, Air pressure and cosmogenic isotope production, Journal of Geophysical Research, Solid Earth, vol. 105, B10, p. 23,753–23,759.

Strobl, M., Hetzel, R., Niedermann, S., Ding, L., and Zhang, L., 2012, Landscape evolution of a bedrock peneplain on the southern Tibetan Plateau revealed by *in situ*-produced cosmogenic [10]Be and [21]Ne, Geomorphology, vol. 153-154, p. 192–204.

Süzen, M.L., Toprak, V., and Rojay, B., 2006, High-altitude Plio-Quaternary fluvial deposits and their implication on the tilt of a horst, western Anatolia, Turkey, Geomorphology, vol. 74, p. 80–99.

Thomson, S.N., and Ring, U., 2006, Thermochronologic evaluation of postcollision extension in the Anatolide orogen, western Turkey, Tectonics, vol. 25, no. 3, TC3005, doi:10.1029/2005TC001833.

van Hinsbergen, D.J., Kaymakci, N., Spakman, W., and Torsvik, T.H., 2010, Reconciling the geological history of western Turkey with plate circuits and mantle tomography, Earth and Planetary Science Letters, vol. 297, no. 3, p. 674–686.

von Blanckenburg, F., 2006, The control mechanisms of erosion and weathering at basin scale from cosmogenic nuclides in river sediment, Earth and Planetary Science Letters, vol. 242, no. 3, p. 224–239.

Whipple, K.X., Forte, A.M., DiBiase, R.A., Gasparini, N.M., and Ouimet, W.B., 2017, Timescales of landscape response to divide migration and drainage capture: Implications for the role of divide mobility in landscape evolution, Journal of Geophysical Research: Earth Surface vol. 122, p. 248–273.

Willett, S.D., Hovius, N., Brandon, M.T., and Fisher, D.M., 2006, Introduction, *in* Willett, S.D., Hovius, N., Brandon, M.T., and Fisher, D.M., eds., Tectonics, Climate and Landscape Evolution: Geological Society of America Special Paper 398, p. vii–xi.

Willett, S. D., McCoy, S.W., Perron, J.T., Goren, L., and Chen, C.-Y., 2014, Dynamic Reorganization of River Basins, Science, vol. 343, no. 6175, p. 1248765.

Wobus, C., Whipple, K.X., Kirby, E., Snyder, N., Johnson, J., Spyropolou, K., Crosby, B., and Sheehan, D., 2006, Tectonics from topography: Procedures, promise, and pitfalls, Geological Society of America Special Papers, vol. 398, p. 55–74.

Wolff, R., Hetzel, R., and Strobl, M., 2018, Quantifying river incision into low-relief surfaces using

local and catchment-wide [10]Be denudation rates, Earth Surface Processes and Landforms, vol. 43, p. 2327–2341.

Wölfler, A., Glotzbach, C., Heineke, C., Nilius, N.-P., Hetzel, R., Hampel, A., Akal, C., Dunkl, I., and Christl, M., 2017, Late Cenozoic cooling history of the central Menderes Massif: Timing of the Büyük Menderes detachment and the relative contribution of normal faulting and erosion to rock exhumation, Tectonophysics, vol. 717, p. 585–598.

Yılmaz, Y., Genç, S.C., Gürer, F., Bozcu, M., Yılmaz, K., Karacık, Z., Altunkaynak, S., and Emlas, A., 2000, When did the western Anatolian grabens begin to develop? In: E. Bozkurt, J.A. Winchester, J.D.A. Piper (eds.) Tectonics and magmatism in Turkey and surrounding regions, Geological Society, London, Special Publications, vol. 173, p. 353–384.

7. Discussion

7.1   Implications on the pre-Miocene evolution of western Anatolia

The preceding chapters unravelled the tectonic evolution of the central Menderes Massif from the Miocene to recent. However, the presented thermochronological data from the hanging wall units of the Gediz, the Büyük Menderes and Demirhan detachments as well as samples from the internal part of the central Menderes Massif provide evidence for an earlier cooling event between 20 and 25 Ma. This late Oligocene to early Miocene cooling event is commonly referred to as stage 1 cooling event of the Menderes Massif, and is observed in the southern, the central and the northern Menderes Massifs (Ring et al. 2003; Thomson & Ring 2006; Cenki-Tok et al. 2015). However, the only extensional structure, which is known to be active during the early Miocene, is the top-to-the NE Simav detachment within the northern Menderes Massif (Işik & Tekeli 2001; Işik et al. 2004; Ring et al. 2003). The structurally higher nappes of the Menderes nappe pile like the Selimiye and Çine nappes, but also the upper units of the Bozdağ nappe constitute the footwall of the Simav detachment (Ring et al. 2003). North of the Simav graben, the Koyunoba and Egrigöz granodiorites are ductilely overprinted by the faulting along the Simav detachment after they were syntectonically emplaced at 21.0 ± 0.2 and 20.7 ± 0.6 Ma, respectively (Ring & Collins 2005). The northern Menderes Massif is bounded to the north by marble, schist and flysch units, which are attributed to the Lycian nappes and represent the hanging wall of the Simav detachment. Relatively small exposures of the hanging wall units also occur as small klippen in the central part of the northern Menderes Massif but south of Selendi and Gördes, hanging wall units were eroded or are probably covered by the widespread middle Miocene volcanic deposits (Ersoy et al. 2011). Therefore, a long-lasting debate exists about how far the Simav detachment reached to the south, and consequently how much extension was accommodated by faulting along the Simav detachment (Ring et al. 2003; Işik et al. 2004; Çemen et al. 2006; van Hinsbergen 2010). Similar late Oligocene to early Miocene cooling ages are also observed in the southern Menderes Massif and consequently, a top-to-the-south detachment in the southern Menderes Massif was tentatively suggested by Ring et al. (2003). However, a related extensional structure in the field is not known (Figure 2). The model by Ring et al. (2003) alternatively proposes that the complete Oligocene/early Miocene cooling of the whole Menderes Massif solely occurred along top-to-the north faulting of the Simav detachment with the north-dipping Datça-Kale fault situated in the gulf of Gökova representing the break-away structure (Seyitoglu et al. 2004; Çemen et al. 2006) (Figure 3). In the central Menderes Massif, the proposed top-to-the-north detachment reappears at the surface, which is linked by Çemen et al. (2006) to the Selimiye shear zone, which in turn is an alpine top-to-the-south thrust fault emplacing the Selimiye nappe over the Çine nappe between 40 to 37 Ma (Hetzel & Reischmann 1996). The Selimiye shear zone is also exposed at the southern margin of the Menderes Massif. There, the overall subhorizontal orientation of the alpine nappe pile in southern Menderes Massif changes to a southward dip. The evolution of this fold, termed South Menderes Monocline, is either associated with a plateau formation to the north, where the south-dipping nappe pile represents the hinge zone (Ring et al. 2017) or with gravitational unloading in the course of top-to-the-north detachment faulting (Çemen et al. 2006). The reconstruction of van Hinsbergen et al. (2010) localizes the break-away fault of the

Simav detachment in the central Menderes Massif and proposes that the Lycian nappes in the southern Menderes Massif were transported southeastward, concurrently with the top-to-the north faulting of the Simav detachment. This southeastward transport of the Lycian nappes is attributed to a gravitational instability of the thickened post-orogenic lithosphere in the late Oligocene (van Hinsbergen 2010).
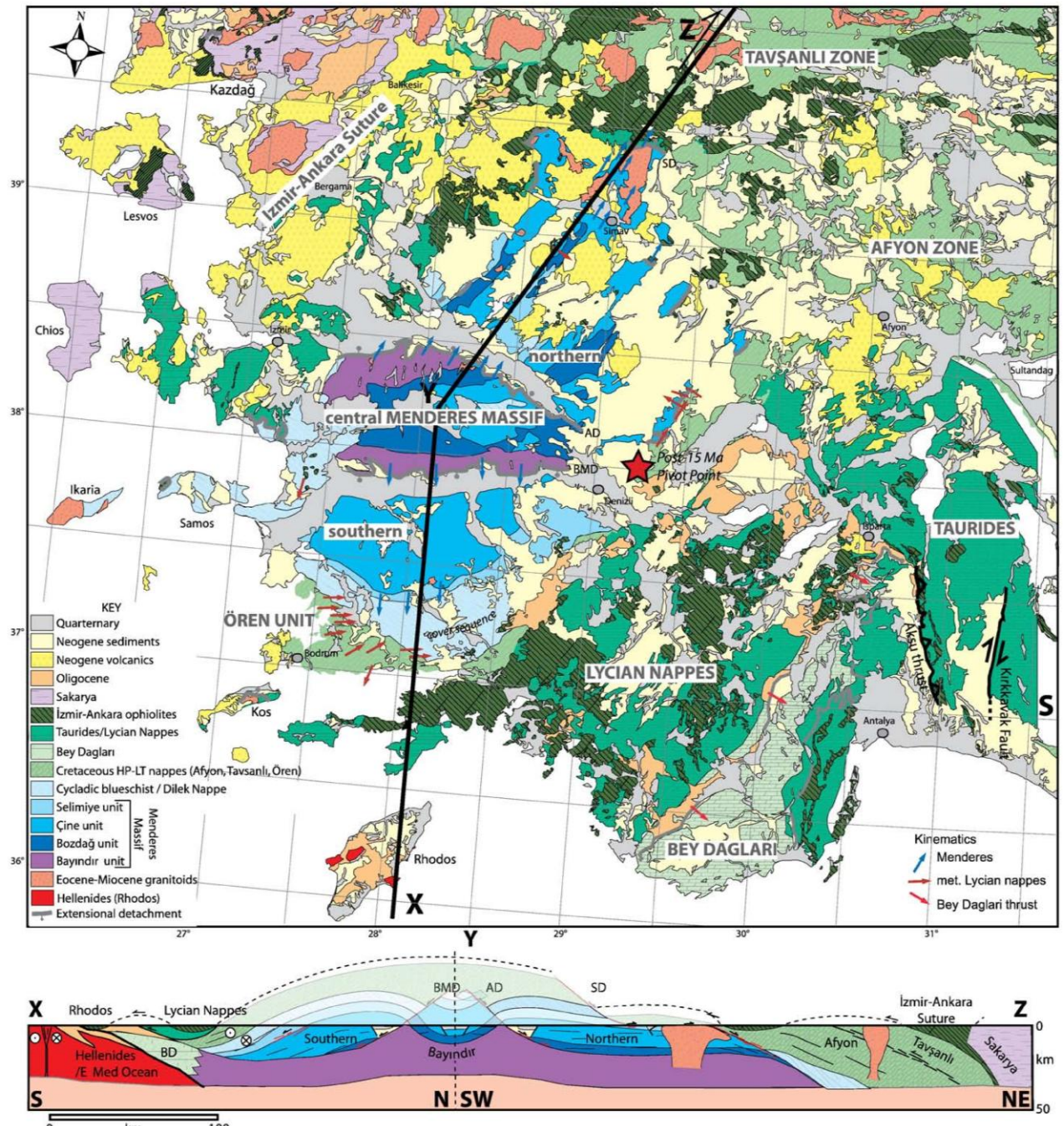
Figure 1: Geological map of western Turkey from van Hinsbergen et al. (2010). Abbreviations: AD = Alaşehir detachment (Gediz detachment), BMD = Büyük Menderes detachment, SD = Simav detachment.
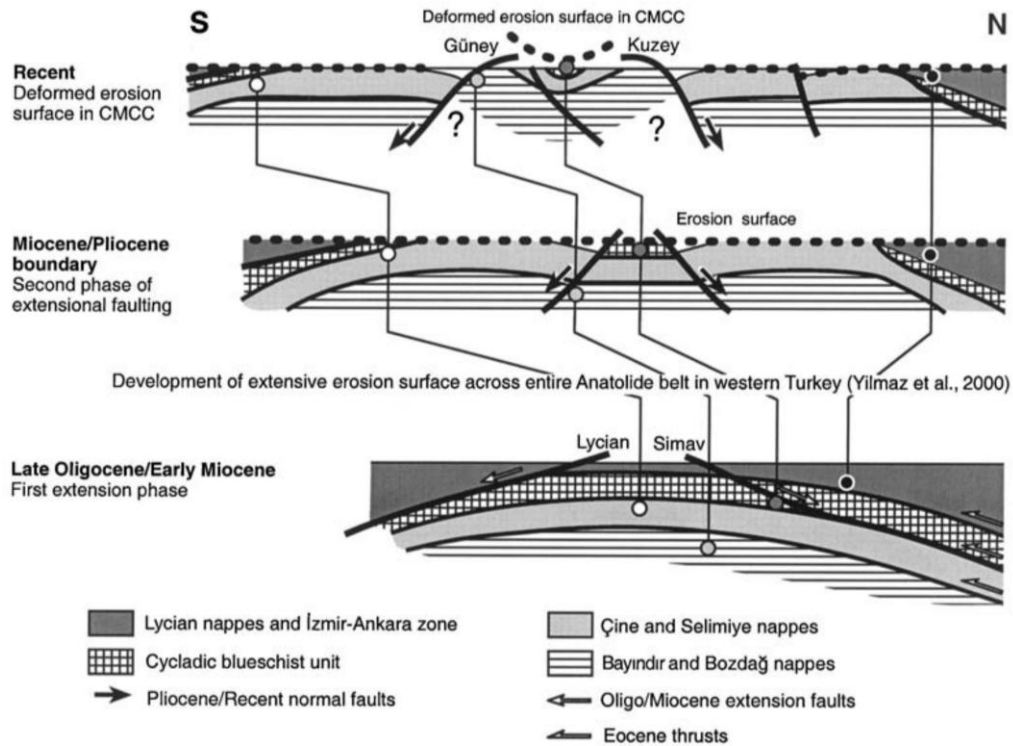
Figure 2: Reconstruction of the geological evolution of western Turkey since the late Oligocene proposing the symmetric exhumation of the northern and southern Menderes Massif during the late Oligocene and early Miocene and subsequent symmetric exhumation of the central Menderes Massif since the late Miocene/Pliocene after Ring et al. (2003). Note the different naming of the Büyük Menderes detachment as Güney detachment and the Gediz detachment as Kuzey detachment.
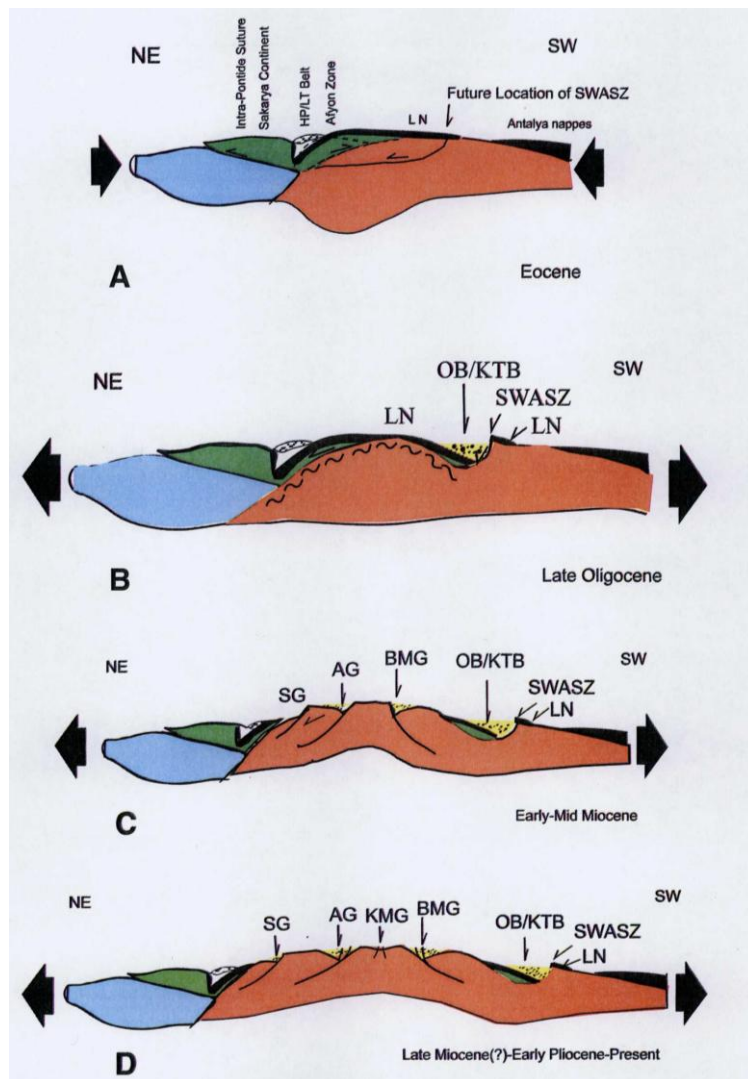
Figure 3: Tectonic evolution model of Çemen et al. (2006). Abbreviations: AG = Alaşehir Graben, BMG = Büyük Menderes Graben, KMG = Kücük Menderes Graben, KTB = Kale-Tavas Basin, LN = Lycian nappe, OB = Ören basin, SG = Simav Graben, SWASZ = South West Anatolian shear zone.

Whether a top-to-the-south extensional structure, which transported the Lycian nappes to the southeast, existed during the late Oligocene in the southern Menderes Massif cannot be tested with our thermochronological dataset. However, the existence of a top-to-the-north detachment at the scale of the whole Menderes Massif should result in high cooling rates of structurally higher units in those parts of the central Menderes Massif, which are not affected by detachment faulting and exhumation associated with the formation of the central Menderes Massif. Therefore, the cooling histories of samples 14M29 and 14M23, located in the Küçük Menderes graben, are modelled as they comprise information from ZHe, AFT and AHe thermochronometers covering the cooling history between 30 to 21 Ma and compared with the tT-history of sample 15M76, originating from the southern part of the northern Menderes Massif (Figure 4)(Tables S2 to S5). For the upper temperature constraint of sample 14M23, the 30.3 ± 2.1 Ma ZFT age of sample 14M29 is used, as this age is very consistent to other samples of the Çine nappe. The thermal history of sample 15M76 is constrained by using the ZHe (22.6 ± 1.5 Ma) and AHe (24.1 ± 0.4 Ma) ages, as well as the 24.8 ± 0.3 Ma ^{39}Ar/^{40}Ar-white mica age of Ring et al. (2003) situated ~2 km north of the sample site of 15M76. For the ^{39}Ar/^{40}Ar-white mica a closure temperature range of 430 to 350 °C is applied (Lister &
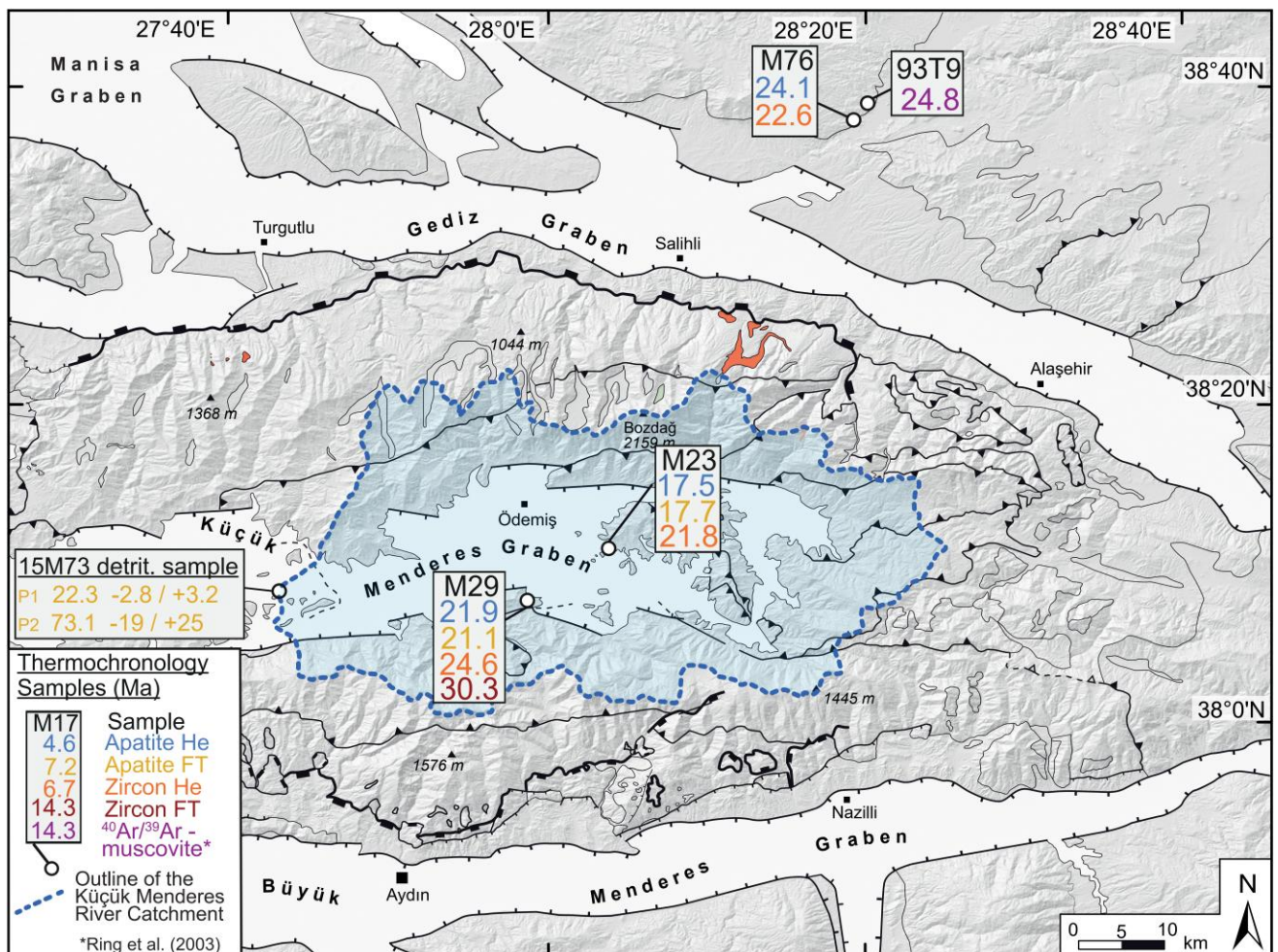
Figure 4: Shaded relief image outlining the catchment area of the Küçük Menderes River at the sample site of 15M73. Single grain AFT ages of sample 15M73 are shown in Figure 6.

Baldwin 1996).

The resulting short time period and the large temperature range over which sample 15M76 cools to near surface temperatures results in a very high cooling rate. However, the high cooling rates of the thermal model fit the observed data for which a realistic cooling path on the basis of this model can be assumed. Comparable cooling rates also occur in the footwall of the Gediz detachment (Chapter 5, Figure 6) advocating that cooling in the southern part of the northern Menderes Massif is related to tectonic denudation in the footwall of the Simav detachment. Further to the south, the thermal models from the Küçük Menderes Graben also reveal Oligocene to early Miocene cooling, but at more moderate rates, which do not necessarily need the existence of a detachment fault. Cooling rates at this order could also be explained by erosional denudation as one would expect to occur by differential uplift close to the break-away fault of the Simav detachment. Furthermore, the detrital AFT sample 15M73 of modern sediments from the Küçük Menderes River comprise two age populations. The largest population reflects the common late Miocene cooling ages with 22.3 ± 2 Ma (90.6 ± 6.9 %) but the second population reveals distinctly older AFT cooling ages, spanning a wide range of Oligocene to Cretaceous ages (Figure 7). This large range causes a relatively large error for the second population yielding 75 ± 22 Ma (9.4 ± 6.9 %) but implies that unmapped parts of tectonic units, which were not involved in the alpine nappe stacking during the Eocene, must exist within the catchment area of the Küçük Menderes river (Figure 4). Possible sources for which late Cretaceous AFT ages are reported exclude Menderes nappes but occur in ophiolitic flysch units of the Lycian nappes, exposed to the south and west of the Menderes Massif and in the Izmir/Ankara zone, exposed north of the Menderes Massif, in the hanging wall of the Simav detachment (Thomson & Ring 2006; Ring et al. 2017). Furthermore, similar late Cretaceous and Eocene detrital AFT ages are reported from small catchments draining the eastern part of the Bozdağ range by Asti et al. (2017). Although, these units might also represent remnants of hanging wall klippen, the moderate late Oligocene cooling rates in the central Menderes Massif compared to the rapid cooling rates in the northern Menderes Massif rather infer that the Simav detachment did not extend over the central Menderes Massif. Therefore, I consider a top-to-the-north detachment spanning across the whole Menderes Massif as unlikely as this implies that the brittle crust would be decoupled from the ductile crust over a distance of ~180 km. Alternatively, I suggest that the Simav detachment reached the surface between the area which became later occupied by the Gediz graben and the Bozdağ range, whereas uplift to the south resulted in enhanced erosional denudation.
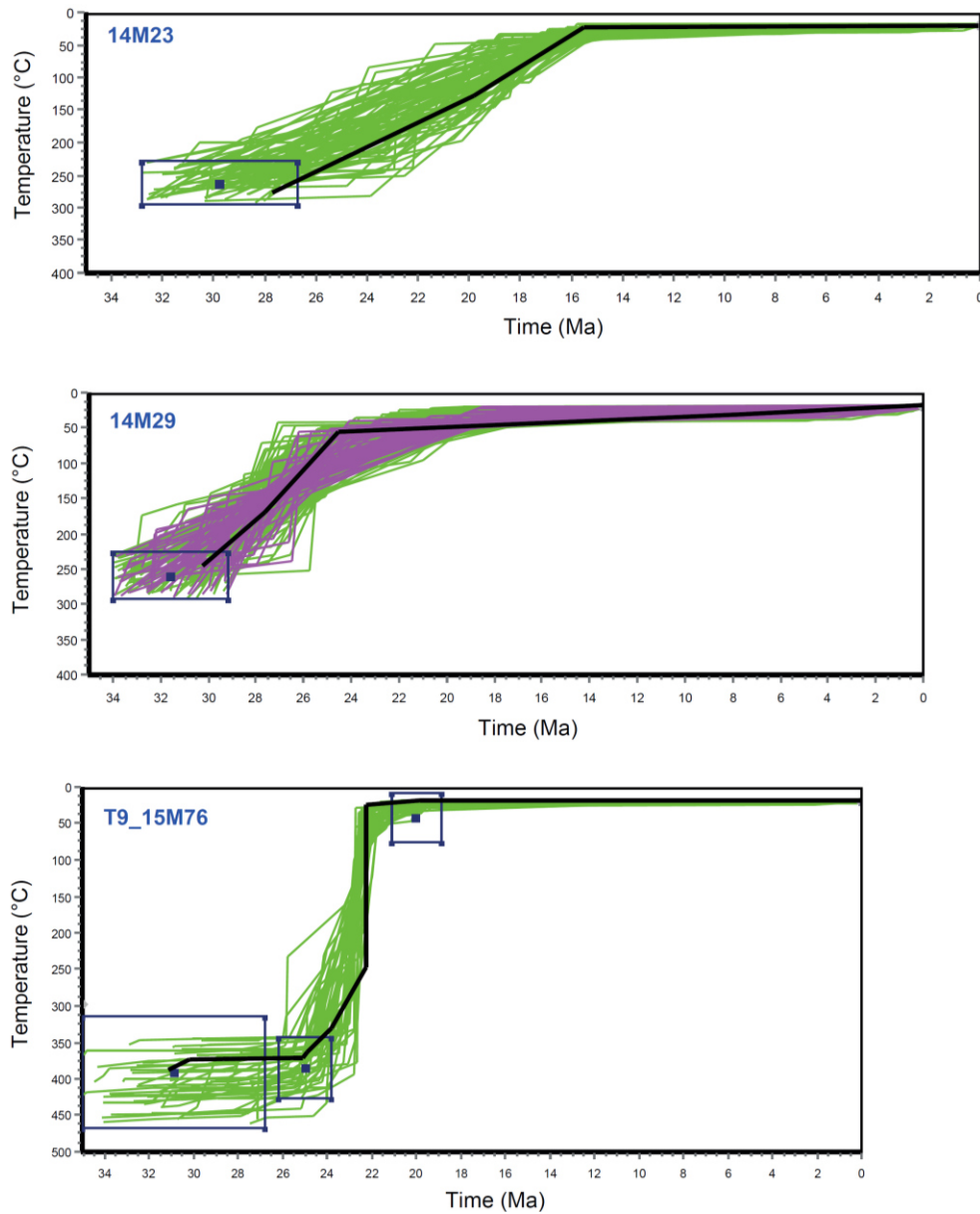
Figure 5: Modelled cooling histories of samples 14M23, 14M29 and T9_15M76, which includes the $^{39}Ar/^{40}Ar$ – age of sample 93T9 of Ring et al. (2003). Green paths comprise a goodness of fit of >0.05, violet path yield a goodness of fit value of >0.5.
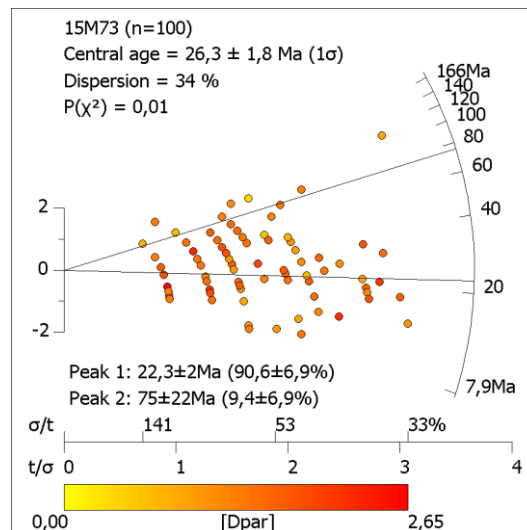
Figure 6: Radial plot of the AFT single grain ages of the detrital apatites from the Küçük Menderes River. Plotted with RadialPlotter of Vermeesch (2009).

7.2   How symmetric was the exhumation of the central Menderes Massif?

The insights into the tectonic history of each detachment fault involved in the exhumation of the central Menderes Massif discussed in detail in chapter 2 and 3 allow to estimate if the exhumation was balanced between the north-dipping Gediz detachment on the one side and the south-dipping Büyük Menderes and Demirhan detachments on the other side or if the exhumation is more asymmetric than symmetric. For the late Miocene and Pliocene period, the robust slip rate and exhumation rate calculations allow a rather straight forward comparison between the eastern part of the Gediz detachment and the Demirhan detachment. In this time interval, two K-Ar fault gouge ages document that the Büyük Menderes detachment was active but only two Pliocene AFT ages (14M41, 15M58) exist in the footwall of the Büyük Menderes detachment, for which it is suggested that the amount of tectonic denudation was rather low. Instead, in the late Miocene and Pliocene most extension was accommodated by the Demirhan detachment, yielding 6 to 8 km of total extension between 7 and 3 Ma (Nilius et al. 2019). The total exhumation in the footwall of the Demirhan detachment adds up to 1.6 km considering the modelled exhumation rate of 0.4 km/Ma between 7 and 3 Ma. At the same time, the eastern part of the Gediz detachment was exhumed with 1.2 to 1.5 km/Ma (11M5 and 11M6, respectively) between 6 and 2 Ma, with a slip rate of ~5 km/Ma between 4 and 2 Ma. This results in a total amount of exhumation of 4.8 to 6 km and ~10 km of slip along the eastern part of the Gediz detachment. However, the estimation of 10 km total slip rather reflects a minimum amount of fault slip as it only covers the period between 4 and 2 Ma, but thermokinematic models imply increased exhumation rates since ~6 Ma. Using the modelled exhumation rate of 0.8 ± 0.5 km/Ma of sample 11M5 between 4.6 and 6.1 Ma (Parameter E2, Table 6, Chapter 5) complements the missing time range with a corresponding slip rate of ~3 km/Ma (using the present-day dip-angle of 15°). Correspondingly, the total amount of extension accommodated by the eastern Gediz detachment since ~6 Ma adds up to ~14.5 km. The middle to late Miocene period is more difficult to comprehend by the missing fault slip rates along the Büyük Menderes detachment and the larger errors on the exhumation rates. However, whereas the temperature in the footwall of the Büyük Menderes detachment was lower or close to the closure temperature of the ZFT system (~240 °C), the Gediz detachment was capable to exhume the Salihli granodiorite, which was emplaced at 630 to 700 °C and subsequently sheared at 530 to 580 °C (Rosetti et al. 2017). Furthermore, exhumation rate modelling of the samples 17M104 (ZHe age of 13.5 Ma at 2150 m.a.s.l.) and 11M15 from the eastern Bozdağ range (ZHe age 8.1 Ma at 982 m.a.s.l.) reveals middle Miocene exhumation rates of > 0.4 km/Ma. As the samples represent a structurally higher part of the Gediz detachment footwall, it is suggested that the resulting ~2.2 km of exhumation between 13.5 and 8.1 Ma is added to the 6 km of exhumation, which occurred since 6 Ma, resulting in > 8.2 km of total exhumation in the eastern Bozdağ range. If one considers a geothermal gradient of ~40 °C for the Miocene and a closure temperature of 240 °C for the ZFT system, the maximum amount of exhumation in the Aydın range did not exceed ~6 km. This amount of exhumation is comparable to the latest Miocene/Pliocene exhumation of the eastern Gediz detachment but in contrast to that, the exhumation in the footwall of the Büyük Menderes detachment occurred over a much longer time range of ~19 and ~5 Ma, although the highest exhumation rates occurred with ~0.5 km/Ma in the middle Miocene (Wölfler et al. 2017; Nilius et al. 2019). Though the exact

numbers are associated with uncertainties, the comparison between the exhumation rates in the Aydın range and the Bozdağ range indicates that the exhumation of the central Menderes Massif was symmetric but not balanced. Whereas exhumation in the footwall of the Büyük Menderes detachment is in the order of < 6 km, the rocks exposed in the footwall of the Gediz detachment were exhumed from depths of > 8 km, as the emplacement depth of the Salihli granodiorite was probably deeper. Therefore, it is proposed that exhumation in the course of extensional detachment faulting along the Gediz detachment exceeded the amount of exhumation along the Büyük Menderes and Demirhan detachments by a factor of 1.4 to 2. This factor is also valid for the total extension accommodated along the detachments since 6 Ma, as the Demirhan detachment accommodated 6 to 8 km of extension compared to ~14.5 km of extension along the Gediz detachment. Considering the slip and exhumation rates only in the Pliocene, the misbalance between the Gediz detachment and the Demirhan detachment seems to be even higher, comparing slip rates of ~5 km/Ma versus ~2 km/Ma and exhumation rates of ~1.5 versus 0.4 km/Ma, respectively.

7.3   Bivergent extension of the central Menderes Massif in the Aegean extensional context

In contrast to continental or oceanic subduction zone settings, where the lithospheric deformation is strongly asymmetric, the deformational mode in large extensional areas like the Aegean or the Basin and Range Province (USA) is more complicated to decipher. Although a single extensional detachment within a region undergoing large scale lithospheric extension can be described by simple shear, a wide region affected by large-scale extension might reflect a more complicated picture comprising multiple detachments with opposing dip-directions. However, in a recent publication of Jolivet et al. (2018), the Aegean domain is used as an example for a region, where the major extensional structures share the same top-to-the north shear sense (The North-Cycladic Detachment System (NCDS), the Naxos-Paros detachment (NPD), Cretan Detachment, Simav Detachment), rendering a strong simple shear component at lithosphere scale (Figure 7a). It is proposed that the asymmetric arrangement with consistent top-to-the-north shearing is associated with the retreat of the Aegean slab, inducing the inflow of asthenospheric mantle towards the trench, which entails basal shearing between the horizontal flow of asthenosphere and the overlying weak lower crust (Jolivet et al. 2018). Although this basal shearing model is an elegant way to describe the extensional tectonic evolution in the Aegean, it should be noted that the NCDS, the Cretan detachment and the Simav detachment share a common history as reactivated alpine shear and/or suture zones (Jolivet et al. 2010). Consequently, the overall Oligocene-Miocene top-to-the north shearing might rather be the related to the inherited alpine structure of the Aegean lithosphere, than induced by a basal shearing of the lower crust. Furthermore, in the western and eastern domains of the Aegean, the existence of the south-westward-dipping West-Cycladic Detachment System (WCDS) and the southward-dipping Büyük Menderes and Demirhan detachments of the central Menderes Massifs imply a less pronounced simple shear component in the lateral domains of the Aegean region, probably due to lower amounts of finite extension compared the central part of the Aegean (Jolivet et al. 2018). However, even the central part of the Aegean cannot be completely described as purely dominated by simple shear extension because the recently discovered Santorini detachment is interpreted as a top-to-the south detachment (Schneider et al. 2018). Yet, the amount of extension

and exhumation along the Santorini detachment was probably much smaller compared to the NCDS, which was able to exhume a migmatite core complex in its footwall. The overall picture in the Aegean thus reflects a more prominent top-to-the north over top-to-the south shearing component, but detailed constraints on the contribution of each detachment fault to the Aegean wide exhumation pattern are missing.

Addressing the aforementioned uncertainties in the Aegean, the results of this thesis might give some implications for the role of asthenospheric shearing, because in contrast the NCDS, and Simav detachment systems, the Gediz detachment as well as the Büyük Menderes and Demirhan detachments are not reactivated alpine structures, as they cross-cut the alpine nappe stack. Although, total amount of extension accommodated along the Gediz and Büyük Menderes detachments are probably much smaller compared to the NCDS and the WCDS (van Hinsbergen & Schmid 2012), the central Menderes Massif also shows a kinematic imbalance between the north-dipping and the south-dipping detachments. Therefore, one possibility to explain the 1.4 to 2 time's higher amount of exhumation in the footwall of the Gediz detachment compared to the Büyük Menderes and Demirhan detachments might be the shearing component induced by horizontal flow of asthenospheric mantle as proposed by Jolivet et al. (2018).
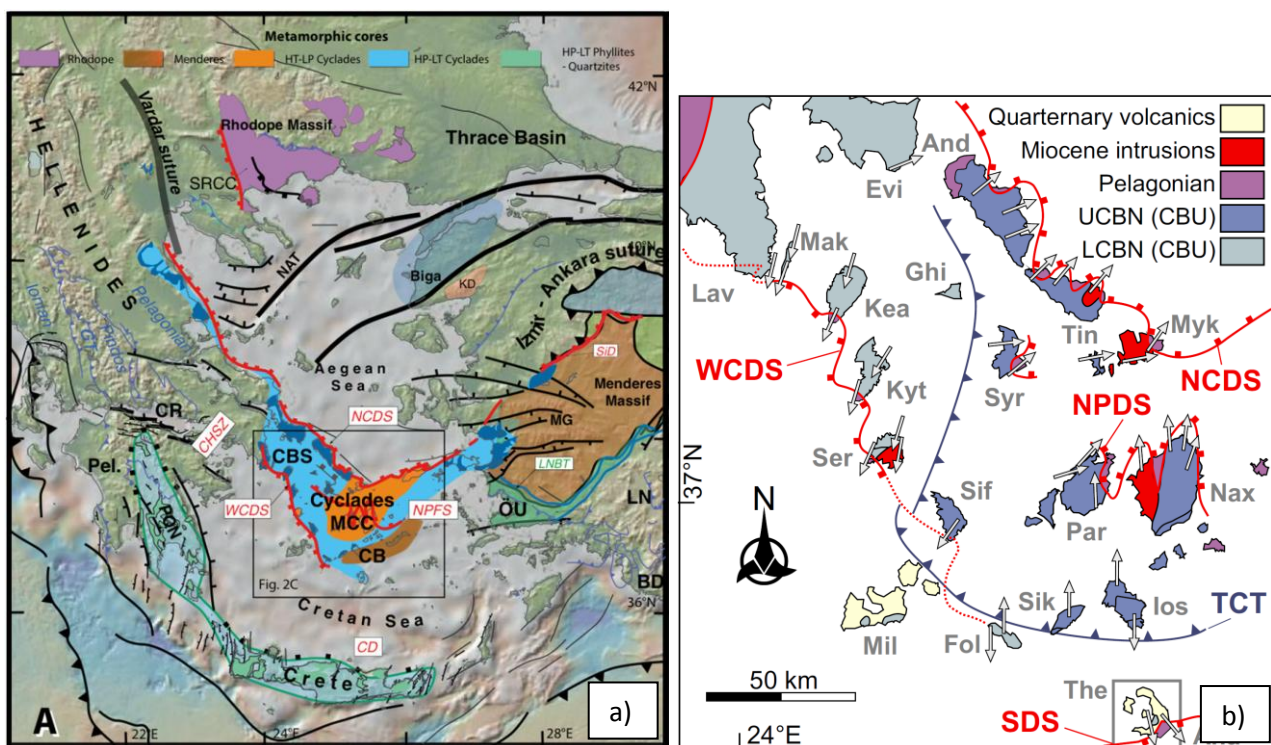
Figure 7a: Overview map of the main Aegean extensional detachments, modified from Jolivet et al. (2018). **b)** A more detailed map of the central part of the Aegean with the position of the newly described Santorini detachment in the south, modified after Schneider et al. (2018). Abbreviations: Ana: Anafi; Evi: Evia; Fol: Folegandros; Ghi: Ghiaros; Kyt: Kythnos; Lav: Lavrion; Mak: Makronisos; Mil: Milos; Myk: Mykonos; Nax: Naxos; Par: Paros; Ser: Serifos; Sif: Sifnos; Syr: Syros; Sik: Sikinos; Tin: Tinos; NCDS: North Cycladic Detachment System; NPDS: Naxos-Paros Detachment System; WCDS: West Cycladic Detachment System; SDS: Santorini Detachment System; TCT: Trans-Cycladic Thrust.

7.4   Conclusions

In the course of this study, high-density thermochronological data to unravel spatiotemporal differences of cooling episodes related to tectonic denudation in combination with the dating of K-Ar fault gouge ages, revealed a detailed exhumation history of the central Menderes Massif. In contrast to the previously debated simultaneity of faulting along the Büyük Menderes and Gediz detachments, as well as whether exhumation of the central Menderes Massif commenced in the middle Miocene or in the Pliocene, our data reveals detailed constraints on the timing of faulting and the spatial exhumation pattern. The oldest indications of faulting in the central Menderes Massif are attributed to K-Ar fault gouge ages of the Büyük Menderes detachment at 22 Ma. This first phase of faulting along the Büyük Menderes detachment might reflect a rather modest intensity of faulting until fast cooling in the footwall occurs between 16 and 13 Ma. This middle Miocene period of fast cooling in the footwall of the Büyük Menderes detachment, correlates with the intrusion of the Salihli and Turgutlu granodiorites and the initiation of detachment faulting along the Gediz detachment. Although the intrusion age and ductile shearing along both granodiorites of the Gediz detachment occurred synchronously along strike, faulting in brittle crustal levels occurred first in the western part of the Gediz detachment, where K-Ar fault gouge and thermochronology ages document detachment faulting between 13 and 6 Ma. The termination of faulting along the western part of the Gediz detachment marks the onset of faulting along its eastern proportion, south of Salihli. Pliocene ZFT ages in the footwall of the eastern Gediz detachment elucidate the intensity of this phase of rapid faulting, which occurs concurrently with the formation of the newly described Demirhan detachment fault in the eastern part of the Aydın range. Structural mapping in the Aydın range identified the Demirhan detachment as an individual detachment situated in the hanging wall of the eastern Büyük Menderes detachment. Thermochronology ages in the footwall imply that the Demirhan detachment operated between ~6 and 3 Ma. The cessation of detachment faulting along the eastern part of the Gediz detachment and the Demirhan detachment is associated with the onset of high-angle normal faulting along the southern and northern graben-bounding faults of the Gediz and Büyük Menderes graben, respectively.

The quantification of core complex formation is inferred by the calculation of detachment slip-rates and thermokinematic modelling of exhumation rates. Slip rates and exhumation rates from the Bozdağ and the Aydın range reveal that faulting and exhumation in the footwall of the Gediz detachment exceeded the rates of the Büyük Menderes and Demirhan detachment by a factor of 2 - 3 during the Pliocene. Whereas middle Miocene exhumation rates in the Aydın range yield ~0.5 km/Ma, the western part of the Bozdağ range experiences exhumation rates of ~1 km/Ma. In the latest Miocene and Pliocene, exhumation rates of 0.4 km/Ma in the footwall of the Demirhan detachment are exceeded by threefold higher exhumation rates in the eastern part of the Gediz detachment of ~1.5 km/Ma. Similarly, the western part of the Gediz detachment yields slip rates of 2.5 km/Ma during the middle Miocene, followed by increasing in slip rates in the Pliocene to ~5 km/Ma in the eastern part of the Gediz detachment. At the same time the Demirhan detachment yields a slip rate of 2 km/Ma. Consequently, the concurrent exhumation of the Bozdağ and Aydın ranges by bivergent faulting along the Gediz and Büyük Menderes and Demirhan detachments can be confirmed for the middle Miocene and Pliocene period. However, the Bozdağ range was continuously

exhumed in the footwall of the long-lived Gediz detachment, whereas the Aydın range shows a discontinuous two-step exhumation history. Furthermore, the slip and exhumation rates imply that the contribution to the symmetric exhumation of the central Menderes Massif of the Büyük Menderes and Demirhan detachments compared to the Gediz detachment was not equally balanced, as the exhumation rates in the Bozdağ range exceeds the exhumation rates in the Aydın range by a factor of ~2 in the middle Miocene and a factor of ~3 during the latest Miocene and Pliocene. Furthermore, the pattern of ^{10}Be catchment-wide erosion rates in the central Menderes Massif emphasizes that a portion of rock exhumation during continental extension can be attributed to erosional denudation, though the relative contribution depends on the local lithology. The much thicker cataclastic surface of the Gediz detachment footwall results in lower erosion rates compared to the more erodible footwalls of the Büyük Menderes and Demirhan detachments in the Aydın range. Hence, fast extension and tectonic denudation of a thick cataclastic footwall might result in a lower contribution of erosion to exhumation compared to extensional detachments comprising slower rates of slip and lower rates of tectonic denudation.

References

Asti, R., Malusà, M.G., Faccenna, C., 2018. Supradetachment basin evolution unravelled by detrital apatite fission track analysis: the Gediz Graben (Menderes Massif, Western Turkey). Basin Research 30(3), 502-521.

Cenki-Tok, B., Expert, M., Işık, V., Candan, O., Monie, P., Bruguier, O., 2016. Complete Alpine reworking of the northern Menderes Massif, western Turkey. International Journal of Earth Sciences 105(5), 1507-1524.

Dunkl, I., 2002. TRAKKEY: a window program for calculation and graphical presentation of fission track data. Computers & Geosciences 28, 3–12.

Hetzel, R., Reischmann, T., 1996. Intrusion of Pan-African gneisses in the southern Menderes massif and the age of cooling after Alpine ductile extensional deformation. Geological Magazine 133, 565–572.

Işik, V., Tekeli, O., 2001. Late orogenic crustal extension in the northern Menderes massif (western Turkey): Evidences for metamorphic core complex formation. International Journal of Earth Sciences 89, 757–765.

Işik, V., Tekeli, O., Seyitoğlu, G., 2004, The $^{40}Ar/^{39}Ar$ age of extensional ductile deformation and granitoid intrusion in the northern Menderes core complex: implications for the initiation of extensional tectonics in western Turkey. Journal of Asian Earth Sciences 23, 555–566.

Jolivet, L., Lecomte, E., Huet, B., Denéle, Y., Lacombe, O., Labrousse, L., Le Pourhiet, L., Mehl, C., 2010. The North Cycladic Detachment System. Earth and Planetary Science Letters 289, 87–104.

Jolivet, L., Menant, A., Clerc, C., Sternai, P., Bellahsen, N., Leroy, S., Pik, R., Stab, M., Faccenna, C., Gorini, C. 2018. Extensional crustal tectonics and crust-mantle coupling, a view from the geological record. Earth-Science Reviews 185, 1187 - 1209.

Nilius, N. P., Glotzbach, C., Wölfler, A., Hampel, A., Dunkl, I., Akal, C., Heineke, C., Hetzel, R. 2019. Exhumation history of the Aydın range and the role of the Büyük Menderes detachment system during bivergent extension of the central Menderes Massif, western Turkey. Journal of the Geological Society, jgs2018-162.

Ring, U., Johnson, C., Hetzel, R., Gessner, K., 2003. Tectonic denudation of a Late Cretaceous-Tertiary collisional belt: regionally symmetric cooling patterns and their relation to extensional faults in the Anatolide belt of western Turkey. Geological Magazine 140, 421–441.

Ring, U., Collins, A.S., 2005. U–Pb SIMS dating of synkinematic granites: timing of core-complex formation in the northern Anatolide belt of western Turkey. Journal of the Geological Society 162(2), 289–298.

Ring, U., Gessner, K., Thomson, S., 2017. Variations in fault-slip data and cooling history reveal corridor of heterogeneous backarc extension in the eastern Aegean Sea region. Tectonophysics 700-701, 108–130.

Schneider, D.A., Grasemann, B., Lion, A., Soukis, K., Draganits, E. 2018. Geodynamic significance of the Santorini Detachment System (Cyclades, Greece). Terra Nova 30(6), 414-422.

Thomson, S.N., Ring, U., 2006. Thermochronologic evaluation of postcollision extension in the Anatolide orogen, western Turkey. Tectonics 25, TC3005, doi:10.1029/2005TC001833.

Ustaszewski, K., Kounov, A., Schmid, S.M., Schaltegger, U., Krenn, E., Frank, W., Fügenschuh, B. 2010. Evolution of the Adria-Europe plate boundary in the northern Dinarides: From

continent-continent collision to back-arc extension. Tectonics 29(6).

van Hinsbergen, D.J., 2010. A key extensional metamorphic complex reviewed and restored: the Menderes Massif of western Turkey. Earth-Science Reviews 102(1-2), 60-76.

van Hinsbergen, D.J., Schmid, S.M., 2012. Map view restoration of Aegean-West Anatolian accretion and extension since the Eocene. Tectonics 31, TC 5005.

Vermeesch, P., 2009, RadialPlotter: a Java application for fission track, luminescence and other radial plots. Radiation Measurements 44 (4), 409-410.

Wölfler, A., Glotzbach, C., Heinecke, C., Nilius, N.P., Hetzel, R., Hampel, A., Akal, C., Dunkl, I., Christl, M., 2017. Late Cenozoic cooling history of the central Menderes Massif: Timing of the Büyük Menderes detachment and the relative contribution of normal faulting and erosion to rock exhumation. Tectonophysics 717, 585-598.

Supplements

Table S1. Mineralogical composition of fault gouge samples (all grain size fractions) that were dated by K-Ar.

Sample number	Grain size	Illite 2M1	Illite 1M	Smectite	Illite/Smectite mixed layer	Kaolinite	Quartz	K-Feldspar	Albite	Dickite	Chlorite	Siderite	Dolomite	Calcite	Goethite
	[μm]	[%]	[%]	[%]	[%]	[%]	[%]	[%]	[%]	[%]	[%]	[%]	[%]	[%]	[%]
Gediz detachment – Bozdağ Range															
15T18	<0.1	26	–	68	–	–	–	–	–	–	6	–	–	–	–
15T18	<2	58	–	37	–	–	<1	–	–	–	4	–	–	–	–
15T18	2–6	57	–	28	–	4	3	–	–	–	8	–	–	–	–
15T22	<0.1	33	–	63	–	4	–	–	–	–	–	–	–	–	–
15T22	<0.4	51	–	41	–	6	1	–	–	–	–	–	–	–	1
15T22	<2	34	–	52	–	6	6	<1	–	–	–	–	–	1	–
15T22	2–6	17	–	37	–	5	25	3	2	–	–	–	<1	11	–
Büyük Menderes detachment – Aydın Range															
15T2	<0.1	10	–	–	81	9	–	–	–	–	–	–	–	–	–
15T2	<2	13	4	–	70	5	6	–	1	–	–	<1	–	–	–
15T2	2–6	7	5	–	62	9	10	–	2	–	–	4	1	–	–
15T3	<0.1 and <0.4	14	13	–	63	10	<1	–	–	–	–	–	–	–	–
15T3	<2	15	10	–	52	12	9	–	–	–	–	1	–	–	–
15T3	2–6	11	8	–	36	12	26	–	–	–	–	5	1	–	–
15T7	<0.4	58	–	15	–	27	–	–	–	–	–	–	–	–	–
15T7	<2	45	–	11	–	35	2	–	–	7	–	–	–	–	–
15T7	2–6	51	–	3	–	32	6	–	–	7	–	–	–	–	–
16T6	<0.4	6	20	5	32	35	1	–	–	–	–	–	–	–	–
16T6	<2	8	21	2	18	42	2	4	3	–	<1	–	–	–	–
16T6	2–6	6	13	2	20	47	2	2	3	–	4	–	–	–	–

Table S2: Complete list of all AFT ages.

Sample	# grains	ρs	Ns	ρi	Ni	ρd	Nd	P(χ²) [%]	Dispersion
11M1**	20	0.885	17	18.490	355	1.9324	4424	100	0
11M3**	6	2.059	7	23.824	81	1.9238	4424	100	0
11M4**	5	2.308	6	7.692	20	1.9246	4424	91	0
11M5**	25	7.075	179	78.577	1988	1.9332	4424	0	0.83
11M6**	25	4.082	78	47.315	904	1.9262	4424	56	0.07
11M7*	10	3.478	32	7.609	70	1.9269	4424	9	0.5
11M8**	10	3.548	16	10.643	48	1.9272	4424	100	0
11M9**	25	3.049	50	3.354	55	1.9285	4424	100	0
11M11**	20	1.636	27	12.545	207	1.9301	4424	99	0
11M12**	22	2.577	50	10.000	194	1.9308	4424	97	0
11M13*	10	1.972	14	21.972	156	1.9316	4424	99	0
11M14**	25	4.217	100	28.251	670	1.9324	4424	76	0
11M15**	25	5.929	123	36.393	755	1.9332	4424	37	0.1
14M17**	20	0.688	24	9.398	328	8.3835	3032	73	0
14M19**	20	0.720	29	13.325	537	8.3596	3032	39	0.35
14M20**	7	0.223	4	4.916	88	8.3477	3032	87	0
14M23**	20	2.587	52	15.473	311	8.3118	3032	26	0
14M24**	20	1.129	14	10.081	125	8.2999	3032	85	0
14M25**	20	1.176	18	9.477	145	8.1326	3032	12	0.32
14M26**	20	2.665	105	20.787	819	8.2760	3032	99	0
14M27**	20	4.135	43	24.135	251	8.2640	3032	90	0
14M29**	20	3.254	82	17.143	432	8.2541	3032	0	0.56
14M30**	20	2.586	30	13.621	158	8.2401	3032	85	0
14M31**	15	2.887	41	17.042	242	8.2282	3032	50	0
14M32**	15	0.655	11	16.190	272	8.2162	3032	77	0
14M33*	4	0.635	4	14.603	92	8.2034	3032	78	0
14M34*	17	0.512	19	11.402	423	8.1923	3032	2	0.67
14M35**	11	0.778	7	15.444	139	8.1684	3032	50	0
14M36*	20	1.395	47	23.383	788	8.1565	3032	86	0
14M37*	20	1.762	77	12.586	550	8.1445	3032	2	0.42
14M38**	15	1.772	14	11.772	93	7.9722	3032	99	0
14M39*	20	1.869	37	9.949	197	8.1206	3032	9	0.54
14M40**	20	0.649	32	2.677	132	8.1087	3032	12	0.61
14M41*	11	0.847	16	18.201	344	8.0967	3032	29	0
15M42	17	1.016	37	3.956	144	5.5313	2796	99	0
15M44	25	0.919	44	9.562	458	5.5103	2796	96	0.02
15M45	25	3.211	122	22.105	840	5.4794	2796	64	0.02
15M46**	20	3.907	53	19.388	263	5.4480	2796	99	0
15M47**	10	2.480	31	13.360	167	5.4174	2796	97	0
15M48**	21	1.298	27	2.740	57	2.1489	2796	100	0
15M49	21	1.507	52	7.072	244	5.3554	2796	92	0.18
15M51	9	4.956	56	19.292	218	5.2934	2796	26	0.22

Table S2: continued

15M52	22	3.215	79	22.543	554	7.4810	2481	100	0
15M54	13	2.331	38	10.061	164	5.2315	2796	81	0.02
15M55	17	1.641	42	8.828	226	5.2005	2796	100	0
15M56	25	1.748	54	7.540	233	5.2005	2796	96	0
15M57**	8	1.383	13	7.234	68	5.1285	2796	99	0
15M58	22	1.546	45	21.306	620	5.1075	2796	80	0.16
15M59	23	1.701	83	12.193	595	4.7896	2796	28	0.15
15M69	17	3.507	101	18.819	542	4.8597	2796	97	
15M70	30	2.732	174	20.235	1289	4.8287	2796	100	0
15M74	62	0.988	120	10.239	1243	4.7668	2796	89	
15M78	26	1.080	73	3.861	261	4.7048	2796	96	
15M84	16	1.373	35	8.824	225	4.6428	2796	100	
16M86	20	1.763	35	5.899	137	7.1850	2481	99	0
16M87	24	3.433	110	23.061	739	7.2356	2481	78	0.16
16M88	17	1.522	63	9.859	408	6.9901	2481	97	0
16M89	17	3.513	67	18.091	345	6.9411	2481	99	0
16M90	35	3.929	163	23.769	986	6.8920	2481	99	0
16M94	23	1.484	42	18.297	518	6.6956	2481	100	0
16M95	14	2.479	29	14.276	167	6.6465	2481	100	0
16M97	7	1.538	13	11.947	101	6.5975	2481	98	0

ρs (ρi) is the spontaneous (induced) track density (10^5 tracks/cm^2); Ns (Ni) is the number of counted spontaneous (induced) tracks; number of tracks counted on the dosimeter; P($\chi2$) is the probability of obtaining Chi-square value ($\chi2$) for n degree of freedom (wher the zeta calibration method (Hurford and Green, 1983), glass dosimeter IRMM540, and zeta values of 226±13 a/cm^2 (samples witho 255±9 (samples with two asterisks) calculated with Durango apatite standards.

Table S3: Complete list of all ZFT ages.

Sample	# grains	ρs	Ns	ρi	Ni	ρd	Nd	P(χ²) [%]	Dispersion	Central age [Ma]	±1σ	U [ppm]
11M1*	20	90.000	531	100.678	594	6.525	2512	2	0.24	32.8	2.9	634
11M2*	20	120.667	543	159.556	718	6.542	2512	15	0.13	26.9	2	1184
11M3*	20	40.707	403	160.101	1585	6.563	2512	11	0.17	9	0.7	1058
11M5*	20	20.396	206	155.050	1566	6.576	2512	0	0.45	4.9	0.6	918
11M6*	20	22.02	218	208.283	2062	6.593	2512	0	0.59	3.8	0.6	1378
11M7*	20	87.705	535	147.541	900	6.610	2512	0	0.25	21	1.8	1016
11M13*	20	28.554	237	131.205	1089	6.643	2512	59	0.02	7.9	0.6	892
11M15*	20	28.723	270	88.936	836	6.677	2512	0	0.34	11.7	1.3	570
14M16*	20	134.054	496	332.432	1230	6.823	2583	10	0.14	15.2	1.1	2147
14M17*	16	37.895	216	100.702	574	6.822	2583	1	0.31	14.3	1.7	652
14M18*	20	24.098	294	129.754	1583	6.821	2583	9	0.15	6.9	0.6	743
14M19*	8	17.755	87	67.347	330	6.821	2583	69	0	9.8	1.2	508
14M29*	20	75.474	717	92.737	881	6.815	2583	10	0.13	30.3	2.1	607
14M30*	20	86.750	694	90.625	725	6.815	2583	10	0.12	35.8	2.5	544
14M31*	20	75.225	835	96.757	1074	6.814	2583	8	0.13	29	1.9	585
14M32*	20	75.714	583	111.299	857	6.814	2583	61	0.04	25.3	1.7	689
14M35*	20	70.571	494	99.571	697	6.812	2583	44	0.08	26.3	1.9	671
14M36*	20	38.485	508	53.864	711	6.812	2583	0	0.32	26.4	2.6	349
15M45	15	24.508	106	53.408	231	6.458	1982	13.39	0.05	22.7	2.9	276
15M47	15	20.534	109	32.026	170	6.822	1982	18.91	0.24	28.2	4.2	152
15M57	20	19.172	147	42.213	316	6.419	1982	19.63	0.2	19.1	2.4	224
15M59	20	25.519	148	37.071	215	6.404	1982	93.85	0.01	33.6	4	185
15M63	20	15.927	155	37.851	368	6.387	1982	27.79	0.27	17.9	2.3	185
15M65	16	19.074	135	52.419	371	6.372	1982	96.53	0	17.7	2	260
15M66	16	17.910	125	52.441	366	6.355	1982	89	0	16.6	1.9	259
15M71	20	18.448	243	21.636	285	6.340	1982	51.54	0.1	35.5	3.4	109.8
15M84	25	9.877	100	33.778	342	6.308	1982	99.32	0	14.1	1.8	228
15M85	25	22.914	232	40.494	410	6.292	1982	93.59	0	27.2	2.6	215.34

ρs (ρi) is the spontaneous (induced) track density (105 tracks/cm²); Ns (Ni) is the number of counted spontaneous (induced) tracks; ρd is the dosimeter track density (105 tracks/cm²); Nd is the number of tracks counted on the dosimeter; P(χ²) is the probability of obtaining Chi-square value (χ²) for n degree of freedom (where n is the number of crystals minus 1); Ages were calculated using the zeta calibration method [Hurford and Green, 1983], glass dosimeter IRMM541, and a zeta value of 153±7 yr/cm² (without asteriks) 109±3 yr/cm² (marked with asteriks) calculated with Fish Canyon Tuff zircon standards.

Table S4: Results of AHe analyses.

Sample	He vol. [ncc]	1s [%]	U238 mass [ng]	1s [%]	conc. [ppm]	Th232 mass [ng]	1s [%]	conc. [ppm]	Th/U ratio	Sm mass [ng]	1s [%]	conc. [ppm]	Ejection correct. (Ft)	*Uncorr.* *He-age* *[Ma]*	Ft-Corr. He-age [Ma]	2s [Ma]	2s [%]	Sample unweighted aver. ± 2 s.e. [Ma]	[Ma]
14M16 a1	0.276	1.3	0.253	1.8	45.4	0.324	2.4	58.3	1.28	0.900	6.1	162	0.78	6.8	8.7	0.7	8	7.2	1.5
14M16 a2	0.024	3.5	0.041	2.2	13.6	0.009	3.5	2.9	0.21	0.424	6.5	142	0.75	4.3	5.7	0.6	11		
14M16 a3	0.073	2.1	0.061	2.0	21.0	0.019	2.9	6.5	0.31	0.431	6.9	148	0.70	8.7	12.4	1.3	11		
14M17 a1	0.035	3.0	0.042	2.2	10.5	0.086	2.5	21.7	2.06	1.416	5.8	358	0.74	3.9	5.3	0.6	10	4.6	0.7
14M17 a2	0.025	3.7	0.042	2.2	13.7	0.071	2.5	22.9	1.68	0.960	6.0	310	0.79	3.1	3.9	0.4	10		
14M18 a3	0.004	8.2	0.016	3.9	3.4	0.012	3.2	2.6	0.78	0.110	9.1	24	0.73	1.8	2.4	0.5	19	3.9	0.5
14M19 a3	0.001	11.0	0.003	16.7	1.7	0.004	4.0	2.3	1.35	0.095	8.2	52	0.70	2.3	3.3	1.0	32		
14M19 a4	0.007	6.7	0.003	18.7	2.0	0.016	3.0	10.4	5.21	0.112	9.1	72	0.69	7.4	10.8	2.4	22		
14M20 a1	0.002	10.6	0.001	48.4	0.8	0.013	3.2	9.7	11.55	0.061	9.5	45	0.69	2.7	3.9	1.3	32		
14M22 a1	0.074	2.2	0.017	3.6	3.1	0.003	4.2	0.6	0.20	0.532	6.1	97	0.74	27.9	37.8	4.0	11		
14M22 a2	0.039	2.7	0.057	2.0	6.5	0.010	3.4	1.2	0.18	0.895	5.9	102	0.78	4.9	6.3	0.6	9		
14M23 a1	0.032	3.3	0.019	3.4	3.9	0.004	4.0	0.9	0.23	0.680	6.4	139	0.73	10.2	14.0	1.7	12		
14M23 a2	0.014	4.8	0.006	8.5	2.9	0.002	5.7	1.1	0.37	0.263	6.7	121	0.65	12.6	19.4	3.6	19		
14M23 a4	0.047	2.6	0.022	3.0	4.2	0.006	3.7	1.1	0.26	0.861	6.0	161	0.66	12.6	19.0	2.4	12	17.5	1.7
14M27 a1	0.009	6.2	0.003	19.2	0.4	0.001	36.6	0.1	0.25	0.047	9.6	7	0.73	21.9	30.0	10.3	35		
14M27 a4	0.013	5.2	0.002	29.9	0.4	0.012	3.3	2.3	6.39	0.041	11.3	8	0.73	20.8	28.5	7.2	25		
14M27 a6	0.072	182.5	0.018	3.4	5.3	0.001	43.9	0.2	0.03	0.044	10.0	13	0.72	32.3	44.8	163.8	365	34.4	5.2
14M29 a1	0.295	1.2	0.120	1.9	14.4	0.022	2.9	2.7	0.19	1.998	5.8	240	0.80	17.2	21.5	1.6	7		
14M29 a2	0.423	1.1	0.163	1.8	17.6	0.031	2.7	3.3	0.19	2.204	5.8	238	0.77	18.6	24.1	1.9	8		
14M29 a5	0.365	1.2	0.153	1.8	14.1	0.048	2.6	4.4	0.31	2.543	5.8	235	0.81	16.3	20.1	1.4	7	21.9	1.2
14M31 a1	0.131	1.5	0.615	1.8	56.5	0.277	2.4	25.4	0.45	0.650	6.2	60	0.81	1.6	2.0	0.1	7		
14M31 a2	0.163	1.5	1.190	1.8	79.2	0.036	2.7	2.4	0.03	0.720	6.0	48	0.80	1.1	1.4	0.1	8		
14M31 a3	0.171	1.4	1.190	1.8	79.4	0.058	2.6	3.9	0.05	0.771	6.0	51	0.80	1.2	1.5	0.1	7	1.6	0.2
14M34 a1	0.001	12.3	0.002	31.5	0.6	0.002	7.7	0.7	1.12	0.035	13.6	12	0.75	2.1	2.8	1.4	50		
14M34 a2	0.000	12.7	0.000	777.1	0.1	0.001	15.1	0.7	12.52	0.018	13.4	11	0.66	2.6	3.9	10.7	273		
14M34 a5	0.010	5.8	0.028	2.6	7.1	0.029	2.7	7.1	1.00	0.149	7.2	37	0.72	2.3	3.2	0.5	15	3.3	0.3
14M35 a5	0.008	6.3	0.011	5.2	6.7	0.007	3.7	4.3	0.64	0.076	9.1	48	0.65	5.1	7.9	1.5	18		
14M35 a7	0.027	3.6	0.081	1.9	11.6	0.056	2.6	8.0	0.69	0.318	6.5	46	0.77	2.3	3.0	0.3	10	5.4	3.5
14M37 a2	0.013	5.1	0.010	5.5	4.2	0.018	3.0	7.3	1.75	0.055	9.3	23	0.76	7.4	9.7	1.4	14	9.7	1.4
15M42 a4	0.013	4.9	0.027	6.2	4.3	0.079	2.6	12.7	2.97	1.174	2.2	190	0.77	1.98	2.6	0.3	13	2.6	0.3
15M44 a1	0.046	2.8	0.056	2.1	5.5	0.216	2.4	21.1	3.84	3.120	3.1	305	0.82	2.87	3.5	0.3	8	3.5	0.3
15M46 a1	0.021	3.7	0.037	4.3	9.3	0.004	19.0	0.9	0.10	0.181	2.2	46	0.65	4.38	6.7	1.0	15	6.7	1.0
15M51 a1	0.033	2.9	0.074	2.0	10.8	0.052	2.6	7.6	0.70	0.194	6.8	28	0.81	3.10	3.8	0.3	9		
15M51 a4	0.140	1.8	0.332	1.8	87.5	0.034	2.8	9.0	0.10	0.143	10.4	38	0.77	3.39	4.4	0.4	8	4.7	0.6
15M56 a1	0.100	1.9	0.050	2.2	7.9	0.003	4.2	0.5	0.07	0.360	5.4	56	0.78	15.29	19.6	1.7	9	19.6	1.7
15M59 a1	0.081	2.2	0.103	1.9	19.2	0.739	2.4	138.0	7.18	0.547	3.8	102	0.73	2.38	3.3	0.3	10		
15M59 a3	2.564	1.2	0.934	1.8	113.2	4.269	2.4	517.5	4.57	0.890	4.2	108	0.78	10.86	13.8	1.0	7		
15M59 a5	1.913	1.4	0.754	1.8	85.5	3.836	2.4	434.8	5.09	0.717	2.2	81	0.78	9.48	12.2	1.0	8	9.8	0.2
15M59 a6	0.847	1.4	0.356	1.9	61.6	2.396	2.4	415.1	6.74	0.432	2.2	75	0.77	7.56	9.8	0.8	8		
15M64 a4	0.006	6.7	0.011	16.1	3.4	0.001	331.2	0.3	0.08	0.145	2.2	45	0.62	3.85	6.3	2.2	35	6.3	2.2
15M65 a3	0.003	8.7	0.003	33.9	2.5	0.004	4.2	3.5	1.40	0.012	29.0	10	0.70	5.86	8.3	4.3	52	8.3	4.3
15M76 a2	0.644	1.1	0.274	1.8	33.7	0.048	2.6	5.9	0.18	0.762	8.3	94	0.773	18.3	23.6	1.9	8	25.5	1.5
15M76 a3	3.896	1.0	1.475	1.8	49.1	0.073	2.5	2.4	0.05	3.997	8.2	133	0.863	21.1	24.5	1.4	6		
16M86 a1	0.005	7.2	0.026	6.1	4.3	0.012	3.0	2.0	0.45	0.814	2.2	135	0.76	1.18	1.6	0.3	18	2.0	0.2
16M86 a3	0.005	7.1	0.014	10.3	3.1	0.005	10.3	1.2	0.37	0.389	2.2	87	0.71	2.39	3.4	0.8	23		

Table S5: Results of zircon (U-Th)/He - analyses

Sample	He vol. [ncc]	1s [%]	U238 mass [ng]	1s [%]	conc. [ppm]	Th232 mass [ng]	1s [%]	conc. [ppm]	Th/U ratio	Sm mass [ng]	1s [%]	conc. [ppm]	Ejection correct. (Ft)	Uncorr. He-age [Ma]	Ft-Corr. He-age [Ma]	2s [Ma]	2s [%]	Sample unweighted aver. ± 2 s.e. [Ma]	[Ma]
14M16 z1	7.128	1.1	9.248	1.8	678	1.638	2.4	120	0.18	0.052	5.8	4	0.90	6.1	6.8	0.3	5.0	7.0	1.6
14M16 z2	16.312	1.1	19.961	1.8	2907	2.136	2.4	311	0.11	0.021	8.2	3	0.80	6.6	8.3	0.6	7.2		
14M16 z3	4.337	1.2	7.570	1.8	1673	0.579	2.4	128	0.08	0.008	12.5	2	0.78	4.7	6.0	0.5	7.8		
14M18 z3	0.767	1.3	2.821	1.8	749	0.335	2.4	89	0.12	0.001	51.3	0	0.80	2.2	2.7	0.2	7.4		
14M18 z4	0.673	1.4	2.083	1.8	375	0.826	2.4	149	0.40	0.015	11.2	3	0.79	2.4	3.1	0.2	7.6		
14M18 z5	0.661	1.4	2.057	1.8	457	0.173	2.4	38	0.08	0.003	21.4	1	0.79	2.6	3.3	0.3	7.7	3.0	0.3
14M19 z2	2.790	1.2	1.785	1.8	156	0.814	2.4	71	0.46	0.027	9.4	2	0.83	11.7	14.1	0.9	6.5		
14M19 z3	1.584	1.2	0.977	1.8	338	0.888	2.4	307	0.91	0.018	9.7	6	0.73	11.0	15.1	1.4	9.0		
14M19 z4	0.503	1.7	1.680	1.8	461	0.430	2.4	118	0.26	0.025	10.6	7	0.74	2.3	3.2	0.3	9.2	14.6	1.9
14M21 z2	1.710	1.2	1.336	1.8	345	0.858	2.4	222	0.64	0.019	8.3	5	0.78	9.2	11.8	0.9	7.7		
14M21 z4	5.634	3.7	2.509	1.8	278	1.398	2.4	155	0.56	0.149	4.9	17	0.81	16.4	20.3	2.0	9.8	16.0	6.0
14M22 z2	0.684	1.0	0.751	1.8	318	0.142	2.4	60	0.19	0.004	33.6	2	0.67	7.2	10.8	1.1	10.6		
14M22 z3	4.291	0.8	3.590	1.8	480	1.694	2.4	226	0.47	0.069	8.1	9	0.77	8.9	11.6	0.9	7.8		
14M22 z4	0.514	1.0	0.662	1.8	164	0.260	2.4	64	0.39	0.004	31.7	1	0.72	5.9	8.2	0.8	9.2	10.2	1.8
14M23 z6	2.105	1.2	1.132	1.8	499	0.134	2.4	59	0.12	0.031	7.6	14	0.68	15.0	22.0	2.3	10.5		
14M23 z7	4.243	1.1	2.340	1.8	829	0.103	2.4	37	0.04	0.005	18.5	2	0.69	14.9	21.5	2.2	10.2	21.8	0.3
14M24 z2	1.551	1.2	1.128	1.8	268	0.410	2.4	98	0.36	0.010	12.7	2	0.80	10.5	13.1	0.9	7.2		
14M24 z3	1.081	1.2	0.850	1.8	276	0.345	2.4	112	0.41	0.012	13.2	4	0.72	9.6	13.3	1.2	9.3		
14M24 z5	0.836	1.3	0.546	1.8	149	0.373	2.4	101	0.68	0.006	18.0	2	0.71	10.9	15.4	1.5	9.6	13.9	0.7
14M29 z1	19.300	0.8	9.024	1.8	1756	1.307	2.4	254	0.14	0.016	19.0	3	0.84	17.1	20.4	1.2	6.1		
14M29 z2	7.266	0.8	3.088	1.8	652	0.264	2.4	56	0.09	0.040	11.3	8	0.72	19.1	26.5	2.4	9.2		
14M29 z5	9.940	0.9	3.583	1.8	377	0.617	2.4	65	0.17	0.067	10.1	7	0.82	22.0	26.9	1.8	6.6	24.6	2.1
14M25 z1	4.983	0.8	3.415	1.8	404	1.977	2.4	234	0.58	0.042	9.0	5	0.82	10.6	13.0	0.8	6.5	13.0	0.8
14M30 z1	3.482	1.2	1.544	1.8	367	0.142	2.4	34	0.09	0.006	20.6	1	0.71	18.3	25.7	2.5	9.6		
14M30 z2	2.879	1.2	1.186	1.8	299	0.113	2.4	28	0.09	0.004	22.9	1	0.74	19.6	26.5	2.3	8.8		
14M30 z3	13.137	1.1	5.219	1.8	467	1.204	2.4	108	0.23	0.091	5.3	8	0.80	19.7	24.7	1.8	7.2	25.7	0.9
14M31 z1	1.476	1.2	0.812	1.8	231	0.180	2.4	51	0.22	0.013	10.2	4	0.76	14.3	18.8	1.6	8.3		
14M31 z3	8.919	1.1	4.403	1.8	737	0.580	2.4	97	0.13	0.108	5.0	18	0.77	16.3	21.1	1.7	8.0	20.0	1.6
14M39 z1	1.810	1.3	1.132	1.8	266	0.517	2.4	121	0.46	0.101	5.6	24	0.71	11.9	16.8	1.6	9.6		
14M39 z2	4.275	1.2	1.802	1.8	366	0.851	2.4	173	0.47	0.059	6.2	12	0.70	17.7	25.2	2.5	9.8	21.0	5.9
14M41 z2	3.249	1.2	1.571	1.8	648	0.326	2.4	135	0.21	0.005	18.4	2	0.73	16.3	22.4	2.0	9.1		
14M41 z3	3.125	1.2	2.314	1.8	286	0.613	2.4	76	0.27	0.006	16.4	1	0.81	10.5	13.0	0.9	7.0		
14M41 z6	0.909	1.3	0.810	1.8	258	0.228	2.4	73	0.28	0.003	25.8	1	0.73	8.7	11.9	1.1	9.1		
14M41 z7	1.773	0.9	1.576	1.8	422	0.484	2.4	129	0.31	0.035	10.5	9	0.74	8.7	11.7	1.0	8.6	12.2	0.7
15M44	3.860	1.3	2.466	1.8	166	0.381	2.4	26	0.15	0.215	15.7	1	0.81	12.5	15.3	1.1	7.0		
15M44	4.250	1.3	3.150	1.8	497	0.821	2.4	130	0.26	0.453	15.7	7	0.80	10.5	13.2	1.0	7.4	14.3	1.5
15M46	8.094	1.3	4.291	1.8	1064	1.200	2.4	297	0.28	0.272	15.7	7	0.74	14.6	19.9	1.8	9.0		
15M46	0.923	1.4	0.634	1.8	265	0.307	2.4	128	0.48	0.336	15.7	14	0.76	10.8	14.2	1.2	8.5		
15M46	1.287	1.4	1.008	1.8	533	0.202	2.4	107	0.20	0.155	15.7	8	0.70	10.1	14.3	1.4	9.9	16.2	1.9
15M47	0.806	2.6	3.739	1.8	1165	0.609	2.4	190	0.16	0.368	15.7	11	0.72	1.7	2.4	0.3	10.5		
15M47	1.724	1.4	1.016	1.8	222	0.729	2.4	160	0.72	0.562	15.7	12	0.78	12.0	15.3	1.2	7.7	15.3	1.2
15M55	1.217	1.4	0.907	1.8	159	0.286	2.4	50	0.32	0.407	15.7	7	0.76	10.3	13.6	1.1	8.4	13.6	1.1
15M56	3.833	1.3	1.611	1.8	439	0.097	2.5	27	0.06	0.179	15.7	5	0.77	19.4	25.3	2.1	8.3		
15M56	0.804	1.5	0.491	1.9	279	0.084	2.5	48	0.17	0.220	15.7	12	0.70	13.0	18.5	1.9	10.0		
15M56	0.375	1.5	0.264	2.0	351	0.127	2.4	168	0.48	0.116	15.7	15	0.69	10.5	15.2	1.6	10.3		
15M56	1.652	1.4	0.611	1.8	458	0.411	2.4	308	0.67	0.063	15.7	15	0.70	19.3	27.5	2.7	9.9	21.6	3.3
15M57	4.611	1.3	3.151	1.8	591	0.502	2.4	94	0.16	0.302	15.7	6	0.78	11.7	15.0	1.2	7.9		
15M57	5.701	1.3	3.664	1.8	832	0.273	2.4	62	0.07	0.210	15.7	5	0.94	12.7	13.5	0.6	4.7		
15M57	6.538	1.3	4.883	1.8	1291	0.528	2.4	140	0.11	0.406	15.7	11	0.76	10.8	14.1	1.2	8.3	14.2	0.4
15M58	4.466	1.3	3.068	1.8	93	1.271	2.4	38	0.41	0.994	15.7	3	0.86	11.0	12.8	0.8	6.0		
15M58	11.496	1.3	8.473	1.8	476	1.118	2.4	63	0.13	0.408	15.7	2	0.84	10.9	12.9	0.8	6.3		
15M58	9.012	1.3	5.666	1.8	351	2.050	2.4	127	0.36	0.740	15.7	5	0.85	12.1	14.3	0.9	6.1	13.3	0.5

ID																			
15M59	**1.085**	2.3	**3.221**	1.8	604	**0.270**	2.4	51	0.08	**0.335**	15.7	6	**0.83**	*2.7*	**3.3**	0.3	7.7		
15M59	**1.598**	1.4	**0.692**	1.8	57	**0.333**	2.4	28	0.48	**0.327**	15.7	3	**0.82**	*17.1*	**20.8**	1.4	6.8		
15M59	**3.984**	1.3	**1.734**	1.8	192	**0.316**	2.4	35	0.18	**0.768**	15.7	9	**0.82**	*18.2*	**22.2**	1.5	6.9	**21.5**	1.0
15M63	**3.580**	1.3	**3.002**	1.8	208	**0.298**	2.4	21	0.10	**0.841**	15.7	6	**0.84**	*9.6*	**11.5**	0.7	6.5		
15M63	**3.386**	1.3	**3.137**	1.8	240	**0.151**	2.4	12	0.05	**0.324**	15.7	2	**0.85**	*8.8*	**10.4**	0.7	6.3		
15M63	**0.300**	1.6	**0.265**	2.0	53	**0.235**	2.4	47	0.88	**0.432**	15.7	9	**0.75**	*7.7*	**10.2**	0.9	8.8	**10.7**	0.4
15M64	**0.405**	1.5	**0.463**	1.9	187	**0.218**	2.4	88	0.47	**0.255**	15.7	10	**0.67**	*6.5*	**9.8**	1.1	11.0		
15M64	**0.394**	8.6	**0.402**	1.9	56	**0.088**	2.5	12	0.22	**0.221**	15.7	3	**0.80**	*7.7*	**9.6**	1.8	18.5		
15M64	**2.900**	1.3	**2.730**	1.8	209	**0.868**	2.4	66	0.32	**0.614**	15.7	5	**0.80**	*8.2*	**10.2**	0.7	7.3	**9.9**	0.2
15M65	**1.562**	1.4	**1.528**	1.8	423	**0.286**	2.4	79	0.19	**0.203**	15.7	6	**0.69**	*8.1*	**11.7**	1.2	10.2		
15M65	**0.409**	1.5	**0.409**	1.9	126	**0.233**	2.4	72	0.57	**0.289**	15.7	9	**0.69**	*7.3*	**10.5**	1.1	10.3		
15M65	**1.763**	1.4	**1.604**	1.8	367	**0.488**	2.4	112	0.30	**0.275**	15.7	6	**0.74**	*8.5*	**11.4**	1.0	8.8	**11.2**	0.4
15M67	**2.110**	1.3	**1.573**	1.8	255	**0.459**	2.4	74	0.29	**0.020**	12.0	3	**0.76**	*10.4*	**13.6**	1.1	8.3		
15M67	**3.352**	1.4	**3.589**	1.8	474	**1.392**	2.4	184	0.39	**0.036**	6.2	5	**0.79**	*7.1*	**9.0**	0.7	7.7	**11.3**	3.3
15M68	**1.425**	1.4	**0.987**	1.8	158	**0.310**	2.4	50	0.31	**0.012**	11.5	2	**0.76**	*11.1*	**14.6**	1.2	8.3		
15M68	**1.429**	1.4	**1.058**	1.8	266	**0.693**	2.4	174	0.65	**0.019**	5.0	5	**0.74**	*9.7*	**13.1**	1.2	8.9		
15M68	**4.537**	1.3	**3.743**	1.8	528	**0.444**	2.4	63	0.12	**0.032**	7.6	5	**0.79**	*9.8*	**12.4**	0.9	7.7		
15M68	**1.898**	1.4	**1.492**	1.8	328	**0.165**	2.4	36	0.11	**0.023**	8.0	5	**0.75**	*10.3*	**13.6**	1.2	8.6	**13.4**	0.5
15M71	**0.436**	1.5	**0.351**	1.9	109	**0.093**	2.4	29	0.27	**0.010**	6.4	3	**0.72**	*9.7*	**13.4**	1.3	9.5		
15M71	**0.791**	1.4	**0.683**	1.8	201	**0.145**	2.4	43	0.21	**0.022**	9.3	6	**0.77**	*9.1*	**11.9**	1.0	8.2		
15M71	**2.201**	1.4	**1.583**	1.8	505	**0.435**	2.4	139	0.27	**0.014**	8.1	5	**0.73**	*10.8*	**14.9**	1.4	9.2	**13.4**	0.9
16M76	**5.601**	1.0	**2.092**	1.8	286	**1.355**	2.4	185	0.65	**0.181**	3.9	25	**0.81**	*19.2*	**23.6**	1.6	6.8		
16M76	**7.012**	1.1	**3.140**	1.8	254	**0.476**	2.4	38	0.15	**0.047**	3.8	4	**0.83**	*17.8*	**21.5**	1.4	6.5	**22.6**	1.5
16M87	**4.814**	1.1	**2.328**	1.8	167	**1.937**	2.4	139	0.83	**0.050**	11.9	4	**0.84**	*14.3*	**17.0**	1.0	6.0		
16M87	**3.617**	1.1	**2.371**	1.8	432	**0.564**	2.4	103	0.24	**0.024**	8.6	4	**0.75**	*12.0*	**15.9**	1.3	8.4		
16M87	**2.452**	1.1	**1.126**	1.8	672	**0.368**	2.4	220	0.33	**0.014**	11.1	8	**0.70**	*16.7*	**23.9**	2.4	9.8	**18.9**	2.5
16M89	**3.686**	1.0	**2.335**	1.8	504	**0.117**	2.4	25	0.05	**0.012**	5.0	3	**0.80**	*12.9*	**16.1**	1.2	7.2		
16M89	**5.710**	1.1	**3.246**	1.8	754	**0.678**	2.4	158	0.21	**0.028**	3.3	7	**0.80**	*13.9*	**17.4**	1.3	7.2	**16.8**	0.9
16M90	**4.474**	1.1	**2.487**	1.8	462	**1.597**	2.4	297	0.64	**0.027**	9.5	5	**0.75**	*12.9*	**17.3**	1.5	8.4		
16M90	**3.637**	1.0	**2.044**	1.8	406	**0.128**	2.4	25	0.06	**0.009**	15.8	2	**0.71**	*14.5*	**20.4**	2.0	9.6	**18.9**	2.2
16M91	**1.653**	1.1	**1.057**	1.8	104	**0.506**	2.4	50	0.48	**0.041**	5.9	4	**0.80**	*11.6*	**14.5**	1.0	7.1		
16M91	**1.000**	1.2	**0.428**	1.9	129	**0.507**	2.4	152	1.18	**0.011**	6.7	3	**0.75**	*15.1*	**20.2**	1.7	8.5		
16M91	**6.736**	1.0	**3.150**	1.8	121	**2.696**	2.4	103	0.86	**0.064**	8.9	2	**0.88**	*14.7*	**16.7**	0.8	5.0	**17.1**	1.7
16M92	**8.192**	1.1	**3.063**	1.8	221	**0.693**	2.4	50	0.23	**0.042**	6.0	3	**0.83**	*21.0*	**25.2**	1.6	6.4		
16M92	**10.274**	1.0	**3.800**	1.8	260	**0.316**	2.4	22	0.08	**0.025**	5.2	2	**0.82**	*21.9*	**26.7**	1.8	6.6		
16M92	**2.437**	1.1	**1.052**	1.8	138	**0.200**	2.4	26	0.19	**0.023**	7.3	3	**0.77**	*18.3*	**23.9**	1.9	8.0	**25.3**	0.8
16M93	**2.434**	1.1	**1.269**	1.8	286	**0.095**	2.5	21	0.08	**0.007**	11.3	2	**0.76**	*15.6*	**20.4**	1.7	8.2		
16M93	**5.806**	1.0	**2.439**	1.8	338	**0.195**	2.4	27	0.08	**0.024**	9.8	3	**0.80**	*19.3*	**24.2**	1.8	7.2		
16M93	**3.011**	1.1	**1.550**	1.8	271	**0.136**	2.4	24	0.09	**0.015**	14.6	3	**0.79**	*15.8*	**20.1**	1.5	7.6	**21.6**	1.3
16M95	**0.986**	1.2	**0.617**	3.5		**0.389**	3.8		0.63				**0.62**	11.5	**18.5**	0.4			
16M95	**2.301**	1.2	**1.254**	5.0		**0.463**	4.8		0.37				**0.95**	14.0	**14.7**	0.7			
16M95	**0.233**	1.3	**0.142**	7.4		**0.107**	5.6		0.75				**0.63**	11.6	**18.4**	0.7		**17.2**	1.2
16M98	**2.765**	1.1	**1.292**	1.8	397	**0.334**	2.4	103	0.26	**0.020**	4.8	6	**0.73**	*16.7*	**22.9**	2.1	9.1		
16M98	**5.110**	1.0	**3.078**	1.8	961	**0.384**	2.4	120	0.12	**0.032**	5.4	10	**0.93**	*13.3*	**14.4**	0.6	4.5	**18.2**	0.3
17M104	**3.488**	1.2	**2.993**	3.2		**0.884**	3.9		0.30				**0.71**	9.0	**12.7**	0.3			
17M104	**1.480**	1.2	**1.021**	3.1		**0.931**	3.5		0.91				**0.76**	9.9	**13.0**	0.3			
17M104	**1.078**	1.2	**0.779**	5.5		**0.291**	4.3		0.37				**0.71**	10.6	**14.9**	0.5		**13.5**	0.7

Curriculum Vitae

Name: Nils-Peter Nilius

Geburtstag: 28.05.1986

Geburtsort: Köln

Staatsangehörigkeit: Deutsch

06/2006	**Abitur**
07/2006 - 04/2007	**Zivildienst**
	Rotes Kreuz Bonn
10/2007 - 09/2008	**Bachelor of Science:** Georesource Management
	RWTH Aachen, Deutschland
10/2008 - 09/2011	**Bachelor of Science**: Geowissenschaften
	Rheinische Friedrich-Wilhelms Universität Bonn, Deutschland
07/2012 - 10/2012	**Post Graduated Studies**: Arctic Geoscience
	UNIS (University Center in Svalbard), Spitzbergen, Norwegen
09/2013	**Doctorate School for Zircon Geochronology**
	Universität Pavia, Italien
10/2011 - 12/2014	**Master of Science: Geowissenschaften**
	Rheinische Friedrich-Wilhelms Universität Bonn, Deutschland
09/2015 – 03/2019	**Wissenschaftlicher Mitarbeiter und Promotionsstudent**
	Institut für Geologie,Leibniz Universität Hannover, Deutschland

Publications

Peer-reviewed papers

Nilius, **N.P.,** Glotzbach C., Wölfler A., Hampel A., Dunkl I., Akal C., Heineke C., Hetzel R. (in prep.): Exhumation patterns in a bivergent core-complex: the central Menderes Massif (western Turkey). Tectonophysics.

Heineke, C., Hetzel, R., **Nilius, N.P**., Zwingmann, H., Todd, A., Mulch, A., Wölfler, A., Glotzbach, C., Akal, C., Dunkl, I., Raven, M., Hampel, A. (subm.). Detachment faulting in a bivergent core complex constrained by fault gouge dating and low-temperature thermochronology. Journal of Structural Geology.

Heineke, C., Hetzel, R., **Nilius, N.P.,** Glotzbach, C., Akal, C., Christl, M., Hampel, A. (in review). Spatial patterns of erosion and landscape evolution in the central Menderes Massif (Western Turkey) revealed by cosmogenic 10Be. GSA Geosphere.

Nilius,N.P., Glotzbach C., Wölfler A., Hampel A., Dunkl I., Akal C., Heineke C. & Hetzel R. 2019: Exhumation history of the Aydın range and the role of the Büyük Menderes detachment system during bivergent extension of the central Menderes Massif, western Turkey. Journal of the Geological Society London. DOI: 10.1144/jgs2018-162

Wölfler, A., Glotzbach, C., Heineke, C., **Nilius, N.P**., Hetzel, R., Hampel, A., Akal, C., Dunkl, I., Christl, M., 2017: Late Cenozoic cooling history of the central Menderes Massif: timing of the Büyük Menderes detachment and the relative contribution of normal faulting and erosion to rock exhumation. Tectonophysics 717, 585-598, doi:10.1016/j.tecto.1017.07.004

Nilius, N.P., Froitzheim, N., Nagel, TJ., Tomaschek, F & Heuser, A., 2016: The Schwarzhorn Amphibolite (Eastern Rätikon, Austria): an Early Cambrian intrusion in the Lower Austroalpine basement. Geologica Carpathica 67; 2; 121-132; doi: 10.1515/geoca-2016-00

Conference contributions

N.P. Nilius, Glotzbach C., Wölfler A., Hampel A., Dunkl I., Akal C., Heineke C., & Hetzel R., 2019: Exhumation patterns in a bivergent metamorphic core complex: The central Menderes Massif (western Turkey). GeoMünster 2019, Münster

N.P. Nilius, Glotzbach C., Wölfler A., Dunkl I., Akal C., Heineke C., Hetzel R., & Hampel A., 2018: Exhumation history of the central Menderes Massif (western Turkey), constrained by low-temperature Thermochronology. Thermo 2018, Quedlinburg

N.P. Nilius, Glotzbach C., Wölfler A., Dunkl I., Akal C., Heineke C., Hetzel R., & Hampel A., 2018: Thermochronological constrains on the symmetric exhumation of the Menderes Massif (western Turkey) along the Gediz and Büyük Menderes detachments. GeoBonn 2018, Bonn

N.P. Nilius, Glotzbach C., Wölfler A., Dunkl I., Akal C., Heineke C., Hetzel R., & Hampel A., 2018: Structural and kinematic constrains on the exhumation of the central Menderes Massif along the Büyük Menderes detachment, western Turkey, EGU General Assembly, Wien, Österreich

N.P. Nilius, Glotzbach C., Wölfler A., Dunkl I., Akal C., Heineke C., Hetzel R., & Hampel A., 2018: Structural and kinematic constrains on the exhumation of the central Menderes Massif along the Büyük Menderes detachment, western Turkey, TSK17, Jena

Nilius NP., Wölfler A., Heineke C., Glotzbach C., Hetzel R., Hampel A., Akal C. & Dunkl I., 2017: Late Cenozoic cooling history of the central Menderes Massif and the contribution of erosion to rock exhumation during active continental extension. EGU General Assembly 2017, Wien, Österreich

Nilius NP., Wölfler A., Glotzbach C., Heineke C., Hetzel R., Hampel A., Akal C. & Dunkl I., 2016: The role of the Büyük Menderes Detachment during Late Cenozoic exhumation of the central Menderes Massif, SW Turkey. Thermo 2016, Maresias, Brasilien.

Nilius NP., Froitzheim N., Nagel T., Tomaschek F., & Heuser A., 2016: From Early Cambrian arc magmatism to Jurassic rifting: Tectonic evolution of the Lower Austroalpine Schwarzhorn Amphibolite (Eastern Rätikon, Austria). GeoTirol 2016, Innsbruck, Austria

Nilius NP, Froitzheim N, Nagel T, Tomaschek F & A Heuser (2014): The Schwarzhorn Amphibolite (Eastern Rätikon, Austria): an Early Cambrian intrusion in the Lower Austroalpine basement. TSK 15, Potsdam